Department of Chemistry

The Photochemistry of Functionalised Rhenium (I) Tricarbonyl Complexes

Nurshadrina Akabar

This thesis is presented for the Degree of
Doctor of Philosophy
of
Curtin University

September 2017

Author's Declaration

To the best of my knowledge and belief this thesis contains no material previously published by any other person except where due acknowledgement has been made.

This thesis contains no material which has been accepted for the award of any other degree or diploma in any university.

[Nurshadrina Akabar]

Date: 13/09/2017

Abstract

This research is centred on studying the fundamental photochemistry of neutral and cationic rhenium(I)-NHC complexes with formula $[Re(\mathbf{N^C})(CO)_3(L)]^{+/0}$, where **N^C** represents a bidentate *N*-heterocyclic carbene ligand and L resembles the ancillary ligand (various pyridine substituents). The basis of this research is to study the potential effect of electron transfer on the photophysics of these rhenium(I) complexes. The presence of amino acids was expected to induce electron transfer processes by providing a "redox-active" group such as tryptophan, as well as serve a purpose for biological applications. The photophysical and photochemical investigation will be carried out on these complexes to enhance an understanding of their functionalities dependent on their structure. Specifically, the photochemistry of cationic rhenium(I)-NHC complexes were studied and their photoproducts identified, based on literature assignments and proposed reaction mechanism.

In addition, the synthesis, structural and photophysical properties of rhenium(I) **phen** tetrazolato complexes coordinated to various amino acid species were explored. The group of complexes are based on the general formula $[Re(\mathbf{phen})(CO)_3(L)]$, where **phen** is 1,10-phenanothroline and L represents a tetrazolato moiety coordinated to various amino acids, comparing *meta* and *para* substituents. In addition, protonation and methylation of the tetrazole ring were carried out and their corresponding photophysical effects were explored. Furthermore, biological studies were initiated on select rhenium(I) complexes to determine whether they were viable in cells.

Acknowledgements

Before listing those I need to thank, I would like to say that no amount of thesaurus-based adjectives and eloquent words can express my gratitude towards the following people who have been a part of this journey! ☺

Firstly to Assoc. Prof. Massimiliano (Max) Massi, for his outstanding supervision and enthusiasm, for sharing his enlightening ideas and knowledge, as well as the constructive feedback during meetings. He makes sure that his students strive towards the best of their abilities. I am grateful to have worked on such a challenging and interesting project. I have learnt a lot about the field of photophysics and photochemistry. Also, thanks for giving me the opportunity to spend a period abroad working in Montreal (Canada).

This leads me to thank Prof. Garry Hanan at UdeM for kindly welcoming me into his lab, as well as sharing his wisdom and innovative ideas. I need to thank Jingwei Luo for helping me settle within my first days in Montreal and for the ESI-MS data. Thanks to Mihaela Cibian, Mathieu Leblanc, Baptiste Laramée-Milette, Amlan Pal for being such a friendly group and motivating me to work hard. I also have to thank Elena Nadezhina for the elemental analysis, as well as Prof Frank Schaper, Dr Michel Simard and Dr Thierry Maris for showing me how the XRD works.

For the biological component of this thesis, I have to thank Dr Delia Nelson for her support, input of ideas and timely feedback. Thanks to Dr Vishal Chaturvendi for analysing my samples and teaching me the ways of cell work. Also, thanks to Dr Connie Jackaman for the microscopy work and training, as well as Jeanne Le Masurier for the flow cytometry training.

I am grateful to Dr Peter V. Simpson for his constant guidance in and outside laboratory, for sharing his wealthy knowledge with peasants such as myself, proof reading my thesis and assisting in every way possible with such patience.

Many thanks go to Ching for his NMR expertise and general laboratory assistance. I would also like to thank Chappy for his technical assistance with the UV-VIS spectrometer. Thanks to Thomas Rodemann at the Central Science Laboratory

(University of Tasmania) and Rob Herman (Curtin University) for running the samples for elemental analysis. Also thanks to Dr Brian Skelton from UWA for the crystallography analysis.

Special thanks to Danica for sharing this amazing experience since undergraduate days and for keeping me company in the office as well as sharing her delicious baked goods. I would also like to shout out to Mel for being such an inspiration and a good role model, Jamila (carbene buddy) for passing on her carbene knowledge and photochemistry skills, Karen for sharing Chemistry puns and sugary cakes, Brodie for helping me with logistics of moving to Canada. I also have to acknowledge the past and present members of the Empire group (including Rene, Phil, Dan, Rhys, Calum, Chiara, Laura, Anna and Stouty); they are quite an ecletic lot. I have had the pleasure to work with such hard working people. Also, to the rest of the Curtin Chemistry group (Erin, Eva, Ben, Gemma and Shifaza) for lunch and tea breaks that kept me both sane and entertained.

Most of all, I would like to express my dearest gratitude to my parents for believing in me and raising me to be the person I am today. They have always been there for me, even though I have been a phantom. Thanks for keeping me fed and supporting me in every way possible. I am also very grateful for the rest of my family (both Salbie and Sukaimi clan) for their tough love and teasing about my weight which resulted in their contribution to feeding me; both old and new friends, especially the 'Friendship 7' crew (you know who you are) for taking my mind off work with crazy shenanigans, and the Bandung crew for sharing some great memories travelling during my break from thesis writing. Thank you all for celebrating my success with me and for putting up with my mood swings, occasional drifting and weekends working (especially during the final year of PhD). I have been very blessed to have such supporting and encouraging people who are proud of my achievements. Thanks for trying to understand the ways of science/academic life.

Dedication

I would like to dedicate this thesis to my family, especially my younger siblings. You can achieve anything with hard work, perseverance, patience and an exceptional attitude.

“Happiness can be found, even in the darkest of times, if one only remembers to turn on the light.”

[Albus Dumbledore]

“Freeze pump thought” – when you think about life whilst waiting for the solution to thaw out.

[Fellow PhD colleague]

Table of Contents

Symbols and Abbreviations

Å	angstroms
δ	NMR chemical shift in ppm
τ	emission lifetime
Φ	quantum yield
λ	wavelength
λ_{em}	excitation wavelength
λ_{ex}	emission wavelength
ε	molar absorptivity, extinction coefficient
mmol	millimole
nm	nanometres
ppm	parts per million
ns	nanoseconds
μs	microseconds
AgOTf	silver triflate (trifluoromethanesulfonate)
app.	apparent
a.u.	arbitrary units
BODIPY	boron-dipyrromethene (also 4,4-difluoro-4-bora-3a,4a-diaza-*s*-indacene)
bipy	2,2′-bipyridine
br.	broad

ca.	circa/approximately
CSA	camphor-sulphonic acid
d	doublet (NMR signal splitting)
DCM	dichloromethane
dec.	decomposition
DMAP	4-dimethylaminopyridine
DMF	dimethylformamide
DMSO	dimethylsulfoxide
eT	electron transfer
ET	energy transfer
EtOAc	ethyl acetate
eq.	equivalents
ES	excited state
GS	ground state
Gly	glycine
HOMO	highest occupied molecular orbital
IC	internal conversion
IL	intraligand
IR	infrared
ISC	intersystem crossing
J	coupling constant in Hz

K	Kelvin
k_{nr}	non-radiative decay rate constant
KPF_6	potassium hexafluorophosphate
k_r	radiative decay rate constant
K^tBuO	potassium *tert*-butoxide
LLCT	ligand-to-ligand charge transfer
LUMO	lowest unoccupied molecular orbital
m	multiplet (NMR), medium (IR)
m.p.	melting point
MC	metal-centred
MLCT	metal-to-ligand charge transfer
MLLCT	metal-to-ligand-to-ligand charge transfer
MeCN	acetonitrile
MeOH	methanol
MeOTf	methyl triflate
NHC	*N*-heterocyclic carbene
NMR	nuclear magnetic resonance
PCET	Protoncoupled electron transfer
PeT	photoinduced electron transfer
Phe	phenylalanine
phen	1,10-phenanthroline

Py	pyridine
r.t.	room temperature
s	singlet (NMR signal splitting), strong (IR)
sh	shoulder
t	triplet (NMR signal splitting)
TEA	triethylamine
TFA	trifluroacetic acid
TfOH	triflic acid
THF	tetrahydrofuran
Trp	tryptophan
UV	ultraviolet
VIS	visible
w	weak (IR)

Commonly used Abbreviations of Compounds

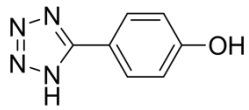

1 **Tz**HPh4OH

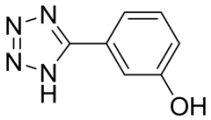

2 **Tz**HPh3OH

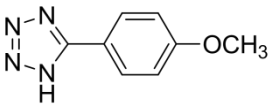

3 **Tz**HPh4OMe

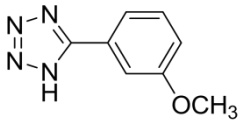

4 **Tz**HPh3OMe

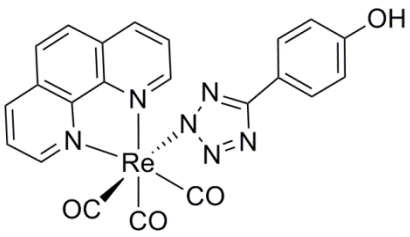

5 [Re(**phen**)$(CO)_3$(**Tz**Ph4OH)]

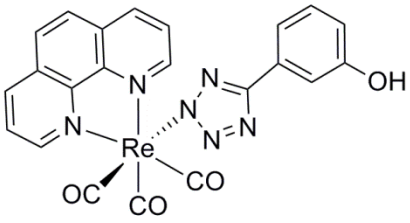

6 [Re(**phen**)$(CO)_3$(**Tz**Ph3OH)]

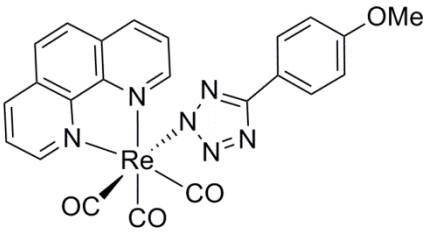

7 [Re(**phen**)$(CO)_3$(**Tz**Ph4OMe)]

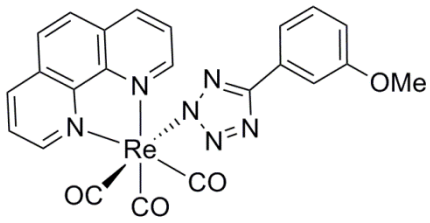

[Re(**phen**)$(CO)_3$(**Tz**Ph3OMe)]

8

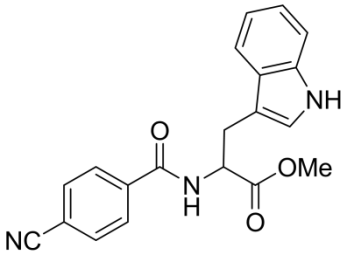

NCPh**Trp**Me

9

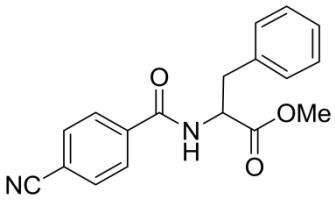

NCPh**Phe**Me

10

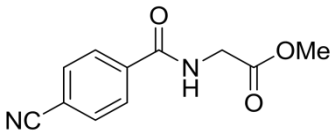

NCPh**Gly**Me

11

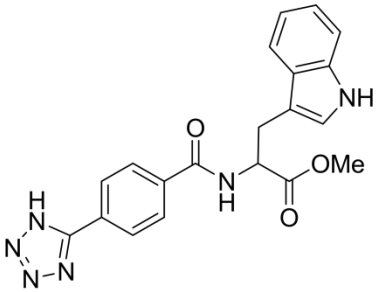

TzHPh**Trp**Me

12

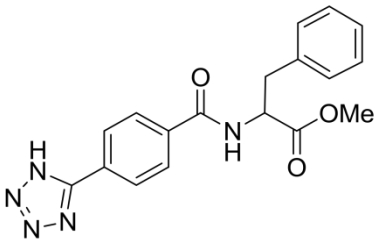

TzHPh**Phe**Me

13

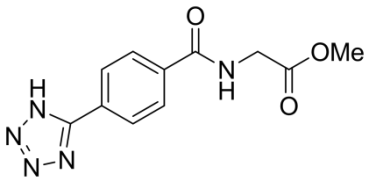

14

TzHPh**Gly**Me

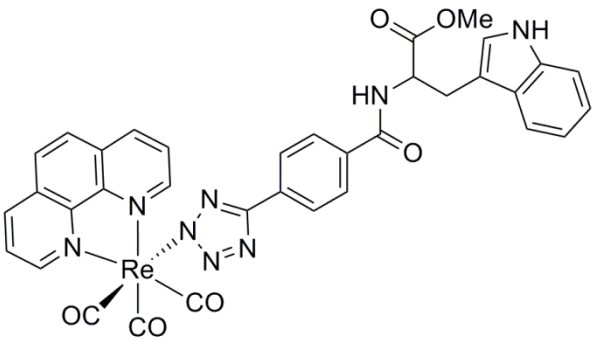

15Trp

[Re(**phen**)$(CO)_3$(**Tz**Ph**Trp**Me)]

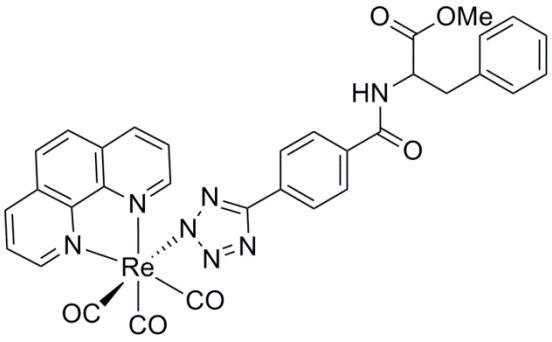

15Phe

[Re(**phen**)$(CO)_3$(**Tz**Ph**Phe**Me)]

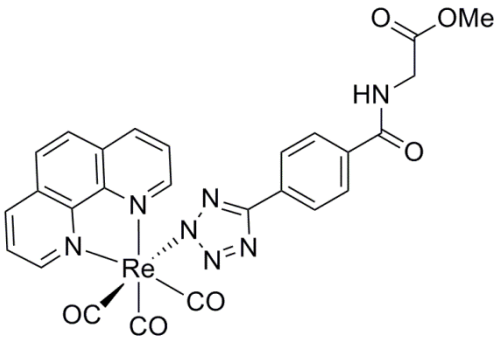

15Gly

[Re(**phen**)$(CO)_3$(**Tz**Ph**Gly**Me)]

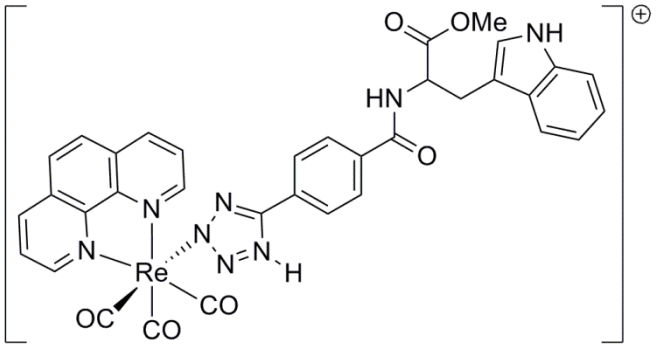

[Re(**phen**)(CO)$_3$(**Tz**HPh**Trp**Me)]PF$_6$

16Trp

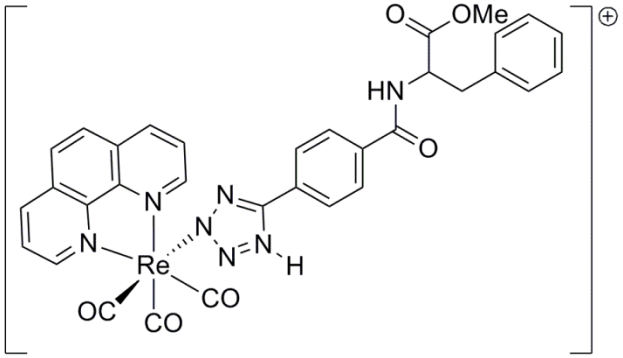

[Re(**phen**)(CO)$_3$(**Tz**HPh**Phe**Me)]PF$_6$

16Phe

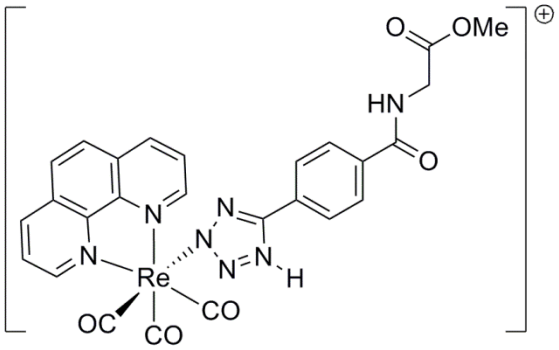

[Re(**phen**)(CO)$_3$(**Tz**HPh**Gly**Me)]PF$_6$

16Gly

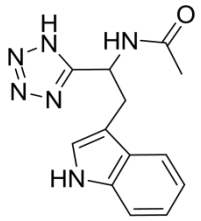

TzH**Trp**

17

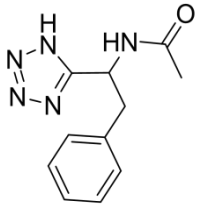

TzH**Phe**

18

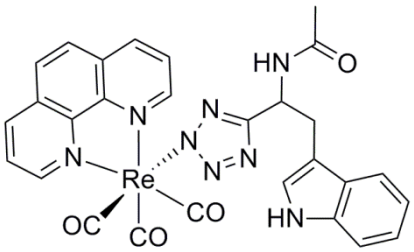

19Trp [Re(**phen**)$(CO)_3$(**TzTrp**)]

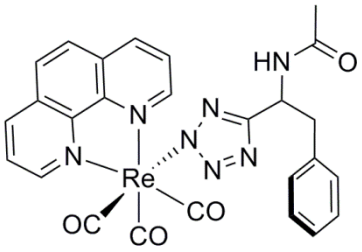

19Phe [Re(**phen**)$(CO)_3$(**TzPhe**)]

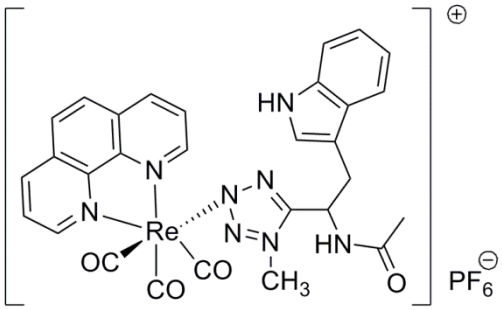

20Trp [Re(**phen**)$(CO)_3$(Me**TzTrp**)]PF_6

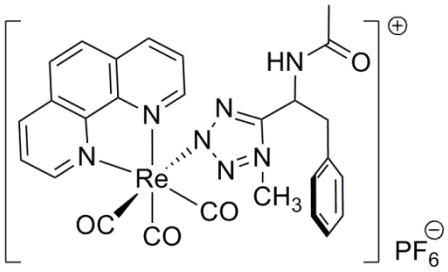

20Phe [Re(**phen**)$(CO)_3$(Me**TzPhe**)]PF_6

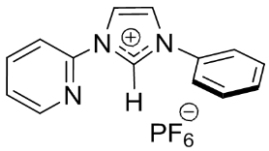

21 [**PyIm**H**Ph**][PF_6]

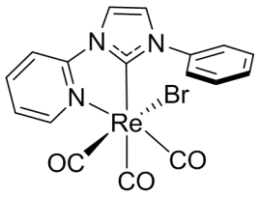

22 [Re(**PyImPh**)$(CO)_3$Br]

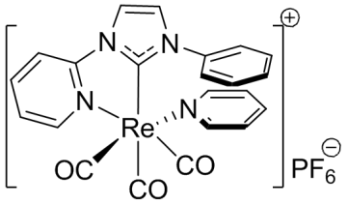

23 [Re(**PyImPh**)$(CO)_3$(Py)]PF_6

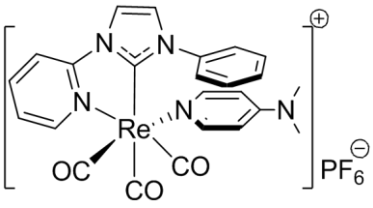

24 [Re(**PyImPh**)$(CO)_3$(DMAP)]PF_6

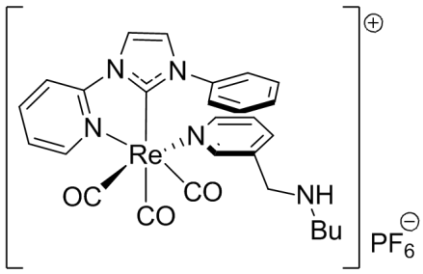

25 [Re(**PyImPh**)$(CO)_3$(PyNHBu)]PF_6

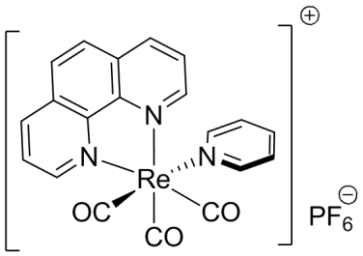

26 [Re(**phen**)$(CO)_3$(Py)]PF_6

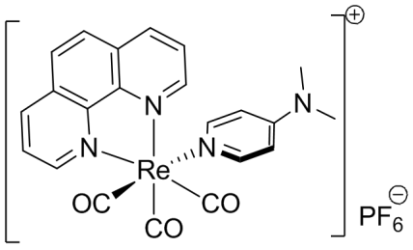

27 [Re(**phen**)$(CO)_3$(DMAP)]PF_6

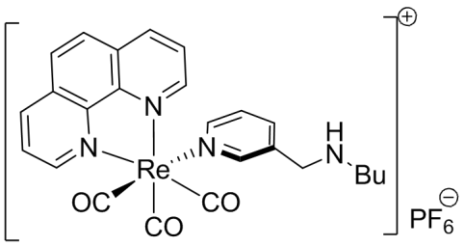

28 [Re(**phen**)$(CO)_3$(PyNHBu)]PF_6

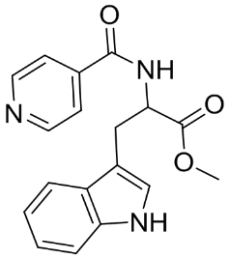

29 Py**Trp**

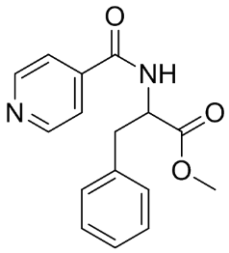

30 Py**Phe**

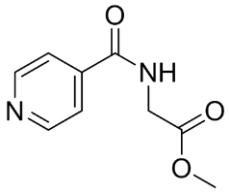

31 Py**Gly**

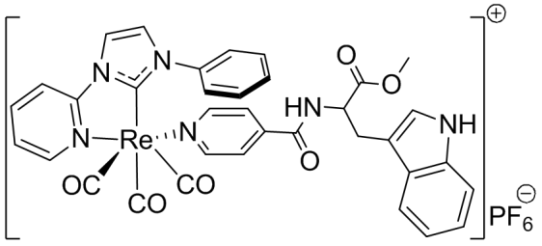

32 [Re(**PyImPh**)(CO)$_3$(Py**Trp**)]PF$_6$

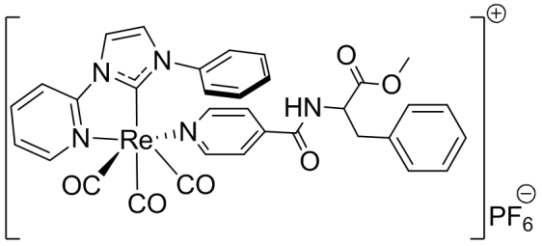

33 [Re(**PyImPh**)(CO)$_3$(Py**Phe**)]PF$_6$

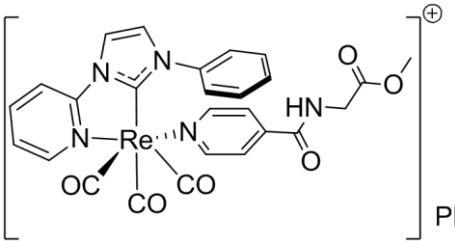

34 [Re(**PyImPh**)(CO)$_3$(Py**Gly**)]PF$_6$

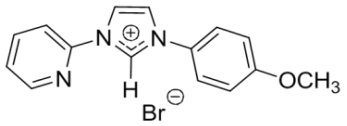

35 [**PyIm**H**Ph**OMe][Br]

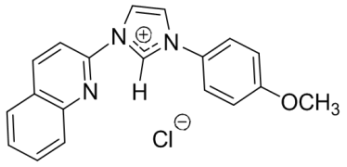

36 [**QuIm**H**Ph**OMe][Cl]

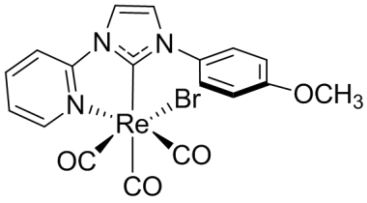

37Br [Re(**PyImPh**OMe)$(CO)_3$Br]

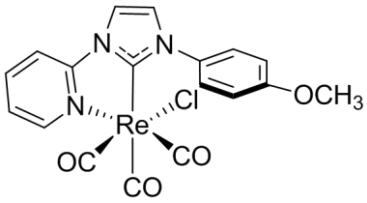

37Cl [Re(**PyImPh**OMe)$(CO)_3$Cl]

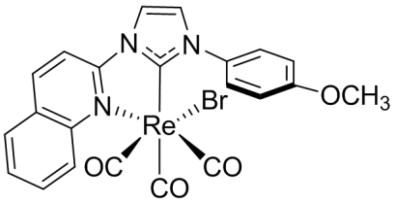

38Br [Re(**QuImPh**OMe)$(CO)_3$Br]

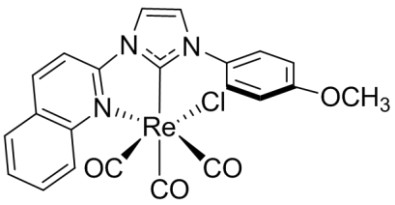

38Cl [Re(**QuImPh**OMe)$(CO)_3$Cl]

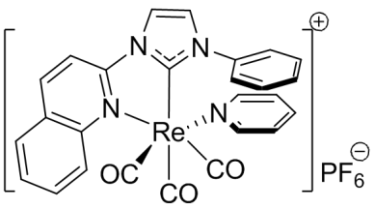

39 [Re(**QuImPh**)$(CO)_3$(Py)]PF_6

Chapter 1

Introduction

1.1 Luminescent Transition Metal Complexes

Transition metal complexes containing Ru(II), Re(I), Ir(III), Pt(II) and Cu(I) have attracted a great deal of attention owing to their phosphorescent nature. The major focus of research into these types of complexes also stems from their wide array of applications in areas of materials (as light emitting devices,[1–4] photovoltaic solar cells[5–7]) and biological sciences (optical imaging[8] and cellular labelling,[9–19] ion and gas sensors,[20–24] as well as phototherapeutic agents).[25–33]

The photophysical properties of the aforementioned transition metal complexes are determined predominantly by their lowest energy excited states.[34,35] These are dependent on the structure of the complex, i.e. based on the presence of different metal centres and nature of the ligand(s).[36,37] **Figure 1.1** illustrates a few different examples of luminescent complexes possessing varying properties.

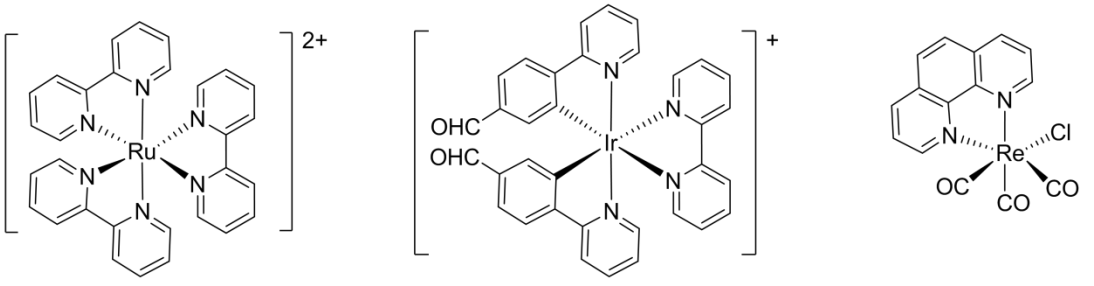

40
λ_{em} = 605 nm
τ = 0.860 μs
QY = 0.062 (MeCN)

41
λ_{em} = 534, 565 (sh) nm
τ = 4.71 μs
QY = 0.27 (MeCN)

42
λ_{em} = 602 nm
τ = 0.173 μs
QY = 0.036 (DCM)

Figure 1.1 Examples of luminescent complexes Ru(II),[38] Ir(III)[39] and Re(I).[40–42]

Polypyridine ruthenium(II) complexes with the general formula $[Ru(\mathbf{N^N})_3]^{2+}$, where **N^N** is a bidentate ligand such as 2,2′-bipyridine (**bipy**), 1,10-phenanthroline (**phen**), or other substituted derivatives, have been most frequently studied and used (as photosensitizers). This is due to the fact that they possess properties such as strong visible absorption, high photochemical stability, efficient luminescence and relatively long-lived excited states.[34,38,43] One of the earliest examples from 1982 is a ruthenium complex containing three bidentate **bipy** ligands, i.e. $[Ru(\mathbf{bipy})_3]^{2+}$ **(40)**, which possesses a red emission (originating from metal-to-ligand charge transfer) at 605 nm and an excited state lifetime at 860 ns in acetonitrile solution. Additionally, the emitting-state energies and excited state redox properties of the photosensitizers can be easily affected by any modifications made to the metal, coordinating ligands and/or solvent.

On the other hand, iridium(III) complexes with the general formula $[Ir(\mathbf{C^N})_2(\mathbf{N^N})]$, where **C^N** is a monoanionic cyclometallating ligand and **N^N** a neutral diimine ligand, are commonly known for their application as light-emitting diodes as they are highly phosphorescent.[44–46] Only recently, these iridium type complexes have increased interest as luminescent imaging agents.[47–50] These complexes possess highly tuneable excitation and emission maxima as well as long lifetimes. The complex $[Ir(pba)_2(\mathbf{bipy})]$ **(41)** where pba is 4-(2-pyridyl)benzaldehyde, displays intense emission at 534 nm with a shoulder band at 565 nm and a long lifetime of 4.71 µs. Similar properties have been shown in other reported iridium complexes.[44,50]

Diimine rhenium(I) tricarbonyl complexes have also been extensively studied since the exploitation of their photophysical properties by Wrighton and Morse in 1974.[41] The authors discovered that $[Re(\mathbf{phen})(CO)_3Cl]$ **(42)** displays room temperature photoluminescence emission at 602 nm (originating from metal-to-ligand charge transfer) and an excited state lifetime decay at 173 ns. Furthermore, the authors discovered that varying the substituents on the **phen** will result in varying the photoluminescence emission properties. The substituent effect on the chelating diimine ligand and ancillary ligand will be discussed further in detail amongst various examples of rhenium(I) complexes which make up the majority of this thesis.

1.1.1 Photophysical Properties of d^6 Metal Complexes

The photophysical properties of these complexes can be determined by examining the electronic transitions that take place. The possible electronic transitions that can occur for low spin d^6 metal complexes are represented in the molecular orbital (MO) diagram illustrated in **Figure 1.2**.

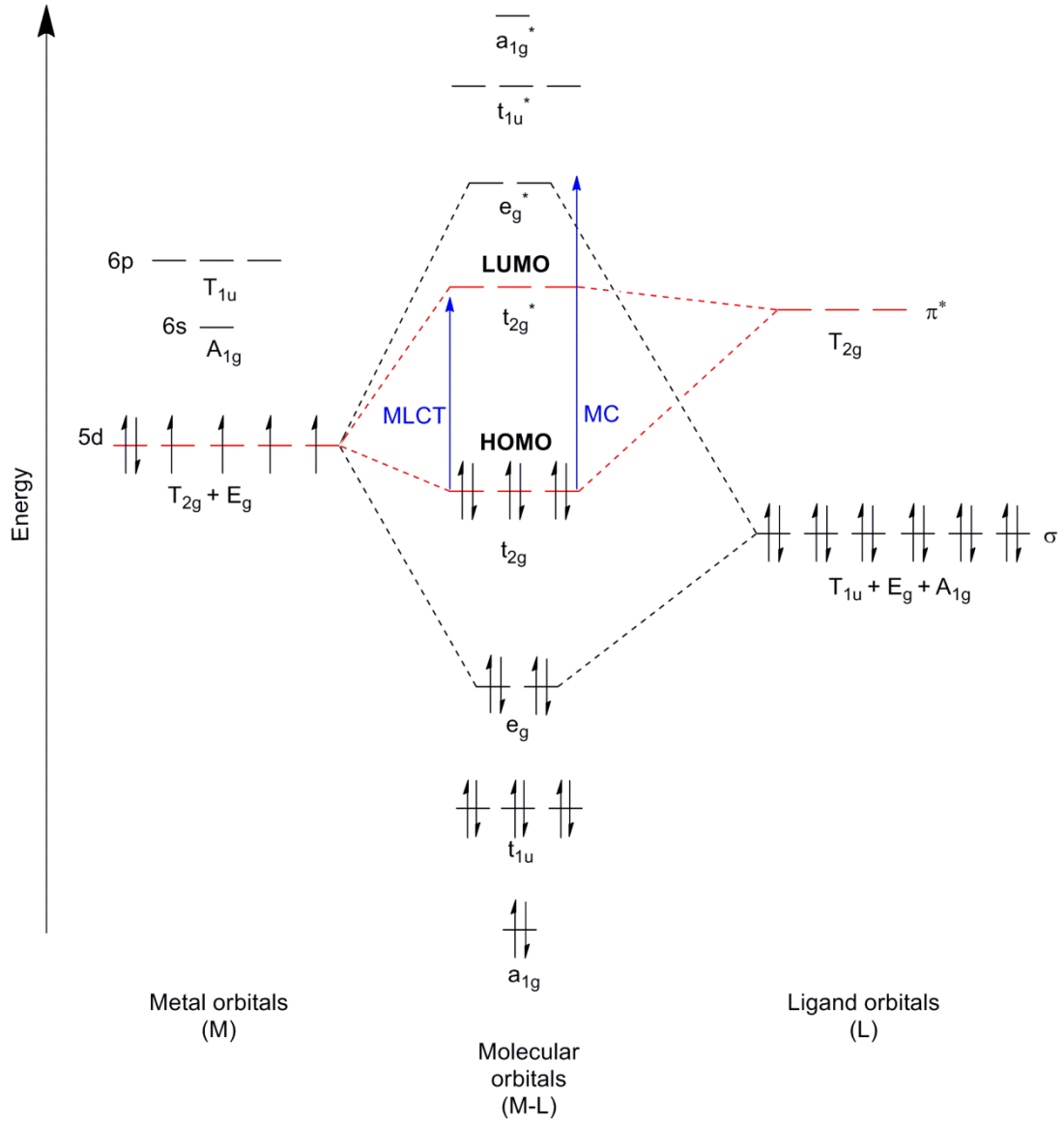

Figure 1.2 MO diagram for d^6 transition metal complexes, coordinated to equivalent π-accepting ligands. Only the T_{2g} orbital formation is considered for simplicity (depicted with red dashed lines). MLCT and MC transitions are depicted in blue.

Figure 1.2 is representative of complexes with second and third row transition metals combined with π* accepting ligands, which experience a strong crystal field. For a complex with an octahedral symmetry, the metal centre contributes to the 5d, 6s and 6p for bonding. These orbitals can be categorised according to their symmetry

in the octahedral point group. The 5d orbitals are represented by symmetry labels T_{2g} and E_g, the 6s orbital is represented as A_{1g} and the 6p orbitals represented as T_{1u}, as shown in **Figure 1.2**.

For simplicity, the ligands surrounding the metal are assumed to be equivalent and only the π* ligand orbitals of T_{2g} symmetry are shown forming molecular orbitals with the metal. **Figure 1.2** shows the bonding orbitals to be completely filled and the anti-bonding orbitals as empty, illustrating the stability of low spin d^6 metal complexes. The highest occupied molecular orbital (HOMO, t_{2g}) is mainly of metal character and the lowest unoccupied molecular orbital (LUMO, t_{2g}*) is mainly of ligand character. The e_g* orbitals have a higher energy than the t_{2g}* orbitals and the relative position of t_{2g} is determined by the presence and specific energies of π* orbitals of ligands.

1.1.1.1 Types of Electronic Transitions of d^6 Metal Complexes

The absorption of a photon can prompt different types of transitions within a metal complex. The different types of electronic transitions that can exist are associated with the arrangement of electrons (relative to the MO diagram presented in **Figure 1.2**) and are described below:[36,37,51,52]

i) Charge transfer (CT) processes arise from the transfer of electrons between orbitals of metal character and orbitals of ligand character. CT transitions can be metal-to-ligand charge transfer (MLCT), ligand-to-ligand charge transfer (LLCT) or ligand-to-metal charge transfer (LMCT).

   a. MLCT states can be described simply as a transfer of an electron from the metal to the ligand. In particular, the transition of an electron from metal-based *d* orbitals (HOMO) to ligand-based antibonding π* orbitals (LUMO). These states are observed when the metal is easily oxidised and the ligand is easily reduced. Generally the ligands would have low-lying π* acceptor orbitals (e.g. CN^-, CO, **phen**, SCN^-).

   b. LLCT states occur if the surrounding ligands are not all equivalent. This type of transition occurs when an electron from the occupied π

orbitals of a ligand is transferred to the π* orbital of a different ligand. This transition is not illustrated in **Figure 1.2**. Furthermore, it is possible that the LLCT can mix with the MLCT to form a MLLCT excited state.

c. LMCT states occur when the metal is electron deficient (making them easily reduced) and the complex contains electron rich ligands such as Br^-, I^- (making them easily oxidised).

ii) Intraligand (IL) or ligand-centred (LC) transitions, also known as π-π* transitions, originate from the transfer of an electron from π-orbital based on the ligand to an empty π* orbital based on the ligands themselves. Typically this type of transition occurs for ligands with extended π-systems including aromatic ligands (such as pyridine, **bipy**, **phen**).

iii) Lastly, ligand field (LF) or metal-centred (MC) "d-d" states are those that appear to lie at rather high energies in the complexes, due to the electron-electron repulsion occurring on the orbitals.[43] This type of transition occurs when an electron is promoted from the t_{2g} orbital to an empty e_g*.

The probability of an electronic transition to occur is directed by selection rules, which are associated with spin multiplicity and symmetry of the ground state and excited state. Based on the selection rules, a transition can be considered as forbidden or allowed. The spin conservation rule states that transitions are only allowed between states of the same spin multiplicity. Therefore a singlet (S = 0) to singlet transition is allowed, whereas a singlet cannot undergo transition to a triplet (S = 1). The rule is summarised as $\Delta S = 0$ for spin-allowed transitions.[53] An electronic transition is allowed when there is a change in parity between ground and excited states, which is the basis of the Laporte selection rule. This selection rule applies to centrosymmetric molecules. This restriction can be relaxed by a "vibronic coupling" process that involves non-symmetric vibrations of the molecule, which remove the centre of inversion. As a result of this process, forbidden transitions may be observed, for example the d-d transition state occurring in octahedral metal complexes, as mentioned earlier.

Upon absorption of a photon, a number of vibrational excited states (of the electronically excited state) will be populated. The population of many vibronic levels is directly related to the Franck-Condon principle and is based on the Born-Oppenheimer approximation, which states that electronic transitions are very rapid compared to nuclear motions, due to the light weight of electrons in relation to the large and heavy nuclei. According to the Franck-Condon principle, when a molecule undergoes an electronic transition, the nuclear configuration of the molecule does not involve a significant change. Therefore vertical electronic transitions will be favoured when there is a minimal change in the position of the nuclei.[54] Typically, a molecule will reside in the upper vibrational level of an electronically excited state and then relax to the lowest vibrational level of the excited state.[37] This radiationless process is known as vibrational relaxation (VR) which occurs between vibrational levels of the same excited state. On the other hand, the non-radiative process that occurs between different electronic levels is known as internal conversion (IC). **Figure 1.3** illustrates the Franck-Condon principle, where the electronic transitions are indicated by vertical arrows.

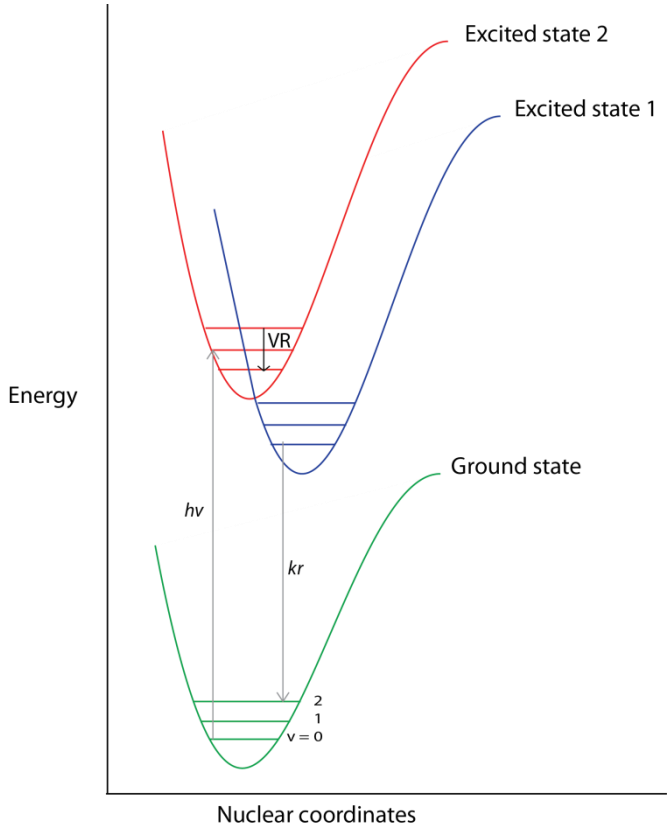

Figure 1.3 Franck-Condon priniciple for electronic transitions.

1.1.2 Photophysics of Rhenium(I) Complexes

The photophysical properties of rhenium(I) complexes possessing these electronic transitions can also be portrayed through a simplified Jablonski diagram, see **Figure 1.4**. First, the absorption of a photon excites the rhenium(I) complex to a singlet state (either ^{1}MLCT, ^{1}MC, ^{1}IL depending on its energy). The complex then undergoes VR and IC to the lowest excited state in accordance with Kasha's rule.[55] IC involves a transition between states of the same multiplicity and is represented in **Figure 1.4** by a curly arrow line between the singlet states. Due to the heavy atom effect, the complex then shifts between states of different multiplicities, where the transition is known as intersystem crossing (ISC) and is represented by a curly arrow as a transition between singlet and triplet states. ISC is considered a forbidden transition as it does not obey the spin selection rule.[37,56] The complex finally decays to the ground state either through radiative or non-radiative processes. The radiative emission from triplet to singlet state is known as *phosphorescence*. The non-radiative processes refer to excitation energy being converted to thermal energy *via* collisional quenching and vibrational relaxation.

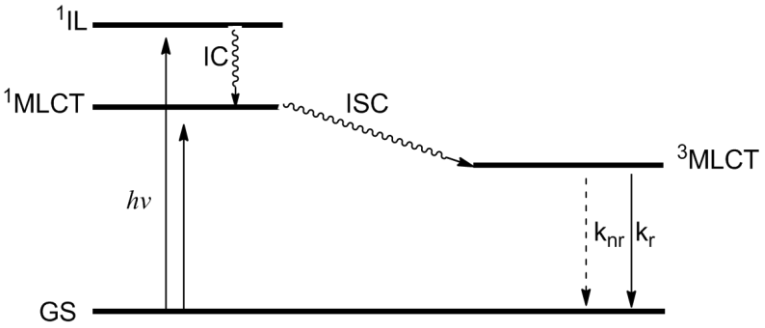

Figure 1.4 Simplified Jablonski diagram showing general electronic transitions.

The radiative decay (k_r) and non-radiative (k_{nr}) decay rate constants for the emission are correlated with the quantum yield, Φ and the observed lifetime, τ_{obs} using the equations below:

$$\tau_{obs} = \frac{1}{(k_r + k_{nr})} \qquad (eqn\ 1.1)$$

$$\Phi = \frac{k_r}{(k_r + k_{nr})} \qquad (eqn\ 1.2)$$

$$\Phi = (k_r)(\tau_{obs}) \qquad (eqn\ 1.3)$$

$$(1 - \Phi) = (k_{nr})(\tau_{obs}) \qquad (eqn\ 1.4)$$

The overall decay rate of an excited state species will be a sum of both radiative and non-radiative decay constants. The lifetime will then be the inverse of the the overall decay (eqn 1.1). The quantum yield of emission can be described as a ratio of the number of photons emitted over the number of photons absorbed. Therefore, the quantum yield can be determined as a fraction of the rate of radiative decay to the overall decay from the excited state (eqn 1.2). In practical terms, absolute quantum yields are vital as they allow one to assess the sensitivity of a proposed fluorophore.[57]

As mentioned previously, the photophysical properties of the metal complexes are mainly determined by the lowest energy excited states, which are greatly dependent on the structure. Specifically for rhenium, photophysical properties such as energy, lifetime, and decay are dependent on both the axial and diimine ligands.[43] The origin of the excited electron depends on the actual complex composition (i.e. axial ligand nature), while the presence of an electron accepting diimine ligand allows for charge transfer (CT) electronic transitions.[43]

These transitions are relative to the Jablonski diagram illustrated in **Figure 1.4**. The introduction of σ donor ligands adjusts the energy levels of the dπ orbitals in the metal centre, while the use of π accepting ligands lowers the t_{2g} energy level. Introducing functional groups (EWG or EDG) with different properties to the diimine ligand will also adjust the π* orbital energy level. Many different methods can be applied to change the properties of d^6 transition metal complexes.[58]

The overall charge of the rhenium complex can be tuned by modifying the ancillary ligand (L), where L is a halogen or anionic heterocycle to form an overall neutral complex or a neutral ligand such as pyridine to form an overall cationic complex. The difference in charges can have varying effects on the MLCT transition and consequently the photophysical and photochemical properties. These can be tuned according to the specific application in use.

The energy gap can be modified by changing the donor strength and conjugation of ligands. Generally, strong σ donor ligands increase the electron density on metals and highly conjugated ligands reduce the energy level of the LUMO; this leads to a smaller energy gap resulting in a red-shifted emission. On the other hand, weak σ

donor ligands (or cationic complexes) decrease the electron density on the metal centre, which leads to a larger energy gap and blue-shifted emission.

1.1.2.1 Rigidochromism

"Luminescence rigidochromism" refers to the behaviour of an emissive complex in a frozen matrix (77 K temperature). The most evident feature is the blue shifted emission profile, which may also differ in structural band character compared to the fluid solution (at room temperature, 298 K). This phenomenon was first discovered by Wrighton and Morse, who observed that the emission spectrum of rhenium(I) species at lower temperatures became more structured and blue-shifted compared to those measurements at room temperature.[41] This can be explained by the fact that when solvent molecules are frozen, they can no longer rearrange their dipoles to stabilise the excited state. As a result, the energy level of the excited ^{3}MLCT is raised in energy (destabilised) compared to the ground state.[59,60] This increases the energy gap, which results in a hyposchromic shift in the emission maximum. The rigidochromic effect usually indicates that the emission originates from a charge transfer state.[61,62] On the other hand, π-π* transitions are usually less sensitive to this effect as the transition does not involve a large change in dipole moment.

In addition, the emission lifetime and quantum yields of the complexes significantly increase upon cooling the solution to 77 K, due to less quenching effects of the excited bimolecular deactivation processes. Non-radiative decay *via* VR is also reduced due to the rigidity of the system, which also increases the observed excited state lifetime.

1.1.2.2 Solvatochromism

Solvatochromism can be described as the change in absorption and emission properties due to a change in solvent polarity. Solvatochromism specifies that there is a significant shift in electron density as a result of the electronic transition. Charge transfer bands (LLCT, MLCT) are more sensitive to solvent polarity, compared to π-π* (IL) or MC transitions. The CT bands are more distinguished due to the large change in dipole between the ground state and excited state. More specifically, a bathochromic shift describes a red shift in the CT band upon increasing solvent polarity, where excited state is more polar than ground state. A hypsochromic shift

(also referred to as "negative solvatochromism") is a blue shifted transition present in more polar solvents.[63,64]

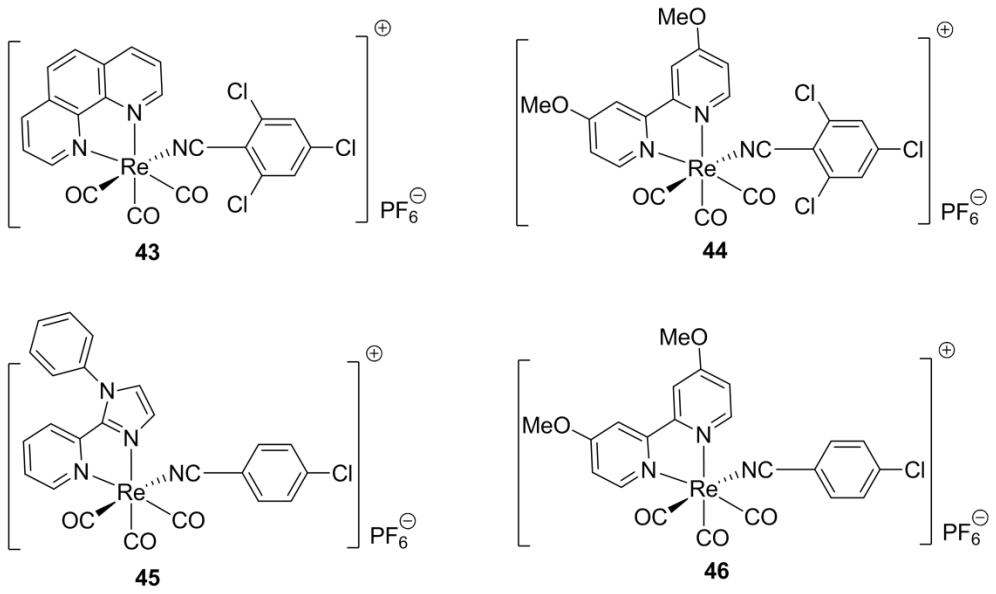

Figure 1.5 A few of the rhenium(I) complexes investigated by Yiu *et al*. showing variation in diimine ligands.

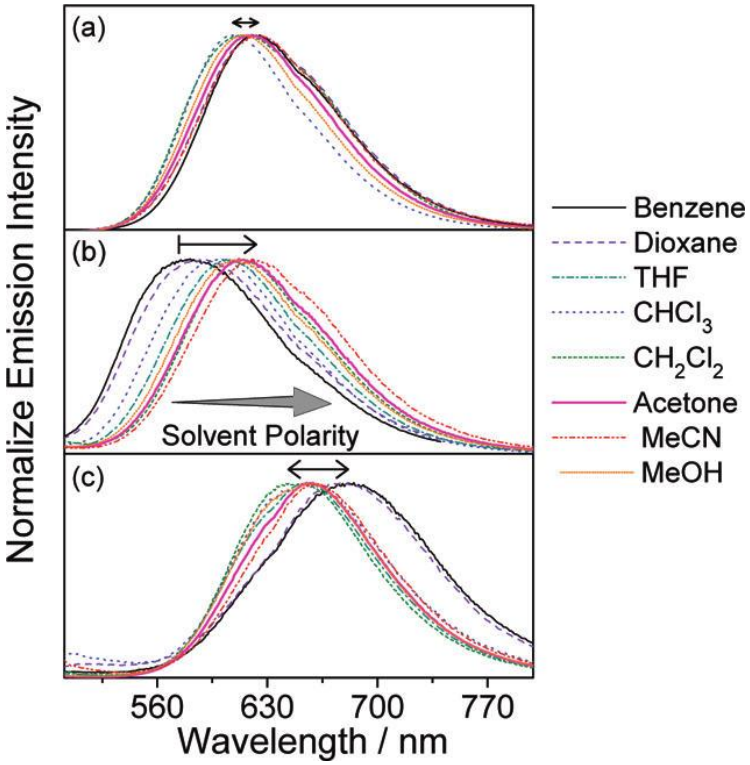

Figure 1.6 Emission spectra of (a) **43**, (b) **44**, and (c) **45** in different solvents at 298 K [reprinted with permission from ref[65]]

A publication by Yiu *et al* reported a series of rhenium(I) isocyano complexes (see **Figure 1.5**) with emissions having great sensitivity to change of the solvent environment.[65] The authors found that the degree of solvent dependence varies with the nature of diimine ligand and its substituents. The emission of the complexes were investigated in a variety of organic solvents such as benzene, dioxane, THF, $CHCl_3$, CH_2Cl_2, acetone, MeCN and MeOH. The emission spectrum for complex **44** (see **Figure 1.6**b) displays a red shift in emission with increasing solvent polarity from benzene to methanol solution. An opposite trend was shown for complex **45** (which had an unsymmetrical diimine ligand attached) that displayed a blue shifted emission with increasing solvent polarity (see **Figure 1.6**c). In addition, the degree of solvent dependence was also found to decrease for complexes with trisubstituted (**43** and **44**) phenyl isocyanide ligands compared to those with monosubstituted (**45** and **46**) phenyl isocyanide ligands. This lower solvent sensitivity was attributed to better shielding in the presence of sterically bulk ligands.

1.1.3 Examples of Luminescent Rhenium(I) Complexes

The rich photophysical properties of rhenium complexes have attracted considerable interest due to their application in a variety of fields including OLEDs[2], sensors[66], catalysis[67] and biological labelling.[68,69] The most investigated rhenium complexes are those of the rhenium(I) tricarbonyl core with the general formulation of *fac*-$[Re(\mathbf{N\hat{}N})(CO)_3(L)]^{+/0}$, where **N^N** is a polypyridyl bidentate chelating ligand (such as **bipy** or **phen)** and L is a neutral or anionic monodentate ancillary ligand (such as a halogen or pyridyl group). The emission of these complexes can be ascribed to phosphorescent decay, the excited state energy of which can be fine-tuned by subtle variation of the **N^N** ligand and/or ancillary ligand.

Organometallic rhenium complexes have occupied a noticeable area in the photophysics and photochemistry of transition metal complexes. Wrighton and Morse[41] first explored the photophysical and photochemical properties of stable and inert rhenium(I) complexes of the type *fac*-$[Re(\mathbf{N\hat{}N})(CO)_3(L)]^{0/+}$. Ever since their contribution to this research field, rhenium(I) diimine complexes have played a significant role in understanding the photophysical processes alongside the photoinduced electron transfer and electronic energy transfer processes (which will be discussed further in Section 1.3 of this chapter).

A large number of articles have been reported in the past exploiting various chelating and ancillary ligands to study the relationship between structural and photophysical properties of rhenium(I) complexes. In particular, the interesting properties of rhenium(I) tricarbonyl diimine complexes have gained increasing attention on their potential as cellular imaging reagents. A few important features of complexes to be viable for biological imaging are that they should have large Stokes shift, long emission lifetime and be photostable in aqueous media. The examples discussed below follow such criteria.

In 2009, Louie *et al.* designed rhenium(I) tricarbonyl polypyridine complexes of the type $[Re(\mathbf{N}\text{^}\mathbf{N})(CO)_3(Py\text{-}DPAT)]^+$ as intracellular zinc ion sensors, where DPAT is 2,2′-dipicolylamine (derived from tyramine) as shown in **Figure 1.7**.[20] Upon excitation, the DPAT complexes display emission at 489-554 nm and a lifetime of 0.54-3.15 μs in degassed solutions. The DPAT complexes (**47**) showed lower emission quantum yields (Φ_{em} = 0.0085-0.028) and shorter lifetimes compared to those DPAT-free analogues (**48**) (Φ_{em} = 0.045-0.23, τ = 0.77-6.06 μs). The authors have attributed this to the DPAT unit quenching the emission through electron transfer. Additional experiments indicated a pH dependent emission on the DPAT complexes; lower pH displayed increased emission intensity and upon increasing pH the emission intensity decreased. Particularly, this trend was attributed to the deprotonation of the ammonium group (on the DPAT) which produced a tertiary amine capable of a quenching process.[70] Another factor that explains the reduction of emission intensity at high pH was the interaction of hydroxide ions with the thiourea unit (on the pyridine ligand). On the other hand, this electron transfer process was shown to be inhibited by the addition of Zn^{2+} and Cd^{2+} ions which gave enhanced emission and extended lifetime.

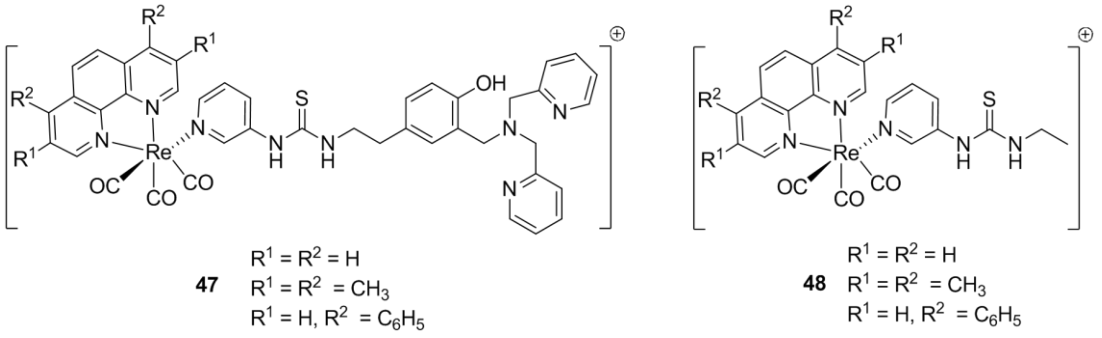

Figure 1.7 Structures of $[Re(\mathbf{N}\text{^}\mathbf{N})(CO)_3(Py\text{-}DPAT)]^+$ and $[Re(\mathbf{N}\text{^}\mathbf{N})(CO)_3(Py\text{-}Et)]^+$ where Py-Et = 3-(ethylthioureidyl)pyridine.

In terms of bioimaging, one of the very first luminescent complexes to target specific organelles was that of $[Re(\mathbf{bipy})(CO)_3(Py\text{-}R)]^+$ where R = CH_2Cl, studied by Coogan *et al.*, shown in **Figure 1.8**. The specific targeting of this cell imaging reagent was demonstrated by co-localisation studies (using MCF-7, human mammary adenocarcinoma cells) which was shown to accumulate specifically in the mitochondria.[9,15,71] Both chloro- (**49**) and hydroxy- (**50**) complexes display similar photophysical properties, although the chloro derivative shows more specificity towards mitochondria. This would indicate that the variability in the structure of the coordinated ligands changes the permeability and toxicity in cells, even though the emission properties were found to be quite similar.

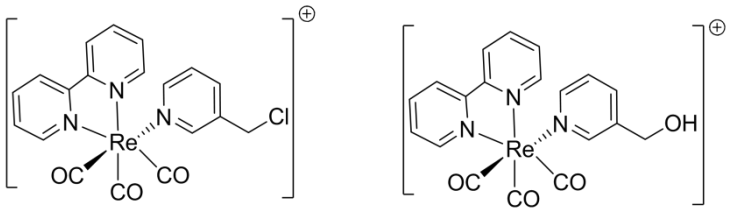

Figure 1.8 Structures of rhenium(I) diimine complexes studied by Coogan.

1.2 Photochemistry of Transition Metal Complexes

Early publications of photochemical investigation of transition metal complexes involved metal carbonyls. General photochemical reactions of metal-carbonyl complexes involve dissociation of carbon monoxide, CO (which is usually followed by substitution for another ligand). An example of a photochemical reaction (shown below) is of tungsten hexacarbonyl losing a CO ligand which is then replaced with a phosphine ligand.[59]

$$[W(CO)_6] + PPh_3 + h\nu \rightarrow [W(CO)_5(PPh_3)] + CO$$

Photochemical substitution of CO by a ligand in metal carbonyl complexes is a convenient synthetic method to prepare other metal carbonyl derivatives. This can be done using a wide variety of substituting ligands. Another advantage of these photochemical substitution reactions is that they can be carried out at room

temperature, which avoids the use of high temperatures potentially causing decomposition of unstable ligands and/or complexes. The preparation of a solvent-substituted derivative is carried out by irradiating the complex in a weakly coordinating solvent (such as acetone, acetonitrile, pyridine or tetrahydrofuran).

A good understanding of how a photochemical reaction proceeds is crucial in order to take advantage of complexes with photochemical properties and tune them to specific applications such as phototherapy. A photochemical process specific to some d^6 metals occurs when a complex absorbs light and is transferred to a singlet excited state, which then undergoes intersystem crossing (ISC) to its triplet excited state (^{3}MLCT). Following this transition, the complex can either decay radiatively as phosphorescence or it can populate another 'reactive state' to open up a photochemical pathway causing CO loss or solvent exchange (see **Figure 1.9**).

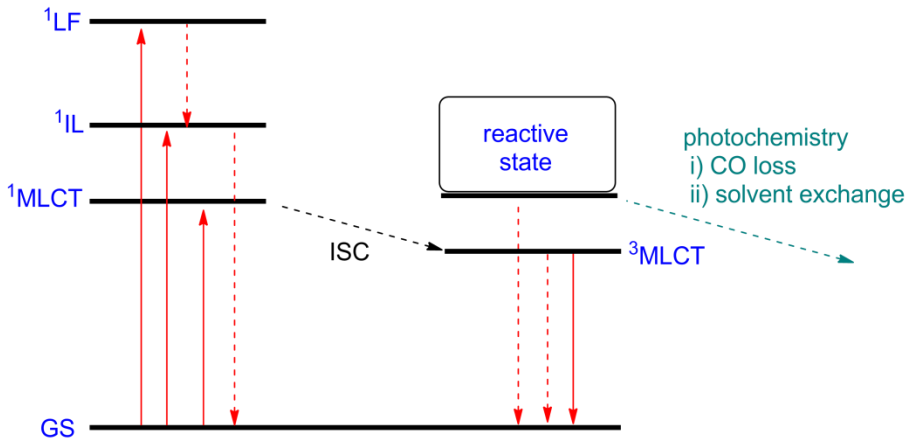

Figure 1.9 Jablonski diagram showing photochemical processes that can occur upon absorption of a photon.

1.2.1 Photochemistry of Rhenium(I) Complexes

As mentioned previously, extensive studies of complexes with the generic type *fac*-$[Re(CO)_3(\mathbf{N}\text{^}\mathbf{N})(L)]^{0/+}$ have shown that small structural modification of either the ancillary and/or chelating ligand can result in a significant difference in the excited state electron transfer properties (in terms of excited state lifetime, quantum yield and luminescent emission). Interestingly, the photochemistry of these complexes have not been reported as much as their photophysics.[51,64] Only recently there have been research which involved photochemical methods to synthesise various rhenium(I) complexes,[24–26] which were found to be high yielding and highly stereoselective.

In 2000, Koike *et al*. discovered new synthetic routes to prepare a class of biscarbonylrhenium(I) complexes with formula $[Re(X_2\textbf{bipy})(CO)_2(PR_3)(L)]^+$ through photochemical ligand substitution reactions (PLS), see **Scheme 1.1**.[75] Using strong field organophosphorous ligands (such as triethylphosphite and triphenylphosphine) bound to rhenium(I) showed a photochemical displacement of CO ligand *trans* to the phosphorous ligand. This photochemical reaction occurred at 365 nm. The progress of the photochemical substitution was monitored by *in situ* solution IR measurements. The changes in the spectra following irradiation (focussing on CO-stretching region) showed two new bands belonging to the product **52** appearing as the bands of **51** decrease. It was found that the PLS occurred at the axial CO ligand, for complexes with a phosphorous ligand. However, this type of PLS was not observed when L included halide or pyridine derivatives.

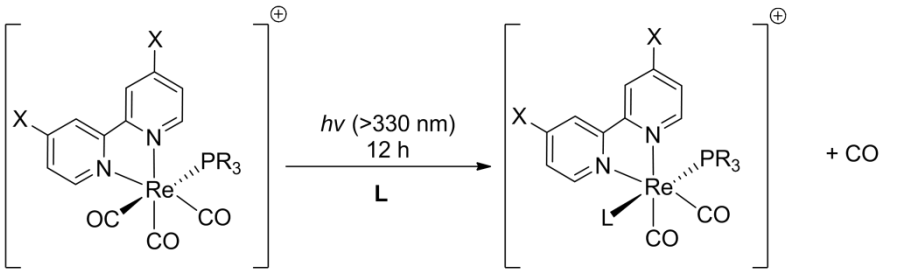

51a: X = H, R = $P(OEt)_3$
51b: X = H, R = PPh_3
51c: X = Me, R = $P(OEt)_3$
51d: X = CF_3, R = $P(OEt)_3$

52a: X = H, R = $P(OEt)_3$, L = MeCN
52b: X = H, R = PPh_3, L = MeCN
52c: X = Me, R = $P(OEt)_3$, L = $P(OEt)_3$
52d: X = CF_3, R = $P(OEt)_3$, L = $P(OEt)_3$

Scheme 1.1 Structures of rhenium phosphine complexes with varying substituents X, and ancillary ligands L (outlined in scheme).

A few years later, the same research group deduced the mechanism for the PLS reaction of $[Re(\textbf{bipy})(CO)_3(PR_3)]^+$ complexes, utilising ^{13}C NMR spectroscopy techniques. By monitoring the intensity change in the ^{13}C NMR signals for the axial and equatorial CO ligands in a $CDCl_3$ solution during irradiation, they were able to identify that the PLS reaction operates through a site-selective substitution of the axial CO ligand. This was indicated by results showing the axial ^{13}CO peaks to have a significant change and equatorial ^{13}CO peaks showed no change. This reaction mechanism can be seen in **Scheme 1.2**, and was determined to go through a dissociative step. This was evident as the photochemical yield of the product formation was not affected by concentration or nucleophilicity of the entering ligand.

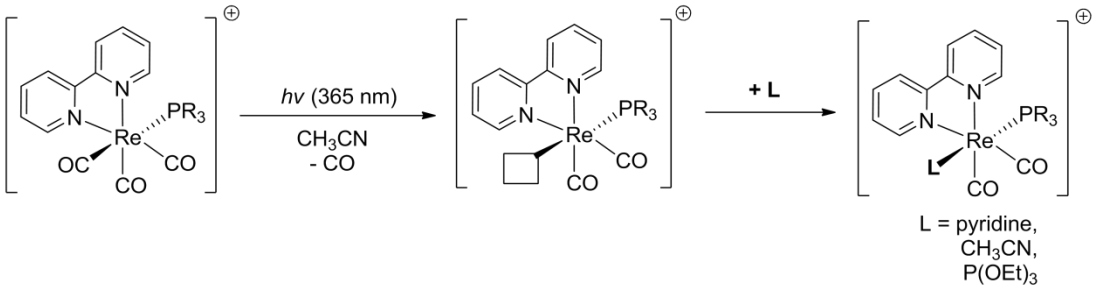

Scheme 1.2 Proposed mechanism for the PLS of [Re(**bipy**)$(CO)_3(PR_3)]^+$ complexes.

In addition, the authors hypothesised that the PLS reaction proceeded through either ^{3}MLCT state or another excited state that was thermally accessible from the ^{3}MLCT state. The lifetime and quantum yield of the ^{3}MLCT excited state emission displayed temperature dependence. These results suggested that the PLS reaction occurred through an excited state thermally accessible from the ^{3}MLCT state.[76] In other literature involving PLS reactions of transition metal diimine complexes, it is well known that the reaction occurs *via* ^{3}LF excited state that is thermally accessible from the ^{3}MLCT state.[77] This can be depicted through the use of a Jablonski diagram, shown in **Figure 1.10**.

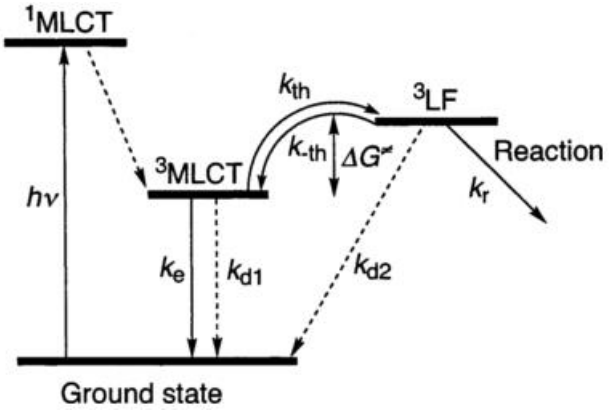

Figure 1.10 Jablonski diagram showing thermally accessible state. [Reproduced from ref [76]].

The investigation of photochemical properties of rhenium(I) complexes having phosphines [19–22] or phosphites, diimines [23] and isonitriles as ligands appear to have a common factor suggesting the photochemical process occurs due to their presence of a strong *trans* effect from the ligand. However, this is not the case for all photochemical reactions, as will be described further in the chapter.

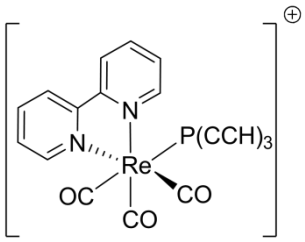

53

Figure 1.11 Chemical structure of [Re(**bipy**)$(CO)_3$(TEP)]$^+$ complex.

In 2005, Hightower and co-workers discovered an unusual photochemical behaviour of [Re(**bipy**)$(CO)_3$(TEP)]$^+$ **(53)** where TEP is triethynylphosphine **(Figure 1.11**), compared to analogous phosphine [Re(**bipy**)$(CO)_3(PR_3)]^+$ complexes (where R is Ph).[82] The distinctive photochemistry is due to the complex having more than one photochemical channel available. These types of complexes undergo a single photosubsitution (from excitation into MLCT excited state manifold) of CO which also competes with a radiative decay from a low-lying triplet state. TEP acts as a better acceptor ligand than PPh_3 and substantially raises the emission energy.[82] This is because TEP possesses properties similar to that of a CO ligand rather than typical PR_3 ligands. This was suggested as a result of the emitting state of **53** displaying high energy π-π* character. Another piece of evidence which validates the better acceptor ability of the TEP ligand would be IR analysis of the CO wavenumber values, where higher frequency wavenumbers (compared to PPh_3 complex) indicates better acceptor ability, due to the reduced electron density on the rhenium.

The authors were able to identify the products from photolysis in MeCN through monitoring the progression using IR and ^{31}P NMR spectroscopy. They observed the products to be *fac*-[Re(**bipy**)$(CO)_3(NCCH_3)]^+$, free TEP ligand and a new complex characterised as *cis, trans*-[Re(**bipy**)$(CO)_2$(TEP)$(NCCH_3)]^+$. It has been established by previous studies that an apparent excited-state *trans* effect labilises the ligand on the strong field axis, which is responsible for photo-substitution of CO.[76]

A few years later, Sato *et al* [83] were the first to report a photochemical ligand substitution (PLS) of [Re(**bipy**)$(CO)_3$Cl] without a phosphorous ligand. Their investigations showed that the reactions do not proceed through the lowest ^{3}MLCT excited states, as they are quite photostable when excited at λ = 365 nm. But instead they occur through higher vibrational levels of the ^{1}MLCT (Re→**bipy** and Re→CO) and/or higher electronic states such as π-π*. Only for complexes with phosphorous

ligand, the PLS reaction proceeds *via* triplet (^{3}MC) excited state, which is in thermal equilibrium with the ^{3}MLCT state.

PLS reaction occurred for [Re(**bipy**)$(CO)_3$Cl] when using shorter wavelength (313 nm) light. When the complex was photolysed at 313 nm in acetonitrile, CO dissociation occurred to form dicarbonyl photoproducts as two geometric isomers (which can be distinguished in the ^{1}H NMR spectra showing eight non-equivalent protons for **56** [*cis,cis*-] and four equivalent protons for **55** [*trans, trans*-]).[83] The structures of the complexes can be seen in **Scheme 1.3**. In addition, the *cis, cis*-complex **56** was found to undergo further isomerisation in acetonitrile to form **57**.

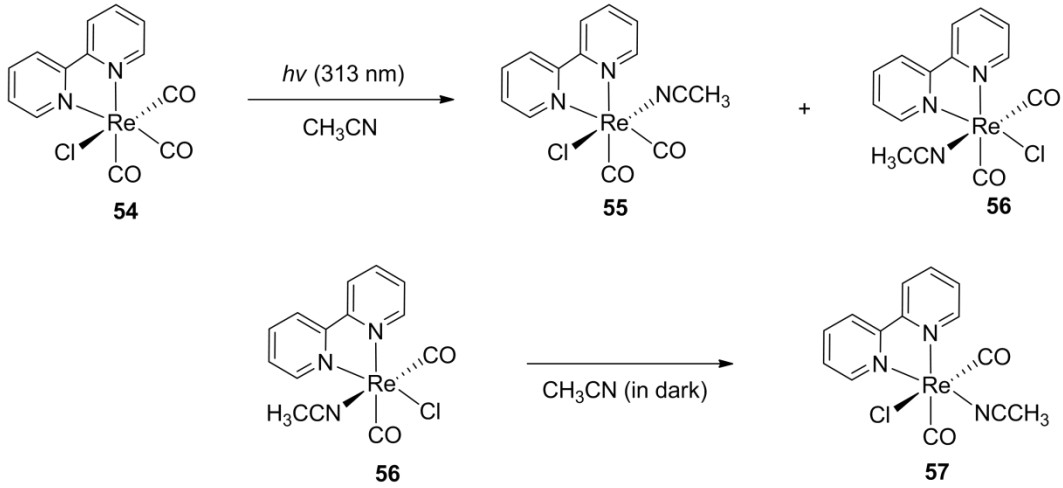

Scheme 1.3 PLS reaction of [Re(**bipy**)$(CO)_3$Cl] showing different products formed, adapted from Sato.

The authors conclude that PLS reactions require excitation at higher electronic excited states and/or higher vibration levels of the lowest ^{1}MLCT state. This was suggested by the quantum yield values which decrease with decreasing irradiation wavelength, i.e. 0.0145 (365 nm) and 0.0129 (313 nm). The difference between the quantum yield of non-emissive and reactive state is about 0.11 and the authors claimed this result to indicate that higher excited states of the complex undergo ultrafast process that competes with population of lowest ^{3}MLCT state. The photochemical reactions shown in the paper indicate that the quantum yields of the photochemical reaction are dependent on the wavelength of light used for irradiation (i.e. <330 nm induces reaction, whereas 365 nm does not). In addition, TRIR analysis indicates that the reaction takes place within 50-100 ps. The aforementioned observations conclude that the PLS and isomerisation reactions do not occur through the lowest ^{3}MLCT excited state.

Following this publication, the same group undertook further investigations on complex **54** and showed that irradiation (313 nm) in THF did not induce a CO loss, but rather caused photochemical isomerisation to give the *mer*- isomer **58** (**Scheme 1.4**).[84,85] This complex could then be further reacted thermally, with other ligands (such as MeCN, $P(OEt)_3$, pyridine), to form rhenium(I) diimine dicarbonyl complexes as illustrated in **Scheme 1.4**. Interestingly, rearrangement of the ligand occurs only for the MeCN solvate and not the others.

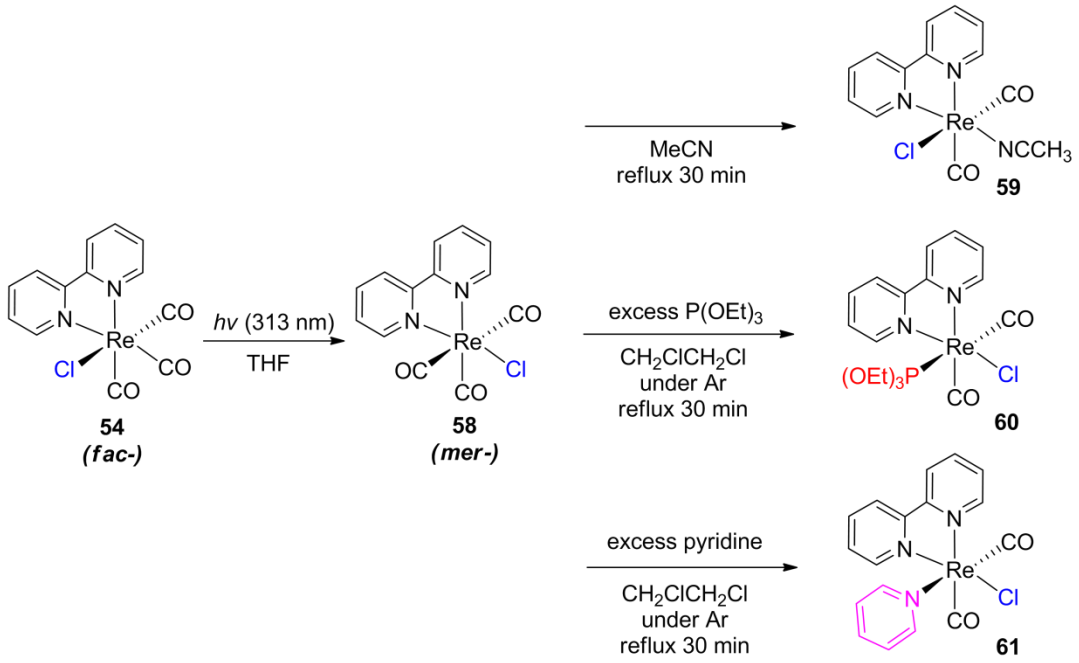

Scheme 1.4 Photoisomerisation reaction of [Re(**bipy**)$(CO)_3$Cl] and further reactions.

An in-depth investigation to further elucidate the photochemical mechanism for the PLS reaction of [Re(**bipy**)$(CO)_3$Cl] was published a few years later.[86] With the aid of advanced techniques such as time-resolved infrared (TRIR), UV-VIS and emission spectroscopy, the authors were able to propose that the PLS reaction occurs from the population of higher excited states. **Scheme 1.4** illustrates three different mechanistic pathways (depending on the solvent used for the experiment). Photochemical reactions were carried out in different solvents. When complex **58** was heated under reflux conditions in acetonitrile solution, complex **59** was produced. When the same complex **58** was heated at reflux in 1,2-dichloroethane solution and contained excess $P(OEt)_3$ or pyridine, **60** and **61** were formed respectively. The mechanisms for the formation of the photoproducts were varied according to concentration of MeCN and temperature.

Another example of $[Re(\mathbf{N^N})(CO)_3(PR_3)]^+$ complexes to undergo PLS reactions have been investigated by McLean *et al.* in 2012, where **N^N** is a dipyrrinato ligand, see **Scheme 1.5**.[78] The PLS reaction took place upon irradiation with a 355 nm laser in acetonitrile solution. Analysis by NMR and IR showed spectral changes that gave evidence towards coordination of deuterated acetonitrile in replacement of a CO ligand.

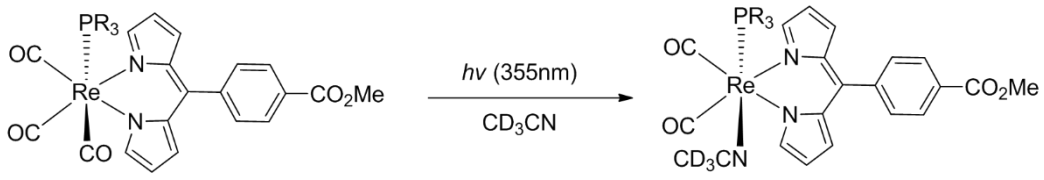

R = Ph, Bu

62 **63**

Scheme 1.5 PLS reaction of rhenium(I)-dipyrrinato complex in acetonitrile-d_6.

In addition to the classical pyridine-based diimine ligands, the photoreactivity of rhenium carbonyl complexes with iminopyridines as chelating ligands have been studied by the group of Knör.[87] These complexes (see **Figure 1.12**) have exhibited MLCT emission (λ_{em} = 750 nm) in the visible region. The PLS reaction occurred from continuous wave irradiation using Xe-lamp light in acetonitrile solution of these compounds. Spectral changes were observed in the UV-VIS absorbance plots.

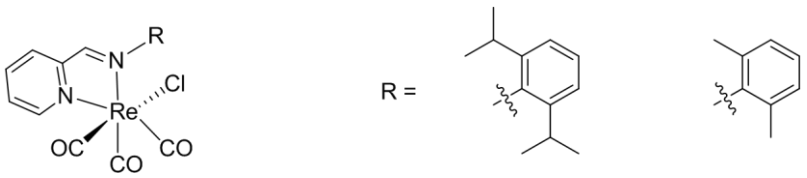

64 a b

Figure 1.12 Structure of rhenium carbonyl complexes with iminopyridine ligands.

1.2.2 Application as Phototherapeutic Agent

Photochemistry plays an important role in designing organometallic complexes that deliver bioactive molecules to physiological targets. The delivery of gasotransmitters such as nitric oxide (NO), hydrogen sulphide (H_2S) and carbon monoxide (CO) are generally of interest.[88–90] In particular, CO has been found to possess therapeutic properties (especially its anti-inflammatory effects).[90–94] CO also has an advantage to react exclusively with transition metals unlike NO and H_2S which interact with several intracellular targets. Additionally, the use of fluorescence microscopy

imaging techniques allows the identification of luminescent complexes and the location of said gas release.[95]

The photosensitivity of metal carbonyls has been well established and the mechanisms associated with the CO release upon irradiation have been extensively studied.[96] This particular type of complexes is referred to as "photoCORMs", i.e. photoinduced CO releasing molecules. However, many challenges are associated with designing and developing the ideal photoCORM. The most important feature is that the complex must be stable in the dark and the release of CO must be controlled upon irradiation of specific wavelength of light.[97] Another feature is the biocompatibility, i.e. solubility and stability in aqueous media, and of course minimal cytotoxicity.[88,93,98]

In addition to mononuclear metal carbonyl complexes, there have also been studies showing the photoreactivity of dinuclear metal complexes, such as dimanganese decarbonyl $[Mn_2(CO)_{10}]$ (**65**) see **Figure 1.13**.[99–102] The first compound reported as a CORM was **65**. Motterlini *et al* have established that **65** can release CO that stimulates specific vascular activities (such as vasorelaxation in rat aortic rings). The rate of CO release was quantified spectrophotometrically by measuring the conversion of deoxy-myoglobin (deoxy-Mb) to carboxy-myoglobin (Mb-CO). This principal method uses UV-VIS to measure the absorbance of Mb-CO at 540 nm. The formation of Mb-CO did not appear in the dark and was only observed upon extended photolysis. The photoactivated complex was reported to aid in vasoconstriction of isolated rat hearts. However, their poor bioavailability and high toxicity of these metal carbonyls restricted their use for other applications. Furthermore, the possibilities to tune their photophysical properties were also deficient. This then led to using compounds that were activated by hydrolysis, such as $[Ru(CO)_3Cl_2]$ and $[Ru(CO)_3Cl(glycinate)]$ *aka* CORM-3.[103–105]

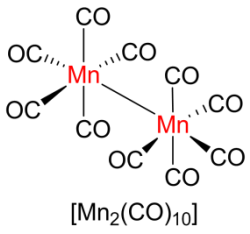

Figure 1.13 Structure of dimanganese decacarbonyl complex.

There have been many studies that incorporate the photochemical properties in view of their application as photoCORMs.[89,100,106] Examples shown in **Figure 1.14** include ruthenium[107], manganese[106,108–110] and rhenium[95] complexes, which will be discussed below. The vast majority of photoCORMs show sensitivity to UV light (300-450 nm), but these conditions are unfavourable for phototherapeutic applications. Recent efforts have been made to develop CORMs that can be triggered by visible/near-IR light.[111]

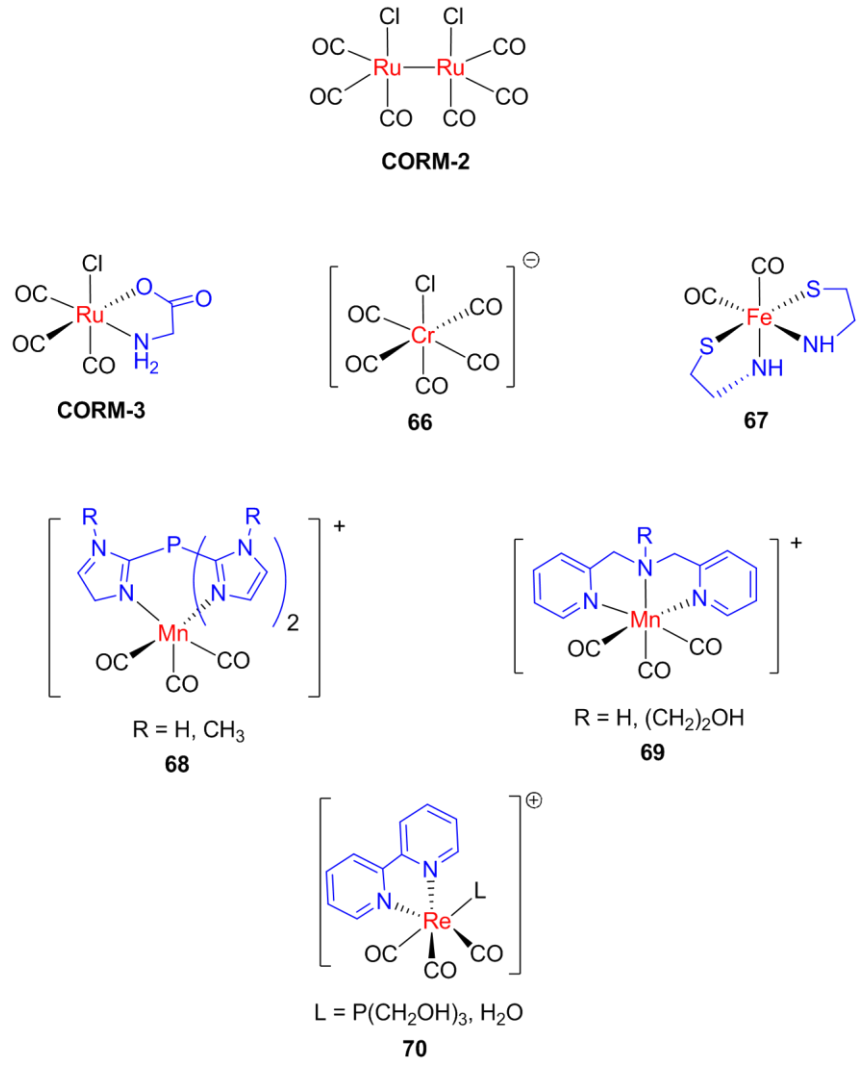

Figure 1.14 Some examples of currently reported photoCORMs[103,106,112,113] in literature.

A paper by Knör *et al*. studied a neutral [Re(1,2-diimine)$(CO)_3$Cl] complex (see **Figure 1.15**) that undergoes a photochemical reaction leading to spectral changes monitored by UV-VIS absorption.[114] In agreement with earlier studies,[115,116] the spectral changes were interpreted as light-induced isomerisation (*fac*- to *mer*-) and a photosubstituion of chloro ligand with the solvent molecule. The low quantum yields

reported for these complexes are favourable towards their application as photoCORMs. The authors suggest that the more bulky aryl substituents on the diimine favour the release of the chloro ligand on the rhenium. The reactivity is most likely due to the direct population of a high-lying ^{1}MC excited state that does not lead to permanent CO loss, which is consistent with IR data.

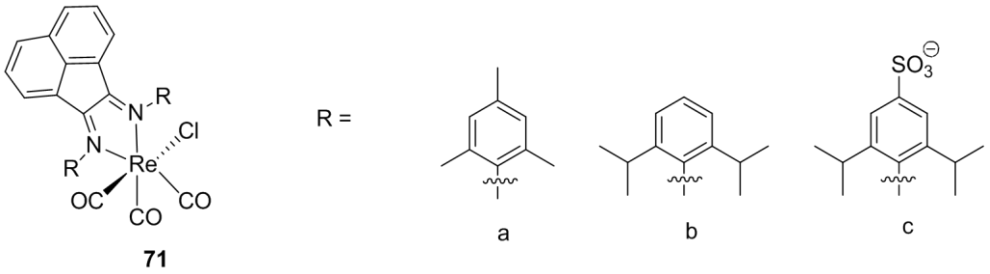

71

Figure 1.15 Structures of [Re(1,2-diimine)$(CO)_3$Cl] complexes with varying R substituents.

Carrington *et al.* have developed a number of complexes incorporating both manganese and rhenium metal centres (see **Figure 1.16**), which release CO upon irradiation with visible light.[117] These complexes are stable in solution in darkness and are also stable in aerobic conditions, which are important factors for biological compatibility and controlled release of CO. Manganese complexes exhibit excellent photoactivity upon exposure to low-power visible light (10-15 mW cm^{-2}). The irradiation causes rapid changes in the absorption spectra due to CO loss and distinct isobestic points indicate clean conversion of the complexes to corresponding photoproducts.[115]

The ligand 2-phenyazopyridine (azpy) illustrated in **Figure 1.16** was chosen as it resembles diimine ligands such as **bipy** and **phen**, but contains extended conjugation. Also, other research groups have used this ligand frame to develop similar photoCORMs.[95,106,118] The data in the paper shows that the rate of CO release for rhenium complexes **74** and **75** were significantly slower than those from the manganese complexes **72** and **73**.[117] This suggests that despite the identical structures, the metal centre plays an important role in the rate of CO release.

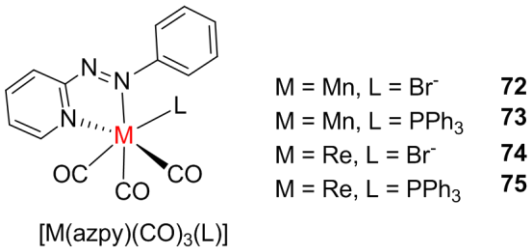

Figure 1.16 General structure of complex with varying metals and ligands.

In 2012, a luminescent and biocompatible photoCORM based on rhenium(I) complex was developed by Pierri *et al.*[95] The [Re(**bipy**)$(CO)_3$(thp)]$^+$ complex, where thp = tris(hydroxymethyl)phosphine shows strong luminescence properties, before (**76**, blue emitter) and after (**77**, green emitter) irradiation at 405 nm (**Scheme 1.6**). This feature can be used to track the conversion and loss of CO inside cellular entities, which is a great advantage in cell imaging. Upon photolysis, the absorption spectrum shows a red shift in the MLCT band from 345 to 405 nm, indicating a loss of CO. IR analysis is consistent with the dissociated CO shown by a shift to lower frequency.

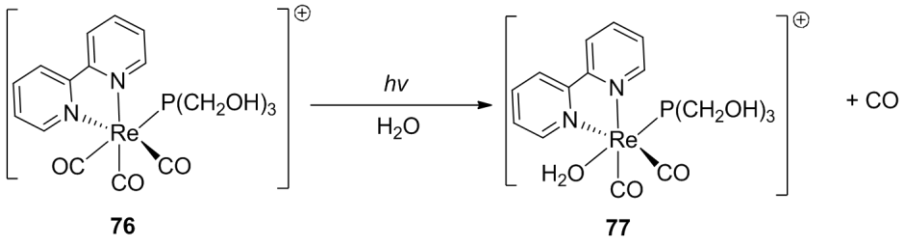

Scheme 1.6 Reaction scheme showing photolysis of rhenium complex in water.

Another example of a photoCORM stems from a dicarbonyl ruthenium(II) complex with functionalised chelating ligands, shown in **Figure 1.17**. The CO release was investigated using the myoglobin assay, showing the complex to be stable in the dark for up to 1 hour and then releasing CO upon illumination at 365 nm.[107]

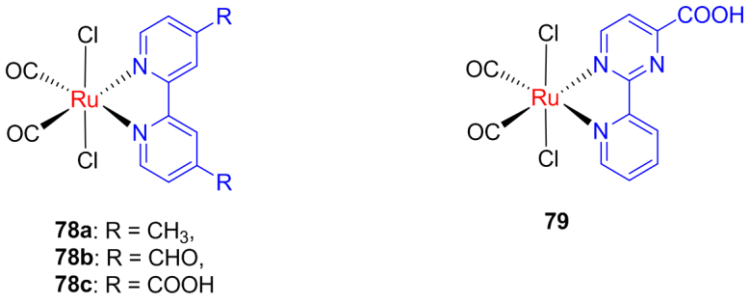

Figure 1.17 Structures of ruthenium(II) complexes, adapted from Bischof.

1.3 Photoinduced Electron Transfer

Electron transfer processes are important because they can be used to quench an electronically excited state (preventing its luminescence or reactivity) and also to sensitize other species.[119] Electron transfer (eT) plays a vital role in biochemical systems, particular for important processes such as photosynthesis and respiration.[120,121] It has been well established long ago that in photosynthesis, the excited chlorophyll mediates redox reactions which originate in one-electron transfer reactions of the excited magnesium complex (**Figure 1.18**).

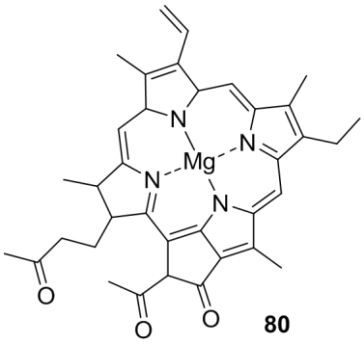

80

Figure 1.18 Structure of chlorophyll (**80**).

For any eT process to occur, there must exist two redox active molecular units – an electron donor (D) and an electron acceptor (A). Electron transfer can occur either intra- (within) or inter- (between) molecularly. When D and A are free in solution, the eT process is bimolecular, i.e. the two reactants have to diffuse together to form D---A. However, when D and A are covalently linked to each other, an intramolecular eT process occurs.

Photoinduced electron transfer (PeT) occurs where upon excitation with light, an electron is transferred from the excited D* to A, which then forms a charged complex. It has been stated that "an electronically excited molecule has an increased tendency to give away an electron as well as replace the one which was removed", therefore the complexes become both better oxidants and reductants compared to their respective electronic ground state.[122]

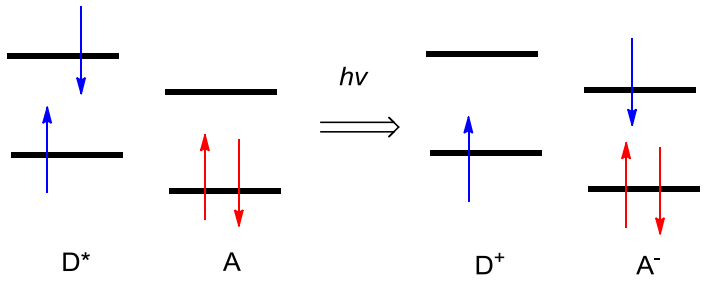

Figure 1.19 Simplified energy level diagram showing transfer of electron from donor to acceptor.

This process can also be illustrated using an energy level diagram (**Figure 1.19**), where the absorption of light activates the D or A for electron transfer by promotion of an electron in the highest occupied molecular orbital (HOMO) to higher levels. This results in an empty space in the HOMO, making the molecule a stronger oxidant. Then the promoted electron will end up on the lowest unoccupied molecular orbital (LUMO), where the high energy electron on the LUMO makes the molecule a stronger reductant.

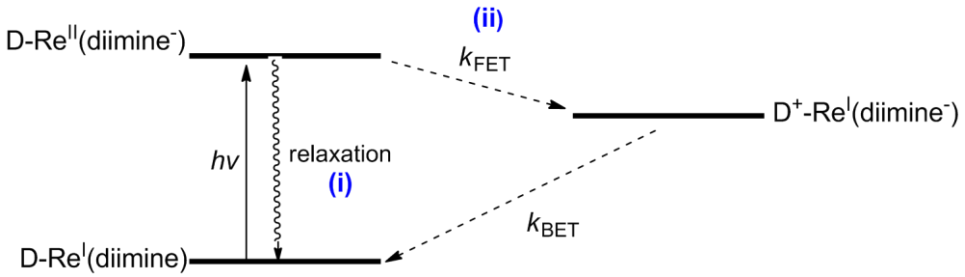

Figure 1.20 General excited state diagram for an electron donor-substituted Re(I) complex. [Reproduced from ref[123]].

Figure 1.20 shows an excited-state diagram which illustrates the photoinduced intramolecular electron transfer in rhenium(I) chromophore-quencher systems.[123] Photoexcitation results in the electron transporting from ground state to excited MLCT state, which can consequently decay by two different pathways, i.e. (i) radiative and non-radiative decay, (ii) intramolecular forward electron transfer (FET). This FET quenching step involves transfer of an electron from the donor to electron-deficient metal centre, which results in formation of ligand-to-ligand charge transfer (LLCT). Following this, decay of the LLCT state occurs by back electron transfer (BET).

A common example is $[Ru(\mathbf{bipy})_3]^{2+}$ which has been extensively studied in terms of its photophysical properties.[124–126] The ^{3}MLCT excited state is both a strong oxidant

and reductant, simultaneously containing an oxidising Ru(III) and reducing **bipy**$^{\bullet-}$ sites. This was demonstrated by vast studies of reductive and oxidative quenching of $[Ru(\mathbf{bipy})_3]^{2+}$ phosphorescence.[124,127]

PeT has been quite an active area of research having a vast number of books and review articles currently available. The following examples will shed some light on a range of compounds known to possess functional groups that take part in electron transfer processes, beginning with organic probes and moving towards transition metal complexes.

1.3.1 From Organic Molecules to Metal Complexes

A functional group capable of introducing PeT through a redox process include phenol compounds.[128] What makes phenols a highly attractive group to study electron transfer is the fact that phenols can act as both electron and proton donors, because their phenolic proton becomes highly acidic upon oxidation.[129] In most PeT-based systems, deprotonation of the phenol can encourage PeT, resulting in reduction of fluorescence. This type of phenomenon was first demonstrated by Gareis *et al*. through the use of a phenol-modified BODIPY fluorophore (see **Figure 1.21).**[130] BODIPY complexes are highly interesting as fluorophores due to their advantageous photophysical properties. Gareis *et al*. looked at the phenol/phenolate-dependent on/off-switching of luminescence of BODIPY bearing phenolic substituents. Deprotonation (using pyridine as the proton acceptor) to form the phenolate displayed a PeT-like quenching mechanism. The fluorescence titrations of the complex in $CHCl_3$ by successive addition of pyridine showed a significant decrease in fluorescence intensity, which can be explained by an electron transfer process. This was also demonstrated by the fluorescence intensity-pH profiles, showing a low intensity (fluorescence off-swithcing) at higher pH. Also, reprotonation by addition of TFA restores the fluorescence; showing a reversible fluorescence on/off states. The same titration experiments were performed on a reference BODIPY compound without the phenolic substituents. There was no base dependent response observed for the reference compound, proving that the changes in fluorescence intensity were due to the presence of the phenolic OH.

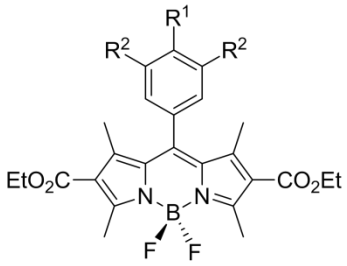

R^1 = OH, R^2 = H
R^1 = OH, R^2 = Bu^t
R^1 = R^2 = H

81

Figure 1.21 Structure of BODIPY compound, with various R substituents.

So far, there have been quite a few examples of pH-systems carrying phenolic PeT groups based on such organic dyes. Only recently, increasing interest has been shifted toward electron transfer of photoexcited molecules or metal complexes.[131] These examples will be discussed in the following section.

The excited state processes of organometallic complexes were rarely studied until 1978 when Wrighton first investigated the electron transfer processes of the ground and excited state of tricarbonyl rhenium complexes.[132] In general, transition metal complexes (d^6 and d^8 electronic configuration) provide a strong platform to investigate the concept of PeT because of their well-defined structures (being chemically inert and photostable) and synthetically tuneable excited state properties. The most popular inorganic sensitizers include complexes of ruthenium(II), rhenium(I), osmium(II), iridium(III/I) and platinium(II).[49,133–135] With their unique photoredox properties, the specific photosensitizer may be used either as an excited state reductant or oxidant, depending on the exact values of the ground state potentials and MLCT energies. Typically, rhenium(I) and iridium(III) systems fall under the excited state acceptor category, osmium(II) complexes are donors and ruthenium(II) can be both. With respect to this thesis, the following examples that will be discussed are generally tricarbonyl diimine rhenium(I) complexes that have been investigated as electron transfer dyes in proteins and as biological sensors due to their suitable photophysical properties.[136]

Electron transfer (eT) as well as energy transfer in phosphorescent d^6 metal complexes can cause quenching of the excited state, resulting in a reduction of the lifetime and quantum yield.[137] The reduction of these photophysical properties is not favourable when the application is targeted toward molecular imaging agents.

However, electron transfer processes can be utilised to facilitate luminescent switching (on-off mechanism) through manipulation of pH. The use of pH (protonation/deprotonation processes) as an external stimulus for the prompt switching of molecular properties (including luminescence) has been demonstrated by Maity *et al.* investigating the photophysical properties of homo- and hetero-bimetallic dyads of ruthenium(II) and rhodium(III).[137] The study investigated compounds based on two different polypyridine bridging ligands, where one was a bidentate chelating site like **bipy** or **phen**, and the other being a tridentate chelating site such as **tpy**. These highly conjugated and rigid structures make it suitable for electronic and photophysical applications. The complexes studied were $[(\mathbf{bipy})_2Ru^{II}(phen\text{-}Hbzim\text{-}\mathbf{tpy})Ru^{II}(\mathbf{tpy}/\mathbf{tpy}\text{-}PhCH_3/H_2pbbzim)]^{4+}$ (**82**) and $[(\mathbf{bipy})_2Ru^{II}(\mathbf{phen}\text{-}Hbzim\text{-}\mathbf{tpy})\text{-}Rh^{III}(\mathbf{tpy}\text{-}PhCH_3/H_2pbbzim)]^{5+}$ **(83)** where **phen**-Hbzim-**tpy** = 2-[4-(2,6-dipyridin-2-ylpyridin-4-yl)phenyl]-1H-imidazole[4,5-*f*][1,10]phenanthroline, **bipy** = 2,2′-bipyridine, **tpy** = 2,2′:6′,2″-terpyridine, **tpy**-$PhCH_3$ =4′-(4-methylphenyl)-2,2′:6′,2″- terpyridine, and H_2pbbzim = 2,6-bis(benzimidazol-2-yl)- pyridine (**Figure 1.22**).

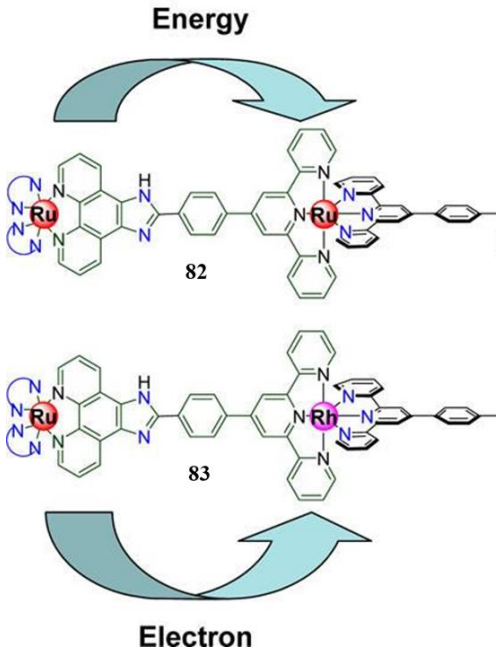

Figure 1.22 Structure of homo-metallic Ru dyads (top) and hetero-metallic Ru-Rh dyads (bottom). [Adapted and reproduced with permission from ref [137]].

The authors of the paper have demonstrated an efficient intramolecular energy transfer to occur in all unsymmetrical homobimetallic complexes, from $[(\mathbf{bipy})_2Ru(\mathbf{phen}\text{-}Hbzim\text{-}\mathbf{tpy})]^{2+}$ to [(**phen**-Hbzim-**tpy**)Ru(**tpy**/**tpy**-$PhCH_3/H_2$pbbz-

im)]. This was illustrated through comparison of the luminescence properties of bimetallic ruthenium complexes to the monometallic compounds; the bimetallic complexes have a lower emission intensity (quantum yield) and shorter excited state lifetime than their monometallic derivatives.[137] The rate constant k_{en} for energy transfer was calculated using the following equation:

$$k_{en} = 1/\tau - 1/\tau^0 \qquad (eqn\ 1.6)$$

where τ^0 is the emission lifetime of the monometallic precursor complex (151 ns) and τ is the lifetime of the unsymmetrical bimetallic complex (15.7 - 76.8 ns). The values of k_{en} at room temperature were found to lie in the range of $6.4 \times 10^6 - 5.7 \times 10^7$ s^{-1}, showing fast energy transfer.

In addition, for heterometallic complexes, an efficient intramolecular photo-induced electron transfer takes place from the Ru moiety to the Rh unit (see complex **83** in **Figure 1.22**). This was illustrated through comparison of the quantum yield of the model monometallic Ru(II) complex **82** with those of the heterometallic Ru(II)-Rh(III) complex **83**, showing a significant quenching of emission to occur for the heterometallic complex (see **Figure 1.23**).

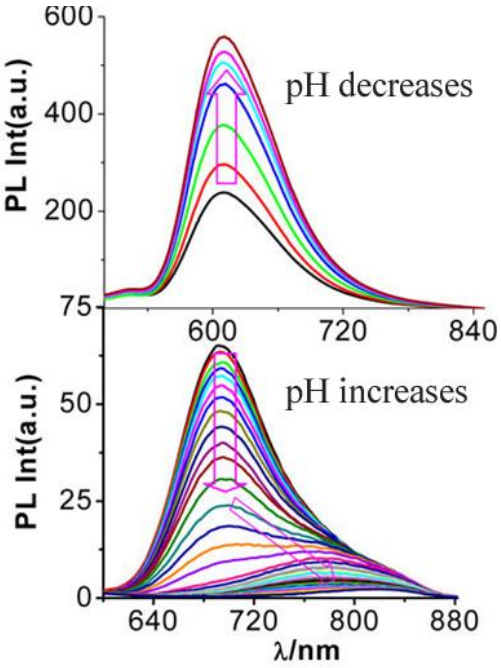

Figure 1.23 Emission plots showing changes in different pH levels for complex **82** (top) and **83** (bottom). [Adapted and reproduced with permission from ref [137]].

Further investigation was carried out to study the influence of pH on the absorption, steady-state and time-resolved emission properties of the complexes.[137] This was based on prior knowledge that the imidazole NH proton of the **phen**-Hbzim-**tpy** ligand becomes acidic upon coordination to the metal centre(s). Spectrophotometric titrations of the complexes were carried out in acetonitrile-water (3:2) solutions and monitored by absorption spectroscopy (see **Figure 1.24**) over the pH range 2.5 - 12. The spectral changes clearly show that deprotonation occurred.

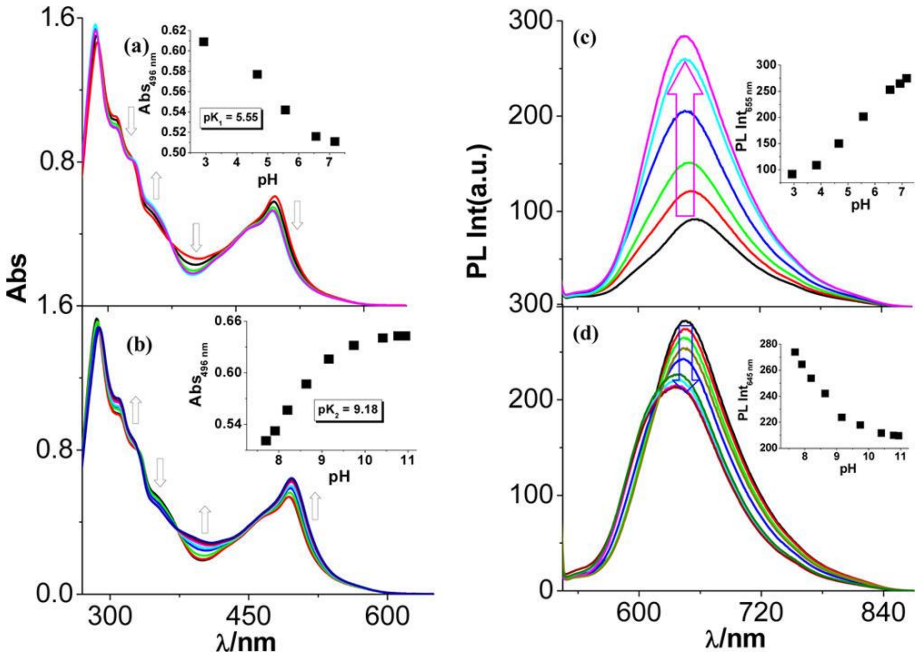

Figure 1.24 Changes in absorption (a and b) and emission spectra (c and d) with variation of pH in acetonitrile-water. [Adapted and reproduced with permission from ref [137]].

The authors of the paper have shown that the directional flow of electron and/or energy is enabled by lack of symmetry, through introducing ligands that differ in donor-acceptor properties or using heterometallic sites.[137] In addition, it has been demonstrated that emitting properties of these complexes are strongly dependent on protonation state of the imidazole rings. Not only do rigidity, conjugation and overall charge of the complex played a vital role to electron transfer rate and efficiency, but other features associated with bridging ligand such as length (distance of donor-acceptor) also played a role.[137]

1.3.2 Distance Dependence of Donor-Acceptor

In general, molecules involved in electron transfer do not normally occur between two reactants which are spatially separated by 10 Å or more. However long distance charge transfer has been observed naturally and is involved in two individually important biological processes such as photosynthesis and respiration.[138] In order to investigate the progress of artificial long-range electron transfer in a sequential manner, a common approach is to use redox active compounds that can be triggered by light.

Kuss-Petermann *et al*. investigated a series of compounds where the phenol unit is covalently linked to a rhenium(I) tricarbonyl diimine core through a number of *p*-xylene spacers (n = 0-3), where the xylene spacer has a length of 4.3 Å (see **Figure 1.25**).

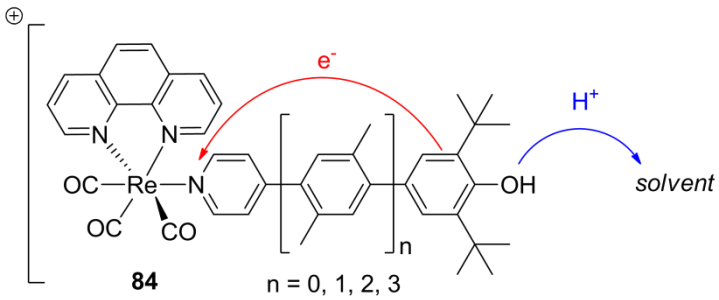

Figure 1.25 Rhenium(I) tricarbonyl diimine complex (Re-xy$_n$-PhOH) illustrating electron and proton transfer process.

2,6-Di-*tert*-butylphenol acts as a combined electron-proton donor, the tricarbonyl rhenium(I) complex is the photooxidant, and a solvent molecule (neighbouring the phenol) acts as the proton acceptor. The distance between the two redox partners ranged from 7.9 to 20.8 Å (*via* introducing 1-3 xylene units), which led to an increase in the distance between the electron-accepting centre and the proton-accepting site.[139] It was found that the dyads (n = 0, 1, 2) exhibit intramolecular photoinduced electron transfer (phenol-to-rhenium). As the donor-acceptor distance decreased, the luminescence (emission intensity) of the complex Re-xy$_n$-PhOH became weaker. This was attributed to the PeT process which was quite significant when n = 0. In addition, the lifetime of Re-xy$_n$-PhOH where n = 1 is significantly different than n = 3 because electron transfer is not as efficient as distance increases.

This demonstrates that the rapid electronic communication between the phenol and rhenium metal centre decreases as a function of distance.

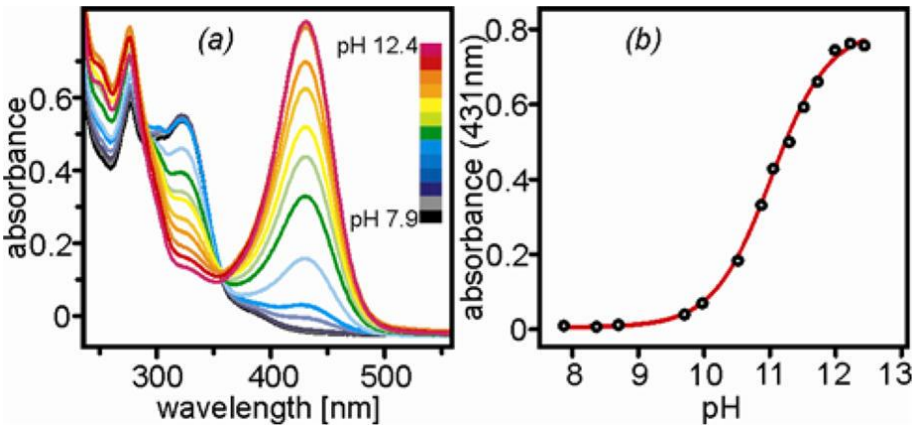

Figure 1.26 (a) Absorption spectra of Re-xy$_0$-PhOH at different pH values and (b) titration curve. [Reproduced with permission from ref [129]].

They also investigated the effects of phenol deprotonation by addition of NaOH solution and monitored the absorption change using UV-VIS spectroscopy (see **Figure 1.26**). As the longer dyads were deprotonated, there were less prominent changes in the spectra, due to the phenol-pyridine coupling being weaker as distance increases. Upon deprotonation, the phenol-pyridine charge transfer (CT) state was energetically stabilised (because it was a phenolate), which led to emission quenching and also provided the driving force for the transfer of electron density from the phenolate unit towards the metal centre. **Figure 1.27** illustrates the energy level diagram describing the process before and after deprotonation.

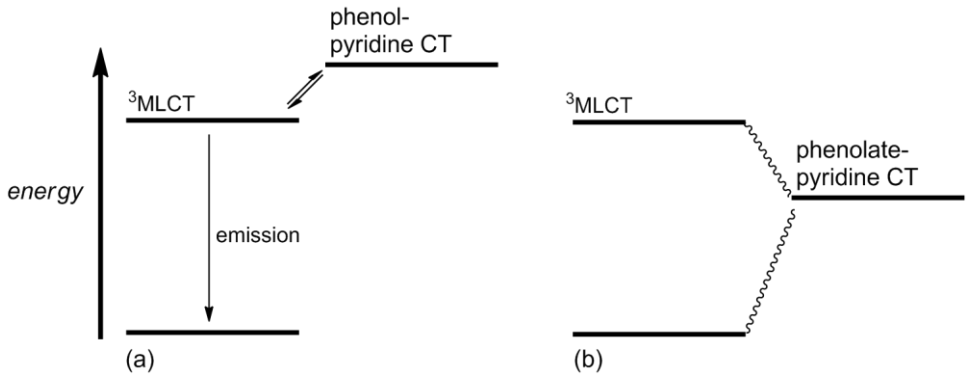

Figure 1.27 Energy-level scheme showing relevant excited states of Re-xy0-PhOH, (a) before and (b) after deprotonation. [Adapted from ref [129]].

1.3.3 Luminescence Switching via Acid-Base Chemistry and its Application As Biosensors

In 2010, a study by Liu and Heinze have found that some platinum(II) and rhenium(I) diimine complexes appended to an acidic phenol group exhibit pH-sensitive behaviour (see **Figure 1.28**).[136,140] The acid-base chemistry of these complexes were investigated and demonstrated that reversible deprotonation of the hydroxy substituted complexes resulted in significant changes in their optical properties.[140]

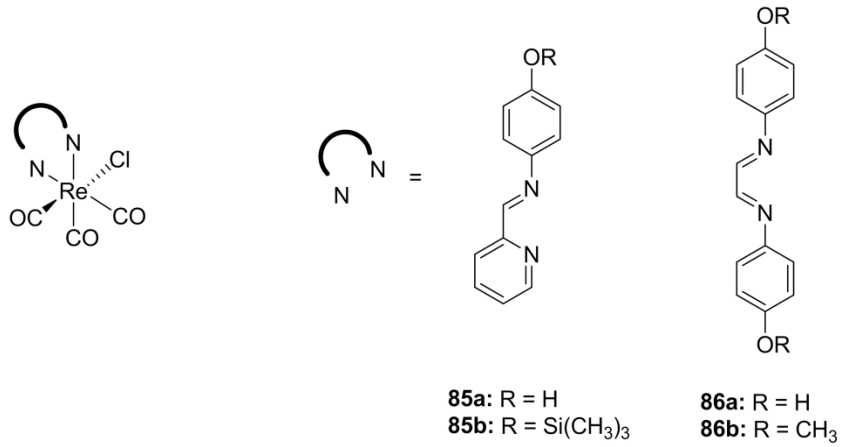

Figure 1.28 Structure of various diimine rhenium(I) complexes studied by Liu and Heinze.[140]

The authors obtained UV-VIS absorbance spectra of the complexes in THF solutions. Complex **85a** and **85b** displayed a structured band around 370-380 nm, whereas **86a** and **86b** shifted around 440 nm. This bathochromic shift can be attributed to an increase in conjugation. In addition, deprotonation of complex **85a** with P_1-*t*Bu (*tert*-butylimino-tris(dimethylamino)phosphorane) results in a significant spectral change, showing a decline of the band at 377 nm and a simultaneous appearance of a new band at 589 nm (**Figure 1.29**). The authors claim that the two isosbestic points indicate an equilibrium between complex **85a** and its conjugate base, and that a reversible behaviour is observed when acetic acid is added to the solution.

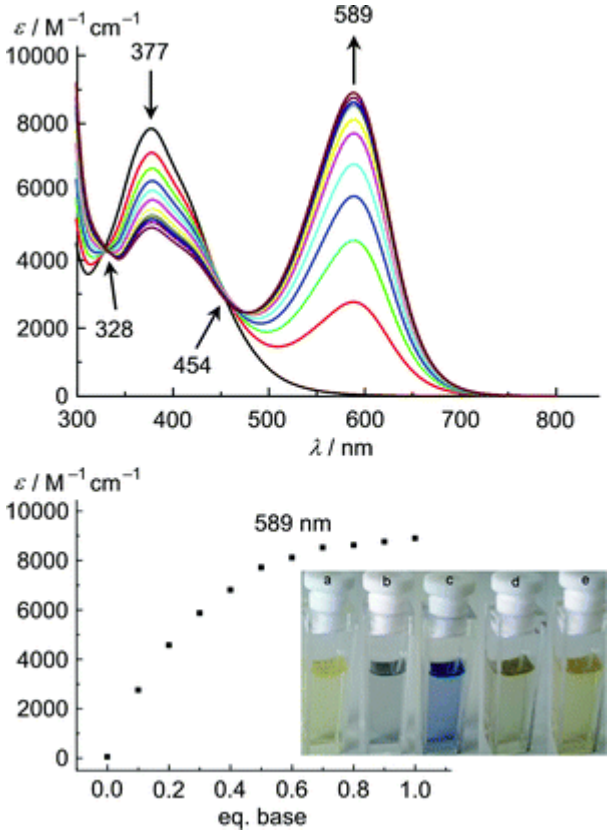

Figure 1.29 Absorption spectra of **85a** in THF upon addition of P_1-*t*Bu base. [Reproduced with permission from Royal Society of Chemistry, ref [136]]

The new absorption band at 589 nm has been attributed to an intraligand π-π* charge transfer from the phenolate substituent to the rhenium(I) diimine unit. The electron accepting strength of the tricarbonyl rhenium core can be seen by changes of the CO stretching frequencies of **85a** upon deprotonation of the OH group, specifically for the totally symmetric A_1 stretch being shifted from 2041 to 2019 cm^{-1} in THF indicating stronger π back-bonding of rhenium(I) to the CO ligands. To conclude, the hydroxyl substituted complexes **85a** and **86a** both feature intermolecular H bonding and deprotonation of these complexes resulted in significant changes in the absorption spectra.

Further investigation of similar rhenium(I) complexes with diimine phenolic ligands (see **Figure 1.30**) by Chanawanno *et al.* looked at how the identity of the halide and the position of the phenol group would affect the pH-dependent UV-VIS absorption properties.[136] Their results showed that upon deprotonation with TMAH (tetramethyl ammonium hydroxide) in THF, the compounds with the phenol situated in the *para*-position exhibited significant changes to their absorption spectra.

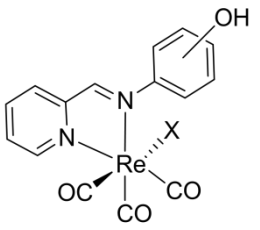

87

a; *p*-OH, X = Cl
b; *m*-OH, X = Cl
c; *o*-OH, X = Cl
d; *p*-OH, X = Br
e; *m*-OH, X = Br
f; *o*-OH, X = Br

Figure 1.30 Structure of rhenium complex studied by Chanawanno *et al*. with various hydroxyl substituents and halides.

Upon treatment of the compound with TMAH, the UV VIS absorption spectrum for *para*-hydroxide compounds **87a** and **87d** showed a gradual decrease in intensity for the band at 380 nm and a growth of a new band at 586 nm; there was a prominent colour change from yellow to blue which was also observed (**Figure 1.31**a). For the case of *ortho*- compounds **87c** and **87f**, there was a less dramatic increase of absorbance intensity and only a slight colour change where the yellow solutions turned darker (**Figure 1.31**b). Whereas the *meta*- compounds **87b** and **87e** showed no change in the absorption spectrum upon addition of base and no colour change observed.

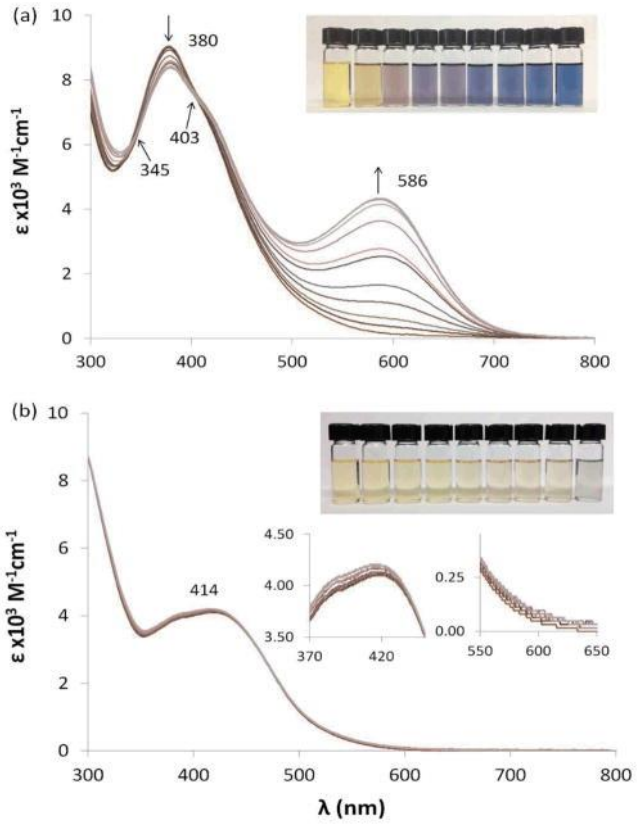

Figure 1.31 UV VIS absorption spectra of **87d** and **87f** [Reproduced with permission from Royal Society of Chemistry, ref [136]].

The authors explain the intense spectral changes from **87a** and **87d** to arise from an extended conjugation system formed upon deprotonation. **Scheme 1.7** illustrates how deprotonation of the *para*- compounds leads to an extended π-system. Whereas, for *ortho*- compounds there is possibly a restricted rotation that prevents an extended conjugated system. Therefore, the relative position of the hydroxide does have an effect on the UV-VIS properties, and the photophysical properties were not dependent on the identity of the halide. These diimine type complexes coordinated to a base-sensitive phenol have been shown to exhibit pH-dependent UV-visible transitions, which can be used for applications in sensing.

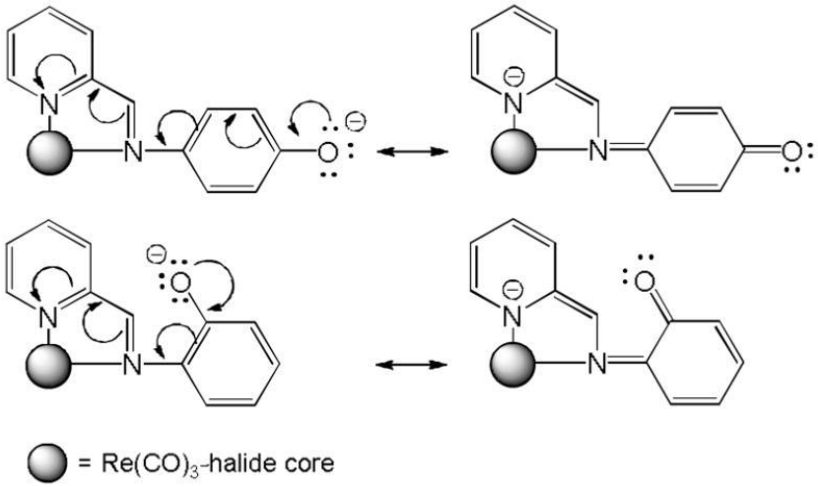

Scheme 1.7 Proposed electron flow of *para*- (top) and *ortho*- (bottom) complexes [reproduced with permission from Royal Society of Chemisty, ref [136]].

Another paper by Herzog, Bronner, Wenger *et al*. reported a rhenium(I) complex to induce intermolecular eT with the phenol (when photoexcited at ^{3}MLCT state). This was simultaneously accompanied by intramolecular proton transfer (PT) between the phenol and pyridine (see **Scheme 1.8**).[141] There was no significant luminescence quenching (in terms of fluorescence intensity or in lifetime decay) observed for PhOH. However, the emission intensity of [Re(**phen**)$(CO)_3$(Py)]$^+$ was significantly quenched in the presence of PhOH-CH_2-py. To conclude, the hydrogen-bonded pyridylphenols have shown to quench the ^{3}MLCT excited state of [Re(**phen**)$(CO)_3$(Py)]$^+$ significantly compared to ordinary reference phenols. This can be explained by the lower oxidation potentials of the pyridylphenols (0.66 V) as opposed to the reference phenols (1.25 V), making them easier to oxidise/donate electrons. The lower oxidation potentials are the result of proton-coupled oxidation processes.

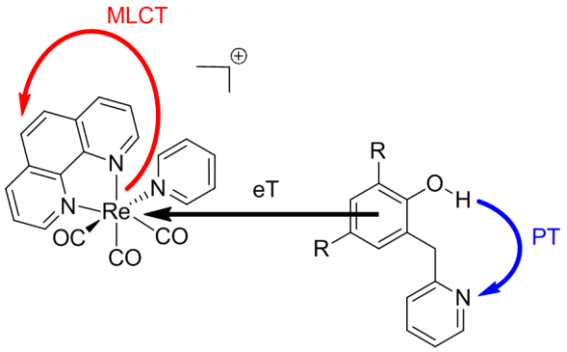

Scheme 1.8 Structure of the rhenium photosensitizer and pyridylphenol quencher, where R = H or ^{t}Bu.

PeT in organometallic systems are commonly seen in complexes with the electron donor on the chelating ligand as well as the ancillary ligand.[128,136,142] In his paper published in 2010, Pope investigated a number of functionalised 4-aminomethylpyridine ligands (L = **88** to **91**, **Figure 1.32** and their coordination to [Re(**N^N**)$(CO)_3$(**L**)] complexes (here referred to as Re-**L**), where **N^N** = 4,4'-dimethyl-2,2'-bipyridine (dmb) or 2,9-dimethyl-1,10-phenanthroline (dmp). The objective was to develop luminescent and responsive probes that are able to target certain metal ions that are important in physiological aspects. The intent of designing the initial ligand **88** was based on a quinoline system known to have affinities for both Zn(II) and Cu(II) cations; while the thiophene-substituted ligands were synthesised to target Hg(II).[143] The various ancillary ligands could participate in a photophysical sense and could also act as a quencher by participating in either energy or electron transfer processes. The authors anticipated that both of these characteristics could be manipulated through the binding of the metal ion to the ancillary ligand.

The complexes Re-**88** and Re-**90** were shown to detect a given cation, such as Cu(II), Zn (II), Hg(II), by monitoring the change in ^{3}MLCT emission lifetimes with and without the presence of the analyte. Specifically, the lifetime of Re(dmp)-**89** changed dramatically with the addition of Cu(II) and Zn(II); initially from 81 ns to 264 ns (bound to Cu(II)) and 215 ns (bound to Zn(II)). However, Re-**91** were unaffected by either electron or energy transfer quenching processes as expected by the reference compound, due to the thiophene units (highlighted in green, **Figure 1.32**) not participating in any ^{3}MLCT quenching processes. In terms of lifetime decay, the Re-**88,** Re-**89** and Re-**90** complexes were shorter compared to the Re-**91** analogues. This would suggest that some sort of quenching mechanism (electron or energy transfer

process) was involved. Additionally, the **89** and **90** ligands induced a greater reduction (about 75%) in lifetime compared to the **91** analogues. With these results accompanied by oxidative potentials, Pope concluded that the quenching process involving **88** are likely to be directed by energy transfer. Whereas the species involving **89** and **90** are more likely to have both electron and energy transfer processes occurring, due to the presence of the OH group (highlighted in blue).

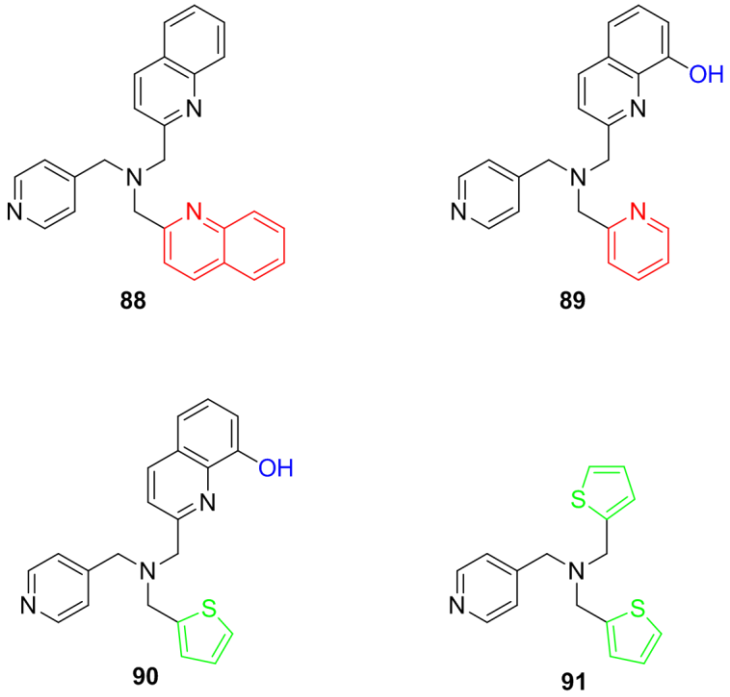

Figure 1.32 Structures of various functionalised 4-aminomethylpyridine ligands which are coordinated to [Re(**N^N**)$(CO)_3$(L)] core, where **N^N** = dmb or dmp.

1.4 Overview of Rhenium(I)-NHC Complexes

While a vast number of luminescent rhenium(I) complexes have been investigated and reported, complexes of the type *fac*-[Re(**N^C**)$(CO)_3$(L)], where **N^C** represents a bidentate *N*-heterocyclic carbene (NHC) ligand, have not been studied extensively. The most studied rhenium-NHC complexes are those of Re(V),[144] Re(VI)[145] and Re(VII)[145]. However, rhenium(I)-NHC complexes have only been recently studied. The first example of rhenium(I)-NHC complexes was reported by Xue *et al.* in 1998, who discovered that the [Re(**N^N**)$(CO)_3$(imidazolyl)]$^+$ complex, where the **N^N** is a diimine ligand (see **Figure 1.33**), exhibits luminescence properties.[146] The

photophysical study suggested that the excited state was of metal-to-ligand charge transfer (MLCT) nature, involving the dimine ligand as π-acceptor.

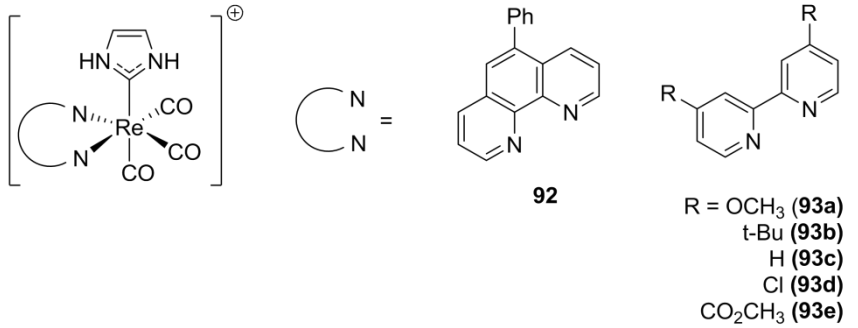

Figure 1.33 The first set of examples of emissive Re(I)-NHC complexes.

In 2011, research was conducted on a new class of *fac*-tricarbonyl rhenium(I)-NHC complexes (see **Figure 1.34**), featuring the NHC ligand as a direct contributor to the luminescent properties of the complex. Casson *et al*. found that the NHC ligands were acting as π-acceptors and that these compounds possessed some blue-shifted emission compared to the class of neutral rhenium(I) tricarbonyl diimine (**bipy** or **phen**) complexes.[147,148] This was due to the overall lower conjugation of the NHC ligand with respect to the diimine.

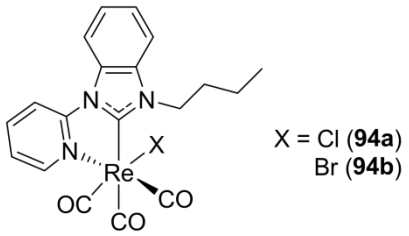

Figure 1.34 Structure of [Re(**N^C**)$(CO)_3$X], where **N^C** is 3-butyl-1-(2′-pyridyl)benzimidazol-2-ylidene).

The room-temperature steady state photoluminescence spectra in diluted dichloromethane solutions of the chloro and bromo [Re(**N^C**)$(CO)_3$X] species consists of a broad and structureless emission profile at 510 and 503 nm, respectively. This blue emission is not commonly seen for neutral rhenium(I) complexes. Additionally, the time resolved data exhibited significant behavioural differences, where the excited state lifetimes were found to be 89 ns (chloro) and 16 ns (bromo). This short excited state lifetime for the bromo derivative was attributed to a factor of lability, illustrating the bromo complex to be easily dissociated in solution compared to the chloro derivative. Another contribution could be that the radiative emission of the complex competes with a photochemical process when

excited to the lowest MLCT state. This was confirmed by recording a successive/continuous steady-state photoluminescence spectra of [Re(**N^C**)$(CO)_3$Br] in air-equilibrated acetonitrile. The structureless emission band at 506 nm slowly disappeared, while the growth of another emission band at 596 nm simultaneously occurred (see **Figure 1.35**). The appearance of the red-shifted band was attributed to a displacement of the bromide being replaced by the acetonitrile solvent. This transformation was also evidenced by the lifetime decays, comparing the acetonitrile sample of [Re(**N^C**)$(CO)_3$Br] before and after multiple emission scans; where the initial mono-exponential lifetime turned into a bi-exponential fit.

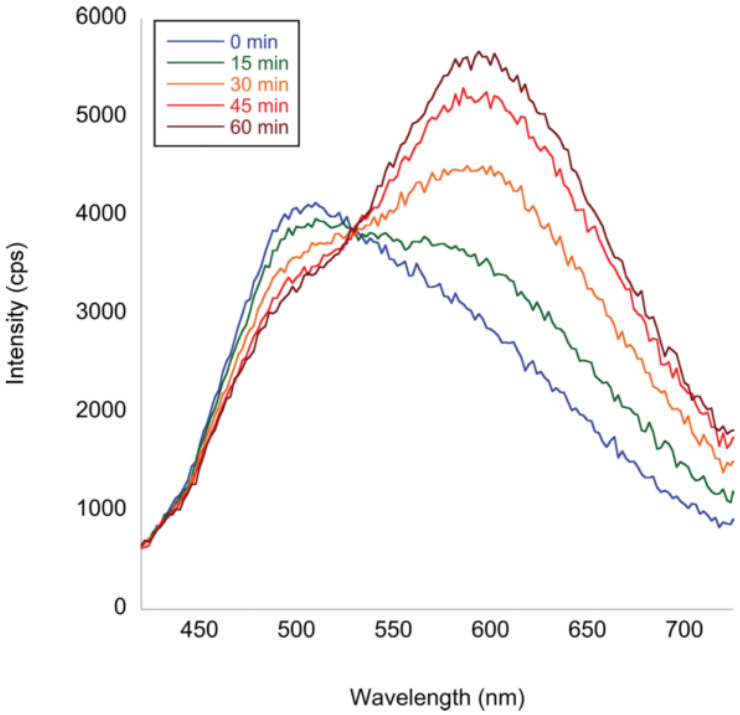

Figure 1.35 Multiple emission spectra of a solution of [Re(**N^C**)$(CO)_3$X] in air-equilibrated acetonitrile, excitation at 365 nm. [Reproduced from ref [147]].

Later in 2013, another paper was published by the same research group which investigated the series of complexes [Re(**N^C**)$(CO)_3$X] further by variation of the R-substituents on the N3 atom of the central imidazole frame (see **Figure 1.36**).[149] It was found that the synthesised rhenium(I)-NHC complexes all exhibited luminescence emission from ^{3}MLCT excited states. In addition, the different variations of R-substituents (both alkyl and aryl in nature) on the NHC ligand did not have a major influence on the electronics or photophysical properties.[149] The authors concluded that the relative energy of the emitting states appeared to be strongly influenced by the substituent on the N1 atom of the imidazole ring, i.e. the various

conjugated N-donor groups such as pyridyl (**95**), pyrimidyl (**96**) and quinoxyl (**97**). In terms of emission spectroscopy, the pyridyl complexes were more blue-shifted (λ_{em} = 515-520 nm) in comparison to the more electron deficient pyrimidyl complexes (λ_{em} = 570-580 nm).

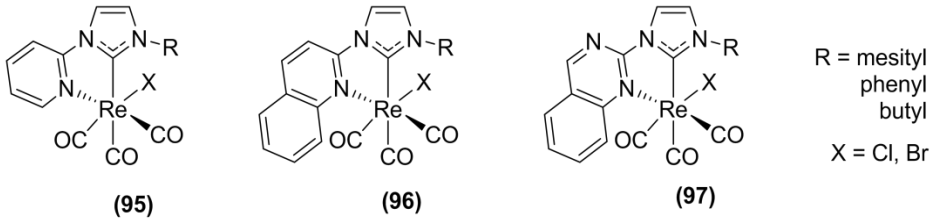

(95) **(96)** **(97)**

Figure 1.36 Rhenium(I)-NHC complexes with varying N-donor ligands and R substituents.

In 2014, an extended exploration on these rhenium(I)-NHC complexes provided a primary photochemical reaction mechanism.[148] Temperature-dependent photochemical experiments illustrated that CO dissociation occurred at very low temperatures (233 K), which suggested that the photochemical mechanism derived from excited states of MLCT nature rather than thermally accessible LF state. The authors have also managed to categorise the rhenium(I)-NHC into photoactive and photostable groups; the pyridyl complexes were found to be photoactive, whereas the pyrimidyl and quinoxyl complexes were photostable.

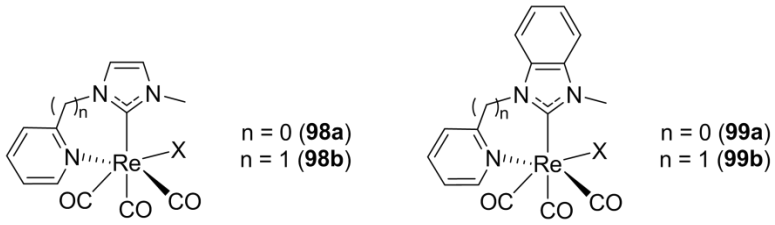

Figure 1.37 Structure of rhenium(I) tricarbonyl with imidazole and benzimidazole rings.

In 2012, Li and co-workers published their work on rhenium(I) tricarbonyl complexes with pyridine-functionalised NHCs (see **Figure 1.37**).[150] They concluded that complexes **98b** and **99b** (with methylene linkers) have very weak emission, whilst complexes **98a** and **99a** showed interesting photoluminescence properties. This was a result of the difference in molecular structures; complexes **98a** and **99a** are quite rigid due to the imidazole and benzimidazole ring positioned coplanar to the pyridine ring. Whereas complexes **98b** and **99b** have a more flexible structure due to the presence of the methylene bridge.

1.5 Objectives of Research Project

The aforementioned rhenium(I) NHC type complexes have been identified to possess certain photochemical properties. With this knowledge in mind, this research attempts to control the photochemistry *via* a process of electron transfer (eT). As this is a new area in the field of rhenium chemistry, initial studies involved complexes that are known to have no photochemical response, i.e. rhenium(I) diimine complexes.

Chapter 2 explores the synthesis, structural and photophysical properties of rhenium(I) **phen** tetrazolato complexes conjugated to a phenol. The hydroxy group being acidic should be sensitive in basic conditions. However, photophysical analysis of the phenolic complexes did not show any response under the experimental conditions reported. The methoxy group was also introduced and synthesised to be used as a reference compound, however no significant differences between the hydroxy and methoxy groups were found.

This investigation will expand on previous photophysical and structure-property relationships of rhenium(I) tetrazolato complexes. Chapter 3 examines rhenium(I) **phen** tetrazolato complexes attached to amino acid methyl esters, such as tryptophan and phenylalanine. Based on reported literature by Blanco-Rodriguez *et al,* the complex attached to the tryptophan (**Trp**) was expected to undergo photoinduced electron transfer (PeT) to the rhenium metal centre, resulting in emission quenching and reduced lifetime as well as quantum yield. The phenylalanine (**Phe**) analogue was used as a reference compound to compare the effects of the quenching.

Apart from the series of rhenium(I) diimine complexes, the purpose of this research was to perform a thorough exploration on rhenium(I) NHC complexes, which have a potential to provide therapeutic benefits as photoinduced CO releasing molecules. Their photochemical activity is important towards their application as photoCORMs. Therefore it is vital that the understanding of both the photophysics and photochemistry of these rhenium(I) NHC complexes be developed. This was achieved by synthesising and characterising a library of neutral and cationic rhenium(I) complexes attached to varying ancillary ligands. Chapter 4 examines a series of cationic rhenium(I) NHC complexes attached to various pyridyl ancillary

ligands, whilst Chapter 5 emphasises on manipulating substituents on the NHC chelating ligand as neutral complexes.

Finally, Chapter 6 focusses on the biological investigation of the synthesised rhenium(I)-**phen** complexes described in Chapter 3. The complexes were tested in various malignant and healthy cell lines, in view of their imaging and sensing properties.

Chapter 2

Phenol-Phenolate Tetrazolato Rhenium(I) Complexes

2.1 Abstract

The synthesis, structural and photophysical characterisation of novel rhenium(I) diimine tricarbonyl complexes will be disussed herein. This group of complexes are based on the general formula [Re(**phen**)$(CO)_3$(**Tz**PhOR)], where **phen** is 1,10-phenanothroline and **Tz**PhOR is a phenyltetrazole substituted with R being either a hydroxy or methoxy group (see **Figure 2.1**). In order to determine whether the hydroxy complexes were sensitive to photophysical changes upon deprotonation, the complexes were treated with a base such as triethylamine (TEA) and potassium *tert*-butoxide (K^tOBu). Both the hydroxy and methoxy complexes showed similar photophysical properties. The substituent groups were also synthesised in both *para* and *meta* positions to explore the variable "electron hopping" distances and how they would affect the potential electron transfer pathway.

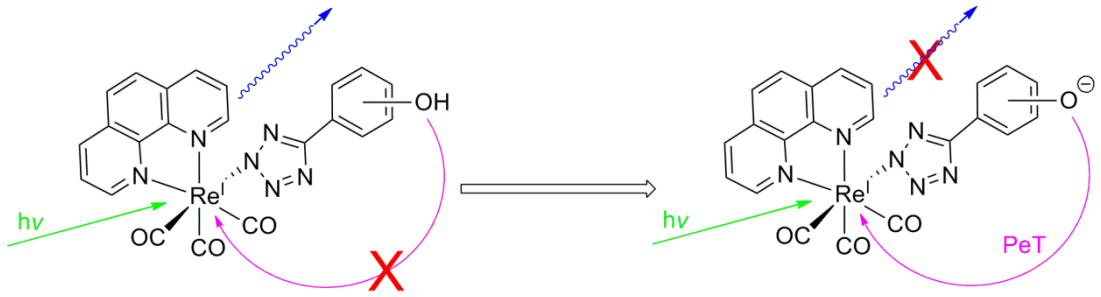

Figure 2.1 Proposed mechanism for PeT of phenolic rhenium(I) complex.

2.2 Introduction

Phenol groups are capable of introducing PeT through a redox process.[128] So far, there have been quite a few examples of pH-dependent complexes carrying phenolic PeT groups based on such organic dyes. Only recently, increasing interest has been shifted toward electron transfer of photoexcited molecules or metal complexes.[131] These examples have been discussed briefly in the main introduction.

In this chapter, the pH dependency of phenol-substituted tetrazolato rhenium(I) complexes (**Figure 2.2**) will be discussed. The methoxy analogues were used as a reference incapable of exhibiting any pH-dependent electron transfer for comparison. The investigation will focus mainly on the photophysical properties (particularly emission, excited lifetime decay and quantum yield) and will also cover the effects of the different position of the phenol group, being *para*- and *meta*- substituted. Deprotonation experiments (where any changes through addition of a base were monitored by absorption, emission and lifetime measurements) were conducted to investigate any electron transfer effect occurring on the phenol-phenolate complexes. Furthermore, the addition of acid on the deprotonated complexes was conducted to identify any reversibility trends.

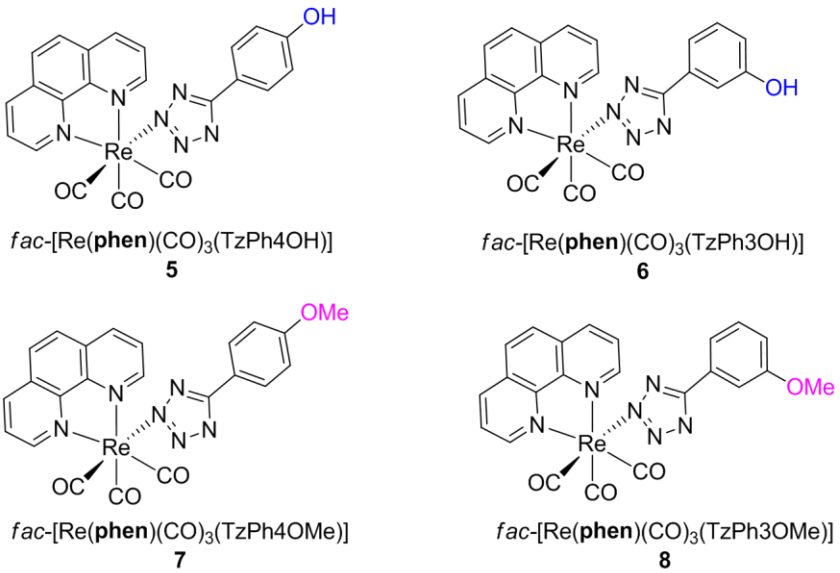

fac-[Re(**phen**)(CO)$_3$(TzPh4OH)] **5**

fac-[Re(**phen**)(CO)$_3$(TzPh3OH)] **6**

fac-[Re(**phen**)(CO)$_3$(TzPh4OMe)] **7**

fac-[Re(**phen**)(CO)$_3$(TzPh3OMe)] **8**

Figure 2.2 Structures of target rhenium(I) tetrazolato complexes prepared in this study.

2.3 Synthesis of the Ligands

The *para*- and *meta*- hydroxybenzonitrile precursors were commercially available and used without further purification to synthesise the corresponding tetrazole ligands (**Scheme 2.1**), following the well-established method by Koguro.[151] On the other hand, the *para*- and *meta*- methoxybenzonitrile precursors (**102** and **103**) were prepared by methylation of the corresponding hydroxybenzonitrile precursors (**101**) with iodomethane and potassium carbonate, heated under reflux conditions in acetonitrile (**Scheme 2.1**).[152] This was then followed by the synthesis of the **Tz**PhOH and **Tz**PhOMe tetrazole molecules, which were achieved by 1,3-dipolar cycloaddition of sodium azide to the corresponding nitrile-containing substrates, according to a previously published methodology.[151]

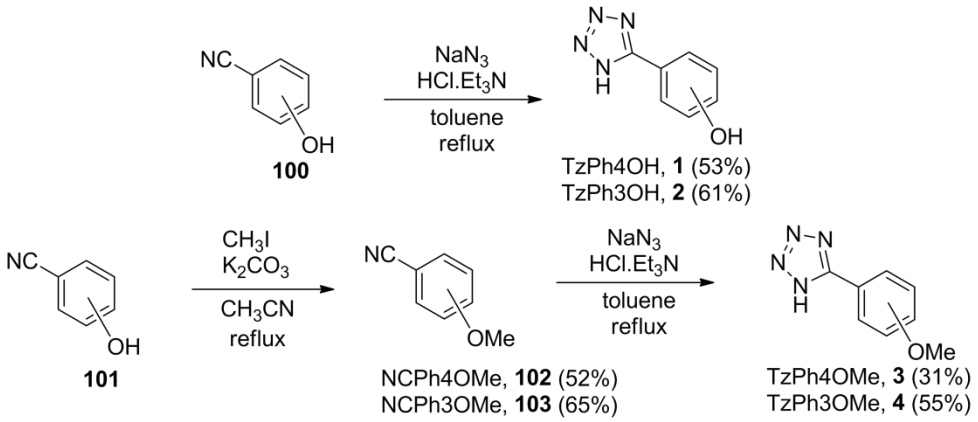

Scheme 2.1 Reaction scheme for preparation of tetrazole compounds, phenol-substituted (top) and methoxy-substituted (bottom).

The formation of the substituted tetrazoles was indicatedby analysis *via* IR spectroscopy, where the NH and aromatic C=N stretching peaks were observed at 3100 and 1600 cm^{-1} respectively. In addition, the absence of the sharp nitrile C≡N band around 2200 cm^{-1} indicated the disappearance of the starting material.

Analysis by ^{13}C NMR spectroscopy shows the tetrazolic carbon (Ct) signal to be around 158-160 ppm, confirming the formation of the tetrazole. Butler *et al*. have performed thorough NMR investigation on the tautomerism of substituted 5-aryltetrazoles and have distinguished between two tautomeric forms where the tetrazolic proton resides on either the N1 or N2 atom (see **Scheme 2.2**).[153] The chemical shifts ranging from 152-156 ppm indicate a dominant N1 tautomer, whereas values ranging from 162-165 ppm are attributed to the N2 tautomer.

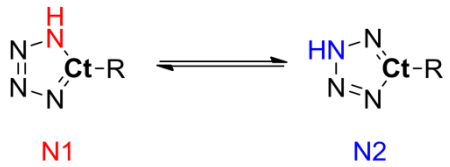

Scheme 2.2 Chemical structures showing the N1 and N2 tautomers of tetrazoles.

2.4 Synthesis of the Complexes

To prepare the neutral rhenium(I) complexes shown in **Figure 2.2**, the halogen on the precursor *fac*-[Re(**phen**)$(CO)_3$Cl] was directly substituted with the corresponding tetrazole ligand after deprotonation using triethylamine in acetonitrile at reflux. In contrast, previously reported procedures use solvato[154] or triflato[155] rhenium precursors, which have not been implemented in this study due to the use of light-sensitive silver salts to remove the halogen ligand from the rhenium centre. Alternatively, the use of microwave irradiation for a few hours at 130 °C using the same reagents and solvents also afforded the product in good yield. Following this reaction, the rhenium(I) complexes were isolated by flash column chromatography. **Scheme 2.3** shows the different reaction conditions applied to synthesise the complexes. Microwave irradiation was advantageous due to shorter reaction times and comparable product yield. In both cases, unreacted starting material was also retrieved by flash chromatography.

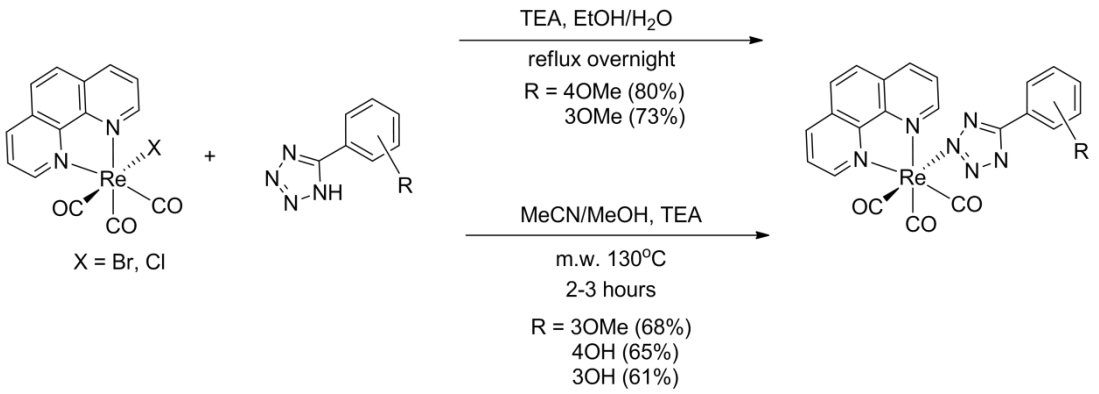

Scheme 2.3 Reaction scheme for preparation of rhenium(I) tetrazolato complexes under conventional conditions (top) and microwave conditions (bottom).

2.4.1 Spectroscopic Characterisation

Formation of the tetrazolato-rhenium(I) complexes were confirmed through ^{1}H NMR, ^{13}C NMR, infrared spectroscopy, elemental analysis, and single crystal X-ray

diffraction, by means of the experimental data in agreement with the proposed structures. Analysis of IR spectra revealed that all the complexes exhibit three characteristic carbonyl stretching bands between 2030-1860 cm^{-1}, showing the totally symmetric in-phase stretching A′(1), the totally symmetric out-of-phase stretching A′(2) and the asymmetric stretching A″. The values of the recorded stretching frequencies are summarised in **Table 2.1**.

Table 2.1 Stretching frequencies (cm^{-1}) of the CO bands of the tetrazolato Re(I) complexes.

Complex	CO A′ (1)	CO A′ (2)/A″
fac-[Re(**phen**)$(CO)_3$Cl] [a]	2014	1923, 1885
fac-[Re(**phen**)$(CO)_3$(**Tz**Ph)] [a]	2019	1909, 1881
fac-[Re(**phen**)$(CO)_3$(**Tz**Ph4OH)] (**5**)	2024	1931, 1893
fac-[Re(**phen**)$(CO)_3$(**Tz**Ph3OH)] (**6**)	2022	1898 [b]
fac-[Re(**phen**)$(CO)_3$(**Tz**Ph4OMe)] (**7**)	2016	1916, 1886
fac-[Re(**phen**)$(CO)_3$(**Tz**Ph3OMe)] (**8**)	2021	1930, 1877

[a] Previously published data[154]; [b] peaks are superimposed into a single broad band

The relative frequencies of the carbonyl bands shown in the infrared spectra (**Table 2.1**) reflect the electron density on the rhenium centre and were consistent with the neutral nature of the complexes, as seen in the literature for [Re(**phen**)$(CO)_3$(**Tz**Ph)], where **Tz**Ph is 5-phenyltetrazole ligand.[154] The tetrazole being a π-acceptor ligand reduced the electron density on the metal centre, which can be observed by the higher frequency of the carbonyl band with respect to the halogenated precursor. All the complexes showed three intense CO bands which was indicative of a *facial* arrangement of the carbonyl ligands, as expected from octahedral complexes with C_s symmetry. Notably, the *facial* and *meriodional* conformations of the rhenium complexes cannot be completely distinguished by the number of IR active CO stretches. However, the value of the CO stretching frequency can distinguish the two species, where higher wavenumbers were observed for *mer*- isomer compared to the *fac*- isomer.[85] In addition, the *trans* effect of CO ligands prevented the *mer*- isomer from forming (under thermal conditions).[156]

The structure of the complexes were distinguished better by ^{1}H NMR spectroscopy, whereby the diimine ligand (with CO ligands in a *facial* arrangement) had a mirror plane symmetry showing only four signals for the equivalent protons.[85] Contrarily, if

the CO ligands were in a *meriodional* arrangement, there will be lack of symmetry and the protons representing the diimine ligand will show eight signals in the proton NMR spectrum.

The ^{1}H NMR and ^{13}C NMR spectra for all complexes shown in **Figure 2.2** were measured in deuterated DMSO solutions. **Table 2.2** reports the chemical shift values for $H_{para,}$ H_{meta}, H_{ortho} of the phenyl, respective R substituents and the Ct of the tetrazole ring. The broad singlet (with integration corresponding to one H atom) found around 9.39-9.51 ppm in the ^{1}H NMR spectrum was indicative of the phenolic proton, whereas the sharp singlet (integration corresponding to three H atoms) found around 3.65-3.69 ppm was indicative of the methyl protons. The four signals found between 8.10-9.60 ppm were typical for phenanthroline protons (showing the symmetric environment of the diimine ligand in the *facial* isomer), consistent with previous studies.[6,81,154] In the ^{13}C NMR, typical Re-tetrazole coordination showed the tetrazolic carbon (Ct) peak around 160 ppm (which indicates an N2 linkage isomeric form), also consistent with previous studies.[6,154] In addition, the fairly weak peaks representing the three carbonyl ligands were found in the 190-200 ppm region.

Table 2.2 Selected NMR chemical shift data (ppm) of the Re(I) complexes in DMSO-d_6 showing the substituted phenyltetrazole peaks.

Complex	H_{para}	H_{meta}	H_{ortho}	R groups	Ct
5	-	7.37-7.27	6.70-6.59	9.51 (OH)	162.3
6	6.79	7.05	6.99, 6.91	9.39 (OH)	162.3
7	-	7.42	6.84	3.69 (OMe)	162.1
8	6.79	7.17	7.08	3.65 (OMe)	n.d.

[a]Previously published data[154]; n.d. not detectable (due to solubility issues)

2.5 X-ray Crystallography

Single crystals were obtained for all the neutral rhenium(I) tetrazolato complexes, except the [Re(**phen**)$(CO)_3$(**Tz**Ph4OH)] (**5**) complex as the crystals that were grown did not adequately diffract. Analysis of the X-ray crystallography data illustrated formation of the Re-N2 linkage isomer in the solid state, in agreement with NMR spectroscopy data and consistent with previously studied rhenium(I) tetrazolato

complexes by Werrett.[154,157] The three CO ligands were arranged in the *facial* conformation, in agreement with IR data and consistent with other diimine rhenium(I) tricarbonyl complexes. The crystal structures for [Re(**phen**)$(CO)_3$(**Tz**Ph3OH)] (**6**), [Re(**phen**)$(CO)_3$(**Tz**Ph4OMe)] (**7**) and [Re(**phen**)$(CO)_3$(**Tz**Ph3OMe)] (**8**) are shown in **Figure 2.3** and **Figure 2.5**, respectively. Additionally, the table of bond lengths and angles for the complexes are presented in Appendix A.1.

[Re(**phen**)$(CO)_3$(**Tz**Ph3OH)] (**6**) crystallised in the triclinic $P\bar{1}$ space group with the rhenium(I) metal centre in a slightly distorted octahedral geometry and coordinated *via* N2 atom of the tetrazole (**Figure 2.3**). There also seems to be some H-bonding interactions (**Figure 2.4**) between sets of molecules, specifically at the N3 atom on the tetrazole ring and OH on the phenol ring. The distance between the OH (phenol, donor) and N (tetrazole, acceptor) was found to be 2.888 Å. This intermolecular H-bonding played a role in the crystal packing, which can be seen in **Figure 2.4**.

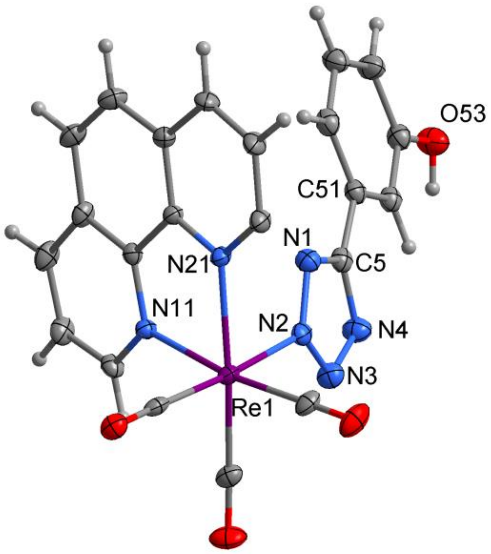

Figure 2.3 Crystal structure of *fac*-[Re(**phen**)$(CO)_3$(**Tz**Ph3OH)] (**6**) where thermal ellipsoids have been drawn at 50% probability.

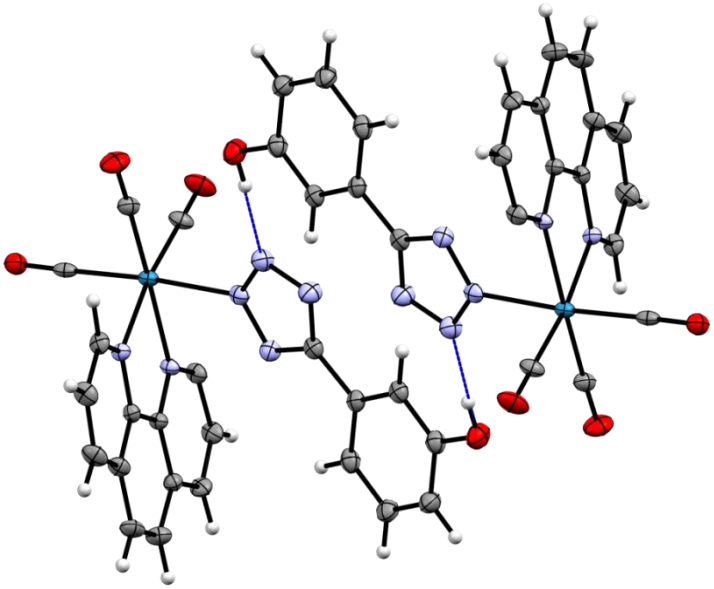

Figure 2.4 Crystal structure of *fac*-[Re(**phen**)$(CO)_3$(**Tz**Ph3OH)] (**6**) showing intermolecular H-bonding interaction (blue dashed line) between the complexes.

Crystal structures of both *para*- and *meta*- methoxy derivatives [Re(**phen**)$(CO)_3$(**Tz**Ph4OMe)] (**7**) and [Re(**phen**)$(CO)_3$(**Tz**Ph3OMe)] (**8**) were obtained and shown in **Figure 2.5**. Both complexes crystallised in the monoclinic $P2_1/n$ space group with slightly distorted octahedral geometry confirmed. In addition, Re-N2 coordination relates to extended interannular conjugation and an extended coplanar arrangement of the aryl and tetrazole rings.[158] The deviation from coplanarity were measured to be 8.63° and 10.48° for [Re(**phen**)$(CO)_3$(**Tz**Ph4OMe)] (**7**) and [Re(**phen**)$(CO)_3$(**Tz**Ph3OMe)] (**8**) respectively.

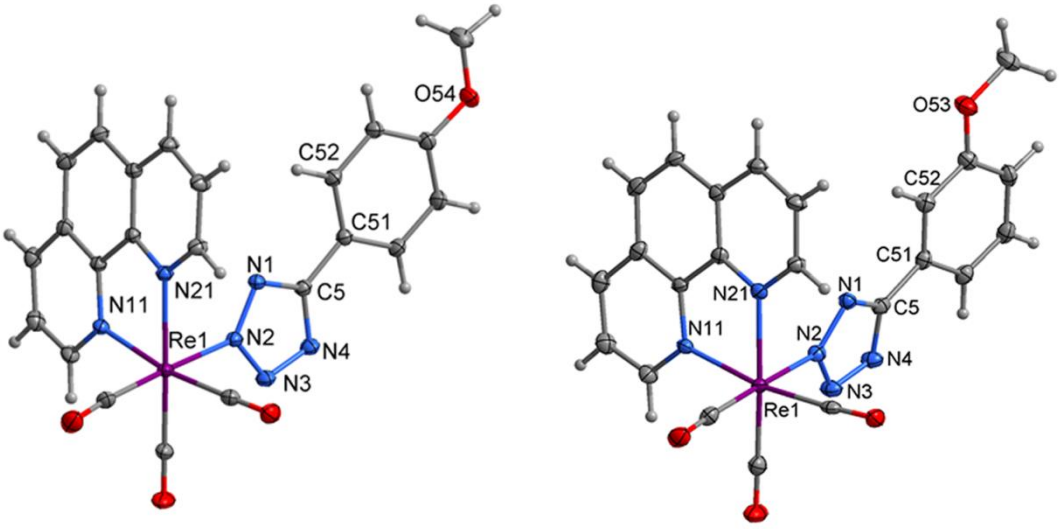

Figure 2.5 Crystal structure of *fac*-[Re(**phen**)$(CO)_3$(**Tz**Ph4OMe)] (**7**), left and *fac*-[Re(**phen**)$(CO)_3$(**Tz**Ph3OMe)] (**8**), right where thermal ellipsoids have been drawn at 50% probability.

2.6 Photophysical Investigation

The photophysical properties of the complexes were studied in acetonitrile solutions at room temperature. A summary of the absorption and emission data is provided in **Table 2.3**. In general, the UV-VIS absorption profiles (**Figure 2.6**) were found to be very similar for all of the complexes, showing an intense higher energy band in the 250-300 nm region which tails off into a lower energy band in the 300-400 nm region. The higher energy band was attributed to intraligand (IL) π- π^* transitions localised on the **phen** and tetrazole ligands, while the lower energy band was attributed to metal-to-ligand charge transfer (MLCT) transitions that involves the 5d orbitals of the rhenium centre and the accessible π^* orbitals of the coordinated aromatic ligands.[159] These MLCT (rhenium to diimine) transitions are mixed with ligand-to-ligand charge transfer LLCT (from tetrazolato to diimine) transitions to give an MLLCT state. This has been confirmed with previous studies by Werrett, where computational DFT calculations have shown the nature of these bands.[154]

Table 2.3 Photophysical properties of the tetrazolato Re(I) complexes from diluted acetonitrile solutions (*ca*. 10^{-5} M).

Complex	λ_{abs} (nm) [10^4 ε, $M^{-1}cm^{-1}$]	λ_{em} (nm)	τ (ns)[a]	τ (ns)[b]	Φ [a, c] (±0.015)	Φ [b, c] (±0.015)
5	259 (3.74), 365 (0.30)	600	86	202	0.0122	0.0641
6	257 (3.27), 367 (0.26)	604	87	206	0.0103	0.0419
7	259 (4.20), 364 (0.35)	613	85	212	0.0107	0.0456
8	257 (3.50), 369 (0.37)	608	100	299	0.0104	0.0363

[a] air equilibrated samples, [b] degassed samples, [c] quantum yield Φ measured against air equilibrated quinine sulfate (in 1M H_2SO_4).

Table 2.4 shows the radiative and non-radiative decay constants for the prepared neutral rhenium(I) complexes. The values obtained for the reported rhenium(I) complexes are within the range and consistent to similar rhenium(I) tetrazolato complexes.[160,161] Generally, a higher k_{nr} is directly related to lower quantum yields and shorter lifetime decays.[162] Refer to equations provided in introduction section 1.1.2 for calculations of decay rate constants.

Table 2.4 Radiative (k_r) and non-radiative decay (k_{nr}) constants for the Re(I) tetrazolato complexes calculated for deaerated acetonitrile solutions (*ca*. 10^{-5} M).

Complex	k_r (10^5 s^{-1})	k_{nr} (10^6 s^{-1})
5	3.17	4.63
6	2.03	4.65
7	2.15	4.50
8	1.21	3.22

Following excitation at 360 nm, each of the neutral tetrazolato rhenium(I) complexes exhibited a broad and structureless emission band from an excited state of ^{3}MLLCT character, with an emission maximum around 600 nm. This orange-red emission was quite typical of tricarbonyl rhenium(I) diimine complexes, where previously reported analogues emitted around 580-590 nm. In addition, the entire series of complexes exhibited a mono-exponential decay in aerated acetonitrile solution at room temperature, with lifetimes around 86-100 ns. When compared to an unsubstituted tetrazolato complex such as [Re(**phen**)$(CO)_3$(**Tz**Ph)], having a lifetime of 92 ns in acetonitrile, the values were quite similar and fell within range. On the other hand, the excited state lifetime decay measured for [Re(**phen**)$(CO)_3$(**Tz**Ph4OMe)] and [Re(**phen**)$(CO)_3$(**Tz**Ph3OMe)] in dichloromethane were 232 and 258 ns respectively. These values were also quite similar when compared to other reported rhenium-tetrazolato complexes such as [Re(**phen**)$(CO)_3$(**Tz**Ph)], [Re(**phen**)$(CO)_3$(Tbdz)] and [Re(**phen**)$(CO)_3$(Tcya)] (where Tbdz = 4-(1H-tetrazol-5-yl)-benzaldehyde and Tcya = 4-(1H-tetrazol-5-yl)-cyanobenzene) in dichloromethane which have a lifetime ranging around 268-382 ns.[161]

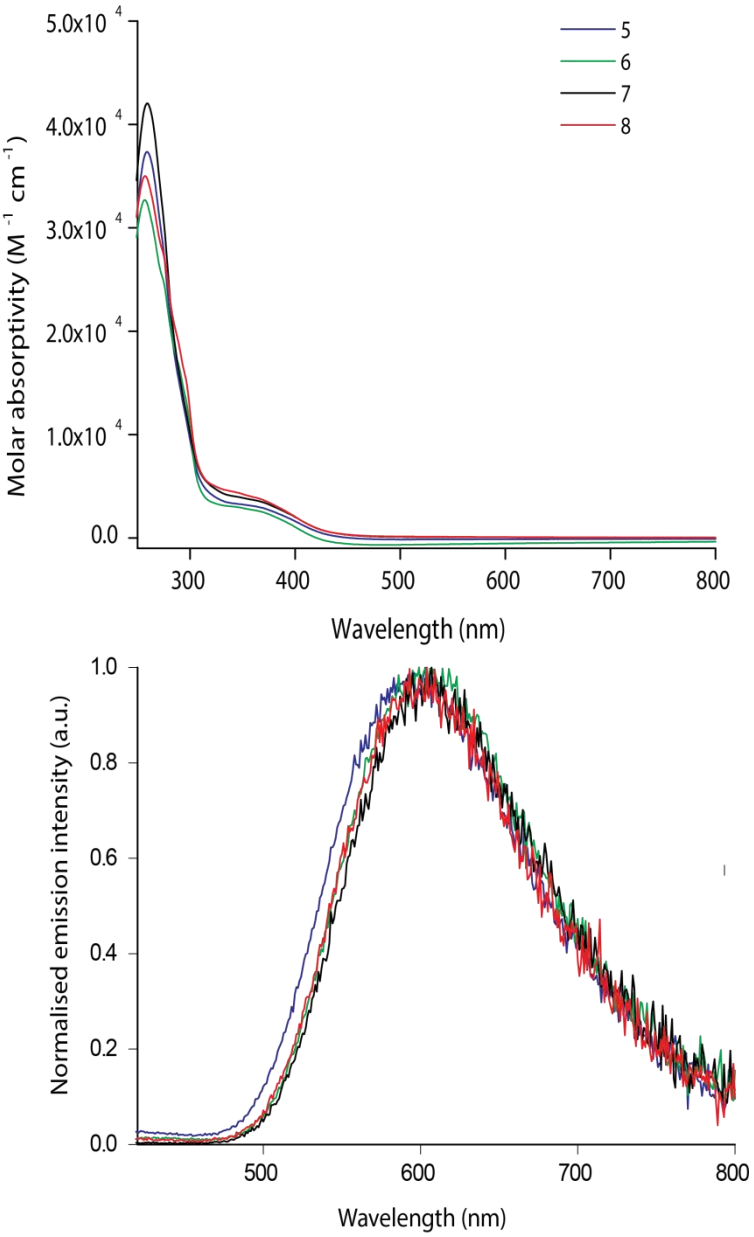

Figure 2.6 Absorption (top) and emission (bottom) profiles for rhenium(I) tetrazolato complexes **5-8** in acetonitrile solution (*ca*. 10^{-5} M). Excitation occurred at 350 nm.

Based on the collective data, we can conclude that the photophysical trends of the electron donating groups (-OMe, -OH) substituted on the phenyltetrazole presented in this chapter are similar (in terms of emission and excite state lifetime decay) to those of the electron withdrawing groups (-CHO, -CN) already reported in the literature.[161] Overall, the substituents on the phenyltetrazole moiety do not greatly affect the electron density of the rhenium centre and hence the energy of the MLLCT state is unchanged.

The excited state lifetime and quantum yield values for the rhenium(I) complexes shown in **Table 2.3** increased (almost three times) upon degassing the solutions. This

evidence supports that emission originates from a state of triplet multiplicity, as the complexes (measured in aerated solution) show sensitivity to molecular oxygen. This was illustrated by the removal of oxygen (by degassing with N_2) which reduces the probability of emission quenching through energy transfer from the triplet excited state of the complex to the triplet ground state of oxygen.[163,164]

Table 2.5 Photophysical properties of the tetrazolato Re(I) complexes from diluted DCM solutions (*ca*. 10^{-5} M) measured at 77 K temperature.

Complex	λ_{em} (nm)	τ (μs)[a]
5	545	8.50
6	551	5.29
7	537	10.64 (67%), 3.88 (33%)
8	540	8.46

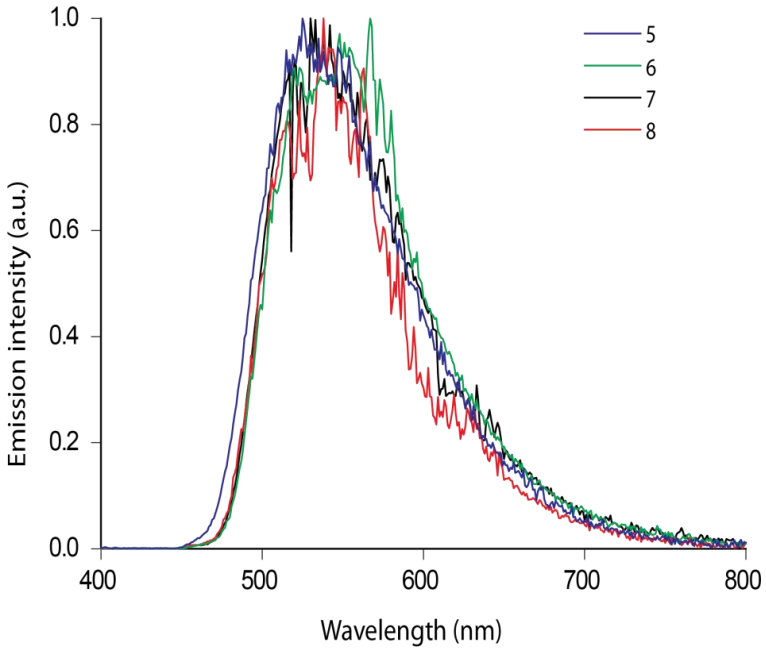

Figure 2.7 Emission profiles for substituted rhenium(I) tetrazolato complexes **5-8** at 77 K. Excitation occurred at 350 nm.

The luminescence of the complexes were also measured in frozen matrix (77 K) and illustrated in **Table 2.5**. Upon cooling from room temperature to 77 K, the emission profiles (**Figure 2.7**) for all complexes were blue shifted by about 50 nm, compared to room temperature measurements. This is due to the destabilisation of the triplet CT state where the solvent is frozen and molecules cannot rearrange to a stable form; commonly referred to as a rigidochromic effect. In addition, the excited state lifetime

decay for these complexes had increased almost ten-fold going from room temperature to 77 K. The anomaly of the bi-exponential decay detected for [Re(**phen**)(CO)$_3$(**Tz**Ph4OMe)] (**7**) has been observed in other studies of similar metal complexes.[154,165] This effect could be attributed to the presence of chemically identical species with different structural arrangements co-existing in the frozen matrix.

2.6.1 Deprotonation Studies with Triethylamine

The primary objective was to study the changes in the photophysical properties of the phenol-phenolate substituents upon deprotonation with a base. Triethylamine (TEA) was initially used as the base (pKa = 10.75), being commercially available and a commonly used reagent. Analysis by ^{1}H NMR spectroscopy was utilised to detect any changes that occurred by deprotonation of the phenol substituent on the phenyltetrazole ring. One equivalent of TEA was added to the rhenium-phenol derivatives in deuterated CD_3CN solution. The ^{1}H NMR spectrum of [Re(**phen**)(CO)$_3$(**Tz**Ph4OH)] (**5**) (**Figure 2.8**) showed an absence of the broad singlet peak (corresponding to the phenolic proton) at 7.00 ppm, however no change in chemical shifts was seen for the peaks corresponding to the tetrazole.

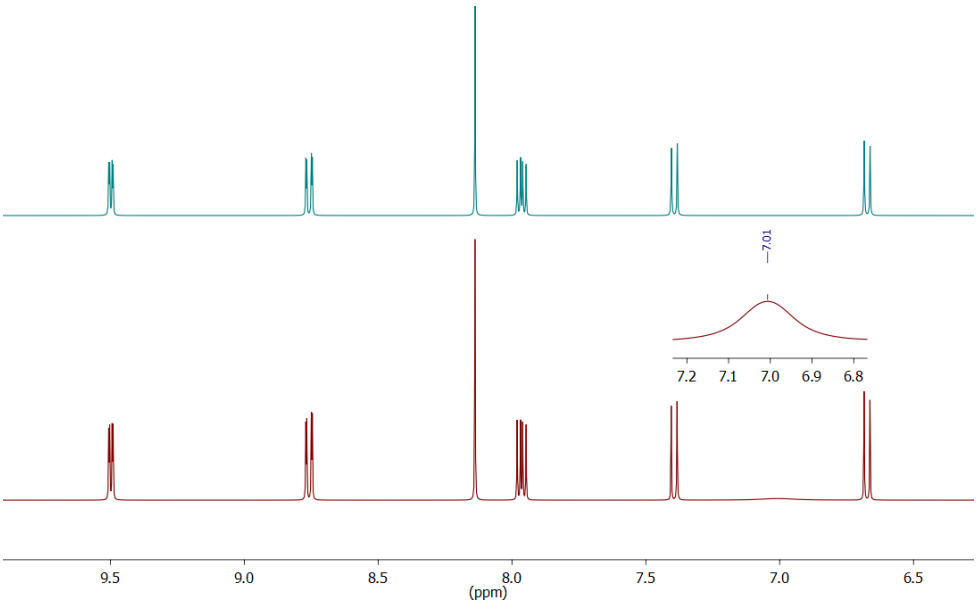

Figure 2.8 Comparison of ^{1}H NMR spectra obtained from CD_3CN solutions containing complex **5** (bottom, red) with addition of TEA (top, blue) and inset showing exchange of proton for deuterium.

Further investigation was pursued by analysing the absorption and emission spectra upon addition of TEA as a base. Aliquots of TEA (0.001 M, 0.5-2.0 eq.) in MeCN were sequentially added to a MeCN solution of rhenium complex. The absorption and emission profiles (Figure 2.9) showed no evident change, which further confirms what was observed by ^{1}H NMR analysis. There was also no significant changes shown in the lifetime decay rates of the deprotonated complexes, see Table 2.6 for summarised data. All deprotonated complexes showed emission around *ca*. 600 nm, which was identical to the initial neutral complex. It was speculated that using TEA as a base for this system was not strong enough to deprotonate the phenolic proton on the phenyltetrazole ring. Thus, a different base was utilised and tested following a similar procedure, except with methanol as a solvent.

Table 2.6 Photophysical data of Re(I) complexes upon addition of TEA in MeCN solutions (*ca*. 10^{-5} M).

Complex	**Initial complex**		**Addition of TEA (1 eq)**	
	λ_{em} (nm)	τ (ns)	λ_{em} (nm)	τ (ns)
5	607	86	600	79
6	604	88	600	78
7	613	85	610	82
8	608	100	595	87

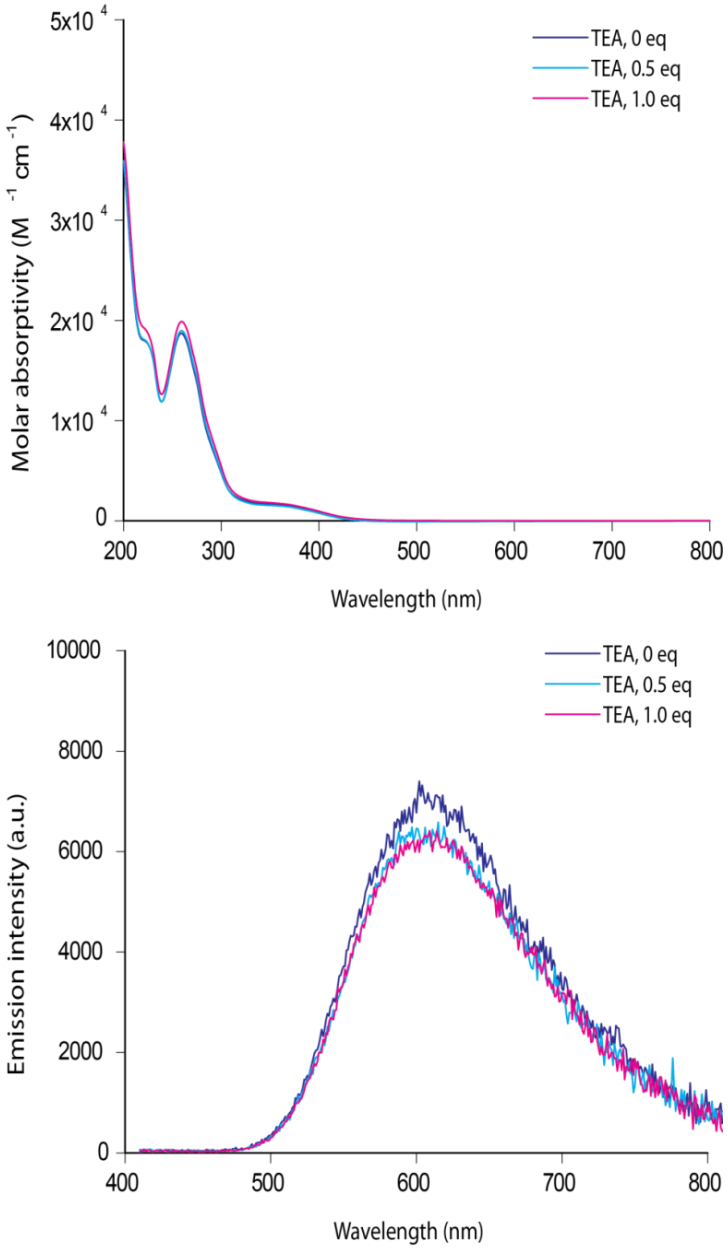

Figure 2.9 Comparison of absorption (top) and emission (bottom) spectra obtained from MeCN solutions at r.t. containing complex [Re(**phen**)$(CO)_3$(**Tz**Ph4OH)] upon addition of TEA. Excitation occurred at 360 nm.

2.6.2 Deprotonation Studies with potassium *tert*-butoxide

The fact that the previous section indicated no changes upon addition of TEA, resulted in the use of a different base, such as potassium *tert*-butoxide (K^tOBu). K^tOBu is considered to be a relatively stronger base (pKa ~ 17) than TEA. The only drawback was that it has limited solubility in some organic solvents. With this in mind, the experiments to be discussed were followed in the same manner as TEA, except using methanol instead of acetonitrile.

Upon addition of one equivalent of K^{t}OBu to deuterated CD_3OD solutions of [Re(**phen**)$(CO)_3$(**Tz**Ph4OH)] (**5**) and [Re(**phen**)$(CO)_3$(**Tz**Ph3OH)] (**6**) complex, a noticeable shift in the peaks shown in the ^{1}H NMR spectrum (**Figure 2.10**) was observed, indicating successful deprotonation. This was illustrated by a doublet peak shifting from 6.65 to 6.46 ppm and 7.36 to 7.17 ppm, which corresponded to the phenyl ring conjugated to the tetrazole, for [Re(**phen**)$(CO)_3$(**Tz**Ph4OH)] (**5**). This change in chemical shift (moving upfield) indicated the formation of a phenoxide which resulted in an increase of electron density on the phenyl ring, compared to the initial phenol complex. The peaks that range between 8.00-9.70 ppm (corresponding to the phenanthroline protons) did not shift, as the chelating diimine ligand was not directly affected by any changes made to the ancillary ligand. As can be seen in **Figure 2.10**, the NMR experiment on the deprotonated species (green trace) showed small detectable peaks (inferred to be starting material) appearing in the baseline which then disappeared upon re-protonation returning to the original spectrum.

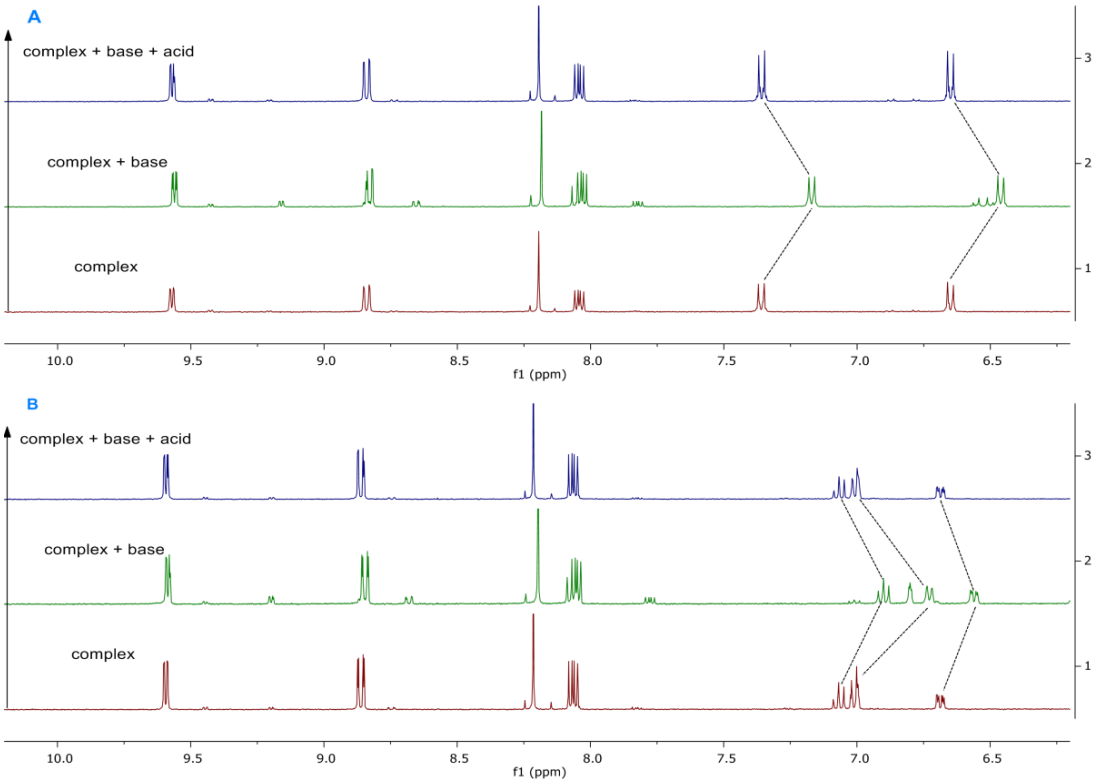

Figure 2.10 Comparison of ^{1}H NMR spectra obtained from MeOD solutions containing complex **5** (top spectrum A) and **6** (bottom spectrum B) showing the initial complex (red trace) with addition of K^{t}OBu (green trace) followed by addition of CSA (blue trace).

Further analyses show that when one equivalent of camphor sulphonic acid (CSA) was added to a solution of the deprotonated phenol complex there was a downfield

shift (returning to its original position), which matched the values of the neutral starting complex (see blue trace in **Figure 2.10**). This illustrated a reversible acid-base process going from phenol (red trace) to phenolate (green trace) and back to the initial complex (blue trace).

The same experiment was conducted on the rhenium-methoxy derivatives, [Re(**phen**)$(CO)_3$(**Tz**Ph4OMe)] (**7**) and [Re(**phen**)$(CO)_3$(**Tz**Ph3OMe)] (**8**) as a reference, to prove that any changes were due to the deprotonation of the phenol reacting with the base. There was no change in the spectra of [Re(**phen**)$(CO)_3$(**Tz**Ph4OMe)] (**7**) and [Re(**phen**)$(CO)_3$(**Tz**Ph3OMe)] (**8**) which can be seen by the absence of a chemical shift on the doublet peak at 7.47 and 6.82 ppm (corresponding to the phenyl ring conjugated to the tetrazole) upon treatment with K^{t}OBu, the former of which is shown (**Figure 2.11**). The spectrum for [Re(**phen**)$(CO)_3$(**Tz**Ph3OMe)] (**8**) derivative was not reported as it was very noisy due to solubility issues in deuterated CD_3OD.

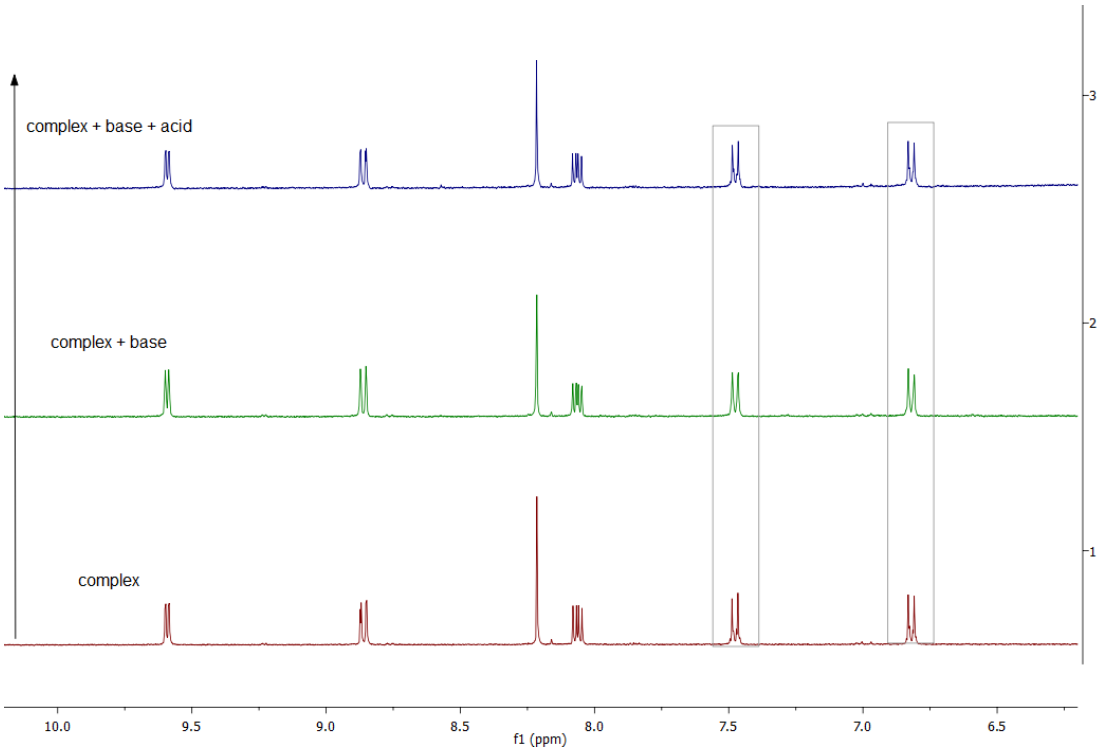

Figure 2.11 ^{1}H NMR spectra obtained from MeOD solution containing complex **7** showing the initial complex (red, 1) with addition of K^{t}OBu (green, 2) and addition of CSA (blue, 3).

The photophysical properties of the neutral complexes and that upon addition of K^{t}OBu showed no significant differences. The absorption and emission profiles for the rhenium-phenol analogues **5-6** (**Figure 2.12**) and the rhenium-methoxy

analogues **7**-**8** (**Figure 2.13**) did not change upon addition of a base. The excited state lifetimes for all the complexes reported (see **Table 2.7**) were also unchanged. Even though the ^{1}H NMR clearly indicated the presence of a deprotonated species, the photophysics were unaffected by the presence of a base.

Table 2.7 Photophysical data of Re(I) complexes upon addition of K^{t}OBu in methanolic solutions (*ca*. 10^{-5} M).

Complex	Initial complex		Addition of K^{t}OBu (1 eq)	
	λ_{em} (nm)	τ (ns)	λ_{em} (nm)	τ (ns)
5	600	93	600	94
6	600	131	600	128
7	586	119	586	119
8	590	132	590	131

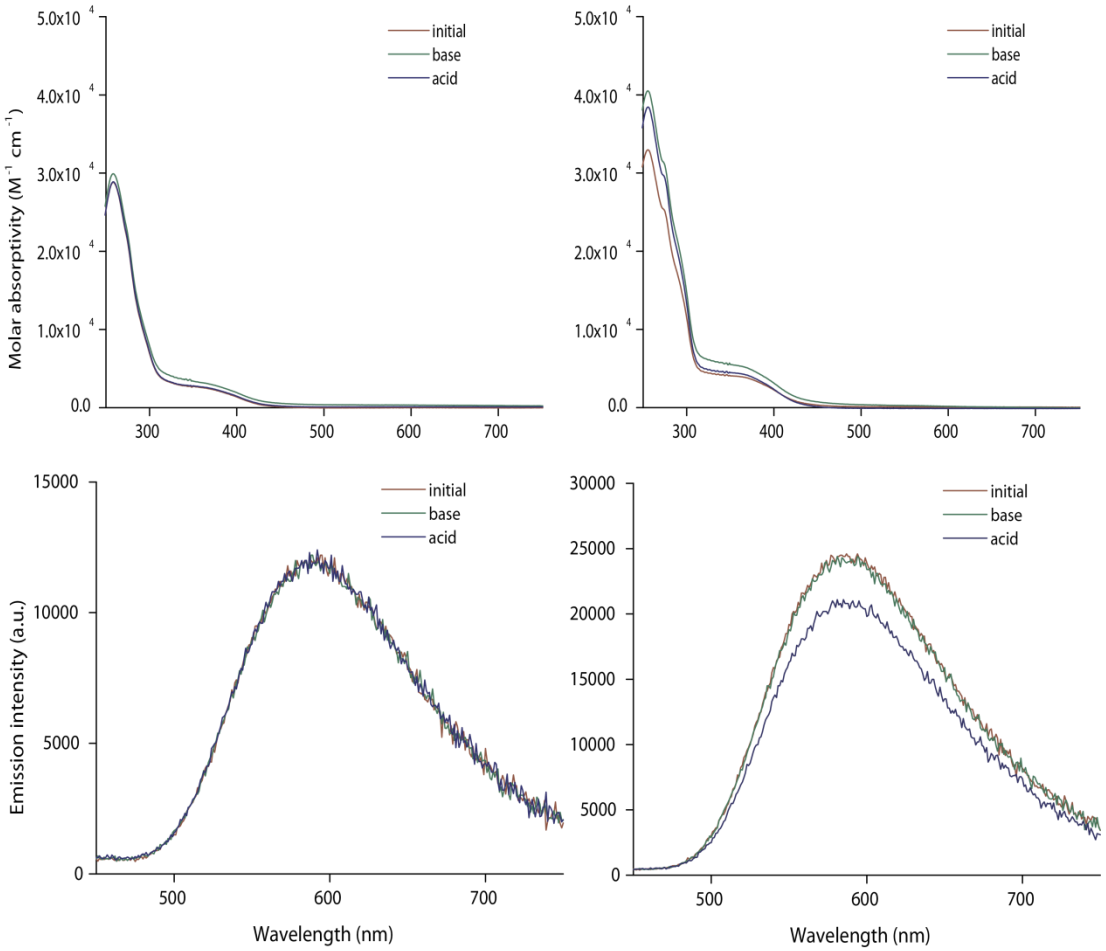

Figure 2.12 Comparison of absorption (top) and emission (bottom) spectra obtained from MeOH solutions at r.t. containing complexes **5** (left) and **6** (right) showing initial complex (dark red) with sequential addition of K^{t}OBu (green) and addition of CSA (blue). Excitation occurred at 350 nm.

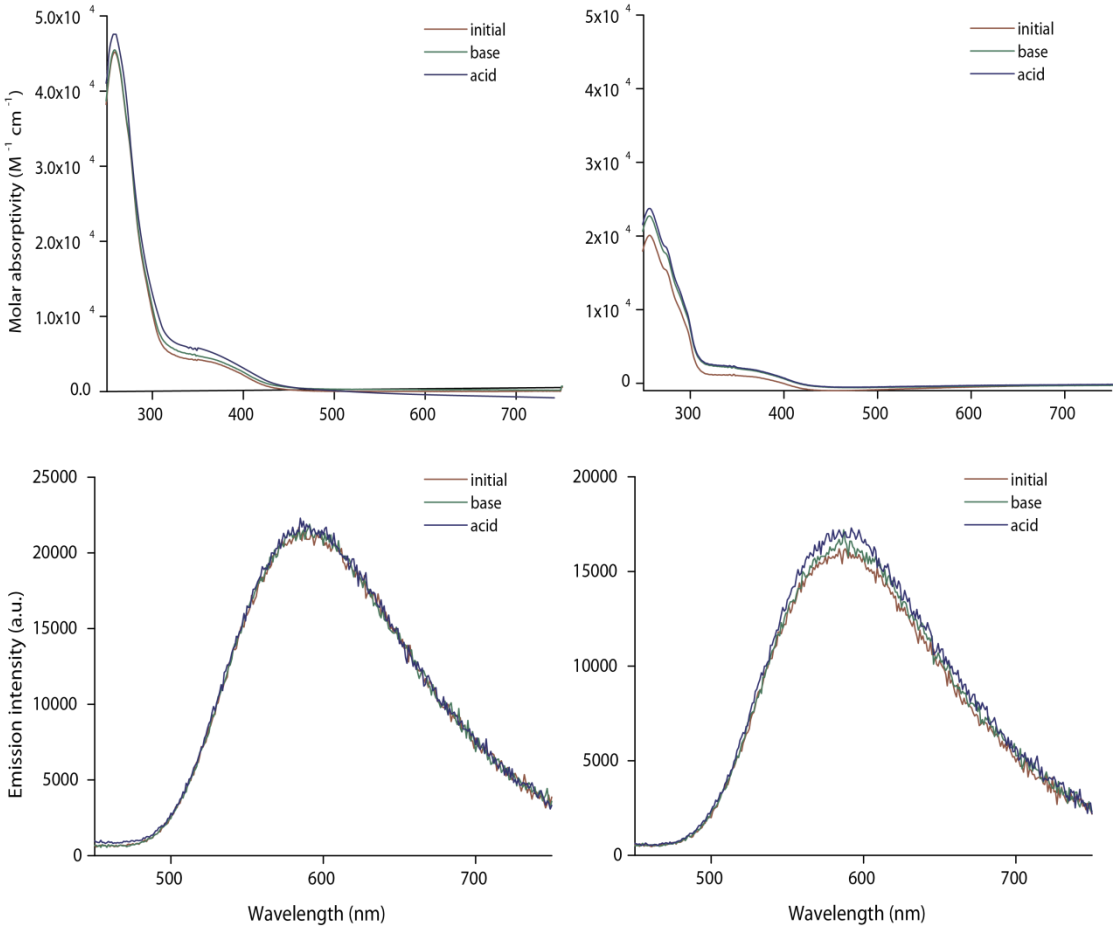

Figure 2.13 Comparison of absorption (top) and emission (bottom) spectra obtained from MeOH solutions at r.t. containing complexes **7** (left) and **8** (right) showing initial complex (dark red) with sequential addition of K^{t}OBu (green) and addition of CSA (blue). Excitation occurred at 350 nm.

It was expected that the phenol-phenolate moiety would show photophysical changes using acid-base chemistry. This was hypothesised based on the fact that any changes made to the ancillary ligand (by deprotonation of the phenol unit) would modify the energy levels of the CT state, therefore affecting the photophysics. It has also been known that phenolate acts as a good quencher.[20,166] However as the absorption and emission spectra resembled the original species (where the plots were superimposable), it seemed that any changes made to the phenol did not affect the excited state luminescence properties in solution with the promotion of photoinduced electron transfer.

2.6.3 Protonation of the Tetrazole Ring

Photophysical changes upon protonation of the complex in solution were also investigated. The protonation experiments were performed by adding a slight excess of triflic acid (0.01 M, 5.0-50 eq.) to dilute (*ca*. 10^{-5} M) acetonitrile solutions of neutral rhenium(I) tetrazolato complexes and the spectral changes monitored by absorbance and emission spectroscopy.

The absorption spectra (**Figure 2.14**) showed a slight red shift in the π-π* transition band around 250-300 nm. However, the MLCT band (350 nm) did not seem to be affected significantly. There was also an evident change in the emission spectrum upon protonation (see **Figure 2.15**) demonstrating a 50 nm blue shift and a significant increase in emission intensity. In addition, the excited state lifetime decay increased from 86-100 ns (neutral) to 146-204 ns (protonated) for both methoxy and phenol substituted complexes.

Protonation of the tetrazole resulted in a reduction of the overall electron density on the rhenium metal centre, due to the decreased σ donation and/or increased π acceptance of the protonated tetrazole.[167,168] This led to a blue shift in emission, because the cationic complex had a larger HOMO-LUMO gap, which in turn explains the elongated excited state lifetime decay of the complexes, according to the energy gap law.[40,162] These findings were also consistent with studies by Werrett *et al*.[167]

Table 2.8 Photophysical properties of the protonated Re(I) complexes from diluted aerated acetonitrile solutions (*ca*. 10^{-5} M).

Complex	**Initial**			**Protonated with TFA (in excess)**		
	λ_{abs} (nm) [10^4 ε, $M^{-1}cm^{-1}$]	λ_{em} (nm)	τ (ns)	λ_{abs} (nm) [10^4 ε, $M^{-1}cm^{-1}$]	λ_{em} (nm)	τ (ns)
5	259 (3.16), 365 (0.29)	607	86	269 (2.60), 362 (0.24)	555	204
6	257 (2.44), 367 (0.25)	604	88	253 (1.99), 271 (1.67), 360 (0.22)	556	179
7	259 (3.48), 364 (0.32)	613	85	265 (2.78), 358 (0.27)	563	169
8	257 (2.50), 369 (0.33)	608	100	255 (2.28), 274 (1.87), 362 (0.33)	564	146

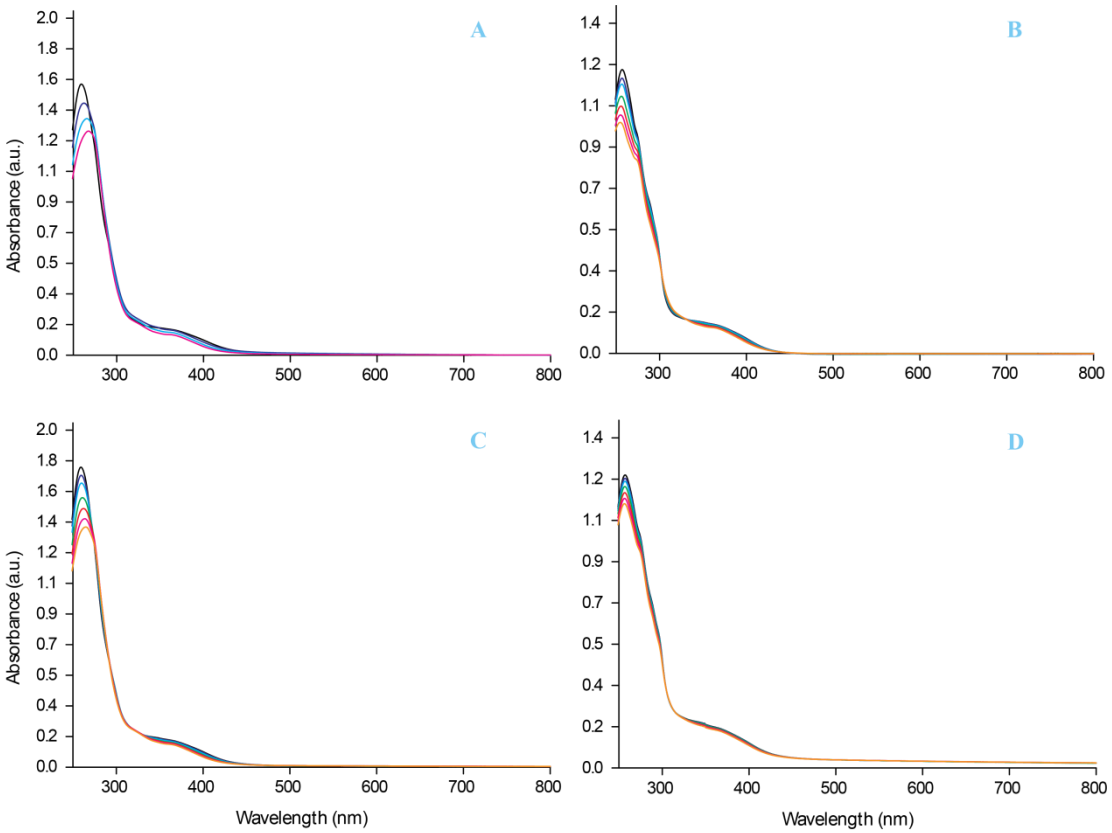

Figure 2.14 Absorption spectra for complexes **5** (A), **6** (B), **7** (C) and **8** (D) in MeCN with sequential addition of acid.

The progression of absorption profiles upon addition of acid for all the complexes were shown in **Figure 2.14**. Isosbestic points were identified at wavelengths of 301 and 330 nm for (**6**), 310 nm for (**8**), and at 275 nm and 333 nm for (**7**). As acid was added sequentially to the solutions, the absorption peaks seen in **Figure 2.14**C (257 nm and 360 nm), **Figure 2.14**B (259 nm and 365 nm), **Figure 2.14**D (257 nm and 360 nm) decreased in intensity. However, there seem to be no significant change or shift in wavelength attributed to either LC or MLCT bands.

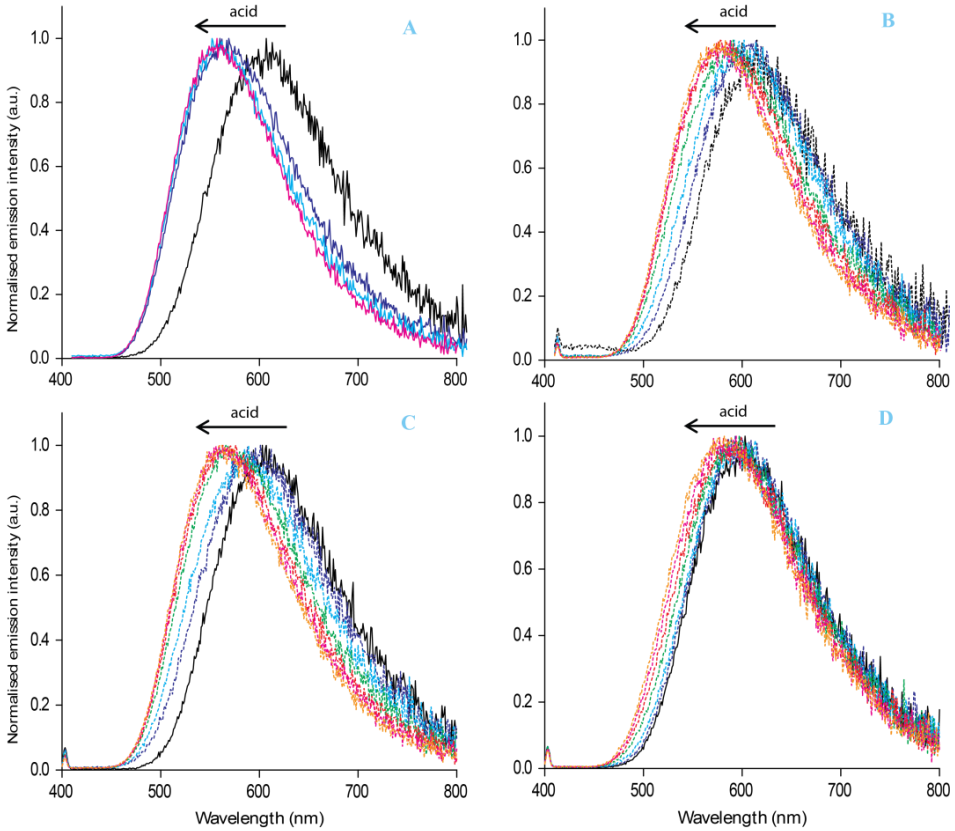

Figure 2.15 Normalised emission spectra for complexes **5** (A), **6** (B), **7** (C) and **8** (D) in MeCN with sequential addition of acid. Excitation occurred at 350 nm.

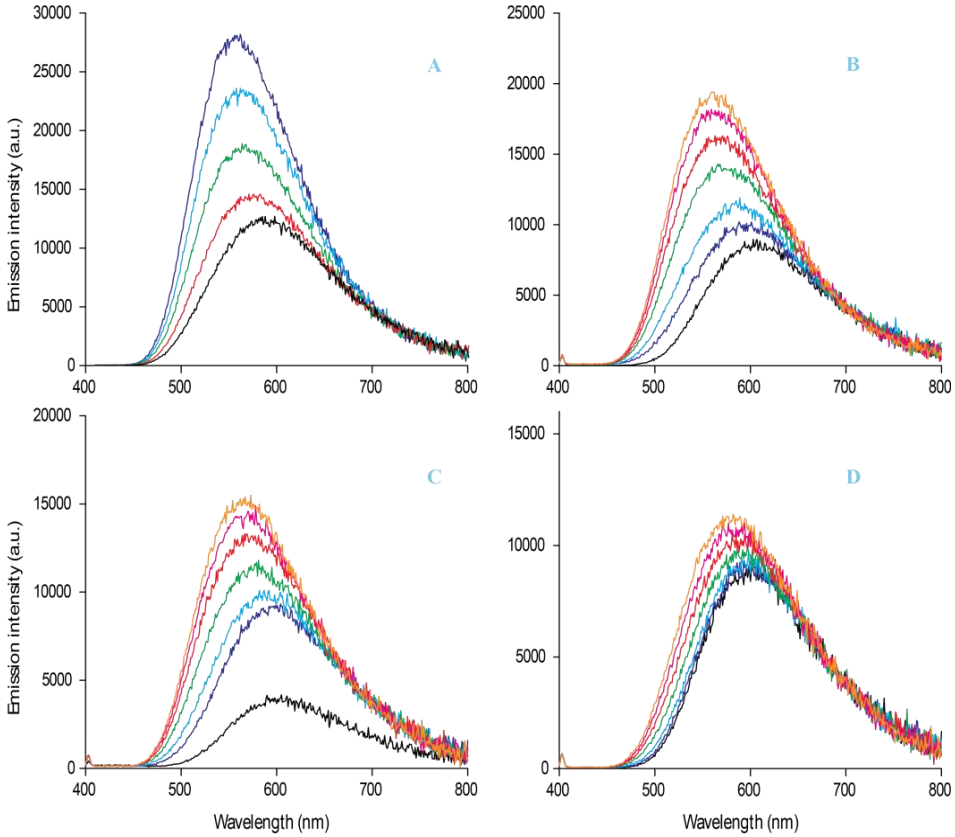

Figure 2.16 Emission spectra for complexes **5** (A), **6** (B), **7** (C) and **8** (D) in MeCN with sequential addition of acid. Excitation occurred at 350 nm.

The emission profiles represented in **Figure 2.15** illustrate the effects of protonation on the complexes. The spectrum shows the starting complex (black trace) with an emission at 600 nm. As acid was progressively added to the solution, this emission peak increased (double) in intensity and also blue shifted by about 50 nm (see **Figure 2.16**). The blue shift is evident of the formation an overall cationic complex, due to the increased HOMO-LUMO energy gap from reduction of electron density on the tetrazole ring. This trend can be seen for all complexes reported within this chapter.

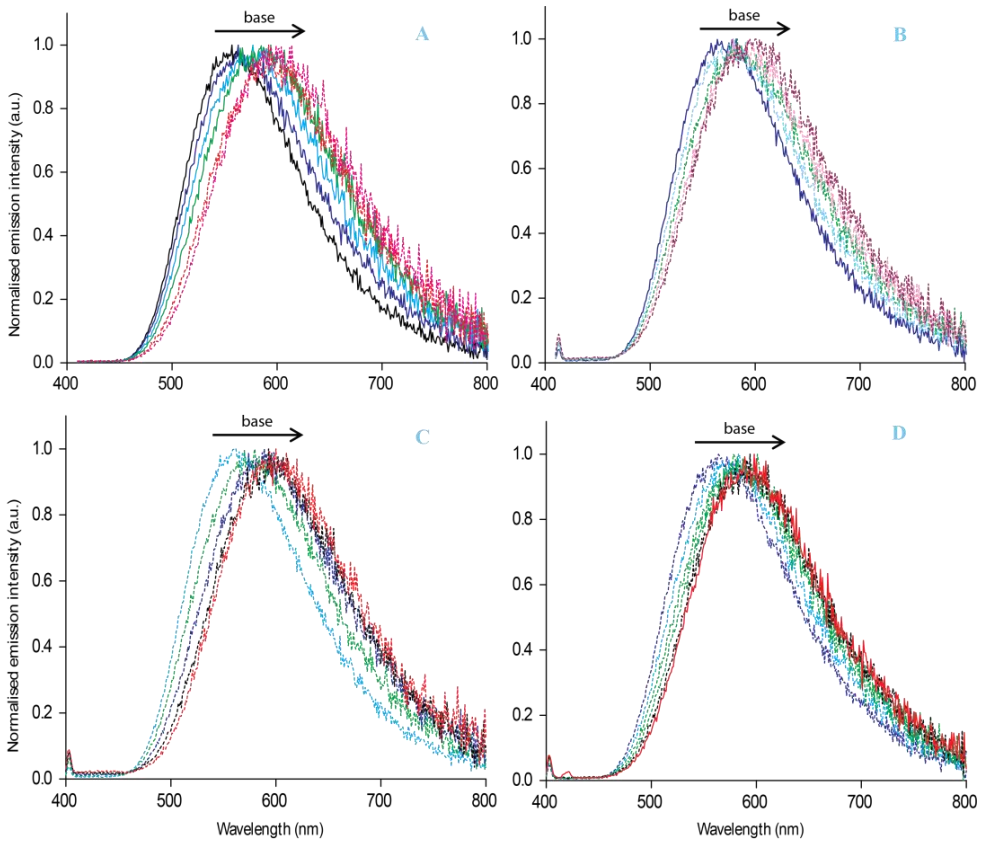

Figure 2.17 Normalised emission spectra for protonated complexes **5** (A), **6** (B), **7** (C) and **8** (D) in MeCN with sequential addition of base showing reversibility. Excitation occurred at 350 nm.

In addition, the protonated compounds can be reconverted to the corresponding initial neutral complex by treatment with a base, such as triethylamine; evident by red shift to original spectrum. This behaviour introduces the possibility for reversibility and modulation of luminescent properties *via* acid-base or deprotonation-protonation system at the tetrazole ring. The plots demonstrating this phenomenon can be seen in **Figure 2.17**.

2.7 Conclusion

This chapter presents a group of four new neutral tetrazolato rhenium(I) diimine tricarbonyl complexes that have been synthesised and characterised by spectroscopy and photophysics. The proton-dependency of the phenol substituted tetrazolato rhenium(I) complexes was investigated. The methoxy analogues **7** and **8** were used as a reference complex incapable of exhibiting any proton-dependency for comparison. Experimental techniques such as ^{1}H NMR spectroscopy, UV-VIS absorbance spectroscopy, emission and excited state lifetime decay were used to monitor any changes that occurred upon titration of a base to a solution of phenol substituted rhenium(I) complex. No base-dependent response could be observed under the experimental conditions reported.

Both the phenol (**5** and **6**) and methoxy (**7** and **8**) substituted tetrazolato rhenium(I) complexes behaved in a similar manner, with respect to their photophysics in acetonitrile solutions. The absorbance, emission and lifetime decay values were roughly the same and had no significant difference. This was also the case regardless of the position of the phenol group being *para*- or *meta*- substituted. The reported data suggests that the phenolic OH (bound to the tetrazole moeity) was not as sensitive to pH as hypothesised. There was no photophysical evidence that suggested electron transfer occurring. In addition, both the methoxy (**7** and **8**) and phenol (**5** and **6**) substituted rhenium(I) complexes behaved in a similar manner (showing similar emission and lifetime decays), with and without the presence of a base. It seems that any type of substituent on the phenyl tetrazole group has minimal effect on the photophysical properties, as it may be too distant from the rhenium centre, or maybe is not strong enough to disturb the high electron density on the tetrazole ring. It was implied that the high electron density on the tetrazole ring inhibited any electron transfer occurring from the phenyl substituent donor to the excited rhenium acceptor component.

Further investigation was applied to these complexes involving protonation of the tetrazole ring, which caused a significant reduction in the electron density and therefore became less σ donating and more π accepting.[168] The decrease in electron density caused an indirect stabilisation of the HOMO level which led to an increase

in the HOMO-LUMO energy gap. This was evident by the blue shifted emission from the protonated rhenium(I) complexes. Additionally, these protonated complexes were able to reconvert to their initial neutral species upon deprotonation with triethylamine, leading to a red shift and decrease in emission intensity. This reversible mode of luminescence present in these complexes provides advantageous features of control and may be applicable as sensors.

2.8 Experimental

2.8.1 General Considerations

All reagents and solvents were purchased from Strem Chemicals, Sigma Aldrich, Alfa Aesar or Ak Scientific and used as received without further purification. Unless stated otherwise, all reactions were conducted under nitrogen atmosphere. Reactions were monitored using thin layer chromatography (TLC) on silica plates, where compounds were visualised under ultraviolet (UV) light. All organic extracts were dried with magnesium sulphate ($MgSO_4$) unless otherwise stated and filtered prior to removal of solvent under reduced pressure. Melting points were determined using the BI Barnsted Electrothermal 9100 melting point apparatus and are reported uncorrected.

Elemental analyses were obtained by Thomas Rodemann at the Central Science Laboratory (University of Tasmania) using a Thermo Finnigan EA 1112 Series Flash, or by Robert Herman at the Department of Chemistry (Curtin University) using a Perkin Elmer EA 2400.

Infrared spectra were obtained on a Perkin-Elmer Spectrometer 100 FTIR using an attenuated total reflectance attachment with a diamond stage; measured in the solid state unless otherwise stated. Compounds were scanned from 4000 to 650 cm^{-1}. The intensities of the IR bands are reported as strong (s), medium (m), or weak (w), with broad (br) and shoulder (sh) bands also specified.

Nuclear magnetic resonance (NMR) spectra were processed on an Ultrashield Bruker Avance 400 spectrometer, where all ^1H NMR spectra were recorded at a 400 MHz

frequency and all ^{13}C NMR spectra were recorded at a 100 MHz frequency at 300 K. ^{1}H and ^{13}C chemical shifts were referenced to residual solvent signals. The assignment of peaks for the compounds are based on the referencing outlined in **Scheme 2.4**.

^{1}H and ^{13}C NMR spectroscopic studies have been carried out on all newly synthesised complexes and the spectra (with expecting integration values) match with the proposed structures. 2D NMR experiments were used to determine the specific assignments of the H_{ortho}, H_{meta} and H_{para} protons on the aryl tetrazolato ligand (see scheme below for NMR referencing).

Scheme 2.4 NMR referencing layout, showing phenanthroline protons (left) and substituted aryl tetrazolato protons (right).

2.8.2 Photophysical Measurements

Absorption spectra were recorded at room temperature on a Cary 400 UV VIS spectrophotometer. Uncorrected steady-state emission and excitation spectra were recorded on an Edinburgh FLSP920 spectrometer equipped with a 450 W xenon arc lamp, double excitation and single emission monochromators, and a Peltier-cooled Hamamatsu R928P photo- multiplier tube (185−850 nm). Emission and excitation spectra were corrected for source intensity (lamp and grating) and emission spectral response (detector and grating) by a calibration curve supplied with the instrument. According to the approach described by Demas and Crosby,[57,169] luminescence quantum yields (Φ_{em}) were measured in optically dilute solutions (OD < 0.1 at excitation wavelength) obtained from absorption spectra on a wavelength scale [nm] and compared to the reference emitter by the following equation:

$$\Phi_x = \Phi_r \left[\frac{A_r(\lambda_r)}{A_x(\lambda_x)}\right]\left[\frac{I_r(\lambda_r)}{I_x(\lambda_x)}\right]\left[\frac{(n_r)^2}{(n_x)^2}\right]\left[\frac{D_x}{D_r}\right]$$

Where *A* is the absorbance at the excitation wavelength (λ), *I* is the intensity of the excitation light at the excitation wavelength (λ), *n* is the refractive index of the

solvent, D is the integrated intensity of the luminescence and Φ is the quantum yield. The subscripts refer to the reference (*r*) and the sample (*x*), respectively. The quantum yields of the complexes were either measured against an air-equilibrated solution of quinine sulfate in 0.1 M H_2SO_4 (Φ = 0.58) or an air-equilibrated solution of $[Ru(\mathbf{bipy})_3]^{2+}$ in water (Φ = 0.028).[170]

Emission lifetimes (τ) were determined with the single photon counting technique (TCSPC) with the same Edinburgh FLSP920 spectrometer using pulsed picosecond LEDs (EPLED 375, fhwm <800 ps) as the excitation source and the above-mentioned R928P PMT as detector. The goodness of fit was assessed by minimizing the reduced χ^2 function and by visual inspection of the weighted residuals.

To record the 77 K luminescence spectra, the samples were placed in quartz tubes (2 mm diameter) and inserted in a special quartz dewar filled with liquid nitrogen.

The solvents (dichloromethane and acetonitrile) used in the preparation of the solutions for the photophysical investigations were of analytical spectrometric grade. Degassed solutions were prepared by the freeze−pump−thaw technique (three cycles). Experimental uncertainties are estimated to be ±8% for lifetime determinations, ±15% for quantum yields, and ±2 and ±5 nm for absorption and emission peaks, respectively.

2.8.3 General Methodology for the Synthesis of Tetrazole Ligands

The synthesis of 5-aryl-1H-tetrazoles was adapted from a previously published procedure by Koguro *et al.*[151] Unless otherwise stated, the following conditions were used. Triethylamine (1.4 eq) and hydrochloric acid (32%, 1.2 eq) were combined in toluene (*ca.* 10 mL) at 0 °C. The flask was immediately stoppered and left to react until no more gas was evolving. The corresponding nitrile (4-methoxybenzonitrile, 3-methoxybenzonitrile, 4-hydroxybenzonitrile, 3-hydroxybenzonitrile) and sodium azide (1.2 eq) were added and the mixture heated at reflux overnight. The reaction mixture was then cooled at room temperature and water (*ca.* 5 mL) was added. The aqueous phase was extracted followed by dropwise addition of hydrochloric acid (5%, 1 mL). The resulting precipitate was collected by vacuum filtration, washed with cold water and air-dried to afford the corresponding tetrazole product.

TzPh4OH (1)

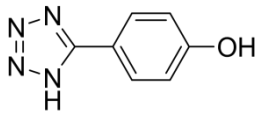

Off-white powder. Yield: 448 mg (60%); m.p. 234-235 °C. ν_{max}(ATR-FTIR)/cm^{-1} (solid state): 3412 br s (OH), 2708-2622 s (tetrazole NH), 1646 w, 1613 s, 1599 s, 1514 m, 1468 m, 1414 s, 1279 m, 1181 m, 1079 m, 835 w, 519 w. ^{1}H NMR (δ, ppm, DMSO-d$_6$): 10.18 (1H, s, O**H**), 7.87 (2H, d, *J* = 8.9 Hz, **H**$_{ortho}$), 6.96 (2H, d, *J* = 8.9 Hz, **H**$_{meta}$). ^{13}C NMR (δ, ppm, DMSO-d$_6$): 160.2 (**C**t), 128.8, 116.2, 114.7, 30.7.

TzPh3OH (2)

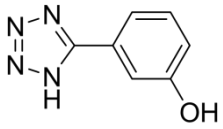

Pale beige solid. Yield: 457 mg (61%); m.p. 218-223 °C. ν_{max}(ATR-FTIR)/cm^{-1} (solid state): 3461 br s (OH), 2629 s (tetrazole NH), 1656 m, 1623 w, 1588 s, 1573 s, 1487 s, 1410 m, 1253 m, 1236 s, 1024 m, 744 w, 682 w. ^{1}H NMR (δ, ppm, DMSO-d$_6$): 9.94 (1H, s, O**H**), 7.52-7.42 (2H, m, **H**$_{ortho}$ and **H**$_{para}$), 7.38 (1H, app. t, *J* = 8.1 Hz, **H**$_{meta}$), 6.98-6.95 (1H, m, **H**$_{ortho}$). ^{13}C NMR (δ, ppm, DMSO-d$_6$): 157.9, 130.6, 118.2, 117.6, 113.6.

TzPh3OMe (3)

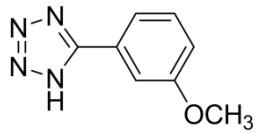

Yield: 226 mg (55%); m.p. 152-155 °C. ν_{max}(ATR-FTIR)/cm^{-1} (solid state): 3096-2621 m (tetrazole NH, aromatic CH and alkane CH), 1655 m, 1619 w, 1585 s, 1563 s, 1490 s, 1439 m, 1287 m, 1398 w, 1287 m, 1234 s, 1141 m, 1046 m, 1001 m, 797 m, 745 m, 683 w. ^{1}H NMR (δ, ppm, DMSO-d$_6$): 7.69-7.58 (2H, m, **H**$_{ortho}$), 7.52 (1H, app. t, *J* = 8.4 Hz, **H**$_{meta}$), 7.17 (1H, d, *J* = 8.4 Hz, **H**$_{para}$), 3.84 (3H, s, OC**H$_3$**). ^{13}C NMR (δ, ppm, DMSO-d$_6$): 159.7 (**C**t), 130.7, 125.3, 119.2, 117.0, 112.1, 55.4 (O**C**H$_3$).

2.8.4 General Methodology for the Synthesis of the Complexes, *fac*-[Re(**phen**)$(CO)_3$(**Tz**PhOR)]

The starting precursor *fac*-[Re(**phen**)$(CO)_3$X] (where X = Cl or Br) and 1.3 equivalents of the corresponding tetrazole (**Tz**PhOH, **Tz**PhOMe) were combined with 1.4 equivalents of triethylamine and MeCN/MeOH (4:1) in a microwave vial. This mixture was heated in a Biotage microwave reactor for 1-2 hours reaching a maximum of 130-160 °C. The resulting product was collected as is after removal of solvent. Specific work up and purification techniques were required depending on the complex.

***fac*-[Re(phen)$(CO)_3$(TzPh4OH)] (5)**

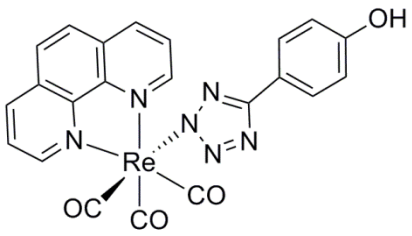

Light yellow star-like needles precipitated out of the mixture over time (after scratching the flask) and were collected *via* vacuum filtration and washed with acetonitrile. Yield: 45 mg (65%); m.p. 295 °C (dec.). ν_{max} (ATR-FTIR)/cm^{-1}: 3070 w, 2024 s (CO, A′(1)), 1931 m (CO, A′(2)), 1893 s (CO, A″), 1617 w, 1487 w, 822 s. ^{1}H NMR (δ, ppm, DMSO-d_6): 9.56 (2H, d, *J* = 8.0 Hz, **phen** $H_{2,9}$), 9.51 (1H, s, phenolic O**H**), 8.98 (2H, d, *J* = 8.3 Hz, **phen** $H_{4,7}$), 8.31 (2H, s, **phen** $H_{5,6}$), 8.12 (2H, d, *J* = 8.3 Hz, **phen** $H_{3,8}$), 7.31 (2H, d, *J* = 8.7 Hz, phenolic **CH**$_{ortho}$), 6.64 (2H, d, *J* = 8.7 Hz, phenolic **CH**$_{meta}$). ^{13}C NMR (δ, ppm, DMSO-d_6): 206.5 (**C**O), 197.0 (**C**O), 194.2 (**C**O), 162.3 (**C**t), 157.7 (phenolic quat. **C**), 154.2 (**phen C**H), 146.5 (**phen** quat. **C**), 139.7 (**phen C**H), 130.3 (**phen** quat. **C**), 127.7 (**phen C**H), 126.9 (**phen C**H), 126.7 (**phen** quat. **C**), 120.3 (phenolic quat. **C**), 115.3 (phenolic **C**H). Elemental Analysis: Calc for $C_{22}H_{13}N_6O_4Re\cdot 0.2H_2O$: C (42.95%), H (2.20%), N (13.66%); found C (42.51%), H (1.67%), N (13.56%).

***fac*-[Re(phen)(CO)$_3$(TzPh3OH)] (6)**

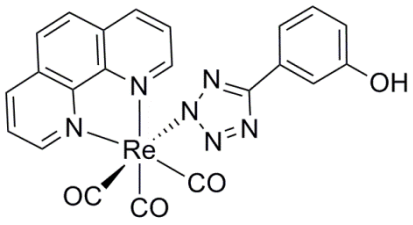

Light yellow precipitate occurred over time (after scratching the flask) and were collected *via* vacuum filtration and washed with cold acetonitrile. Yield: 45 mg (61%); m.p. 305 °C (dec.). ν_{max} (ATR-FTIR)/cm^{-1}: 2021 s (CO, A′(1)), 1896 s (CO, A″). ^{1}H NMR (δ, ppm, DMSO-d$_6$): 9.56 (2H, d, *J* = 6.4 Hz, **phen**, $H_{2,9}$), 9.40 (1H, broad s, phenolic O**H**), 8.99 (2H, d, *J* = 8.3 Hz, **phen** $H_{4,7}$), 8.31 (2H, s, **phen** $H_{5,6}$), 8.13 (2H, d, *J* = 8.3 Hz, **phen** $H_{3,8}$), 7.05 (1H, t, *J* = 7.9 Hz, phenolic **CH**$_{meta}$), 6.99 (s, 1H, phenolic **CH**$_{ortho}$), 6.91 (d, 1H, *J* = 8.0 Hz, phenolic **CH**$_{ortho}$), 6.62 (1H, d, *J* = 8.0 Hz, phenolic **CH**$_{para}$). ^{13}C NMR (δ, ppm, DMSO-d$_6$): 196.9 (**C**O), 194.2 (**C**O), 162.3 (**C**t), 157.3 (phenolic quat. **C**), 154.3 (**phen C**), 146.5 (**phen** quat. **C**), 139.7 (**phen C**H), 130.3 (phenolic **C**H), 129.6 (phenolic quat. **C**), 127.7 (**phen C**H), 126.7 (**phen C**H), 116.3 (phenolic **C**H$_{para}$), 115.5 (phenolic **C**H$_{para}$), 112.3 (phenolic **C**H$_{ortho}$). Elemental Analysis: Calc for $C_{22}H_{13}N_6O_4Re$: C (43.21%), H (2.14%), N (13.74%); found C (42.91%), H (1.71%), N (13.54%).

***fac*-[Re(phen)(CO)$_3$(TzPh4OMe)] (7)**

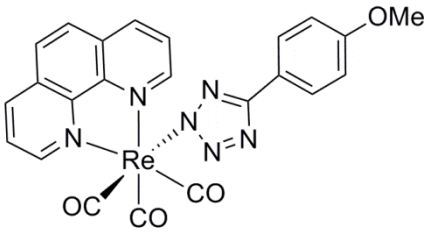

TzPh4OMe (45 mg, 0.26 mmol), [Re(**phen**)(CO)$_3$Cl] (101 mg, 0.21 mmol) and TEA (0.035 mL, 0.25 mmol) were combined with ethanol (9 mL) and water (3 mL) and heated to reflux overnight. The mixture was cooled at room temperature and the concentrated under reduced pressure to minimal solvent. This was cooled in an ice bath and the suspended solids filtered under vacuum to afford a bright yellow solid. Yield: 105 mg (80%); m.p. 274 °C (dec.). ν_{max} (ATR-FTIR)/cm^{-1}: 3065 w, 2940 w, 2840 w, 2507 w, 2016 s (CO, A′(1)), 1916 sh (CO, A′(2)), 1886 s br (CO, A″). ^{1}H NMR (δ, ppm, DMSO-d$_6$): 9.57-9.53 (2H, m, **phen** $H_{2,9}$), 8.99 (2H, d, *J* = 8.4 Hz, **phen** $H_{4,7}$), 8.31 (2H, s, **phen** $H_{5,6}$), 8.13 (2H, d, *J* = 8.3 Hz, **phen** $H_{3,8}$), 7.42 (2H, d,

J = 8.8 Hz, phenyl **CH**$_{meta}$), 6.84 (2H, d, *J* = 8.8 Hz, phenyl **CH**$_{ortho}$), 3.69 (3H, s, O**CH**$_3$). ^{13}C NMR (δ, ppm, DMSO-d$_6$): 197.0 (**C**O), 162.1 (**C**t), 159.5 (**Tz**Ph4OMe quat. **C**), 154.3 (**phen C**H), 146.6 (**phen** quat. **C**), 139.8 (**phen C**H), 130.3 (**phen** quat. **C**), 127.7 (**phen C**H), 126.9 (phenyl **C**H), 126.7 (**phen C**H), 121.8 (**Tz**Ph4OMe quat. **C**), 114.1 (phenyl **C**H), 55.1 (O**C**H$_3$). Elemental Analysis: Calc for $C_{23}H_{15}N_6O_4Re$: C (44.16%), H (2.42%), N (13.43%); found C (44.23%), H (2.56%), N (13.45%). Single crystals suitable for X-ray diffraction were grown by slow diffusion of diethyl ether into a dichloromethane solution of the complex.

***fac*-[Re(phen)(CO)$_3$(TzPh3OMe)] (8)**

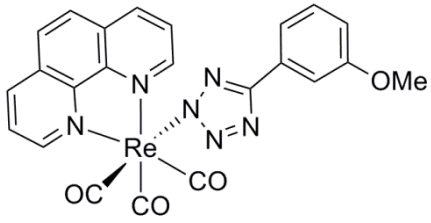

TzPh3OMe (45 mg, 0.26 mmol), [Re(**phen**)(CO)$_3$Cl] (101 mg, 0.21 mmol) and TEA (0.0346 mL, 0.25 mmol) were combined with ethanol (9 mL) and water (3 mL) and heated to reflux overnight. The mixture was cooled to room temperature and the concentrated under reduced pressure to minimal solvent. This was cooled in an ice bath and the suspended solids filtered under vacuum to afford a bright yellow solid. This crude solid was purified *via* flash chromatography (Brockmann II, deactivated alumina) and eluted with dichloromethane to separate the starting rhenium precursor and switched to EtOAc/DCM (50:50) to afford the pure product as fine yellow powder. Yield: 96 mg (73%); m.p. 284 °C (dec.). ν_{max} (ATR-FTIR)/cm^{-1}: 3062 w, 3003 w, 2933 w, 2838 w, 2515 w, 2021 s (CO, A′(1)), 1930 s (CO, A′(2)), 1877 s (CO, A″). ^{1}H NMR (δ, ppm, DMSO-d$_6$): 9.56 (2H, d, *J* = 6.8 Hz, **phen** *H*$_{2,9}$), 8.99 (2H, d, *J* = 8.4 Hz, **phen** *H*$_{4,7}$), 8.31 (2H, s, **phen** *H*$_{5,6}$), 8.13 (2H, d, *J* = 8.4 Hz, **phen** *H*$_{3,8}$), 7.17 (1H, app. t, *J* = 7.9 Hz, **CH**$_{meta}$), 7.08 (1H, d, *J* = 8.8 Hz, **CH**$_{ortho}$), 6.90 (1H, s, **CH**$_{ortho}$), 6.79 (1H, d, *J* = 7.2 Hz, **CH**$_{para}$), 3.65 (3H, s, O**CH**$_3$). ^{13}C NMR (δ, ppm, DMSO-d$_6$): 197.0 (**C**O), 194.2 (**C**O), 162.0 (**C**t), 159.3 (**Tz**Ph4OMe quat. **C**), 154.3 (**phen C**H), 146.6 (**phen** quat. **C**), 139.8 (**phen C**H), 130.5 (phenyl **C**H$_{meta}$), 130.3 (**phen** quat. **C**), 129.9, 127.8 (**phen C**H), 126.8 (**phen C**H), 117.9 (phenyl **C**H$_{ortho}$), 114.3 (phenyl **C**H$_{para}$), 110.5 (phenyl **C**H$_{ortho}$), 54.9 (O**C**H$_3$). Elemental Analysis: Calc for $C_{23}H_{15}N_6O_4Re$·*0.6DCM*: C (41.90%), H (2.41%), N (12.42%); found C (41.75%), H (2.37%), N (12.11%). Single crystals suitable for X-ray

diffraction were grown by slow diffusion of petroleum spirits into a dichloromethane solution of the complex.

2.8.5 X-ray Crystallography

X-ray crystallography diffraction data was collected at 100(2) K and performed by Prof. Brian Skelton at the University of Western Austalia, using an Oxford Diffraction Xcalibur diffractometer fitted with Mo Kα radiation. Following analytical absorption corrections and solution by direct methods, the structure was refined against F^2 with full-matrix least-squares using the program SHELXL-2014.[171] All hydrogen atoms were added at calculated positions and refined by use of riding models with isotropic displacement parameters based on those of the parent atoms. Anisotropic displacement parameters were employed throughout for the non-hydrogen atoms.

Chapter 3

Neutral Rhenium(I) Tetrazolato Complexes Bound to Amino Acids

3.1 Abstract

The synthesis, structural and photophysical characterisation of novel rhenium(I) diimine tricarbonyl complexes will be discussed herein. This group of complexes are based on the general formula [Re(**phen**)$(CO)_3$(L)], where L represents a tetrazolato moiety coordinated to various amino acid ligands. Tryptophan (**Trp**) was chosen as it is known to undergo excited state electron transfer.[172–174] Phenylalanine (**Phe**) and glycine (**Gly**) were used as a reference as they do not share the same excited state behaviour as **Trp**. However, the photophysical properties of the **Trp**-containing neutral rhenium(I) tetrazolato complexes reported in this chapter do not undergo an electron transfer process upon excitation. This was demonstrated for **Trp**, **Phe** and **Gly** complexes, where the quantum yield and excited state lifetime are not significantly different to each other.

Manipulation of these tetrazolato bound amino acids was hypothesised to drive an electron transfer upon photoexcitation. However, after protonation or methylation to reduce the electron density on the tetrazole ring, the photophysical data for both complexes were quite similar. Another approach was to modulate the ligand by shortening the distance between the amino acid (photo-oxidised species) and the rhenium metal centre. The photophysical properties were investigated to see whether this variation has a greater potential for electron transfer to occur.

3.2 Introduction

In 2011, Blanco-Rodriguez *et al*. investigated the excited state properties of complexes containing amino acids (**AA** = **Trp**, **Phe**) with an aromatic side group. The publication reported a series of rhenium(I) diimine tricarbonyl complexes (**Figure 3.1**) that undergo photoinduced electron transfer (PeT) when appended to **Trp** (which acts as a reducing agent).[175] The authors investigated bidentate diimine (**N^N**) chelating ligands such as **phen** and **bipy**. Phenylalanine (**Phe**) was used as a reference as it does not generate PeT within the rhenium(I) complex.

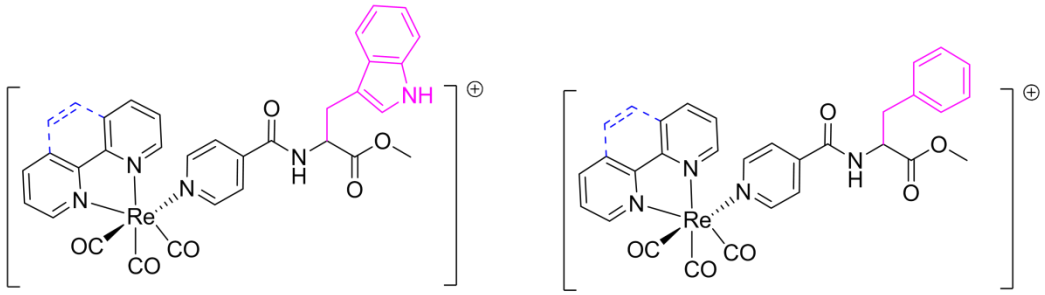

[Re(**bipy**)(CO)$_3$(PyTrp)]$^+$ **(104a)**

[Re(**phen**)(CO)$_3$(PyTrp)]$^+$ **(105a)**

[Re(**bipy**)(CO)$_3$(PyPhe)]$^+$ **(104b)**

[Re(**phen**)(CO)$_3$(PyPhe)]$^+$ **(105b)**

Figure 3.1 Structures of rhenium(I) diimine complexes appended to amino acids.

Upon photoexcitation, the **Phe**-containing complexes (**104b** and **105b**) show a broad, structureless emission with relatively high intensities. However, the **Trp**-containing complexes (**104a** and **105a**) were shown to emit at the same wavelength maxima (λ_{em} = 560 nm) although with a weaker emission intensity. This was attributed to a quenching process *via* electron transfer (eT). In addition, the lifetime data also suggested an electron transfer occurring from **Trp** (indole) group to the MLCT-excited Re^{II} chromophore (see **Scheme 3.1**). For the **Phe** complex **105b,** emission lifetime was reported as 281 ns, whereas the **Trp** derivative **105a** was shown to have an emission lifetime of 26.9 ns. This significant decrease in lifetime was interpreted as an electron transfer process. It was suspected that the generated PeT may have occurred through space (mediated by solvent molecules), or through σ bonds. The report by Blanco-Rodriguez *et al*. has demonstrated that **Trp** can act as an electron flow mediator in photodriven eT systems based on rhenium complexes. With this knowledge, **Trp** has been used as a moiety of interest to investigate any PeT in rhenium and other chromophore-quencher systems.

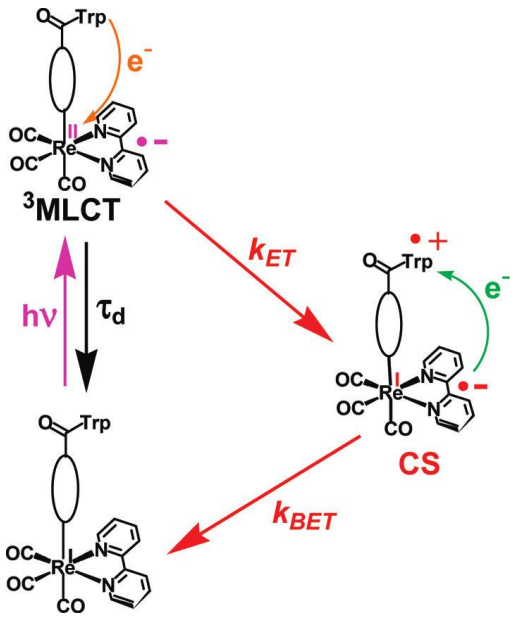

Scheme 3.1 Excited state electron transfer reactivity showing bimolecular quenching involving intramolecular eT pathways [reprinted with permission from ref [175]].

The target rhenium(I) complexes in this chapter (**Figure 3.2**) were based on the species studied by Blanco Rodriguez *et al*, where the chelating ligand is either **phen** or **bipy**, and the ancillary ligand a pyridine appended to an amino acid group. In this investigation, only the **phen** complexes were synthesised and characterised. Also, modifications have been applied to incorporate an aryltetrazole moiety in place of the pyridyl ancillary ligand, resulting in an overall neutral rhenium(I) complex. Based on these variations, the structure-property relationship of the complexes was examined. This was achieved in two different pathways: i) by varying the distance between the amino acid and the metal centre *via* introducing a phenyl linker, and ii) varying the overall charge of the rhenium(I) complex to gain a better driving force for photooxidation of the amino acid *via* protonation or methylation of the tetrazole ring.

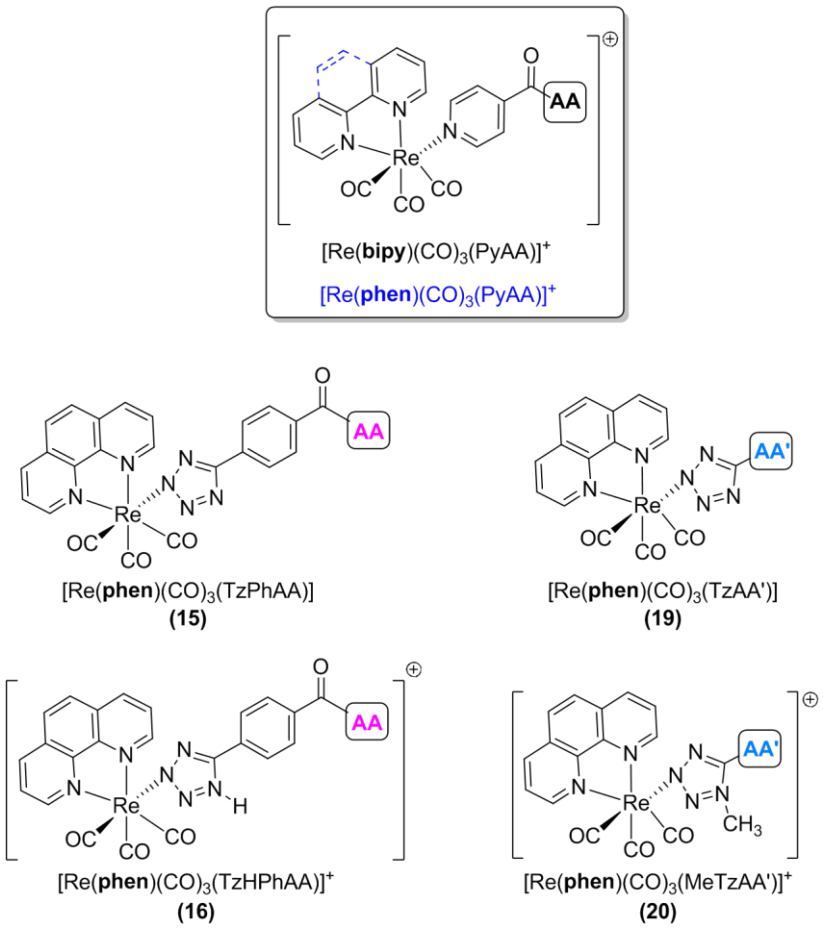

Figure 3.2 Structures of target complexes illustrating differences in charge and ancillary ligand, based on the reference complex shown in the box, where **AA** is **Trp**, **Phe** or **Gly**.

The photophysical properties of the cationic rhenium(I) complexes were compared to the neutral rhenium(I) complexes to establish a structure-property relationship. In addition, a comparison of the complexes having an extra unit (phenyl linked to tetrazole, **15Trp/Phe/Gly**) as opposed to the tetrazole being directly coordinated to the amino acid (without phenyl bridge, **19Trp/Phe**) would provide an insight to whether distance of the reducing agent (from the metal centre) played a significant role in terms of their photophysical properties. The group of complexes that have undergone protonation and methylation are shown in **Figure 3.3** and **Figure 3.4** respectively.

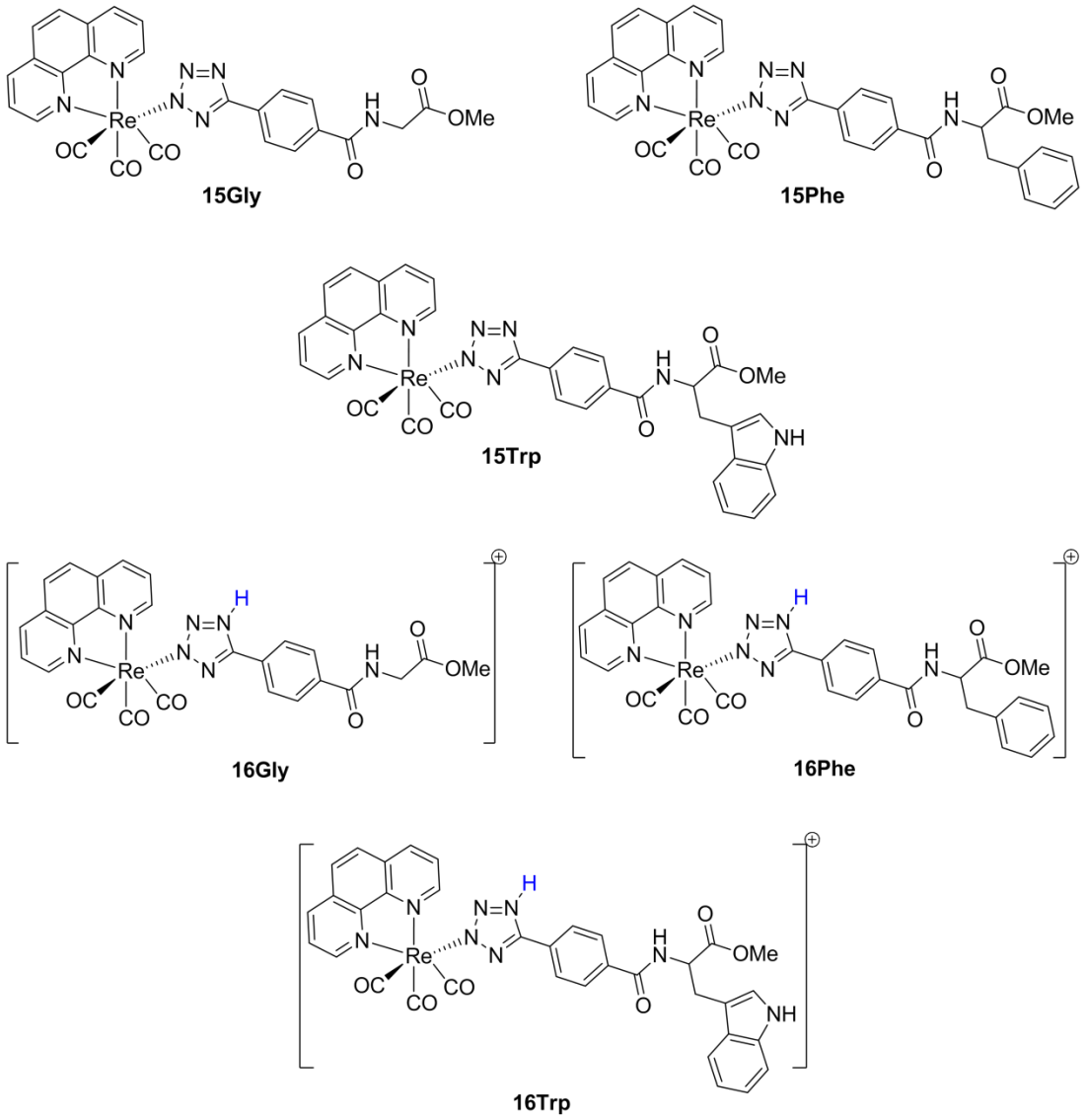

Figure 3.3 Structures of neutral (top) and protonated (bottom) rhenium(I) amino acid appended tetrazolato complexes with phenyl linker.

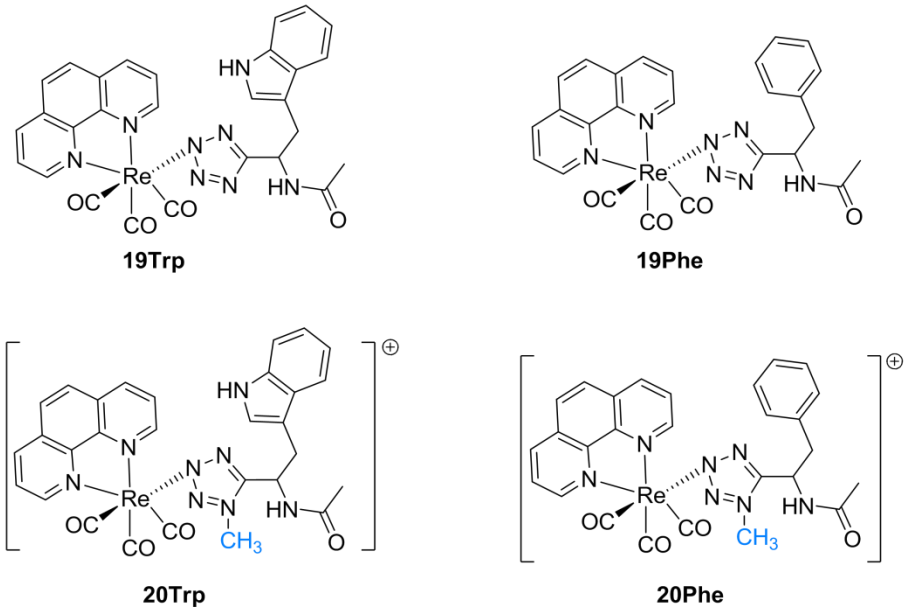

Figure 3.4 Structures of neutral (top) and cationic (bottom) rhenium(I) amino acid appended tetrazolato complexes without phenyl linker.

Previously, Chapter 2 described the photophysical investigation of neutral rhenium(I) complexes appended to phenol substituted tetrazoles. It was deduced that an electron transfer process did not occur upon photoexcitation. Following this discovery, attention was turned towards model rhenium(I) complexes with amino acids known to undergo electron transfer in its excited state. As mentioned earlier, studies by Blanco-Rodriguez *et al* demonstrated that **Trp** can undergo PeT to the rhenium metal centre as opposed to the non-photoactive **Phe** derivative. Based on these results, Chapter 3 aims to explore rhenium(I) **phen** tetrazolato complexes attached to amino acid methyl esters so that meaningful comparisons could be made.

3.3 Synthesis of the Ligands

To prepare the nitrile precursors, 4-cyanobenzoic acid (**106**) was converted into an acyl chloride (**107**), which was then reacted with the corresponding amino acid methyl ester (as the hydrochloride salt in the presence of a base) to afford the compounds **9-11** in moderate to good yields as shown in **Scheme 3.2**. The products were characterised using IR and NMR spectroscopy.

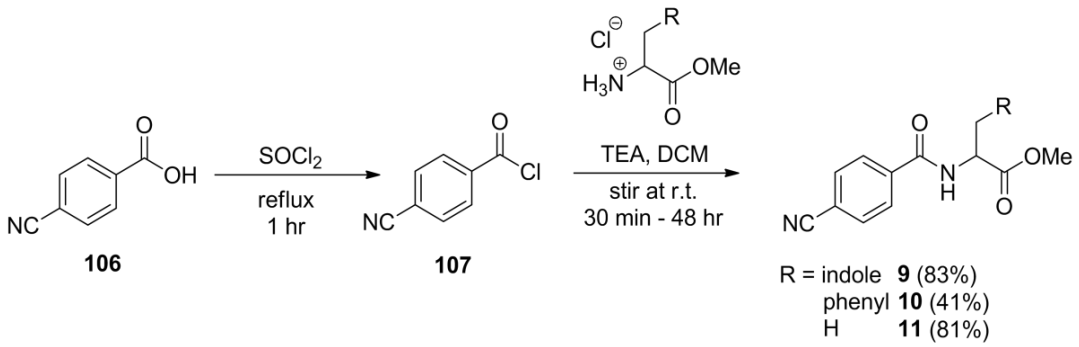

Scheme 3.2 Two-step reaction scheme showing preparation of nitrile compounds.

The amino acid substituted tetrazoles **12-14** shown in **Scheme 3.3** were synthesised by following the Koguro method,[151] but the yields were quite low due to the moderate water solubility of the products, preventing them from fully precipitating upon acidification. Instead a different approach was used to extract and isolate the tetrazole products, i.e. extraction with ethyl acetate after acidification and finally evaporation of the organic solvent to afford the product. Alternatively, the Sharpless method, which involves a stoichiometric amount of zinc salt at reflux in water/isopropanol solvent mixture, was used to generate the tetrazoles.[176,177] In the case of the tetrazoles in this chapter, the latter method was more successful in terms of isolation and yield.

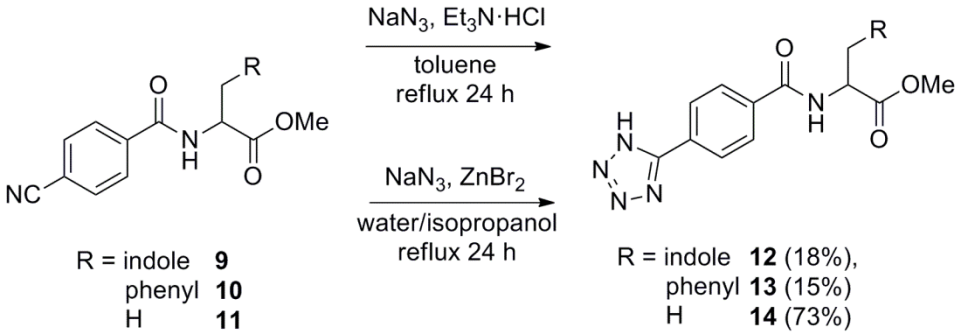

Scheme 3.3 Reaction scheme to prepare tetrazole compounds **12-14**.

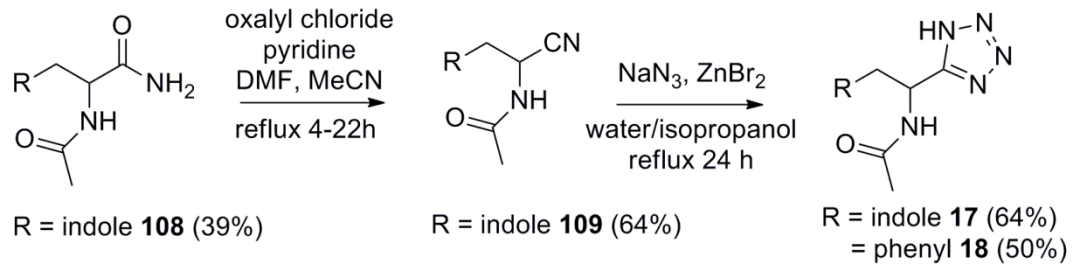

Scheme 3.4. Reaction scheme to prepare tetrazole compounds **17** and **18**.

The preparation of the tetrazole compounds **17** and **18** without the phenyl linker involved a two-step reaction which is shown in **Scheme 3.4**. The *N*-acetyl amide (**108**) was converted to the *N*-acetyl nitrile (**109**) through a dehydration reaction using the Vilsmeier reagent (i.e. chloromethylene iminium salt), following a procedure reported by Bargar and Riley.[178] The Vilsmeier reagent was produced in-situ by combining DMF and oxalyl chloride in MeCN, which formed an immediate precipitate (see **Scheme 3.5**). To this was added the amide and pyridine which were heated at reflux. After the reaction, liquid-liquid extraction and trituration afforded the product in low yields. The nitrile was then converted to the tetrazole using the method reported by Sharpless, where the yields were moderate and a mixture of starting material and product were obtained (see ^{1}H NMR spectrum, **Figure 3.5**), indicating that the reaction did not proceed to completion. Due to the low yields, it was considered not suitable to attempt to further purify the mixture. In addition, tetrazoles cannot generally be purified by column chromatography. Nevertheless, the crude mixture containing the tetrazole **Tz**H**Trp** (**17**) was still used in the metallation step due to prior knowledge that the final product could be more readily purified by column chromatography.

Scheme 3.5 Reaction showing formation of Vilsmeier reagent.

3.3.1 Spectroscopic Characterisation of the Ligands

The formation of the substituted tetrazole compounds **12-14** and **17-18** was consistent with IR spectroscopic analysis, where the NH and C=N stretching peaks were observed at 3000 and 1600 cm^{-1} respectively. In addition, the absence of the sharp nitrile C≡N band around 2200 cm^{-1} indicated the absence of starting material. The CO stretching vibrations for carbonyl groups range from 1810 to 1690 cm^{-1} depending on the electron withdrawing and resonance effects. A higher frequency is observed for an ester (*ca.* 1735 cm^{-1}) and a lower CO frequency for an amide (*ca.* 1690 cm^{-1}).

Analysis by ^{1}H NMR spectroscopy showed the most significant signals for the corresponding tetrazole compounds **12-14** (with linker) to be the amide NH peak (broad singlet, with integration of one proton) found downfield (around 9.0-10.0 ppm) and the upfield methyl ester peak (sharp singlet, with integration of three protons) at 3.60-3.70 ppm. On the other hand, the **Tz**H**Trp** (**17**) ligand (without linker) was not isolated as a pure product as it contained starting material (see **Figure 3.5**).

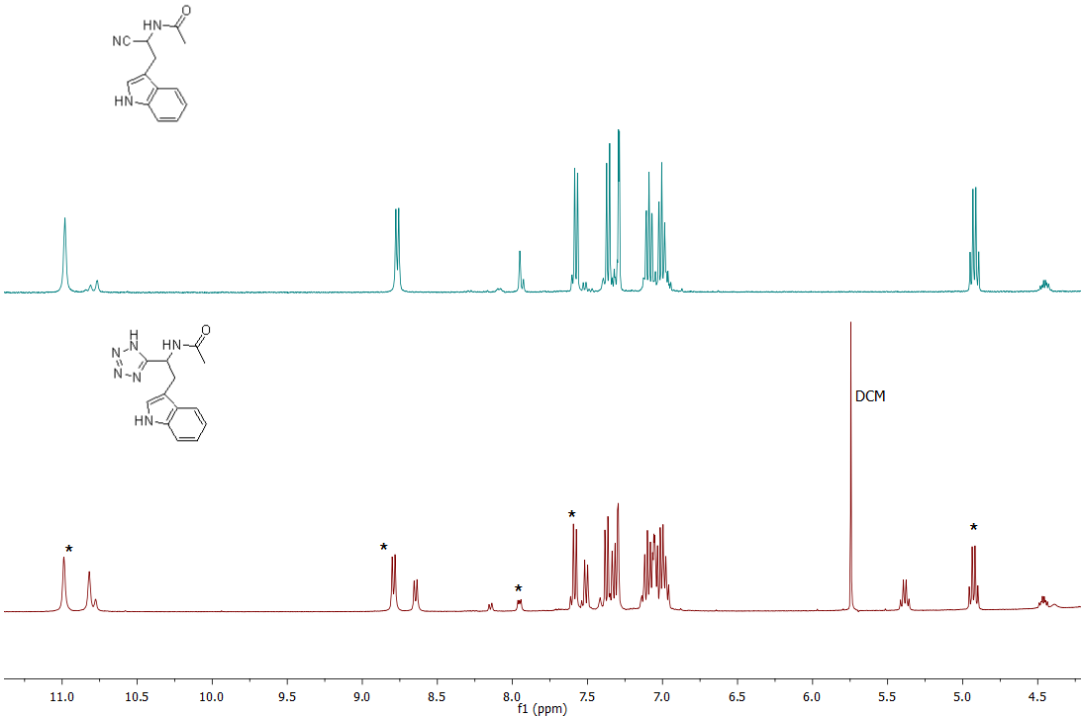

Figure 3.5 ^{1}H NMR spectra comparing starting nitrile **109** (top, blue) and **Tz**H**Trp** tetrazole ligand **17** (bottom, red) in DMSO-d_6 where asterix represent unconverted starting nitrile precursor**.**

3.4 Synthesis of the Complexes

To prepare the neutral rhenium(I) complexes shown in Figure 3.3 and Figure 3.4, the halogenated precursor *fac*-[Re(phen)$(CO)_3$Cl] was reacted by direct substitution of the chloride with the corresponding tetrazole ligand. This was achieved by use of microwave irradiation for 3 hours at 130-160 °C. Purification of the rhenium(I) tetrazolato complexes by flash column chromatography (eluting with 2% MeOH in

EtOAc) afforded the products in moderate yield, with the remaining starting material *fac*-[Re(phen)(CO)$_3$Cl] also being recovered.

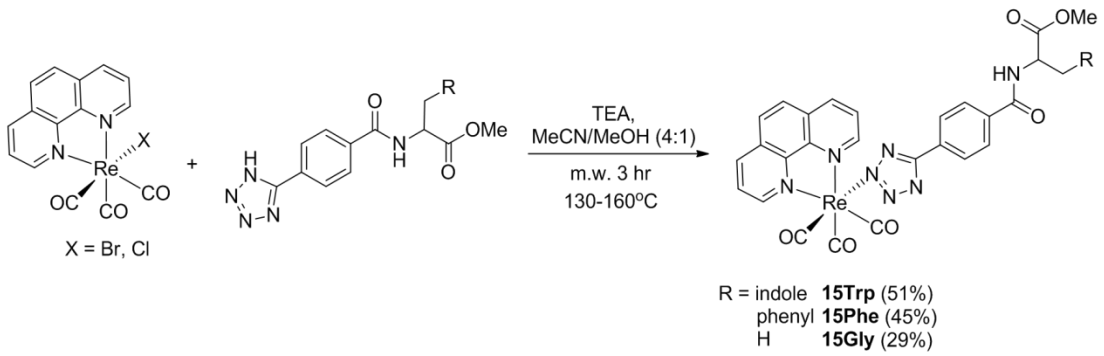

Scheme 3.6 Reaction scheme for preparation of rhenium(I) tetrazolato complexes **15Trp/Phe/Gly**.

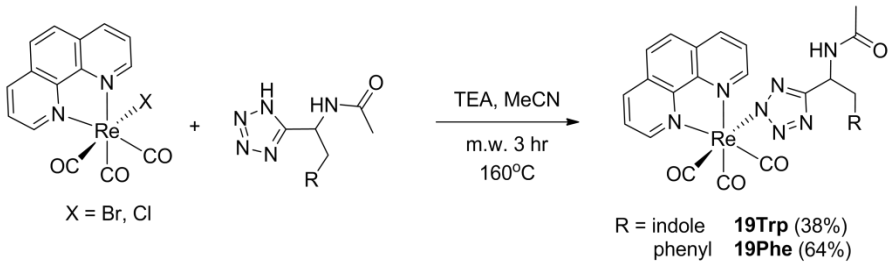

Scheme 3.7 Reaction scheme for preparation of rhenium(I) tetrazolato complexes **19Trp/Phe**.

3.4.1 Spectroscopic Characterisation of the Complexes

Formation of the targeted rhenium(I) complexes was confirmed by ^{1}H NMR, ^{13}C NMR, infrared spectroscopy, elemental analysis and X-ray diffraction; the experimental data were in agreement with the proposed formulae. Analysis by infrared (IR) spectroscopy illustrated that all the complexes exhibit three characteristic carbonyl (CO) stretching bands between 2030-1860 cm^{-1}, showing the totally symmetric in-phase stretching A′(1), the totally symmetric out-of-phase stretching A′(2) and the asymmetric stretching A″. The values of the stretching frequencies are summarised in **Table 3.1**. The A′(1) stretch tends to be the sharpest peak, whereas A′(2) and A″ bands can sometimes collapse to form one broader peak. In the halogenated rhenium precursor complex, the A′(1) stretch is found to be 2014-2015 cm^{-1}, the A′(2) and A″ bands were 1923-1925 cm^{-1} and 1885-1882 cm^{-1} respectively.[154] After coordination to the tetrazolato ligands, the A′(1) stretching frequency increases and the A′(2) frequency decrease. This high stretching frequency of the carbonyl band is a result of the tetrazole reducing the electron density on the

rhenium metal centre. This can be explained by the fact that tetrazoles are better π accepting ligands compared to the halogens.

Table 3.1 Stretching frequencies (cm^{-1}) of the CO bands of the neutral rhenium(I) complexes.

Complex	CO A′(1)	CO A′(2)/A″
[Re(**phen**)$(CO)_3$(**Tz**Ph**Trp**Me)] (**15Trp**)	2023	1915 [a]
[Re(**phen**)$(CO)_3$(**Tz**Ph**Phe**Me)] (**15Phe**)	2024	1908 [a]
[Re(**phen**)$(CO)_3$(**Tz**Ph**Gly**Me)] (**15Gly**)	2026	1921, 1885
[Re(**phen**)$(CO)_3$(**TzTrp**)] (**19Trp**)	2026	1911 [a]
[Re(**phen**)$(CO)_3$(**TzPhe**)] (**19Phe**)	2024	1906 [a]

[a] Single value data, where the peaks are superimposed into a single broad band

Analysis by NMR spectroscopy was used to determine the structure of the complex. The ^{1}H NMR and ^{13}C NMR spectra for all complexes were measured in either deuterated acetone or DMSO solutions. The main signals in the ^{1}H NMR spectrum include a sharp singlet (integration corresponding to three H atoms) found around 3.66-3.68 ppm, which is attributed to the methyl protons of the methyl ester. Another sharp singlet (integration corresponding to three H atoms) found around 1.60-1.80 ppm was attributed to the acetyl group. For the **Trp** derivatives, the NH on the indole can be seen as a broad singlet peak (integrating to one proton) downfield around 10.5 ppm, as opposed to the NH on the amide found around 7.70-7.93 ppm. Furthermore, all the rhenium(I) complexes discussed in this chapter show four signals found between 8.17-10.06 ppm which are typical for phenanthroline protons (confirming the symmetric environment of the diimine ligand in the *facial* isomer), consistent with previous studies.[6,81,154] Specifically for **15Trp** and **15Phe**, the methylene can be seen as two sets of doublets (both integrating for two protons) appearing at 3.42-3.27 ppm (**15Trp**) and 3.28-3.10 ppm (**15Phe**). This can be explained by the fact that the methylene is coupled to the proton on the central asymmetric carbon atom of the amino acid. There may also be a presence of isomers with different structural conformations.

In the ^{13}C NMR, typical Re-tetrazole peaks can be seen at around 160 ppm (which indicates an N2 linkage isomer), also consistent with previous studies.[6,154] **Table 3.2** reports the chemical shift values for the tetrazolic carbon (Ct) on the free tetrazole

ligand compared to when it is coordinated to the rhenium. In addition, the peaks representing the three carbonyl ligands can be found in the 190-200 ppm region.

Table 3.2 NMR chemical shifts (ppm) of the Ct tetrazole for ligands and the Re(I) complexes.

Compound	Tetrazole ligand, DMSO	Re complex
TzPh**Trp**Me	165.5	162.9 (acetone)
TzPh**Phe**Me	165.7	162.9 (acetone)
TzPh**Gly**Me	166.3	162.9 (acetone)
TzTrp	169.3	164.2 (DMSO)
TzPhe	169.2	163.5 (acetone)

3.5 X-ray Crystallography

Single crystals were obtained for rhenium(I) tetrazolato complexes **15Phe**, **15Gly** and **19Phe**. X-ray crystallographic analysis confirms they are all arranged in an octahedral geometry. The table of bond lengths and angles are presented in Appendix A.2. X-ray crystallographic analysis also confirms the formation of the Re-N2 linkage isomer in the solid state, as shown in **Figure 3.6**, **Figure 3.7** and **Figure 3.9**, which is relatively common amongst rhenium(I) tetrazolato complexes. Formation of the N1 linkage isomer was not observed as it tends to favour coordination of the aryl tetrazolato ring at the N2 position, which have also been established by previous studies.[153] In addition, the three carbonyl ligands are positioned in a *facial* arrangement, consistent with the IR and NMR spectroscopic data presented in this chapter.

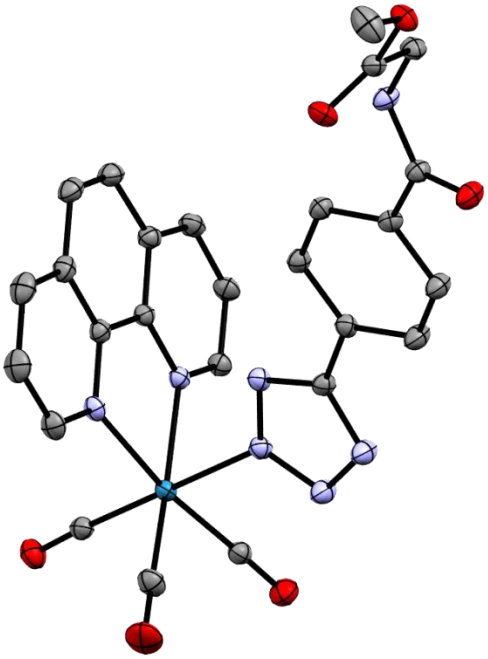

Figure 3.6 Crystal structure of complex **15Gly**, where H atoms omitted for clarity and thermal ellipsoids drawn at 50% probability.

The X-ray crystal structure of **15Gly** is shown in **Figure 3.6**. This complex crystallised in the triclinic space group $P\bar{1}$. The crystal packing of **15Gly** where the **phen** ligands are involved in π-stacking (face-to-face) between neighbouring complexes show a plane-to-plane distance of 3.421 Å. Early publications have reported that π interactions in metal complexes usually occur at distances between 3.3 and 3.8 Å.[179] Comparison with **15Trp** and **15Phe** derivatives could not be made, as single crystals were not obtained for these complexes.

The **Trp** analogues were most difficult to grow crystals of as the position of the tryptophan was speculated to have different conformers that prevent proper stacking of the molecules based on literature; Vlcek predicted the structures of the **Trp** using DFT and found four different conformers possible.[175] The similar stacking of indole has also been demonstrated crystallographically by other published reports.[173,180]

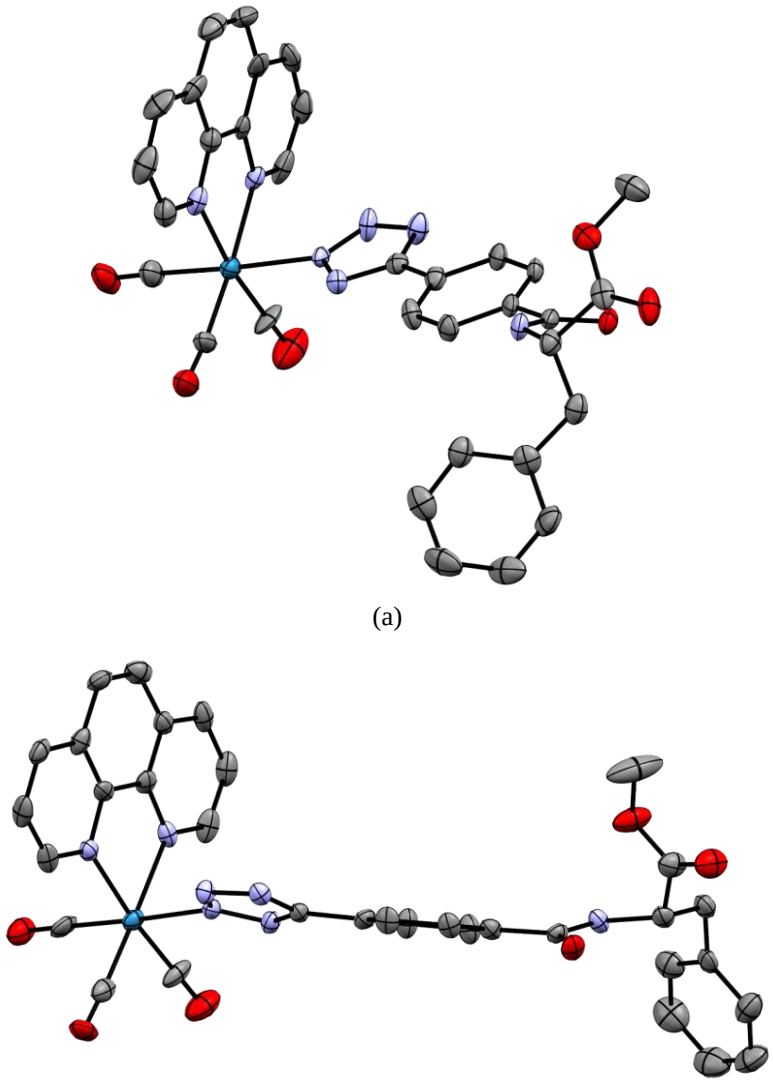

(a)

(b)

Figure 3.7 Crystal structure of **15Phe** showing two different conformations, where phenylalanine is (a) facing up/left and (b) down/right. H atoms omitted for clarity and thermal ellipsoids drawn at 50% probability.

The X-ray crystal structure of **15Phe** is shown in **Figure 3.7**. This complex crystallised in the orthorhombic space group $P2_12_12$. The three carbonyl ligands are in *facial* configuration and the rhenium(I) metal centre coordinated *via* the N2 atom of the tetrazole in agreement with spectroscopic data and consistent with previous studies.[154,157,181] The complex did not exhibit any π stacking, unlike the **15Gly** derivative. It can be seen that this complex can exist in two different conformations, where the phenylalanine is faced up/left or down/right; this is in agreement with the ^{1}H NMR spectrum. There also seems to be some H bonding interaction between the molecules, which is shown in **Figure 3.8**. The distance calculated between the NH and the O atom was 2.963 Å for one set of packing and 2.872 Å for the other set.

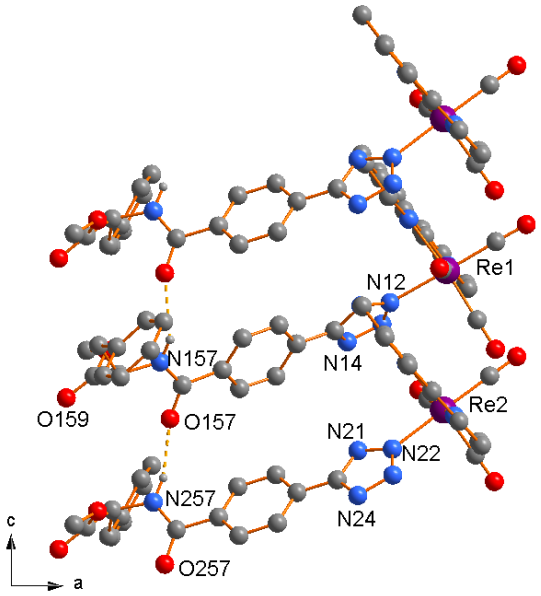

Figure 3.8 Crystal packing showing H bond interactions between **15Phe** molecules.

Furthermore, the structure of **19Phe** is shown in **Figure 3.9** and the complex crystallises in the triclinic space group $P\bar{1}$. It can be seen that the rhenium(I) metal centre is coordinated *via* the N2 atom, which is consistent with previous studies. The crystal packing of **19Phe** between neighbouring complexes shows a plane-to-plane distance of 5.323 Å. This is much larger than **15Phe** and common π interactions with distances of 3.3 to 3.8 Å. There is also some intermolecular H bond interaction present, where the distance between the NH and O atom was found to be 2.923 Å, similar to the H bonding calculated for **15Phe**.

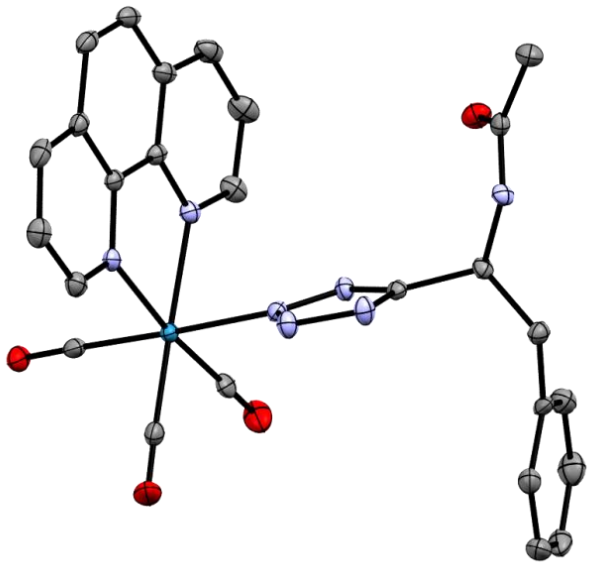

Figure 3.9 Crystal structure of complex **19Phe**, where H atoms and solvent molecules are omitted for clarity. Thermal ellipsoids drawn at 50% probability.

3.6 Photophysical Investigation

The absorption spectra of the neutral rhenium(I) complexes **15Trp**, **15Phe** and **15Gly** were measured in dilute dichloromethane solutions at approximately 10^{-5} M. The absorption profiles (**Figure 3.10**, top graph) exhibit an intense high energy band between 250-300 nm, which can be assigned to intraligand (IL) π-π* transitions and a broad lower energy band between 330-450 nm, which can be assigned to admixtures of metal-to-ligand charge transfer (MLCT) and ligand-to-ligand charge transfer (LLCT) bands. This mixed nature of bands is referred to metal-to-ligand-to-ligand charge transfer (MLLCT) transitions. Both these transitions are characteristic of typical rhenium(I) complexes and fit the description of similar reported complexes. [154,157,181]

The emission profiles (**Figure 3.10**, bottom graph) for the complexes were obtained from dichloromethane solutions and each complex exhibit a broad structureless emission band from an excited state of ^{3}MLLCT character, with an emission maxima around 580-600 nm; this is characteristic of, and consistent with, other reported neutral rhenium(I) diimine complexes that are phosphorescent.[6,154,181] There appear to be no discrepancies in the emission band, regardless of the amino acid present. This would suggest that any substituent on the phenyltetrazole group has no effect on the HOMO/LUMO energy levels.

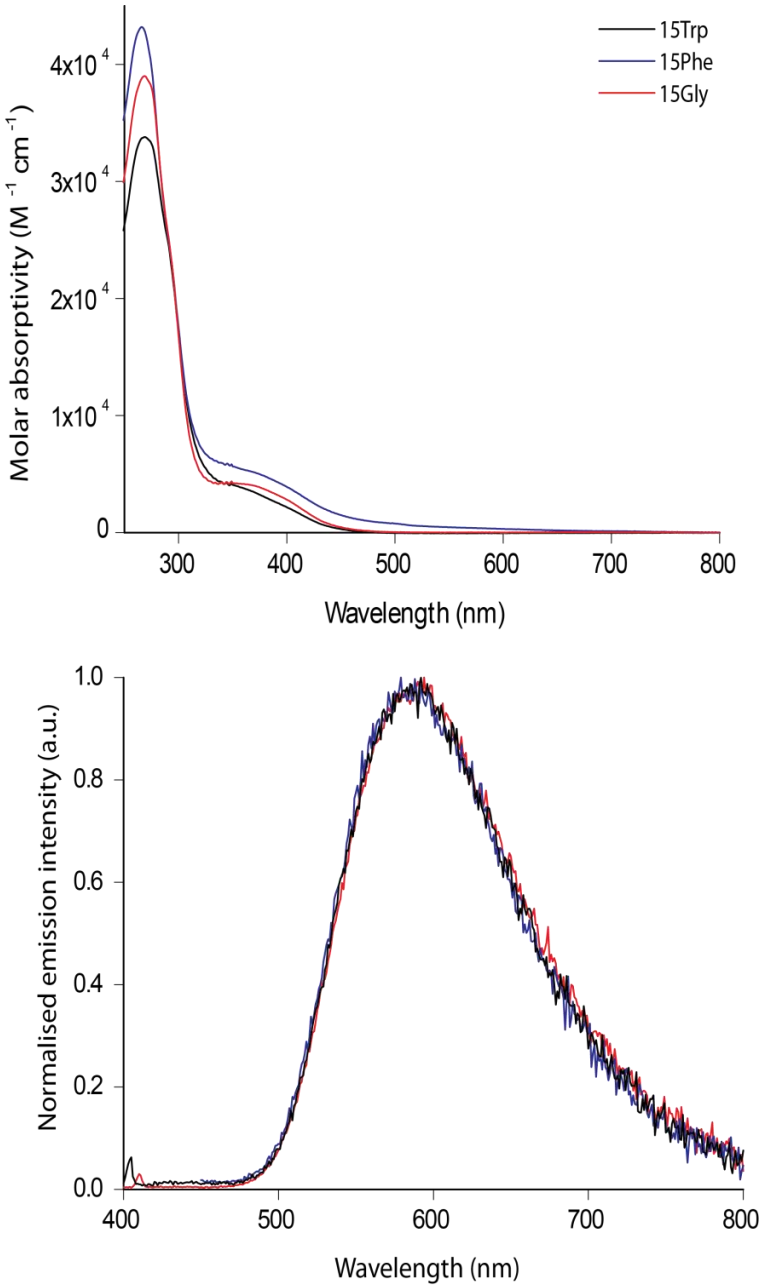

Figure 3.10 Comparison plots showing absorption (top) and normalised emission (bottom) of complexes **15Trp**, **15Phe** and **15Gly** in aerated dichloromethane solution.

The photophysical data for the neutral rhenium(I) complexes **15Trp**, **15Phe** and **15Gly** are summarised in **Table 3.3**. At a glance, the value of the excited state lifetime decay for all complexes is very similar (~300 ns) indicating that electron transfer is not a dominating process. This trend was consistent with the emission profiles, as there was no significant effect from the varying amino acid substituents. Even though the quantum yields for **15Trp** are lower than both the **15Phe** and **15Gly** derivatives, this alone is not strong evidence to indicate quenching *via* an electron transfer process.

Table 3.3 Photophysical properties of the Re(I) complexes from diluted dichloromethane solutions (*ca*. 10^{-5} M) at 298 K.

Complex	λ_{abs} (nm) [10^4 ε, $M^{-1}cm^{-1}$]	λ_{em} (nm)	τ [a] (ns)	τ [b] (ns)	Φ [a, c] (± 0.015)	Φ [b, c] (± 0.015)
15Trp	269 (3.38), 350 (0.41)	588	280	881	0.029	0.083
15Phe	266 (4.32), 355 (0.55)	581	308	1002	0.093	0.275
15Gly	268 (3.89), 358 (0.42)	592	267	806	0.109	0.331

[a] air equilibrated samples, [b] degassed samples, [c] quantum yield Φ measured against air-equilibrated quinine sulfate (in 1M H_2SO_4).

Based on the excited state lifetime decay and quantum yield measurements, the radiative (k_r) and non-radiative (k_{nr}) decay rate constants can be estimated (refer to equations provided in introduction section 1.1.2 for calculations of decay rate constants). The k_r and k_{nr} values obtained for the reported rhenium(I) tetrazolato complexes are summarised in **Table 3.4**. Both the k_r and k_{nr} values for the reported rhenium(I) complexes appear similar to previously reported rhenium(I) tetrazolato complexes.[71,159,161] This would suggest that the π-accepting nature of the tetrazolato ligand is not significantly affected by its coordination with amino acid methyl esters or any other substituent, as mentioned previously.

Table 3.4 Radiative and non-radiative decay constants (k_r and k_{nr}) of the Re(I) complexes calculated for the degassed dichloromethane solutions.

Complex	k_r (10^5 s^{-1})	k_{nr} (10^6 s^{-1})
15Trp	2.46	0.89
15Phe	3.01	0.69
15Gly	1.32	1.11

Upon cooling from room temperature to 77 K, the emission profiles for all complexes (illustrated in **Figure 3.11**) are blue shifted which can be explained by the rigidochromic effect (already discussed in the previous chapter). In addition, the excited state lifetime decay had increased almost 20-fold due to less quenching effects in frozen media. Also, the non-radiative decay is reduced due to the rigidity of the system, which results in longer excited state lifetime. This observation was

consistent with other rhenium(I) complexes.[182,183] **Table 3.5** summarises the luminescence properties of the complexes at low temperatures (77 K).

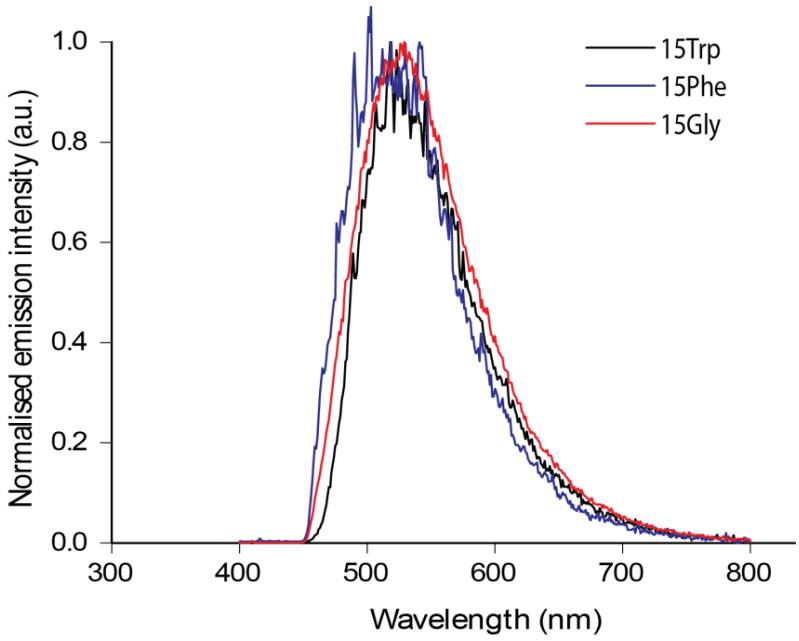

Figure 3.11 Emission profiles of rhenium(I) complexes **15Trp**, **15Phe** and **15Gly** at 77K.

Table 3.5 Emission and excited state lifetime data of Re(I) complexes **15Trp/Phe/Gly** at 77 K frozen media.

Complex	λ_{em} (nm)	τ (μs)
15Trp	521	2.04 (15%) and 8.28 (85%)
15Phe	516	9.07
15Gly	529	6.17

The photophysical data for rhenium(I) complexes **19Trp** and **19Phe** are presented in **Table 3.6**. The absorption profiles exhibit a high energy band between 250-300 nm attributed to IL transitions. The lower energy band between 330-450 nm was attributed to the MLLCT transition. The emission profiles for both **19Trp** and **19Phe** derivatives were relatively similar, appearing as a broad and structureless band at 585 nm (see **Figure 3.12**). In addition, the excited state lifetime decay for **19Trp** is of biexponential nature (percentage component in brackets) with values 224 (57%) and 577 (43%) ns, whereas for the **19Phe** analogue the lifetime decay was monoexponential at 313 ns. This biexponential decay observed for the **Trp** complex was also reported in Blanco-Rodriguez's paper as well as other **Trp** systems.[172,173,180]

The quantum yield for **19Trp** was lower than **19Phe** suggesting a quenching mechanism. However, this is not strong evidence to indicate an electron transfer process occurring as it is not complementary to the lifetime data.

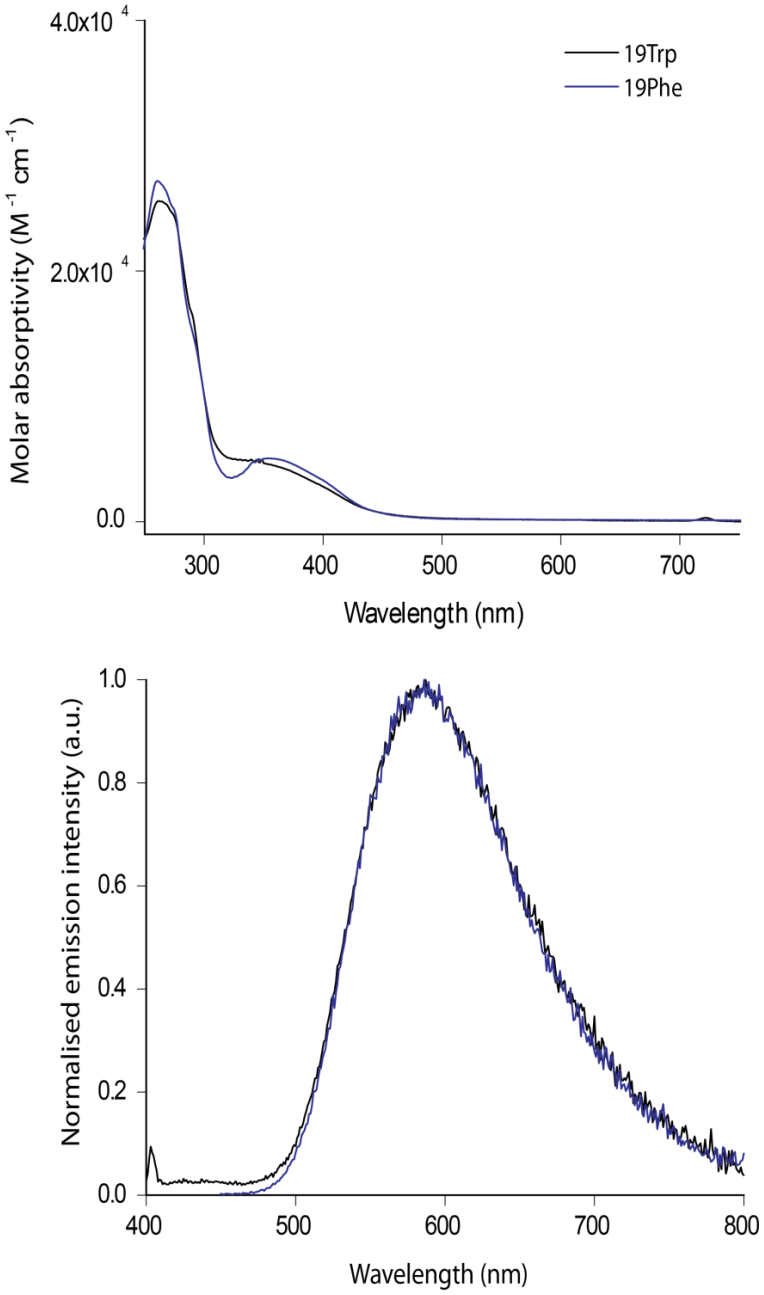

Figure 3.12 Absorption (top) and emission (bottom) plots of complexes **19Trp** and **19Phe** in aerated DCM solution.

Table 3.6 Photophysical properties of the Re(I) complexes from diluted dichloromethane solutions (*ca*. 10^{-5} M) at 298 K.

Complex	λ_{abs} (nm) [10^4 ε, $M^{-1}cm^{-1}$]	λ_{em} (nm)	τ (ns)[a]	τ (ns)[b]	Φ [a, c] (± 0.015)	Φ [b, c] (± 0.015)
19Trp	262 (2.56), 345 (0.49)	585	224 (57%), 577 (43%)	193 (27%), 1546 (73%)	0.009	0.015
19Phe	261 (2.72), 354 (0.51)	586	313	995	0.023	0.088

[a] air equilibrated samples, [b] degassed samples, [c] quantum yield Φ measured against air-equilibrated [Ru(**bipy**)$_3$]Cl$_2$.

3.7 Methylation of the Tetrazole Ring

The luminescence of rhenium(I) tetrazolato complexes can be efficiently modified by lowering the electron-rich nature of the tetrazolato moiety *via* reaction with electrophilic reagents such as H^+ and CH_3^+. This has been observed experimentally by Werrett, through reversible protonation and irreversible methylation of various neutral [Re(**N^N**)(CO)$_3$(L)] complexes.[167,184] The luminescence properties of the charged complexes varied significantly to their neutral analogues, in which the data displayed a 50 nm blue shift in emission with increased intensity, alongside elongated emission lifetimes. A similar trend can also be seen for neutral [Re(**N^N**)(CO)$_3$(L)] complexes in the presence of divalent metal ions such as Zn(II) and Cd(II).[185] Complexation of the neutral rhenium(I) species with these metal cations caused the steady-state emission to blue shift in emission (28-36 nm) and the time-resolved measurements resulted in 1.5 to 2.5-fold elongation of emission lifetimes. In addition to rhenium(I) metal complexes, there have been other reports on tetrazole-based metal complexes that have observed a dramatic effect upon methylation of the complexes. Specifically, the methylation of a tetrazolato-Ru(II) complex reported by Stagni *et al*. which resulted in a slight blue shift in emission (9-30 nm) and a 10-fold increase in excited state lifetime.[186]

Encouraged by these findings, further investigation was carried out to promote a photo-induced electron transfer (PeT) from the amino acid moiety to the excited rhenium metal centre. It was speculated that as a consequence of the electron rich nature of the tetrazole, the PeT could not be achieved with the neutral rhenium(I)

species presented earlier in the chapter. Therefore, the objective of reducing the electron-rich tetrazole by the introduction of electrophilic reagents was pursued. An investigation of the charged rhenium(I) species would then give us an indication of any PeT occurring within the system.

Methylation of the rhenium(I) tetrazolato complex was established by an addition of an electrophile (i.e. a methyl group) to the nucleophilic tetrazole ring. This was achieved by reacting methyl triflate in dichloromethane with the complex at low temperature (see **Scheme 3.8**). The cationic rhenium(I) analogue was formed after leaving the mixture to stir overnight at room temperature, followed by a metathesis to form the PF_6 salt.

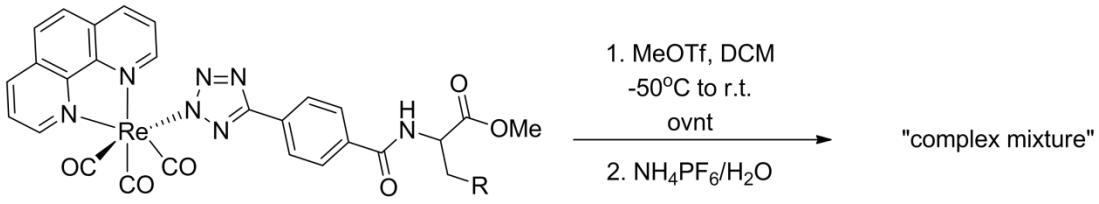

Scheme 3.8 Reaction scheme showing attempted methylation of **15Trp** and **15Phe**.

The methylated complexes **15Trp** and **15Phe** could not be purified and isolated due to the complex mixture of by-products that were difficult to separate. On the contrary, the methylation reaction worked successfully for the tetrazole ligands without a phenyl linker, **20Trp** and **20Phe** (**Scheme 3.9**), and the complexes were characterised by IR and NMR spectroscopy.

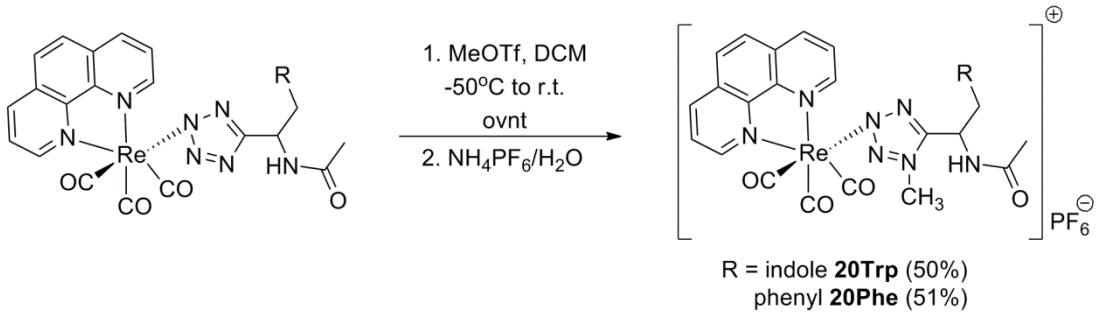

Scheme 3.9 Reaction scheme showing synthesis of methylated complexes **20Trp** and **20Phe**.

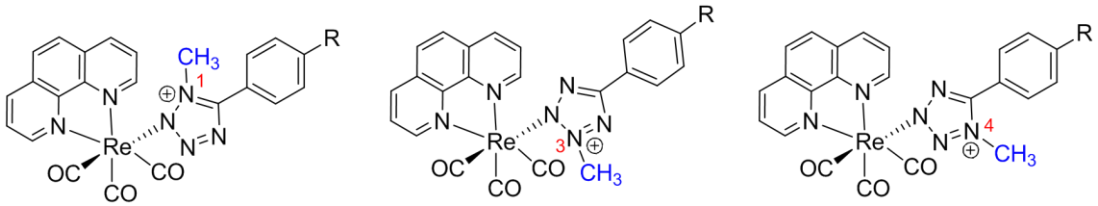

Scheme 3.10 Representation of possible methylated Re(I) tetrazolato complexes at N1, N3 or N4 atom.

There are three prospective positions for methylation to occur, i.e. on the three free nitrogen atoms of the tetrazole ring. However, previous studies have shown that the most favourable position for methylation is on the less hindered N4 atom (shown in **Scheme 3.10**).[158] The formation of the expected methylated complexes was initially confirmed by IR spectroscopy. Particularly, intense sharp CO signals were observed at *ca*. 2030 cm^{-1} and broader signals found at *ca*. 1920 cm^{-1}. **Table 3.7** displays IR stretching frequencies of complexes **19Trp/Phe** and **20Trp/Phe**. The stretching frequency for CO A′(2)/A″ is reported as one value as the bands are collapsed, which is not unusual for these type of rhenium(I) complexes.[184,187] In addition, the frequencies of the CO stretching bands shift to higher wavenumbers upon methylation, which is evident in **Table 3.7**. This is caused by the complex having an overall positive charge and reduced electron density on the rhenium metal centre.

Table 3.7 IR measurements comparing CO stretching frequencies (cm^{-1}) of neutral rhenium complexes and corresponding methylated analogues.

Complex	CO A′(1)	CO A′(2)/A″ *
[Re(**phen**)$(CO)_3$(**TzTrp**)] (**19Trp**)	2026	1911
[Re(**phen**)$(CO)_3$(Me**TzTrp**)]$^+$ (**20Trp**)$^{\#}$	2034	1920
[Re(**phen**)$(CO)_3$(**TzPhe**)] (**19Phe**)	2025	1907
[Re(**phen**)$(CO)_3$(Me**TzPhe**)]$^+$ (**20Phe**)$^{\#}$	2034	1921

$^{\#}$Measured in solution (acetone);
*CO A′(2)/A″ displays peaks that are superimposed into a single broad band

3.7.1 ^{1}H NMR Studies

^{1}H NMR spectroscopy was also used to characterise the methylated complexes. This technique is useful to elucidate a preliminary structure to indicate the formation of the product. The spectrum for the **15Gly** derivative is shown solely, as the **15Phe** and **15Trp** derivatives did not afford a clean product upon methylation due to the formation of inseparable by-products.

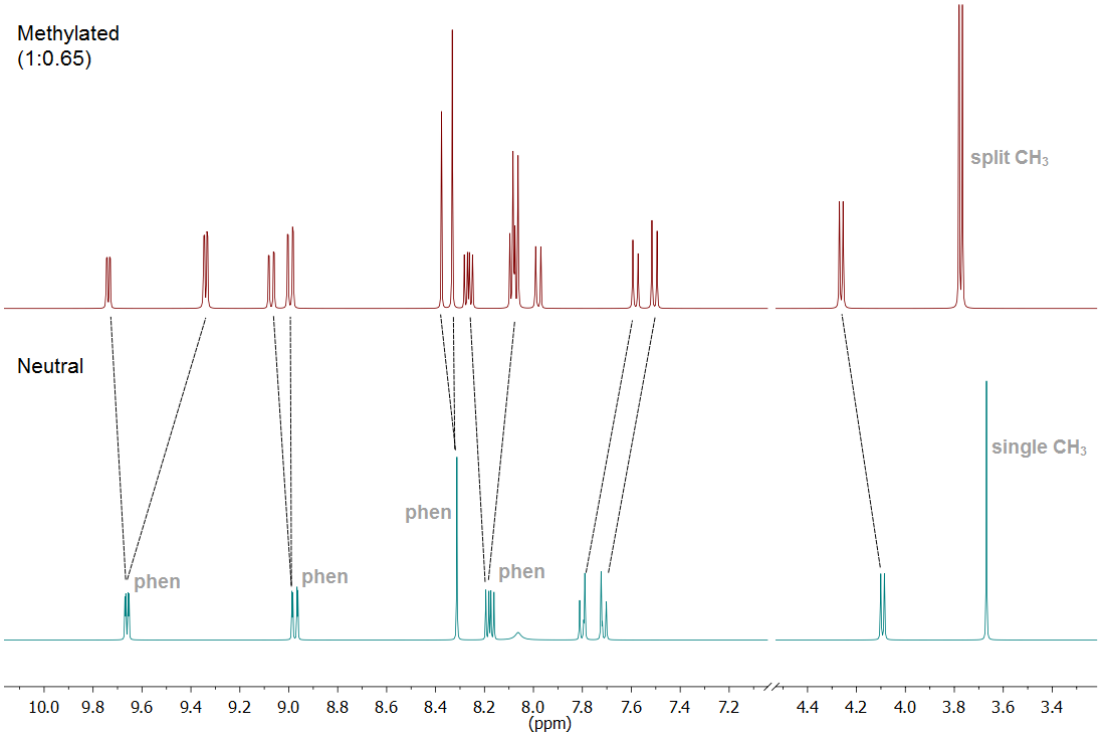

Figure 3.13 ^{1}H NMR spectra of neutral [Re(**phen**)(CO)$_3$(**Tz**Ph**Gly**Me)] complex (bottom, blue) compared to methylated species (top, red) in acetone-d$_6$ solution.

Upon methylation of complex **15Gly**, two distinct signal patterns were observed in the aromatic region of the ^{1}H NMR spectrum (in acetone-d$_6$). **Figure 3.13** shows the change in the number and position of the phenanthroline peaks upon methylation. In the neutral species there is one set of phenanthroline resonances (**Figure 3.13**, bottom) compared to the methylated species presenting two sets of signals (**Figure 3.13**, top). This data suggests that there are two rhenium species existing in solution. The methylation reaction may have produced two separate and different rhenium complexes, or they may be in equilibrium. It is also possible that the two different species could be a mixture of both Re-N1 and Re-N2 linkage isomers.[184] The integration of the peaks in the ^{1}H NMR spectra for the methylated species indicated the two products to occur in a ratio of 1:0.65.

However, this was not the case for [Re(**phen**)(CO)$_3$(**TzTrp**)] and [Re(**phen**)(CO)$_3$(**TzPhe**)] complexes, shown in **Figure 3.14** and **Figure 3.15** respectively. An exception could be seen of the tetrazolato complexes without the phenyl linker, having produced a cleaner ^{1}H NMR spectrum, with only one distinct species present. It could be that the signals are collapsed, with the exception of the

methylene protons (around 3.20-2.80 ppm) appearing as two signals. However, the integration remains the same which suggests it is assigned to one species only.

Additionally, the peaks at 3.77 and 3.78 ppm assigned to the methyl protons for **15Gly** were combined. On the contrary, the methyl peaks for **20Trp** and **20Phe** are well separated. The sharp singlet at 1.68 ppm (**20Trp**) and 1.69 ppm (**20Phe**) with integration of three protons was assigned as the methyl on the acetyl group. On the other hand, the sharp singlet at 3.55 ppm (**20Trp**) and 3.74 ppm (**20Phe**) with integration of three protons was assigned to the methyl on the tetrazole ring.

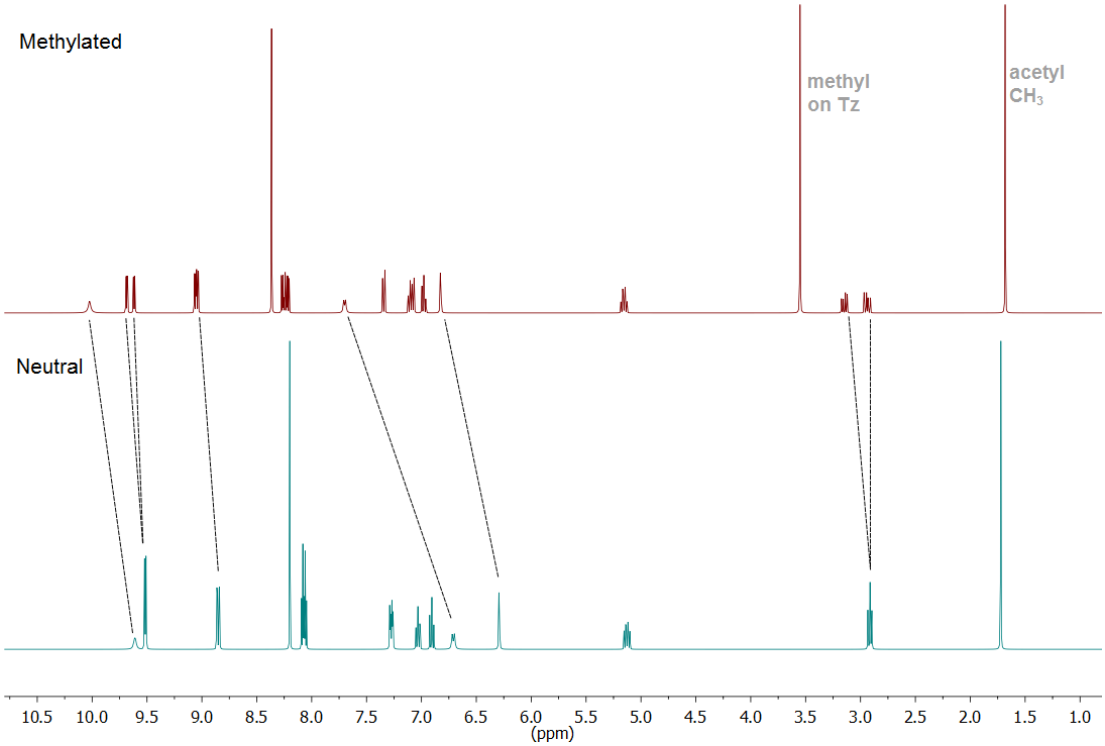

Figure 3.14 ^{1}H NMR spectra of neutral [Re(**phen**)$(CO)_3$(**TzTrp**)] complex (bottom, blue) compared to methylated species (top, red) in acetone-d_6 solution.

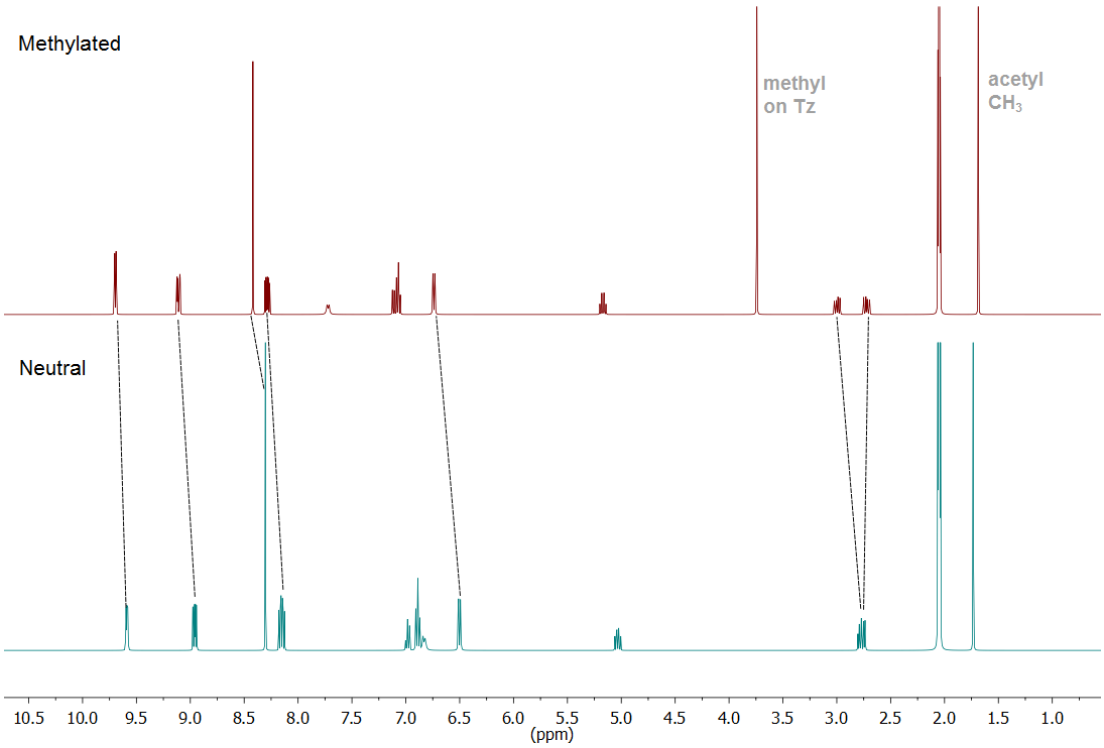

Figure 3.15 ^{1}H NMR spectra of neutral [Re(**phen**)(CO)$_3$(**TzPhe**)] complex (bottom, blue) compared to methylated species (top, red) in acetone-d$_6$ solution.

A condensed view of the **phen** proton signals before and after methylation of rhenium(I) tetrazolato complexes can be seen in **Table 3.8**. It seems that the peaks resembling the **phen** unit all appear to be deshielded (where peaks are upfield in the ^{1}H NMR spectrum) upon methylation. This increase in chemical shift was expected as there was reduced electron density around the **phen** unit, due to the positively charged tetrazole ring. Furthermore, the peak assigned to the NH signal of the amide had also experienced a higher chemical shift upon methylation for **Trp** and **Phe** complexes.

Table 3.8 Comparison of ^{1}H NMR signals (ppm) of the **phen** protons and NH amide signal before and after methylation.

Complex	phen $H_{2,9}$	phen $H_{3,8}$	phen $H_{5,6}$	phen $H_{4,7}$	NH (amide)
[Re(**phen**)(CO)$_3$(**Tz**Ph**Gly**Me)]	9.65	8.97	8.31	8.17	8.06
[Re(**phen**)(CO)$_3$(Me**Tz**Ph**Gly**Me)]$^{+}$	9.74, 9.34	9.08, 8.99	8.38, 8.33	8.26, 8.08	7.98
[Re(**phen**)(CO)$_3$(**TzTrp**)]	9.51	8.85	8.20	8.08	6.70
[Re(**phen**)(CO)$_3$(Me**TzTrp**)]$^{+}$	9.68, 10.02	9.05	8.36	8.24	7.70
[Re(**phen**)(CO)$_3$(**TzPhe**)]	9.58	8.97	8.31	8.14	6.82
[Re(**phen**)(CO)$_3$(Me**TzPhe**)]$^{+}$	9.69	9.10	8.41	8.29	7.72

NMR data from acetone-d$_6$ solutions

3.7.2 Photophysics

In general, the absorption profiles for the methylated rhenium(I) complexes all appear to have high energy bands in the UV region around 260-330 nm, which can be assigned to IL (π-π^*) transitions localised in the **phen** component and a lower energy band around 370 nm assigned to MLCT transitions. With respect to their neutral analogues, the methylated rhenium(I) species all appear to have a blue shifted absorption profile. This trend is similar for both **Trp** (**Figure 3.16**) and **Phe** (**Figure 3.17**) derivatives. The blue shift can be explained by the stabilisation of the HOMO energy level from the reduction of the electron density on the tetrazole ring *via* introduction of a methyl group.

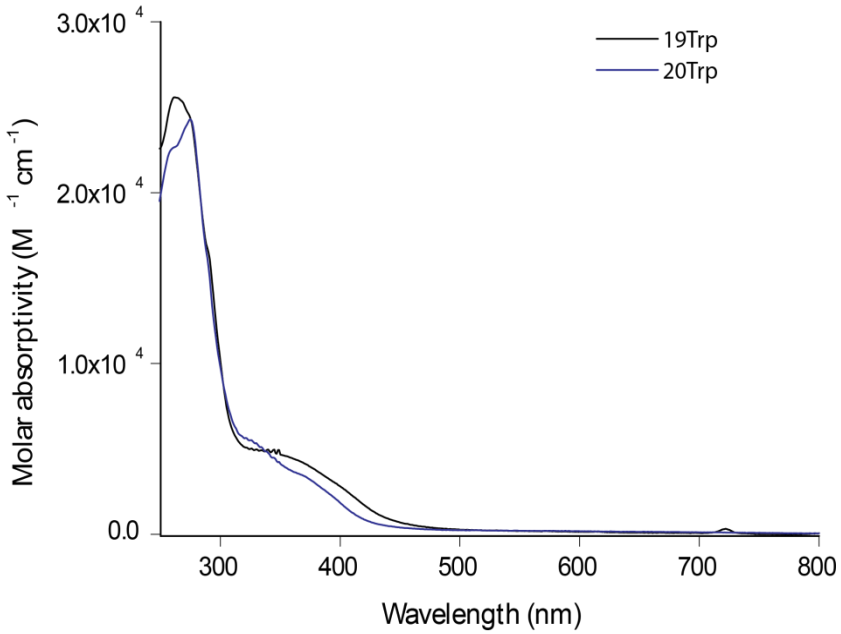

Figure 3.16 Absorption plot of cationic **20Trp** (blue trace) compared to the neutral **19Trp** (black trace) in DCM solution.

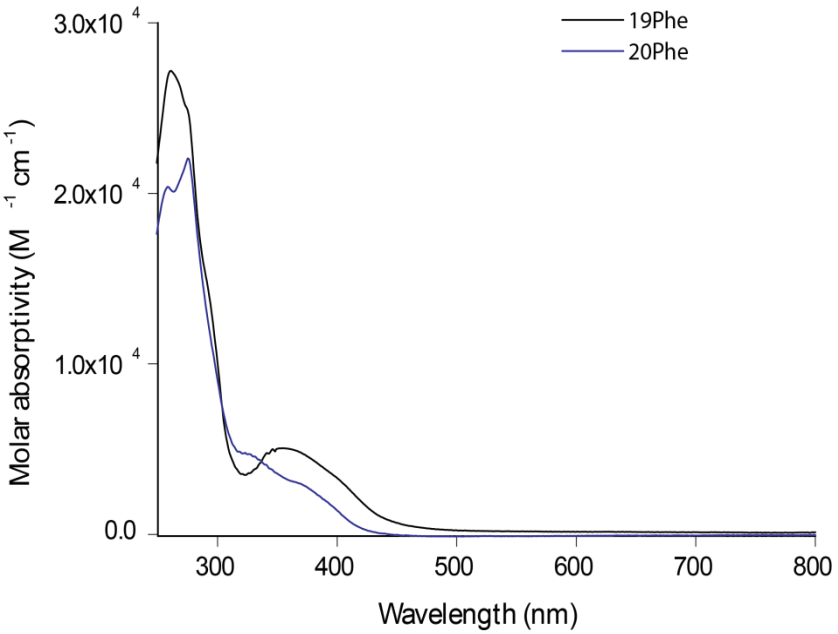

Figure 3.17 Absorption plot of cationic **20Phe** (blue trace) compared to the neutral **19Phe** (black trace) in DCM solution.

The emission profiles of the methylated rhenium(I) complexes in dilute DCM solutions appear to be broad and structureless. Both **Trp** (**Figure 3.18**) and **Phe** (**Figure 3.19**) derivatives have a maximum emission wavelength at 536-538 nm. Similarly observed for the absorption spectra, the emission maxima are blue shifted (~50 nm) with respect to neutral analogues. Again, this can be explained by the increased HOMO-LUMO energy gap apparent for cationic complexes. In addition, the lifetimes of the methylated complexes have lengthened about four times, whereas the quantum yields have doubled (see **Table 3.9** compared to **Table 3.6**). According to the energy gap law, the increased values of lifetime and quantum yield upon methylation can be described by a decreased non-radiative decay, due to the increased relative energy of the ^{3}MLCT excited state.[40,162]

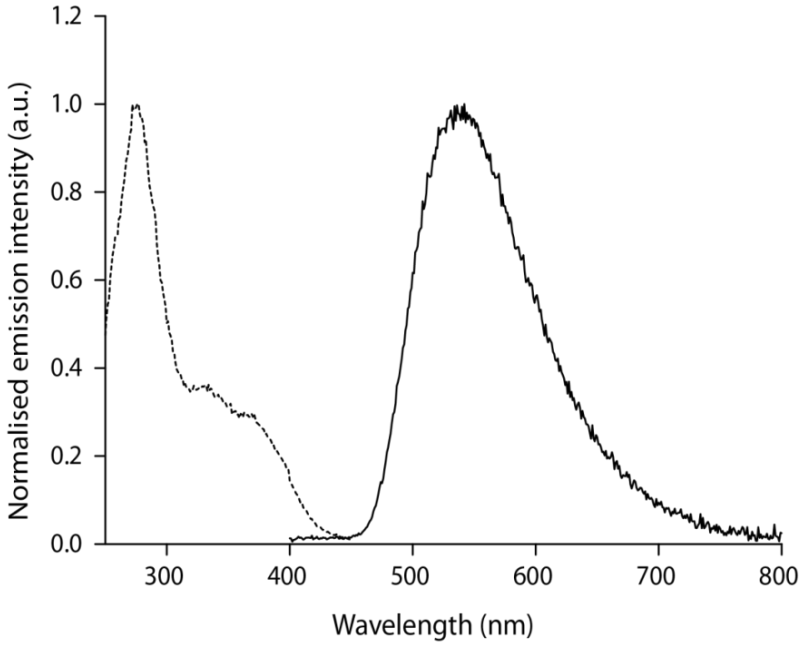

Figure 3.18 Excitation (dashed line) and emission (solid line) of **20Trp** in DCM solution.

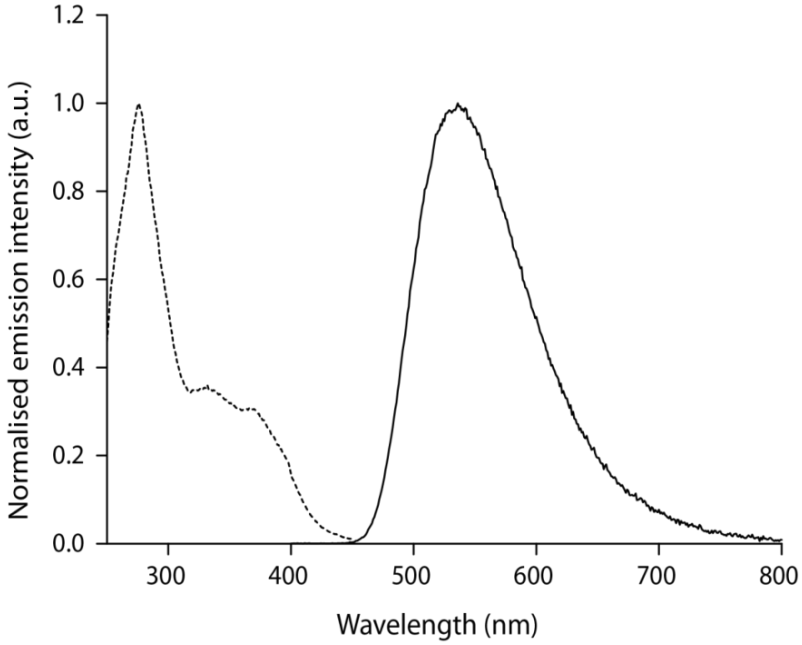

Figure 3.19 Excitation (dashed line) and emission (solid line) of **20Phe** in DCM solution.

Table 3.9 Photophysical properties of the methylated Re(I) complexes from diluted dichloromethane solutions (*ca*. 10^{-5} M).

Complex	λ_{abs} (nm) [10^4 ε, $M^{-1}cm^{-1}$]	λ_{em} (nm)	τ (ns)[a]	τ (ns)[b]	Φ [a, c] (± 0.015)	Φ [b, c] (± 0.015)
20Trp	275 (2.43), 332 (0.55), 370 (0.34)	539	355 (64%), 1096 (36%)	457 (42%), 3216 (58%)	0.019	0.032
20Phe	258 (2.04), 275 (2.21), 365 (0.31)	536	1287	3520	0.087	0.194

[a] air equilibrated samples, [b] degassed samples, [c] quantum yield Φ measured against air-equilibrated [Ru(**bipy**)$_3$]Cl$_2$.

Compared to the neutral rhenium(I) complexes **19Trp/Phe**, the methylated species **20Trp/Phe** was predicted to induce an electron transfer process. This can be explained by the fact that methylating the tetrazole ring would reduce the electron density on the rhenium metal centre, which would increase the potential for the photoexcited **Trp** ligand to donate an electron to the rhenium metal centre. The difference in quantum yield values (shown in **Table 3.9**) for **20Trp/Phe** were greater than those of **19Trp/Phe** (**Table 3.6**). However, analysis of **Table 3.9** demonstrated no significant difference in the lifetime decay for **20Trp/Phe** which disproves any occurrence of an electron transfer process.

3.8 Protonation of the Tetrazole Ring

It has already been known from reported literature that changing the electron rich nature of the tetrazole will result in significant variation of luminescence of the complexes.[181] The results deriving from the methylation of the tetrazole was described earlier in section 3.7. Protonation of the tetrazole was investigated because there were complications with methylation (due to formation of by-products) of complexes **15Trp** and **15Phe**. Regardless of the electrophile being used, both would result in the formation of a charged rhenium(I) complex which have been investigated.

The absorption and emission profiles for protonated rhenium(I) complexes were measured after sequential addition of triflic acid (TfOH) directly in the cuvette until no more change in intensity was observed, which assumed complete conversion to the protonated species. All rhenium complexes of **16Trp**, **16Phe** and **16Gly** derivatives showed different rates of protonation and required different amounts of triflic acid. However this was not investigated any further as the experiment was solely for qualitative purposes. A summary of the photophysical data is shown in **Table 3.10**, and the absorption and emission profiles shown in **Figure 3.20** to **Figure 3.22**.

Table 3.10 Absorption and emission data for the protonated Re(I) tetrazolato complexes (*ca.* 10^{-5} M) in aerated dichloromethane solution.

Complex	λ_{abs} (nm) [10^4 ε, $M^{-1}cm^{-1}$]	λ_{em} (nm)	τ (ns)	Φ [a]	k_r (10^6 s^{-1})	k_{nr} (10^6 s^{-1})
16Trp	260 (4.06), 321 (0.75)	534	1133	0.176	0.155	0.727
16Phe	261 (3.95), 331 (0.47)	536	1106	0.231	0.209	0.695
16Gly	258 (4.27), 374 (0.55)	537	1102	0.561	0.509	0.398

[a] quantum yield Φ measured against air-equilibrated [Ru(**bipy**)$_3$]Cl_2.

The absorption profiles for the protonated rhenium(I) tetrazolato species were relatively similar and all exhibit intense high energy bands between 258-261 nm and lower energy bands between 321-374 nm. The photophysical data was summarised in **Table 3.10**. Upon comparing the absorption profiles for the protonated and neutral species, there is an expected hypsochromic shift of both IL and CT bands. This observation can be described by the fact that protonation of the tetrazole reduces electron density around the rhenium metal centre, which causes indirect stabilisation of the HOMO orbitals and in turn increases the HOMO-LUMO energy gap.

The emission profiles of the protonated rhenium(I) complexes all exhibit broad structureless bands, alongside a significant blue shift in emission and there was also a visible increase in emission intensity compared to the neutral analogues. The spectra in **Figure 3.20** to **Figure 3.22** show the gradual change in emission occurring upon protonation for complexes **16Trp**, **16Phe** and **16Gly** respectively. Upon excitation of the MLCT band at *ca* 350 nm, the neutral rhenium(I) tetrazolato complexes display a

broad emission band in the range of 581-592 nm, whereas the protonated analogues shifted the emission in the range of 534-537 nm. This blue shift in emission can be explained by the increased HOMO-LUMO energy gap caused by protonation of the tetrazole ring.

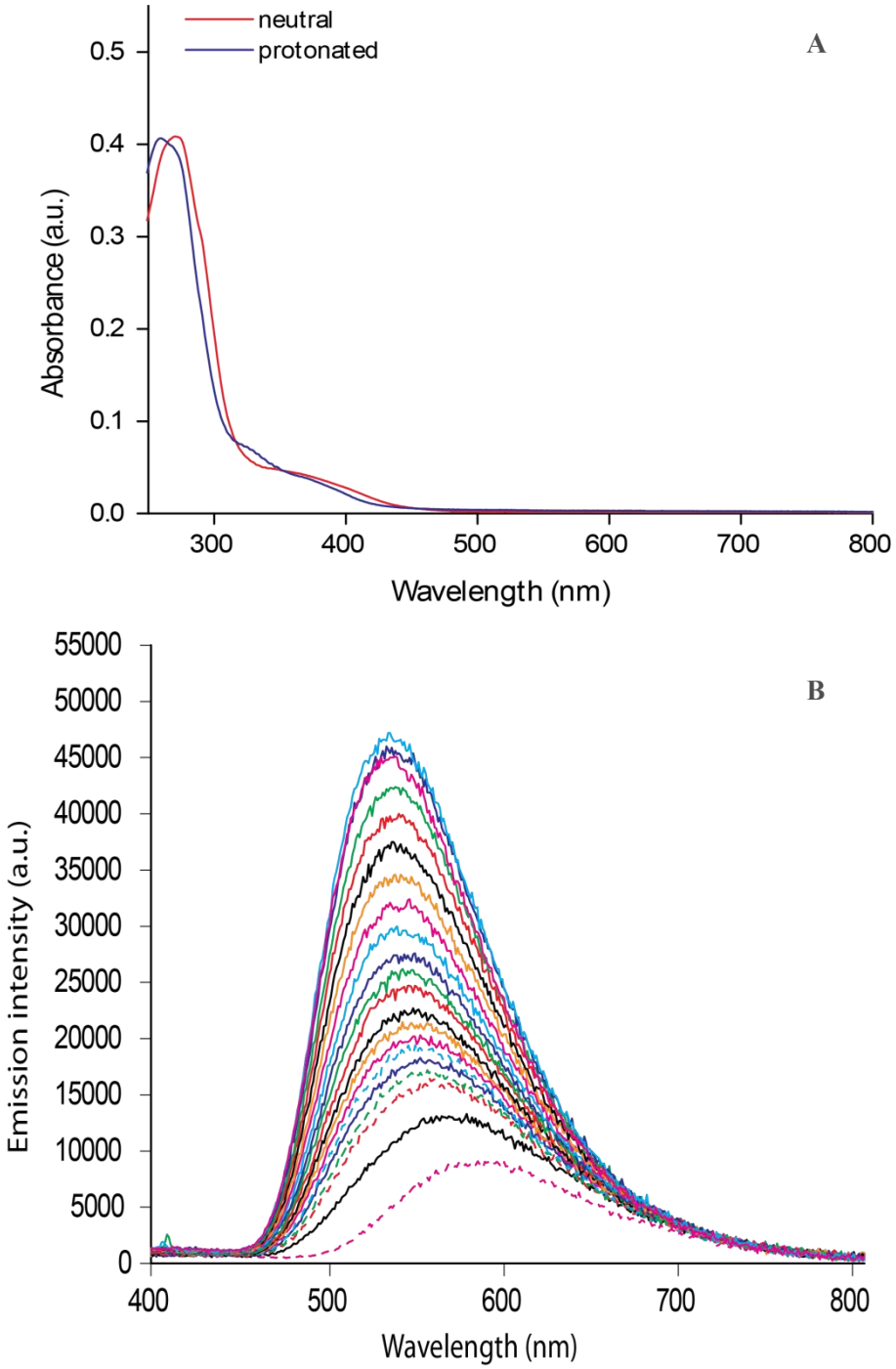

Figure 3.20 (a) Absorption plot of neutral **15Trp** (red trace) vs protonated **16Trp** (blue trace) complexes in DCM; (b) Emission of **16Trp** in DCM, upon sequential addition of TfOH ($1x10^{-5}$ M).

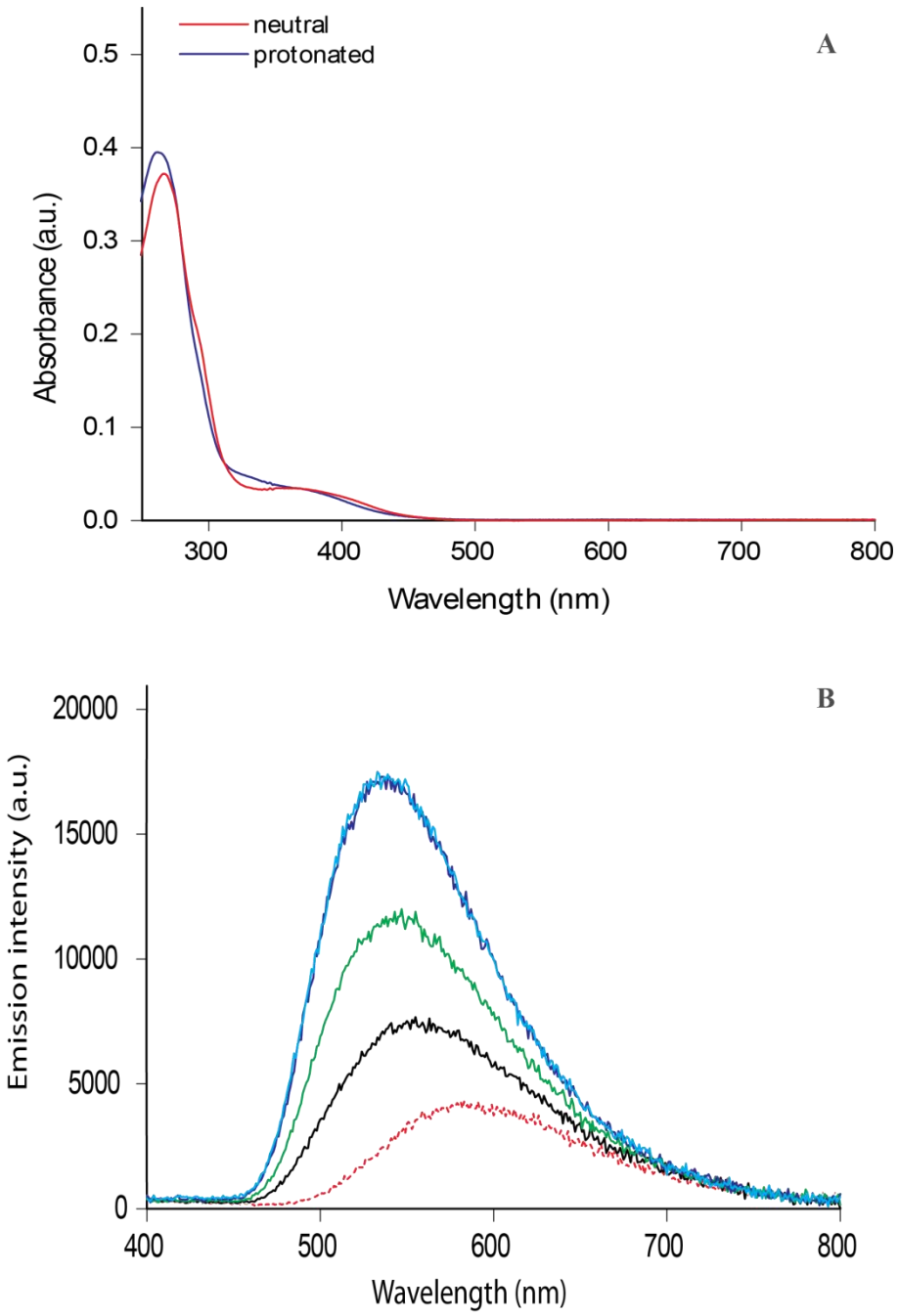

Figure 3.21 (a) Absorption plot of neutral **15Phe** (red trace) vs protonated **16Phe** (blue trace) complexes in DCM; (b) Emission of **16Phe** in DCM, upon sequential addition of TfOH ($1x10^{-5}$ M).

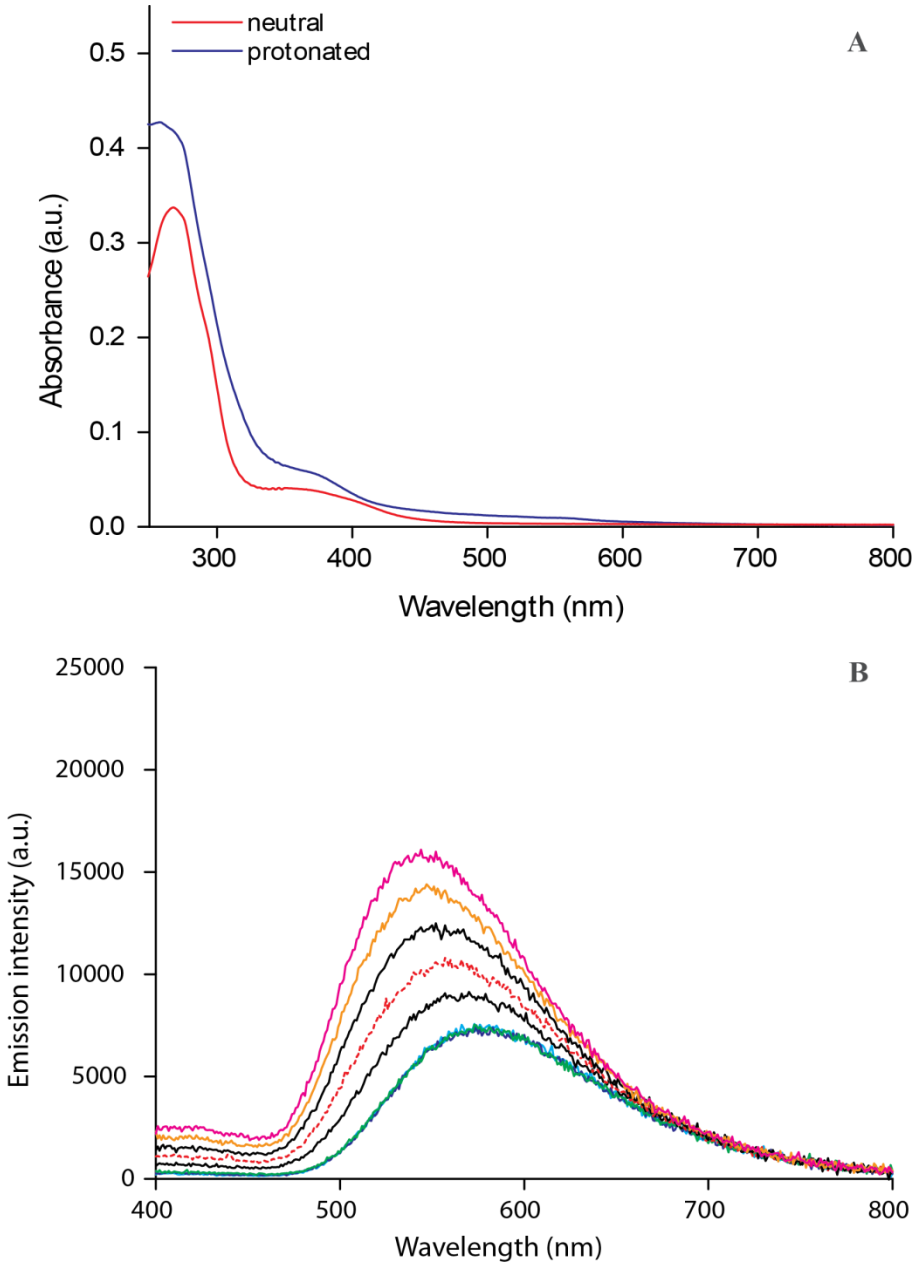

Figure 3.22 (a) Absorption plot of neutral **15Gly** (red trace) vs protonated **16Gly** (blue trace) complexes in DCM; (b) Emission of **16Gly** in DCM, upon sequential addition of TfOH ($1x10^{-5}$ M).

Generally, cationic rhenium(I) complexes display greater photophysical properties than their neutral analogues, which is often rationalised by the energy gap law.[40,188] As such, the excited state lifetime decays for the positively charged rhenium species **16Trp/Phe/Gly** have increased (four-fold) from hundreds of nanoseconds for the neutral analogues to a few microseconds. Moreover, the quantum yields of the protonated complexes are also higher (around ten-fold) than their neutral analogues. The elongated lifetimes and higher quantum yield values were attributed to a decreased non-radiative decay, due to the increased relative energy of the ^{3}MLCT

excited state upon protonation of the tetrazole ring.[40,162] The data for **16Trp**/**Phe**/**Gly** complexes are evident in **Table 3.10**.

It appears that the emission and excited state lifetime decay for the cationic complexes **16Trp**/**Phe**/**Gly** are very similar to each other, despite the difference in the amino acid substituent. This was similar to the photophysical data reported for the neutral analogues. Once again, there is no evidence of an electron transfer process occurring within these rhenium(I) tetrazolato species.

3.9 Conclusion

A series of six new neutral rhenium(I) [Re(**phen**)$(CO)_3$(L)] complexes, where L represents a variety of amino acid linked tetrazole ligands, were synthesised and characterised in terms of their structural and photophysical properties. The hypothesised phenomena of photoinduced electron transfer (PeT) could not be demonstrated or confirmed by photophysical analyses (focussing on excited state lifetime and quantum yield specifically). Even though the quantum yield values of the **Trp** derivative were lower, the lifetime decay and emission maxima were not significantly different to the **Phe** or **Gly** derivatives. Possible reasons as to why PeT was not observed include the fact that the distance of the reducing agent (**Trp**) was further away (due to the presence of a phenyl linker) than that of Blanco-Rodriguez's pyridine conjugated rhenium(I) complex. In addition, pyridine is a neutral ligand which makes the overall rhenium complex positively charged. In comparison, the tetrazole is anionic which makes the overall rhenium complex neutral. Having said this, the rhenium metal centre has a greater electron density (due to the electron rich nature of the tetrazole ring) and was less willing to accept electrons coming from the **Trp** species.

With the reasons mentioned above, several alterations were implemented to increase the driving force for PeT to occur. First, an attempt was to make the tetrazole ligand more electron withdrawing by protonation. This would result in reduced electron density on the rhenium metal centre, which would then induce an electron transfer process from the tryptophan to form a charge separated state. The protonation of the

complexes **16Trp**, **16Phe** and **16Gly** have been investigated and the change in luminescence monitored by emission spectroscopy. Upon protonation of the tetrazole ring, the emission intensity was significantly increased and a blue shift was observed for all the complexes. These photophysical changes can be attributed by a larger HOMO-LUMO energy gap found on the cationic complexes. The new complexes all exhibit improved quantum yields and longer lifetimes, which are characteristic of cationic species. These cationic amino acid rhenium(I) tetrazolato complexes showed different photophysical properties to their neutral analogues. However, when comparing the **Trp** and **Phe** derivatives of the same complex, there was no strong evidence to suggest electron transfer to occur in this system.

Another attempt was made, this time investigating the effects of shortening the distance between the electron donor site (**Trp**) and metal centre to increase the likelihood of an electron transfer mechanism to occur. This was done by removing the phenyl ring linked to the tetrazole, to afford complexes **19Trp** and **19Phe**. However, photophysical data suggest that both types of complexes (with and without the phenyl linker) were not significantly different to each other. The emission band arises at 580-590 nm, with excited state lifetimes of 200-300 ns in aerated dichloromethane solutions for both series of complexes. Therefore, this suggested that the group of complexes without the phenyl linker had more likelihood of participating in PeT process when compared to their analogues with the phenyl linker.

In addition, methylated rhenium(I) tetrazolato complexes **20Trp** and **20Phe** have been synthesised and characterised, structurally and photophysically. The methylation reaction produced a mixture of Re-N1 and Re-N2 linkage isomers, where the methyl was coordinated regioselectively on the N4 atom of the tetrazole ring. Further investigation looking at the change in luminescence was monitored by emission spectroscopy. The photophysical properties were found to be similar to those complexes that were protonated, which was expected due to a change in electron density on the tetrazole.

3.10 Experimental

Refer to general procedures as outlined in Chapter 2, section 2.8.1, unless stated otherwise. For compounds **20Trp** and **20Phe**, it was not possible to obtain reproducible elemental analyses.

The specific assignment of peaks for the amino acid compounds are based on the referencing outlined in **Scheme 3.11**.

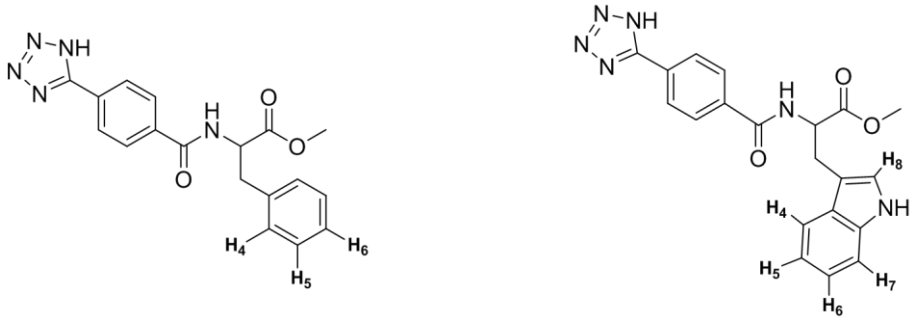

Scheme 3.11 NMR referencing layout for amino acids, phenylalanine (**Phe**, left) and tryptophan (**Trp**, right).

3.10.1 General Methodology for the Synthesis of Ligands

NCPhTrpMe (9)

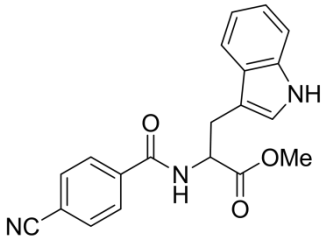

Thionyl chloride (1.8 mL) was added to 4-cyanobenzoic acid (0.61 g, 4.13 mmol) and the mixture heated to reflux for 1 hour. Excess thionyl chloride was removed by rotary evaporation to afford a white solid. This was dissolved in DCM (*ca.* 20 mL) and triethylamine (1.5 mL, 10.7 mmol) was added to this at 0 °C. **Trp**MeHCl (1.06 g, 4.18 mmol) was added and the solution turned dark orange. The mixture was left to stir at room temperature for 30 minutes. The precipitate ($Et_3N{\cdot}HCl$) that formed was filtered off and the orange filtrate washed with D.I. water (3 × 20 mL). The organic extract was dried ($MgSO_4$) and concentrated under reduced pressure to afford oily orange residue. This was left to dry under vacuum over the weekend to afford orange crystalline solid (1.19 g, 83%); m.p. 151-153 °C. ν_{max} (ATR-FTIR)/cm^{-}

[1] (solid state): 3395 br. s, 2952 m, 2850 w, 2231 m (C≡N), 1733 s (C=O ester) 1646 s (C=O amide), 1525 s, 1493 s, 1457 m, 1435 m, 1342 m, 1281 m, 1215 s, 854 w, 742 s. ^{1}H NMR (δ, ppm, $CDCl_3$): 8.24 (1H, s, **NH** amide), 7.75-7.69 (2H, m, phenyl **CH**), 7.67-7.63 (2H, m, phenyl **CH**), 7.51 (1H, d, *J* = 8.0 Hz, indole **CH**), 7.37 (1H, d, *J* = 8.0 Hz, indole **CH**), 7.20 (1H, app. t, *J* = 7.0 Hz, indole **CH**), 7.07 (1H, app. t, *J* = 7.0 Hz, indole **CH**), 7.00 (1H, s, indole **H8**), 6.69 (1H, br. s, **NH** indole) 5.15-5.11 (1H, m, NH-**CH**-$COOCH_3$), 3.76 (3H, s, O**CH$_3$**), 3.52-3.41 (2H, m, NH-CH-**CH$_2$**-indole). ^{13}C NMR (δ, ppm, $CDCl_3$): 172.2 (**C**=O ester), 165.3 (**C**=O amide), 137.9, 136.3, 132.5, 127.9, 127.8, 122.9, 122.6, 119.9, 118.6, 115.4 (**C**N), 111.6, 109.9, 53.9, 52.7, 45.9 (**C**H_3), 27.6 (**C**H_2).

NCPhPheMe (10)

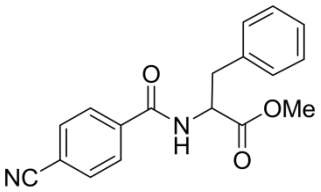

Thionyl chloride (*ca.* 2 mL) was added to 4-cyanobenzoic acid (469 mg, 3.19 mmol) and heated to reflux for 1 hour. Excess thionyl chloride was removed by rotary evaporation to produce dark orange residue. This was dissolved in DCM (*ca.* 20 mL) and triethylamine (2 mL, 14 mmol) was added at 0 °C. HCl gas was evolved and the solution turned dark brown. **Phe**MeHCl (712 mg, 3.3 mmol) was added and the solution left to stir at room temperature over the weekend. The dark brown mixture was washed with D.I. water (2 × 20 mL) and Na_2CO_3 (3 × 10 mL). The organic extract was then dried ($MgSO_4$) and concentrated under reduced pressure to afford a brown solid. This was purified by recrystallization (hexane/chloroform) to produce a beige powder (407 mg, 41%); m.p. 123-126 °C; ν_{max} (ATR-FTIR)/cm^{-1} (solid state): 3286 broad s, 2231 m (C≡N), 1740 s (C=O ester), 1644 s (C=O amide), 1548 s, 1434 m, 1351 m, 1273 m, 1216 m, 1093 w, 996 w, 854 w, 707 w. ^{1}H NMR (δ, ppm, $CDCl_3$): 7.81 (2H, d, *J* = 8.0 Hz, phenyl **CH**), 7.73 (2H, d, *J* = 8.8 Hz, phenyl **CH**), 7.30-7.27 (5H, m, phenyl **H4,5,6**), 6.56 (1H, br. s, **NH**), 5.09-5.05 (1H, m, NH-**CH**-$COOCH_3$), 3.79 (3H, s, O**CH$_3$**) and 3.34-3.26 (2H, m, NH-CH-**CH$_2$**-phenyl). ^{13}C NMR (δ, ppm, $CDCl_3$): 171.9 (**C**=O ester), 165.2 (**C**=O amide), 137.8, 135.7, 132.5, 129.3, 128.7, 127.8, 117.9, 115.4 (**C**N), 53.8, 52.7, 45.9 (**C**H_3), 37.7 (**C**H_2).

NCPhGlyMe (11)

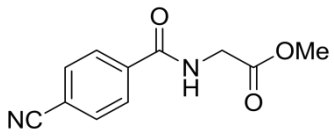

Thionyl chloride (3 mL) was added to 4-cyanobenzoic acid (508 mg, 3.45 mmol) and the mixture heated to reflux for about 1 hour. The white mixture was concentrated under vacuum to afford colourless flakes. This was dissolved in DCM (*ca.* 20 mL) and triethylamine (2 mL, 14 mmol) added to this at 0 °C. The solution turned orange after evolution of gas ceased. Finally, **Gly**MeHCl (488 mg, 3.8 mmol) was added and the solution turned yellow. The reaction mixture was left to stir at room temperature overnight. The precipitate ($Et_3N{\cdot}HCl$) was filtered off and the yellow solution washed with water (3 × 50 mL). The organic extract was dried ($MgSO_4$) and concentrated under reduced pressure to afford bright yellow solid (610 mg, 81%); m.p. 153-164 °C; ν_{max} (ATR-FTIR)/cm^{-1} (solid state): 3320 broad s, 2953 m, 2229 m (C≡N), 1735 s (C=O ester) 1644 s (C=O amide), 1547 s, 1500 m, 1211 s, 863 w, 770 w. ^{1}H NMR (δ, ppm, $CDCl_3$): 7.96-7.93 (2H, m, phenyl **CH**), 7.80-7.78 (2H, m, phenyl **CH**), 6.70 (1H, s, **NH**), 4.26 (2H, d, *J* = 4.0 Hz, NH**CH$_2$**), 3.82 (3H, s, O**CH$_3$**). ^{13}C NMR (δ, ppm, $CDCl_3$): 170.1 (**C**=O ester), 165.6 (**C**=O amide), 132.5 (phenyl **C**H), 127.8 (phenyl **C**H), 115.5 (**C**N), 52.7 (**C**H_3), 41.8 (**C**H_2).

TzHPhTrpMe (12)

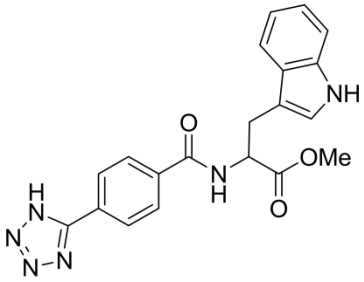

Compound **9** (344 mg, 1.0 mmol), sodium azide (134 mg, 2.0 mmol), zinc bromide (123 mg, 0.5 mmol) were combined in isopropanol/water (1:2) mixture (*ca.* 15 mL) and heated at reflux under nitrogen overnight. After heating, the reaction mixture was left to cool down at room temperature (orange solution with brown precipitate evident). To the mixture was added 3 M HCl until pH 1 was achieved and then EtOAc added until no more solid was evident. The organic layer was separated and the aqueous layer further extracted with EtOAc. The combined organic extracts were dried ($MgSO_4$) and then evaporated *in vacuo* to afford an orange-brown oil (69 mg,

18%); m.p. 180 °C (dec.). ν_{max} (ATR-FTIR)/cm^{-1}: 3393 broad s (NH amide), 1728 s (C=O ester) 1622 s (C=O amide). ^{1}H NMR (δ, ppm, acetone-d_6): 10.08 (1H, s, **NH**), 8.20–8.13 (2H, m, phenyl **CH**$_{ortho}$), 8.05–7.95 (2H, m, phenyl **CH**$_{meta}$), 7.90 (1H, d, *J* = 7.7 Hz, **NH** amide), 7.87–7.80 (1H, m, **NH** indole), 7.72–7.58 (1H, m, **CH** indole), 7.42–7.33 (1H, m, **CH** indole), 7.32–7.27 (1H, m, **CH** indole), 7.16–6.87 (2H, m, **CH** indole), 5.12–4.93 (1H, m, NH-**CH**-$COOCH_3$), 3.70 (3H, s, **CH$_3$**), 3.62–3.27 (2H, m, NH-CH-**CH$_2$**-indole). ^{13}C NMR (δ, ppm, DMSO-d_6): 173.4, 172.4 (**C**=O ester), 165.6 (**C**=O amide), 164.9 (**Ct**), 137.9, 136.0 (phenyl quat. **C**), 135.8 (phenyl quat. **C**), 132.4 (phenyl **C**H), 128.3 (phenyl **C**H), 127.1 (indole quat. **C**), 126.8, 123.5, 120.9, 118.3, 117.9, 113.7 (indole **C**H), 111.4 (indole **C**H), 110.4 (indole **C**H), 109.8 (indole quat. **C**), 53.9 (**C**H), 51.9 (**C**H_3), 26.7 (**C**H_2).

TzHPhPheMe (13)

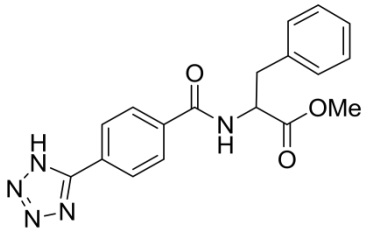

Hydrochloric acid (32%, 1 mL) was added to a vigorously stirred solution of TEA (0.32 mL, 2.29 mmol) in toluene (*ca.* 10 mL) at 0 °C, stoppered and left to stir at room temperature for 10 minutes. Compound **10** (1.0 g, 3.2 mmol) and sodium azide (0.612 g, 9.40 mmol) were added and the yellow mixture heated to reflux whilst stirring for 4 days. After cooling down at room temperature, the yellow-orange mixture was concentrated under reduced pressure to remove toluene. The residue was dissolved in EtOAc and washed with water (3 × 20 mL). The organic extract was concentrated under reduced pressure to afford orange oil. This was washed with water and extracted with DCM, dried and concentrated down to a white solid (170 mg, 15%); m.p. 177-199 °C. ν_{max} (ATR-FTIR)/cm^{-1}(solid state): 1729 s (C=O ester) 1656 s (C=O amide). ^{1}H NMR (δ, ppm, DMSO-d_6): 8.87 (1H, d, *J* = 8.1 Hz, **NH** amide), 8.16–8.04 (2H, m, phenyl **CH**$_{meta}$), 7.97 (2H, d, *J* = 8.5 Hz, phenyl **CH**$_{ortho}$), 7.41–7.10 (5H, m, phenyl **H4, H5, H6**), 4.76–4.53 (2H, m, **CH$_2$**-CH-NH), 3.65 (3H, s, **CH$_3$**), 3.25-3.07 (1H, m, CH_2-**CH**-NH). ^{13}C NMR (δ, ppm, DMSO-d_6): 173.1, 172.2 (**C**=O ester), 165.7 (**C**=O amide), 163.5 (**Ct**), 138.1, 137.7, 136.1 (phenyl quat. **C**), 135.6 (phenyl quat. **C**), 129.1 (phenyl **C**H), 128.4 (phenyl **C**H), 127.0 (phenyl

quat. **C**), 126.6 (phenyl **C**H), 126.5 (phenyl **C**H), 126.3 (phenyl **C**H), 54.4 (**C**H), 52.1 (**C**H_3), 36.4 (**C**H_2).

TzHPhGlyMe (14)

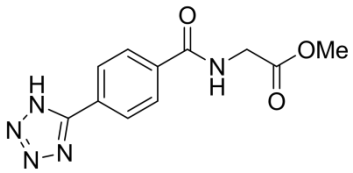

Hydrochloric acid (32%, 0.22 mL) was added to a vigorously stirred solution of TEA (0.32 mL) in toluene (*ca.* 10 mL) at 0 °C, stoppered and left to stir at room temperature for 10 minutes. Compound **11** (257 mg, 1.17 mmol) and sodium azide (255 mg, 3.9 mmol) were added and the yellow mixture heated to reflux whilst stirring for 3 days. After cooling down at room temperature, water (*ca.* 10 mL) was added to the creamy mixture and toluene was removed by separation. The aqueous phase was acidified with HCl to form an off-white precipitate. This was collected by vacuum filtration and air-dried to afford a beige-white solid (233 mg, 73%); m.p. 176-192 °C; ν_{max}(ATR-FTIR)/cm^{-1}(solid state): 3554 s, 3289 s, 1732 s (C=O ester) 1638 s (C=O amide), 1582 m, 1545 s, 1501 m, 1437 m, 1312 w, 1276 m, 1092 w, 859 w, 662 w. ^{1}H NMR (δ, ppm, DMSO-d_6): 9.15 (1H, t, *J* = 5.6 Hz, **NH** amide), 8.17 (2H, d, *J* = 8.8 Hz, phenyl **CH**), 8.08 (2H, d, *J* = 8.4 Hz, phenyl **CH**), 4.05 (2H, d, *J* = 6.0 Hz, NH**C**$\mathbf{H_2}$-COOCH_3), 3.67 (3H, s, O**C**$\mathbf{H_3}$). ^{13}C NMR (δ, ppm, DMSO-d_6): 170.7 (**C**=O ester), 166.2 (**C**=O amide), 136.2 (phenyl quat. **C**), 128.7 (phenyl **C**H), 127.5 (phenyl **C**H), 52.3 (**C**H_3), 41.7 (**C**H_2).

3.10.2 Synthesis of the Complexes

[Re(phen)(CO)$_3$(TzPhTrpMe)] (15Trp)

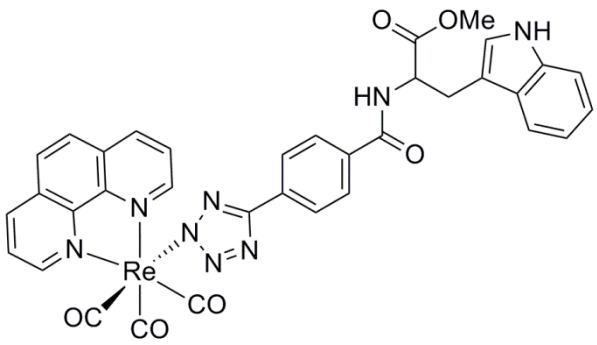

fac-[Re(**phen**)(CO)$_3$Cl] (62 mg, 0.12 mmol) and compound **12** (60 mg, 0.15 mmol) were combined in MeCN (*ca.* 5 mL). TEA (22 µL, 0.16 mmol) was added to this and

reaction mixture heated using microwave reactor at 160 °C for 3 hours. The orange solution was concentrated under reduced pressure to afford light orange residue, which was purified *via* column chromatography (deactivated neutral alumina, Brockmann III); DCM/EtOAc (50:50) eluted first fraction as starting rhenium precursor and EtOAc (2% MeOH) eluted second fraction as product (27 mg, 51%). ν_{max} (ATR-FTIR)/cm^{-1} (solid state): 2023 s (CO, A′(1)), 1915 s (CO), 1617 w, 1488 m.

^{1}H NMR (δ, ppm, Acetone-d_6) 10.06 (1H, s, **NH** amide), 9.65 (2H, d, *J* = 8.0 Hz, **phen** $H_{2,9}$), 8.97 (2H, d, *J* = 8.4 Hz, **phen** $H_{3,8}$), 8.30 (2H, s, **phen** $H_{5,6}$), 8.17 (2H, d, *J* = 8.4 Hz, **phen** $H_{4,7}$), 7.72–7.58 (5H, m, phenyl $\mathbf{H_{ortho}}$, $\mathbf{H_{meta}}$, **NH** indole), 7.59 (1H, d, *J* = 9.2 Hz, **CH** indole), 7.35 (1H, d, *J* = 8.8 Hz, **CH** indole), 7.23 (1H, s, indole $\mathbf{H_8}$), 7.08 (1H, app. t, *J* = 6.8 Hz, **CH** indole), 7.00 (1H, app. t, *J* = 8.0 Hz, **CH** indole), 4.93-4.91 (1H, m, NH-**CH**-$COOCH_3$), 3.66 (3H, s, $\mathbf{CH_3}$), 3.42–3.27 (2H, m, NH-$\mathbf{CH_2}$-indole). ^{13}C NMR (δ, ppm, Acetone-d_6) 197.9 (**C**O), 194.8 (**C**O), 173.2 (**C**$OOCH_3$), 166.9 (**C**t), 162.9, 155.1 (**phen C**H), 148.2 (**phen** quat. **C**), 140.4 (**phen C**H), 137.6 (phenyl quat. **C**), 134.6 (phenyl quat. **C**), 133.8 (indole quat. **C**), 131.7 (indole quat. **C**), 128.7 (phenyl **C**H), 128.3 (phenyl **C**H), 127.4 (**phen C**H), 126.4 (**phen C**H), 124.4 (indole **C**H), 122.2 (**phen C**H), 119.6 (indole **C**H), 119.1 (indole **C**H), 112.3 (indole **C**H), 111.0 (indole **C**H), 54.6 (NH-**C**H-$COOCH_3$), 52.3 (O**C**H_3), 28.1 (NH-**C**H_2-indole). Elemental Analysis: Calc for $C_{35}H_{25}N_8O_6Re$·*DCM*·*EtOAc*: C (47.43%), H (3.48%), N (11.06%); found C (46.70%), H (3.49%), N (11.05%).

[Re(phen)(CO)$_3$(TzPhPheMe)] (15Phe)

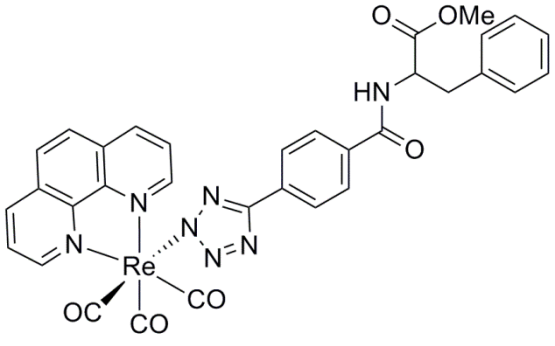

fac-[Re(**phen**)$(CO)_3$Cl] (58 mg, 0.12 mmol) and compound **13** (56 mg, 0.16 mmol) were combined in MeCN (*ca*. 5 mL). TEA (22 µL, 0.16 mmol) was added to this and reaction mixture heated using microwave reactor at 160 °C for 2 hours. The orange solution was concentrated under reduced pressure to afford light orange residue,

which was purified *via* column chromatography (deactivated neutral alumina, Brockmann III); DCM/MeCN (70:30) eluted first fraction (yellow) as starting rhenium precursor and MeCN/MeOH (70:30) eluted second fraction (orange) as product. An orange solid was produced after concentrating the column fractions under reduced pressure (43 mg, 45%). ν_{max} (ATR-FTIR)/cm^{-1} (solid state): 2024 s (CO, A′(1)), 1908 s (CO), 1741 m, 1655 m.

^{1}H NMR (δ, ppm, Acetone-d_6) 9.67 (2H, d, *J* = 8.0 Hz, **phen** $H_{2,9}$), 8.99 (2H, d, *J* = 8.0 Hz, **phen** $H_{4,7}$), 8.33 (2H, s, **phen** $H_{5,6}$), 8.19 (2H, d, *J* = 8.0 Hz, **phen** $H_{3,8}$), 7.80 (1H, s, **NH** amide), 7.74–7.67 (4H, m, 2 × $\mathbf{H_{ortho}}$ and 2 × $\mathbf{H_{meta}}$), 7.32–7.20 (5H, m, phenyl **H4, H5, H6**), 4.98–4.75 (1H, m, NH-**CH**-$COOCH_3$), 3.68 (3H, s, $\mathbf{CH_3}$), 3.28–3.10 (2H, m, NH-CH-$\mathbf{CH_2}$-phenyl). ^{13}C NMR (δ, ppm, Acetone-d_6): 197.9 (**C**O), 194.9 (**C**O), 172.9 (**C**$OOCH_3$), 170.9, 166.9 (**C**t), 162.9, 155.1 (**phen C**H), 148.2, 140.4 (**phen C**H), 138.4, 134.5, 133.9, 131.7, 130.0, 129.2 (**Phe**), 128.7 (**phen C**H), 128.3 (phenyl **C**H), 127.5, 127.4 (**phen C**H), 126.4 (phenyl **C**H), 55.2 (NH-**CH**-$COOCH_3$), 52.3 (O**C**H_3), 38.0 (NH-CH-$\mathbf{CH_2}$-Phe). Elemental Analysis: Calc for $C_{33}H_{24}N_7O_6Re$: C (49.50%), H (3.02%), N (12.24%); found C (48.96%), H (2.95%), N (11.75%).

[Re(phen)(CO)$_3$(TzPhGlyMe)] (15Gly)

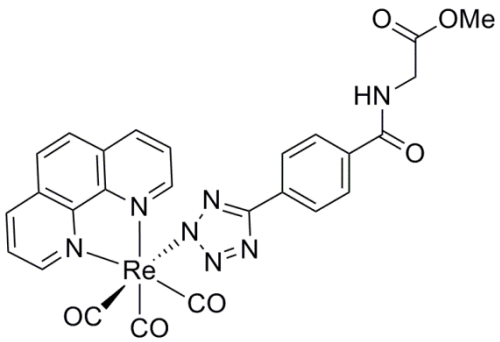

fac-[Re(**phen**)$(CO)_3$Cl] (188 mg, 0.39 mmol) and AgOTf (110 mg, 0.41 mmol) were stirred in DCM (*ca.* 20 mL) at room temperature for 2 hours. The grey precipitate (AgCl) was filtered *via* bed of celite. To the resulting bright yellow filtrate, compound **14** (107 mg, 0.4 mmol) was added and the reaction mixture heated to reflux for 3 hours. Heating was stopped and the mixture left to cool down before removing solvent under reduced pressure, which afforded yellow residue. This was dissolved in DCM, then TEA (0.055 mL, 0.40 mmol) was added and the reaction mixture left to stir at room temperature overnight. The yellow solution was

concentrated under reduced pressure to afford yellow oil. This was purified *via* flash column chromatography (deactivated neutral alumina, Brockmann III), where EtOAc/DCM (60:40) eluted the first fraction as starting material and MeOH was used to elute the second fraction as the desired product (55 mg, 29%). Yellow crystals were grown by slow evaporation of DCM. ν_{max} (ATR-FTIR)/cm^{-1} (solid state): 2026 (CO, A′(1)), 1921 (CO, A′(2)), 1885 (CO, A″), 1750 (C=O ester), 1650 (C=O ester).

^{1}H NMR (δ, ppm, $CDCl_3$): 9.53 (2H, d, *J* = 8.0 Hz, phenyl **CH**), 8.57 (2H, d, *J* = 8.0 Hz, phenyl **CH**), 7.99 (2H, s, **phen** $H_{2,9}$), 7.91-7.88 (2H, m, **phen** $H_{3,8}$), 7.83 (2H, d, *J* = 6.4 Hz, **phen** $H_{5,6}$), 7.69 (2H, d, *J* = 8.4 Hz, **phen** $H_{4,7}$), 6.79 (1H, app. t, *J* = 5.2 Hz, N**H**), 4.19 (2H, d, *J* = 5.2 Hz, NH**CH**$_2$COOCH$_3$), 3.77 (3H, s, O**CH**$_3$). ^{13}C NMR (δ, ppm, $CDCl_3$): 214.6 (**C**O), 210.9 (**C**O), 202.4 (**C**O), 154.2 (**phen C**H), 153.2 (**phen C**H), 138.1 (phenyl **C**H), 126.6 (phenyl **C**H), 125.9 (**phen C**H), 124.6 (**phen C**H), 69.9, 55.1, 53.9 (O**C**H$_3$), 31.8, 27.7 (**C**H$_2$). Elemental Analysis: Calc for $C_{26}H_{18}N_7O_6Re$: C (43.94%), H (2.55%), N (13.80%); found C (43.85%), H (2.61%), N (13.63%).

[Re(phen)(CO)$_3$(TzTrp)] (19Trp)

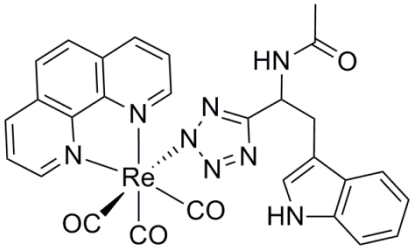

TEA (11 µL, 0.078 mmol) was added to a mixture of *fac*-[Re(**phen**)(CO)$_3$Cl] (28 mg, 0.05 mmol) and compound **17** (23 mg, 0.09 mmol) in MeCN/MeOH (*ca*. 5 mL). This was heated in microwave reactor for a total of 2.5 hours at 160 °C. The resulting orange solution was concentrated under reduced pressure to afford orange residue. This was purified by column chromatography using deactivated neutral alumina (Brockmann III); DCM/EtOAc (50:50) eluted first fraction as a bright yellow product identified as starting material and EtOAc (2-5% MeOH) eluted second fraction as pale yellow product. A yellow powder (22 mg, 78%) was collected after concentrating the column fractions under reduced pressure. ν_{max} (ATR-IR, acetone)/cm^{-1}: 2026 (CO, A′(1)) and 1911 (CO, A′(2)).

^{1}H NMR (δ, ppm, DMSO-d_6): 10.48 (1H, s, **NH** indole), 9.51-9.47 (2H, m, **phen** *H*$_{2,9}$), 8.93 (2H, d, *J* = 8.4 Hz, **phen** *H*$_{3,8}$), 8.26 (2H, s, **phen** *H*$_{5,6}$), 8.08 (2H, d, *J* = 8.4 Hz, **phen** *H*$_{4,7}$), 7.93 (1H, d, *J* = 8.4 Hz, **NH** amide), 7.24 (2H, d, *J* = 8.0 Hz, **CH** indole), 7.01 (1H, app. t, *J* = 8.0 Hz, **CH** indole), 6.89 (1H, app. t, *J* = 6.8 Hz, **CH** indole), 6.35 (1H, s, **CH** indole), 4.93-4.87 (1H, m, CH_2-**CH**-NH), 2.80-2.70 (2H, m, **CH_2**-CH-NH), 1.63 (3H, s, **CH_3** acetyl). ^{13}C NMR (δ, ppm, DMSO-d_6): 197.1 (**C**O, collapsed), 194.2 (**C**O), 168.3 (**C**=O acetyl), 164.2 (**C**t), 154.1 (**phen C**H), 146.5 (**phen** quat. **C**), 139.7 (**phen C**H), 135.8 (indole quat. **C**), 130.3, 127.7 (**phen C**H), 126.6 (**phen C**H), 122.7 (indole **C**H), 120.7, 118.2 (indole **C**H), 111.2 (indole quat. **C**), 110.6 (indole **C**H), 45.7 (CH_2-**C**H-NH), 30.2 (**C**H_2-CH-NH), 22.5 (acetyl **C**H_3). Elemental Analysis: Calc for $C_{28}H_{21}N_8O_4Re$: C (46.73%), H (2.94%), N (15.57%); found C (46.77%), H (2.96%), N (14.61%).

[Re(phen)(CO)$_3$(TzPhe)] (19Phe)

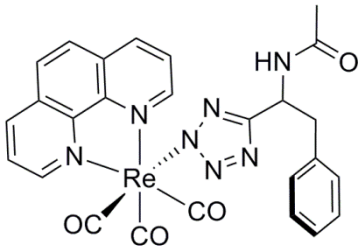

fac-[Re(**phen**)(CO)$_3$Cl] (31 mg, 0.063 mmol), compound **18** (19 mg, 0.082 mmol) and triethylamine (11 µL, 0.078 mmol) were combined in MeCN (*ca*. 5 mL), subjected to microwave irradiation at 160 °C for 3 hours. The mixture was purified *via* flash chromatography using deactivated neutral alumina (Brockmann III); first fraction of starting material eluted with DCM/EtOAc (50:50) and second fraction of product eluted with EtOAC (2% MeOH). Yield: 33 mg (78%). Single crystals (bright yellow in colour) suitable for X-ray diffraction were grown by slow evaporation of an acetone solution of the complex. ν_{max} (ATR-IR, acetone)/cm^{-1}: 2025 (CO, A′(1)) and 1907 (CO, A′(2)).

^{1}H NMR (δ, ppm, Acetone-d_6): 9.60-9.57 (2H, m, **phen** *H*$_{2,9}$), 8.98-8.94 (2H, m, **phen** *H*$_{3,8}$), 8.30 (2H, s, **phen** *H*$_{5,6}$), 8.18-8.13 (2H, m, **phen** *H*$_{4,7}$), 7.00-6.96 (1H, m, phenylalanine **H$_5$**), 6.89 (2H, t, *J* = 7.6 Hz, phenylalanine **H$_6$**), 6.83 (1H, d, *J* = 8.0 Hz, **NH** amide), 6.50 (2H, d, *J* = 8.4 Hz, phenylalanine **H$_7$**), 5.05-5.00 (1H, m, CH_2-**CH**-NH), 2.86-2.72 (2H, m, **CH_2**-CH-NH), 1.73 (3H, s, acetyl **CH_3**). ^{13}C NMR (δ,

ppm, Acetone-d_6): 196.9 (**C**O), 168.1 (**C**=O acetyl), 163.5 (**C**t), 154.2 (**phen C**H), 146.3 (**phen** quat. **C**), 139.7 (**phen C**H), 137.9, 130.3, 128.7, 127.7 (**phen C**H), 127.6, 126.7, 125.8, 46.4 (CH_2-**C**H-NH), 39.5 (**C**H_2-CH-NH), 22.3 (acetyl **C**H_3). Elemental Analysis: Calc for $C_{26}H_{23}N_7O_4Re$: C (45.67%), H (3.39%), N (14.34%); found C (46.07%), H (2.92%), N (13.73%).

3.10.2.1 General Methodology for the Methylation of the Neutral *fac*-[Re(**phen**)$(CO)_3$(L)] Complexes

The preparation of the methylated complexes was carried out following procedures adapted from literature.[184] Previously synthesised [Re(**phen**)$(CO)_3$(L)] (1 eq) was dissolved in DCM and the solution allowed to cool using EtOAc/LN_2 cool bath. Once the reaction vessel had cooled until frozen, a solution of MeOTf (1.2 eq) in DCM was added. The reaction was stirred under nitrogen for approximately 30 minutes in the cool bath, before allowed to reach to room temperature and stirred overnight. An excess of KPF_6 in water was added to the reaction mixture and stirred for 30 minutes. This was then extracted with DCM and the organic component dried ($MgSO_4$). The solvent was removed *in vacuo* to afford glassy yellow residue for both complexes **20Trp** and **20Phe**.

[Re(phen)$(CO)_3$(MeTzTrp)]PF_6 (20Trp)

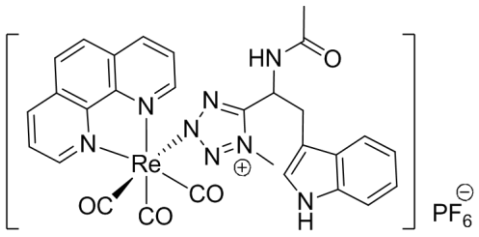

ν_{max} (ATR-IR, acetone)/cm^{-1}: 2034 (CO, A′(1)) and 1920 (CO, A′(2)), 1696, 1522, 1430, 840. Yield: 10 mg, 51%. ^{1}H NMR (δ, ppm, Acetone-d_6): 10.03 (1H, s, **NH** indole), 9.69 (1H, d, *J* = 4.0 Hz, **phen** $H_{2,9}$), 9.62 (1H, d, *J* = 4.0 Hz, **phen** $H_{2,9}$), 9.07-9.03 (2H, m, **phen** $H_{3,8}$), 8.37 (2H, s, **phen** $H_{5,6}$), 8.28-8.21 (2H, m, **phen** $H_{4,7}$), 7.71 (1H, s, **NH** amide), 7.34 (1H, d, *J* = 8.0 Hz, **CH** indole), 7.15-7.04 (2H, m, **CH** indole), 6.98 (1H, app. t, *J* = 8.0 Hz, **CH** indole), 6.83 (1H, app. s, **NH**), 5.18-5.13 (2H, m, CH_2-**CH**-NH), 3.55 (3H, s, **CH_3** methyl), 3.23-3.05 (2H, m, **CH_2**-CH-NH), 2.99-2.88 (2H, m, **CH_2**-CH-NH), 1.68 (3H, s, **CH_3** acetyl). A satisfactory ^{13}C NMR spectrum could not be obtained due to the low concentration of the solution.

[Re(phen)(CO)$_3$(MeTzPhe)]PF$_6$ (20Phe)

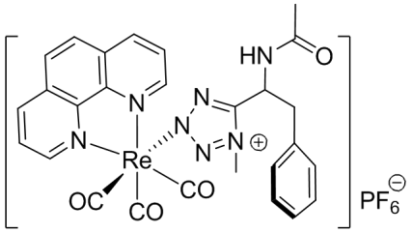

ν_{max} (ATR-IR, acetone)/cm^{-1}: 2034 (CO, A′(1)) and 1921 (CO, A′(2)), 1675, 1521, 1432, 840. Yield: 5 mg, 51%. ^{1}H NMR (δ, ppm, Acetone-d$_6$): 9.70 (2H, d, *J* = 4.0 Hz, **phen** *H$_{2,9}$*), 9.13-9.06 (2H, m, **phen** *H$_{3,8}$*), 8.42 (2H, s, **phen** *H$_{5,6}$*), 8.31-8.26 (2H, m, **phen** *H$_{4,7}$*), 7.72 (1H, d, *J* = 7.2 Hz, **NH**), 7.14-7.05 (3H, m, 3 × phenylalanine **CH**), 6.74 (2H, d, *J* = 6.4 Hz, 2 × phenylalanine **CH**), 5.20-5.14 (2H, m, CH$_2$-**CH**-NH), 3.74 (3H, s, **CH$_3$** methyl), 3.02-2.97 (1H, m, CH$_2$-**CH**-NH), 2.75-2.69 (1H, m, **CH$_2$**-CH-NH), 1.69 (3H, s, acetyl **CH$_3$**). A satisfactory ^{13}C NMR spectrum could not be obtained due to the low concentration of the solution.

Chapter 4

Photophysics and Photochemistry of Cationic Rhenium(I)-NHC Complexes

4.1 Abstract

A series of cationic rhenium(I)-NHC complexes appended to substituted pyridines were investigated in terms of their photophysical and photochemical properties. Rhenium(I)-**phen** complexes with the same pyridyl ligands were synthesised as a reference and confirmed to be photostable, when excited at ^{3}MLCT state in a coordinating solvent such as acetonitrile. The progress of the photolysis reactions were monitored at regular intervals using ^{1}H NMR and IR spectroscopy. The collective findings have confirmed that the photoactive component stems from the NHC ligand. Recent studies by Mukuta *et al*. have revealed the mechanism of the photochemical ligand substitution (initially proposed by Vaughan) using time-resolved measurements. Additionally, the identification of the photoproducts will be discussed within this chapter.

4.2 Introduction

Complexes of the type [Re(**N^C**)$(CO)_3$(L)] are associated with blue-shifted and weaker emission properties, along with shorter lifetimes. This is relative to their diimine (**phen** or **bipy**) analogues which have much favourable emission quantum yields and relatively longer excited state lifetimes. On the other hand, [Re(**N^C**)$(CO)_3$(L)] complexes possess unique photochemical properties. The main

feature is identified as the dissociation of a CO ligand that occurs upon excitation of a complex in a coordinating solvent. Usually this type of photochemical transformation occurs on complexes bound to ligands (L) with strong *trans* effect such as phosphines, phosphites or isonitriles.[19–22] More specifically, the CO dissociation of these complexes was proposed to occur from a reactive state (^{3}LF) that was thermally accessible from the ^{3}MLCT state. This was suggested as a result of the excited state emission properties displaying a temperature dependence. However, this type of photochemical mechanism does not apply to [Re(**PyImPh**)$(CO)_3$X] complexes. Extended investigation has proved that the loss of CO upon photoexcitation occurs from MLCT excited states rather than thermally accessible LF excited states. This was initiated by photochemical experiments persisting at temperatures as low as 233 K.[148]

Recently, the detailed photochemical processes of [Re(**PyImPh**)$(CO)_3$Br] which have been initially proposed by Vaughan,[148,149] have been explored further by Mukuta *et al*. using time-resolved measurements.[189] The possible photoproducts which can appear upon irradiation of [Re(**PyImPh**)$(CO)_3$Br] by UV light are depicted in **Figure 4.1**. Product **I** can be described as a cationic tricarbonyl solvato complex, [Re(**PyImPh**)$(CO)_3(CH_3CN)]^+$ in which the Br ligand has been substituted by the MeCN molecule. Product **II** is a neutral dicarbonyl species, [Re(**PyImPh**)$(CO)_2(CH_3CN)$Br] where the CO ligand positioned *trans* to the NHC ligand has been exchanged with the MeCN molecule. Product **III** is a cationic dicarbonyl species, [Re(**PyImPh**)$(CO)_2(CH_3CN)_2]^+$ in which both the Br ligand and the CO *trans* to the NHC ligand has been substituted with the MeCN molecule.

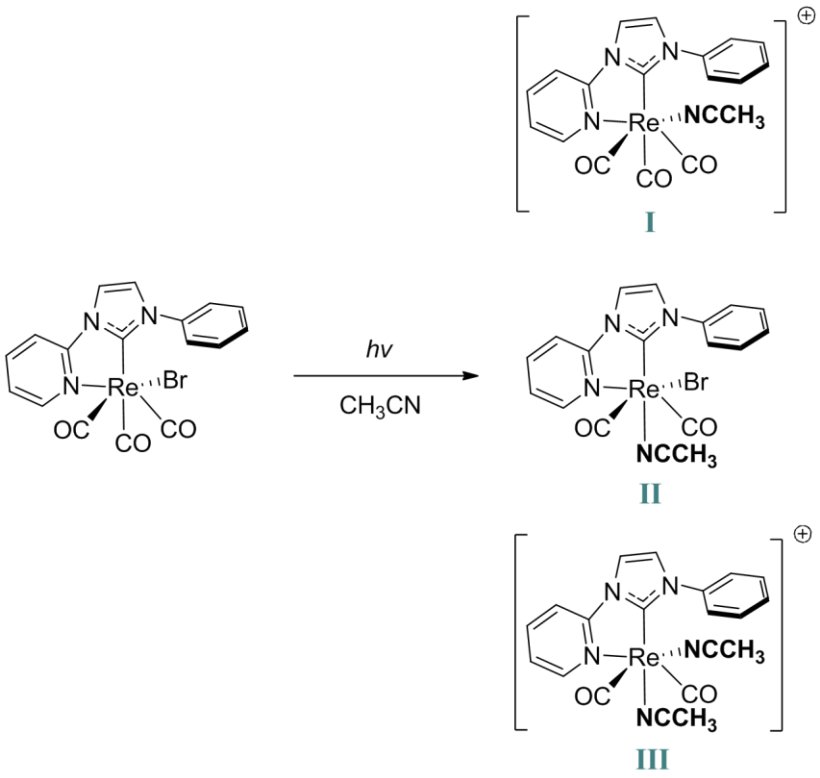

Figure 4.1 Structures of photoproducts upon irradiation of [Re(**PyImPh**)$(CO)_3$Br] with UV light in a solution of MeCN.

The use of techniques such as time-resolved infrared spectroscopy (TR-IR) allowed Mukuta *et al.* to elucidate a mechanism of the photoreaction process. This was achieved by first identifying the intermediate species from the vibrational spectral pattern. The photoexcitation of [Re(**PyImPh**)$(CO)_3$Br] at 355 or 400 nm was measured in MeCN solution (photoactive) as well as in DCM solution (non-photoactive). The TRIR measurements in the picosecond time scale showed similar spectra for both MeCN and DCM solutions, where the intensity and position of the bands appear identical. This data indicates that no CO dissociation reaction occured in the picosecond range. On the other hand, the TRIR measurements in the nanosecond time scale display different responses for different solvents. For the complex in DCM solution, the intensity of the spectra decreased over time but without any change in the spectral shape. The authors attributed this observed spectral change to relaxation from the lowest ^{3}MLCT excited state to the ground state (GS). Whereas for the complex in MeCN solution, the intensity of the spectra also decreased but at a faster rate and the spectral shape differs significantly from the initial scan. This distinctive spectral progression implied the formation of a product after photoexcitation. The identity of the product was determined by the examination

of the remaining transition absorption bands. As the bands are found at high wavenumbers relative to those of the reactant in the GS, it was implied that the product has a lower electron density on the Re atom. Between the three possible photoproducts shown in **Figure 4.1**, products **II** and **III** have less number of CO ligands which suggests a higher electron density on the Re atom. Based on this respect, product **I** was proposed to be the most likely species to appear after a few nanoseconds.

Combining the data from TR-IR spectroscopy and calculations based on transition-state theory, the detailed reaction mechanism of the unique photochemical ligand substitution was revealed. Optimised geometries of [Re(**PyImPh**)$(CO)_3$Br] in the singlet ground state (S_0) and triplet excited state (T_1) exposed a significant change in the bending of the Br-Re-CO linkage, as shown in **Figure 4.2**.

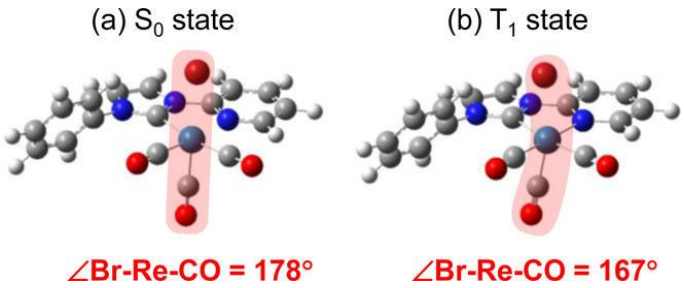

Figure 4.2 Optimised geometries of [Re(**PyImPh**)$(CO)_3$Br] in (a) singlet and (b) triplet states. [Reprinted with permission from ref[189]]

This non-symmetric structure in the ^{3}MLCT state allowed space for a solvent molecule to enter and form a seven-coordinate state *via* an associative mechanism, which gives rise to a higher transition state represented by ^{3}MLCT(2) in the diagram shown in **Figure 4.3**. Under non-reactive conditions (red trace), the complex undergoes non-radiative decay quickly returning to the GS, as a DCM molecule cannot coordinate to the rhenium metal centre. On the other hand, under reactive conditions (blue trace), the MeCN-solvato complex is produced as it can coordinate to the rhenium, even though it also undergoes non-radiative decay from ^{3}MLCT(2) to GS.

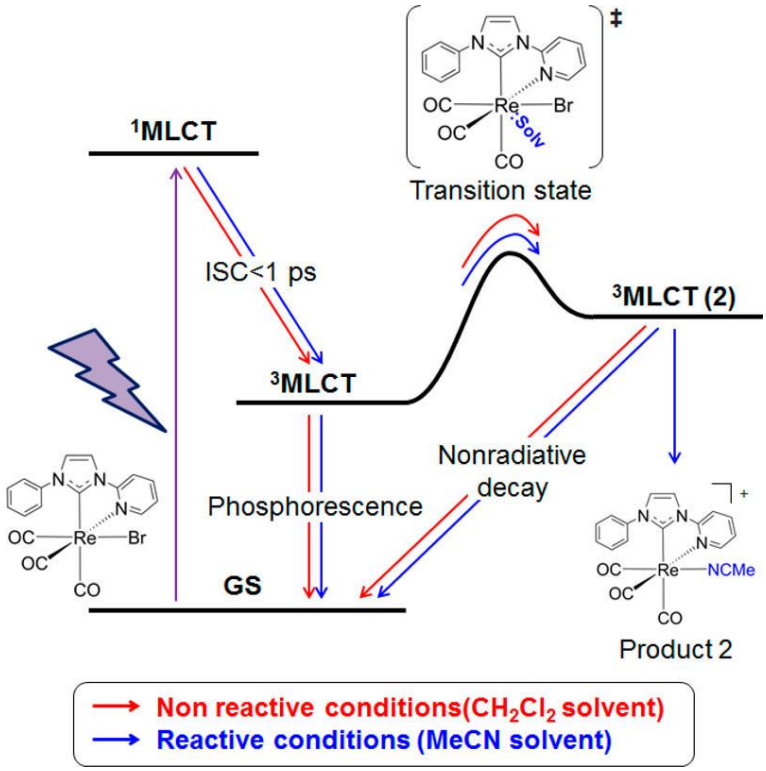

Figure 4.3 Proposed mechanism of the photochemical reaction of [Re(**PyImPh**)$(CO)_3$Br] in DCM (red trace) and MeCN (blue trace) solutions. [Reprinted with permission from ref[189]]

Analyses of reported literature have revealed that neutral rhenium(I) pyridyl NHC complexes possess unique photochemical and photophysical properties. The objective of this chapter is to study various cationic rhenium(I) pyridyl NHC complexes (**23-25**, see **Figure 4.4**), where the different ancillary ligands bound to the metal serve as a dependent variable to manipulate the emissive states. It would also serve as a mean to qualitatively investigate the velocity of dissociation upon photoirradiation. Cationic rhenium(I) diimine analogues (**26-28**, see **Figure 4.4**) were also synthesised as reference complexes to compare the photostabilty of the complexes.

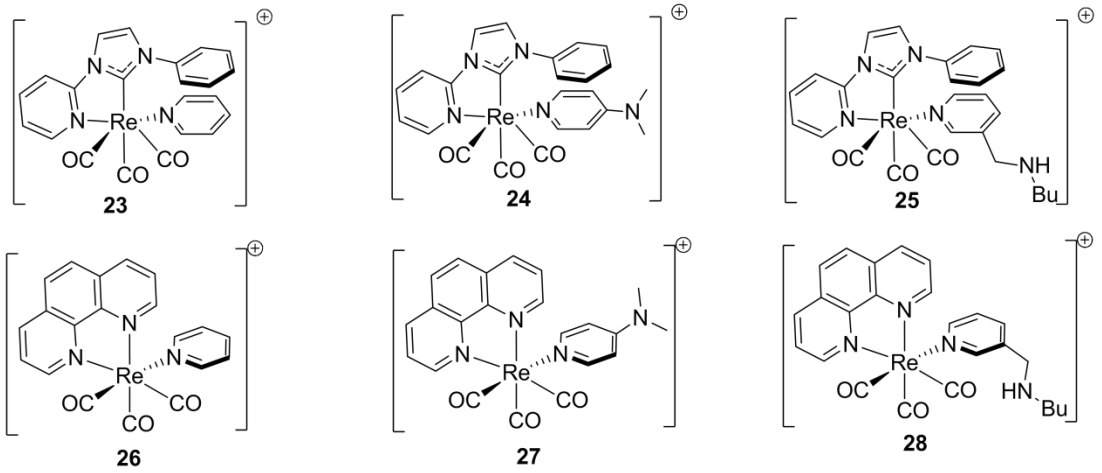

Figure 4.4 New [Re(**PyImPh**)$(CO)_3(L)]^+$ complexes **23-25** and model [Re(**phen**)$(CO)_3(L)]^+$ complexes **26-28** prepared in this study.

In addition, excited state processes such as electron transfer will be investigated using various amino acid pyridine ligands which have been reported in literature[175]. This time they will be incorporated to the rhenium NHC frame and any effects it may have on the photochemistry will be assessed, then finally comparing them to the literature work by Blanco-Rodriquez *et al.* on non-photoactive rhenium(I) **phen** analogues.

4.3 Synthesis and Structural Characterisation of the Ligands

4.3.1 Synthesis of the NHC Chelating Ligand

The target aryl-substituted imidazolium salt [**PyIm**H**Ph**][PF_6] in **Scheme 4.2** was prepared using a procedure adapted from the literature.[149] The previously published paper reported the synthesis of imidazolium salts by heating a solvent-free mixture of a halopyridine with a N1 substituted imidazole in a sealed pressure vessel at 170 °C. The syntheses of aryl functionalised azolium salts have been well established and typically occur *via* nucleophilic aromatic substitution (NAS).

Firstly, 1-phenylimidazole was prepared *via* an Ullmann coupling reaction of iodobenzene (**110**) and imidazole (**111**) in the presence of a copper catalyst (**Scheme 4.1**) and a base in DMSO. Ullmann coupling reactions are used to synthesise

symmetric biaryls or couple an aryl group with a nucleophile using aryl halides. When the copper catalyst, $Cu(OAc)_2 \cdot H_2O$ was used,[190] 1-phenylimidazole (**112**) was isolated in 23% yield. However, when copper (I) oxide was used as the catalyst,[191] this procedure gave an improved yield of 56%.

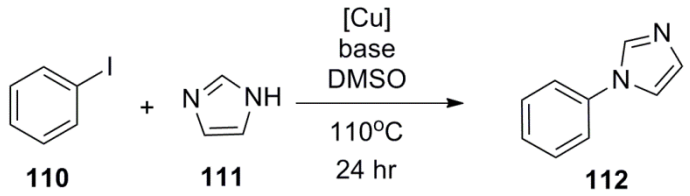

Scheme 4.1 Reaction scheme showing preparation of 1-phenylimidazole (**112**).

Following procedures in literature[149,192], the NAS reaction of 2-chloropyridine and 1-phenylimidazole (**112**) afforded the [**PyIm**H**Ph**][PF_6] salt in low yields (**Scheme 4.2**). The moderate yields (65%) could be due to difficulties in isolation *via* vacuum filtration, as the compounds rapidly absorb water. These hygroscopic and deliquescent properties of such NHC salts are commonly known. This was overcome by converting the chloride salt to a PF_6 salt by metathesis, which provided a more air-stable product.

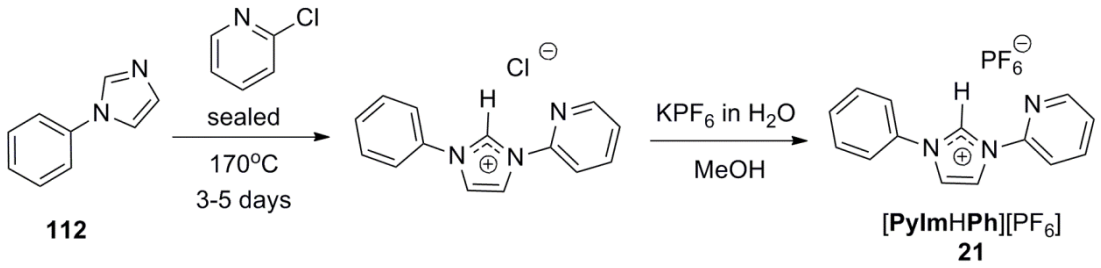

Scheme 4.2 Preparation of 1-(2-pyridyl)-3-phenylimidazolium hexafluorophosphate, [**PyIm**H**Ph**][PF_6].

Analysis of the aryl-substituted imidazolium salt [**PyIm**H**Ph**][PF_6] by ^{1}H NMR spectroscopy in $CDCl_3$ confirmed the isolation of the desired compound. The H2 proton (see **Figure 4.30** for numbering) for the salt appeared at 12.43 ppm. This hydrogen atom (represented by a singlet peak) was much more deshielded compared to the corresponding aryl-imidazole H2 proton signal at 7.92 ppm for 1-phenylimidazole. This was expected due to the electron withdrawing effects of the two neighbouring nitrogen atoms on the positively charged imidazolium salt.

4.3.2 Synthesis of the Pyridyl Ancillary Ligands

The rationale behind the choice of ligands synthesised below was that they must be easily oxidised (from the lone pair of electrons on the amino nitrogen atom). This was preferable in order to induce an electron transfer from the ligand to the excited metal complex.

Before attempting any lengthy multiple step synthesis, primary investigations involved using pyridine as a model (with no amino group) to compare with the substituted pyridines. On the other hand, *N*-(pyridin-3-ylmethyl)butan-1-amine (**115**), was prepared by reductive amination reaction following previously published procedures.[193] This stepwise procedure involved initial imine formation followed by reduction with sodium borohydride, as shown in **Scheme 4.3**.

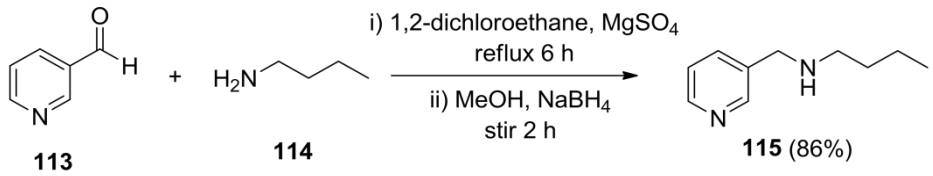

Scheme 4.3 Reductive amination of pyridine carboxaldehye to produce **115**.

Additionally, 4-(amino acid) pyridine ligands (abbreviated as Py**Trp**, Py**Phe** and Py**Gly**) shown in **Scheme 4.4** were synthesised according to previously published procedures.[172] The reaction involved a mixture of isonicotinic acid chloride and the respective amino acid methyl ester (as hydrochloride salt) in dichloromethane, with triethylamine as a base. The acyl chloride reacts with the amine to form a substituted amide in moderate yields.

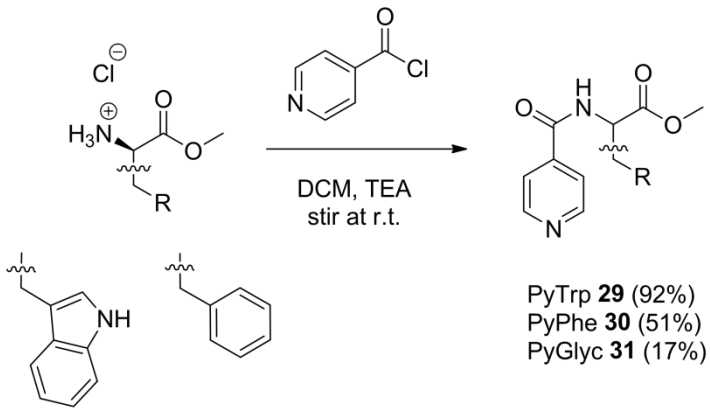

Scheme 4.4 Reaction scheme for synthesis of 4-(amino acid) pyridine ligands, **29-31**.

4.4 Synthesis and Structural Characterisation of the Complexes

The preparation of target rhenium(I)-NHC complexes followed the work of Casson and co-workers, implementing an *in-situ* synthesis.[147] This work involved combining benzimidazolium salt, [$Re(CO)_5Cl$] and potassium carbonate in toluene, heated at reflux for 2 days. Two carbonyl ligands are substituted for the bidentate neutral **PyBzimPh** ligand. This substitution can result in two possible geometric isomers; however only the *facial* isomer is formed due to the strong *trans effect* of the carbonyl ligands. Following the procedure reported, except using imidazolium salt [**PyIm**H**Ph**][PF_6] as opposed to the benzimidazolium salt, the corresponding rhenium complex [Re(**PyImPh**)$(CO)_3$Br] was synthesised in moderate 70% yield. The chloro analogue was also synthesised, however in lower yields of 40%.

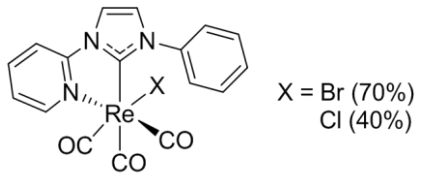

22

Figure 4.5 Structure of [Re(**PyImPh**)$(CO)_3$X] complex, where X = bromo or chloro.

Formation of [Re(**PyImPh**)$(CO)_3$X] shown in **Figure 4.5** was confirmed by ^{1}H NMR, ^{13}C NMR and infrared spectroscopy. Analysis of the ^{1}H NMR spectrum illustrated an absence of the H2 proton singlet around 12 ppm, which indicated that the **PyImPh** salt has been deprotonated. Analysis of the ^{13}C NMR spectrum which displayed four downfield signals present around 198-189 ppm in DMSO-d_6; three signals belonging to CO group, and the NCN carbene carbon signal at 190 ppm, confirmed the formation of the tricarbonyl rhenium(I) complex. Also, the IR stretching frequency values of the CO peaks were similar to other previously reported tricarbonyl rhenium(I) NHC species.[146,147,149]

The next step was to replace the halogen with a series of substituted pyridine ancillary ligands (see **Scheme 4.5** and **Scheme 4.6**). The substitution of the halo ligand occurred through the method of silver-halide-abstraction. This reaction involved the use of a silver source ($AgBF_4$ or AgOTf) and heating the rhenium precursor under reflux conditions in a coordinating solvent. Since acetonitrile is a

coordinating solvent, it easily bound to the rhenium and replaced the halide. This was confirmed by infrared analysis, where the frequencies of the CO bands increased due to the reduced electron density on the rhenium metal because acetonitrile is a poor σ donor. The addition of pyridine then replaced the acetonitrile easily because acetonitrile is labile. Again, IR analysis show the frequencies of CO bands decreased due to the increased electron density on the rhenium metal, as pyridine is a better σ donor. The complexes were isolated and purified by the addition of diethyl ether to a solution of the complex in dichloromethane, giving moderate yields of 50-86%. In some cases, the impurities from the reaction were significant and this required purification by column chromatography using Brockmann II acidic alumina. The **phen** derivatives were prepared in a similar manner as shown in **Scheme 4.7**.

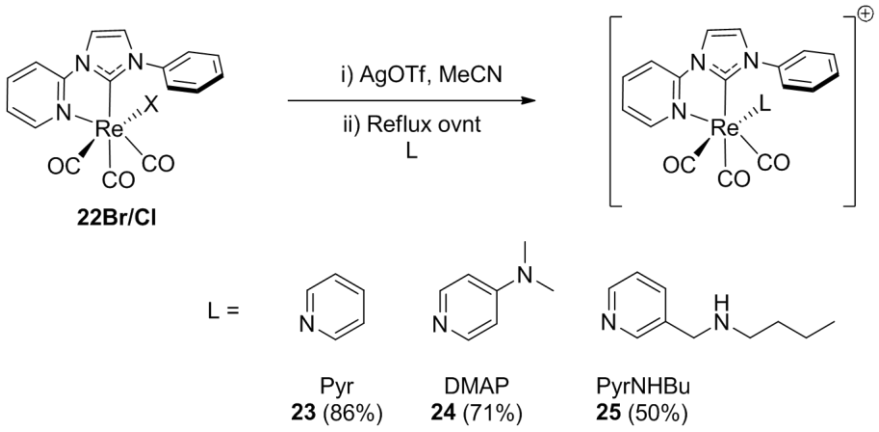

Scheme 4.5 Synthetic preparation of rhenium(I)-NHC complexes **23-25**.

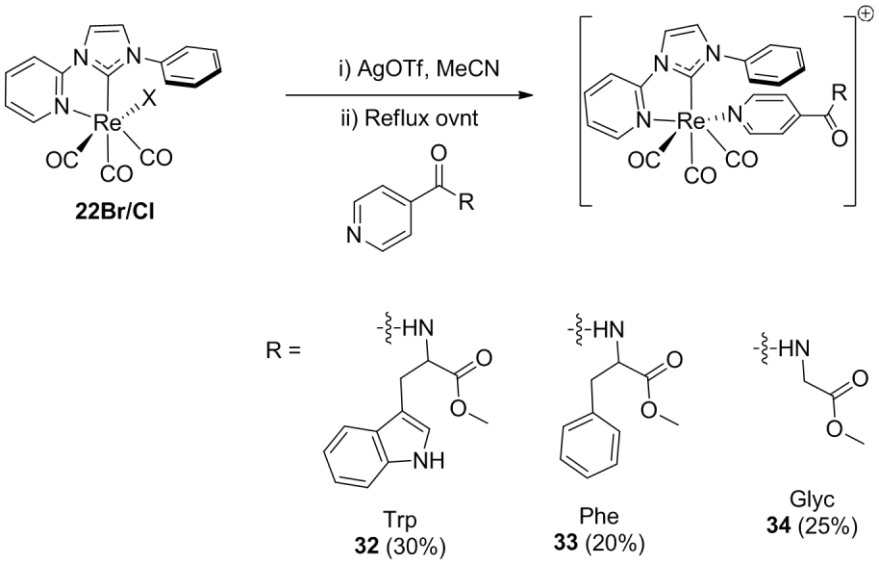

Scheme 4.6 Synthetic preparation of rhenium(I)-NHC complexes **32-34**.

Formation of the new rhenium(I)-NHC complexes were confirmed by ^{1}H NMR, ^{13}C NMR, infrared spectroscopy, elemental analysis, and single crystal X-ray diffraction, with the experimental data in agreement with the proposed formulae. All the complexes exhibit characteristic carbonyl stretching bands between 2020-1900 cm^{-1}, showing the totally symmetric in-phase stretching A′(1), the totally symmetric out-of-phase stretching A′(2) and the asymmetric stretching A″. The carbonyl C≡O ligands are arranged in a *facial* manner and can be seen as three distinct stretching frequencies as summarised in **Table 4.1**. All the cationic rhenium(I) complexes reported have a higher stretching frequency with respect to the neutral halogenated precursor. This is a result of reduced electron density on the rhenium metal centre as the overall charge on the complex is now positive due to the coordinated ancillary ligand being neutral.

Table 4.1 Stretching frequencies (cm^{-1}) of the CO bands of the Re(I)-NHC complexes.

Complex	CO A′ (1)	CO A′ (2)/A″
[Re(**PyImPh**)$(CO)_3$Cl]	2010	1921, 1890
[Re(**PyImPh**)$(CO)_3$(Py)].OTf (**23**)	2022	1926, 1909
[Re(**PyImPh**)$(CO)_3$(DMAP)].PF_6 (**24**)	2016	1916, 1905
[Re(**PyImPh**)$(CO)_3$(PyNHBu)].PF_6 (**25**)	2027	1951, 1926
[Re(**PyImPh**)$(CO)_3$(Py**Trp**)].PF_6 (**32**)	2031	1935, 1927
[Re(**PyImPh**)$(CO)_3$(Py**Phe**)].PF_6 (**33**)	2028	1918[a]
[Re(**PyImPh**)$(CO)_3$(Py**Gly**)].PF_6 (**34**)	2022	1913, 1902

[a] peaks are superimposed into a single broad band

The ^{1}H NMR and ^{13}C NMR spectra for the targeted cationic rhenium(I) NHC complexes matched the expected structural formulae with indicative peaks in the ^{1}H NMR spectrum showing two sharp singlet peaks at approximately 8.60 and 7.90 ppm representing the protons on the imidazolium backbone. Generally, the most downfield signal resembling a “doublet” peak at *ca* 9.20 ppm in the ^{1}H NMR spectrum was always assigned to the pyridyl-H6′ proton coordinated to the rhenium. In addition, the presence of four downfield signals observed in the region 197-190 ppm (in acetone-d_6) of the ^{13}C NMR spectra represent the three CO ligands and the NCN carbene carbon as expected. The intensities for these signals were fairly weak as they were chemically equivalent to each other. In order to distinguish the CO

peaks from the NCN peaks, HMBC 2D NMR was applied to assign the spectrum. This technique displayed the correlation between carbon resonance and proton of the imidazolium backbone.

In order to compare the photochemical properties of the rhenium(I)-NHC complexes, analogous complexes containing a diimine chelating ligand (**phen**) instead of the carbene ligand were synthesised. The complexes were prepared by the same method as described above and isolated as PF_6 salts (**Scheme 4.7**), although the yields were significantly lower than the rhenium(I)-NHC complexes. This may be due to incomplete abstraction of the halide to the triflate solvato complex, therefore addition of the ligand to the reaction mixture was not completely successful.

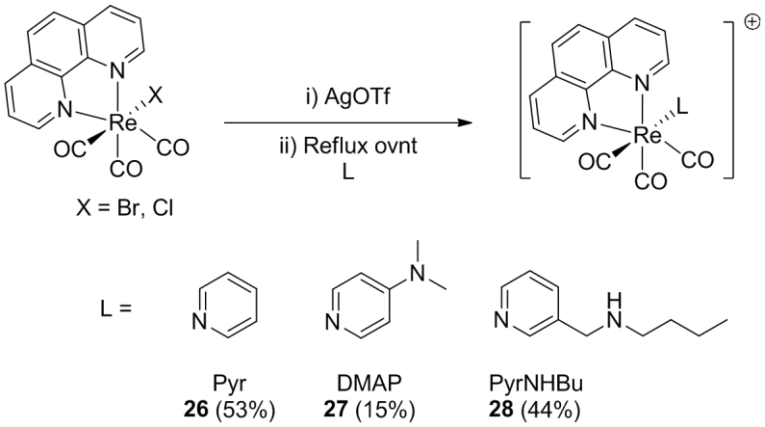

Scheme 4.7 Reaction scheme for preparation of rhenium(I)-**phen** complexes **26-28**.

Similarly to the rhenium(I)-NHC complexes, all the cationic rhenium(I)-phen complexes reported in **Table 4.2** have a higher CO stretching frequency as a result of reduced electron density on the rhenium metal centre.

Table 4.2 Stretching frequencies (cm^{-1}) of the CO bands of the reference Re(I)-diimine complexes.

Complex	CO A′ (1)	CO A′ (2)/A″
[Re(**phen**)$(CO)_3$(Py)].PF_6 (**26**)	2026	1922, 1902
[Re(**phen**)$(CO)_3$(DMAP)].PF_6 (**27**)	2027	1910 [a]
[Re(**phen**)$(CO)_3$(PyNHBu)].PF_6 (**28**)	2033	1919 [a]

[a] peaks are superimposed into a single broad band

4.5 X-ray Crystallography

Single crystals were obtained for the rhenium(I)-NHC complexes and analysed by XRD. Analysis of the crystallographic data illustrated a distorted octahedral geometry with the three CO ligands arranged in a *facial* configuration for all complexes. The crystal structures for complexes [Re(**PyImPh**)$(CO)_3$(Py)]$^+$ (**23**) and [Re(**PyImPh**)$(CO)_3$(DMAP)]$^+$ (**24**) are shown in **Figure 4.6**. The former complex crystallised in the orthorhombic Pbca space group, while the latter complex crystallised in the triclinic P1 space group. The bond distances for Re-CO all lie in the 1.9 Å range, consistent with other rhenium(I)-NHC complexes.[147,149]

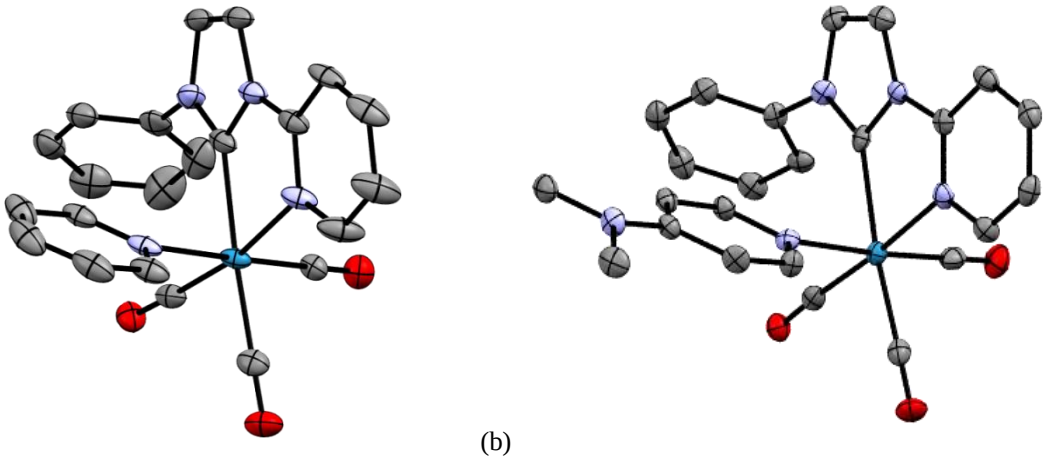

(a) (b)

Figure 4.6 X-ray crystal structures of [Re(**PyImPh**)$(CO)_3$(Py)]$^+$ (**23**, a) and [Re(**PyImPh**)$(CO)_3$(DMAP)]$^+$ (**24**, b). Hydrogen atoms, solvent molecules and counterion omitted for clarity. Thermal ellipsoids drawn at 50% probability.

The ancillary DMAP ligand was suspected to have a possible iminium-type structure (see **Scheme 4.8**). This was illustrated by the amino group being planar to the pyridine, whereas a free DMAP compound would have the amino positioned slightly angled (tilted perpendicularly) to the pyridine. Another indication was derived by analysing the bond length, where a single bond is typically 1.54 Å and a double bond is 1.34 Å.[194] The bond length of the amino group (pyridine C-N$(CH)_3$) on the DMAP ligand was found to be 1.354 Å for the NHC derivative, which confirms the presence of an iminium-type structure. Similar structural features for the DMAP (where bond length is 1.36 Å) can be seen on Zn, Cd and Hg complexes coordinated to two DMAP molecules.[195,196]

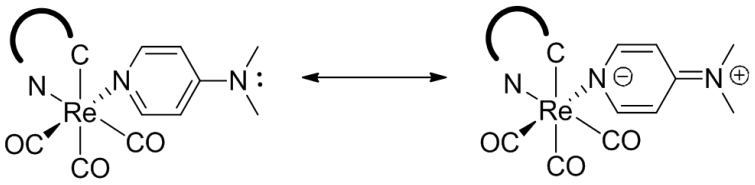

Scheme 4.8 Complex structure showing possible iminium form of DMAP.

The crystal structures for the model rhenium(I) diimine complexes were also collected and shown in **Figure 4.7**. The bond length of the amino group (pyridine C-$N(CH)_3$) on the DMAP ligand was measured to be 1.345 Å for the diimine derivative, which is similar to the NHC derivative.

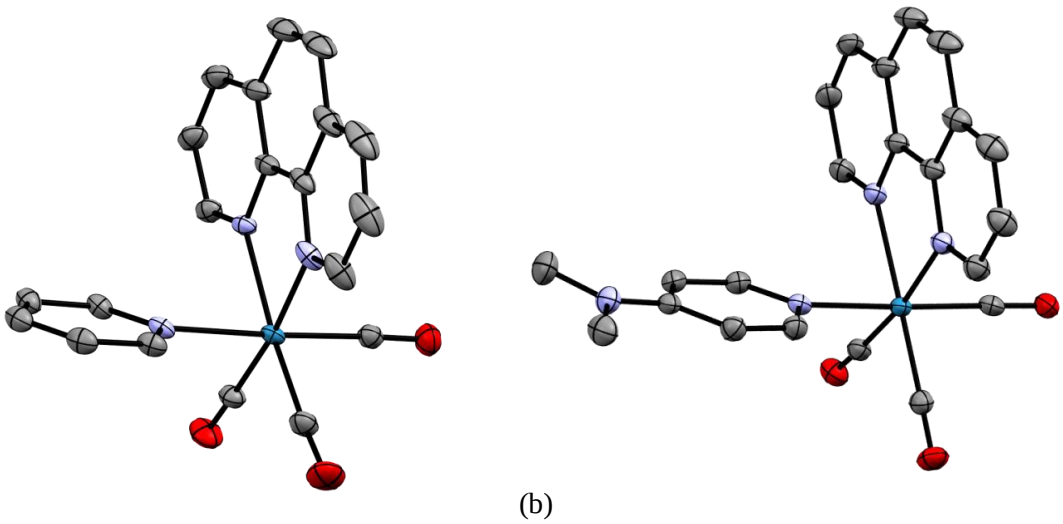

(a) (b)

Figure 4.7 Crystal structure of (a) [Re(**phen**)$(CO)_3$(Py)]$^+$ (**26**) and (b) [Re(**phen**)$(CO)_3$(DMAP)]$^+$ (**27**). Hydrogen atoms, solvent moleculess and counterion omitted for clarity. Thermal ellipsoids drawn at 50% probability.

4.6 Photophysical Investigation

The excited state properties of the reported complexes were initially investigated in dichloromethane solutions. In addition, a more polar and coordinating solvent such as acetonitrile was used to investigate the photochemical properties of the complexes (as it was previously found to have interesting features in such conditions).

A summary of the photophysical data for complexes [Re(**PyImPh**)$(CO)_3$(Py)]$^+$ (**23**), [Re(**PyImPh**)$(CO)_3$(DMAP)]$^+$ (**24**) and [Re(**PyImPh**)$(CO)_3$(PyNHBu)]$^+$ (**25**) is provided in **Table 4.3** and **Table 4.4**, for dichloromethane and acetonitrile solutions,

respectively. In general, the UV-VIS absorption profiles show an intense higher energy band in the 250-300 nm region which tails off into a lower energy band in the 300-400 nm region. These are characteristic of a typical rhenium(I)-NHC complex.[147–149,197] The higher energy band is attributed to intraligand (IL) π- π* transitions localised within the NHC ligand, while the lower energy band is attributed to metal-to-ligand charge transfer (MLCT) transitions that involves the 5d orbitals of the rhenium centre and the accessible π* orbitals of the coordinated imine type N-donor ligands.

The absorption plots (see **Figure 4.8**) for [Re(**PyImPh**)$(CO)_3$(Py)]$^+$ (**23**) and [Re(**PyImPh**)$(CO)_3$(PyNHBu)]$^+$ (**25**) show similar features, where the higher energy IL transition resides around 267-272 nm and the lower energy ^{3}MLCT band at around 330 nm. On the other hand, [Re(**PyImPh**)$(CO)_3$(DMAP)]$^+$ (**24**) display a much higher intensity IL band which could be attributed not only to π-π* transitions localised within the NHC ligand but also on the conjugated DMAP-iminium species. There seems to be a slight red shifted absorption for **24** by *ca.* 10 nm relative to the other analogues, which could be attributed to the extended conjugation on the DMAP ligand lowering the π-π* level and thus decreasing the HOMO-LUMO energy gap. This is evidence to suggest that the ancillary ligand has a large influence on the photophysical properties of the metal complex, due to variation of MO energies.

Following excitation of the complexes at 360 nm, each of the cationic rhenium(I)-NHC pyridyl substituted complexes **23-25** exhibit a broad and structureless emission band from an excited state of ^{3}MLCT character. Complexes **23-25** displayed an excited state emission of around 480-500 nm in aerated DCM. Compared to their neutral halogenated precursor **22** (λ_{em} = 522 nm in DCM), the cationic rhenium(I)-NHC complexes all exhibit a blue-shifted emission (~30 nm). This can be attributed to an increase of the HOMO-LUMO energy gap caused by pyridine being a weaker σ donor and greater π acceptor than the halogen. The coordinated pyridine ligand reduces the electron density on the rhenium metal centre, stabilising the HOMO energy level and thus increasing the HOMO-LUMO gap.

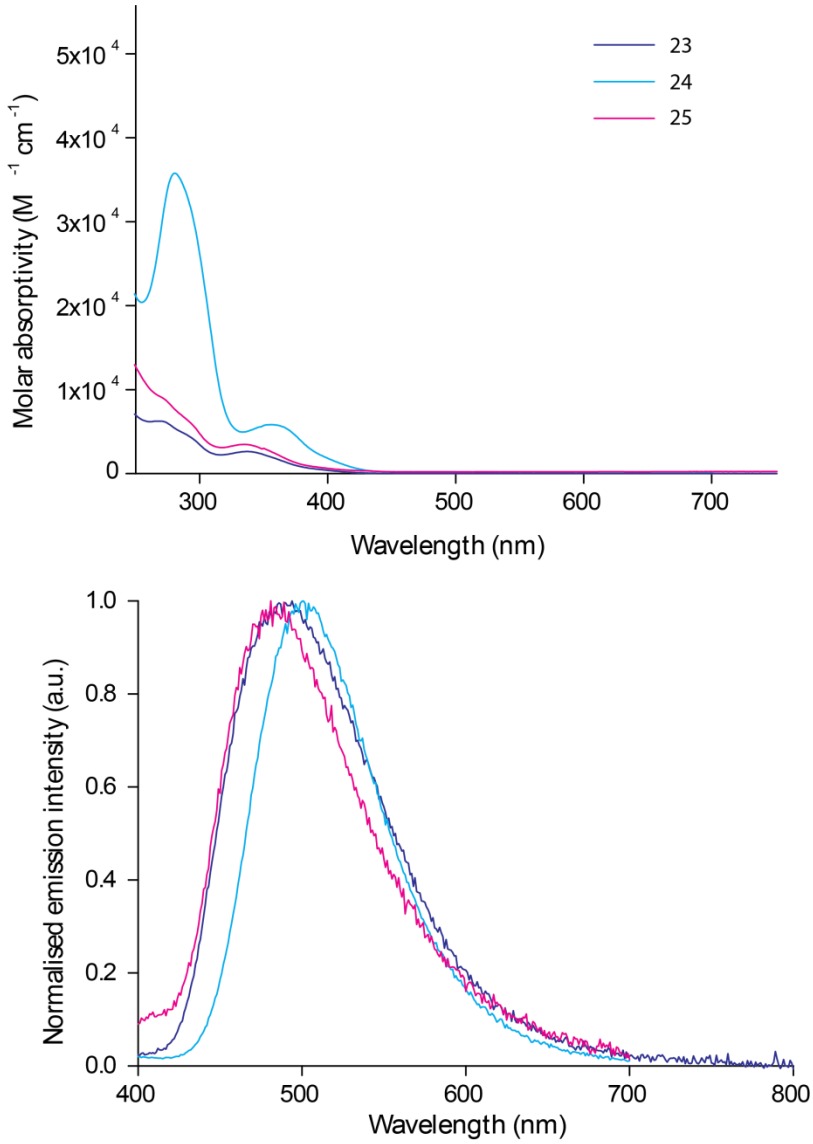

Figure 4.8 Absorption (top) and emission (bottom) spectra for [Re(**PyImPh**)$(CO)_3$(Py)]$^+$ (**23**, blue), [Re(**PyImPh**)$(CO)_3$(DMAP)]$^+$ (**24**, cyan) and [Re(**PyImPh**)$(CO)_3$(PyNHBu)]$^+$ (**25**, magenta) in aerated DCM solution. Excitation occurred at 360 nm.

The excited state lifetime for [Re(**PyImPh**)$(CO)_3$(Py)]$^+$ (**23**) in aerated DCM was measured to be 60 ns, which is identical to that of the neutral halogenated precursor **22Cl**. Also, the lifetime decays for **24** (τ = 83 ns) and **25** (τ = 52 ns) are not significantly different to each other. Conversely, the quantum yield value for **23** (Φ = 0.08%) and **25** (Φ = 0.25%) is significantly lower than **22Cl** (Φ = 3.00%) in aerated DCM. Despite the differences in quantum yield, the relaxation from the lowest ^{3}MLCT excited state to the ground state, (i.e. non-radiative decay) of all complexes are very similar.

Table 4.3 Photophysical properties of the Re(I)-NHC complexes from diluted dichloromethane solutions at room temperature (*ca.* 10^{-5} M).

Complex	λ_{abs} (nm) [10^4 ε, $M^{-1}cm^{-1}$]	λ_{em} (nm)	Lifetime [a] (τ, ns)	Lifetime [b] (τ, ns)	Φ [a, c] (±0.015)	Φ [b, c] (±0.015)
22Cl [149]	277 (0.89), 361 (0.33)	522	60	140	0.03	0.09
23	267 (0.625), 337 (0.263)	494	61 [#]	133 [#]	0.00083	0.00097
24	281 (6.18), 358 (0.764),	501	83	126	0.011	0.028
25	272 (0.891), 334 (0.348)	481	52	107 [#]	0.0025	0.0053

[a] air equilibrated samples, [b] degassed samples, [c] quantum yield Φ measured against air equilibrated quinine sulfate (in 1M H_2SO_4). [#] A short component was also detected (<10% contribution).

The complexes were also investigated in acetonitrile solutions (see **Figure 4.9**) to observe any solvent-assisted displacement of the ancillary ligand (which has been previously reported for the halide derivative).[147] Firstly, the absorption plots showed a slight blue shift upon measuring the complexes in acetonitrile solution. However, the emission plots were relatively the same and displayed structureless bands at a maximum wavelength of 480-500 nm. There was no significant shift upon changing the solvent from dichloromethane to acetonitrile. Furthermore, the most significant change was that of the excited state lifetime decay of the complexes in acetonitrile.

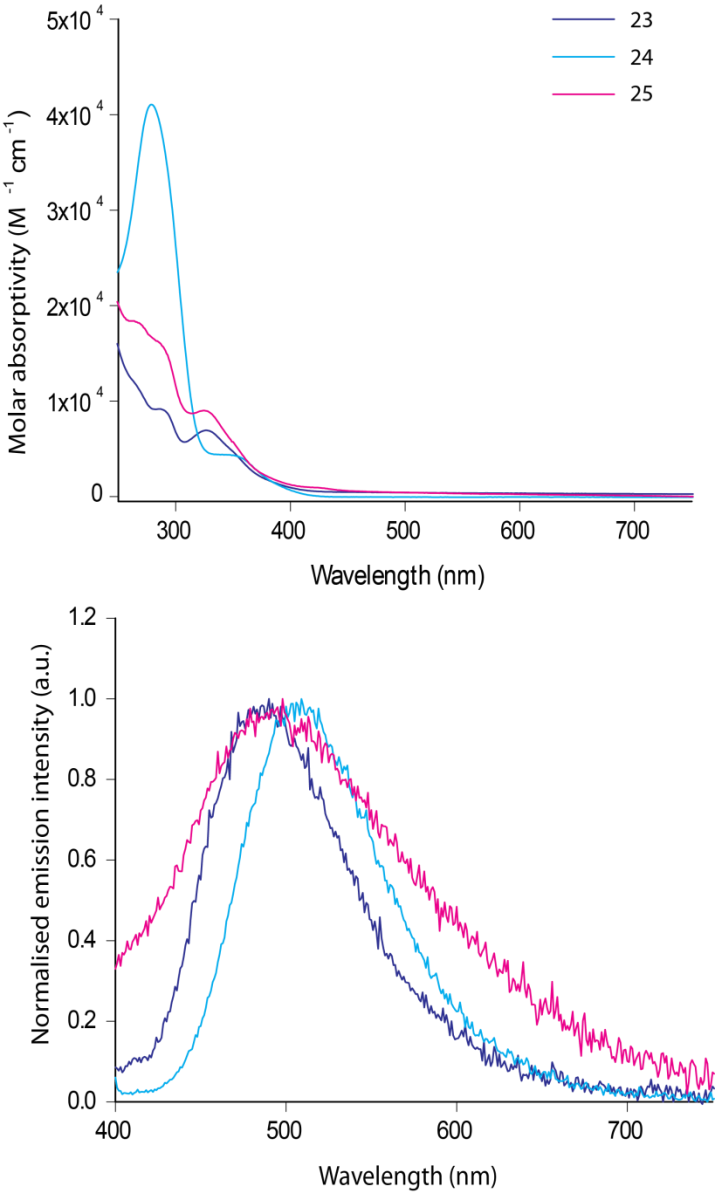

Figure 4.9 Absorption (top) and emission (bottom) spectra for [Re(**PyImPh**)$(CO)_3$(Py)]$^+$ (**23**, blue), [Re(**PyImPh**)$(CO)_3$(DMAP)]$^+$ (**24**, cyan) and [Re(**PyImPh**)$(CO)_3$(PyNHBu)]$^+$ (**25**, magenta) in aerated MeCN solution. Excitation occurred at 360 nm.

Even though there appears to be no solvatochromic shift in emission, the excited state lifetime decay and quantum yield measurements indicate that these cationic complexes are solvent-dependent (i.e. non-reactive in dichloromethane and reactive in acetonitrile). The lifetime for **23** in aerated acetonitrile was significantly lower than when measured in aerated dichloromethane; exhibiting a biexponential decay of 2 and 12 ns in aerated acetonitrile. The biexponential data suggests that two species are present in solution, i.e. one component representing the original complex and the other representing the solvated complex upon photoexcitation with acetonitrile. Interestingly, upon degassing the solution, the lifetime did not increase or change

significantly. This would also suggest that the species which exist in solution is not affected by the presence of oxygen. This trend was also evident for **25** with a biexponential and short lifetime decay of 3 and 10 ns in acetonitrile. The lifetime for **24** in aerated acetonitrile displayed a longer lifetime than complex **23** and **25**, albeit still short relative to other rhenium(I) tricarbonyl complexes.

In addition, the quantum yield values for complexes **23-25** are significantly lower in aerated acetonitrile solution. Upon degassing the solution, there was no significant change in the lifetime decay which was similar to the trend in dichloromethane. The reduced quantum yield and shorter excited state lifetime suggests a quenching mechanism taking place, which can be explained by photochemistry. This can be confirmed by monitoring multiple successive scans of the complex in acetonitrile, when excited at its ^{3}MLCT state. These findings will be discussed in detail in the photochemical investigation section of this chapter.

Table 4.4 Photophysical properties of the Re(I)-NHC complexes from diluted acetonitrile solutions at room temperature (*ca*. 10^{-5} M).

Complex	λ_{abs} (nm) [10^4 ε, $M^{-1}cm^{-1}$]	λ_{em} (nm)	Lifetime [a] (τ, ns)	Lifetime [b] (τ, ns)	Φ [a, c] (±0.015)	Φ [b, c] (±0.015)
23	285 (0.918), 327 (0.694)	482	1.9 (74%), 12.2 (26%)	1.9 (42%), 14.6 (58%)	0.00053	0.00055
24	279 (4.11), 347 (0.438)	506	29.6	35.1	0.006	0.017
25	268 (1.93), 324 (0.992)	497	3.4 (47%), 9.9 (53%)	3.2 (42%), 9.7 (58%)	0.0007	0.0010

[a] air equilibrated samples, [b] degassed samples, [c] quantum yield Φ measured against air equilibrated quinine sulfate (in 1M H_2SO_4).

In comparison to the rhenium(I)-NHC complexes, the photophysical properties of the rhenium(I)-**phen** analogues were also investigated. The absorption and emission profiles for [Re(**phen**)$(CO)_3$(Py)]$^+$ (**26**), [Re(**phen**)$(CO)_3$(DMAP)]$^+$ (**27**) and [Re(**phen**)$(CO)_3$(PyNHBu)]$^+$ (**28**) in aerated dichloromethane are shown in **Figure 4.10**. Complexes **26-28** exhibit a red shift in emission by *ca*. 50-80 nm compared to the NHC analogues. Also, the DMAP complex **27** displayed further red shifted emission compared to **26** and **28**, consistent with the rhenium(I)-NHC complex

reported earlier. The red shifted emission can be attributed to the extended conjugation of the **phen** chelating ligand. This increased conjugation stabilises the energy level of the LUMO which results in a smaller HOMO-LUMO energy gap causing the red shift. In addition, the excited state lifetimes for the rhenium(I)-**phen** complexes are almost ten times longer (in the microsecond range) than that of the NHC analogues (nanosecond range). This is a result of the **phen** being less distorted in the excited state compared to the NHC complexes.

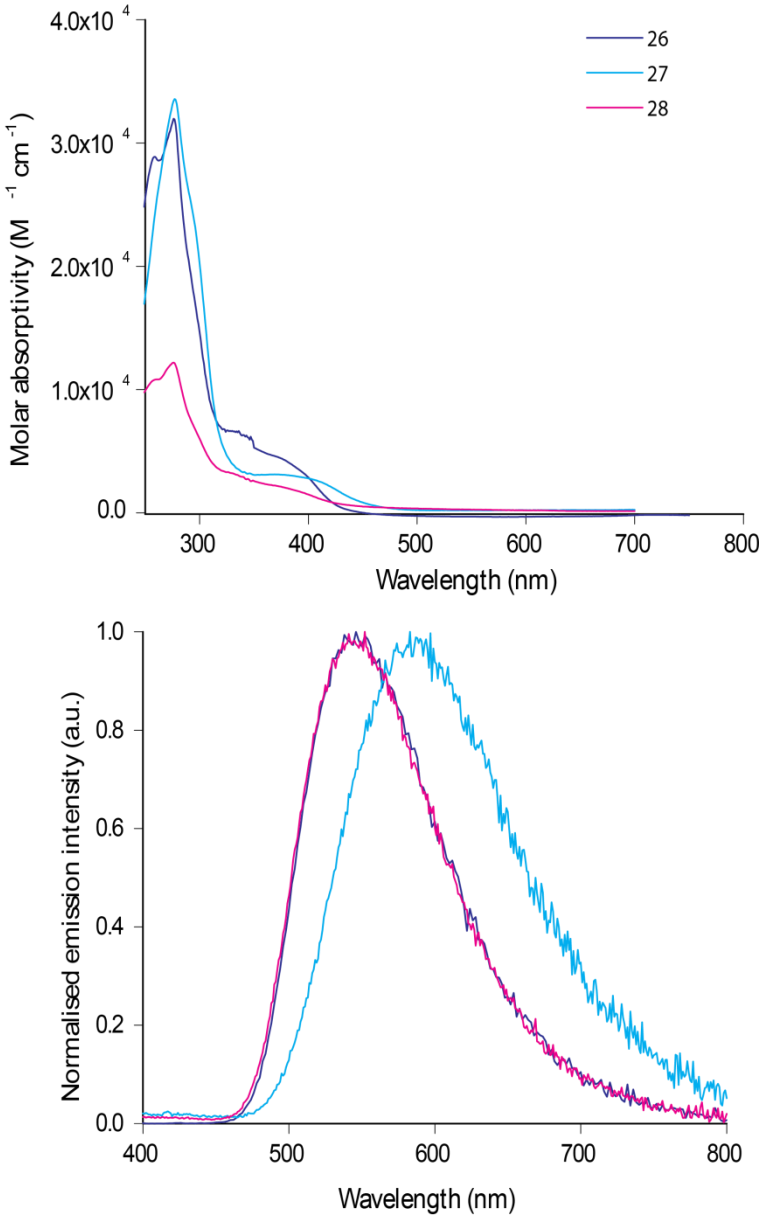

Figure 4.10 Absorption (top) and emission (bottom) spectra for [Re(**phen**)$(CO)_3$(Py)]$^+$ (**26**, blue), [Re(**phen**)$(CO)_3$(DMAP)]$^+$ (**27**, cyan) and [Re(**phen**)$(CO)_3$(PyNHBu)]$^+$ (**28**, magenta) in aerated DCM solution. Excitation occurred at 360 nm.

The photophysical properties of the rhenium(I)-**phen** analogues were also investigated in acetonitrile solutions as shown in **Figure 4.11**. The absorption plots for complex **26-28** in acetonitrile are almost identical to those in dichloromethane. The high energy band at ~275 nm in the absorption spectrum is assigned to IL transitions as they do not display any solvatochromic behaviour.

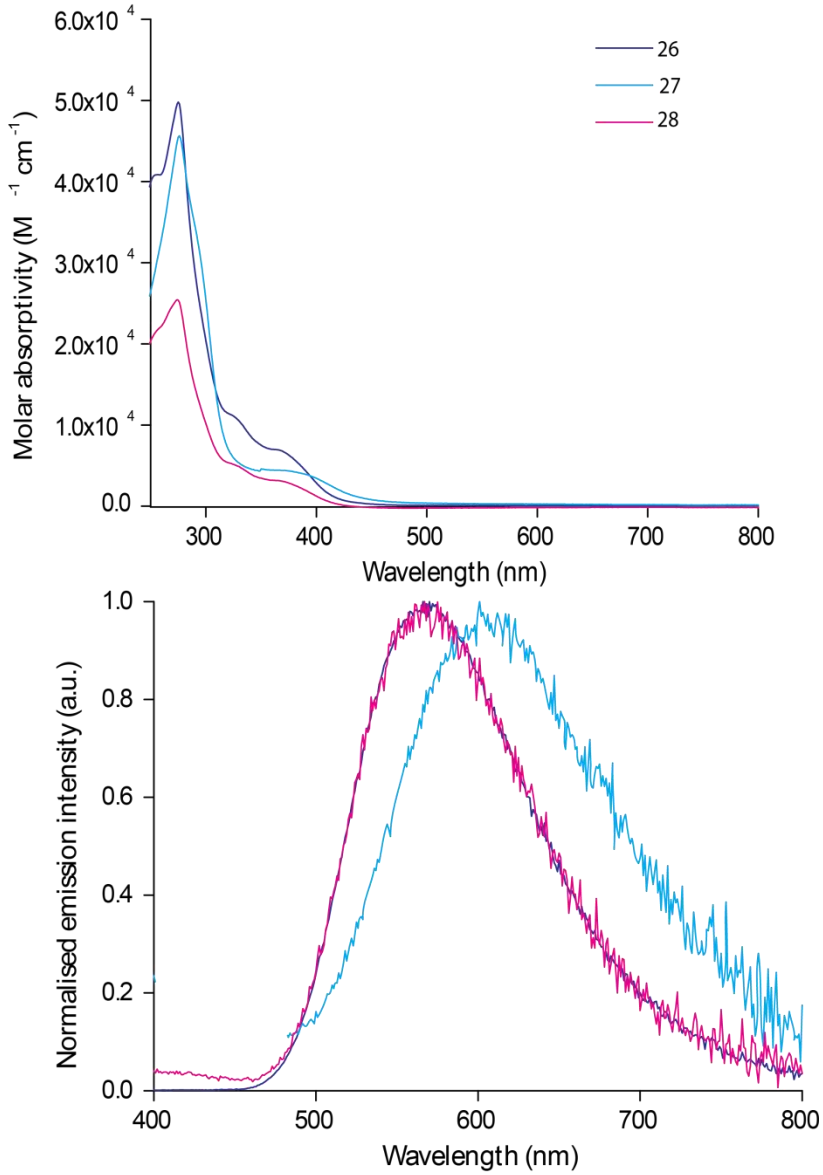

Figure 4.11 Absorption (top) and emission (bottom) spectra for [Re(**phen**)$(CO)_3$(Py)]$^+$ (**26**, blue), [Re(**phen**)$(CO)_3$(DMAP)]$^+$ (**27**, cyan) and [Re(**phen**)$(CO)_3$(PyNHBu)]$^+$ (**28**, magenta) in aerated MeCN solution. Excitation occurred at 360 nm.

In acetonitrile solution, all the complexes exhibit a red shift in emission by *ca* 20 nm compared to the measurements in dichloromethane. This solvatochromic behaviour is indicative of a charge transfer state. The structureless emission band is attributed to ^{3}MLCT transition from the rhenium metal centre to the **phen** ligand. In particular,

the emission maxima of complex **27** displayed a red shift compared to **26** and **28**. The difference in emission energies is attributed to the DMAP substituent lowering the energy of the LUMO and giving the complex an overall smaller energy gap. As a result, the k_{nr} increases and this relates to the shorter lifetime decay (318 ns) for **27**, in accordance with the energy gap law.[162,198] These data are consistent with those reported by Sacksteder.[198] **Table 4.5** provides a summary of the photophysical data for complexes **26-28** in both dichloromethane and acetonitrile solutions.

Table 4.5 Summary of photophysical data for Re(I)-**phen** complexes **26-28** in diluted DCM and MeCN solutions at room temperature (*ca.* 10^{-5} M).

	DCM			**MeCN**		
Complex	λ_{abs} (nm) [10^4 ε, $M^{-1}cm^{-1}$]	λ_{em} (nm)	Lifetime [a] (τ, ns)	λ_{abs} (nm) [10^4 ε, $M^{-1}cm^{-1}$]	λ_{em} (nm)	Lifetime [a] (τ, ns)
26	277 (3.19), 355 (0.507)	544	1052	277 (4.87), 375 (0.630)	570	238
27	277 (5.02), 373 (0.41)	588	318	275 (4.55), 379 (0.427)	603	71 (68%), 199 (32%)
28	276 (1.22), 360 (0.23)	545	1226	274 (2.54), 360 (0.319)	565	220

4.6.1 Amino Acid Complexes

In order to make meaningful comparisons to the rhenium(I) diimine complexes studied by Blanco-Rodriguez *et al.*, the excited state processes of rhenium(I)-NHC complexes coordinated to pyridyl amino acids were investigated. The photophysical data in dichloromethane solutions for the complexes [Re(**PyImPh**)$(CO)_3$(Py**Trp**)]$^+$ (**32**), [Re(**PyImPh**)$(CO)_3$(Py**Phe**)]$^+$ (**33**) and [Re(**PyImPh**)$(CO)_3$(Py**Gly**)]$^+$ (**34**) are summarised in **Table 4.6**. The absorption spectrum illustrated in **Figure 4.12** displays two distinct bands: a high intensity band at ~270 nm and a low intensity broad band at 330 nm. The higher energy band is assigned to intraligand (IL) transitions involving the π system of the NHC ligand, whereas the lower energy broad band is assigned to MLCT transition. The absorption profiles for **32-34** are very similar to **23-25**, despite the changes in ancillary ligand with the amino acids present. In addition, all the complexes display broad and structureless emission centred around 490-520 nm. The emission maxima for **33** and **34** are slightly shifted,

due to the variation of the amino acid substituent. In addition, the excited state lifetime decays for **32-34** are of biexponential nature and lower than those reported for **23-25**. Upon degassing the solution, the lifetime for complexes **32-34** increases. This suggests that the emission originates from a triplet excited state, which is consistent with previously reported rhenium(I)-NHC complexes.[147,149]

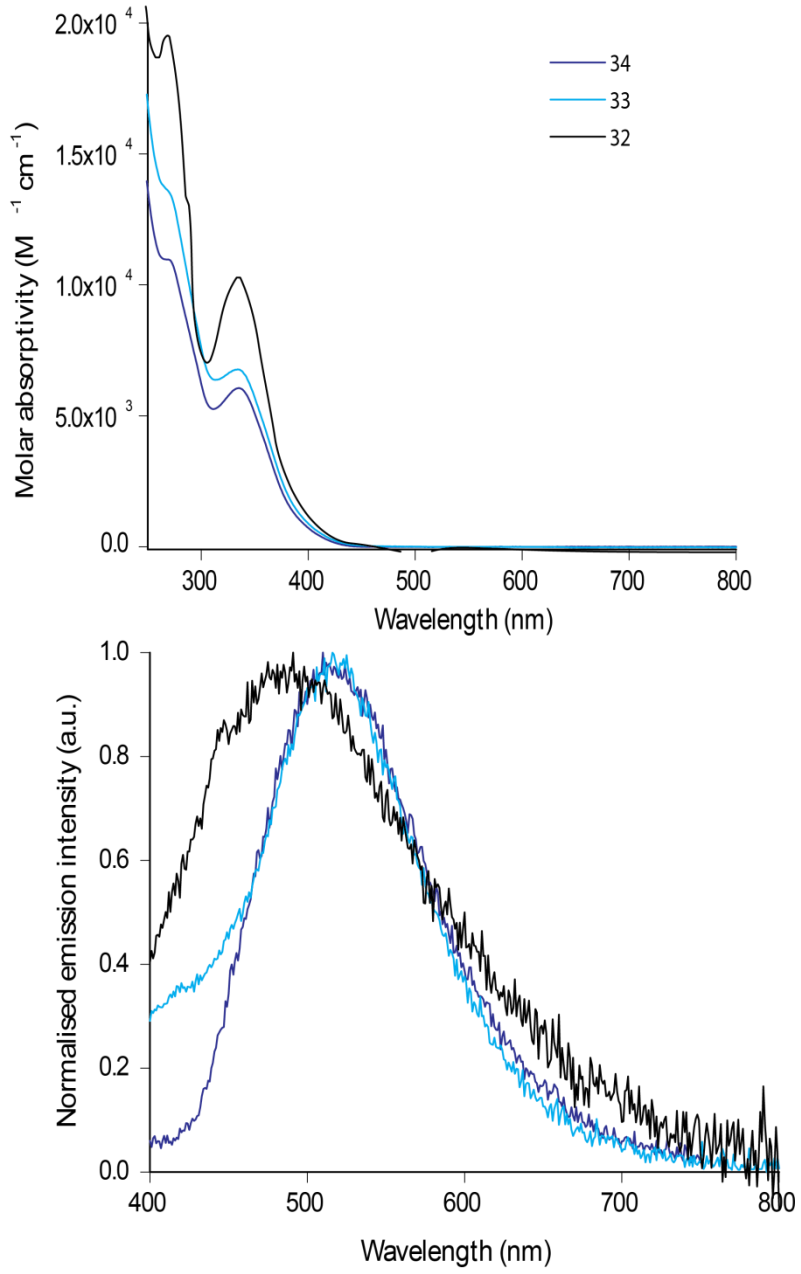

Figure 4.12 Absorption (top) and emission (bottom) spectra for **34** (cyan), **33** (blue) and **32** (black) in aerated DCM solution.

Table 4.6 Photophysical properties of the Re(I)-NHC complexes from diluted dichloromethane solutions at room temperature (*ca.* 10^{-5} M).

Complex	λ_{abs} (nm) [10^4 ε, $M^{-1}cm^{-1}$]	λ_{em} (nm)	Lifetime [a] (τ, ns)	Lifetime [b] (τ, ns)	Φ [a, c] (± 0.015)	Φ [b, c] (± 0.015)
32	269 (2.02), 334 (1.10)	491	4 (19%), 24 (81%)	140	0.001	0.002
33	270 (1.35), 334 (0.67)	520	5 (16%), 59 (84%)	22 (4%), 150(96%)	0.004	0.005
34	269 (1.09), 335 (0.61)	517	6.1 (11%), 41 (89%)	13 (27%), 60 (73%)	0.014	0.042

[a] air equilibrated samples, [b] degassed samples, [c] quantum yield Φ measured against air equilibrated quinine sulfate (in 1M H_2SO_4).

The photophysical data for the complexes in acetonitrile are presented in **Figure 4.13**. The absorption profile of the **Trp** (**32**) and **Gly** (**34**) analogue are almost identical displaying a broad MLCT band at *ca.* 325 nm, despite their unique differences present for IL transitions coming from their amino acid structures. On the other hand, the emission profiles for **32** with respect to **34** vary greatly and the integration of the band is significantly different. This indicates a quenching mechanism occurring in solution. In addition, the emission band for **32** appears to have a contribution of mixed IL and MLCT transitions which tails off at the end. This mixed phosphorescence has also been seen in literature.[43] In addition, the excited state lifetime decay for **32** is very short with biexponential nature at 2 and 8 ns, compared to complex **34** at 30 ns; this is also suggestive of a quenching mechanism. The photophysical data in acetonitrile are summarised in **Table 4.7**. The quantum yield values are very low, which also support the short excited state lifetime data. These can be attributed to quenching from electron transfer. Additionally, the electron transfer rate constant (k_{eT}) can be calculated following the approach from Blanco Rodriguez, using the following equation:

$$k_{eT} = \tau_{\mathbf{Trp}}^{-1} - \tau_{\mathbf{Gly}}^{-1}$$

where $\tau_{\mathbf{Trp}}$ is the excited state lifetime of the **Trp** complexes and $\tau_{\mathbf{Gly}}$ is the essential component being the excited state lifetime of the corresponding unreactive **Gly** complexes. The rate of electron transfer for compound **34** was calculated to be 6.4 ×

10^8 s^{-1} when measured in aerated acetonitrile. This rate falls within the range of an electron transfer mechanism as reported by Blanco-Rodriguez.

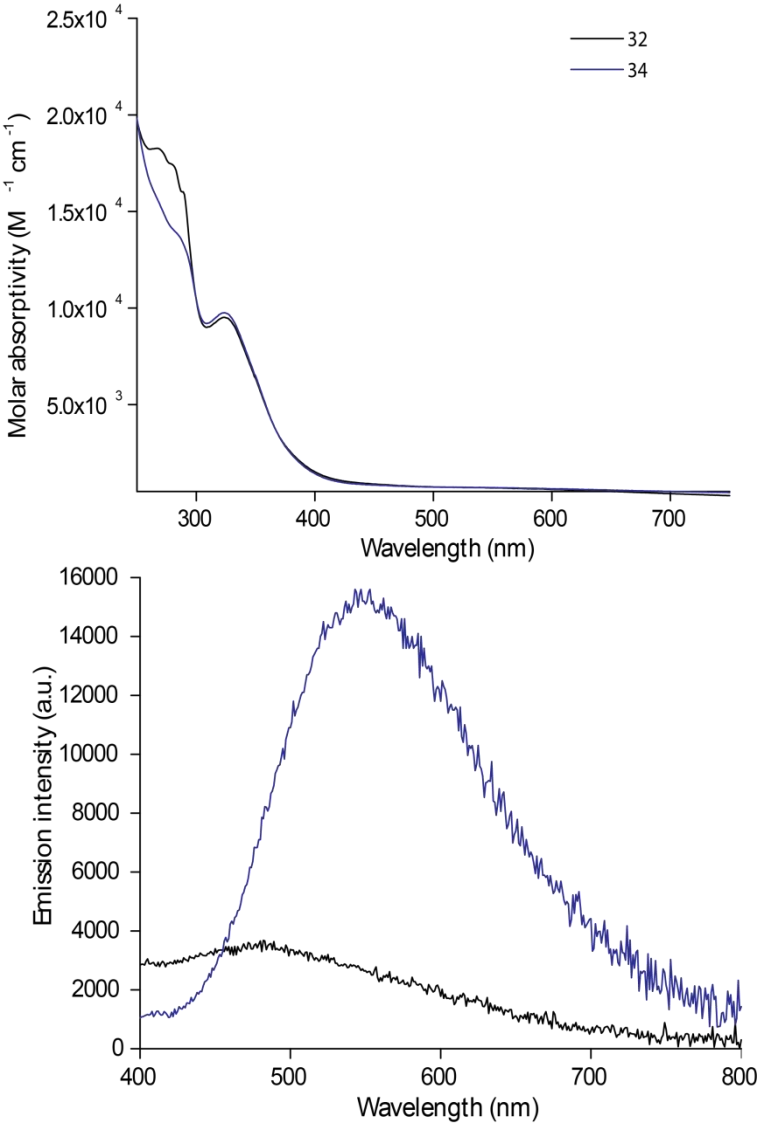

Figure 4.13 Absorption and emission plots of **32** (black trace) and **34** (blue trace) in MeCN.

Table 4.7 Photophysical properties of the Re(I) complexes from diluted acetonitrile solutions at room temperature (*ca.* 10^{-5} M).

Complex	λ_{abs} (nm) [10^4 ε, $M^{-1}cm^{-1}$]	λ_{em} (nm)	Lifetime [a] (τ, ns)	Lifetime [b] (τ, ns)	Φ [a, c] (± 0.015)	Φ [b, c] (± 0.015)
32	290 (1.64), 324 (1.03)	482	2 (56%), 8 (43%)	3 (82%), 16 (18%)	0.0004	0.0005
34	289 (1.34), 324 (0.97)	548	31	153	0.0005	0.0007

[a] air equilibrated samples, [b] degassed samples, [c] quantum yield Φ measured against air equilibrated quinine sulfate (in 1M H_2SO_4).

4.7 Photochemical Investigation

Before each experiment was undertaken, the complex was dissolved in acetonitrile solution and left overnight in darkness to assess its stability. After subsequent NMR scans, the final and initial spectra were superimposable and confirmed that all complexes were stable in darkness. Therefore any reaction that took place was due to the photochemical reaction and not a result of hydrolysis or solvent exchange in solution.

Previous studies by Vaughan *et al.*, demonstrated that the neutral complex [Re(**PyImPh**)$(CO)_3$X], where X is a halide, is photoactive in a coordinating solvent such as acetonitrile.[148] The key step was the formation of cationic tricarbonyl solvato species (I). Further studies revealed that the reaction goes through an associative transition state, where the complex structure bends and allows space for the coordinating solvent to enter.[189] This helped identify the species formed post photolysis (see **Figure 4.14**).

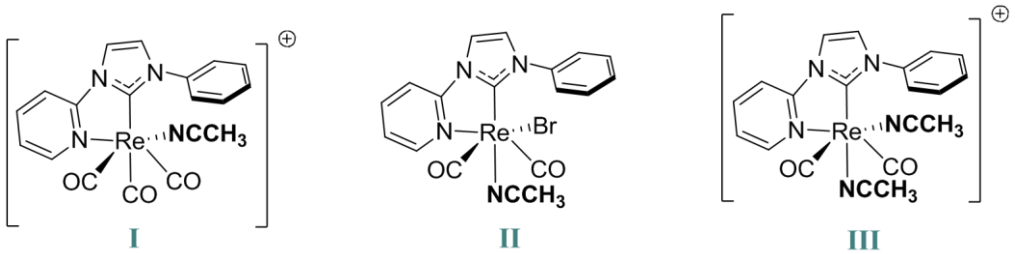

Figure 4.14 Possible photoproducts present upon irradiation of [Re(**PyImPh**)$(CO)_3$(L)] in MeCN with UV light.

In this investigation, the appropriate conditions for the photochemical experiments outlined in experimental section 4.9.2 were followed for each of the subsequent complexes. The cationic species being investigated have the general formula, [Re(**PyImPh**)$(CO)_3$(L)]$^+$, where L is a pyridine with various substituents. The main spectroscopic techniques that were utilised to emphasise the possible photochemical mechanism and associated photoproducts were NMR and IR spectroscopy.

4.7.1 [Re(**PyImPh**)$(CO)_3$(Py)]$^+$

Firstly, the emission profile of [Re(**PyImPh**)$(CO)_3$(Py)]$^+$ in diluted acetonitrile solution was monitored by recording consecutive scans upon constant excitation at

λ_{ex} = 370 nm, for a total duration of 4 hours. Refer to experimental section 4.9.2 for specific parameters. The emission profile of complex [Re(**PyImPh**)$(CO)_3$(Py)]$^+$ showed a change after photolysis in MeCN solution. The change is distinguished by the disappearance of the blue-coloured emission centred at 490 nm, and the simultaneous appearance of an orange-coloured emission centred at 580 nm. The initial and final emission profiles are shown in the **Figure 4.15**. The change in the spectrum can also be physically observed by the pale yellow colour of the initial solution progressively becoming dark yellow/orange. This new band can be attributed to either of the photoproducts **II** and **III** (see **Figure 4.1**). It cannot be the MeCN-solvato complex **I** as this would show a colourless solution which is not emissive.

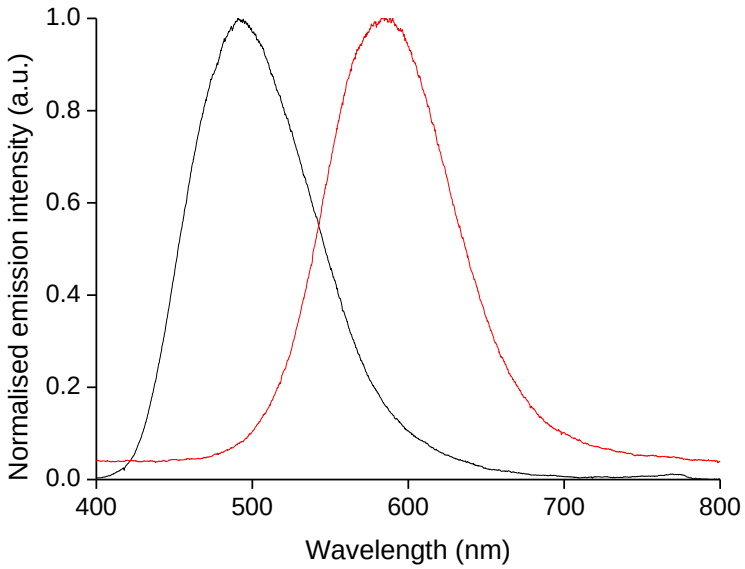

Figure 4.15 Emission profile for [Re(**PyImPh**)$(CO)_3$(Py)]$^+$ before (black trace) and after (red trace) photolysis in acetonitrile solution. The photolysis was performed by irradiating the sample at λ_{ex} = 370 nm.

The photochemical properties of the complexes in acetonitrile solutions were also analysed using ^{1}H NMR spectroscopy, following irradiation of the sample with 365 nm light corresponding to the excitation at the MLCT manifold. ^{1}H NMR spectroscopy was implemented to monitor any structural changes that occurred during the photolysis of the complexes. The sequential ^{1}H NMR spectra of the photolysis of [Re(**PyImPh**)$(CO)_3$(Py)]$^+$ at 365 nm can be seen in **Figure 4.16**. The most distinctive changes in the spectrum were those occurring to the downfield signal associated to the pyridyl-H6′ proton at 9.01 ppm. This peak resembled a

"doublet" and was used as a spectroscopic handle as it was the clearest to observe for spectral changes due to being well separated from all other signals.

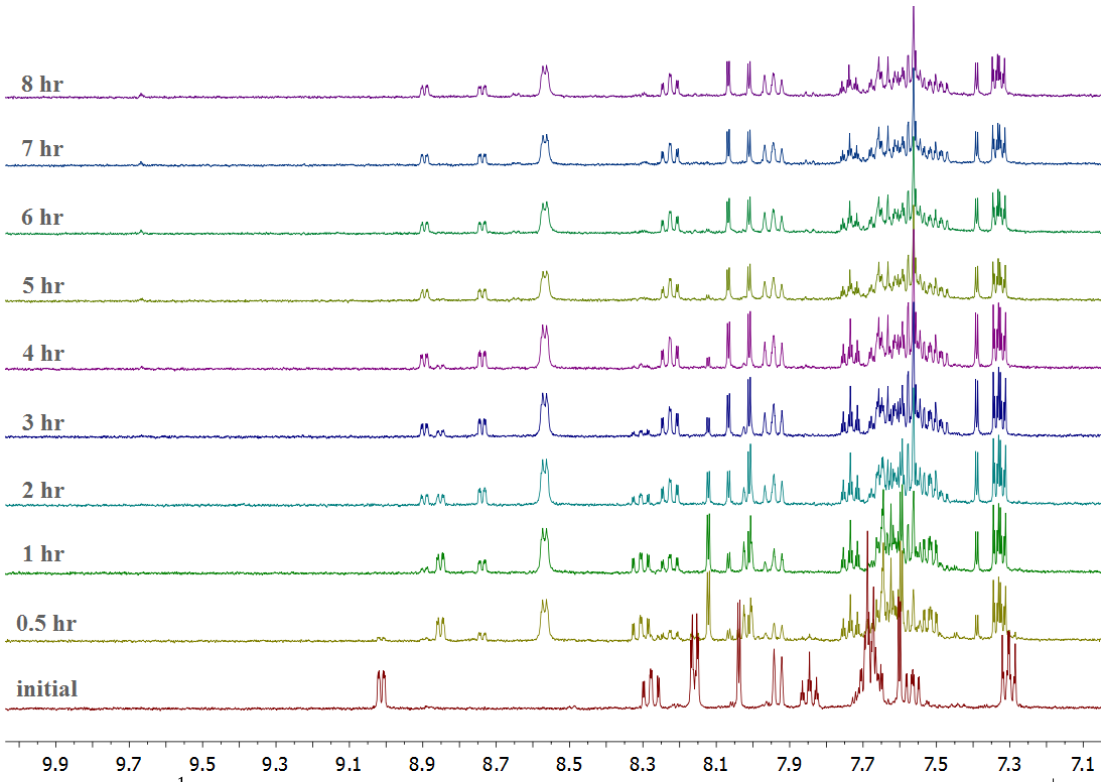

Figure 4.16 ^{1}H NMR progression of the photolysis of [Re(**PyImPh**)(CO)$_3$(Py)]$^+$ in deuterated acetonitrile solution. The photolysis was performed by irradiating the sample at 365 nm (pen ray lamp) over a period of 8 hours.

After the first 30 minutes of photolysis, the initial doublet had started to disappear and was completely absent after 1 hour (see **Figure 4.17**). This was accompanied by the appearance of three new upfield doublet peaks at 8.85, 8.74 and 8.57 ppm, which can be attributed to formation of new species assigned as photoproducts **I**, **II** and pyridine respectively. The peak at 8.57 ppm corresponds to free pyridine as a result of the pyridine dissociating from the rhenium. After about 2 hours, the signal at 8.85 ppm (**I**) started decreasing in intensity and completely disappeared after 4 hours of photolysis. Accompanying this disappearance was a new signal appearing at 8.90 ppm which was assigned as photoproduct **III**. In addition, another new downfield signal at 9.70 ppm appears with very weak intensity, which is characteristic of the H2 hydrogen in an imidazolium salt. This was characterised as a detachment of the NHC ligand, which is common upon hydrolysis and has been shown to occur in similar conditions in previous studies. [149,197]

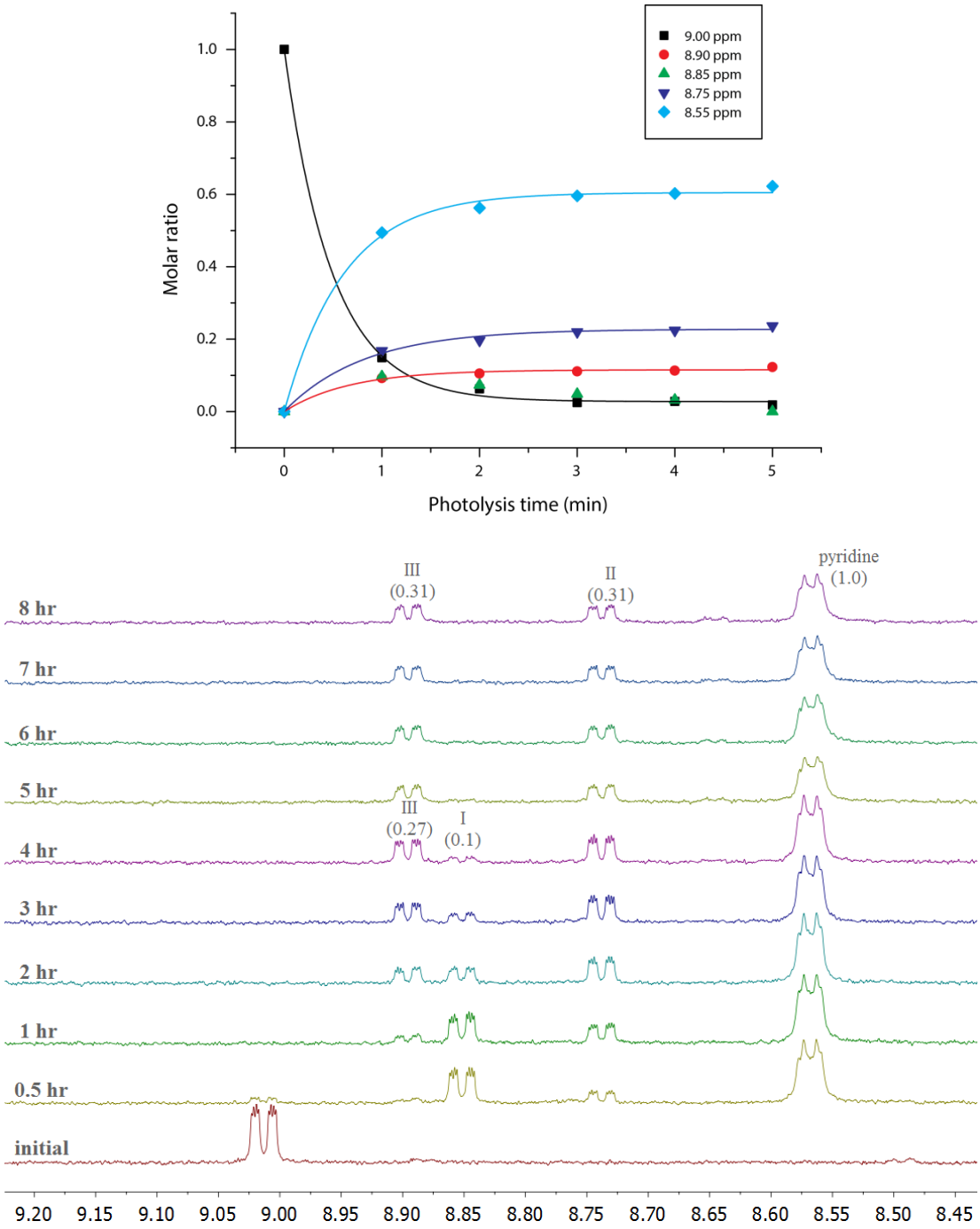

Figure 4.17 Top: Rate of photolysis as molar ratio (derived from peak integration) showing appearance and disappearance of products over time. Bottom: Magnified ^{1}H NMR spectrum showing changes in the peak associated with H6 proton of [Re(**PyImPh**)$(CO)_3$(Py)]$^+$. Integration of photoproducts shown in brackets.

The top graph in **Figure 4.17** represents the trend related to the appearance and disappearance of peaks in the ^{1}H NMR spectrum; it takes into account the molar ratio, which correlates the integration of peak of interest and the combined integration of total peaks present. All the peaks appear to follow a general exponential trend, with the exception of the peak at 8.85 ppm, which was found to be

an intermediate component of the reaction, assigned as the tricarbonyl acetonitrile solvato complex (**I**).

To gain a better understanding of the photochemical processes occurring and to further identify the products, an acetonitrile solution of the complex was photolysed and periodically monitored by IR spectroscopy, particularly paying attention to the carbonyl bands of the complex. The IR spectrum of the reaction mixture in CD_3CN solution after photolysis was obtained according to experimental procedure outlined in section 4.9.2 and compared to the spectrum of the original solution prior to photolysis. Another spectrum was collected midway through the experiment. The three spectra were overlaid and illustrated in **Figure 4.18**. The spectra only show the range from 2050 to 1800 cm^{-1} in order to focus specifically on the features of the carbonyl stretches. Analysis of the IR spectrum corresponding to the original sample (**Figure 4.18**, black trace) featured carbonyl stretches at 2025 (sharp peak) and 1907 (broad peak with shoulder, indicating two signals overlapping) cm^{-1}, which can be identified as a cationic rhenium(I) tricarbonyl complex. Analysis of the IR spectrum of the photolysed sample (**Figure 4.18**, green trace) displayed the carbonyl stretches at 1930 and 1854 cm^{-1}. The stretching frequency of the carbonyl band had shifted to lower wavenumbers on account of an increased electron density on the metal, suggesting the loss of a CO ligand. Considering the spectrum taken midway (blue trace), the initial CO band had shifted from 2025 to 2030 cm^{-1}, indicating the formation of an intermediate tricarbonyl complex (**I**, identified as [Re(**PyImPh**)$(CO)_3(CH_3CN)]^+$). Subsequently, this band then decreased in intensity until it had completely disappeared, suggesting the conversion into a dicarbonyl complex (**III,** identified as [Re(**PyImPh**)$(CO)_2(CH_3CN)_2]^+$).

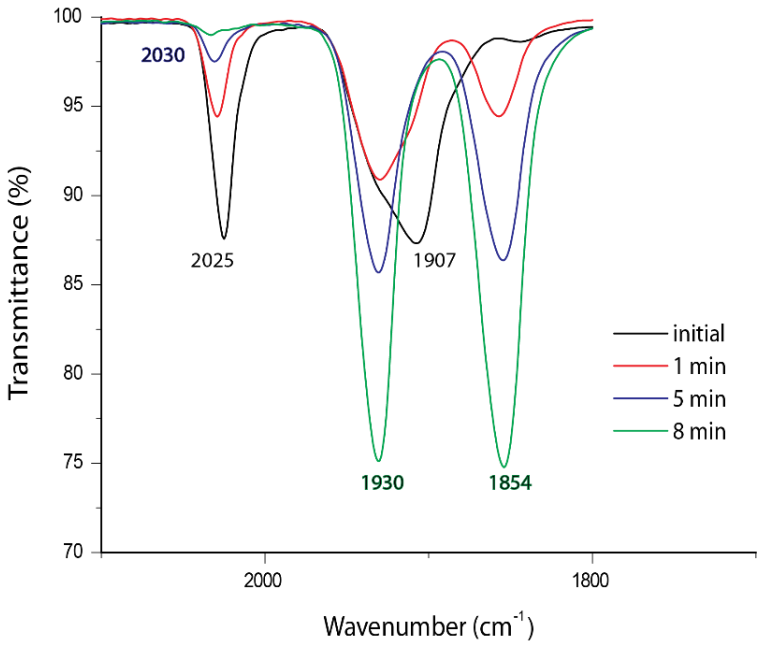

Figure 4.18 IR progression of the photolysis of [Re(**PyImPh**)$(CO)_3$(Py)]$^+$ in deuterated acetonitrile solution. The photolysis was performed by irradiating the sample at λ_{ex} = 350 nm (polilamp) over a period of 8 minutes.

Based on analysis of the ^{1}H NMR data in combination with the IR data, it would appear that there are three species present in the reaction mixture post photolysis, i.e. two rhenium dicarbonyl products and free pyridine. The proposed photochemical mechanism and structures of the complexes can be seen in **Scheme 4.9**. When [Re(**PyImPh**)$(CO)_3$(Py)]$^+$ is photolysed in acetronitrile, it forms the acetonitrile solvate, [Re(**PyImPh**)$(CO)_3(CH_3CN)]^+$ **(I)** *via* pathway 'A1' (**Scheme 4.9**). This solvato complex then further reacts *via* pathway 'A2' to form photoproduct **III**, which is hypothesised to be a dicarbonyl complex as indicated by the two carbonyl stretches observed in **Figure 4.18**. It has been predicted that the CO *trans* to the NHC ligand would be the most labile, as it should be experiencing a strong *trans* effect because the NHC ligand is a strong σ donor. Thus, the labile carbonyl ligand *trans* to the NHC ligand can then be replaced by a neutral acetonitrile ligand to form the dicarbonyl species, [Re(**PyImPh**)$(CO)_2(CH_3CN)_2]^+$ **(III)** as shown in **Scheme 4.9**.

The second reaction that can take place during the photolysis of [Re(**PyImPh**)$(CO)_3$(Py)]$^+$ is the direct formation of a dicarbonyl product *via* pathway 'B'. The structural identity of this product was assigned to be [Re(**PyImPh**)$(CO)_2(CH_3CN)$(Py)]$^+$ **(II)** by process of elimination. In addition, the IR spectrum of the photolysed solution indicates the presence of a dicarbonyl species.

However, through this alternative pathway, instead of the ancillary ligand being replaced by a solvent, only the labile CO positioned *trans* to the NHC is dissociated and exchanged for an acetonitrile molecule.

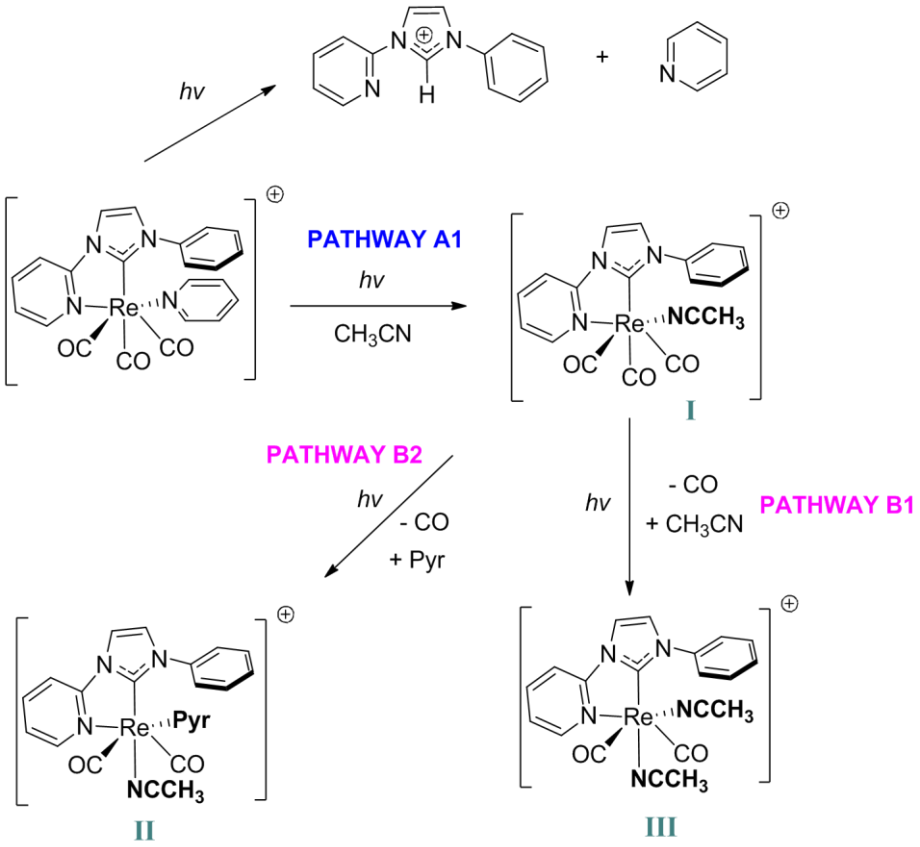

Scheme 4.9 Photochemical reaction pathway illustrating transformation of [Re(**PyImPh**)$(CO)_3$(Py)]$^+$ complex when excited using UV light in acetonitrile solution.

In order to confirm the identity of the photoproducts through structural analysis, the complex photolysed mixture needed to be isolated as a single crystal. However, multiple attempts and various methods such as slow evaporation of the solvent and slow diffusion of the sample into a solvent were not successful.

Furthermore, [Re(**phen**)$(CO)_3$(Py)]$^+$ was irradiated under the same conditions and no spectral changes were found in the ^{1}H NMR spectrum, therefore it was concluded to be photostable in CD_3CN, see Appendix **Figure A2**. Furthermore, it can be deduced that the photochemical factor comes from the chelating NHC ligand, as described by previously published papers.[147–149]

4.7.2 [Re(**PyImPh**)(CO)$_3$(DMAP)]$^+$

Following similar conditions as described in section 4.7.1, photochemical investigation were undertaken on complexes with substituted pyridine ligands, to see whether this has any effect on the rate and mechanism of photochemical reactions.

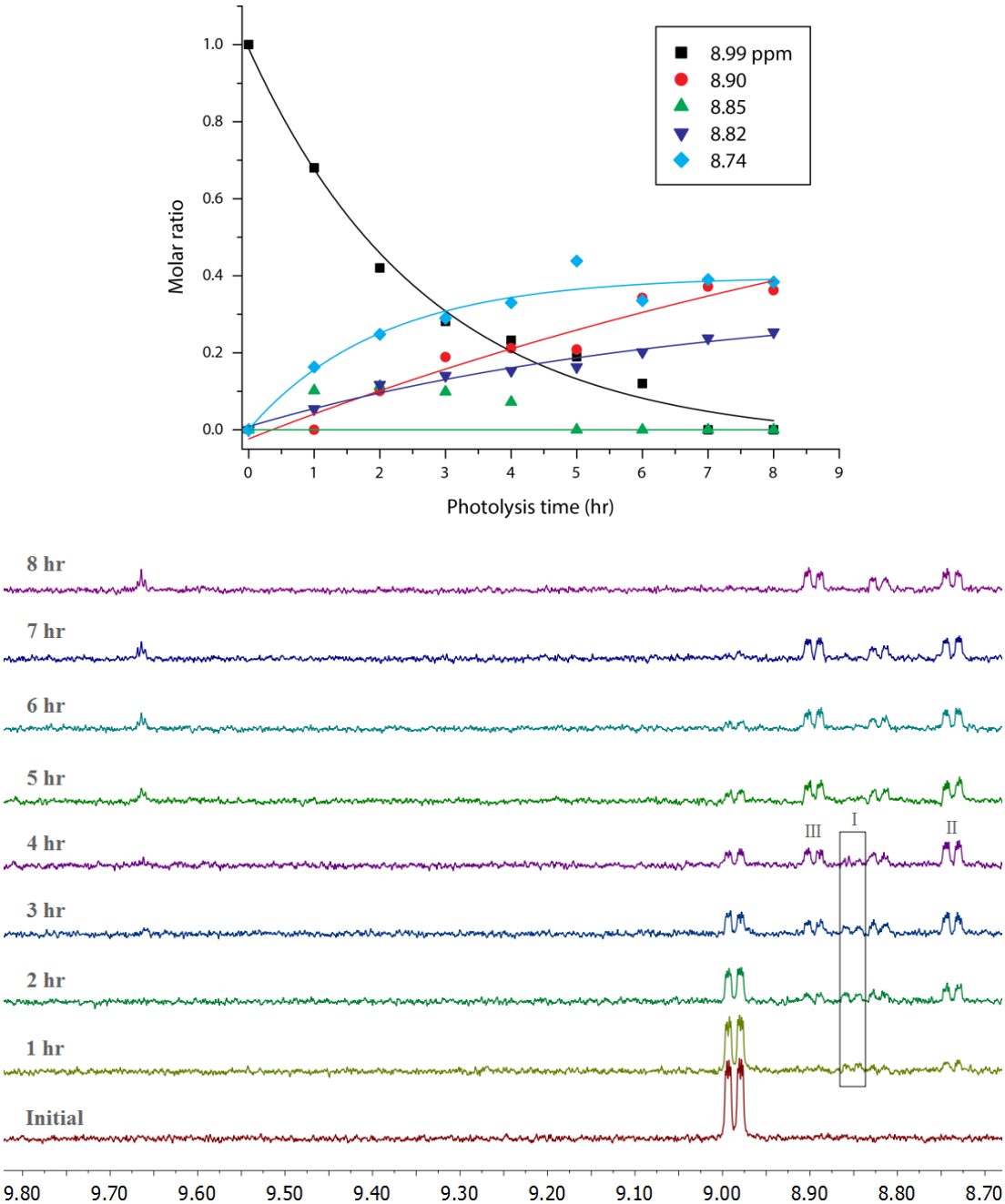

Figure 4.19 Top: Rate of photolysis as molar ratio (derived from peak integration) showing appearance and disappearance of products over time. Bottom: ^{1}H NMR progression of the photolysis of [Re(**PyImPh**)(CO)$_3$(DMAP)]$^+$ in deuterated acetonitrile solution. The photolysis was performed by irradiating the sample at 365 nm (pen ray lamp) over a period of 8 hours.

Analysis by ^{1}H NMR spectroscopy of the photolysed solution of complex [Re(**PyImPh**)$(CO)_3$(DMAP)]$^{+}$ in acetonitrile (**Figure 4.19**) illustrates the pyridyl H6′ proton as a doublet at 8.99 ppm. Over the duration of the photolysis, the peak slowly decreases in intensity and is completely absent after 8 hours of irradiation at 365 nm. After two hours, the appearance of four new upfield doublet peaks was evident at 8.89 (**III**), 8.85 (**I**), 8.82 (unknown) and 8.74 (**II**) ppm, which was attributed to the formation of new species. The highlighted box in **Figure 4.19** illustrates the formation and subsequent conversion of the photoproduct identified as **I**, which was also evident in the photolysis of [Re(**PyImPh**)$(CO)_3$(Py)]$^{+}$. Another similar trend found was the appearance of a downfield signal at 9.70 ppm corresponding to the H2 hydrogen of the imidazolium salt. The peak at 8.82 ppm has yet to be identified, although the possibility of it being the free DMAP ligand has been eliminated. This was confirmed by collecting a ^{1}H NMR spectrum of free DMAP in acetonitrile solution and comparing this to the photolysed solution. The aromatic signals of the DMAP do not overlap with any signals of the photolysed solution, neither does the methyl signal (see **Figure 4.20**). In addition, the imidazolium proton (9.70 ppm) to unknown peak has a ratio of 1:2, also eliminating the possibility of the peak belonging to the imidazolium salt that has dissociated from the rhenium.

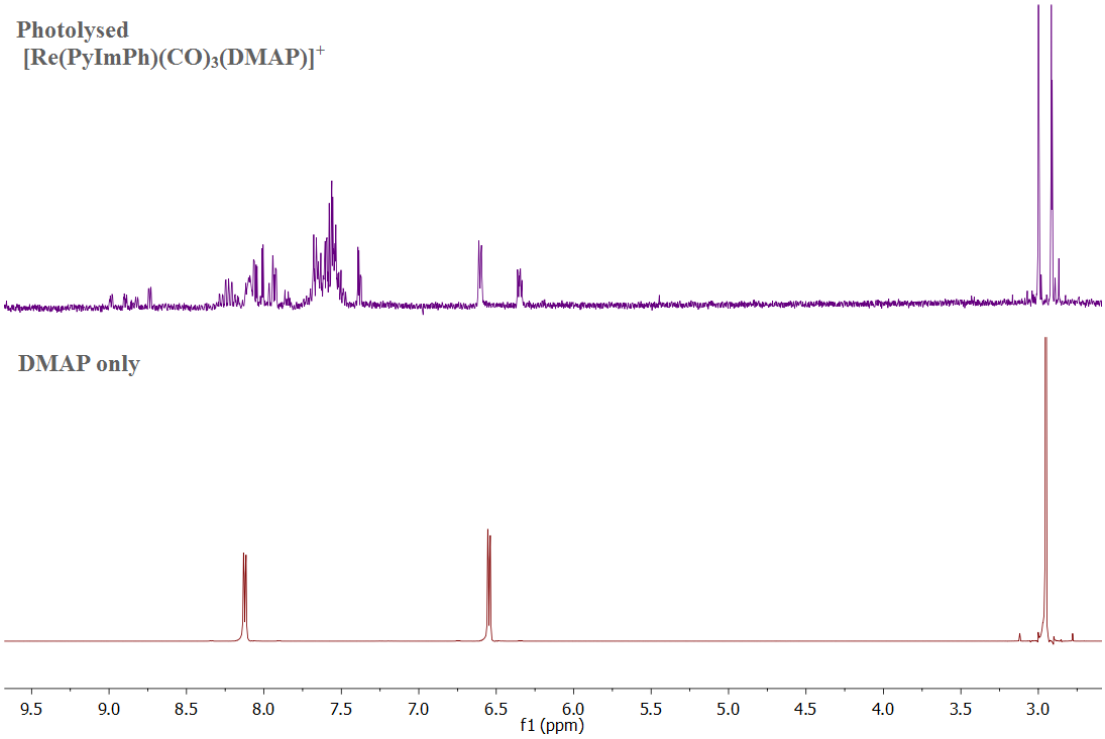

Figure 4.20 Overlaid ^{1}H NMR spectrum of photolysed [Re(**PyImPh**)$(CO)_3$(DMAP)]$^+$ complex (top) and free DMAP (bottom) in acetonitrile solution.

The IR spectrum of the reaction mixture in CD_3CN solution after photolysis was obtained according to experimental outlined in section 4.9.2 and compared to the spectrum of the original solution prior photolysis. The two spectra were overlaid and illustrated in **Figure 4.21**. Analysis of the IR spectrum corresponding to the original sample (blue trace) specifies carbonyl stretches at 2021 (sharp peak) and 1904 (broad, two peaks overlapping) cm^{-1}. The frequencies of these bands are consistent with previous reported cationic rhenium tricarbonyl complexes. Analysis of the IR spectrum of the photolysed sample after 8 hours (red trace), displayed the carbonyl stretches to shift to lower frequencies at 1930 and 1855 cm^{-1}. This was indicative of a loss of a carbonyl ligand as evident in **Figure 4.21** and similar to the IR spectrum of photolysed [Re(**PyImPh**)$(CO)_3$(Py)]$^+$ discussed earlier.

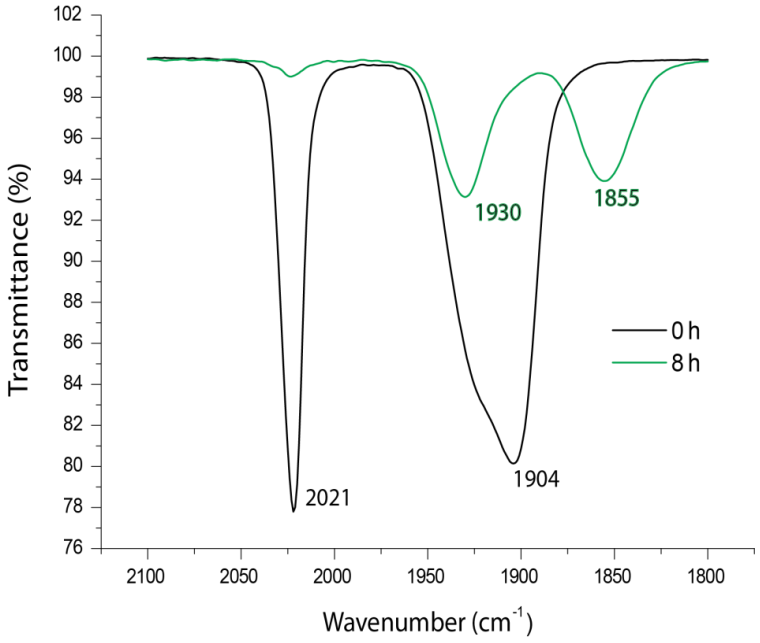

Figure 4.21 IR progression of the photolysis of [Re(**PyImPh**)$(CO)_3$(DMAP)]$^+$ in deuterated acetonitrile solution. The photolysis was performed by irradiating the sample at λ_{ex} = 365 nm (pen ray lamp) over a period of 8 hours.

In order to confirm that the photoactive component is the NHC ligand and not the ancillary ligand, a comparison was drawn with the diimine derivative, i.e. [Re(**phen**)$(CO)_3$(DMAP)]$^+$ complex. This was photolysed under the same conditions and monitored by NMR spectroscopy. Photolysis under UV light in acetonitrile showed no change in spectra over 4 hours (see Appendix, **Figure A3**), which confirms its photostability.

4.7.3 [Re(**PyImPh**)$(CO)_3$(PyNHBu)]$^+$

Analysis by ^{1}H NMR spectroscopy of the photolysed solution of complex [Re(**PyImPh**)$(CO)_3$(PyNHBu)]$^+$ in acetonitrile illustrates the pyridyl H6′ proton as a doublet at 9.03 ppm (**Figure 4.22**).

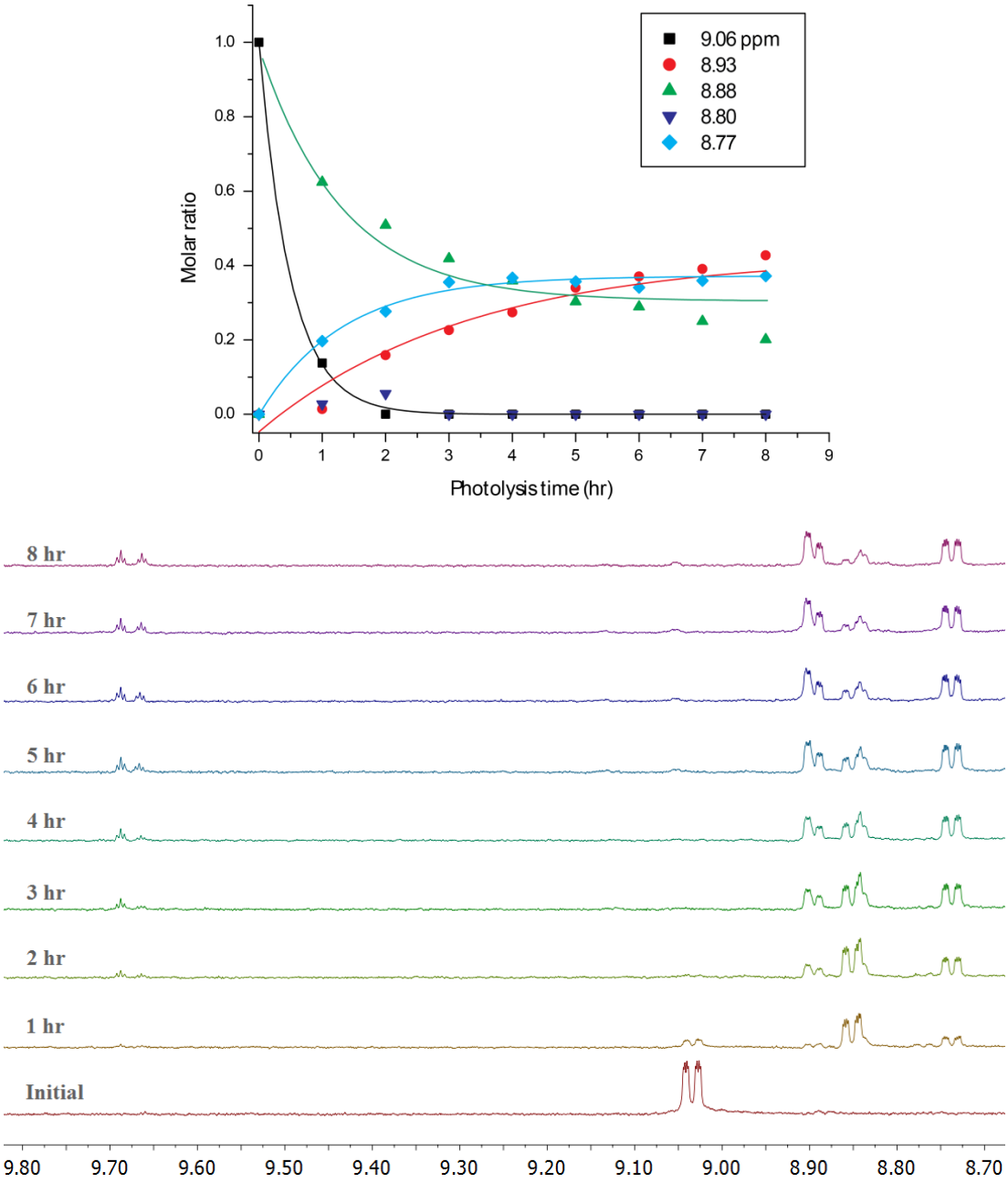

Figure 4.22 Top: Rate of photolysis as molar ratio (derived from peak integration) showing appearance and disappearance of products over time. Bottom: ^{1}H NMR progression of the photolysis of [Re(**PyImPh**)$(CO)_3$(PyNHBu)]$^{+}$ in deuterated acetonitrile solution. The photolysis was performed by irradiating the sample at 365 nm (pen ray lamp) over 8 hours.

The reaction was fairly quick and after 1 hour the initial doublet had already disappeared. The appearance of four new upfield doublet peaks was evident at 8.90, 8.85, 8.77 and 8.74 ppm, which was attributed to the formation of new species. The peak at 8.77 ppm was only present for a short while, and then disappeared completely after 2 hours. Also, the peak at 8.85 ppm appeared to be slowly decreasing in intensity over the duration of the photolysis.

The IR spectrum of the reaction mixture in CD_3CN solution after photolysis was obtained and compared to the IR spectrum of the original spectrum prior photolysis. The two spectra were overlaid and illustrated in **Figure 4.23**. Analysis of the IR spectrum corresponding to the original sample featured carbonyl stretches at 2027, 1932 (shoulder) and 1913 cm^{-1}. Analysis of the IR spectrum of the photolysed sample after 4 hours also displayed three carbonyl stretches at 2033, 1932 and 1858 cm^{-1}. The appearance of the stretching band at 1858 cm^{-1} was consistent with formation of new dicarbonyl species.

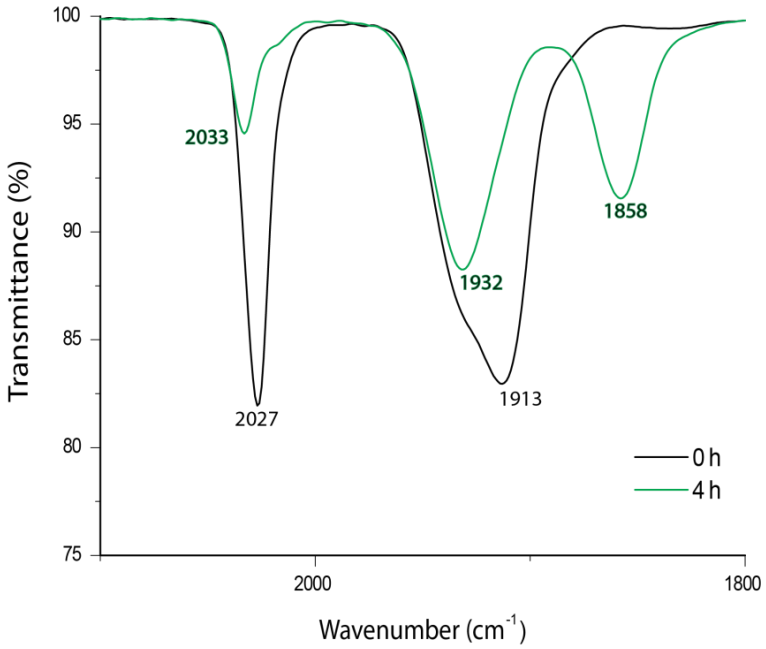

Figure 4.23 IR progression of the photolysis of [Re(**PyImPh**)$(CO)_3$(PyNHBu)]$^+$ in deuterated acetonitrile solution. The photolysis was performed by irradiating the sample at λ_{ex} = 365 nm (pen ray lamp) over a period of 8 hours.

4.7.4 [Re(**PyImPh**)$(CO)_3$(Pyaa)]$^+$

In addition, the pyridyl amino acid complexes were also investigated for their photochemical properties. Analysis by ^{1}H NMR spectroscopy of the photolysed solution of complex [Re(**PyImPh**)$(CO)_3$(Py**Gly**)]$^+$ in acetonitrile illustrated the pyridyl H6′ proton as a doublet at 9.04 ppm, shown in **Figure 4.24**. After 1 hour of irradiation, the initial doublet slowly decreased in intensity and completely disappeared after 3 hours. The appearance of three new upfield doublet peaks was evident at 8.88, 8.76 and 8.68 ppm, which was attributed to the formation of new species. Also, the peak at 9.70 suggested that the imidazolium salt dissociated similarly to previous compounds.

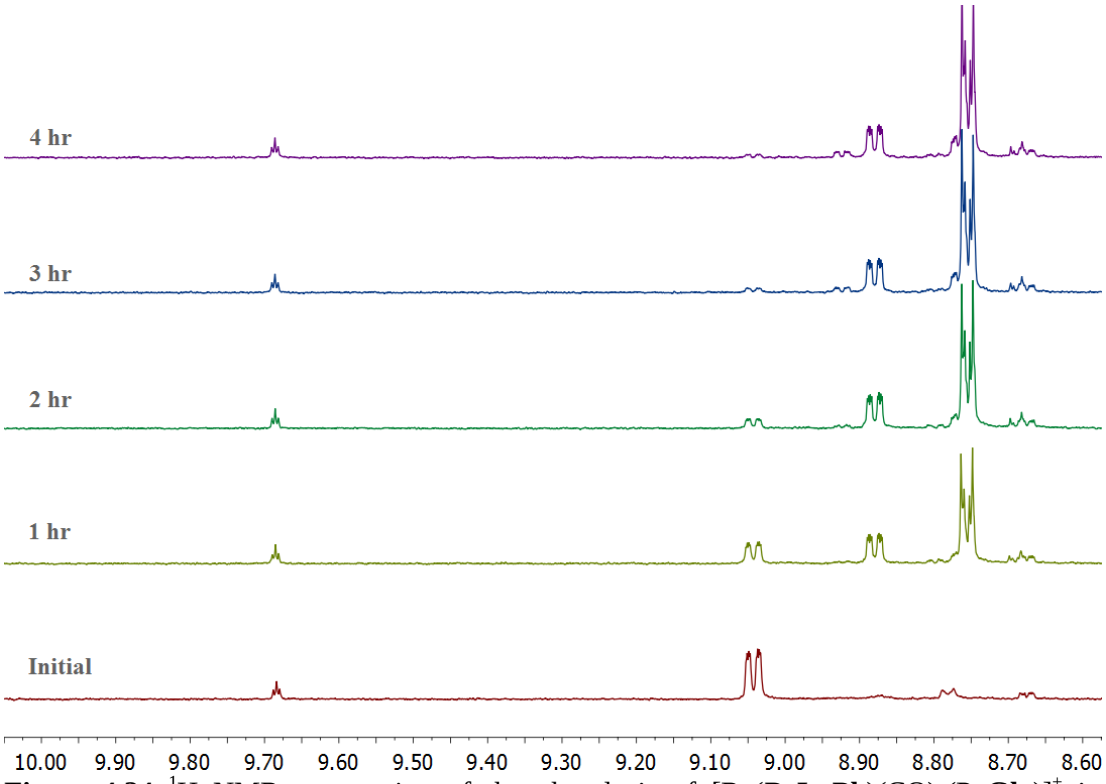

Figure 4.24 ^{1}H NMR progression of the photolysis of [Re(**PyImPh**)(CO)$_3$(Py**Gly**)]$^+$ in deuterated acetonitrile solution. The photolysis was performed by irradiating the sample at 365 nm (pen ray lamp) over a period of 4 hours.

The IR spectrum of the photolysed solution of complex [Re(**PyImPh**)(CO)$_3$(Py**Gly**)]$^+$ in acetonitrile after photolysis (green trace) was obtained and compared to the IR spectrum of the original solution prior to photolysis (black trace). The two spectra were overlaid and illustrated in **Figure 4.25**. Analysis of the IR spectrum corresponding to the original sample featured carbonyl stretches at 2029 (sharp peak) 1934 (shoulder) and 1916 (broad) cm^{-1}. Analysis by IR spectroscopy of the photolysed sample displayed the carbonyl stretches at 1929 and 1857 cm^{-1}. The stretching frequency of the carbonyl band shifted to lower wavenumbers due to an increased electron density on the metal, suggesting the loss of a CO ligand.

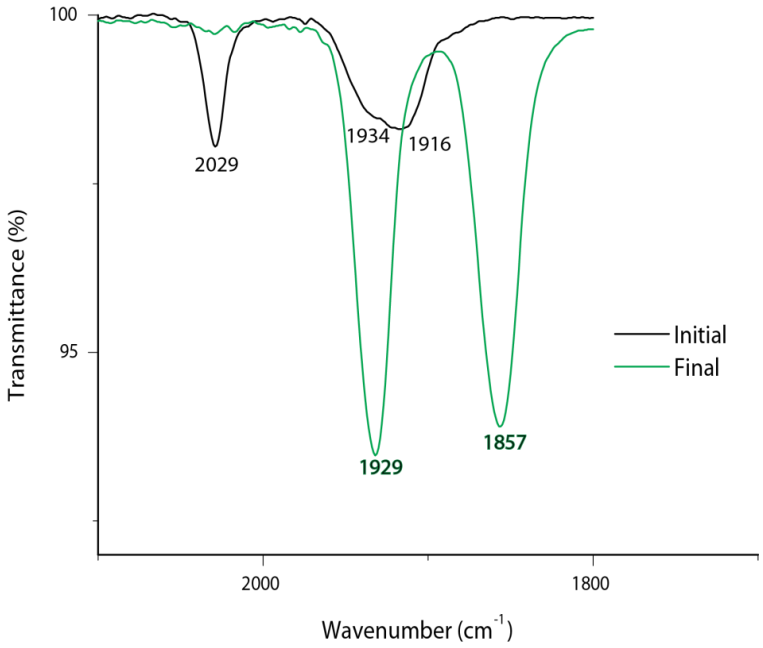

Figure 4.25 IR progression of the photolysis of [Re(**PyImPh**)$(CO)_3$(Py**Gly**)]$^+$ in deuterated CD_3CN solution by irradiating the sample at λ_{ex} = 365 nm over a period of 4 hours.

The emission of the photolysed solution was measured before and after in order to attempt to identify the species which may exist (see **Figure 4.26**). There appeared to be a significant change, where the emission band at 548 nm disappeared and simultaneously a red-shifted emission band at 618 nm appeared with greater intensity. This new band was unfamiliar with respect to previous pyridyl complexes; as the MeCN-solvato complex would have an emission of *ca*. 580 nm as reported previously in literature.

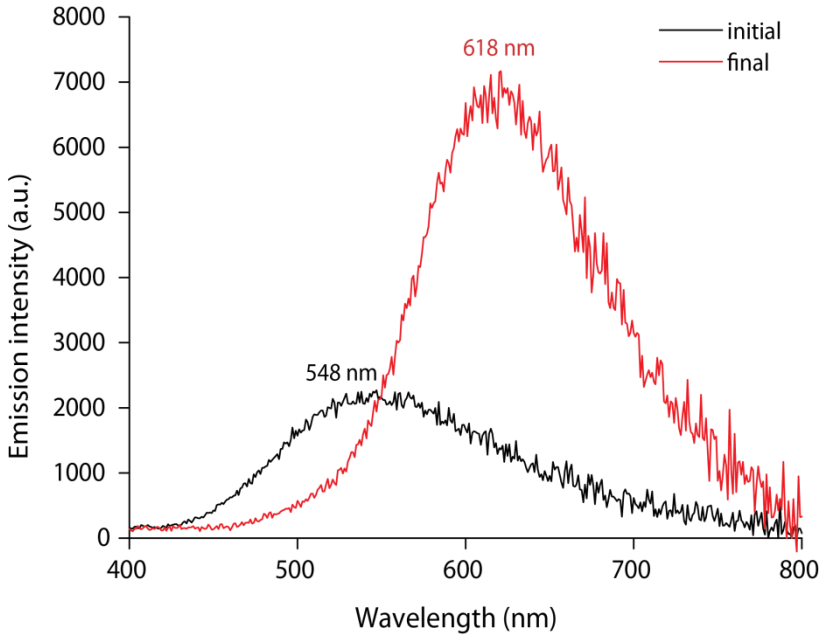

Figure 4.26 Emission scan for [Re(**PyImPh**)(CO)$_3$(Py**Gly**)]$^+$ before (black trace) and after (red trace) photolysis in acetonitrile solution for 4 hours at λ_{ex} = 370 nm.

Photolysis of [Re(**PyImPh**)(CO)$_3$(Py**Trp**)]$^+$ was also investigated to compare whether the presence of tryptophan had any effect on the photochemistry with respect to the glycine analogue. Analysis by ^{1}H NMR spectroscopy of the photolysed solution of complex [Re(**PyImPh**)(CO)$_3$(Py**Trp**)]$^+$ in deuterated acetonitrile was illustrated in **Figure 4.27**. Over the course of the 4 hour irradiation, there seems to be no significant spectral changes in the ^{1}H NMR spectrum. However, careful analysis shows tiny peaks evident at 8.87, 8.70 and 8.15 ppm. Even though it appears that no visible photochemical reaction occurs, it could just be that the rate of reaction is very slow under these conditions. On the other hand, the complex should have reacted similar to the **Gly** analogue as both complexes possess similar structures. It seems that the presence of the tryptophan played a role in slowing the photochemistry. The hypothesised electron transfer from the indole group to the excited rhenium centre may have inhibited the photochemical pathway.

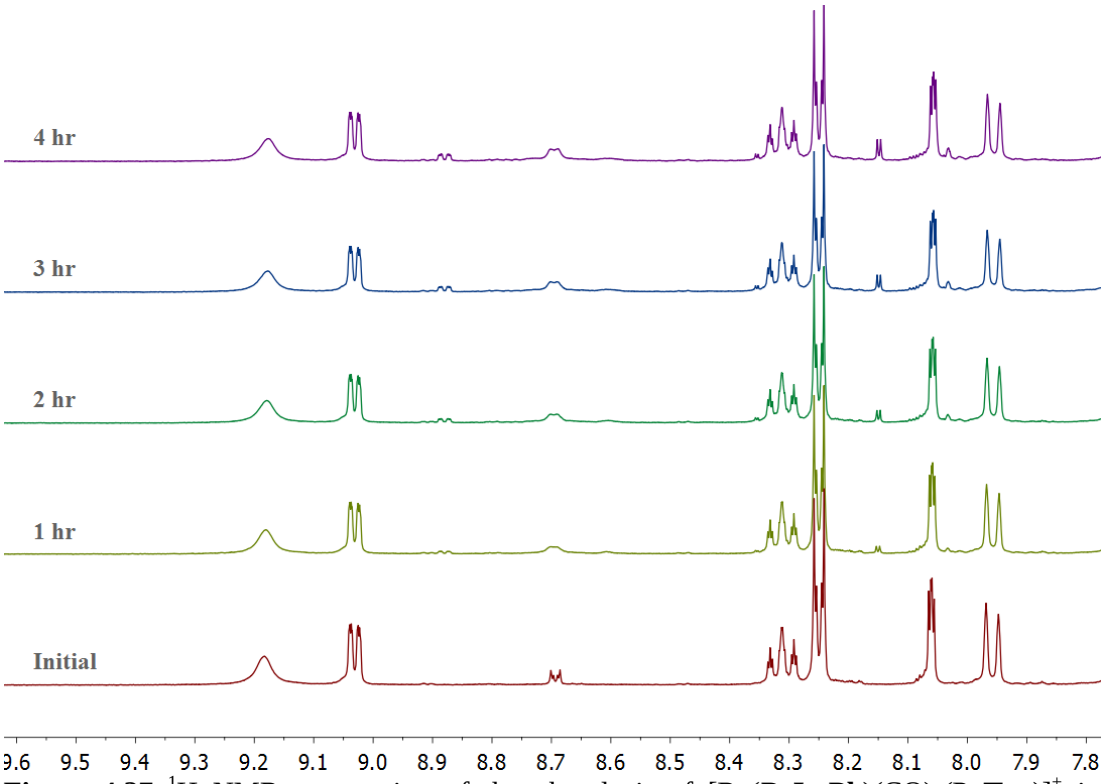

Figure 4.27 ^{1}H NMR progression of the photolysis of [Re(**PyImPh**)$(CO)_3$(Py**Trp**)]$^{+}$ in deuterated acetonitrile solution. The photolysis was performed by irradiating the sample at 365 nm (pen ray lamp) over a period of 4 hours.

In addition, analysis of the CO bands in the IR spectrum (**Figure 4.28**) gave more meaningful information as opposed to the ^{1}H NMR data showing minimal changes. The CO bands in the IR spectrum indicated a photochemical reaction taking place as the change in frequencies indicated a change in electron density on the rhenium. However the rate was very slow compared to the **Gly** analogue. Furthermore, analysis of the emission spectrum indicated that there was starting material (consistent with the NMR spectrum) still present as well as the appearance of a new photoproduct.

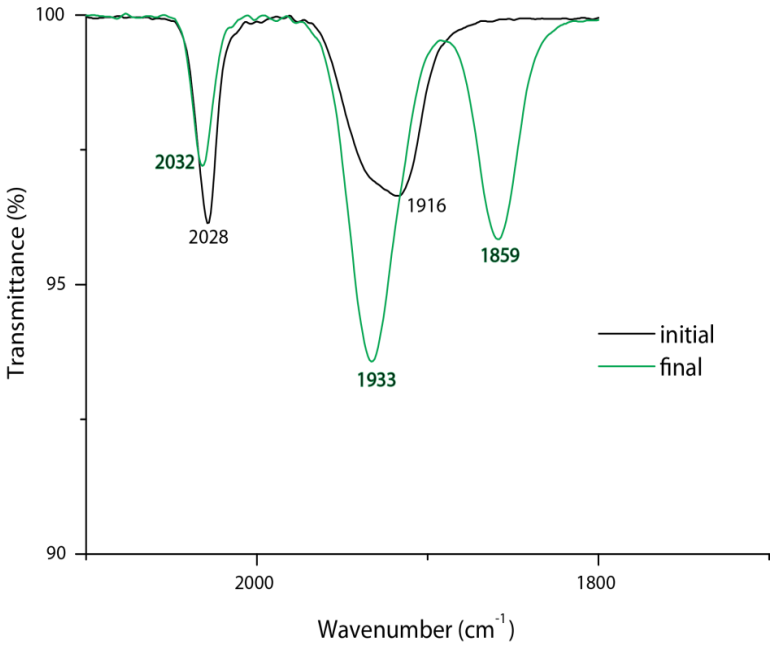

Figure 4.28 IR progression of the photolysis of [Re(**PyImPh**)(CO)$_3$(Py**Trp**)]$^+$ in deuterated acetonitrile solution. The photolysis was performed by irradiating the sample at λ_{ex} = 365 nm (pen ray lamp) over a period of 4 hours.

The emission of the photolysed solution was measured before and after in order to attempt to identify the photoproducts which may exist (see **Figure 4.29**). There appears to be a drastic change; the weakly emissive band at 482 nm seems to split into two new bands at 438 nm and 614 nm. The red-shifted band was also apparent for the **Gly** analogue. However, the band at 438 nm is unknown and unique as it does not appear in the photolysis for other complexes. It was assumed to be the Py**Trp** ligand detaching upon photolysis, however this can be ruled out as the emission lies at 330 nm. A review of the literature was undertaken to interpret this band, focussing on photodegradation and isomerisation of the tryptophan and its derivatives. All reports showed a fluorescence band of **Trp** to appear at 300-350 nm.[199–202] This eliminates **Trp** to be a possible photoproduct. This strange peak at 430 nm could be attributed to the dissociation of the carbene ligand, which was also present in the ^{1}H NMR spectrum as a tiny peak around 9.70 ppm. It is unknown why the peak at 430 nm is only present for this complex, when other complexes also show dissociation of the carbene ligand. Nevertheless, it could be a result of a unique property found on the indole of the tryptophan. Further investigation is needed using alternative techniques such as TRIR, similar to those reported by Vlcek on tryptophan oxidation.[174]

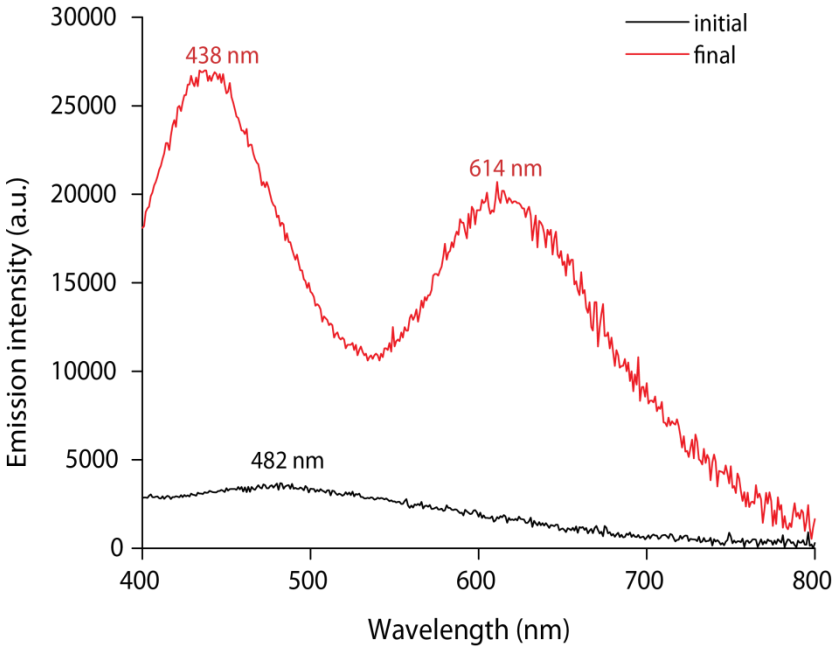

Figure 4.29 Emission scan for [Re(**PyImPh**)$(CO)_3$(Py**Trp**)]$^+$ before (black trace) and after (red trace) photolysis in acetonitrile solution for 4 hours at λ_{ex} = 370 nm.

4.8 Conclusion

A series of cationic rhenium(I)-NHC tricarbonyl complexes appended to substituted pyridines were investigated in terms of their photophysical and photochemical properties. Rhenium(I)-**phen** complexes with the same pyridyl ligands were synthesised as a reference. The collective findings have shown that the photophysical properties of the complexes in dichloromethane displayed absorption around 325-345 nm and ^{3}MLCT emission at 480-490 nm range, which was very blue shifted compared to their diimine analogues. On the other hand, the photophysics of the complexes when measured in acetronitrile displayed more of a blue shifted emission, which illustrates the solvatochromism that exists within these complexes. Also the excited state lifetime decay were found to be very short in the 3-10 ns range. This could be accounted for the photoactive component in the coordinating solvent.

The photophysical properties of all newly synthesised cationic rhenium(I)-NHC compounds were investigated and they were found to possess similar properties to other reported rhenium(I)-NHC compounds. Modifications to the pyridyl ancillary ligand had a significant effect to the photophysical output, due to the variation of MO

energies. This was especially prominent for the DMAP containing complexes, which displayed longer lifetimes and higher quantum yields.

The photochemical activity of all reported rhenium(I)-NHC tricarbonyl compounds was assessed using fundamental spectroscopic techniques such as IR and ^{1}H NMR spectroscopy. The rhenium(I)-NHC complexes in acetonitrile solutions were found to be stable in the dark. Only when excited at the MLCT manifold (365 nm), were the complexes perceived to undergo photochemical changes. The detected changes were characterised as photochemical ligand substitution reactions, which resulted in the formation of new photoproducts. The PLS reaction mechanism was proposed to follow a similar pathway to Vaughan, which assisted in identifying the species. One of the photoproducts was confirmed to be the acetonitrile solvato species [Re(**PyImPh**)$(CO)_3(CH_3CN)]^+$ as an intermediate and the others were proposed to be dicarbonyl species. There was no crystallography characterisation that would be able to confirm the structure of the complex. However the conclusions were based on previously published reports of similar compounds. Further analysis would need to be carried out to assess the photoproducts of [Re(**PyImPh**)$(CO)_3$(Pyaa)]$^+$ complexes.

In the paper published by Blanco Rodriguez *et al*., the authors attributed the tryptophan group to undergo a photooxidation process; this electron transfer mechanism was evident by the quenched emission intensity and reduced lifetime when compared to the reference species. In the case of rhenium(I)-NHC systems, the photophysical properties are significantly different when comparing the **Trp** and **Gly** analogues. Evidence shows the **Trp** analogue to display a weaker emission and lower lifetime decay than **Gly**. Also, the rate of electron transfer (in aerated acetonitrile) for [Re(**PyImPh**)$(CO)_3$(Pyaa)]$^+$ complexes was calculated to be 6.4×10^8 s^{-1} which is much longer than [Re(**phen**)$(CO)_3$(Pyaa)]$^+$ complexes reported by Blanco Rodriguez *et al*. with a rate of 3.3×10^7 s^{-1}. Hence, it can be concluded that this phenomenon follows an electron transfer mechanism.

4.9 Experimental

4.9.1 General Comments

Refer to general procedures as outlined in Chapter 2, section 2.8.1, unless stated otherwise. For compounds **25** and **28**, it was not possible to obtain reproducible elemental analyses.

4.9.2 Photolysis Experiments

Monitored photolysis experiments were carried out using a Hitachi F-7000 spectrofluorimeter. The compound was measured in a dilute acetonitrile solution (*ca.* 10^{-5} M) placed in a quartz cuvette. The solutions were irradiated at λ_{ex} = 370 nm with slit widths set to 20 nm (excitation) and 5 nm (emission). A total of 99 consecutive scans, with no delay between replicates, were run per solution at a speed of 240 nm min^{-1} with the detector set to acquire a signal between 400 and 800 nm. Under these experimental conditions, the solution was constantly irradiated for a period of approximately 4 hours. The emission spectra were recorded uncorrected for the detector response.

Lamp photolysis experiments were carried out using a UVP Blak-Ray B-100AP High Intensity UV lamp with a 100 W bulb at a single wavelength output of 365 nm. The experiments were performed in the darkness, where the apparatus was covered in foil. The reaction vessel consisted of either a glass NMR tube, containing a deuterated solution of the complex, or a quartz cuvette with a magnetic stirrer; both positioned 3 cm away from the lamp.

Other lamp photolysis (high intensity) were carried out using Rofin Forensic Polilight PL500 with a 500 W xenon arc lamp set at UV wavelength output of 350 nm. The experiments were performed in darkness, where the apparatus was covered in black bin liners. The reaction vessel consisted of a glass NMR tube positioned 1 cm away from the lamp.

For monitored photolysis using ^{1}H NMR spectroscopy, an initial spectrum of the freshly dissolved sample in the deuterated solvent was collected. The NMR tube was then clamped (positioned 3 cm away from the light source) and after 1 hour of

continuous photolysis, the lamp was switched off and a second ^{1}H NMR spectrum was collected. Subsequently, the NMR solution was re-positioned in front of the lamp and photolysed further. This was repeated every hour and until no more changes in the spectrum was observed. Generally, the sample was photolysed for a total of 8 hours.

At the end of the photolysis, an IR spectrum was collected by drop-casting the solution onto the diamond stage of the Perkin-Elmer 100 FT-IR spectrometer. The drop of solution was allowed to evaporate before repeating the drop-casting procedure, until the sample was concentrated enough to visualise the carbonyl bands. The IR spectrum of the photolysed sample was overlaid with the IR spectrum of the same complex prior to photolysis.

4.9.3 Synthesis

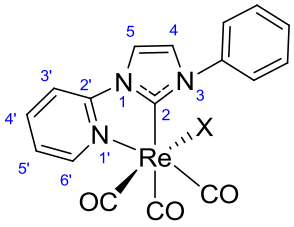

Figure 4.30 NMR referencing layout for rhenium(I)-NHC complexes.

_N_-(pyridin-3-ylmethyl)butan-1-amine (PyNHBu)

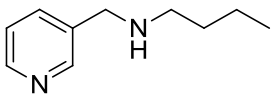

N-butylamine (225 µL, 2.3 mmol) and 3-pyridine-carboxaldehyde (200 µL, 2.1 mmol) were dissolved in 1,2-dichloroethane (*ca.* 25 mL) and $MgSO_4$ (337 mg) added to the clear solution. The mixture was heated at reflux under N_2 for 6 hr with stirring. After cooling down at room temperature, the orange solution was filtered to remove the $MgSO_4$ and then concentrated under reduced pressure to afford orange oil. This was dissolved in methanol (*ca.* 3 mL) and whilst stirring, sodium borohydride (60 mg, 1.58 mmol) was added until it ceased to effervesce. The solution resulted in a dark yellow colour. The solution was stirred for a further 2 hr. After this, an aqueous HCl solution (40 mL, 50%) was added until the solution turned pH 2, and then

NaOH solution (10 mL, 2 M) was added until the solution turned pH 10. The product was extracted with DCM (3 × 20 mL), dried over $MgSO_4$, and concentrated under reduced pressure to yield light orange oil (400 mg, 86%). ^{1}H NMR (δ, ppm, $CDCl_3$): 8.54 (1H, s, pyridyl **CH**), 8.48 (1H, broad s, pyridyl **CH**), 7.66 (1H, d, *J* = 8.0 Hz, pyridyl **CH**), 7.26-7.22 (1H, m, pyridyl **CH**), 3.78 (2H, s, **CH$_2$**NHBu), 2.61 (2H, t, *J* = 7.2 Hz, **CH$_2$**$CH_2CH_2CH_3$), 1.62 (1H, broad s, **NH**), 1.53-1.41 (2H, m, CH_2**CH$_2$**CH_2CH_3), 1.39-1.29 (2H, m, CH_2CH_2**CH$_2$**CH_3), 0.89 (3H, t, *J* = 7.6 Hz, $CH_2CH_2CH_2$**CH$_3$**). ^{13}C NMR (δ, ppm, $CDCl_3$): 149.8, 148.5, 135.9, 135.8, 123.5, 53.5, 51.5, 32.3, 20.5, 14.1. Spectroscopic data are in agreement to those already reported in literature.[193]

4.9.3.1 General Methodology for Synthesis of Amino Acid Substituted Pyridine Ligands (Pyaa)

Isonicotinic acid chloride hydrochloride was prepared by suspension of isonicotinic acid in thionyl chloride at reflux for 1 hour. Isonicotinic acid chloride hydrochloride (1.0 eq.) was then suspended in DCM (*ca.* 30 mL) and TEA (*ca.* 2 mL) was added until most solid dissolved. The amino acid methyl ester hydrochloride (1.14 eq.) was added and the solution turned blood orange. The reaction mixture was left to stir at room temperature for 20 min. The precipitate (Et_3N·HCl) was filtered and the DCM filtrate washed with water (4 × 50 mL). The organic extract was dried ($MgSO_4$), filtered and concentrated under reduced pressure to afford the desired ligands characterised below.

PyTrp (29)

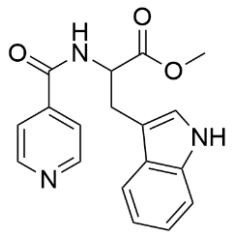

Golden-yellow crystalline solid. Yield: 1.13 g (92%); m.p. 73-75 °C.

^{1}H NMR (δ, ppm, $CDCl_3$): 8.88 (1H, broad s, indole **NH**), 8.56 (2H, d, *J* = 5.6 Hz, pyridyl **CH**), 7.50 (1H, d, *J* = 8.0 Hz, indole **CH**), 7.43 (2H, d, *J* = 6.0 Hz, pyridyl **CH**), 7.30 (1H, d, *J* = 8.0 Hz, indole **CH**), 7.14 (1H, t, *J* = 8.0 Hz, indole **CH**), 7.07-

6.99 (2H, m, indole **CH**), 6.96 (1H, s, **NH**), 5.12-5.08 (1H, m, **CH**), 3.72 (3H, s, **CH_3**), 3.48-3.47 (2H, m, **CH_2**). ^{13}C NMR (δ, ppm, $CDCl_3$): 172.1 (**C**=O ester), 165.2 (**C**=O amide), 150.3, 140.9, 136.3, 127.6, 123.0, 122.3, 121.0, 119.7, 118.4, 111.6, 109.4, 53.8, 52.6, 45.8, 27.4, 8.50 ppm. ν_{max} (ATR-FTIR, DCM solution)/cm^{-1}: 3312 broad w, 3053 w, 1740 s (C=O ester), 1658 s (C=O amide), 1519 m, 1265 m, 730 s. Already reported in literature.[172]

PyPhe (30)

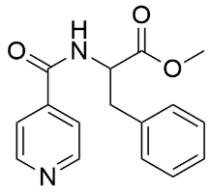

Yellow oil. Yield: 569 mg (51%).

^{1}H NMR (δ, ppm, $CDCl_3$): δ 8.76 (2H, d, *J* = 4.8 Hz, pyridyl **CH**), 7.65 (2H, d, *J* = 4.8 Hz, pyridyl **CH**), 7.33-7.24 (3H, m, phenyl **CH**), 7.12 (2H, d, *J* = 8.0 Hz, phenyl **CH**), 6.74 (1H, s, **NH**), 5.09-5.05 (1H, m, **CH**), 3.81 (3H, s, **CH_3**), 3.34-3.22 (2H, m, **CH_2**). Already reported in literature.[172]

PyGly (31)

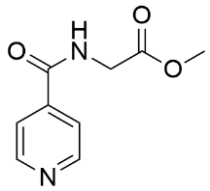

Beige-cream crystalline solid. Yield: 298 mg (17%); m.p. 106-108 °C.

^{1}H NMR (δ, ppm, $CDCl_3$): 8.77 (2H, d, *J* = 6.1 Hz, pyridyl **CH**), 7.65 (2H, d, *J* = 6.1 Hz, pyridyl **CH**), 6.75 (1H, s, **NH**), 4.26 (2H, d, *J* = 5.0 Hz, **CH_2**), 3.82 (3H, s, **CH_3**). ^{13}C NMR (δ, ppm, $CDCl_3$): 170.3 (**C**=O ester), 165.7 (**C**=O amide), 150.8 (pyridyl **C**H), 140.9 (pyridyl quat. **C**), 121.1 (pyridyl **C**H), 52.9 (**C**H_3), 41.9 (**C**H_2). ν_{max} (ATR-FTIR, solid)/cm^{-1}: 3267 s/br, 3081 w, 2956 w, 1744 s (ester C=O), 1651 s (amide C=O), 1547 s, 1490 w, 1429 m, 1405 m, 1365 m, 1327 m, 1206 m, 1171 m, 1011 w, 853 w, 760 w.

4.9.3.2 General Methodology for the Synthesis of Rhenium(I)-NHC Complexes

[Re(**PyImPh**)$(CO)_3$X] (1.0 eq) was added to AgOTf (1.1 eq) in the solvent of choice. The corresponding pyridine-type ligand (1.0 eq) was added to the mixture and heated at reflux under nitrogen, whilst stirring in darkness for duration of time. The resulting AgX precipitate was filtered off and the resulting filtrate was concentrated under reduced pressure to afford product. This was dissolved in MeOH and then saturated solution of KPF_6 was added to afford precipitate.

Some complexes required further purification by re-precipitation or column chromatography.

***fac*-[Re(PyImPh)(Py)]PF_6 (23)**

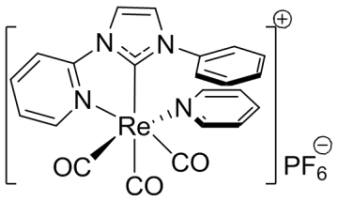

Followed procedure described in section 4.9.3.2, using pyridine (*ca.* 3 mL) as solvent. Re-precipitation by diethyl ether of compound in dichloromethane afforded beige-yellow powder (62 mg, 86%); m.p. 210-213 °C; ν_{max} (ATR-FTIR, solid)/cm^{-1}: 3124 w, 2022 s (CO, A′(1)), 1926 sh (CO, A′(2)), 1909 s (CO, A″), 1617 m, 1486 m, 1258 m, 1029 m, 758 w, 695 w. ^{1}H NMR (δ, ppm, acetone-d_6): 9.27 (1H, d, *J* = 5.6 Hz, pyridyl C**H**), 8.59 (1H, app. s, imidazoyl C**H**), 8.49-8.38 (4H, m, 4 × pyridyl C**H**), 7.99 (1H, app. t, *J* = 8.0 Hz, pyridine solvate), 7.96 (1H, app. s, imidazoyl C**H**), 7.83-7.71 (6H, m, 5 × phenyl C**H** and pyridyl C**H**), 7.48 (2H, app. t, *J* = 4.0 Hz, pyridine solvate). ^{13}C NMR (δ, ppm, acetone-d_6): 197.7 (**C**O), 195.8 (**C**O), 191.9 (**C**O), 191.3 (N**C**N), 155.0 (pyridyl **C**H), 154.8 (pyridyl **C**H), 154.7 (pyridyl quat. **C**), 144.4 (imidazoyl **C**H), 140.4 (phenyl **C**H), 140.1 (pyridine solvate **C**H), 131.2 (phenyl **C**H), 127.8 (pyridine solvate **C**H), 127.4 (phenyl quat. **C**), 127.0 (pyridine solvate **C**H), 126.4 (phenyl **C**H), 119.6 (pyridyl **C**H), 114.9 (pyridyl **C**H). Elemental Analysis: Calc for $C_{23}H_{16}N_4O_6F_3SRe$·*0.2H_2O 0.5DCM*: C (36.86%), H (2.29%), N (7.32%); found: C (36.97%), H (1.85%), N (7.38%).

***fac*-[Re(PyImPh)(DMAP)]PF_6 (24)**

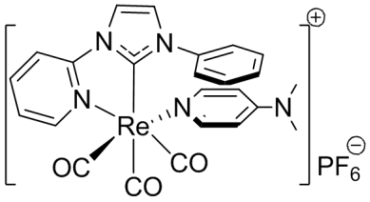

Followed procedure described in section 4.9.3.2, using toluene (*ca.* 6 mL) as solvent. Light golden yellow powder (65 mg, 71%); m.p. 248 °C (dec.); ν_{max} (ATR-FTIR, acetone solution)/cm^{-1}: 2925 w, 2016 s (CO, A′(1)), 1916 sh (CO, A′(2)), 1905 s (CO, A″), 1701 w, 1625 w, 1487 w, 840 s. ^{1}H NMR (δ, ppm, acetone-d_6): 9.23 (1H, d, *J* = 6.4 Hz, pyridyl C**H**), 8.58 (1H, s, imidazolyl C**H**), 8.48 (1H, t, *J* = 7.6 Hz, pyridyl C**H**), 8.38 (1H, d, *J* = 7.6 Hz, pyridyl C**H**), 7.98 (1H, s, imidazolyl C**H**), 7.81-7.71 (8H, m, 5 × phenyl C**H** and 2 × **DMAP**), 6.52 (2H, d, *J* = 6.8 Hz, **DMAP**), 3.01 (6H, s, N(C**H**$_3$)$_2$); ^{13}C NMR (δ, ppm, acetone-d_6): 197.6 (**C**O), 196.1 (**C**O), 192.2 (**C**O), 190.9 (N**C**N), 155.7, 154.8, 154.5 (pyridyl **C**H), 153.9 (pyridyl quat. **C**), 152.7 (phenyl **C**H), 149.5 (pyridyl **C**H), 143.9 (pyridyl **C**H), 139.4 (quat. **C**), 130.7 (phenyl **C**H), 126.9 (phenyl **C**H), 126.6 (phenyl quat. **C**), 125.9 (imidazolyl **C**H), 119.5 (imidazolyl **C**H), 114.5 (pyridyl **C**H), 108.9 (phenyl **C**H), 107.6 (DMAP quat. **C**), 39.1 (**C**H_3), 38.9 (**C**H_3). Elemental Analysis: Calc for $C_{24}H_{21}N_5O_3F_6PRe$·*0.2acetone*; C (38.36%), H (2.91%), N (9.09%); found: C (38.83%), H (2.31%), N (9.03%).

***fac*-[Re(PyImPh)(PyNHBu)]PF_6 (25)**

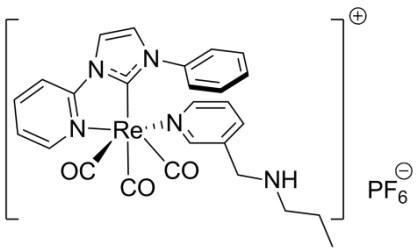

Followed procedure described in section 4.9.3.2, using toluene (*ca.* 4 mL) as solvent. Orange solid (24 mg, 50%). ν_{max} (ATR-FTIR, solid)/cm^{-1}): 2930 w, 2027 s, 1951 m, 1926 s, 1617 w, 1487 w, 822 s. ^{1}H NMR (δ, ppm, acetone-d_6): 9.21 (1H, d, *J* = 8.0 Hz, pyridyl C**H**), 8.45 (1H, s, imidazoyl C**H**), 8.25 (2H, t, *J* = 8.0 Hz, 2 × pyridyl C**H**), 8.24 (2H, d, *J* = 8.0 Hz, 2 × pyridyl C**H**), 7.98-7.87 (2H, m, pyridyl C**H**), 7.86 (1H, s, imidazoyl C**H**), 7.78 (2H, m, 2 × pyridyl C**H**), 7.79-7.72 (5H, m, 5 × phenyl C**H**), 7.41 (1H, app. t, *J* = 8.0 Hz, pyridyl C**H**), 2.59 (2H, t, *J* = 8.0 Hz,

C**H**$_2$CH$_2$CH$_2$CH$_3$), 1.46 (2H, m, CH$_2$C**H**$_2$CH$_2$CH$_3$), 1.26 (2H, m, CH$_2$CH$_2$C**H**$_2$CH$_3$), 0.83 (3H, t, *J* = 8.0 Hz, CH$_2$CH$_2$CH$_2$C**H**$_3$). ^{13}C NMR (δ, ppm, acetone-d$_6$): 197.7 (**C**O), 195.8 (N**C**N), 192.0 (**C**O), 191.5 (**C**O), 154.9 (pyridyl **C**H), 154.6 (pyridyl **C**H), 154.5 (aminopyridyl **C**H), 144.3 (pyridyl **C**H), 139.8 (pyridyl **C**H), 131.1 (phenyl **C**H), 127.2 (pyridyl **C**H), 126.9 (imidazoyl **C**H), 126.4 (phenyl **C**H), 119.4 (imidazoyl **C**H), 114.7 (pyridyl **C**H), 50.9 (py**C**H$_2$NH-Bu), 49.6 (**C**H$_2$CH$_2$CH$_2$CH$_3$), 32.8 (CH$_2$**C**H$_2$CH$_2$CH$_3$), 21.0 (CH$_2$CH$_2$**C**H$_2$CH$_3$), 14.3 (CH$_2$CH$_2$CH$_2$**C**H$_3$).

***fac*-[Re(PyImPh)(PyTrp)]PF$_6$ (32)**

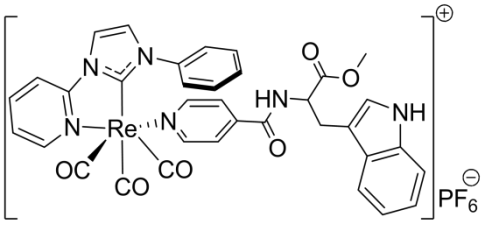

Followed procedure described in section 4.9.3.2, using methanol (*ca.* 4 mL) as solvent to afford bright yellow solid (16 mg, 30%). ν_{max} (ATR-FTIR, solid)/cm^{-1}: 2031 s (CO, A′(1)), 1935 s (CO, A′(2)), 1927 s (CO, A″). ^{1}H NMR (δ, ppm, acetone-d$_6$): 10.06 (1H, s, **NH** indole), 9.27 (1H, d, *J* = 8.0 Hz, pyridyl **CH**), 8.54-8.46 (4H, m, imidazolyl **CH**), 8.34 (1H, d, *J* = 8.0 Hz, pyridyl **CH**), 8.23 (1H, d, *J* = 12 Hz, pyridyl C**H**), 7.96 (1H, s, imidazolyl **CH**), 7.83-7.70 (8H, m, 4 × pyridyl **CH,** 4 × phenyl **CH**), 7.53 (1H, d, pyridyl **CH**), 7.38-7.35 (1H, m, indole C**H**), 7.21 (1H, s, C**H**), 7.11-7.05 (1H, m, indole C**H**), 6.99-6.94 (1H, m, indole C**H**), 4.92-4.89 (1H, m, indole C**H**), 3.67 (3H, split s, OC**H**$_3$), 3.41-3.26 (2H, m, C**H**$_2$). ^{13}C NMR (δ, ppm, acetone-d$_6$): 197.4 (**C**O), 195.6 (N**C**N), 191.9 (**C**O), 191.0 (**C**O), 172.4, 170.9 (**C**=O ester), 164.1 (**C**=O amide), 155.5, 155.1 (pyridyl **C**H), 154.7 (pyridyl **C**H), 144.3 (imidazolyl **C**H), 140.0 (phenyl **C**H), 137.6, 131.3, 131.2 (phenyl **C**H), 127.4 (phenyl **C**H), 126.9, 126.4, 125.3 (imidazolyl **C**H), 122.3, 119.7, 119.6 (pyridyl **C**H), 119.00, 114.9 (pyridyl **C**H), 112.3, 110.7, 60.5, 54.9, 52.5 (O**C**H$_3$). ESI-MS calculated for ReC$_{35}$H$_{28}$O$_6$N$_6$ ([M]$^+$): 814.57, observed: 815.16 ([M + H]$^+$). Elemental Analysis: Calc for C$_{35}$H$_{28}$N$_6$O$_6$RePF$_6$; C (43.78%), H (2.90%), N (8.75%); found C (44.32%), H (2.79%), N (8.74%).

***fac*-[Re(PyImPh)(PyGly)]PF_6 (34)**

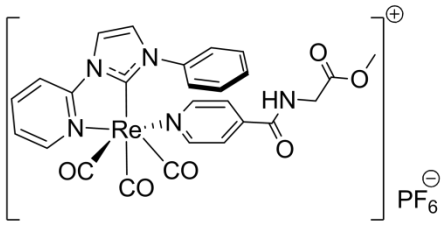

Followed procedure described in section 4.9.3.2, using methanol (*ca.* 4 mL) as solvent to afford bright yellow powder (12 mg, 25%).

^{1}H NMR (δ, ppm, acetone-d_6): 9.28 (1H, d, *J* = 8.0 Hz, pyridyl C**H**), 8.74 (1H, broad s, imidazolyl C**H**), 8.58-8.54 (3H, m, pyridyl C**H**), 8.47 (1H, t, *J* = 8.0 Hz, phenyl C**H**), 8.35 (1H, d, *J* = 4.0 Hz, pyridyl **C**H), 7.97 (1H, s, imidazolyl C**H**), 7.86-7.73 (4H, m, phenyl C**H**), 7.79-7.72 (4H, m, pyridyl C**H**), 4.08 (2H, d, *J* = 8.0 Hz, C$\mathbf{H}_2$), 3.66 (3H, s, OC$\mathbf{H}_3$). ^{13}C NMR (δ, ppm, acetone-d_6): 197.5 (**C**O), 195.6 (**C**O), 191.9 (N**C**N), 191.0 (**C**O), 170.3 (**C**=O ester), 164.5 (**C**=O amide), 155.7 (pyridyl **C**H), 155.1 (pyridyl quat. **C**), 144.4 (pyridyl C**H**), 140.1, 131.3 (pyridyl C**H**), 131.2, 127.5, 127, 126.4 (imidazolyl C**H**), 125.3, 119.6 (imidazolyl **C**H), 114.9, 52.3 (O**C**H_3), 42.0. ν_{max} (ATR-FTIR, solid)/cm^{-1}: 2022 s (CO, A′(1)), 1913 s (CO, A′(2)), 1902 s (CO, A″). Elemental Analysis: Calc for $C_{26}H_{21}N_5O_6F_6PRe\cdot 0.2H_2O$; C (37.59%), H (2.54%), N (8.43%); found: C (37.06%), H (2.25%), N (8.34%).

4.9.3.3 General Methodology for Synthesis of Rhenium(I)-Diimine Complexes

***fac*-[Re(phen)$(CO)_3$(Py)]PF_6 (26)**

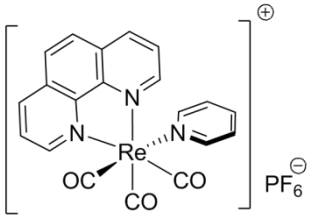

fac-[Re(**phen**)$(CO)_3$Br] (28 mg, 0.05 mmol) was added to AgOTf (21 mg, 0.08 mmol) in pyridine (*ca.* 4 mL) under nitrogen. This was heated at reflux whilst stirring in darkness overnight. After the reaction cooled down at room temperature, the yellow solution was concentrated in vacuo to afford yellow residue. DCM was added and the grey precipitate filtered *via* celite. The resulting bright yellow filtrate was reduced to <1 mL and diethyl ether added to precipitate bright yellow crystals.

These were dissolved in MeOH and precipitated with sat. KPF_6 solution to afford the product as a pale yellow solid (14 mg, 53%).

ν_{max} (ATR-FTIR)/cm^{-1} (solid state): 2026 (CO, A′(1)), 1922 (CO, A′(2)), 1902 (CO, A″), 1631, 1607, 1585, 1521, 1448, 1429 w, 1359, 1220, 1149, 1220, 832 m, 763, 699 w. ^{1}H NMR (δ, ppm, $CDCl_3$): 9.51 (2H, d, *J* = 8.0 Hz, **phen**), 8.79 (2H, d, *J* = 7.6 Hz, pyridine solvate), 8.19-8.12 (6H, m, **phen**), 7.71 (1H, t, *J* = 6.8 Hz, pyridine solvate), 7.31 (2H, t, *J* = 6.8 Hz, pyridine solvate) ppm. ^{13}C NMR (δ, ppm, acetone-d_6): 155.8 (phen **C**), 153.1, 147.5 (quat. **C**), 141.5, 141.0, 132.3 (quat. **C**), 129.2, 128.4, 127.7 (pyr **C**). Previously reported in literature.[182,203]

***fac*-[Re(phen)(CO)$_3$(DMAP)]PF$_6$ (27)**

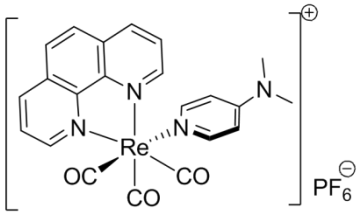

fac-[Re(**phen**)$(CO)_3$Cl] (100 mg, 0.21 mmol) and 4-dimethylaminopyridine (153 mg, 1.23 mmol) were added to AgOTf (80 mg, 0.31 mmol) in DCM (20 mL). This mixture was heated at reflux under N_2 overnight. After cooling down to room temperature, the silver salt in the mixture was filtered *via* celite and washed with DCM. The organic extract was concentrated under reduced pressure and the crude residue purified *via* chromatography (deactivated neutral alumina, Brockmann III) using EtOAc/DCM (50:50) to elute starting [Re(**phen**)$(CO)_3$Cl] and DCM/MeOH (98:2) to elute product as yellow residue (18 mg, 15%).

ν_{max} (ATR-FTIR)/cm^{-1} (MeCN solution): 2027 (CO, A′(1)), 1910 (CO, A′(2)/A″). ^{1}H NMR (δ, ppm, acetone-d_6): δ 9.86 (2H, d, *J* = 5.1 Hz, **phen**), 9.10 (2H, d, *J* = 8.3 Hz, **phen**), 8.38 (2H, s, **phen**), 8.36-8.32 (2H, m, **phen**), 7.86 (2H, d, *J* = 7.4 Hz, **DMAP**), 6.38 (2H, d, *J* = 7.4 Hz, **DMAP**), 2.91 (6H, s, N(C**H$_3$**)$_2$). ^{13}C NMR (δ, ppm, acetone-d_6): 154.8, 154.6, 150.2, 146.4, 140.4, 131.3, 128.3, 127.3, 108.0, 38.2. Spectroscopic data is agreeable to that already reported in literature (although measured in different solvent).[204]

***fac*-[Re(phen)(CO)$_3$(PyNHBu)]PF$_6$ (28)**

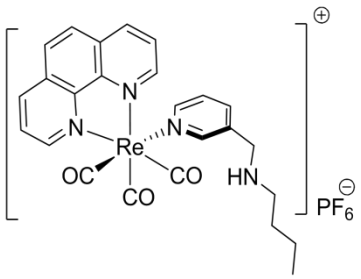

fac-[Re(**phen**)(CO)$_3$Br] (32 mg, 0.06 mmol) and *N*-(pyridine-3-ylmethyl)butan-1-amine (10 µL) was added to AgOTf (21 mg, 0.08 mmol) in toluene (*ca*. 4 mL). This was heated to reflux under N_2, whilst stirring in darkness (covered in foil) for 3 hr. After the mixture cooled down at room temperature, the yellow solution was washed with water and extracted with DCM. It was then re-precipitated with hexanes. The crude product was dissolved in MeOH and a saturated solution of KPF_6 added to yield orange powder (20 mg, 44%), which was collected by vacuum filtration.

ν_{max} (ATR-FTIR)/cm^{-1} (MeCN solution): 2033 (CO, A′(1)), 1919 (CO, A′(2)/A″). ^{1}H NMR (δ, ppm, acetone-d$_6$): 9.90 (2H, d, *J* = 4.0 Hz, **phen**), 9.10 (2H, d, *J* = 4.0 Hz, **phen**), 8.77 (1H, broad s, N**H**), 8.53 (1H, d, *J* = 8.0 Hz, pyridyl C**H**), 8.36 (2H, s, **phen**), 8.35-8.33 (2H, m, **phen**), 8.01 (1H, d, *J* = 8.0, pyridyl C**H**), 7.40-7.36 (1H, m, pyridyl C**H**), 2.79 (2H, t, *J* = 8.0 Hz, **CH$_2$**CH$_2$CH$_2$CH$_3$), 1.55-1.47 (2H, m, CH$_2$**CH$_2$**CH$_2$CH$_3$), 1.34-1.25 (2H, m, CH$_2$CH$_2$**CH$_2$**CH$_3$), 0.91 (3H, t, *J* = 8.0 Hz, CH$_2$CH$_2$CH$_2$**CH$_3$**). A satisfactory ^{13}C NMR spectrum could not be obtained due to the low concentration of the solution.

Chapter 5

Rhenium(I)-NHC Complexes with Varying Chelating Ligands

5.1 Overview

In the previous chapters, manipulation of the ancillary ligand on the rhenium carbene and rhenium diimine complexes had shown minimal changes on the photophysical properties. In this investigation, attention will be focused towards manipulating the NHC chelating ligand by introducing an acidic phenol unit on the N1 position of the imidazole. The objective was to study its acid/base chemistry and pH dependent photophysical properties. In a similar fashion to Chapter 4, analogous methoxy derivatives that should not undergo any acid/base chemistry were made as reference compounds. However, the targeted phenol analogues could not be synthesised successfully and only the methoxy complexes were investigated.

Studies by Vaughan[148] have already established that changing the substituents on the N1 position of the **PyImPh** ligand does not change the photophysical properties. Based on this, the introduction of a base-sensitive substituent provides a good comparison when manipulating this framework. This chapter will explore complexes of both pyridyl (photoactive) and quinolynyl (not photoactive) containing NHC ligands as shown in **Figure 5.1** to assess the effects on the photophysical and photochemical properties.

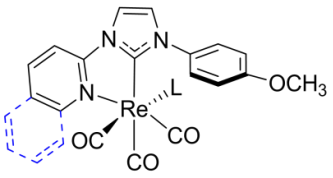

[Re(**PyImPh**OMe)X] **(37)**
[Re(**QuImPh**OMe)X] **(38)**

X = Br, Cl

Figure 5.1 Structure of various substituted rhenium(I)-NHC complexes prepared in this study.

5.2 Synthesis of the Target Compounds

The azolium salt precursors were first synthesised *via* a copper catalysed Ullmann coupling reaction, following the procedure outlined in **Scheme 4.1**. After forming the *N*-substituted imidazoles, the next step was to functionalise on the N3 position to form the desired azolium salts (**N^C** type bidentate chelating ligand) as shown in **Figure 5.2**.

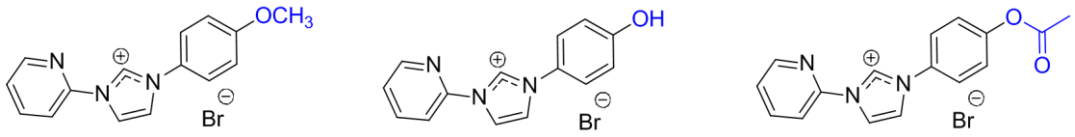

116 **117** **118**

Figure 5.2 Structures of target azolium salts.

In contrast to the preparation of 1-phenylimidazole (**112**) in Chapter 4, 1-(4-hydroxyphenyl)-imidazole (**120**) could not be synthesised *via* a copper catalysed Ullmann coupling reaction under the set experimental conditions (see **Scheme 5.1**). Instead, compound **120** was purchased from Sigma-Aldrich and used as is to form the imidazolium salt (**117**) by reacting with 2-bromopyridine in a sealed pressure tube for 3-5 days. An aliquot of the reaction mixture was analysed by ^{1}H NMR and a downfield peak at 10.40 ppm attributed to the NCHN peak was apparent. This indicated the formation of the imidazolium salt. Unfortunately, the target compound was present in a mixture of by-products that could not be separated after various attempts to isolate and purify the compound. This reaction could not be optimised and was not explored any further.

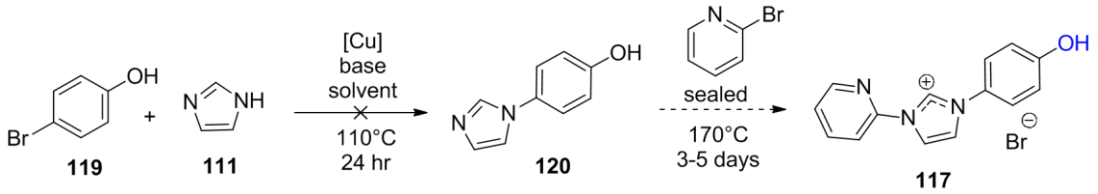

Scheme 5.1 Reaction scheme showing attempted synthesis of phenol-substituted NHC salt.

Instead, a different approach was utilised by first synthesising the 1-(4-methoxyphenyl)-imidazole (**122**) following a procedure adapted from the literature.[192,205] The rationale behind synthesising the methoxy derivative (**35**) was so that the hydroxy (**117**) can be produced in the final stage. The first stage of the reaction involved treating *p*-anisidine (**121**) with glyoxal, followed by ammonium chloride, formaldehyde and a strong acid (such as phosphoric acid) to afford compound **122** in 71% yield (see **Scheme 5.2**). The synthesised compound **122** was finally reacted with 2-bromopyridine at 170 °C in a sealed flask for 3-5 days to form the imidazolium salt [**PyIm**H**Ph**OMe][Br] in 27% yield (see **Scheme 5.2**). This reaction occurred *via* a NAS pathway which is typical between halopyridines and imidazoles, and has been mentioned in Chapter 4 previously. It was noted that the halopyridine must be in slight excess (1.1 eq) in order for the reaction to succeed. If a huge excess (6 eq, which was used for the synthesis of [**PyIm**H**Ph**][Br]), was added to the reaction, polymerisation would occur with formation of unwanted by-products that are difficult to separate.

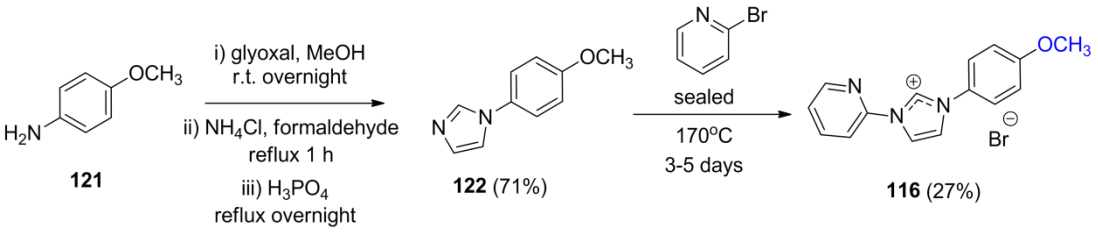

Scheme 5.2 Reaction scheme showing synthesis of methoxy-substituted NHC salt, [**PyIm**H**Ph**OMe][Br].

Analysis of the aryl-substituted imidazolium salt [**PyIm**H**Ph**OMe][Br] by ^{1}H NMR spectroscopy in DMSO-d_6 was consistent with the isolation of the desired compound. This was inferred by the appearance of a downfield peak at 10.54 ppm as shown in **Figure 5.3**, attributed to the H2 proton of the NCHN carbene.

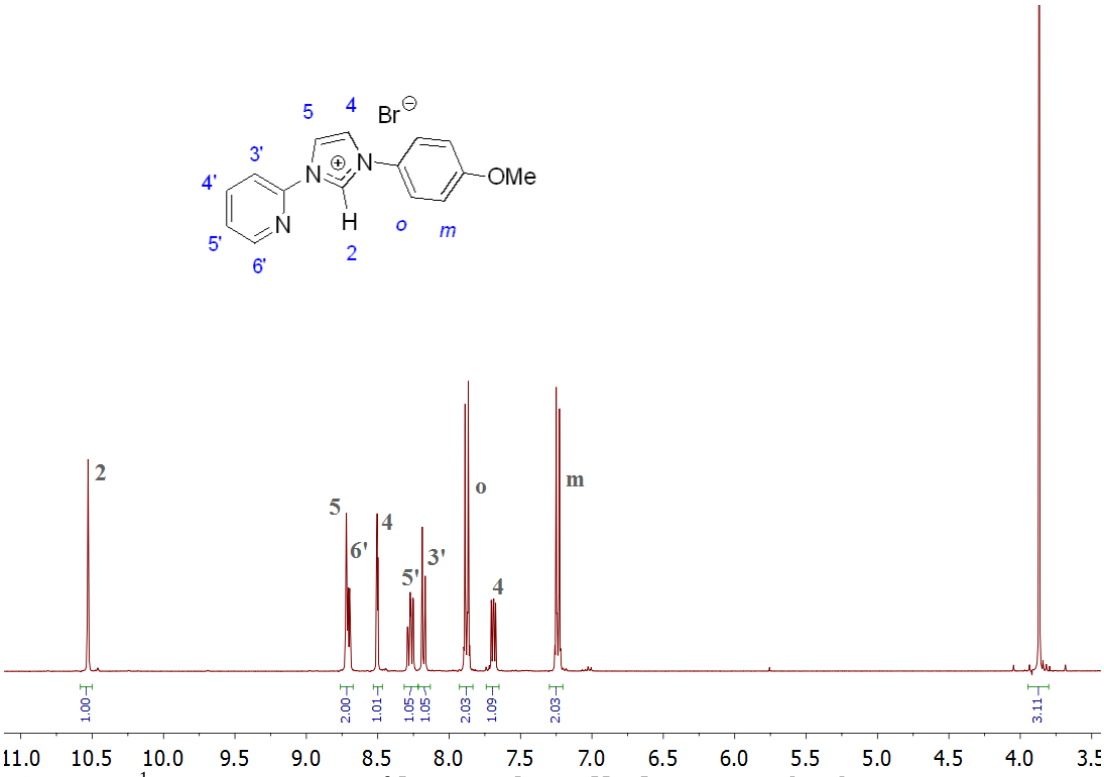

Figure 5.3 ^{1}H NMR spectrum of [**PyIm**H**Ph**OMe][Br] in DMSO-d_6 solution.

The second target aryl-substituted imidazolium salt [**QuIm**H**Ph**OMe][Cl] was prepared in a similar manner to the pyridyl analogues (see Chapter 3) adapted from literature (**Scheme 5.3**).[149] NAS reaction of 2-chloroquinoline and 1-(4-methoxyphenyl)-imidazole afforded the product in high yields (75%). These quinolinyl compounds appeared to be less hygroscopic compared to the pyridyl analogues.

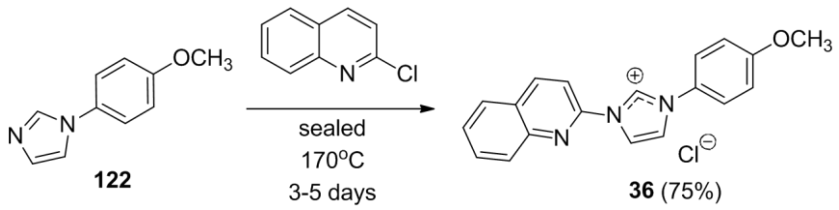

Scheme 5.3 Reaction scheme of quinolinyl- substituted imidazolium salt, [**QuIm**H**Ph**OMe][Cl].

Characterisation of the quinolinyl-substituted imidazolium salt by ^{1}H NMR spectroscopy in DMSO-d_6 was consistent with the isolation of the compound (**Figure 5.4**). The ^{1}H NMR spectrum displayed a notable signal corresponding to the imidazolium H2 proton that appeared as a singlet at 10.69 ppm. The number of peaks, chemical shifts and integration values were consistent with the proposed structure.

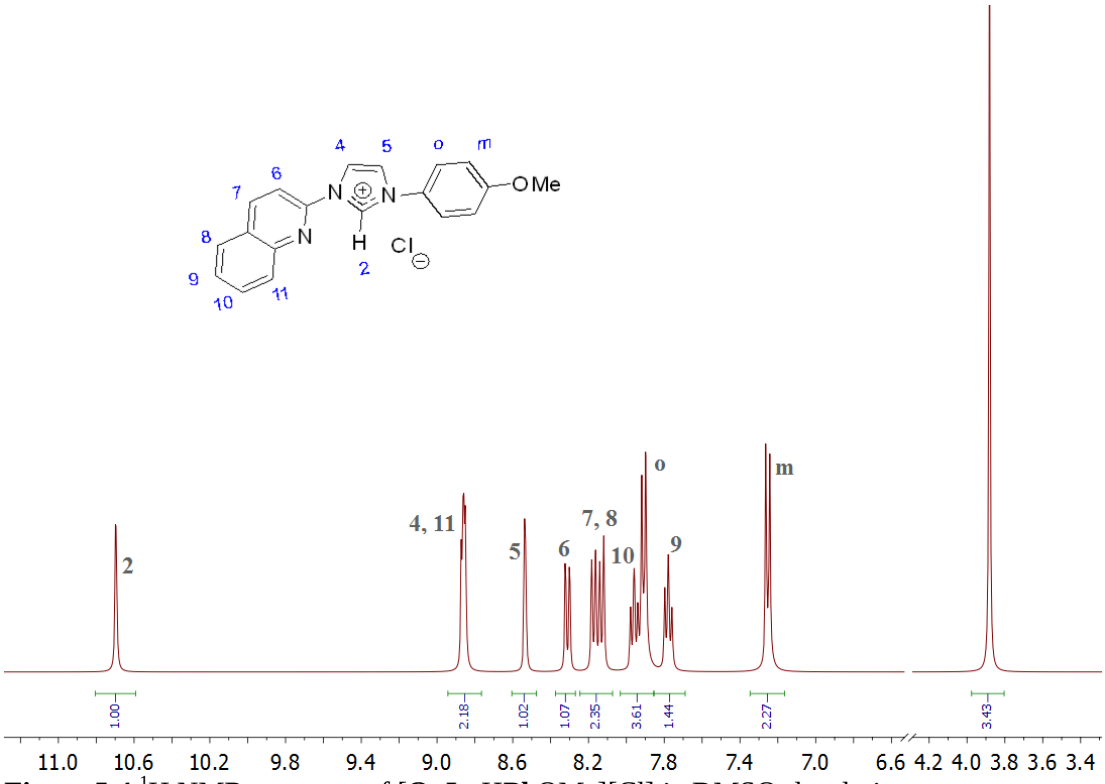

Figure 5.4 ^{1}H NMR spectrum of [**QuIm**H**Ph**OMe][Cl] in DMSO-d_6 solution.

The pyridyl azolium salt series would be used as a direct comparison to the quinolynyl azolium series to assess whether increasing the conjugation of the *N*-donor ring on the NHC ligand system affects the properties of the rhenium(I)-NHC tricarbonyl complex.

After successful synthesis of the methoxy analogues, an alternative technique was attempted to prepare the hydroxy analogue. It has been reported in the literature that one of the methods to cleave a methyl ether would be the use of 47% HBr in acetic acid, heated at reflux for 30 mins.[206] What seemed like a simple procedure actually led to complications and the formation of by-products. This procedure was applied for the demethylation of the ligand **36** alone (see **Scheme 5.4**) and the same conditions were applied to the demethylation of the complex **38Cl** (see **Scheme 5.5**). However, the presence of the methyl peak at 3.80 ppm was still apparent in the ^{1}H NMR spectrum which indicated no conversion occurred.

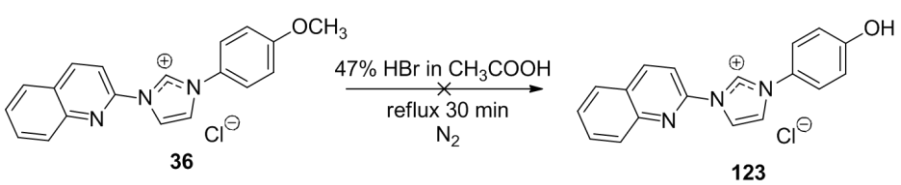

Scheme 5.4 Reaction scheme showing attempted demethylation of ligand (**36**).

5.3 Synthesis and Structural Characterisation of the Complexes

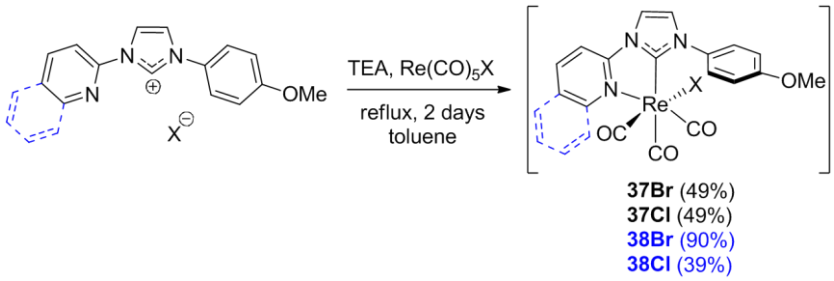

Scheme 5.5 Reaction scheme for preparation of [Re(**PyImPh**OMe)$(CO)_3$X] (**37**) and [Re(**QuImPh**OMe)$(CO)_3$X] (**38**) complexes.

The preparation of target rhenium(I)-NHC tricarbonyl complexes followed the work of Vaughan and co-workers, implementing an *in-situ* synthesis.[149] The reaction consisted of the methoxy substituted imidazolium salt and triethylamine alongside pentacarbonylrhenium halide, heated at reflux in toluene (see **Scheme 5.5**). The formation of the complexes was judged by NMR and IR spectroscopy. The successful synthesis of the rhenium(I)-NHC complexes was indicated by the disappearance of the H2 proton of the imidazolium salt (located around 10.50 ppm in DMSO-d_6 of the ^{1}H NMR spectrum, see **Figure 5.5**). The ^{13}C NMR spectrum displayed four downfield signals present around 198-189 ppm in DMSO-d^6. The three signals belonging to the CO group, and the NCN carbene carbon signal at 190 ppm, confirmed the formation of the tricarbonyl rhenium(I) complex. In addition, the stretching frequency values of the CO peaks in the IR spectrum was consistent with the formation of a tricarbonyl complex.

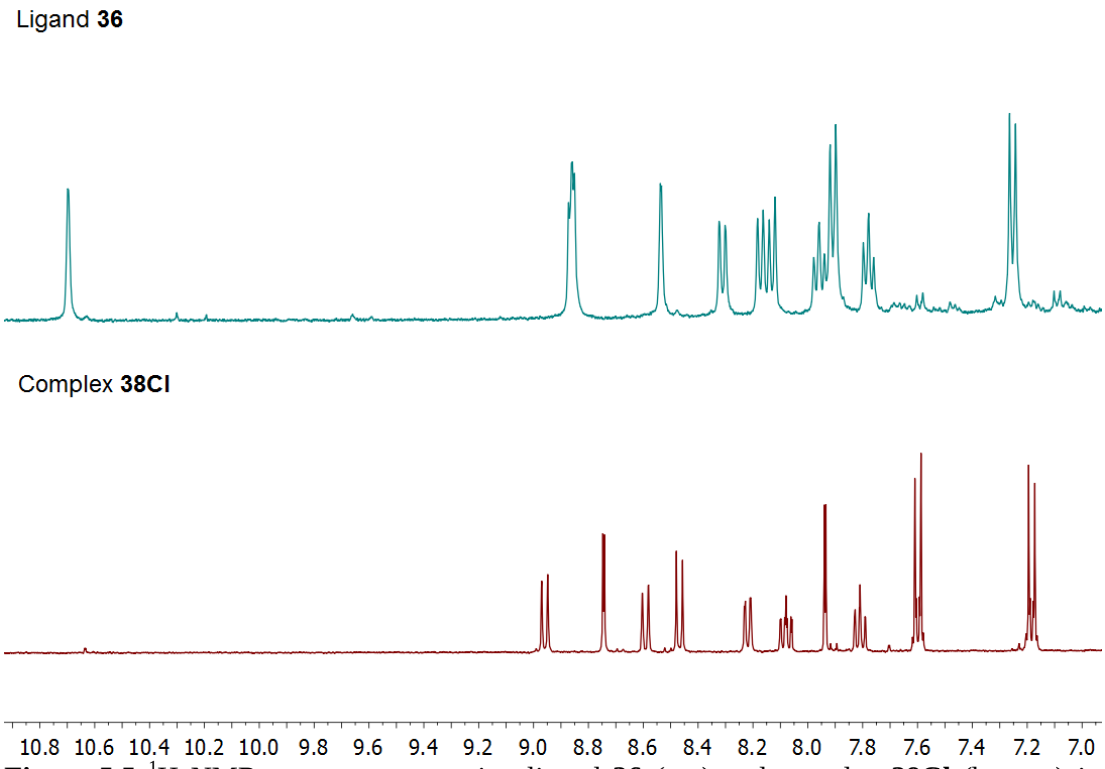

Figure 5.5 ^{1}H NMR spectrum comparing ligand **36** (top) and complex **38Cl** (bottom) in DMSO-d_6 solution.

IR analysis indicated the formation of the rhenium(I) tricarbonyl complex, where the two CO ligands have been replaced by the bidentate NHC ligand. This conversion from a pentacarbonyl to a tricarbonyl species was suggested by the lower stretching frequencies as a result of increased electron density on the metal due to the NHC ligand being a strong σ donor.

The next step was to replace the halogen with a pyridine molecule *via* a silver-halide-abstraction reaction (see **Scheme 5.6**). The formation of the cationic complex was verified by IR analysis. The stretching frequencies of the CO bands displayed an increase in wavenumber as there is less electron density on the rhenium metal centre. This was consistent with similar complexes reported in the previous chapter.

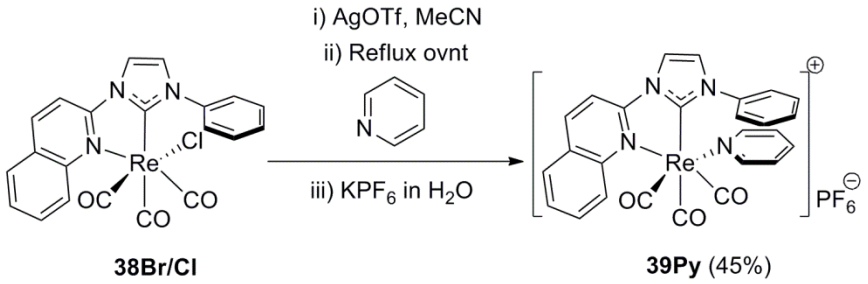

Scheme 5.6 Synthetic preparation of cationic rhenium(I)-NHC complex **39Py**.

All of the pyridyl N-donor complexes **37Br/Cl** displayed three CO stretching bands (in the range of 2030 to 1850 cm^{-1}) which are evident in the IR spectrum, summarised **Table 5.1**. These stretching frequencies are typical of neutral *fac*-rhenium(I) tricarbonyl complexes. On the other hand, the quinolinyl N-donor complexes **38Br/Cl** display three CO stretching bands in the IR spectrum with some observed splitting of the peaks.

Table 5.1 Stretching frequencies (cm^{-1}) displaying CO bands of the Re(I)-NHC complexes.

Complex	CO A′ (1)	CO A′ (2)/A″
[Re(**PyImPh**)$(CO)_3$Br] (**22Br**) [149]	2010	1923, 1894
[Re(**PyImPh**)$(CO)_3$Cl] (**22Cl**) [149]	2010	1921, 1890
[Re(**PyImPh**OMe)$(CO)_3$Br] (**37Br**)	2014	1882 [a]
[Re(**PyImPh**OMe)$(CO)_3$Cl] (**37Cl**)	2015	1916, 1884
[Re(**QuImPh**)$(CO)_3$Br] [149]	2011, 1912	1880, 1857
[Re(**QuImPh**)$(CO)_3$Cl] [149]	2010, 1910	1876, 1852
[Re(**QuImPh**)$(CO)_3$(Py)]$^+$	2025	1930, 1898
[Re(**QuImPh**OMe)$(CO)_3$Br] (**38Br**)	2015, 1943	1907, 1882
[Re(**QuImPh**OMe)$(CO)_3$Cl] (**38Cl**)	2014, 1942	1912, 1878

[a] peaks are superimposed into a single broad band

Following examination of the stretching frequencies (reported in Table 5.1) of complexes **37Br/Cl** compared to **22Br/Cl**, it appeared that the CO peaks are quite similar even after introducing the methoxy group; this implied it had no significant effect on the electron density around the metal centre due to the lack of conjugation. In addition, there appeared to be no obvious differences on the CO stretching frequencies upon alternating the N-donor ring between pyridyl **37Br/Cl** and quinolinyl **38Br/Cl** groups. This implied that the electron density around the rhenium metal centre and the back-bonding to the carbonyl ligands were not significantly affected by these modifications. Furthermore, no difference was apparent upon changing the halogen between bromide and chloride, consistent with literature examples previously reported.[149,207]

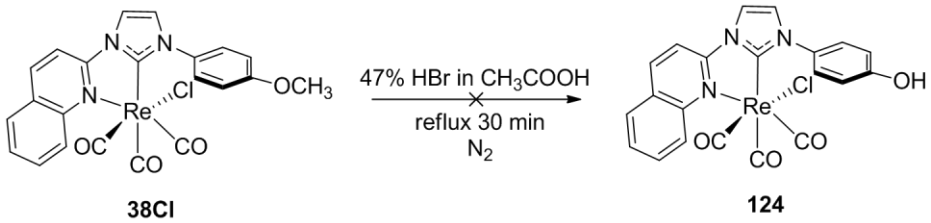

Scheme 5.7 Reaction scheme showing attempted demethylation of complex (**38Cl**).

The demethylation of the complex was attempted following the experimental conditions that were set out for the demethylation of the ligand (see **Scheme 5.7**). However, after reaction completion, analysis showed that the presence of the methyl peak was still apparent in the ^{1}H NMR spectrum and no hydroxy peak was present in the IR spectrum. It was evident that a complicated mixture was present as the methyl peak did not integrate for three protons anymore. Even after separation of by-products through column chromatography, there was no evidence of the hydroxy peak in both the NMR and IR spectrum.

5.4 X-ray Crystallography

Single crystals suitable for X-ray diffraction studies were obtained for **37Br**, **37Cl** and **38Br**. However, **38Cl** did not produce single crystals suitable for analysis. The structures can be seen in **Figure 5.6**. The structures are consistent with the proposed formulae of the complexes, with each complex having the carbonyl ligands arranged in a *facial* manner. An overall distorted octahedral geometry is observed.

The rhenium-carbene carbon (Re-C) bond distance for the [Re(**PyImPh**OMe)$(CO)_3$X] complexes is 2.149(2) and 2.157(3) Å for the bromide and chloride analogues, respectively. These distances appear to be longer than those reported for pyridyl, 2.123(4) or pyrimidyl, 2.118(5) Å substituted imidazolyl units containing a mesityl group.[197] The rhenium-carbene carbon (Re-C) bond distances for [Re(**PyImPh**)$(CO)_3$X] complexes are 2.145(3) Å for bromide and 2.1488(10) Å for chloride analogues.[149] The rhenium-carbene carbon distances give an indication on the donating ability of the carbene ligands.

According to **Table 5.2**, the distance of the rhenium-carbonyl (Re-CO) bond *trans* to the carbene carbon is 1.943 and 1.940 Å for **37Br** and **37Cl** respectively, which

appears longer than the remaining carbonyl ligands with a distance of around 1.909-1.920 Å. This suggests the strong donating ability of the carbene pushing the carbonyl further away from the rhenium centre. This confirms that the Re-CO bond *trans* to the strong σ donor ligand would elongate as expected.

Table 5.2 Selected bond lengths (Å) of the Re(I)-NHC complexes.

Complex	**Bond length (Å)**		
	Re-CO *trans* to N atom	Re-CO *trans* to C atom	Re-CO *trans* to ancillary ligand (halogen or pyridine)
[Re(**PyImPh**OMe)$(CO)_3$Br] (**37Br**)	1.912(3)	1.943(3)	1.909(3)
[Re(**PyImPh**OMe)$(CO)_3$Cl] (**37Cl**)	1.920(3)	1.940(3)	1.913(3)
[Re(**QuImPh**OMe)$(CO)_3$Br] (**38Br**)	1.905(4)	1.964(4)	1.865(6)
[Re(**QuImPh**)$(CO)_3$(Py)]$^+$	1.906	1.971	1.924

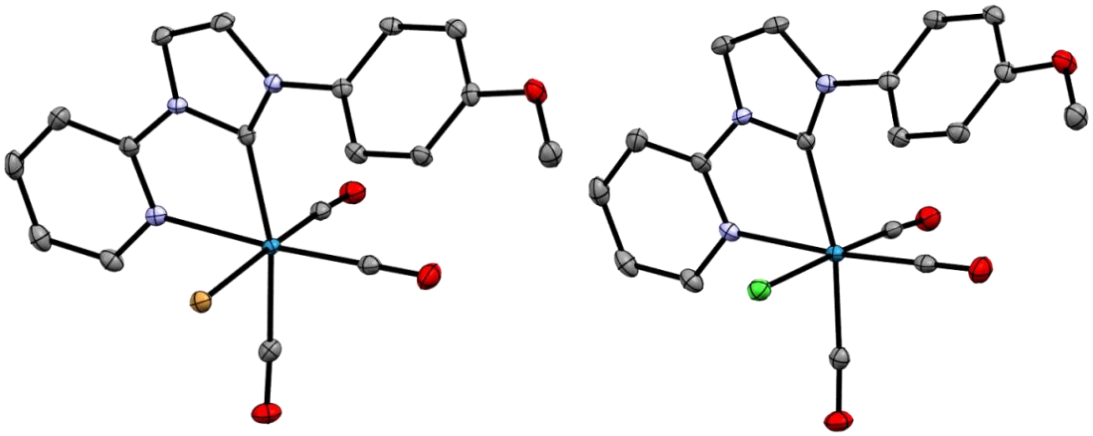

Figure 5.6 X-ray crystal structure of [Re(**PyImPh**OMe)$(CO)_3$Br], left and [Re(**PyImPh**OMe)$(CO)_3$Cl], right. Ellipsoids are displayed at the 50% probability level; hydrogen atoms omitted for clarity.

The crystal structure for [Re(**QuImPh**OMe)$(CO)_3$Br] can be seen in **Figure 5.7**. The rhenium-carbene carbon bond distance for [Re(**QuImPh**OMe)$(CO)_3$Br] complex is 2.111 Å which is longer than the pyridyl analogues. However, this distance is very similar to [Re(**QuImPh**)$(CO)_3$Br] previously reported.[149] The distance of the rhenium-carbonyl bond *trans* to the carbene carbon is 1.964 Å, which is significantly longer than the remaining carbonyl ligands with a distance of 1.906 and 1.866 Å. In addition, the rhenium-bromide bond distance is 2.590 Å, which is longer than the

pyridyl analogues. Although it appears shorter to [Re(**QuImPh**)$(CO)_3$Br] with a rhenium-bromide distance of 2.6243 Å.

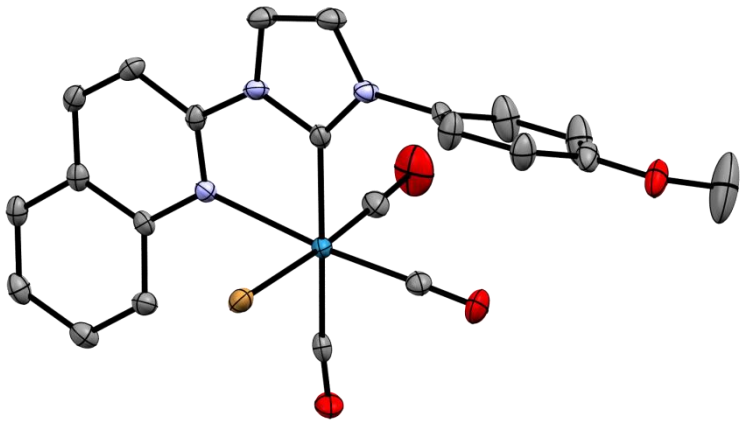

Figure 5.7 X-ray crystal structure of [Re(**QuImPh**OMe)$(CO)_3$Br], where thermal ellipsoids have been drawn at 50% probability and hydrogen atoms omitted for clarity.

The crystal structure for [Re(**QuImPh**)$(CO)_3(Py)]^+$ can be seen in **Figure 5.8**. The rhenium-carbene carbon bond distance for [Re(**QuImPh**)$(CO)_3(Py)]^+$ complex is 2.118 Å which is slightly longer than the other quinolinyl analogues. The distance of the rhenium-carbonyl bond *trans* to the carbene carbon is 1.971 Å, which is significantly longer than the remaining carbonyl ligands with a distance of 1.906 and 1.924 Å. In addition, the rhenium-pyridine bond distance is 2.229 Å, which is actually shorter than those with the halide ancillary ligand, specifically [Re(**QuImPh**)$(CO)_3$Br] with a rhenium-bromide distance of 2.6243 Å.

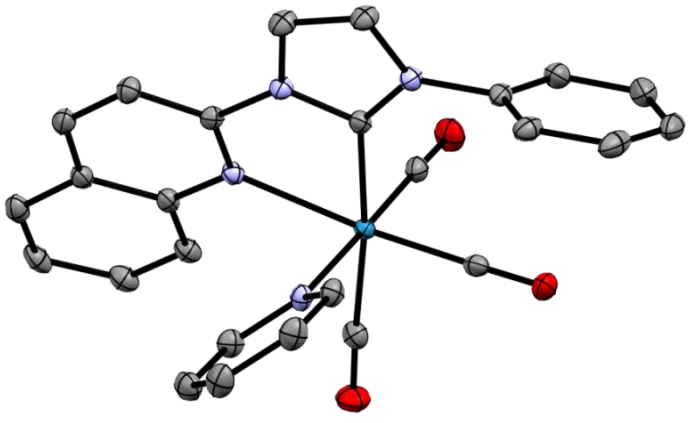

Figure 5.8 X-ray crystal structure of [Re(**QuImPh**)$(CO)_3(Py)]^+$, where thermal ellipsoids have been drawn at 50% probability.

An interesting aspect of the crystal structures of these complexes is the angle between the planes of the imidazole and pyridyl rings. The imidazole unit is almost

completely co-planar with the pyridyl group, having an interplanar angle of just 7.53°. However, the methoxyphenyl ring for complexes **37Br/Cl** is not co-planar with the imidazole and N-donor ring, having an interplanar angle of 51.9°. For the quinolyinyl complexes **38Br/Cl**, the imidazole unit is almost completely co-planar with the quinolynl group, having an interplanar angle of just 6.52°. However, the methoxyphenyl ring is not co-planar with the imidazole and N-donor ring, having an interplanar angle of 71.3°. This angle is much larger when compared to the pyridyl series. Additionally, both complexes exhibit distorted octahedral geometry, where the bite angle of the **N^C** ligand was measured to be 74.3° and 73.9° for pyridyl and quinolynyl analogues, respectively.

5.5 Photophysical Investigation

The photophysical properties of the aforementioned rhenium(I)-NHC complexes [Re(**PyImPh**OMe)$(CO)_3$X] (**37Br/Cl**) and [Re(**QuImPh**OMe)$(CO)_3$X] (**38Br/Cl**) have been investigated and will be discussed throughout this section. A summary of the photophysical data in diluted dichloromethane solutions for the complexes are shown in **Table 5.3**.

Table 5.3 Photophysical data of complexes in diluted DCM solution (*ca*. 10^{-5} M) at 298 K.

Complex	λ_{abs} (nm) [10^4 ε, $M^{-1}cm^{-1}$]	λ_{em} (nm)	Lifetime [a] (τ, ns)	Lifetime [b] (τ, ns)	Φ [a] (± 0.015)	Φ [b] (± 0.015)
[Re(**PyImPh**OMe)$(CO)_3$Br] (**37Br**)	283 (1.44), 363 (0.41)	518	18	22	0.006 [c]	0.008 [c]
[Re(**PyImPh**OMe)$(CO)_3$Cl] (**37Cl**)	282 (1.19), 358 (0.42)	522	53	131	0.008 [c]	0.015 [c]
[Re(**QuImPh**OMe)$(CO)_3$Br] (**38Br**)	284 (0.47), 333 (0.35), 386 (0.105)	625	242	1345	0.014 [d]	0.052 [d]
[Re(**QuImPh**OMe)$(CO)_3$Cl] (**38Cl**)	285 (0.32), 332 (0.32), 383 (0.093)	634	228	842	0.013 [d]	0.042 [d]
[Re(**QuImPh**)$(CO)_3$Br] (**39Br**) [149]	255 (3.15), 323 (0.77), 382 (0.36)	622	263	993	0.030 [c]	0.100 [c]
[Re(**QuImPh**)$(CO)_3$Cl] (**39Cl**) [149]	257 (4.73), 336 (0.76), 392 (0.38)	626	240	1065	0.030 [c]	0.130 [c]
[Re(**QuImPh**)$(CO)_3$(Py)]$^+$ (**39Py**)	329 (0.61), 360 (0.32)	572	997	9033	0.020 [c]	0.180 [c]

[a] air equilibrated samples, [b] degassed samples, Φ quantum yield measured against air-equilibrated reference [c] [Ru(**bipy**)$_3$]Cl_2 or [d] quinine sulfate (in 1M H_2SO_4).

As can be seen in **Figure 5.9**, the absorption profiles for [Re(**PyImPh**OMe)$(CO)_3$Br] (**37Br**) and [Re(**PyImPh**OMe)$(CO)_3$Cl] (**37Cl**) in dichloromethane are very similar. The complexes **37Br/Cl** exhibit a high intensity band at 282 nm assigned to an IL transition involving the NHC ligand and the low intensity broad band centred at 360 nm assigned to an MLCT band. The absorption profiles for **37Br/Cl** are quite similar to **22Br/Cl** in dichloromethane solutions, despite the presence of methoxy substituent on the former complex. Also, the emission profiles for **37Br/Cl** display a structureless band at maximum wavelength of *ca*. 520 nm (**Figure 5.9**), similar to that of **22Br/Cl** in dichloromethane solution**.** In addition, both complexes **37Br/Cl** and **22Br/Cl** exhibit quite short excited state lifetime decays (typical of rhenium carbene complexes) in dichloromethane solutions. However, the quantum yields for [Re(**PyImPh**OMe)$(CO)_3$X] are very low at 0.6% (**37Br**) and 0.8% (**37Cl**), compared to [Re(**PyImPh**)$(CO)_3$X] at 2.0% (**22Br**) and 3.0% (**22Cl**) in aerated dichloromethane solutions.

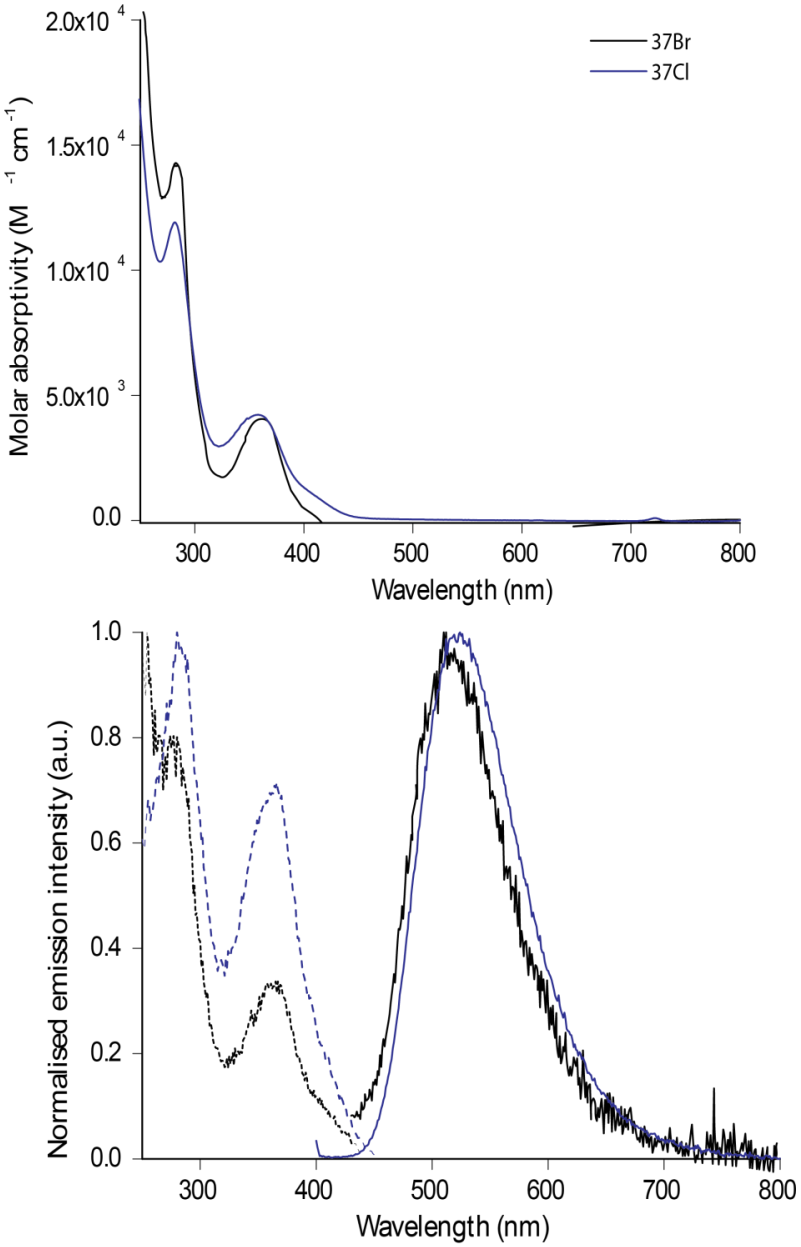

Figure 5.9 Top: Absorption profile of **37Br/Cl** and bottom: emission (solid) and excitation (dashed) profiles of **37Br/Cl** in DCM.

Compared to the pyridyl series, the absorption profiles for both [Re(**QuImPh**OMe)$(CO)_3$Br] (**38Br**) and [Re(**QuImPh**OMe)$(CO)_3$Cl] (**38Cl**) in dichloromethane exhibit a more structured spectrum with three distinct bands at 284 nm, 330 nm and a low intensity band centred at 380 nm (see **Figure 5.10**). The higher energy band (IL) for complexes **38Br/Cl** are red shifted (~30 nm) in dichloromethane with respect to **39Br/Cl**, i.e. [Re(**QuImPh**)$(CO)_3$X]. This would be due to the electron donating nature of the methoxy on the phenyl ring which would partially affect the LUMO. However, the MLCT band does not seem to shift significantly for the varying complexes (**38Br/Cl** vs **39Br/Cl**). This would be

because the methoxy substituent has no significant effect on the HOMO, and hence the MLCT transitions are similar. On the other hand, the cationic complex [Re(**QuImPh**)$(CO)_3$(Py)]$^+$ (**39Py**) displays a blue shifted emission (*ca*. 50 nm) compared to its halogenated precursors. This is attributed to a larger HOMO-LUMO gap as a result of the coordinated pyridine reducing the electron density on the rhenium and stabilising the HOMO. In addition, the excited state lifetime decay is almost three times longer in aerated solution.

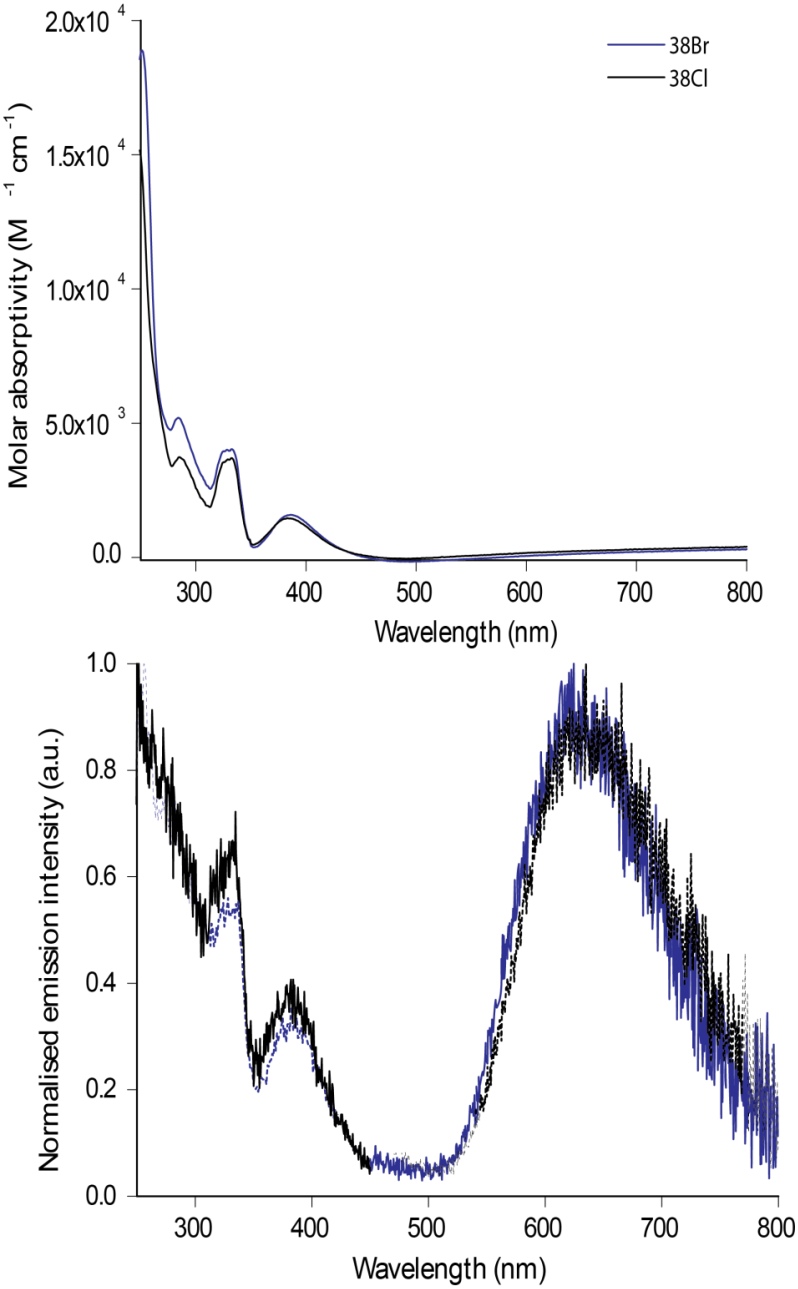

Figure 5.10 Top: Absorption profile of **38Br/Cl** and bottom: emission (solid) and excitation (dashed) profiles of **38Br/Cl** in DCM.

The absorption and emission profiles for [Re(**QuImPh**OMe)$(CO)_3$X] were quite similar to the analogues without the methoxy substituent, [Re(**QuImPh**)$(CO)_3$X] in dichloromethane solutions. On the other hand, the quinolinyl complexes all exhibit a red-shifted emission (~110 nm) compared to the pyridyl analogues. This could be due to an increased conjugation on the chelating ligand, stabilising and lowering the energy of the LUMO, thus resulting in a smaller HOMO-LUMO gap. In addition, the excited state lifetime decays are longer than the pyridyl analogues. The observed excited state lifetime for all complexes increased upon degassing which is suggestive of emission originating from a triplet state. The excited state lifetime decays for degassed solutions are doubled for the pyridyl series. However, the quinolynl series seem to have a much greater increase (triple) upon degassing. This could be attributed to the increased conjugation on the quinoline group.

The radiative and non-radiative decay constants are presented in **Table 5.4**. The value of the non-radiative decay (k_{nr}) for **37Br** appears much higher relative to that of **38Br**. There appears to be a structural trend which affects the k_r and k_{nr} values, as a result of the different emission energies between pyridyl **37Br/Cl** and quinolynyl **38Br/Cl** complexes.

Table 5.4 Radiative and non-radiative decay constants for the Re(I) complexes calculated for deaerated DCM solutions (*ca*. 10^{-5} M).

Complex	k_r (10^5 s^{-1})	k_{nr} (10^6 s^{-1})
[Re(**PyImPh**OMe)$(CO)_3$Br] (**37Br**)	3.64	45.1
[Re(**PyImPh**OMe)$(CO)_3$Cl] (**37Cl**)	1.15	7.52
[Re(**QuImPh**OMe)$(CO)_3$Br] (**38Br**)	0.37	0.71
[Re(**QuImPh**OMe)$(CO)_3$Cl] (**38Cl**)	0.49	1.14

A summary of the photophysical data in diluted acetonitrile solutions for the complexes were shown in **Table 5.5**. The absorption and emission profiles for the imidazolium salts were only measured in acetonitrile as they were insoluble in dichloromethane solutions. The absorption profile of the [**PyIm**H**Ph**OMe][Br] salt consists of only one major band centred at around 275 nm (13900 M^{-1} cm^{-1}). This band can be assigned to π-π* (IL) transitions. The broad band at 350 nm is absent in

the absorption spectrum (**Figure 5.11**) of the precursor azolium [**PyIm**H**Ph**OMe][Br] salt with respect to the coordinated complex and therefore attributed to a transition involving the metal centre. In addition, the ligand emits *via* fluorescence at 428 nm which is illustrated in **Figure 5.11**. The absorption and emission profile for the [**QuIm**H**Ph**OMe][Cl] salt is illustrated in **Figure 5.12**. The absorption spectrum exhibits a structured profile with three distinct bands, i.e. a high intensity band at 277 nm (15600 M^{-1} cm^{-1}) which tails off in the lower energy into two visible peaks at 310 nm (9220 M^{-1} cm^{-1}) and 324 nm (7280 M^{-1} cm^{-1}). These bands are assigned to ligand-centred π-π* transitions. The emission band is centred at 434 nm which is typical of a short-lived fluorescent component.

Table 5.5 Photophysical data of complexes in diluted MeCN solution (*ca*. 10^{-5} M).

Complex	**λ_{abs} (nm) [10^4 ε, $M^{-1}cm^{-1}$]**	**λ_{em} (nm)**	**Lifetime [a] (τ, ns)**	**Lifetime [b] (τ, ns)**	**Φ [a]**	**Φ [b]**
[Re(**PyImPh**OMe)$(CO)_3$Br] (**37Br**)	278 (0.614), 355 (0.149)	524	2	4	0.0006 [c]	0.0008 [c]
[Re(**PyImPh**OMe)$(CO)_3$Cl] (**37Cl**)	274 (1.06), 347 (0.3)	523	15	23	0.0023 [c]	0.0035 [c]
[Re(**QuImPh**OMe)$(CO)_3$Br] (**38Br**)	329 (0.591), 369 (0.264)	630	96	1488	0.0020 [d]	0.0030 [d]
[Re(**QuImPh**OMe)$(CO)_3$Cl] (**38Cl**)	327 (0.656), 367 (0.308)	638	91	646	0.0016 [d]	0.0018 [d]
[Re(**QuImPh**)$(CO)_3$(Py)]$^+$ (**39Py**)	326 (0.812), 350 (0.454)	579	323	5753	0.023 [c]	0.176 [c]

[a] air equilibrated samples, [b] degassed samples, Φ quantum yield measured against air-equilibrated reference [c] [Ru(**bipy**)$_3$]Cl_2 or [d] quinine sulfate (in 1M H_2SO_4).

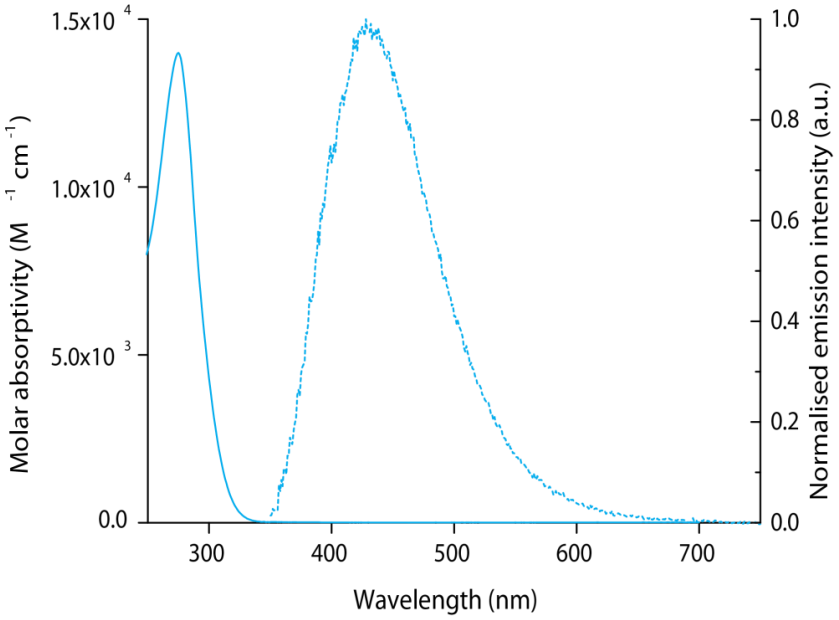

Figure 5.11 Absorption (solid) and emission (dashed) profile for [**PyIm**H**Ph**OMe][Br] salt in MeCN.

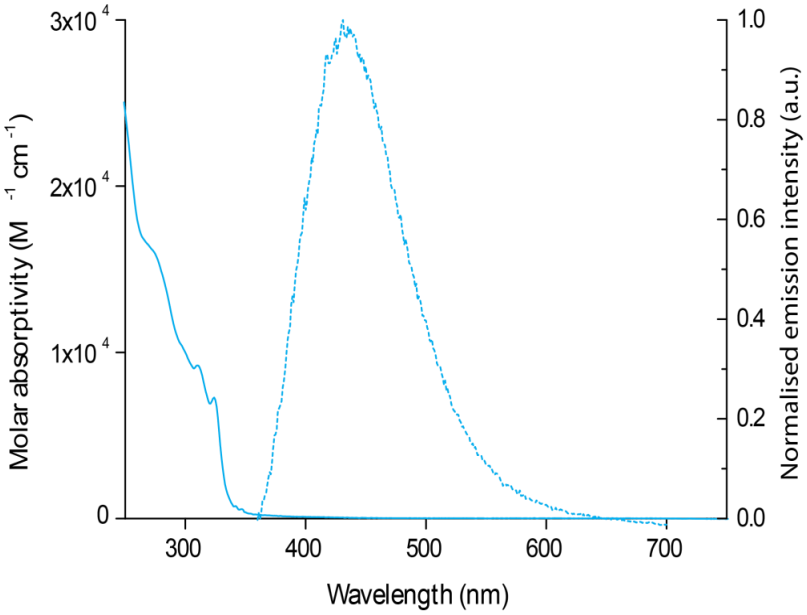

Figure 5.12 Absorption (solid) and emission (dashed) profile for [**QuIm**H**Ph**OMe][Cl] in MeCN.

The absorption, excitation and emission profiles of the [Re(**PyImPh**OMe)$(CO)_3$X] complexes in air equilibrated acetonitrile solutions are shown in **Figure 5.13**. The absorption profile for complex **37Br/Cl** displays a high intensity band at 270 nm and a low intensity band at 350 nm. The complexes display a broad and structureless emission centred around 520 nm. This is typical of a charge transfer emission originating from ^{3}MLCT state.

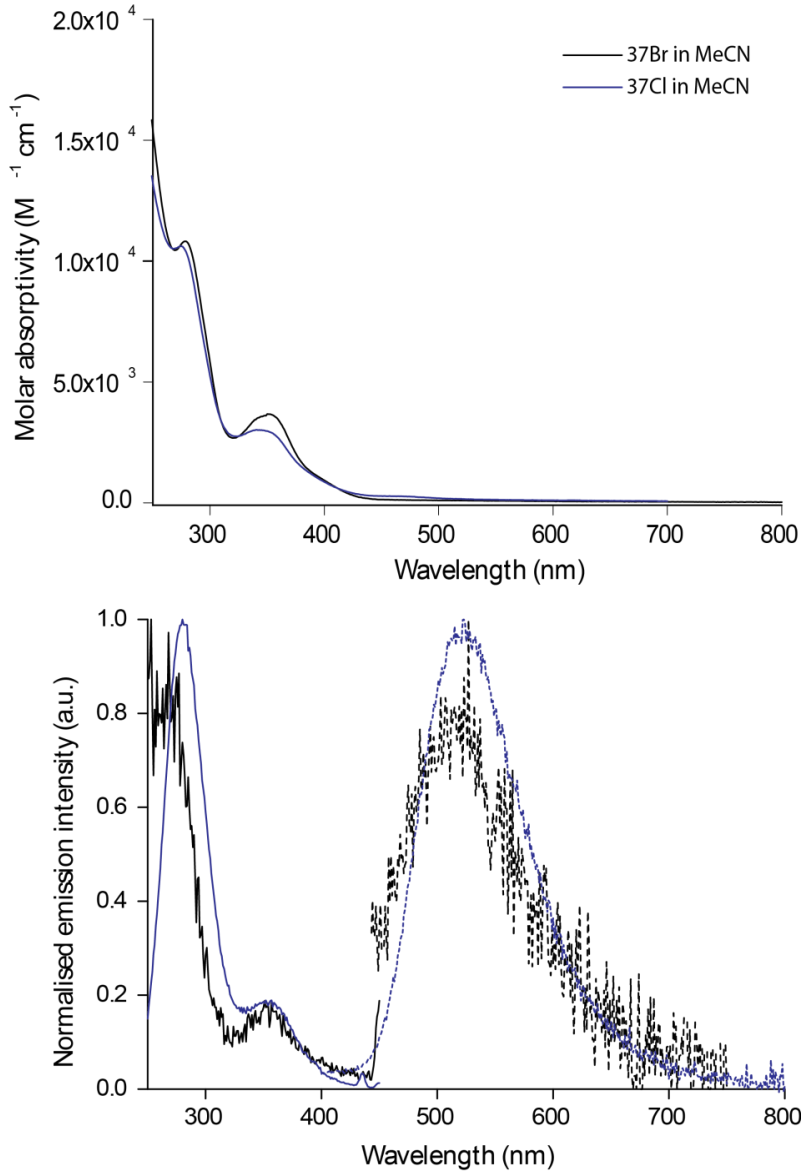

Figure 5.13 Top: Absorption profile of **37Br/Cl** and bottom: emission (solid) and excitation (dashed) profiles of **37Br/Cl** in MeCN.

The absorption, excitation and emission profiles of the [Re(**QuImPh**OMe)$(CO)_3$X] complexes in air equilibrated acetonitrile solutions are shown in **Figure 5.14**. The complexes display a broad and structureless emission centred around 630-640 nm. Again, these characteristics are typical of a charge transfer emission of ^{3}MLCT state as stated previously. The emission maxima are very similar between bromo and chloro analogues as expected.

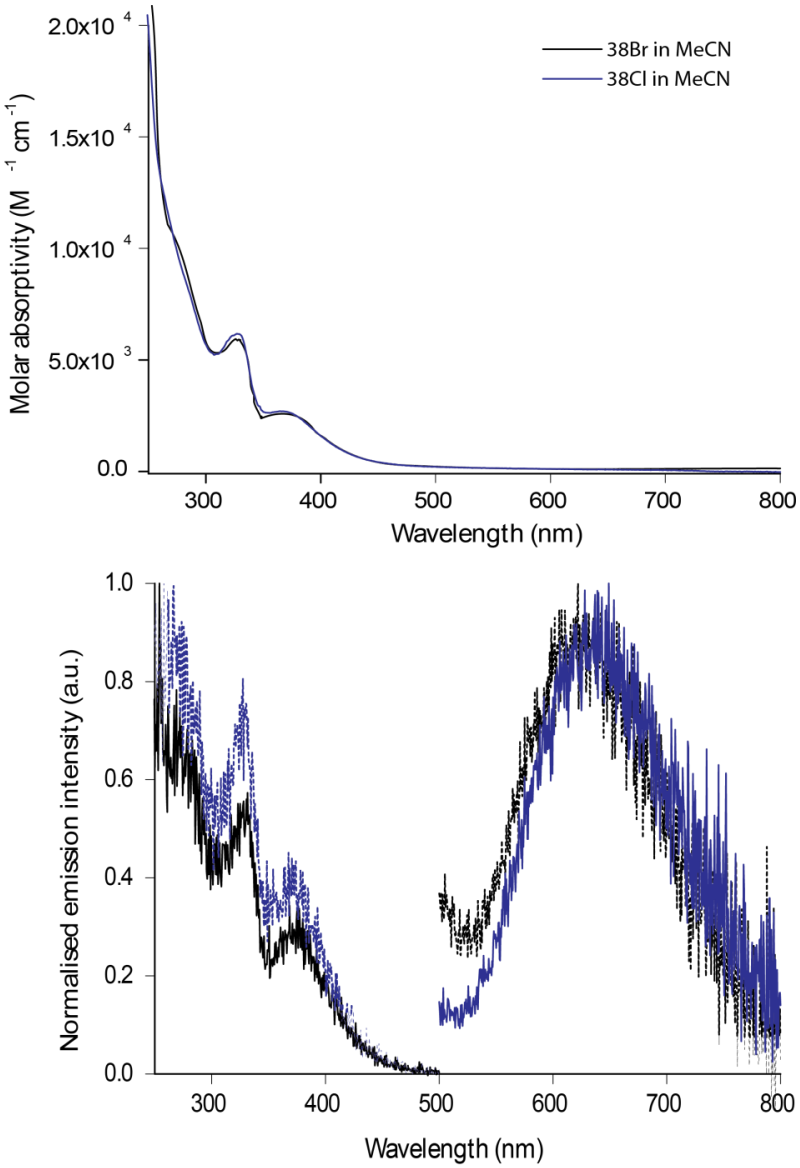

Figure 5.14 Top: Absorption profile of **38Br/Cl** and bottom: emission (solid) and excitation (dashed) profiles of **38Br/Cl** in MeCN.

Comparing pyridyl and quinolinyl series, the [Re(**QuImPh**OMe)$(CO)_3$X] complexes have an emission red shifted about 100 nm. This bathochromic shift can be explained due to the increased conjugation of the N-donor ring that lowers the energy of the LUMO, thus reducing the HOMO-LUMO gap.

The observed excited state lifetime values of **37Br** in air equilibrated acetonitrile solutions display a very short lifetime of 2 ns. When degassed, the lifetime slightly increases to 4 ns. On the other hand, **38Br** displayed a lifetime of about 10 ns when aerated and 16 ns when degassed. This discrepancy of the bromo analogue having a reduced lifetime compared to the chloro can be attributed to the higher lability of the bromo ligand. Also, the presence of a second excited state, MLCT(2), may exist in

reactive conditions of acetonitrile as seen in the work of Mukuta.[189] However, this trend was not consistent with the [Re(**QuImPh**OMe)$(CO)_3$X] type complexes. This could be due to the fact that quinolynyl complexes are not reactive in acetonitrile.

5.5.1 Photophysical Investigation at 77 K

The emission maxima and excited state lifetime values for all complexes measured at 77 K are compiled in **Table 5.6**. The emission profiles for complexes **37Br/Cl** and **38Br/Cl** in frozen dichloromethane at 77 K are depicted in **Figure 5.15** and **Figure 5.16**, respectively. The emission profiles for both complexes displayed a smooth and structureless band. This observation was divergent to those 77 K data shown in previous chapters showing structured profiles. The structured profiles (of the complex in the previous chapter) could be due to the energy of the emissive ^{3}MLCT state lying above the ^{3}LC state; this is consistent to what has been reported in literature.[198] This is not the case for the complexes reported in this chapter. Nonetheless, the emission maxima were blue-shifted compared to the solutions measured at room temperature which can be attributed to the rigidochromic effect. The emission can be characterised as occurring from ^{3}MLCT state. Furthermore, the excited state lifetime values at 77 K were significantly elongated compared to those measured at room temperature. This is due to the absence of collisional quenching and also a reduction of non-radiative decay due to the rigidity of the system.

For the pyridyl N-donor complexes **37Br/Cl**, the emission maximum measured at 77 K (**Figure 5.15**) is centred at 480 nm. In addition, the excited state lifetime decay for **37Br** at 77 K was measured to be 2 µs, which is almost a 100-fold increase with respect to the lifetime decay at room temperature. On the other hand, **37Cl** also displayed a longer lifetime but at a bi-exponential decay of 1 µs (8%) and 6 µs (92%). For the quinolinyl N-donor complexes **38Br/Cl**, the emission maximum would be *ca*. 560 nm as displayed in **Figure 5.16**. In addition, the excited state lifetime decay was slightly longer than their pyridyl analogues, at 6 µs for **38Br** and 10 µs for **38Cl**.

Table 5.6 Summarised data of complexes measured at 77 K in frozen DCM solution.

Complex	λ_{em} (nm)	Lifetime (τ, µs)
[Re(**PyImPh**OMe)$(CO)_3$Br] (**37Br**)	487	1.91
[Re(**PyImPh**OMe)$(CO)_3$Cl] (**37Cl**)	474	1.20 (8%), 5.50 (92%)
[Re(**QuImPh**OMe)$(CO)_3$Br] (**38Br**)	559	6.16
[Re(**QuImPh**OMe)$(CO)_3$Cl] (**38Cl**)	565	10.1
[Re(**QuImPh**)$(CO)_3$(Py)]$^+$ **(39Py)**	545	20.25

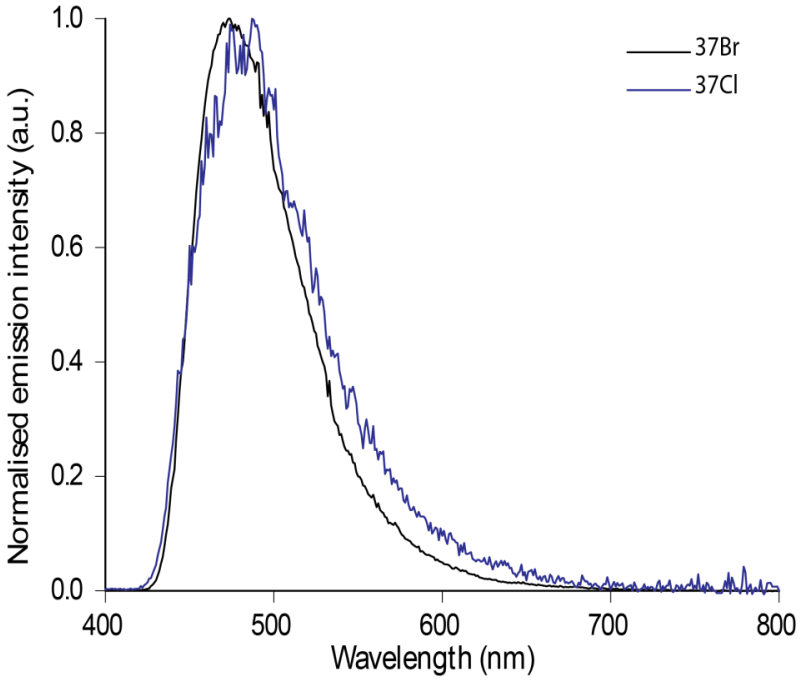

Figure 5.15 Emission profile for [Re(**PyImPh**OMe)$(CO)_3$X] complexes in DCM at 77K frozen media.

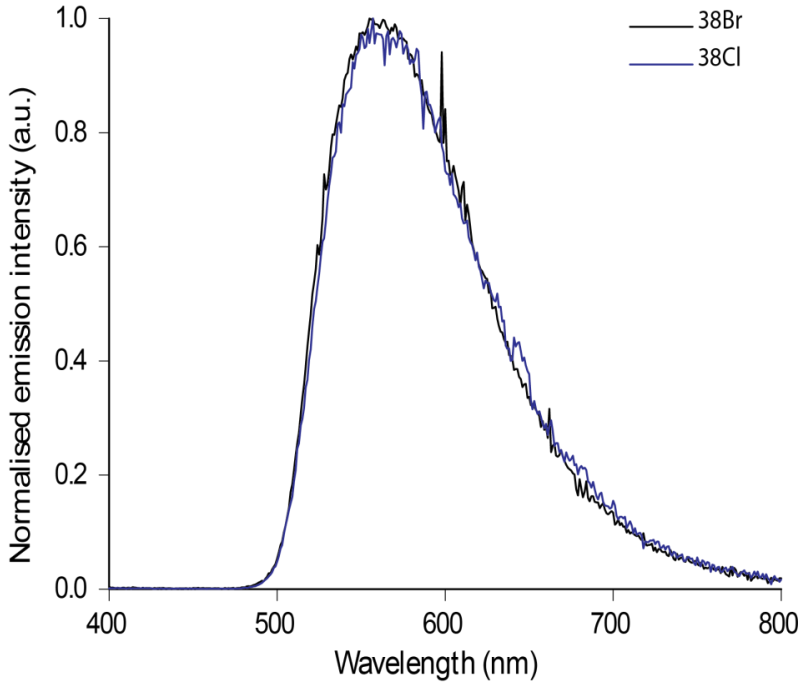

Figure 5.16 Emission profile for [Re(**QuImPh**OMe)$(CO)_3$X] complexes in DCM at 77K frozen media.

5.6 Photochemical Investigation

The photochemistry of all rhenium(I)-NHC complexes were investigated by irradiation in acetonitrile under UV (λ_{ex} = 365 nm) light, following the procedure outlined in section 4.9.2. These experiments were performed over the course of 4 to 8 hours, depending on the reactivity of the complexes. At regular 1 hour intervals, ^{1}H NMR spectrum was collected to monitor the progression of the peaks. In addition, the IR spectrum of the photolysed solution was collected every 2 hours. The photoproducts predicted to form after irradiation of the complex is outlined in **Figure 5.17**.

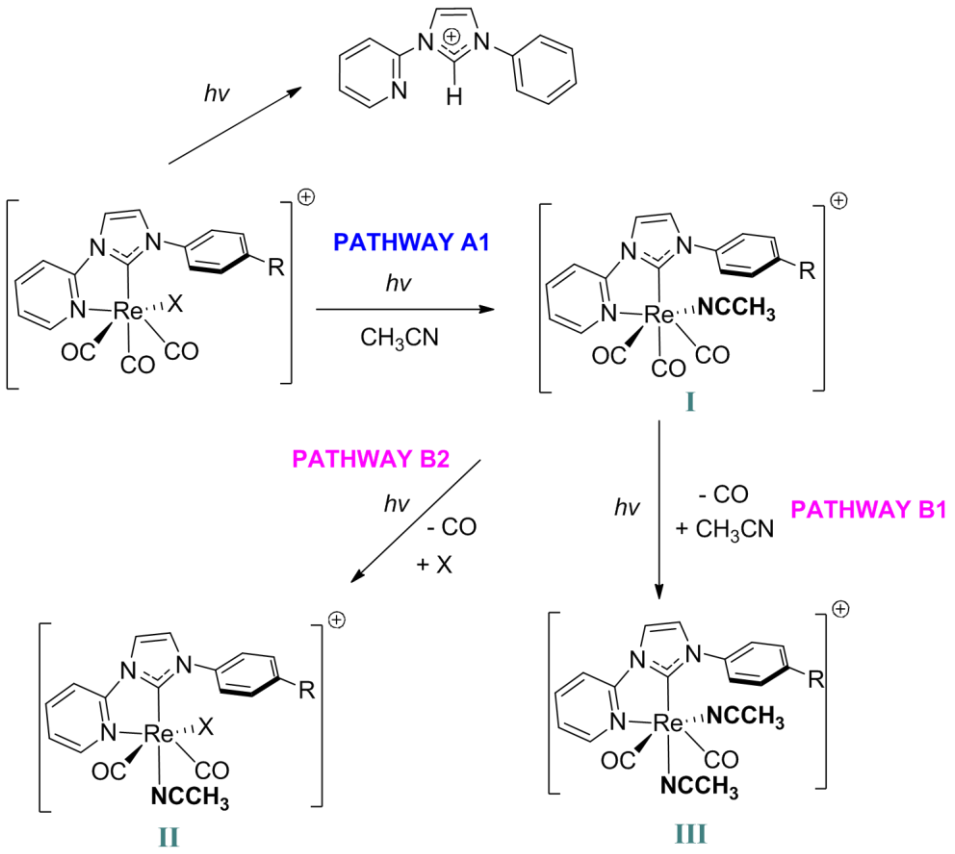

Figure 5.17 Structures of photoproducts upon irradiation of [Re(**PyImPh**OMe)$(CO)_3$X] with UV light in a solution of MeCN.

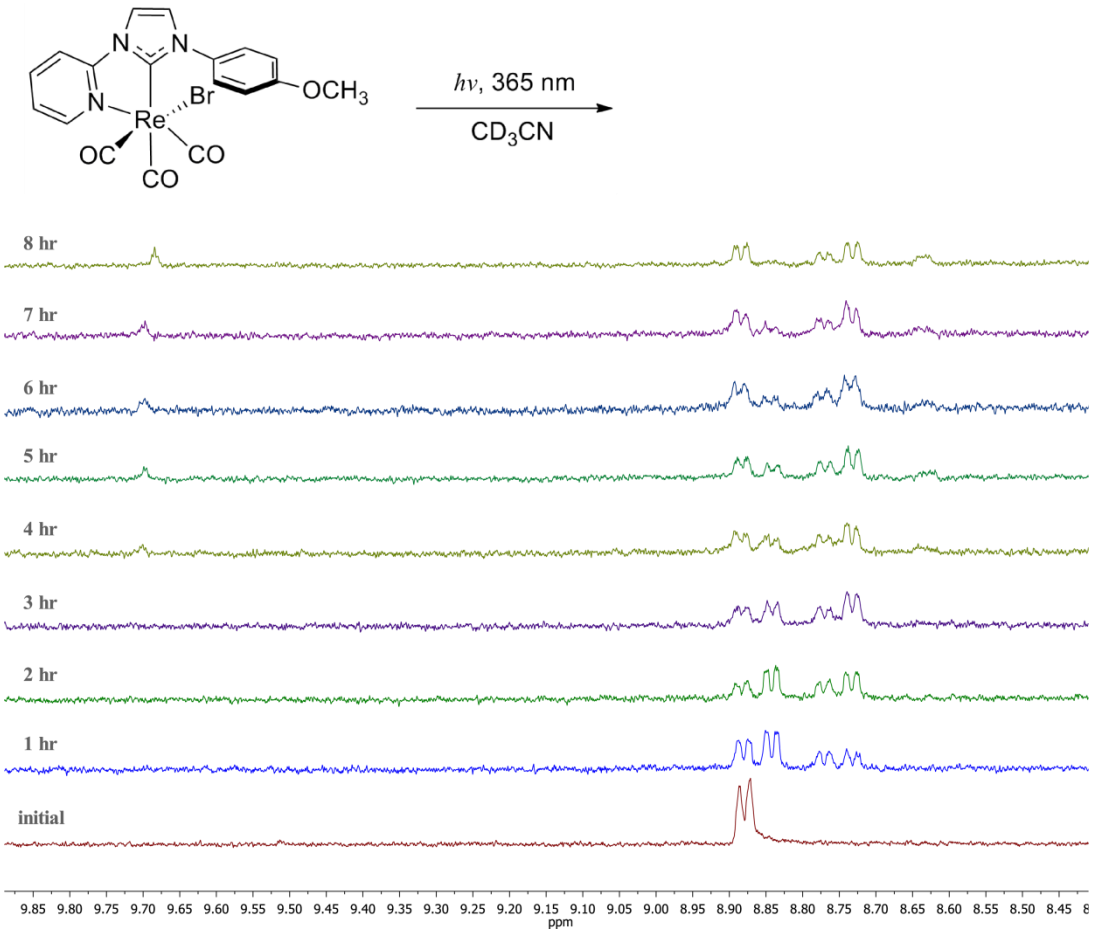

Figure 5.18 ^{1}H NMR spectra (stacked) monitoring photolysis of [Re(**PyImPh**OMe)(CO)$_3$Br] in CD_3CN.

Photolysis (λ_{ex} = 365 nm) of [Re(**PyImPh**OMe)(CO)$_3$Br] in CD_3CN over the duration of 8 hours is depicted in **Figure 5.18**. There is a disappearance of the doublet peak at 8.88 ppm (assigned to the pyridyl H6′ atom) and an appearance of three new upfield doublet peaks at 8.84, 8.77 and 8.73 ppm. The apparent triplet peak (low intensity) located at 9.70 ppm is assigned to the dissociation of the imidazolium salt, which has been evident in previous photolysis experiments as discussed in the previous chapter. The peak at 8.84 ppm is assigned as product **I** (see **Figure 5.17**) which is the intermediate [Re(**PyImPh**OMe)(CO)$_3$(CH_3CN)]$^+$ that appears after 1 hour and disappears over time to form the other products. The peak at 8.73 ppm has been assigned as product **III** (see **Figure 5.17**), i.e. the dicarbonyl species [Re(**PyImPh**OMe)(CO)$_2$(CH_3CN)$_2$]$^+$. The other photoproduct (minor) at 8.77 ppm could then be identified as product **II**, i.e. [Re(**PyImPh**OMe)(CO)$_2$(CH_3CN)(X)]$^+$.

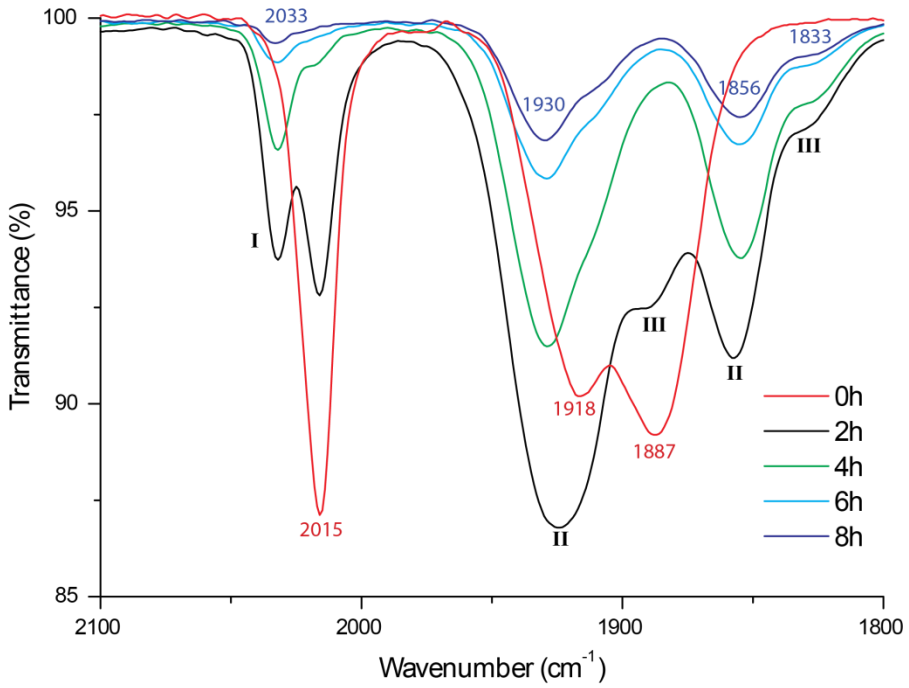

Figure 5.19 IR spectra over 8 hour photolysis of [Re(**PyImPh**OMe)$(CO)_3$Br] in CD_3CN.

Analysis of IR spectrum (**Figure 5.19**, black trace) before photolysis displays CO bands at 2015, 1918 and 1887 cm^{-1}, corresponding to the initial tricarbonyl complex. Whereas, after photolysis the CO bands shift to higher wavenumbers at 2033 (weak), 1930 and 1856 cm^{-1}. After 2 hours of irradiation (red trace), formation of intermediate product **I** was apparent through the growth of a band at 2032 cm^{-1}. This was also present alongside starting material indicated by the two CO bands at 2016 and 1888 cm^{-1}. After 4 hours (green trace), the peaks representing the starting material had completely disappeared, which meant the tricarbonyl complex was no longer apparent. However in the ^1H NMR spectrum, the peak attributed to starting material still appear to be present with a mixture of photoproducts. Only after 8 hours of irradiation did the dissociation of CO complete to form a dicarbonyl complex as product **II** (blue trace). This was also evident in the ^1H NMR spectrum, where the peak at 8.84 ppm (assigned to product **I**) completely disappeared, which confirmed a completely new product had formed.

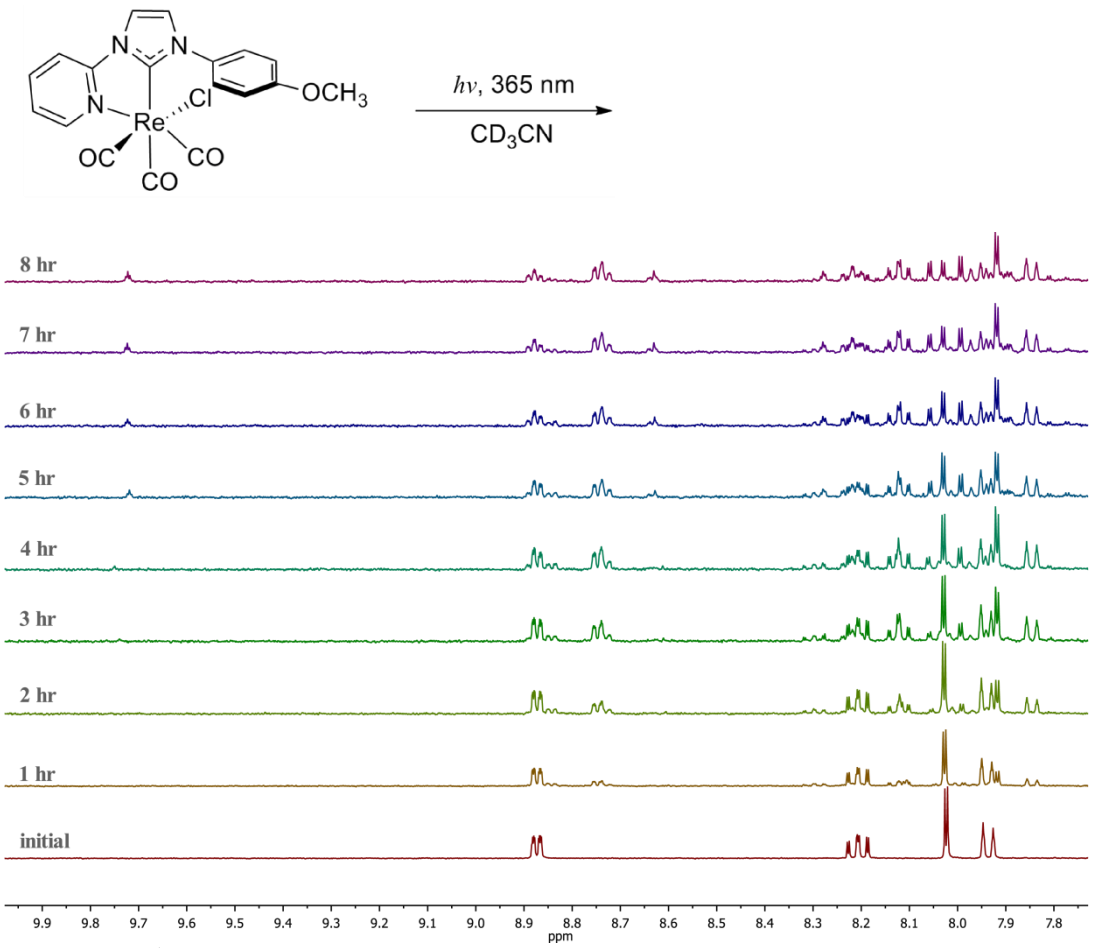

Figure 5.20 ^{1}H NMR spectra (stacked) monitoring photolysis of [Re(**PyImPh**OMe)(CO)$_3$Cl] in CD_3CN.

Photolysis (λ_{ex} = 365 nm) of [Re(**PyImPh**OMe)(CO)$_3$Cl] in CD_3CN is depicted in **Figure 5.20**. There was a disappearance of the doublet peak at 8.88 ppm (assigned to the pyridyl H6′ atom) and a very slow appearance of two new doublet peaks. In comparison to the bromo analogue, the rate of disappearance of the peak appears much slower for the chloro. It was hypothesised that the photolysis of the bromo ligand happens faster as a result of being more labile than the chloro ligand. Furthermore, evidence of the imidazolium peak at 9.70 ppm only appears after 5 hours of irradiation.

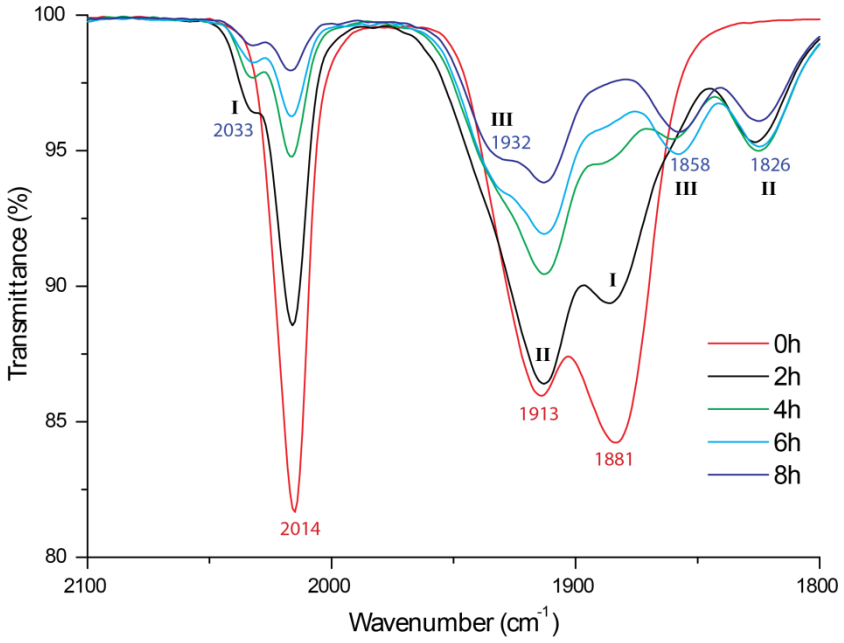

Figure 5.21 IR spectra over 8 hour photolysis of [Re(**PyImPh**OMe)$(CO)_3$Cl] in CD_3CN.

Analysis of the IR spectrum for [Re(**PyImPh**OMe)$(CO)_3$Cl] before photolysis (**Figure 5.21**, red trace) displays CO bands at 2014, 1913 and 1881 cm^{-1}. After 2 hours of irradiation (black trace), the intensities of the CO bands begin to change but no shift is apparent yet. After 4 hours of irradiation (green trace), the band at 1881 disappears and the growth of a new set of CO bands at 1858 and 1826 cm^{-1} was evident. Alongside the low intensity peak at 2014 cm^{-1}, there also appears to be a shoulder band at 2033 cm^{-1}. This low intensity shoulder peak can be assigned to the intermediate product, i.e. the acetonitrile solvato complex **I**. The dicarbonyl product **II** corresponds to the CO bands at 1913 and 1826 cm^{-1}, which have been similarly reported by Vaughan.[208] Thus, the CO bands at 1932 and 1858 cm^{-1} will be deduced as product **III**. The ^1H NMR spectrum supports the formation of a photoproduct due to the presence of two small new peaks at 8.84 and 8.74 ppm.

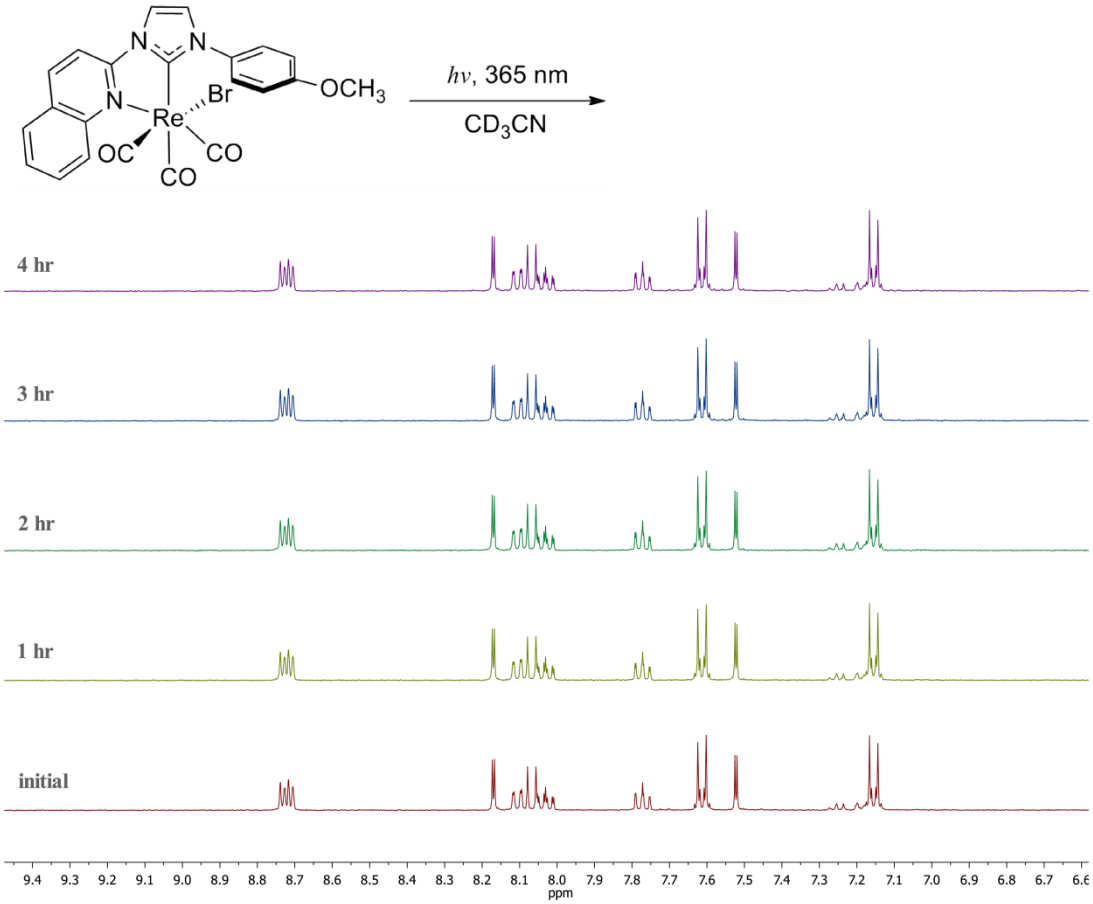

Figure 5.22 ^{1}H NMR spectra for photolysis of [Re(**QuImPh**OMe)(CO)$_3$Br] in CD_3CN.

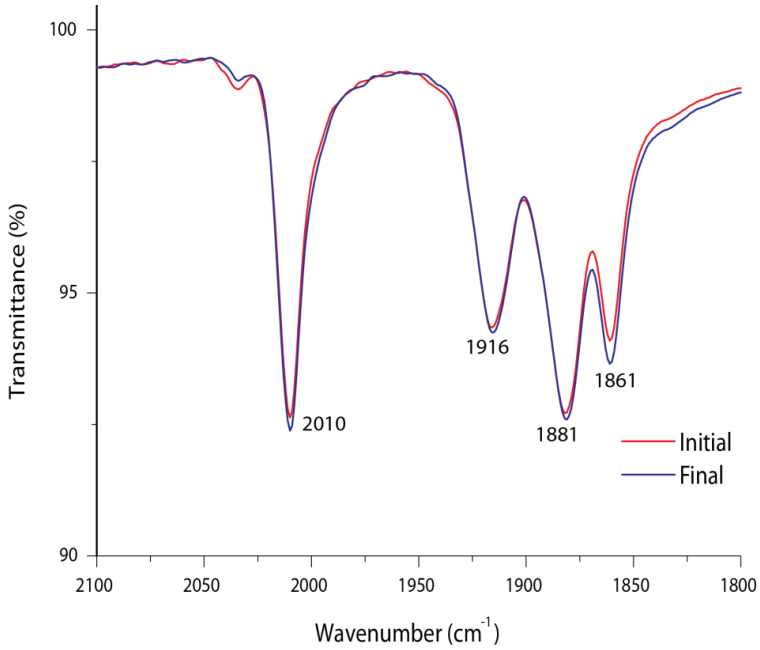

Figure 5.23 IR spectrum of [Re(**QuImPh**OMe)(CO)$_3$Br] in CD_3CN before (red) and after (blue) photolysis.

Photolysis (λ_{ex} = 365 nm) of [Re(**QuImPh**OMe)$(CO)_3$Br] in CD_3CN was depicted in **Figure 5.22** and showed no spectral changes in the ^{1}H NMR. Analysis of the IR spectrum of the photolysed species shows four distinguishable CO stretches at 2010, 1916, 1881 and 1861 cm^{-1} which were also present in the initial sample before photolysis. This IR data (**Figure 5.23**) seems to be consistent with NMR data, showing no observable spectral changes, therefore inferring no photochemical reaction to occur for this particular species. The photochemical activity of [Re(**QuImPh**OMe)$(CO)_3$Br] in deuterated acetonitrile was also consistent with previous studies by Vaughan, who found that both quinolinyl and quinoxlinyl rhenium(I)-NHC complexes were not photoactive and do not participate in PLS reactions under these conditions.[148]

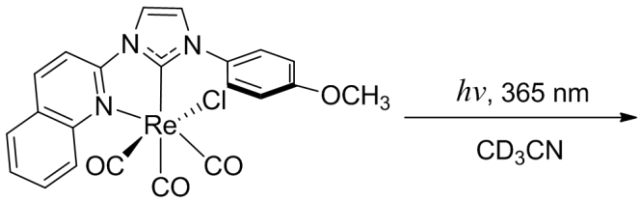

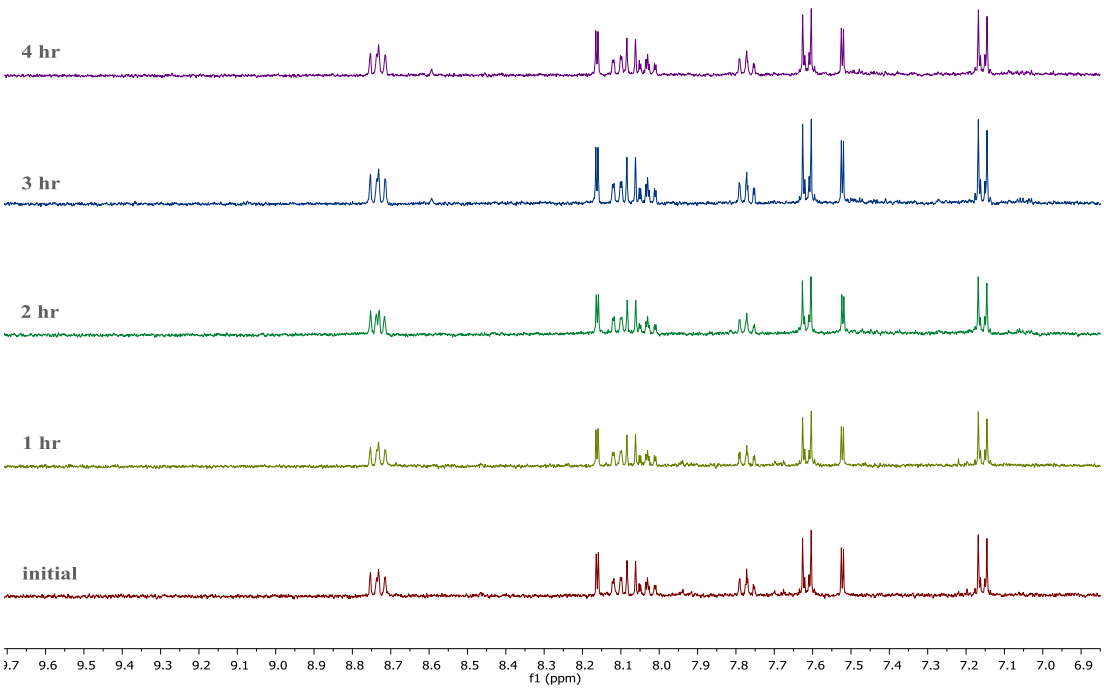

Figure 5.24 ^{1}H NMR spectra (stacked) monitoring photolysis of [Re(**QuImPh**OMe)$(CO)_3$Cl] in CD_3CN.

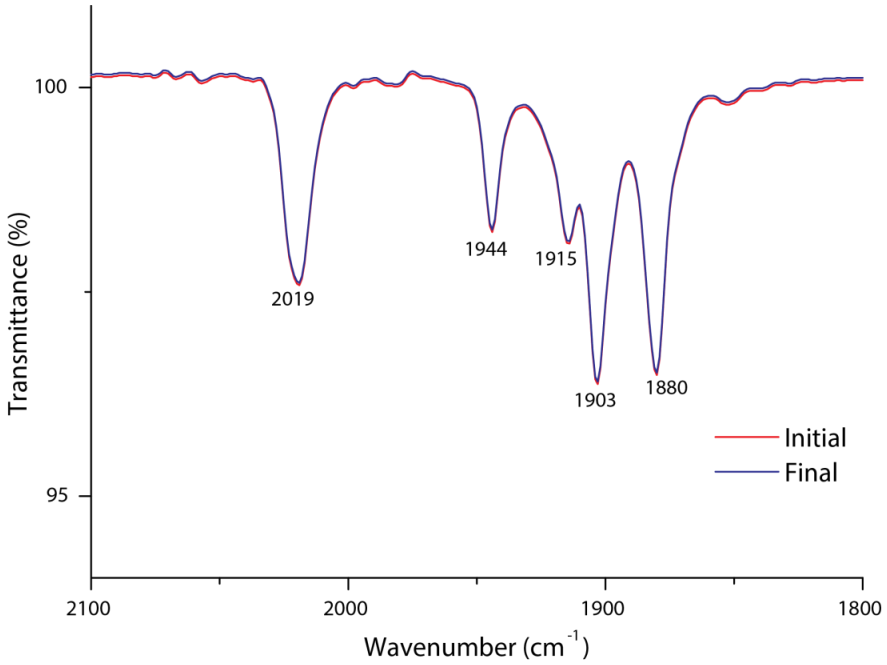

Figure 5.25 IR spectrum of [Re(**QuImPh**OMe)$(CO)_3$Cl] in CD_3CN before (red) and after (blue) photolysis.

Photolysis (λ_{ex} = 365 nm) of [Re(**QuImPh**OMe)$(CO)_3$Cl] in CD_3CN was depicted in **Figure 5.24** and also showed no spectral changes in the ^{1}H NMR, which was consistent with the bromo analogue. In addition, the IR spectrum (**Figure 5.25**) of the complex before photolysis is superimposable to that after photolysis. This suggests no photochemical reactivity which is consistent to the bromo analogue.

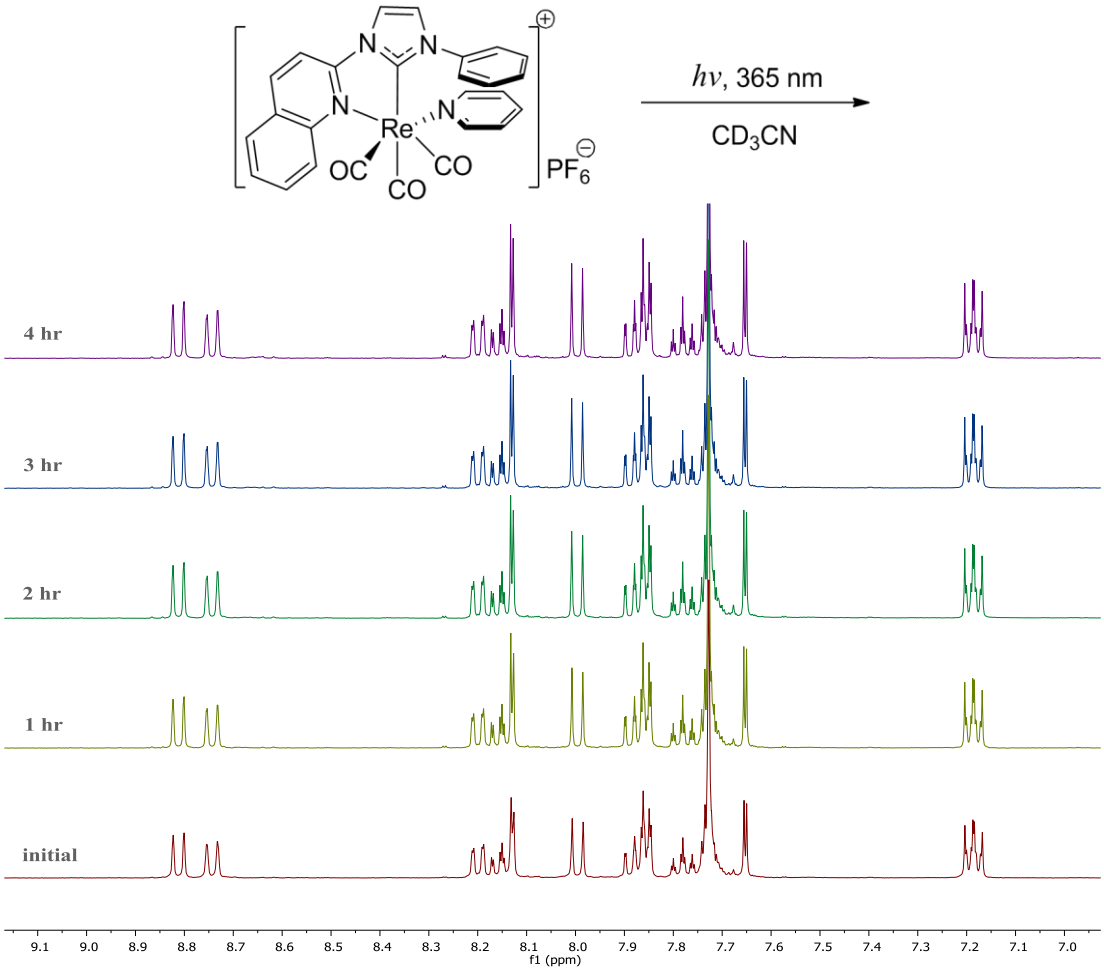

Figure 5.26 ^{1}H NMR spectra (stacked) monitoring photolysis of [Re(**QuImPh**)$(CO)_3$(Py)]$^{+}$ in CD_3CN.

Furthermore, photolysis (λ_{ex} = 365 nm) of the cationic pyridine-solvate complex [Re(**QuImPh**)$(CO)_3$(Py)]$^{+}$ in CD_3CN also shows no visible photochemical reaction upon analysing the ^{1}H NMR spectrum in **Figure 5.26**. This was also consistent with the IR data presented in **Figure 5.27**. It was assumed that the cationic complex would be more photosensitive and follow the same trend as the pyridyl complexes in Chapter 4. This was derived from the blue-shifted emission and greater HOMO-LUMO energy gap, which would indicate the energy of the MLCT state to be higher and thermally accessible to the MLCT(2) state. However, this was not the case as the determining factor for photochemical reactivity is the chelating ligand and not the ancillary ligand. It has already been established that quinolynl type complexes do not undergo PLS. This was evident in both the ^{1}H NMR and IR spectrum shown in **Figure 5.26** and **Figure 5.27** respectively.

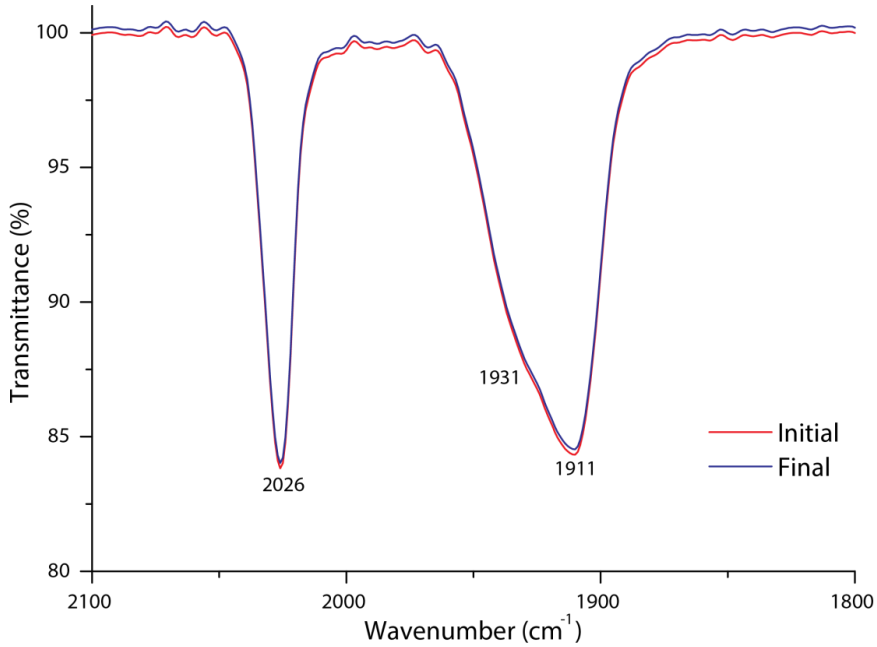

Figure 5.27 IR spectrum of [Re(**QuImPh**)$(CO)_3$(Py)]$^+$ in CD_3CN before (red) and after (blue) photolysis.

5.7 Conclusion

The photophysical properties of four new methoxy substituted rhenium(I)-NHC complexes **37Br/Cl** and **38Br/Cl**, were investigated and found to perform similar to their analogues without the methoxy group. The emission maxima did not significantly differ upon changing the substituent on the phenyl ring. This indicates that introducing a substituent on the phenyl ring of the imidazolium frame has no significant effect on the HOMO, and hence the MLCT transitions are similar. This was attributed to the phenyl ring not lying completely co-planar with the imidazole-pyridyl system. Both the pyridyl and quinolinyl series were found to be emissive at room temperature (originating from ^{3}MLCT state) in both DCM and MeCN solutions. The emission maximum was observed to red shift for the quinolinyl complexes (**38Br/Cl**) as the N-donor ring was more electron deficient and more conjugated compared to the pyridine complexes (**37Br/Cl**). Furthermore, modifications to the halo ancillary ligand did not affect the photophysical properties significantly (which had also been demonstrated in previous publications by Vaughan). In addition, all the complexes had apparent solvatochromic behaviour, where the broad emission band slightly blue shifts by 5-10 nm for each complex

upon changing the solvent from dichloromethane to more polar acetonitrile. As this broad band does not appear in the absorption spectra of the ligand precursors, it is attributed to a MLCT transition from the rhenium metal centre to the NHC ligand.

The photochemical reactivity for complexes **37Br/Cl** were found to perform similarly to complexes **22Br/Cl** reported by Vaughan and co-workers.[148,149,189] This was also reflected in the photophysical data presented, as the only difference was the introduction of a methoxy group onto the phenyl ring of the **PyImPh** frame. Similarly, the photolysis of the bromo analogue reacted faster than the chloro in acetonitrile due to differences in lability. On the other hand, the quinolynyl type complexes **38Br/Cl** did not react under photochemical conditions.

X-ray crystallography data shows that the phenyl ring on the **PyImPh** moiety is not co-planar with the imidazole and N-donor ring; they can be considered as a separate aromatic system to the heterocyclic ring system which could potentially affect the photophysical properties.

The intended target phenol-NHC derivatives could not be synthesised successfully, despite various attempts towards the product. Future work to consider would be to first synthesise a compound with an acetyl group which then could hydrolyse to form the phenol analogue (see **Scheme 5.8**). The photophysical, photochemical and acid/base chemistry properties should then be explored.

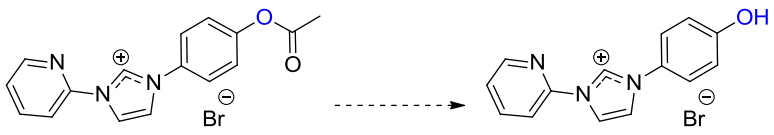

118 **117**

Scheme 5.8 Reaction scheme towards formation of compound **117**.

Another alternative would be to synthesise an amide- or ester-based NHCs similar to those reported by Chan *et al.* in **Figure 5.28**. The authors' intent was to design luminescent rhenium(I) NHC complexes for biological imaging and sensor applications.[209] This stategy could be used for preparing azolium salts conjugated to biomolecules in the future.

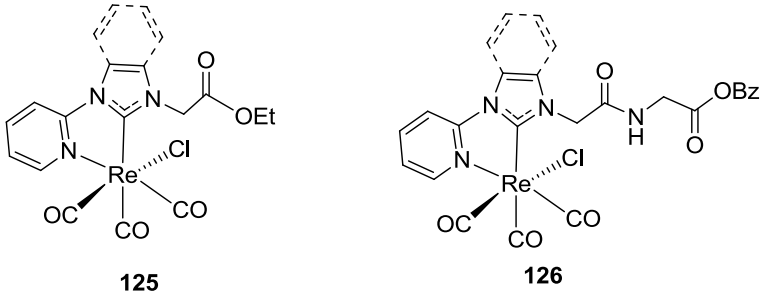

Figure 5.28 Luminescent rhenium(I) complexes with ester and amide based NHC ligand.

Further investigation on the cationic complexes such as **39Py** is required to assess the excited states of those non-photoactive quinolynyl complexes. Furthermore, synthesis and characterisation of the methoxy analogues **37Py** and **38Py** (coordinated to pyridine solvate) would provide a good comparison in terms of their photophysical and photochemical properties.

5.8 Experimental

1-(4-Methoxyphenyl)-imidazole was prepared using published procedures. [205]

5.8.1 General procedure for the Synthesis of Imidazolium Salts:

A mixture of the corresponding imidazole (1.0 eq) and halogenated pyridine or quinoline (1.1 eq) were heated in a sealed vessel at 170 °C neat for 2 days. After cooling down at room temperature, DCM was added to the reaction mixture and the insoluble solids present were collected *via* vacuum filtration. A saturated aqueous solution of KPF_6 was added to a methanolic solution of the imidazolium salt to afford fluffy precipitate. The precipitate was collected by vacuum filtration and dried to afford the product.

1-(2-pyridyl)-3-(methoxyphenyl)imidazolium bromide, [PyImHPhOMe]Br

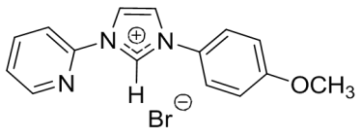

Pale yellow powder (182 mg, 27%); m.p. 231-235 °C. ^{1}H NMR (δ, ppm, DMSO-d_6): 10.53 (1H, app. s, imidazolium **H2**), 8.76-8.67 (2H, 2 × m, **H5** and **H6′**), 8.50 (1H, s, **H4**), 8.27 (1H, app. t, *J* = 8.2 Hz, **H5′**), 8.18 (1H, d, *J* = 8.0 Hz, **H3′**), 7.93-7.83 (2H, m, phenyl C**H$_o$**), 7.71-7.67 (1H, m, **H4′**), 7.30-7.20 (2H, m, phenyl C**H$_m$**), 3.87 (3H, s, OC**H**$_3$). ^{13}C NMR (δ, ppm, DMSO-d_6): 160.3 (phenyl quat. **C**), 149.3 (**C6′**), 146.3 (pyridyl quat. **C**), 140.6 (**C5′**), 133.9 (imidazole **C**H), 127.7 (phenyl quat. **C**), 125.4 (**C4′**), 123.8 (phenyl **C**H$_o$), 122.5 (**C4**), 119.7 (**C5**), 115.1 (phenyl **C**H$_m$), 114.7 (**C3′**), 55.81 (O**C**H$_3$). Elemental Analysis: Calc for $C_{15}H_{14}N_3BrO$; C (54.23%), H (4.25%), N (12.64%); found: C (51.50%), H (4.30%), N (11.97%).

1-(2-quinolynyl)-3-(methoxyphenyl)imidazolium chloride, [QuImHPhOMe]Cl

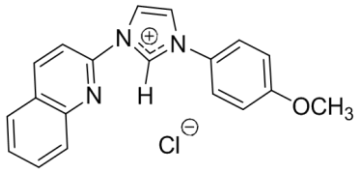

Dark grey-brown solid (140 mg, 75%); m.p. 237-243 °C. ^{1}H NMR (δ, ppm, DMSO-d_6): 10.69 (1H, br. s, imidazolium **H2**), 8.87-8.85 (2H, m, **H4** and **H11**), 8.54 (1H, br s, imid. **H5**), 8.31 (1H, d, *J* = 8.8 Hz, quin. **H6**), 8.18-8.12 (2H, m, quin. **H7** and **H8**), 7.98-7.90 (3H, m, quin. **H10** and phenyl C**H$_o$**), 7.80-7.76 (1H, m, quin **H9**), 7.25 (2H, d, *J* = 8.0 Hz, phenyl C**H$_m$**), 3.88 (3H, s, OC**H**$_3$). ^{13}C NMR (δ, ppm, DMSO-d_6): 160.4 (phenyl quat. **C**), 145.6 (quinolyl quat. **C**), 145.2 (quinolyl quat. **C**), 141.3 (**C4**), 134.4, 131.8 (**C10**), 128.3 (**C9**), 128.1 (**C7**), 127.9 (**C8**), 127.7 (phenyl quat. **C**), 123.8 (phenyl **C**H$_o$), 122.6 (**C5**), 119.8 (**C11**), 115.1 (phenyl **C**H$_m$), 112.8 (**C6**), 54.9 (O**C**H$_3$). Elemental Analysis: Calc for $C_{19}H_{16}N_3ClO$; C (67.74%), H (4.78%), N (12.46%); found: C (66.69%), H (4.73%), N (12.34%).

5.8.2 Synthesis of Complexes

[Re(PyImPhOMe)Br] (37Br)

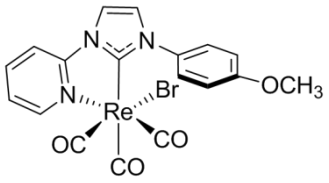

[**PyIm**H**Ph**OMe][Br] salt (41 mg, 0.123 mmol) and triethylamine (120 µL, 0.861 mmol) were stirred in toluene under nitrogen for 10 mins, then pentacarbonylrhenium bromide (41 mg, 0.123 mmol) was added to the mixture and heated to reflux for 2 days. After cooling down at room temperature, the solvent was removed *in vacuo* to afford yellow residue. This was dissolved in DCM and washed with water. The organic extract was dried over $MgSO_4$ and concentrated under reduced pressure to afford the desired compound as a yellow powder (37 mg, 49%).

ν_{max} (ATR-IR, acetone)/cm^{-1}: 2014 s (CO, A′(1)), 1882 s (CO, A″) collapsed band.

^{1}H NMR (δ, ppm, DMSO-d_6): 8.88 (1H, d, *J* = 5.6 Hz, pyridyl **H6**′), 8.66 (1H, app. s, imid. C**H**), 8.39-8.33 (2H, m, pyridyl C**H**), 7.92 (1H, app. s, imid. C**H**), 7.62-7.56 (2H, m, phenyl C**H**), 7.55-7.52 (1H, m, pyridyl C**H**), 7.21-7.13 (2H, m, phenyl C**H**), 3.84 (3H, s, OC**H**$_3$). ^{13}C NMR (δ, ppm, DMSO-d_6): 197.8 (**C**O), 196.6 (**C**O), 190.6 (N**C**N), 189.2 (**C**O), 160.3 (phenyl quat. **C**), 153.9 (pyridyl **C**H), 153.2 (pyridyl quat. **C**), 142.7 (pyridyl **C**H), 132.6 (phenyl quat. **C**), 127.9 (phenyl **C**H), 125.9 (imidazole **C**H), 124.6 (pyridyl **C**H), 118.3 (imidazole **C**H), 115.1 (phenyl **C**H), 113.6 (pyridyl **C**H), 56.10 (O**C**H$_3$). Elemental Analysis: Calc for $C_{18}H_{13}N_3BrO_4Re$; C (35.95%), H (2.18%), N (6.99%); found: C (35.75%), H (1.90%), N (6.92%).

[Re(PyImPhOMe)Cl] (37Cl)

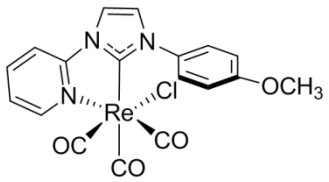

[**PyIm**H**Ph**OMe][PF_6] salt (55 mg, 0.14 mmol) and triethylamine (58 µL, 0.41 mmol) were stirred in toluene (*ca.* 10 mL) under nitrogen for 10 mins, then pentacarbonylrhenium chloride (50 mg, 0.14 mmol) was added to the mixture and heated to reflux for 2 days. After cooling down at room temperature, the solvent was

removed *in vacuo* to afford yellow residue. This was washed with water (10 mL) and extracted with DCM (5 × 10 mL) The organic extract was dried over $MgSO_4$ and concentrated under reduced pressure. The crude product was purified by a plug of deactivated acidic alumina (Brockmann III) and eluted with DCM/EtOAc (50:50). The eluted solution was concentrated *in vacuo* to afford light yellow solid (38 mg, 49%). Crystals (cubic, yellow) suitable for XRD were grown by slow evaporation of the compound in acetone.

ν_{max} (ATR-FTIR)/cm^{-1}: 2015 s (CO, A′(1)), 1916 s (CO, A′(2)), 1884 s (CO, A″).

^{1}H NMR (δ, ppm, acetone-d_6): 8.97 (1H, d, *J* = 5.6 Hz, pyridyl C**H**), 8.43 (1H, s, imid. C**H**), 8.34 (1H, app. t, *J* = 8.4 Hz, pyridyl C**H**), 8.26 (1H, d, *J* = 8.4 Hz, pyridyl C**H**), 7.73 (1H, s, imid. C**H**), 7.68-7.66 (2H, m, phenyl C**H**), 7.58 (1H, app. t, *J* = 5.6 Hz, pyridyl C**H**), 7.15 (2H, d, *J* = 8.9 Hz, phenyl C**H**), 3.90 (3H, s, OC**H**$_3$). ^{13}C NMR (δ, ppm, acetone-d_6): 199.2 (**C**O), 197.6 (**C**O), 193.5 (N**C**N), 189.9 (**C**O), 161.1 (pyridyl quat. **C**), 154.1 (pyridyl **C**H), 142.7 (pyridyl **C**H), 133.3 (phenyl quat. **C**), 128.3 (phenyl **C**H), 125.8 (imidazole **C**H), 124.7 (pyridyl **C**H), 118.4 (imidazole **C**H), 115.4 (phenyl **C**H), 113.9 (pyridyl **C**H), 56.0 (O**C**H$_3$). Elemental Analysis: Calc for $C_{18}H_{13}N_3ClO_4Re$; C (38.82 %), H (2.35%), N (7.54%); found: C (38.00%), H (2.01%), N (7.29%).

[Re(QuImPhOMe)Br] **(38Br)**

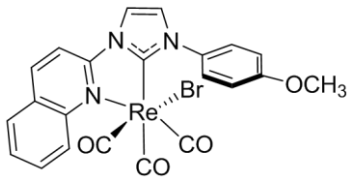

Pentacarbonylrhenium bromide (55 mg, 0.135 mmol) was added to a mixture of [**QuIm**H**Ph**OMe][PF_6] salt (50 mg, 0.112 mmol) and triethylamine (85 µL, 0.615 mmol) in toluene (*ca*. 10 mL). The reaction mixture was heated to reflux under nitrogen for 2 days. Over time, yellow precipitate formed. After heating was stopped and reaction left to cool down at room temperature, the mixture was washed with water and extracted with DCM. The dark yellow organic extracts were dried ($MgSO_4$) and concentrated under reduced pressure to afford orange-grey solid (101 mg, 90%). M.p. 258 °C (dec.).

ν_{max} (ATR-IR)/cm^{-1} (solid state): 2015 s (CO, A′(1)), 1943 s (CO), 1907 s (CO), 1882 s (CO, A″).

^{1}H NMR (δ, ppm, DMSO-d_6): 8.98 (1H, d, *J* = 8.9 Hz, quinolinyl C**H**), 8.81 (1H, s, imid. C**H**), 8.59 (1H, d, *J* = 8.8 Hz, quinolinyl C**H**), 8.51 (1H, d, *J* = 8.9 Hz, quinolinyl C**H**), 8.22 (1H, d, *J* = 8.2 Hz, quinolinyl C**H**), 8.11-8.07 (1H, m, quinolinyl C**H**), 7.98 (1H, s, imid. C**H**), 7.84-7.80 (1H, m, quinolinyl C**H**), 7.61 (2H, d, *J* = 8.9 Hz, phenyl C**H**), 7.20 (2H, d, *J* = 8.9 Hz, phenyl C**H**), 3.85 (3H, s, OC**H**$_3$). ^{13}C NMR (δ, ppm, DMSO-d_6): 197.8 (**C**O), 194.6 (**C**O), 192.0 (N**C**N), 188.9 (**C**O), 160.0 (phenyl quat. **C**), 154.4 (quinolinyl quat. **C**), 145.7 (quinolinyl quat. **C**), 143.6 (quinolinyl **C**H), 132.9 (quinolinyl **C**H), 132.2 (), 129.5 (quinolinyl **C**H), 128.9 (quinolinyl **C**H), 127.7 (phenyl quat. **C**), 127.6 (quinolinyl **C**H), 126.9, 125.9 (imidazole **C**H), 118.7 (imidazole **C**H), 114.8 (phenyl **C**H), 111.9 (quinolinyl **C**H), 55.7 (O**C**H$_3$). Elemental Analysis: Calc for $C_{22}H_{15}N_3BrO_4Re$; C (40.58%), H (2.32%), N (6.45%); found: C (40.65%), H (1.98%), N (6.31%).

[Re(QuImPhOMe)Cl] (38Cl)

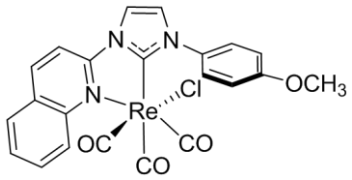

Pentacarbonylrhenium chloride (32 mg, 0.088 mmol) was added to a mixture of [**QuIm**H**Ph**OMe][Cl] salt (27 mg, 0.081 mmol) and triethylamine (57 µL, 0.415 mmol) in toluene (*ca*. 5 mL). The reaction mixture was heated to reflux under nitrogen for 2 days. Over time, brown precipitate formed. After heating was stopped and reaction left to cool down at room temperature, the mixture was washed with water and extracted with DCM. The dark yellow organic extracts were dried ($MgSO_4$) and concentrated under reduced pressure to afford yellow-grey solid (20 mg, 39%). M.p. 258 °C (dec.).

ν_{max} (ATR-IR)/cm^{-1} (solid state): 3104 w, 3052 w, 2843 w, 2014 s (CO, A′(1)), 1942 s (CO), 1912 s (CO), 1878 s (CO, A″), 1612 w, 1598 w, 1511 m, 1436 m, 1247 m, 828 w.

^{1}H NMR (δ, ppm, DMSO-d_6): 8.96 (1H, d, *J* = 8.0 Hz, quinolinyl C**H**), 8.75 (1H, s, imid. C**H**), 8.59 (1H, d, *J* = 8.0 Hz, quinolinyl C**H**), 8.47 (1H, d, *J* = 8.0 Hz, quinolinyl C**H**), 8.22 (1H, d, *J* = 8.0 Hz, quinolinyl C**H**), 8.10-8.06 (1H, m, quinolinyl C**H**), 7.94 (1H, s, imid. C**H**), 7.83-7.79 (1H, m, quinolinyl C**H**), 7.6 (2H, d, *J* = 8.0 Hz, phenyl C**H**), 7.18 (2H, d, *J* = 8.0 Hz, phenyl C**H**), 3.83 (3H, s, OC**H**$_3$). ^{13}C NMR (δ, ppm, DMSO-d_6): 198.7(**C**O), 195.3(**C**O), 193.06(N**C**N), 189.7(**C**O), 160.2 (phenyl quat. **C**), 154.4 (quinolinyl quat. **C**), 145.7 (quinolinyl quat. **C**), 143.9 (quinolinyl **C**H), 133.1 (quinolinyl **C**H), 132.3 (quinolinyl quat. **C**), 129.7 (quinolinyl **C**H), 128.9 (quinolinyl **C**H), 127.9 (quinolinyl **C**H), 127.7 (phenyl **C**H), 127.1 (phenyl quat. **C**), 125.8 (imidazole **C**H), 118.8 (imidazole **C**H), 114.9 (phenyl **C**H), 112.1 (quinolinyl **C**H), 55.8 (O**C**H$_3$), 45.9. Elemental Analysis: Calc for $C_{22}H_{15}N_3ClO_4Re$; C (43.53%), H (2.49%), N (6.92%); found: C (43.31%), H (2.38%), N (6.08%).

Chapter 6

Biological Investigation of Tetrazolato Rhenium(I) Diimine Complexes

6.1 Overview

Optical imaging is a biological imaging technique used to visualise cells and tissues and identify specific biological processes and, where relevant, disease in some cases.[210,211] This method uses the properties of harmless visible and infrared light to visualise the area of interest. Thus, optical imaging is a high resolution technique using contrast agents (which exhibit fluorescence) that can be used for basic or fundamental research, and for early disease diagnosis.[212] Previous studies have shown d^6 metal complexes as popular bioimaging agents due to their favourable photophysical properties, inertness and the fact that they prevent photobleaching.[213] These complexes can also bind to specific intracellular components *via* use of bioconjugated ligands.[214] By using metal complexes as biological imaging agents, we can develop an understanding of the mechanisms of action, uptake and localisation of specific molecules of interest.

Biological imaging experiments were conducted by incubating selected rhenium(I) complexes with malignant (lung cancer and mesothelioma) and healthy cell lines. The purpose of these experiments was to determine the behaviour of the rhenium(I) complexes in biological media. Confocal and fluorescence microscopy were used to visualise cellular uptake and intracellular localisation. Whereas, quantitative flow cytometry experiments were used to determine toxic effects investigating cell viability and induction of cell death *via* apoptosis, as well as determining the number of cells stained and staining intensity.

Biological testing and analyses of these complexes (**Figure 6.1**) were carried out by Dr Vishal Chaturvendi under the supervision of Dr Delia Nelson, within the CHIRI Biosciences Precinct (Building 305, Curtin University) laboratory facilities.

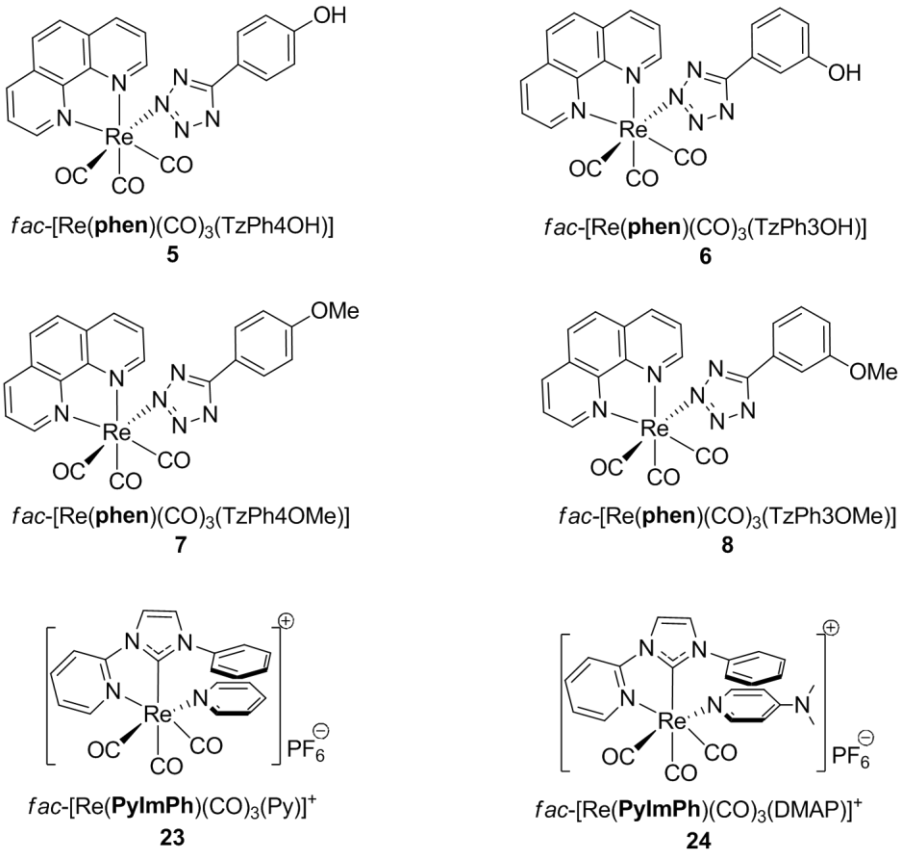

Figure 6.1 Rhenium(I) complexes investigated in this study.

6.2 Background

6.2.1 Cell Culture

Cell culture is referred to the growth of cells which have been removed from animal or plant tissue. These cells grow under certain favourable conditions within an artificial environment. Therefore, culture conditions vary and depend on the specific cell type used. The artificial environment in which cells are cultured consists of an appropriate chamber containing a suitable culture media that supplies essential nutrients (amino acids, carbohydrates, vitamins and minerals). In addition, cell growth factors are influenced by external conditions, such as temperature and humidity levels. These external conditions are controlled by using an incubator (or

humidifier), to simulate the environment experienced by cells *in vivo*. A physico-chemical environment must also be regulated through the use of buffering agents to maintain pH levels. A CO_2 atmosphere (5%) is generally required to maintain the pH of the mammalian cell culture media. The CO_2 functions as a buffer system to maintain the pH of the media at approximately 7.4. Furthermore, the temperature for mammalian cell cultures must reach 37 °C with 95% humidity.[215]

A primary culture refers to cells freshly isolated from tissue and grown *in vitro* under appropriate conditions until they reach confluence, where the cells occupy most of the available substrate, in the case of adherent cells this generally means covering (adhering to) approximately 80% of the base of the tissue culture flask. Once confluent, cells have to be subcultured by transferring a proportion of cells to a new flask with fresh growth medium to continue growth and expansion. At this stage, cells are often cloned, especially if they are tumour cells, as they were already immortalised, i.e. they undergo a process that results in the production of genetically identical cells, that are referred to as a cell line.[215,216]

The human JU77 mesothelioma cell line used in this study was derived from the pleural fluid (in the lungs) of male patients with confirmed malignant mesothelioma in 1991; the patient had known exposure to crocidolite asbestos fibres, the causative agent of mesothelioma. The morphology of JU77 cells is epithelial-like and spindle-shaped with few vacuoles.[217] As JU77 cells are tumor cells, the study also used a 'healthy' cell line for comparison. RAW264.7 cells are murine macrophages (immune cells) sourced from the peritoneal ascites (fluid) induced after intraperitoneal injection of Abselon murine leukaemia virus into a male mouse.[218]

6.2.2 Confocal Microscopy

Microscopy is a powerful optical technique used in biology to analyse and detect the structure, physiology and function of cells. In conventional "wide-field" light microscopy, the entire depth of a sample is constantly excited, which allows out-of-focus light to be detected. This causes images to appear blurry and lack contrast of fine details.

Confocal microscopy offers several advantages over conventional optical microscopy, which includes the ability to control depth-of-field, eliminate image

degrading out-of-focus information, and the ability to reconstruct a 3D view of the specimen by collecting a series of optical sections from thick specimens.[219,220] This is made possible through use of an excitation pinhole which is focussed by objective lens onto the specimen. Following this, a second pinhole positioned in front of the detector filters out-of-focus light.

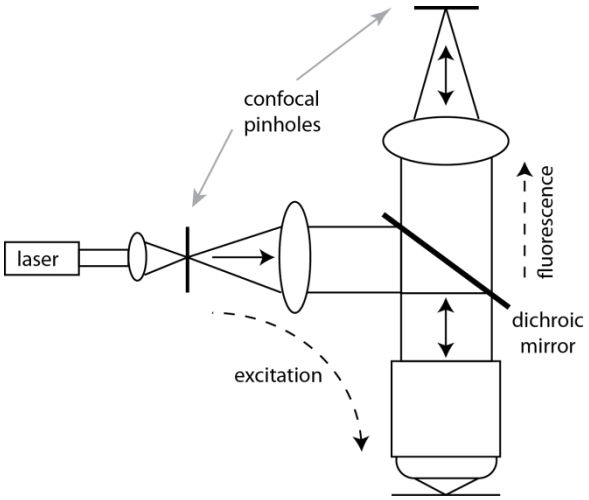

Figure 6.2 Schematic diagram of confocal fluorescence microscopy illustrating excitation of specimen by a laser.

Confocal fluorescence microscopy illuminates the specimen by use of a laser, whereby excitation of fluorophores (through absorption) causes detectable fluorescence. Light originating from the laser passes through an excitation pinhole, is reflected by a dichroic mirror and focused by a microscope objective to a small area in the specimen. The dichroic mirror reflects light of a shorter wavelength, while transmitting that of a longer wavelength. This is depicted in the schematic diagram shown in **Figure 6.2**.

6.2.3 Flow Cytometry

Flow cytometry has the ability to measure the properties of individual particles. The principles of the flow cytometer can be categorised into four main parts – the fluidics system, optics and detection, signal processing and electrostatic cell sorting. Firstly, when a sample in solution is introduced into a flow cytometer, the fluidic system transports particles from a randomly distributed sample suspension into an orderly stream of particles travelling in a single-file. Focussing particles into single-file can be achieved in one of two ways – hydrodynamic or acoustic focussing. The

hydrodynamic method uses a flowing sheath fluid to focus the sample fluid into a narrow core and the diameter can be changed depending on the pressure of the fluid used. Under optical conditions, the fluid in the central chamber will not mix with the sheath fluid. Without hydrodynamic focussing, it would not be possible to analyse individual cells at a time.

After hydrodynamic focussing, each particle is distributed through one or more light beams. Light scattering provides information about the particle's properties. Light that is scattered in the forward direction (20° offset from the laser beam's axis) is collected by the forward scatter detector (FSD). The intensity of the FSD is roughly proportional to the particle's size and can also be used to distinguish the cellular debris and living cells. On the other hand, light that is approximately 90° to the laser beam is called side scatter. The side scatter detector (SSD) provides information about the granular content and complexity of the particle.

Flow cytometers use separate channels to detect light emitted. The specificity of detection is controlled by optical filters, which block certain wavelengths while letting others pass. There are three major filter types – 'long pass' filters allows light above 500 nm to transmit, 'short pass' allows light below 560 nm and 'band pass' transmits light within a specified narrow range of wavelengths (e.g. 630/15 nm band pass permits everything in the 615-645 nm band width). When a filter is positioned at a 45° angle to the light, it becomes a dichroic mirror. This produces two functions – to pass specific wavelengths in the forward direction and deflect blocked light at a 90° angle.

Lastly, when light hits the photodetector, a small current is generated. The voltage associated with the current has an amplitude proportional to the total number of photons received by the detector. This is then converted to electrical signals that are plotted graphically on the computer system.

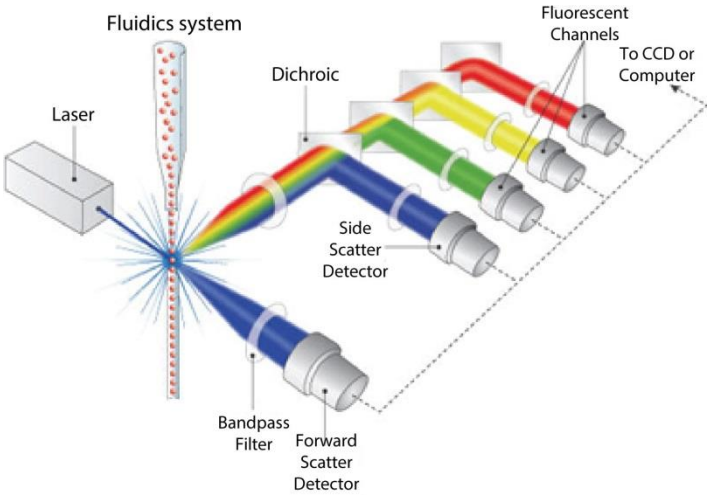

Figure 6.3 Basic schematic diagram of flow cytometry.

Flow cytometry was used to determine the spectral emission profile of each label by interrogating all channels (detectors) on a BD LST Fortessa flow cytometer; this flow cytometer has four fixed wavelength excitation lasers, i.e. red, blue, violet and UV, and can detect 18 emitted wavelength colours.

6.2.4 Rhenium(I) Complexes in Optical Imaging

Typical phosphorescent complexes used for cell imaging are based around the rhenium(I) tricarbonyl frame with varying polypyridyl chelating ligands. These neutral complexes [Re(**N^N**)$(CO)_3$X] (X = Br, Cl) usually possess long excited state lifetimes in the order of hundreds of ns and quantum yield in the 0.1% range. These photophysical properties make them applicable in the field of biological imaging.

The first rhenium complex appropriate for optical imaging was reported in 2004 from the work of Zubieta *et al.* [214] The structure of the metal complex was based around the rhenium(I) tricarbonyl frame with quinoline ligands conjugated to a small peptide (see **Figure 6.4**). This peptide was initially used as a targeting vector in radioimaging. After the complex was incubated in human leukocytes, fluorescence microscopy revealed localisation on the edge of the leukocytes (see **Figure 6.5**). The authors of the paper concluded that this complex has suitable luminescence properties for *in vitro* microscopy studies.

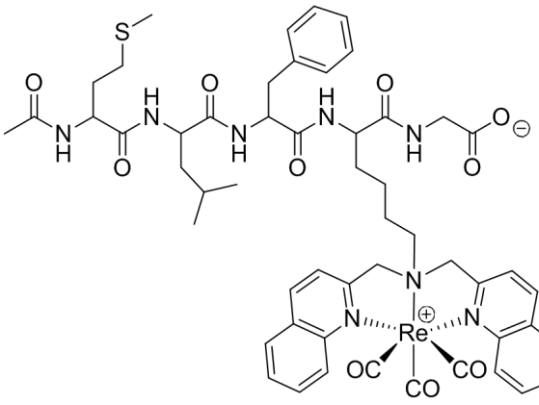

100

Figure 6.4 Structure of complex **100** conjugated to a peptide.

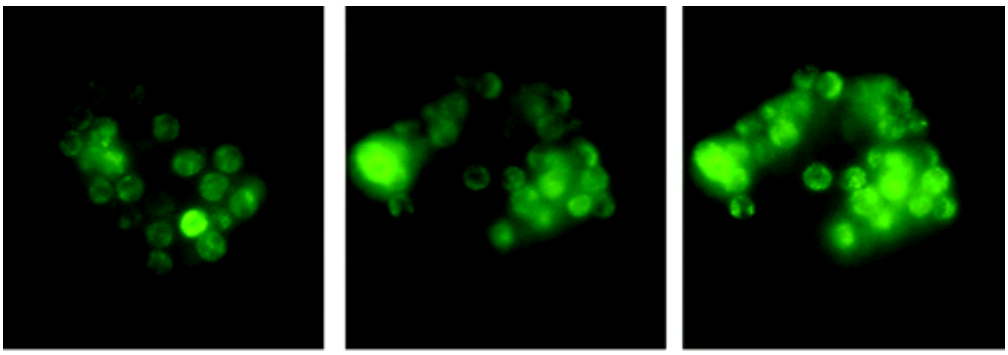

Figure 6.5 Fluorescence microscopy images of human leukocytes incubated with varying concentrations (1-50 nM) of complex **100**. **[**Reproduced with permission from ref[214]**].**

The majority of subsequent studies focussed on diimine ligands such as **bipy** or **phen** rather than bisquinoline ligands. This was influenced by the fact that complexes with quinoline ligands require a shorter wavelength (such as 360 nm in this case) which makes it undesirable in terms of tissue penetration and damage.

The same rhenium(I) tricarbonyl frame comprised of **bipy** and various substituted **phen** as well as incorporating a variety of pyridyl ancillary ligands. An example of the very first luminescent complex to target specific organelles (such as the mitochondria) was discovered by Coogan *et al* in 2007 (which has been mentioned in the general introduction section).[9,15] The structure of the rhenium(I) **bipy** complex is shown in **Figure 6.6**. The specificity of complex **45** was incubated with yeast and did not show significant uptake. However, when incubated with human breast adenocarcinoma MCF-7 cells, distinct uptake and localisation was observed (see **Figure 6.7**). Confocal microscopy studies showed the complexes retained fluorescence in biological environments, proving that rhenium(I) diimine complexes are viable as biological probes for imaging.

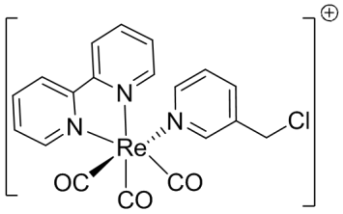

45

Figure 6.6 Structure of chloromethyl rhenium complex.

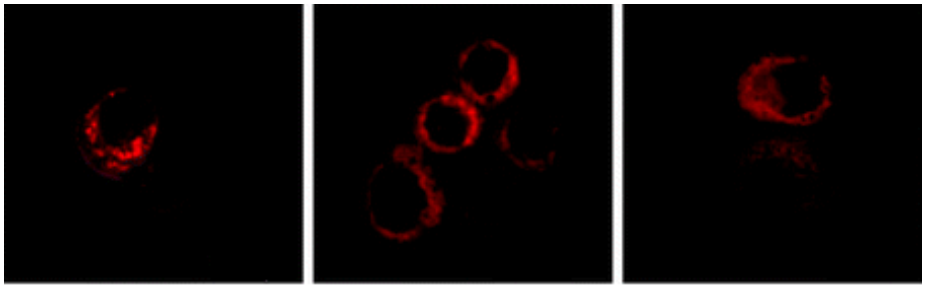

Figure 6.7 Confocal fluroescence microscopy images of complex **45** incubated with MCF-7 cells. **[**Reproduced with permission from ref[9]].

In 2012, a series of tricarbonyl rhenium(I) **bipy** complexes coordinated to *meta*- and *para*- bioconjugated pyridyl derivatives (see **Figure 6.8**) were investigated by Fernandez-Moreira *et al.*[221] The authors of the publication demonstrated that ligand design of the complex was vital towards the application of either cell imaging or phototherapy. The results revealed that even the slightest change in ligand structure can result in varying biological properties. The photophysical properties of these complexes displayed bright emission (*ca*. 540 nm), long lifetimes (270-370 ns) and large Stokes shift (>140 nm) which suggests these bioconjugated complexes could make strong candidates for cell imaging. The complexes were incubated with MCF-7 cells and displayed clear uptake, however the effect on the cells were significantly different between the *para*- **Re(1-3)** and *meta*- **Re(4-6)** substituted analogues.

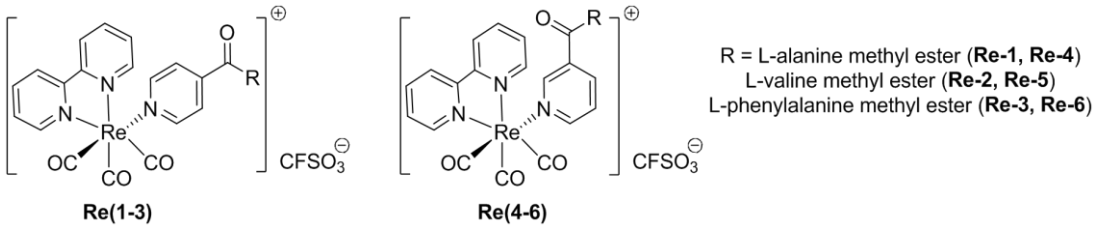

Figure 6.8 Structure of rhenium(I) coordinated to *para*- **Re**(**1-3**) and *meta*- **Re**(**4-6**) bioconjugated pyridyl derivatives.

The *para*- derivatives suffered photobleaching upon irradiation, damaged cell structure and promoted cell death; clusters of dead cells were observed (see **Figure**

6.9). On the other hand, the *meta*- derivatives demonstrated passive uptake mechanism in cells that localised to the cytoplasm. No photobleaching, cell clustering or phototoxicity was evident. **Figure 6.10** shows cytoplasmic staining in the cells.

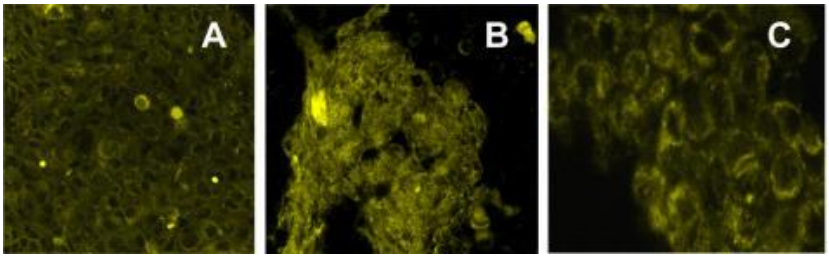

Figure 6.9 Cell imaging with complexes Re-1 to Re-3 (A-C, respectively) showing clustering [reprinted with permission from ref [221]].

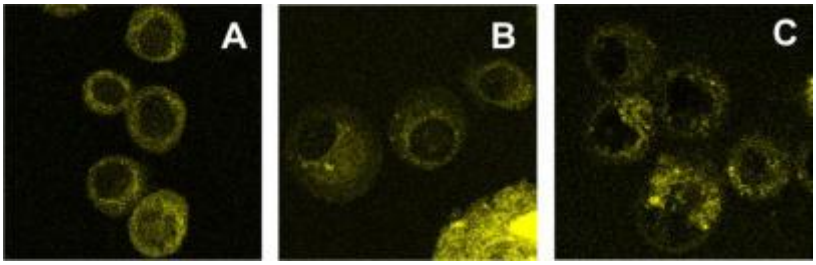

Figure 6.10 Cell imaging with complexes Re-4 to Re-6 (A-C, respectively) showing localisation [reprinted with permission from ref [221]].

6.3 Results and Discussion

6.3.1 Lipophilic Character of the Rhenium(I) Complexes

In order to evaluate the potential of the complexes to be incubated in cell culture, it is vital to assess their lipophilic character. The *n*-octanol/water distribution coefficients (log $D_{7.4}$) of the complexes were measured using the shake-flask method[110,222] and are summarised in **Table 6.1**. The cellular uptake is usually related to the overall charge of the complex, the size and substituent group attached. In this case, all the complexes demonstrated similar values to other neutral rhenium(I) diimine complexes in the range of 1.63 to 2.66 reported in literature.[222] Moreover, the substituent type (OH or OMe) did not appear to significantly alter the lipophlicity.

Table 6.1 Distribution coefficient (log $D_{7.4}$) values for the complexes obtained from *n*-octanol/water solutions.

Complex	log $D_{7.4}$
[Re(**phen**)$(CO)_3$(**Tz**Ph4OH)] (**5**)	1.55 ± 0.03
[Re(**phen**)$(CO)_3$(**Tz**Ph3OH)] (**6**)	2.10 ± 0.08
[Re(**phen**)$(CO)_3$(**Tz**Ph4OMe)] (**7**)	1.49 ± 0.05
[Re(**phen**)$(CO)_3$(**Tz**Ph3OMe)] (**8**)	1.25 ± 0.05

6.3.2 Flow Cytometry Analysis

The cellular uptake characteristics were investigated further by flow cytometry techniques. Flow cytometry was used to detect the level of fluorescence emitted by the rhenium(I) complexes that were associated with viable JU77 and/or RAW264.7 cells. **Figure 6.11** below shows representative plots of gated viable cells (stained with Zombie NIR) at varying concentrations of 5, 10 and 20 µM, which emit luminescence excited by the violet laser and are detected in the 605/12 nm channel. The data is read similarly to a histogram and displays the population of cells which are luminescent in that particular channel.

An increase in concentration leads to increase in emission intensity of the complexes inside the cells. Complex **5** (**Figure 6.11**a) was weakly emissive with only a low cell number of stained viable cells detected (1071 cells) that were above the control cells. In comparison to its *meta* derivative **6** (**Figure 6.11**b) that demonstrated a higher number of brightly stained cells relative to the controls (26533 cells). On the other hand, complex **7** (**Figure 6.11**c) demonstrated a clear dose-related staining response with a medium count of 3457 emissive cells, whilst its *meta* derivative **8** (**Figure 6.11**d) also showed a clear dose-related staining response with the two higher concentrations delivering very bright signals in association with a higher count of 10492 stained cells. Full statistical data are tabulated and can be referred to in Appendix D. These results were interesting as they showed discrepancies when comparing the methoxy- analogues **7** and **8** to the phenol- analogues **5** and **6**, even though the photophysics data showed that they emitted at the same wavelength (λ_{em} = 600 nm) after excitation by light (λ_{ex} = 350 nm). In addition, the position of the

phenol group seemed to have a significant effect as shown in the flow cytometry data below (**Figure 6.11**a and b). Particularly, the phenol group which was positioned *para* (**5)** to the tetrazole showed very few cells to be emissive. On the other hand, the *meta*-phenol analogue **6** showed more fluorescent cells.

This is not a unique finding as it has previously been reported in the literature by Fernandez-Moreira *et al*. which confirmed that having identical substituents in different positions can vary the biological properties.[221] Even though the substituents were identical and the complexes had similar solubilities and lipophilicities, the emission intensities within the cells varied.

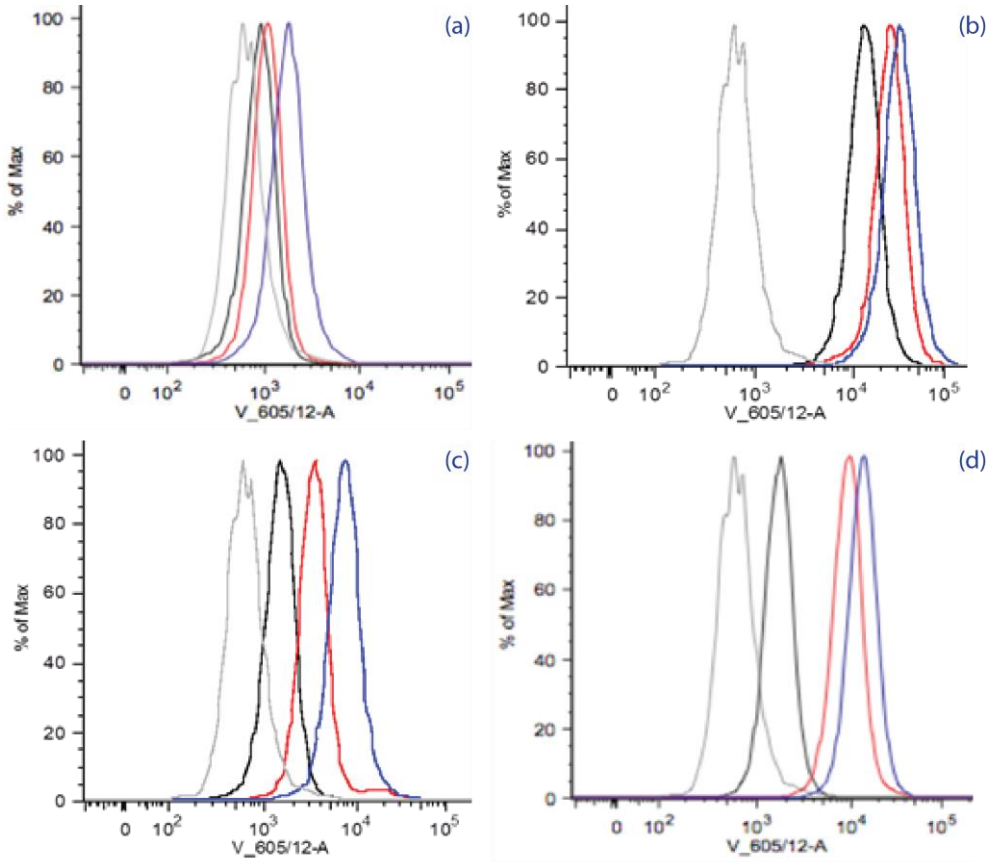

Figure 6.11 Representative flow cytometry histogram data of mean fluorescence intensities for JU77 cells stained with complexes **5-8** (a to d, respectively) at 5 µM (black), 10 µM (red), 20 µM (blue) compared to control cells (grey) that were not stained with a rhenium(I) complex. All cells were stained with Zombie NIR to detect gate viable cells. The data are representative from reproducible experiments performed three times.

For rhenium(I) complexes **23** and **24**, it appeared that very few cells were emissive upon increasing concentration up to 10 µM (see **Figure 6.12**). Either the emission was short-lived, or it could be that the complexes did not efficiently enter the cells.

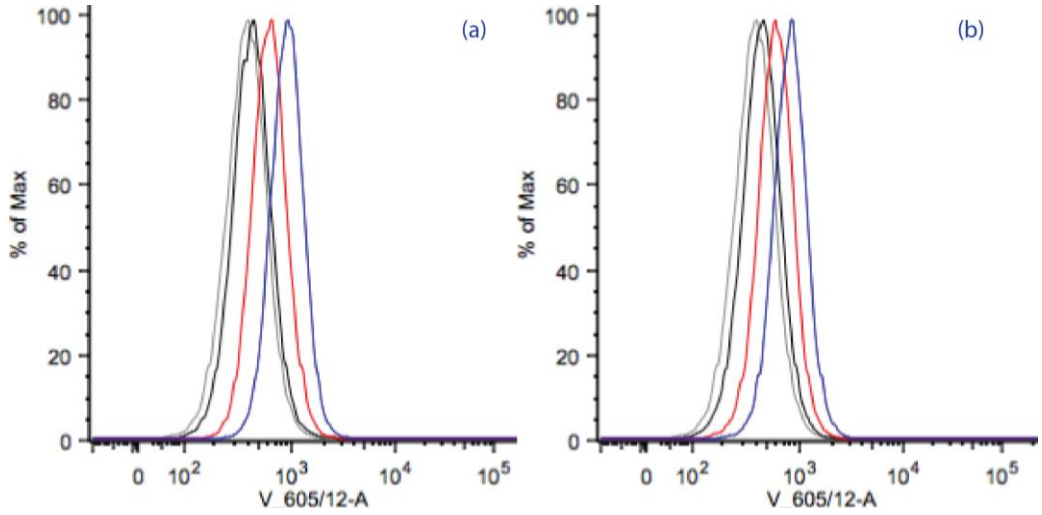

Figure 6.12 Representative flow cytometry histogram data of mean fluorescence intensities for RAW264.7 cells stained with complexes **23** (a) and **24** (b) at 1 µM (black), 5 µM (red), 10 µM (blue) compared to control cells (grey) that were not stained with a rhenium(I) complex. All cells were stained with Zombie NIR to detect gate viable cells. The data are representative from reproducible experiments performed three times.

6.3.3 Confocal Imaging of Complexes

The application of these complexes in luminescence imaging of RAW264.7 cells was investigated by the use of a spinning disk confocal microscope. Approximately 30 minutes after incubation with the rhenium(I) complexes, the cells were visualised. Confocal microscopy imaging for [Re(**phen**)$(CO)_3$(**Tz**Ph4OH)] (**5**), [Re(**phen**)$(CO)_3$(**Tz**Ph3OH)] (**6**), [Re(**phen**)$(CO)_3$(**Tz**Ph4OMe)] (**7**) and [Re(**phen**)$(CO)_3$(**Tz**Ph3OMe)] (**8**) are depicted in **Figure 6.13**. Examination of individual cells showed a generalised staining pattern for all rhenium labels, with plasma membranes emitting a strong emissive signal and the nuclear region showing no uptake. Localisation of these rhenium(I) complexes appears specifically outside of the nucleus. Complexes **6-8** emit a bright emissive signal, whilst complex **5** shows weaker emission, which was also reflected in the flow cytometry data (**Figure 6.11**a). Interestingly, even though the photophysical data of these complexes appear to have similar emission profiles, the imaging data shown in **Figure 6.13** does not reflect this trend. This would suggest that the anomaly of complex **5** could be due to the phenolic OH group reacting within the cells, resulting in emission quenching. Or, it may have difficulty entering the cells which was reflected in the low cell count from the flow cytometry analysis.

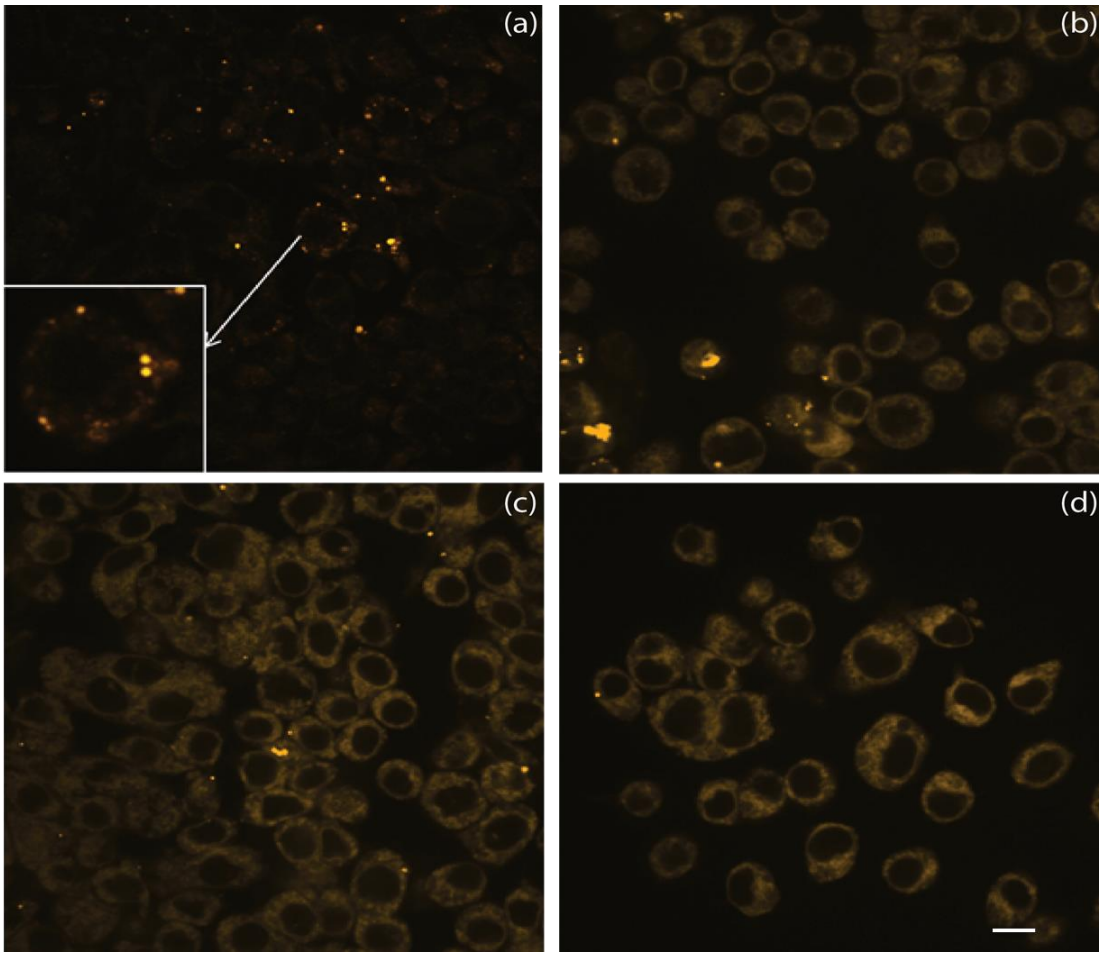

Figure 6.13 Microscopy imaging for complexes **5-8** (a to d, respectively) in RAW264.7 cells; samples at 10 µM concentration. The images are representative from reproducible experiments performed three times; scale bar 100 µm.

The microscopy imaging for complexes **23** and **24** are not shown as they were very weakly emissive in the channel and could not be captured efficiently.

6.3.4 Cytotoxicity

The cytotoxicity of phosphorescent heavy metal complexes is dependent on their chemical structures. The cytotoxic effects of the rhenium(I) complexes on cell lines was analysed using a live/dead (Zombie) dye, i.e. an amine reactive fluorescent dye that is permeant to dead cells with compromised membranes, and non-permeant to live cells, and can be detected by flow cytometry. At concentrations of 5 µM and 10 µM, the rhenium complexes **5-8** caused minimal cell death (<12%) which was comparable to control cells (6%) that had not been exposed to the rhenium(I) complexes in JU77 cells (see **Figure 6.14**). Even at the higher concentration of 20 µM, the complexes were not very toxic to the cells and never exceeded 15% cell death. This trend was also observed in RAW264.7 cells, presented in **Figure 6.15**.

For the rhenium(I)-NHC complexes, **23** displayed similar cell death (12%) as **24** (14%) in JU77 cells at high concentration (20 µM) as shown in **Figure 6.15**. However when in RAW264.7 cells, **24** appeared most toxic with 33% cell death compared to **23** with only 5% cell death, in high concentration (20 µM), see **Figure 6.17**. These data suggest that the rhenium(I) complexes have good biocompatibility and are suitable for cell imaging.

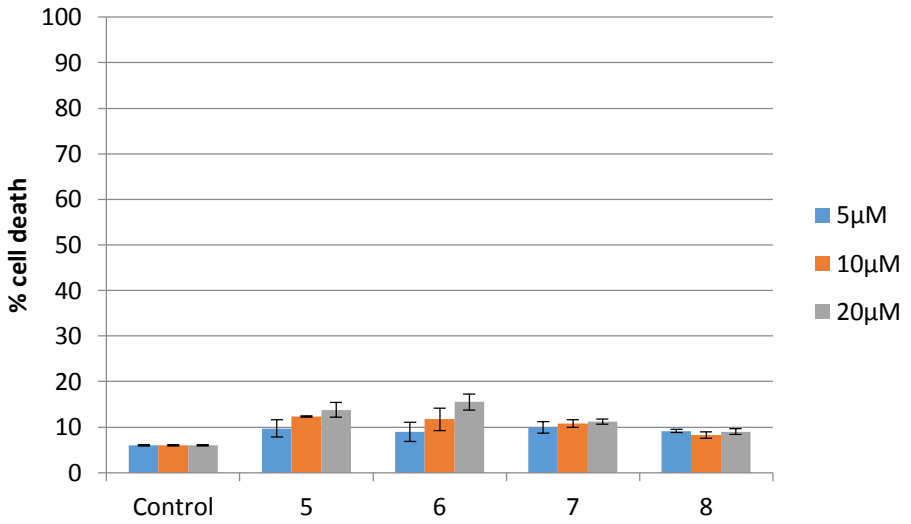

Figure 6.14 Live/dead assay of control and rhenium complexes **5-8** on JU77 cells, showing error bars (SD, n=3, triplicate).

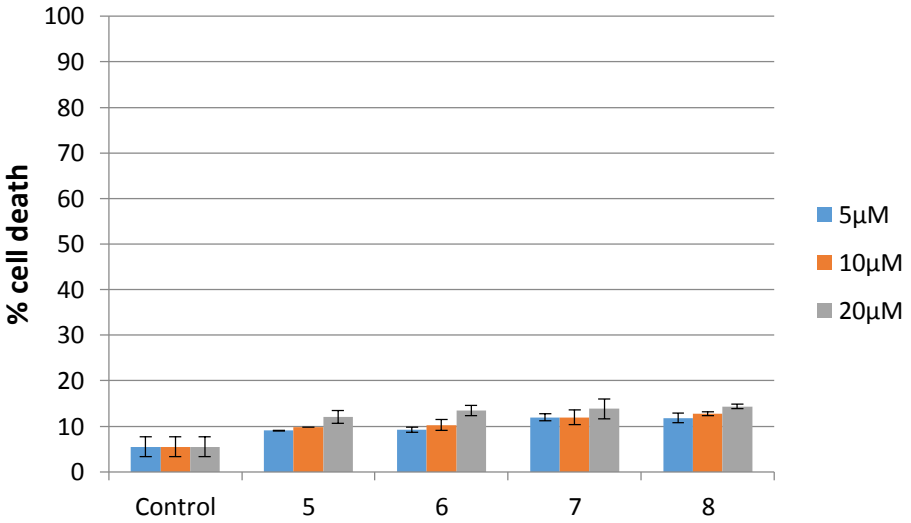

Figure 6.15 Live/dead assay of control and rhenium complexes **5-8** on RAW264.7 cells, showing error bars (SD, n=3, triplicate).

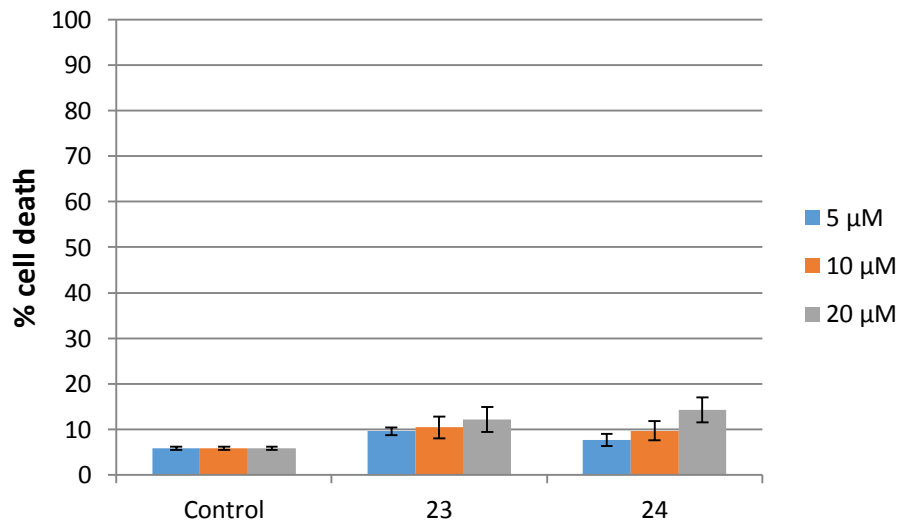

Figure 6.16 Live/dead assay of control and rhenium complexes **23** and **24** on JU77 cells, showing error bars (SD, n=3, triplicate).

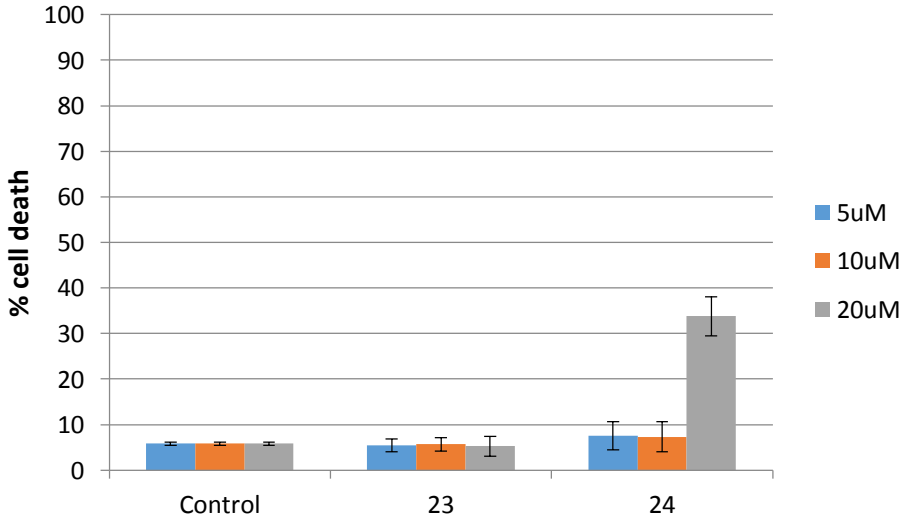

Figure 6.17 Live/dead assay of control and rhenium complexes **23** and **24** on RAW264.7 cells, showing error bars (SD, n=3, triplicate).

6.4 Conclusion

A series of neutral rhenium(I) tetrazolato complexes, [Re(**phen**)$(CO)_3$(**Tz**Ph4OH)] (**5**), [Re(**phen**)$(CO)_3$(**Tz**Ph3OH)] (**6**), [Re(**phen**)$(CO)_3$(**Tz**Ph4OMe)] (**7**), and [Re(**phen**)$(CO)_3$(**Tz**Ph3OMe)] (**8**) were tested in malignant and healthy cell lines in order to determine the behaviour of these complexes in biological media. Live/dead assay detected by flow cytometry displayed minimal cell death (<12%) at 10 µM concentration for all complexes in both RAW264.7 and JU77 cells. On the other

hand, neutral rhenium(I)-NHC complexes **23** and **24** were also tested in cell lines and found to behave in a similar manner.

Confocal microscopy imaging for the rhenium(I) complexes **5-8** displayed strong emission in the plasma membrane and no uptake in the nuclear region. **Figure 6.13** displays the localisation of the rhenium(I) complexes to appear specifically outside the nucleus. Results show that complex **6-8** can efficiently enter the cells, whereas complex **5** has poor cell uptake efficiency, which agree with results of live cell imaging and flow cytometry experiments. The collective data suggests that these rhenium(I) complexes have good biocompatibility and are suitable as cell imaging probes. Further investigation of the rhenium(I) complexes involving different concentrations and longer incubation times will be required in order to assess their full capacity as optical imaging agents.

6.5 Experimental Procedure

6.5.1 Cell Lines

The JU77 human mesothelioma cell line was derived from the pleural effusion of a patient[217] and RAW264.7 murine macrophage cells were a kind gift from Jay Steer (University of Western Australia, Perth, Australia). Both cell types were cultured in RPMI-1640 (Life Technologies, Carlsbad, CA) supplemented with 10% Foetal Bovine Serum (FBS) (HyClone, Thermo Scientific, Waltham, MA), 2 mM L-Glutamine, penicillin-streptomycin (100 units/mL) and 10 mM HEPES buffer (all from Life Technologies). Cells were maintained in a humidifier at 37 °C and 5% CO_2 and subcultured when they were 70-80% confluent. RAW 264.7 cells were used at a passage number <20 for all experiments to ensure maintenance of their macrophage characteristics.

6.5.2 Flow Cytometry: Live/Dead Assay with Zombie NIR

RAW264.7 cells were first stained with the provided rhenium(I) labels at three different concentrations: 5 µM, 10 µM and 20 µM respectively. Briefly, cells were

cultured for 2 days in complete medium until 70-80% confluent, trypsinized and centrifuged at 1200 rpm for 5 min at room temperature. Cells were re-suspended in PBS, counted using a haemocytometer and 0.5 million cells were incubated with the respective labels for 30 min at 37 °C under 5% CO_2. Following incubation, cells were washed with PBS, centrifuged at 1200 rpm for 5 min at RT and the cell pellet re-suspended in 500 µL of PBS and incubated with 0.5 µL of Zombie NIR (BioLegend, San Diego, CA) with an Ex_{max} of 719 nm and Em_{max} of 746 nm. After 30 min, cells were washed once with 10% FBS/1% BSA in PBS, centrifuged at 1200 rpm for 5 min at RT and pellet was resuspended in 100 µL PBS. Flow cytometry data was acquired immediately using an LSR Fortessa flow cytometer (BD Biosciences, San Jose, CA) and FACSDiva software; the data analysed was using FlowJo software version 10.0.8 (TreeStar, Oregon, USA).

6.5.3 Confocal Microscopy

JU77 human mesothelioma cells (5×10^4) seeded in a 35mm high µ-Dish (Ibidi GmbH, Martinsried, Germany) were cultured for 2 days, then washed once with serum free RPMI1640 and incubated with 10 µM of the pyridine labels for 30 min at RT. Cells were then washed with PBS and imaged using an UltraVIEW VoX Spinning Disc Confocal Microscope (PerkinElmer, Waltham, MA). Images were analysed using the Volocity software (PerkinElmer).

6.5.4 Sample Preparation

The neutral rhenium(I) diimine complexes known to have strong photophysical characteristics were selected for testing and cell imaging experiments as described. DMSO was used to dissolve the complexes into aqueous cellular media, as it is a common solvent used in biology to prepare stock solutions of fluorophores.

6.5.5 Determination of Lipophilicity

The *n*-octanol/water distribution coefficients (log $D_{7.4}$) of the complexes were measured using the shake-flask method.[110] PBS buffer (pH 7.4) and *n*-octanol were mixed together over 72 hours to ensure saturation of both phases. Each complex (~1 mg) was dissolved in 250 µL of DMSO. To a 1:1 solvent system of PBS buffer and *n*-octanol (750 µL each), 50 µL of the complex in DMSO was added and mixing

using a laboratory vortex. The resulting solution was centrifuged to allow separation of the two phases. The absorption profile of the complex in each phase was measured by UV-VIS spectroscopy. The absorbance at 280 nm was recorded and used to determine the log $D_{7.4}$ value where:

$$\text{Log } D_{7.4} = \log A_o - \log A_w$$

Where A_o and A_w are the absorbance values of the complex in the *n*-octanol and water phases measured at λ = 280 nm respectively. The method assumed constant molar absorptivitiy between the two solvents so that, according to Beer's law, the values of concentration are linearly proportional to the values of absorbance.

Chapter 7

Conclusions and Future Work

7.1 Summary

The research reported throughout this thesis extends the work revolved around rhenium(I) tricarbonyl complexes, specifically those utilising *N*-heterocyclic carbene ligands. The chosen structural motif of NHCs were based on those previously reported pyridylimidazolium salts, which possessed luminescent features when coordinated to rhenium(I). The imidazolium salts were used to synthesise a series of novel rhenium(I)-NHC tricarbonyl complexes with varying ancillary ligands. Furthermore, some new bidentate NHC ligands were synthesised in addition to previously reported NHC ligands; to make comparison between effects of R substituent on the NHC. Modification of the ligand at this particular site did not achieve any difference in photophysical properties of the rhenium(I)-NHC complexes, see **Figure 7.1**.

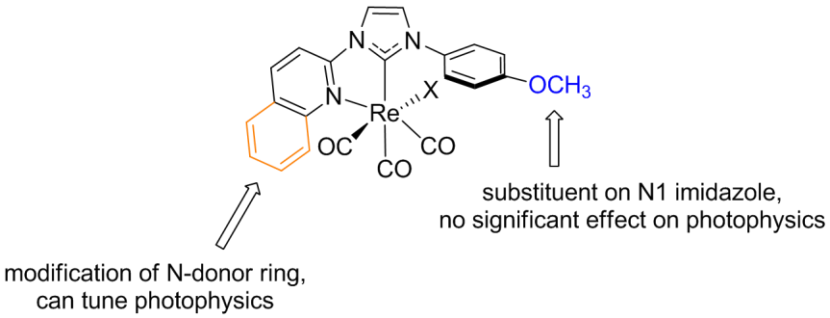

Figure 7.1 Summary of modifications made towards Re(I)-NHC complexes.

The newly synthesised complexes were fully characterised structurally by IR, ^{1}H and ^{13}C NMR spectroscopy, as well as X-ray crystallography and elemental analyses. The experimental data presented were in agreement with the proposed structural

formulae. X-ray quality crystals were obtained for most of the complexes and analyses confirmed that the carbonyl ligands were arranged in a *facial* configuration. It was also established that the complexes all displayed a distorted octahedral geometry, which were quite typical of rhenium(I)-NHC complexes. Additionally, the photophysical and photochemical properties of these complexes were investigated.

The photophysical properties of the reported cationic rhenium(I)-NHC complexes coordinated to pyridyl ligands, [Re(**PyImPh**)$(CO)_3$(L)]$^+$ were found to perform differently to the previously published neutral rhenium(I)-NHC complexes, although still emissive at room temperature in dichloromethane solutions. This was mainly due to the cationic nature of the complexes, which displayed blue shifted emission (490 nm) compared to their neutral analogues (520 nm). The emission of the complexes originated from ^{3}MLCT state, which was evident by observing the change upon degassing solutions. The observed excited state lifetime and quantum yield for these cationic complexes appeared lower than their neutral analogues. Furthermore, the cationic rhenium(I)-NHC complexes appended to pyridyl amino acids exhibited very weak emission and extremely short excited state lifetimes in acetonitrile solutions. This was attributed to the presence of both photochemical and electron transfer mechanisms. The rate of electron transfer (k_{eT}) for [Re(**PyImPh**)$(CO)_3$(Py**Trp**)]$^+$ was calculated to be 6.4×10^8 s^{-1} which was very similar to the **phen** analogues reported by Blanco-Rodriguez *et al* with a rate of $k_{eT} = 3.3 \times 10^7$ s^{-1}.

The photochemical properties of these cationic rhenium(I)-NHC complexes were also investigated in acetonitrile. These compounds were stable in the dark, but tend to undergo photochemical changes when excited at the ^{3}MLCT manifold. This was only the case for the pyridyl-imidazolium complexes **37Br/Cl**, whereas the quinoline-imidazolium complexes **38Br/Cl** were found to not be photoactive. When the photoactive rhenium(I)-NHC complexes were irradiated with UV light, a photochemical ligand substitution reaction occurred and formed new photoproducts. One of the identified photoproducts was confirmed to be the acetonitrile solvato species [Re(**PyImPh**)$(CO)_3(CH_3CN)]^+$ as an intermediate which further reacted to form dicarbonyl species. The use of fundamental techniques such as IR and ^{1}H NMR spectroscopy assisted in identifying the structure of the species. Further

characterisation by crystallography would be vital in confirming the complex structure, however no single crystals could be produced after exhaustive photolysis in acetonitrile solutions.

As well as investigating the behaviour of rhenium(I)-NHC complexes, an expansion on the work of rhenium(I)-diimine complexes were also undertaken in this thesis. In particular, the moiety of interest was of amino and phenol functional groups capable of driving an electron transfer effect. Chapter 2 presented phenol substituted tetrazoles, while Chapter 3 presented amino acid (tryptophan, phenylalanine, glycine) based tetrazole ligands. The series of tetrazolato coordinated rhenium(I) diimine tricarbonyl complexes were characterised by spectroscopy and investigated in terms of their photophysical properties. Any potential for acid-base chemistry was also examined. It seemed that any potential for electron transfer from the amino acid to the rhenium metal was inhibited, due to the presence of the electron rich tetrazole ring.

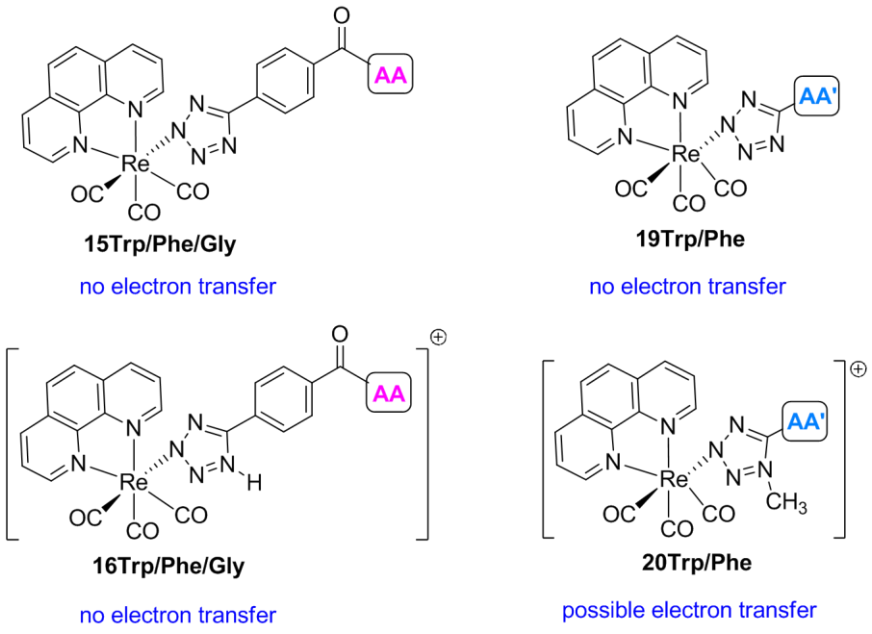

Figure 7.2 Summary of complexes investigated for electron transfer.

However, various alterations were implemented to counteract this by manipulation of the tetrazole ring through either protonation (reversible) or methylation (irreversible) of the neutral tetrazolato rhenium(I) diimine complexes. Upon protonation to afford complexes **16Trp/Phe/Gly**, there was a drastic change in the photophysical properties where emission intensity increased and a blue shift was apparent, as well as elongation of lifetime decay, with respect to neutral analogues **15Trp/Phe/Gly**.

However, when comparing reactive (**Trp**) and non-reactive (**Phe**) amino acids, there was no strong evidence to suggest an electron transfer occurred within these systems. In addition, upon methylation to afford complexes **20Trp/Phe**, the resulting cationic complexes had similar photophysical output to the protonated complexes, i.e. blue shifted emission and elongated lifetime decay. Furthermore, when comparing **Trp** and **Phe** analogues, the electron transfer rate constant was closer to that of literature, thus proving that electron transfer is viable within these systems if modulated at the right parameters. This summary is depicted in **Figure 7.2**.

7.2 Future Work

The data presented in this thesis mainly consists of steady state luminescence measurements. Thus would require further analyses using advanced techniques such as ultrafast transient spectroscopy (time-resolved absorption (TR-UV), time-resolved infrared (TR-IR) to name a few), which can detect molecular processes in the femto/picosecond range. This could then identify any electron transfer mechanism that the fluorescence spectrometer could not distinguish. Electrochemistry is also another useful experimental technique that could be implemented to identify the redox potentials of the rhenium(I) complexes and assess their ability for electron transfer (in the ground state). Another technique that could provide more evidence and identify orbital energy levels would be computational studies such as time-dependent density functional theory (TD-DFT) calculations. This can be used to simulate the energetics of the complexes and indicate the lower energy transitions involved.

To assess the possibility of an electron transfer at shorter distance, *meta* substituents of the amino acid complexes should also be synthesised and compared to their *para* analogues. Literature has already proved that a minor change such as position of substituent results in major effects in biological aspects. An example was that of Fernandez-Moreira *et al*. investigation on tricarbonyl rhenium(I) **bipy** complexes coordinated to *meta* and *para* pyridyl derivatives.[221]

To evaluate the possibility of the rhenium(I)-NHC complexes as photoCORMs, it is suggested that the synthesised complexes be tested in biological media to determine their solubility and lipophilic character. In addition, the myoglobin UV-VIS assay experiments would provide information of the rates of CO release from the tricarbonyl complexes. If not suitable, alternatives can be considered where the NHC motif is modified with relevant functional groups and/or biocompatible amino acids. On the other hand, the use of a different metal centre such as manganese provides more viability and sensitivity as photoCORMs. When manganese is coordinated to a diimine or NHC motif, their different reactivities can be compared to those of rhenium complexes. This research is currently undergoing in the Massi research group focussing on these aspects.

Bibliography

(1) Kalinowski, J.; Fattori, V.; Cocchi, M.; Williams, J. A. G. *Coord. Chem. Rev.* **2011**, *255* (21-22), 2401–2425.

(2) Zhao, G.-W.; Hu, Y.-X.; Chi, H.-J.; Dong, Y.; Xiao, G.-Y.; Li, X.; Zhang, D.-Y. *Opt. Mater. (Amst).* **2015**, *47*, 173–179.

(3) Noh, Y.-Y.; Lee, C.-L. L.; Kim, J.-J.; Yase, K. *J. Chem. Phys.* **2003**, *118* (6), 2853.

(4) Lee, P.-I.; Hsu, S. L.-C.; Chung, C.-T. *Synth. Met.* **2006**, *156* (14-15), 907–970.

(5) Baranov, D. S.; Popov, A. G.; Uvarov, M. N.; Kulik, L. V. *Mendeleev Commun.* **2014**, *24* (6), 383–385.

(6) Wright, P. J.; Muzzioli, S.; Werrett, M. V.; Raiteri, P.; Skelton, B. W.; Silvester, D. S.; Stagni, S.; Massi, M. *Organometallics* **2012**, *31* (21), 7566–7578.

(7) Wadman, S. H.; Lutz, M.; Tooke, D. M.; Spek, A. L.; Hartl, F.; Havenith, R. W. A.; van Klink, G. P. M.; van Koten, G. *Inorg. Chem.* **2009**, *48* (5), 1887–1900.

(8) Zhao, Q.; Huang, C.; Li, F. *Chem. Soc. Rev.* **2011**, *40* (5), 2508–2524.

(9) Amoroso, A. J.; Arthur, R. J.; Coogan, M. P.; Court, J. B.; Fernandez-Moreira, V.; Hayes, A. J.; Lloyd, D.; Millet, C.; Pope, S. J. A. *New J. Chem.* **2008**, *32* (Copyright (C) 2013 American Chemical Society (ACS). All Rights Reserved.), 1097–1102.

(10) Lo, K. K.-W.; Louie, M.-W.; Sze, K.-S.; Lau, J. S.-Y. *Inorg. Chem.* **2008**, *47* (Copyright (C) 2013 American Chemical Society (ACS). All Rights Reserved.), 602–611.

(11) Kam-Wing Lo, K.; Chun-Ming Ng, D.; Hui, W.-K.; Cheung, K.-K. *J. Chem. Soc. Dalt. Trans.* **2001**, *3* (18), 2634–2640.

(12) Zhang, K. Y.; Tso, K. K.; Louie, M.; Liu, H.; Lo, K. K. *Organometallics* **2013**, *3* (I).

(13) Louie, M.-W.; Choi, A. W.-T.; Liu, H.-W.; Chan, B. T.-N.; Lo, K. K.-W. *Organometallics* **2012**, *31* (16), 5844–5855.

(14) Choi, A. W.-T.; Louie, M.-W.; Li, S. P.-Y.; Liu, H.-W.; Chan, B. T.-N.; Lam, T. C.-Y.; Lin, A. C.-C.; Cheng, S.-H.; Lo, K. K.-W. *Inorg. Chem.* **2012**, *51* (24), 13289–

13302.

(15) Amoroso, A. J.; Coogan, M. P.; Dunne, J. E.; Fernandez-Moreira, V.; Hess, J. B.; Hayes, A. J.; Lloyd, D.; Millet, C.; Pope, S. J. A.; Williams, C. *Chem. Commun. (Cambridge, U. K.)* **2007**, No. Copyright (C) 2013 American Chemical Society (ACS). All Rights Reserved., 3066–3068.

(16) Fernández-Moreira, V.; Thorp-Greenwood, F. L.; Amoroso, A. J.; Cable, J.; Court, J. B.; Gray, V.; Hayes, A. J.; Jenkins, R. L.; Kariuki, B. M.; Lloyd, D.; Millet, C. O.; Williams, C. F.; Coogan, M. P.; Fernandez-Moreira, V. *Org. Biomol. Chem.* **2010**, *8* (Copyright (C) 2013 American Chemical Society (ACS). All Rights Reserved.), 3888–3901.

(17) Balasingham, R. G.; Thorp-Greenwood, F. L.; Williams, C. F.; Coogan, M. P.; Pope, S. J. a. *Inorg. Chem.* **2012**, *51* (3), 1419–1426.

(18) Yu, M.; Zhao, Q.; Shi, L.; Li, F.; Zhou, Z.; Yang, H.; Yi, T.; Huang, C. *Chem. Commun. (Cambridge, U. K.)* **2008**, No. Copyright (C) 2013 American Chemical Society (ACS). All Rights Reserved., 2115–2117.

(19) Zhao, Q.; Yu, M.; Shi, L.; Liu, S.; Li, C.; Shi, M.; Zhou, Z.; Huang, C.; Li, F. *Organometallics* **2010**, *29* (Copyright (C) 2013 American Chemical Society (ACS). All Rights Reserved.), 1085–1091.

(20) Louie, M.-W.; Liu, H.-W.; Lam, M. H.-C.; Lau, T.-C.; Lo, K. K.-W. *Organometallics* **2009**, *28* (15), 4297–4307.

(21) Choi, A. W.-T.; Yim, V. M.-W.; Liu, H.-W.; Lo, K. K.-W. *Chemistry* **2014**, *20* (31), 9633–9642.

(22) Zhao, Q.; Huang, C. *Chem Soc Rev* **2010**, *39*, 3007–3030.

(23) Guerchais, V.; Fillaut, J.-L. *Coord. Chem. Rev.* **2011**, *255* (21-22), 2448–2457.

(24) Sun, S.; Lees, A. J. *Coord. Chem. Rev.* **2002**, *230* (1-2), 171–192.

(25) Fernández-Moreira, V.; Marzo, I.; Gimeno, M. C. *Chem. Sci.* **2014**, *5*, 4434–4446.

(26) García-gallego, S.; Bernardes, G. J. L. G. J. L. *Angew. Chem. Int. Ed. Engl.* **2014**, *53* (37), 9712–9721.

(27) Li, Y.; Tan, C.-P.; Zhang, W.; He, L.; Ji, L.-N.; Mao, Z.-W. *Biomaterials* **2015**, *39*,

95–104.

(28) Habtemariam, A.; Garino, C.; Ruggiero, E.; Alonso-de Castro, S.; Mareque-Rivas, J. C.; Salassa, L. *Molecules* **2015**, *20* (4), 7276–7291.

(29) Mari, C.; Pierroz, V.; Ferrari, S.; Gasser, G. *Chem. Sci.* **2015**, *6*, 2660–2686.

(30) Mandal, S.; Poria, D. K.; Ghosh, R.; Ray, P. S.; Gupta, P. *Dalton Trans.* **2014**, *43* (46), 17463–17474.

(31) Leonidova, A.; Pierroz, V.; Rubbiani, R.; Heier, J.; Ferrari, S.; Gasser, G. *Dalton Trans.* **2014**, *43* (11), 4287–4294.

(32) Wähler, K.; Ludewig, A.; Szabo, P.; Harms, K.; Meggers, E. *Eur. J. Inorg. Chem.* **2014**, No. 5, 807–811.

(33) Albani, B. a; Peña, B.; Dunbar, K. R.; Turro, C. *Photochem. Photobiol. Sci.* **2014**, *13* (2), 272–280.

(34) Sacksteder, L.; Lee, M.; Demas, J. N.; Degraff, B. A. *J. Am Chem Soc* **1993**, *115* (18), 8230–8238.

(35) Vlček Jr, A. *Coord. Chem. Rev.* **2000**, *202*, 933–977.

(36) Balzani, V. In *Handbook of Photochemistry*; 2006; pp 50–82.

(37) Balzani, V.; Sebastiano, B.; Ciamician, C. G.; Bologna, U.; Inorganica, C.; Analitica, C.; Fisica, C.; Messina, U. *Top Curr Chem* **2007**, *280* (June), 1–36.

(38) Calvert, J. M.; Caspar, J. V.; Binstead, R. A.; Westmoreland, T. D.; Meyer, T. J. *J. Am Chem Soc* **1982**, *104*, 6620–6627.

(39) Lo, K. K.-W.; Chung, C.-K.; Zhu, N. *Chem. Eur. J.* **2003**, *9* (2), 475–483.

(40) Caspar, J. V.; Meyer, T. J. *J. Phys. Chem.* **1983**, *87* (6), 952–957.

(41) Wrighton, M. S.; Morse, D. L. *J. Am. Chem. Soc.* **1974**, *96* (4), 998–1003.

(42) Kalyanasundaram, K. *J. Chem. Soc. Faraday Trans. 2* **1986**, *82* (12), 2401–2415.

(43) Stufkens, D. J.; Vlček Jr, A. *Coord. Chem. Rev.* **1998**, *177*, 127–179.

(44) Nazeeruddin, K.; Humphry-Baker, R.; Berner, D.; Rivier, S.; Zuppiroli, L.; Graetzel,

M. *J. Am Chem Soc* **2003**, No. 125, 8790–8797.

(45) Lamansky, S.; Djurovich, P.; Murphy, D.; Abdel-Razzaq, F.; Kwong, R.; Tsyba, I.; Bortz, M.; Mui, B.; Bau, R.; Thompson, M. E. *Inorg. Chem.* **2001**, *40* (7), 1704–1711.

(46) Cao, H.; Shan, G.; Yin, Y.; Sun, H.; Wu, Y.; Xie, W.; Su, Z. *Dye. Pigment.* **2015**, *113*, 655–663.

(47) Thorp-Greenwood, F. L.; Balasingham, R. G.; Coogan, M. P. *J. Organomet. Chem.* **2012**, *714*, 12–21.

(48) Fernandez-Moreira, V.; Thorp-Greenwood, F. L.; Coogan, M. P. *Chem. Commun. (Cambridge, U. K.)* **2010**, *46* (Copyright (C) 2013 American Chemical Society (ACS). All Rights Reserved.), 186–202.

(49) Coogan, M. P.; Fernández-Moreira, V. *Chem. Commun. (Camb).* **2014**, *50* (4), 384–399.

(50) Lo, K. K.-W.; Chung, C.-K.; Lee, T. K.-M.; Lui, L.-H.; Tsang, K. H.-K.; Zhu, N. *Inorg. Chem.* **2003**, *42* (21), 6886–6897.

(51) Kirgan, R. A.; Sullivan, B. P.; Paul, D. *Top Curr Chem* **2007**, *281*, 45–100.

(52) Vogler, A.; Kunkely, H. *Coord. Chem. Rev.* **2000**, *200-202*, 991–1008.

(53) Housecroft, C. E.; Sharpe, A. G. *Inorganic Chemistry*, Second edi.; Pearson, 2001.

(54) Sauer, M.; Hofkens, J.; Enderlein, J. *Handbook of Fluorescence Spectroscopy and Imaging*; Wiley-VCH Verlag GmbH & Co. KGaA, 2011.

(55) Birks, J. B. *Standardisation in spectrophotometry and luminescence measurements*; 1975.

(56) Lakowicz, J. R. *Principles of Fluorescence Spectroscopy Principles of Fluorescence Spectroscopy*; 2006.

(57) Demas, J. N.; Crosby, G. A. *J. Phys. Chem.* **1971**, *75* (8), 991–1024.

(58) Tsubaki, H.; Sekine, A.; Ohashi, Y.; Koike, K.; Takeda, H.; Ishitani, O. *J. Am. Chem. Soc.* **2005**, *127* (44), 15544–15555.

(59) Geoffroy, G. L. *J. Chem. Educ.* **1983**, *60* (10), 861.

(60) Stufkens, D. J. *Comments Inorg. Chem.* **1992**, *13* (6), 359–385.

(61) Lees, A. J. *Comments Inorg. Chem.* **1995**, *17* (6), 319–346.

(62) Sousa, S. F.; Sampaio, R. N.; Barbosa Neto, N. M.; Machado, A. E. H.; Patrocinio, A. O. T. *Photochem. Photobiol. Sci.* **2014**.

(63) Liptay, W. *Angew. Chem. Int. Ed. Engl.* **1969**, *8* (3), 177–188.

(64) Kumar, A.; Sun, S.; Lees, A. J. *Top Organomet Chem* **2010**, No. 29, 1–35.

(65) Ko, C. C.; Siu, J. W. K.; Cheung, A. W. Y.; Yiu, S. M. *Organometallics* **2011**, *30* (10), 2701–2711.

(66) Patrocinio, A. O. T.; Iha, N. Y. M. *Inorg. Chem.* **2008**, *47* (23), 10851–10857.

(67) Liu, C.; Dubois, K. D.; Louis, M. E.; Vorushilov, A. S.; Li, G. *ACS Catal.* **2013**, *3*, 655–662.

(68) Lo, K. K.-W.; Zhang, K. Y.; Li, S. P.-Y. *Eur. J. Inorg. Chem.* **2011**, *2011* (Copyright (C) 2013 American Chemical Society (ACS). All Rights Reserved.), 3551–3568.

(69) Lo, K. K.-W.; Hui, W.-K.; Chung, C.-K.; Tsang, K. H.-K.; Ng, D. C.-M.; Zhu, N.; Cheung, K.-K. *Coord. Chem. Rev.* **2005**, *249* (13-14), 1434–1450.

(70) Chen, P.; Westmoreland, T. D.; Danielson, E.; Schanze, K. S.; Anthon, D.; Neveux, P. E.; Meyer, T. J. *Inorg. Chem.* **1987**, *26* (7), 1116–1126.

(71) Coogan, M. P.; Fernández-Moreira, V.; Hess, J. B.; Pope, S. J. a.; Williams, C. *New J. Chem.* **2009**, *33* (5), 1094.

(72) Ishitani, O.; Kanai, K.; Yamada, Y.; Sakamoto, K. *Chem. Commun.* **2001**, No. 16, 1514–1515.

(73) Ko, C.-C.; Cheung, A.; Lo, L. T.-L.; Siu, J. W.-K.; Ng, C.-O.; Yiu, S.-M. *Coord. Chem. Rev.* **2012**, *256* (15-16), 1546.

(74) Ko, C.-C.; Lo, L. T.-L.; Ng, C.-O.; Yiu, S.-M. *Chemistry* **2010**, *16* (46), 13773–13782.

(75) Koike, K.; Tanabe, J.; Toyama, S.; Tsubaki, H.; Sakamoto, K.; Westwell, J. R.;

Johnson, F. P. A.; Hori, H.; Saitoh, H.; Ishitani, O. *Inorg. Chem.* **2000**, *39* (13), 2777–2783.

(76) Koike, K.; Okoshi, N.; Hori, H.; Takeuchi, K.; Ishitani, O.; Tsubaki, H.; Clark, I. P.; George, M. W.; Johnson, F. P. A.; Turner, J. J. *J. Am. Chem. Soc.* **2002**, *124* (38), 11448–11455.

(77) Vlček Jr, A. *Coord. Chem. Rev.* **1998**, *177*, 219–256.

(78) McLean, T. M.; Moody, J. L.; Waterland, M. R.; Telfer, S. G. *Inorg. Chem.* **2012**, *51* (1), 446–455.

(79) Hori, H.; Koike, K.; Ishizuka, M.; Takeuchi, K.; Ibusuki, T.; Ishitani, O. *J. Organomet. Chem.* **1997**, *530* (1-2), 169–176.

(80) Morimoto, T.; Ito, M.; Koike, K.; Kojima, T.; Ozeki, T.; Ishitani, O. *Chemistry* **2012**, *18* (11), 3292–3304.

(81) Cheung, A.; Lo, L. T.-L.; Ko, C.-C.; Yiu, S.-M. *Inorg. Chem.* **2011**, *50* (11), 4798.

(82) Hightower, S. E.; Corcoran, R. C.; Sullivan, B. P. *Inorg. Chem.* **2005**, *44* (26), 9601–9603.

(83) Sato, S.; Sekine, A.; Ohashi, Y.; Ishitani, O.; Blanco-Rodríguez, A. M.; Vlček Jr, A.; Unno, T.; Koike, K. *Inorg. Chem.* **2007**, *46* (9), 3531–3540.

(84) Sato, S.; Matubara, Y.; Koike, K.; Falkenström, M.; Katayama, T.; Ishibashi, Y.; Miyasaka, H.; Taniguchi, S.; Chosrowjan, H.; Mataga, N.; Fukazawa, N.; Koshihara, S.; Onda, K.; Ishitani, O. *Chemistry* **2012**, *18* (49), 15722–15734.

(85) Sato, S.; Morimoto, T.; Ishitani, O. *Inorg. Chem.* **2007**, *46* (22), 9051–9053.

(86) Sato, S.; Ishitani, O. *Coord. Chem. Rev.* **2015**, *282-283*, 50–59.

(87) Kianfar, E.; Kaiser, M.; Knör, G. *J. Organomet. Chem.* **2015**, *799-800*, 13–18.

(88) Pierri, A. E.; Muizzi, D. A.; Ostrowski, A. D.; Ford, P. C. In *Struc Bond*; 2014; pp 1–45.

(89) Zhang, W.-Q.; Whitwood, A. C.; Fairlamb, I. J. S.; Lynam, J. M. *Inorg. Chem.* **2010**, *49* (19), 8941–8952.

(90) Motterlini, R.; Otterbein, L. E. *Nat. Rev. Drug Discov.* **2010**, *9*, 728–743.

(91) Rochette, L.; Cottin, Y.; Zeller, M.; Vergely, C. *Pharmacol. Ther.* **2013**, *137* (2), 133–152.

(92) Otterbein, L. E. *Respir. Care* **2009**, *54* (7), 925–932.

(93) Marques, A. R.; Kromer, L.; Gallo, D. J.; Penacho, N.; Rodrigues, S. S.; Seixas, D.; Gonc, A. M. L.; Matos, M. N. De; Bento, I.; Otterbein, L. E.; Roma, C. C. *Organometallics* **2012**, *31*, 5810–5822.

(94) Romão, C. C.; Blättler, W. a; Seixas, J. D.; Bernardes, G. J. L. *Chem. Soc. Rev.* **2012**, *41* (9), 3571–3583.

(95) Pierri, A.; Pallaoro, A.; Wu, G.; Ford, P. C. *J. Am. Chem. Soc.* **2012**, *134* (44), 18197.

(96) Gonzales, M. a; Mascharak, P. K. *J. Inorg. Biochem.* **2014**, *133*, 127–135.

(97) Schatzschneider, U. *Eur. J. Inorg. Chem.* **2010**, *2010* (10), 1451–1467.

(98) Seixas, J. D.; Mukhopadhyay, A.; Santos-Silva, T.; Otterbein, L. E.; Gallo, D. J.; Rodrigues, S. S.; Guerreiro, B. H.; Gonçalves, A. M. L.; Penacho, N.; Marques, A. R.; Coelho, A. C.; Reis, P. M.; Romão, M. J.; Romão, C. C. *Dalton Trans.* **2013**, *42* (17).

(99) Motterlini, R.; Clark, J. E.; Foresti, R.; Sarathchandra, P.; Mann, B. E.; Green, C. J. *Circ. Res.* **2002**, *90* (2), e17–e24.

(100) Schatzschneider, U. *Inorganica Chim. Acta* **2011**, *374* (1), 19–23.

(101) Levenson, R. A.; Gray, H. B. *J. Am. Chem. Soc.* **1975**, *97* (21), 6042–6047.

(102) Wrighton, M. S.; Ginley, D. S. *J. Am Chem Soc.* **1975**, *97* (8), 2065–2072.

(103) Clark, J. E. *Circ. Res.* **2003**, *93* (2), 2e – 8.

(104) Johnson, T. R.; Mann, B. E.; Teasdale, I. P.; Adams, H.; Foresti, R.; Green, C. J.; Motterlini, R. *Dalton Trans.* **2007**, No. 15, 1500–1508.

(105) Long, R.; Salouage, I.; Berdeaux, A.; Motterlini, R.; Morin, D. *Biochim. Biophys. Acta - Bioenerg.* **2014**, *1837* (1).

(106) Rimmer, R. D.; Pierri, A. E.; Ford, P. C. *Coord. Chem. Rev.* **2012**, *256* (15-16),

1509–1519.

(107) Bischof, C.; Joshi, T.; Dimri, A.; Spiccia, L.; Schatzschneider, U. *Inorg. Chem.* **2013**, *52* (16), 9297–9308.

(108) Ward, J. S.; Lynam, J. M.; Moir, J. W. B.; Sanin, D. E.; Mountford, A. P.; Fairlamb, I. J. S. *Dalton Trans.* **2012**, *41* (35), 10514–10517.

(109) Berends, H.-M.; Kurz, P. *Inorganica Chim. Acta* **2012**, *380*, 141–147.

(110) Huber, W.; Linder, R.; Niesel, J.; Schatzschneider, U.; Spingler, B.; Kunz, P. C. *Eur. J. Inorg. Chem.* **2012**, *2012* (19), 3140–3146.

(111) Gonzalez, M. a; Carrington, S. J.; Fry, N. L.; Martinez, J. L.; Mascharak, P. K. *Inorg. Chem.* **2012**, *51* (21), 11930–11940.

(112) Kunz, P. C.; Huber, W.; Rojas, A.; Schatzschneider, U.; Spingler, B. *Eur. J. Inorg. Chem.* **2009**, *2009* (35), 5358–5366.

(113) Schatzschneider, U. *Br. J. Pharmacol.* **2015**, *172* (6), 1638–1650.

(114) Kianfar, E.; Schäfer, C.; Lornejad-Schäfer, M. R.; Portenkirchner, E.; Knör, G. *Inorganica Chim. Acta* **2015**, *435*, 174–177.

(115) Carrington, S. J.; Chakraborty, I.; Mascharak, P. K. *Chem. Commun. (Camb).* **2013**, *49* (96), 11254–11256.

(116) Farrell, I. R.; Vlček Jr, A. *Coord. Chem. Rev.* **2000**, *208* (1), 87–101.

(117) Chakraborty, I.; Carrington, S. J.; Mascharak, P. K. *ChemMedChem* **2014**, *9*, 1266–1274.

(118) Schatzschneider, U. *Inorganica Chim. Acta* **2011**, *374* (1), 19–23.

(119) Balzani, V.; Ceroni, P. In *The Exploration of Supramolecular Systems and Nanostructures by Photochemical Techniques*; Springer, 2012; pp 21–38.

(120) Ramirez, B. E.; Malmstrom, B. G.; Winkler, J. R.; Gray, H. B. *Proc. Natl. Acad. Sci. U. S. A.* **1995**, *92*, 11949–11951.

(121) Bixon, M.; Jortner, J.; Michel-Beyerle, M. E. *Biochim. Biophys. acta - Bioenerg.* **1991**, *1056* (3), 301–315.

(122) Rabinowich, E. *Photosynthesis and related systems*; New York, 1945.

(123) Schanze, K. S.; Macqueen, D. B.; Perkins, T. A.; Cabana, L. A. *Coord. Chem. Rev.* **1993**, *122*, 63–89.

(124) Ajayakumar, G.; Sreenath, K.; Gopidas, K. R. *Dalton Trans.* **2009**, No. 7, 1180–1186.

(125) Alstrum-Acevedo, J. H.; Brennaman, M. K.; Meyer, T. J. *Inorg. Chem.* **2005**, *44* (20), 6802–6827.

(126) Juris, A.; Balzani, V.; Barigelletti, F.; Campagna, S.; Belser, P.; Zelewsky, A. von. *Coord. Chem. Rev.* **1988**, *84*, 85–277.

(127) Sjödin, M.; Styring, S.; Wolpher, H.; Xu, Y.; Sun, L.; Hammarström, L. *J. Am. Chem. Soc.* **2005**, *127* (11), 3855–3863.

(128) Aigner, D.; Freunberger, S. a; Wilkening, M.; Saf, R.; Borisov, S. M.; Klimant, I. *Enhancing Photoinduced Electron Transfer Efficiency of Fluorescent pH-Probes with Halogenated Phenols.*; 2014.

(129) Kuss-Petermann, M.; Wolf, H.; Stalke, D.; Wenger, O. S. *J. Am. Chem. Soc.* **2012**, *134* (30), 12844–12854.

(130) Gareis, T.; Huber, C.; Wolfbeis, O. S.; Daub, J. *Chem. Commun.* **1997**, 1717–1718.

(131) Bronner, C.; Wenger, O. S. *Inorg. Chem.* **2012**, *51* (15), 8275–8283.

(132) Luong, J. C.; Nadjo, L.; Wrighton, M. S. *J. Am. Chem. Soc.* **1978**, *100* (18), 5790–5795.

(133) El Nahhas, A.; Consani, C.; Blanco-Rodríguez, A. M.; Lancaster, K. M.; Braem, O.; Cannizzo, A.; Towrie, M.; Clark, I. P.; Zális, S.; Chergui, M.; Vlček Jr, A. *Inorg. Chem.* **2011**, *50* (7), 2932–2943.

(134) Hanss, D.; Freys, J. C.; Bernardinelli, G.; Wenger, O. S. *Eur. J. Inorg. Chem.* **2009**, *2009* (32), 4850–4859.

(135) Lovell, J. F.; Liu, T. W. B.; Chen, J.; Zheng, G. *Chem. Rev.* **2010**, *110* (5), 2839–2857.

(136) Chanawanno, K.; Engle, J. T.; Le, K. X.; Herrick, R. S.; Ziegler, C. J. *Dalt. Trans.*

2013, *42*, 13679–13684.

(137) Maity, D.; Bhaumik, C.; Karmakar, S.; Baitalik, S. *Inorg. Chem.* **2013**, *52* (14), 7933–7946.

(138) Wenger, O. S. *Coord. Chem. Rev.* **2009**, *253* (9-10), 1439–1457.

(139) Kuss-Petermann, M.; Wolf, H.; Stalke, D.; Wenger, O. S. *J. Am. Chem. Soc.* **2012**, *134* (30), 12844–12854.

(140) Liu, W.; Heinze, K. *Dalton Trans.* **2010**, *39* (40), 9554–9564.

(141) Herzog, W.; Bronner, C.; Löffler, S.; He, B.; Kratzert, D.; Stalke, D.; Hauser, A.; Wenger, O. S. *Chemphyschem* **2013**, *14* (6), 1168–1176.

(142) Badaeva, E.; Albert, V. V; Kilina, S.; Koposov, A.; Sykora, M.; Tretiak, S. *Phys. Chem. Chem. Phys.* **2010**, *12* (31), 8902–8913.

(143) Mullice, L. A.; Pope, S. J. A. *Dalton Trans.* **2010**, *39* (25), 5908–5917.

(144) Braband, H.; Zahn, T. I.; Abram, U. *Inorg. Chem.* **2003**, *42* (20), 6160–6162.

(145) Braband, H.; Kueckmann, T. I.; Abram, U. *J. Organomet. Chem.* **2005**, *690* (24-25), 5421–5429.

(146) Xue, W.-M.; Chan, M. C.-W.; Su, Z.-M.; Cheung, K.-K.; Liu, S.-T.; Che, C.-M. *Organometallics* **1998**, *17*, 1622–1630.

(147) Casson, L. a; Muzzioli, S.; Raiteri, P.; Skelton, B. W.; Stagni, S.; Massi, M.; Brown, D. H. *Dalton Trans.* **2011**, *40* (44), 11960–11967.

(148) Vaughan, J. G.; Reid, B. L.; Wright, P. J.; Ramchandani, S.; Skelton, B. W.; Raiteri, P.; Muzzioli, S.; Brown, D. H.; Stagni, S.; Massi, M. *Inorg. Chem.* **2014**, *53* (7), 3629–3641.

(149) Vaughan, J. G.; Reid, B. L.; Ramchandani, S.; Wright, P. J.; Muzzioli, S.; Skelton, B. W.; Raiteri, P.; Brown, D. H.; Stagni, S.; Massi, M. *Dalton Trans.* **2013**, *42* (39), 14100–14114.

(150) Li, X.-W.; Li, H.-Y.; Wang, G.-F.; Chen, F.; Li, Y.-Z.; Chen, X.-T.; Zheng, Y.-X.; Xue, Z.-L. *Organometallics* **2012**, *31* (10), 3829–3835.

(151) Koguro, K.; Oga, T.; Mitsui, S.; Orita, R. *Synthesis (Stuttg).* **1998**, *6*, 910–914.

(152) Bocharov, V. N.; Bureiko, S. F.; Golubev, N. S.; Shajakhmedov, S. S. *J. Mol. Struct.* **1998**, *444* (1-3), 57–62.

(153) Butler, R. N.; Garvin, V. C.; Lumbroso, H.; Liegeois, C. *J. Chem. Soc. Perkin Trans. II* **1984**, 721–725.

(154) Werrett, M. V; Chartrand, D.; Gale, J. D.; Hanan, G. S.; MacLellan, J. G.; Massi, M.; Muzzioli, S.; Raiteri, P.; Skelton, B. W.; Silberstein, M.; Stagni, S. *Inorg. Chem.* **2011**, *50* (4), 1229–1241.

(155) Hevia, E.; Pérez, J.; Riera, V.; Miguel, D.; Kassel, S.; Rheingold, A. *Inorg. Chem.* **2002**, *41* (18), 4673–4679.

(156) Coe, B. J.; Glenwright, S. J. *Coord. Chem. Rev.* **2000**, *203*, 5.

(157) Wright, P. J.; Muzzioli, S.; Werrett, M. V.; Raiteri, P.; Skelton, B. W.; Silvester, D. S.; Stagni, S.; Massi, M. *Organometallics* **2012**, *31* (21), 7566–7578.

(158) Palazzi, A.; Stagni, S.; Bordoni, S.; Monari, M.; Selva, S. *Organometallics* **2002**, *21* (18), 3774–3781.

(159) Worl, L. a.; Duesing, R.; Chen, P.; Ciana, L. Della; Meyer, T. J. *J. Chem. Soc. Dalt. Trans.* **1991**, 849.

(160) Vlček Jr, A. In *Top Organomet Chem*; Lees, A. J., Ed.; Springer, 2009; pp 115–158.

(161) Werrett, M. V. Design , Synthesis and Application of Luminescent Metal Tetrazolato Complexes in Optical Imaging, Curtin University, 2014.

(162) Caspar, J. V; Kober, E. M.; Sullivan, B. P.; Meyer, T. J. *J. Am Chem Soc* **1982**, *104*, 630–632.

(163) Abdel-Shafi, A. A.; Worrall, D. R. *J. Photochem. Photobiol. A Chem.* **2005**, *172* (2), 170–179.

(164) Schweitzer, C.; Schmidt, R. *Chem. Rev.* **2003**, *103*, 1685–1757.

(165) Makal, A.; Benedict, J.; Trzop, E.; Sokolow, J.; Fournier, B.; Chen, Y.; Kalinowski, J. A.; Graber, T.; Henning, R.; Coppens, P. *J. Phys. Chem. A* **2012**, *116* (13), 3359–3365.

(166) Bare, W. D.; Mack, N. H.; Demas, J. N.; Degraff, B. A. *Highly Efficient pH-Induced Intramolecular Quenching of Luminescence in Rhenium Complexes Containing the Hydroxypyridine ligand*; 2001; Vol. 4199.

(167) Werrett, M. V; Muzzioli, S.; Wright, P. J.; Palazzi, A.; Raiteri, P.; Zacchini, S.; Massi, M.; Stagni, S. *Inorg. Chem.* **2014**, *53*, 229–243.

(168) Palazzi, A.; Stagni, S.; Selva, S.; Monari, M. *J. Organomet. Chem.* **2003**, *669* (1-2), 135–140.

(169) Demas, J. N.; Crosby, G. A. *J. Am Chem Soc* **1970**, *93* (12), 2841.

(170) Eaton, D. F. *Pure Appl. Chem* **1988**, *60* (7), 1107–1114.

(171) Sheldrick, G. M. *Acta Crystallogr. Sect. C Struct. Chem.* **2015**, *71* (Md), 3–8.

(172) Blanco-Rodríguez, A. M.; Towrie, M.; Sýkora, J.; Záliš, S.; Vlček, A. *Inorg. Chem.* **2011**, *50* (13), 6122–6134.

(173) Blanco-Rodríguez, A. M.; Di Bilio, A. J.; Shih, C.; Stanislav, Z.; Vlček Jr, A. *Chemistry (Easton).* **2011**, *17* (19), 5350–5361.

(174) Vlcek, A.; Kvapilova, H.; Towrie, M.; Stanislav, Z. *Acc. Chem. Res.cc* **2015**, *48* (3), 868–876.

(175) Blanco-rodríguez, A. M.; Towrie, M.; Stanislav, Z.; Vlček Jr, A. *Inorg. Chem.* **2011**, *50*, 6122–6134.

(176) Demko, Z. P.; Sharpless, K. B. *J. Org. Chem* **2001**, *66* (24), 7945–7950.

(177) Demko, Z. P.; Sharpless, K. B. *Org. Lett.* **2002**, *4* (15), 2525–2527.

(178) Bargar, T. M.; Riley, C. M. *Synth. Commun.* **2006**, *10* (6), 479–487.

(179) Janiak, C. *J. Chem. Soc., Dalt. Trans.* **2000**, 3885–3896.

(180) Shih, C.; Museth, A. K.; Abrahamsson, M.; Blanco-Rodríguez, A. M.; Di Bilio, A. J.; Sudhamsu, J.; Crane, B. R.; Ronayne, K. L.; Towrie, M.; Vlček Jr, A.; Richards, J. H.; Winkler, J. R.; Gray, H. B. *Science (80-.).* **2008**, *320* (5884), 1760–1762.

(181) Wright, P. J.; Affleck, M. G.; Muzzioli, S.; Skelton, B. W.; Raiteri, P.; Silvester, D. S.; Stagni, S.; Massi, M.; Phillip, J.; Mark, G. A.; Brian, W.; Debbie, S.; Ligand-

induced, M. *Organometallics* **2013**, *32* (13), 3728–3737.

(182) Wallace, L.; Rillema, D. P. *Inorg. Chem.* **1993**, *32* (18), 3836–3843.

(183) Ziessel, R.; Juris, A.; Venturi, M. *Inorg. Chem.* **1998**, *37*, 5061–5069.

(184) Werrett, M. V; Huff, G. S.; Muzzioli, S.; Fiorini, V.; Zacchini, S.; Skelton, B. W.; Maggiore, A.; Malicka, J. M.; Cocchi, M.; Gordon, K. C.; Stagni, S.; Massi, M. *Dalton Trans.* **2015**, *44*, 8379–8393.

(185) Fiorini, V.; Ranieri, A. M.; Muzzioli, S.; Magee, K. D. M.; Zacchini, S.; Akabar, N.; Stefan, A.; Ogden, M. I.; Massi, M.; Stagni, S. *Dalton Trans.* **2015**, *44* (47), 20597–20608.

(186) Stagni, S.; Orselli, E.; Palazzi, A.; De Cola, L.; Zacchini, S.; Femoni, C.; Marcaccio, M.; Paolucci, F.; Zanarini, S. *Inorg. Chem.* **2007**, *46* (22), 9126–9138.

(187) Bullock, J. P.; Carter, E.; Johnson, R.; Kennedy, A. T.; Key, S. E.; Kraft, B. J.; Saxon, D.; Underwood, P. *Inorg. Chem.* **2008**, *47* (17), 7880–7887.

(188) Baiano, J. a.; Murphy, W. R. *Inorg. Chem.* **1991**, *30* (24), 4594–4598.

(189) Mukuta, T.; Simpson, P. V; Vaughan, J. G.; Skelton, B. W.; Stagni, S.; Massi, M.; Koike, K.; Ishitani, O.; Onda, K. *Inorg Chem* **2017**.

(190) Xu, Z.-L.; Li, H.-X.; Ren, Z.-G.; Du, W.-Y.; Xu, W.-C.; Lang, J.-P. *Tetrahedron* **2011**, 5282–5288.

(191) Huang, Y.-Z.; Miao, H.; Zhang, Q.-H.; Chen, C.; Xu, J. *Catal Lett* **2008**, *122* (3-4), 344–348.

(192) Liu, J.; Chen, J.; Zhao, J.; Zhao, Y.; Li, L.; Zhang, H. *Synthesis (Stuttg).* **2003**, No. 17, 2661–2666.

(193) Deng, J.; Mo, L.-P.; Zhao, F.-Y.; Hou, L.-L.; Yang, L.; Zhang, Z.-H. *Green Chem.* **2011**, *13* (9), 2576.

(194) Berg, J.; Tymoczko, J.; Stryer, L. In *Biochemistry*; New York, 2002.

(195) Tyrra, W.; Naumann, D.; Pantenburg, I. *J. Fluor. Chem.* **2003**, *120* (1), 13–19.

(196) Secondo, P. M.; Land, J. M.; Baughman, R. G.; Collier, H. L. *Inorganica Chim. Acta*

2000, *309* (1-2), 13–22.

(197) Simpson, P. V.; Skelton, B. W.; Raiteri, P.; Massi, M. *New J. Chem.* **2016**, 22–25.

(198) Sacksteder, L.; Zipp, A. P.; Brown, E. a.; Streich, J.; Demas, J. N.; DeGraff, B. a. *Inorg. Chem.* **1990**, *29* (21), 4335–4340.

(199) Borkman, R. F.; Hibbard, L. B.; Dillon, J. *Photochem. Photobiol.* **1986**, *43* (1), 13–19.

(200) Creed, D. *Photochem. Photobiol.* **1984**, *39* (4), 537–562.

(201) Igarashi, N.; Onoue, S.; Tsuda, Y. *Anal. Sci.* **2007**, *23* (8), 943–948.

(202) Catalfo, A.; Bracchitta, G.; De Guidi, G. *Photochem. Photobiol. Sci.* **2009**, *8* (10), 1467–1475.

(203) Fredericks, S. M.; Luong, J. C.; Wrighton, M. S. *J. Am. Chem. Soc.* **1979**, *101* (24), 7415–7417.

(204) Probst, B.; Guttentag, M.; Rodenberg, A.; Hamm, P.; Alberto, R. *Inorg. Chem.* **2011**, *50* (8), 3404–3412.

(205) Pratt, D. A.; Pesavento, R. P.; Donk, W. A. Van Der. *Org. Lett.* **2005**, *7* (13), 2735–2738.

(206) Haslam, E. **1973**, 372–382.

(207) Vaughan, J. G.; Reid, B. L.; Wright, P. J.; Ramchandani, S.; Brian, W.; Raiteri, P.; Muzzioli, S.; Brown, D. H.; Stagni, S. No. I.

(208) Vaughan, J. G.; Reid, B. L.; Ramchandani, S.; Wright, P. J.; Muzzioli, S.; Skelton, B. W.; Raiteri, P.; Brown, D. H.; Stagni, S.; Massi, M. *Dalton Trans.* **2013**, *42* (39), 14100–14114.

(209) Chan, C. Y.; Pellegrini, P. a; Greguric, I.; Barnard, P. J. *Inorg. Chem.* **2014**, *53* (20), 10862–10873.

(210) Leblond, F.; Davis, S. C.; Valdes, P. A.; Pogue, B. W. *J. Photochem. Photobiol. B* **2010**, *98* (1), 77–94.

(211) Hadjipanayis, C. G.; Jiang, H.; Roberts, D. W.; Yang, L. *Semin Oncol* **2011**, *38* (1),

109–118.

(212) Goldys, E. M. *Fluorescence Applications in Biotechnology and the Life Sciences*; Wiley-Blackwell, 2009.

(213) Lowry, M. S.; Hudson, W. R.; Pascal, R. A.; Bernhard, S. *J. Am. Chem. Soc.* **2004**, *126* (43), 14129–14135.

(214) Stephenson, K. A.; Banerjee, S. R.; Besanger, T.; Sogbein, O. O.; Levadala, M. K.; McFarlane, N.; Lemon, J. A.; Boreham, D. R.; Maresca, K. P.; Brennan, J. D.; Babich, J. W.; Zubieta, J.; Valliant, J. F. *J. Am. Chem. Soc.* **2004**, *126* (28), 8598–8599.

(215) Clarke, S.; Dillon, J. In *Animal Cell Culture: Essential Methods*; Davis, J. M., Ed.; John Wiley and Sons, 2011; pp 1–31.

(216) ThermoFisherScientific. Introduction to Cell Culture https://www.thermofisher.com/au/en/home/references/gibco-cell-culture-basics/introduction-to-cell-culture.html.

(217) Manning, L. *Int. J. Cancer* **1991**, *47* (2), 285–290.

(218) Rasche, W. C.; Baird, S.; Ralph, P.; Nakoinz, I. *Cell* **1978**, *15*, 261–267.

(219) Smith, C. L. In *Current Protocols in Molecular Biology*; John Wiley and Sons, 2008; pp 1–18.

(220) Foldes-Papp, Z.; Demel, U.; Tilz, G. P. *Int. Immunopharmacol.* **2003**, *3* (13-14), 1715–1729.

(221) Fernandez-Moreira, V.; Ortego, M. L.; Williams, C. F.; Coogan, M. P.; Villacampa, M. D.; Gimeno, M. C. *Organometallics* **2012**, *31* (16), 5950–5957.

(222) Werrett, M. V.; Wright, P. J.; Simpson, P. V; Raiteri, P.; Skelton, B. W.; Stagni, S.; Buckley, A.; Rigby, P.; Massi, M. *Dalt. Trans.* **2015**, No. 47, 20636–20647.

Appendix A X-ray Crystallography Data

A.1 Chapter 2

Table A 1. Crystal data and structure refinement for complex **7.**

Identification code	**7**
Empirical formula	$C_{23}H_{15}N_6O_4Re$
Formula weight	625.61
Temperature	100(2) K
Wavelength	0.71073 Å
Crystal system	Monoclinic
Space group	$P2_1/n$
Unit cell dimensions	a = 10.08970(10) Å
	b = 10.88040(10) Å
	c = 19.7094(3) Å
	β= 95.7110(10)°
Volume	2152.96(4) Å^3
Z	4
Density (calculated)	1.930 Mg/m^3
μ	5.689 mm^{-1}
Crystal size	0.61 x 0.32 x 0.16 mm^3
θ range for data collection	2.185 to 38.592°.
Index ranges	-17<=h<=17, -18<=k<=18, -34<=l<=34
Reflections collected	79395
Independent reflections	11957 [R(int) = 0.0328]
Completeness to θ = 36.000°	100.0 %
Absorption correction	Analytical
Max. and min. transmission	0.473 and 0.140
Refinement method	Full-matrix least-squares on F^2
Data / restraints / parameters	11957 / 0 / 308
Goodness-of-fit on F^2	1.094
Final R indices [I>2σ(I)]	R1 = 0.0205, wR2 = 0.0458
R indices (all data)	R1 = 0.0238, wR2 = 0.0469
Largest diff. peak and hole	1.566 and -0.633 e.Å^{-3}

Table A 2. Selected bond lengths [Å] and angles [°] for complex **7.**

Re(1)-C(3)	1.9215(14)
Re(1)-C(2)	1.9238(15)
Re(1)-C(1)	1.9237(14)
Re(1)-N(2)	2.1645(12)
Re(1)-N(21)	2.1752(12)
Re(1)-N(11)	2.1813(11)
C(3)-Re(1)-C(2)	87.25(6)
C(3)-Re(1)-C(1)	88.28(6)
C(2)-Re(1)-C(1)	89.02(6)
C(3)-Re(1)-N(2)	91.46(5)
C(2)-Re(1)-N(2)	177.98(5)
C(1)-Re(1)-N(2)	89.40(5)
C(3)-Re(1)-N(21)	171.62(6)
C(2)-Re(1)-N(21)	98.24(5)
C(1)-Re(1)-N(21)	98.10(5)
N(2)-Re(1)-N(21)	83.22(4)
C(3)-Re(1)-N(11)	97.36(5)
C(2)-Re(1)-N(11)	97.99(5)
C(1)-Re(1)-N(11)	171.18(5)
N(2)-Re(1)-N(11)	83.70(4)
N(21)-Re(1)-N(11)	75.68(4)
N(2)-N(1)-C(5)	103.46(11)
N(3)-N(2)-N(1)	111.07(11)
N(3)-N(2)-Re(1)	122.35(8)
N(1)-N(2)-Re(1)	126.07(9)

Table A 3. Crystal data and structure refinement for complex **8**.

Identification code	**8**
Empirical formula	$C_{23}H_{15}N_6O_4Re$
Formula weight	625.61
Temperature	100(2) K
Wavelength	0.71073 Å
Crystal system	Monoclinic
Space group	$P2_1/n$
Unit cell dimensions	a = 9.7182(2) Å
	b = 10.7464(2) Å
	c = 20.5528(3) Å
	β= 99.7700(10)°.
Volume	2115.31(7) Å^3
Z	4
Density (calculated)	1.964 Mg/m^3
μ	5.790 mm^{-1}
Crystal size	0.37 x 0.10 x 0.03 mm^3
θ range for data collection	2.764 to 31.978°.
Index ranges	-14<=h<=14, -15<=k<=15, -30<=l<=29
Reflections collected	39769
Independent reflections	7023 [R(int) = 0.0605]
Completeness to θ = 30.000°	99.9 %
Absorption correction	Analytical
Max. and min. transmission	0.856 and 0.342
Refinement method	Full-matrix least-squares on F^2
Data / restraints / parameters	7023 / 0 / 308
Goodness-of-fit on F^2	1.047
Final R indices [I>2σ(I)]	R1 = 0.0330, wR2 = 0.0668
R indices (all data)	R1 = 0.0430, wR2 = 0.0715
Largest diff. peak and hole	1.884 and -1.610 e.Å^{-3}

Table A 4. Selected bond lengths [Å] and angles [°] for complex **8.**

Re(1)-C(2)	1.918(4)
Re(1)-C(1)	1.922(4)
Re(1)-C(3)	1.929(4)
Re(1)-N(21)	2.165(3)
Re(1)-N(2)	2.171(3)
Re(1)-N(11)	2.187(3)
C(2)-Re(1)-C(1)	89.50(14)
C(2)-Re(1)-C(3)	86.97(15)
C(1)-Re(1)-C(3)	89.39(14)
C(2)-Re(1)-N(21)	98.24(13)
C(1)-Re(1)-N(21)	96.41(12)
C(3)-Re(1)-N(21)	172.21(13)
C(2)-Re(1)-N(2)	178.32(13)
C(1)-Re(1)-N(2)	90.43(12)
C(3)-Re(1)-N(2)	91.35(13)
N(21)-Re(1)-N(2)	83.43(10)
C(2)-Re(1)-N(11)	96.27(12)
C(1)-Re(1)-N(11)	170.90(12)
C(3)-Re(1)-N(11)	97.92(12)
N(21)-Re(1)-N(11)	75.83(10)
N(2)-Re(1)-N(11)	84.01(10)

Table A 5. Crystal data and structure refinement for complex **6**.

Identification code	**6**
Empirical formula	$C_{22}H_{12}N_6O_4Re$
Formula weight	610.58
Temperature	100(2) K
Wavelength	0.71073 Å
Crystal system	Triclinic
Space group	$P\bar{1}$
Unit cell dimensions	a = 9.2949(3) Å
	b = 9.5006(3) Å
	c = 12.6357(4) Å
	α= 95.587(2)°
	β= 104.913(3)°
	γ = 108.209(3)°
Volume	1004.85(6) Å^3
Z	2
Density (calculated)	2.018 Mg/m^3
μ	6.092 mm^{-1}
Crystal size	0.20 x 0.145 x 0.06 mm^3
θ range for data collection	2.300 to 35.000°.
Index ranges	-15<=h<=15, -15<=k<=15, -20<=l<=20
Reflections collected	32529
Independent reflections	8860 [R(int) = 0.0575]
Completeness to θ = 35.00°	100.0 %
Absorption correction	Semi-empirical from equivalents
Max. and min. transmission	1.000/ 0.649
Refinement method	Full-matrix least-squares on F^2
Data / restraints / parameters	8860 / 1 / 303
Goodness-of-fit on F^2	1.034
Final R indices [I>2σ(I)]	R1 = 0.0328, wR2 = 0.0599
R indices (all data)	R1 = 0.0425, wR2 = 0.0627
Largest diff. peak and hole	2.114 and -1.867 e.Å^{-3}

Table A 6. Selected bond lengths [Å] and angles [°] for complex **6**.

Re(1)-C(3)	1.924(3)
Re(1)-C(2)	1.924(3)
Re(1)-C(1)	1.926(3)
Re(1)-N(11)	2.171(2)
Re(1)-N(2)	2.174(2)
Re(1)-N(21)	2.177(2)
C(3)-Re(1)-C(2)	88.47(11)
C(3)-Re(1)-C(1)	88.54(12)
C(2)-Re(1)-C(1)	88.77(12)
C(3)-Re(1)-N(11)	97.49(10)
C(2)-Re(1)-N(11)	95.48(10)
C(1)-Re(1)-N(11)	172.70(10)
C(3)-Re(1)-N(2)	92.94(10)
C(2)-Re(1)-N(2)	174.93(10)
C(1)-Re(1)-N(2)	96.13(11)
N(11)-Re(1)-N(2)	79.51(8)
C(3)-Re(1)-N(21)	173.14(10)
C(2)-Re(1)-N(21)	93.89(9)
C(1)-Re(1)-N(21)	97.94(10)
N(11)-Re(1)-N(21)	75.89(8)
N(2)-Re(1)-N(21)	84.17(8)

Table A 7. Hydrogen bonds for complex **6** [Å and °].

D-H...A	d(D-H)	d(H...A)	d(D...A)	<(DHA)
O(53)-H(53)...N(3)[1]	0.886(18)	2.004(18)	2.888(3)	176(3)

Symmetry transformations used to generate equivalent atoms: [1] 2-x,1-y,-z

A.2 Chapter 3

Table A 8. Crystal data and structure refinement for complex **15Phe**.

Identification code	**15Phe**
Empirical formula	$C_{33}H_{24}N_7O_6Re$, $11/8(CH_2Cl_2)$
Formula weight	917.57
Temperature	100(2) K
Wavelength	1.54178 Å
Crystal system	Orthorhombic
Space group	$P2_12_12$
Unit cell dimensions	a = 33.5824(6) Å
	b = 22.2724(7) Å
	c = 9.69150(10) Å
Volume	7248.9(3) Å^3
Z	8
Density (calculated)	1.682 Mg/m^3
μ	8.884 mm^{-1}
Crystal size	0.21 x 0.14 x 0.03 mm^3
θ range for data collection	3.30 to 67.37°.
Index ranges	-39<=h<=38, -26<=k<=26, -11<=l<=11
Reflections collected	60037
Independent reflections	12914 [R(int) = 0.0946]
Completeness to θ = 67.37°	99.2 %
Absorption correction	Analytical
Max. and min. transmission	0.777 and 0.347
Refinement method	Full-matrix least-squares on F^2
Data / restraints / parameters	12914 / 30 / 951
Goodness-of-fit on F^2	1.024
Final R indices [I>2σ(I)]	R1 = 0.0477, wR2 = 0.1151
R indices (all data)	R1 = 0.0549, wR2 = 0.1217
Absolute structure parameter	-0.052(11)
Largest diff. peak and hole	3.209 and -2.052 e.Å^{-3}

Table A 9. Selected bond lengths [Å] and angles [°] for complex **15Phe.**

Re(1)-C(12)	1.911(9)
Re(1)-C(13)	1.923(7)
Re(1)-C(11)	1.928(9)
Re(1)-N(111)	2.171(6)
Re(1)-N(121)	2.174(6)
Re(1)-N(12)	2.184(6)
Re(2)-C(23)	1.922(8)
Re(2)-C(22)	1.932(9)
Re(2)-C(21)	1.942(8)
Re(2)-N(211)	2.155(6)
Re(2)-N(221)	2.172(7)
Re(2)-N(22)	2.189(6)
C(12)-Re(1)-C(13)	88.6(3)
C(12)-Re(1)-C(11)	88.4(4)
C(13)-Re(1)-C(11)	89.8(4)
C(12)-Re(1)-N(111)	96.7(3)
C(13)-Re(1)-N(111)	97.4(3)
C(11)-Re(1)-N(111)	171.2(3)
C(12)-Re(1)-N(121)	91.8(3)
C(13)-Re(1)-N(121)	173.1(3)
C(11)-Re(1)-N(121)	97.1(3)
N(111)-Re(1)-N(121)	75.7(2)
C(12)-Re(1)-N(12)	177.9(3)
C(13)-Re(1)-N(12)	93.2(3)
C(11)-Re(1)-N(12)	92.7(3)
N(111)-Re(1)-N(12)	81.9(2)
N(121)-Re(1)-N(12)	86.3(2)
C(23)-Re(2)-C(22)	88.1(4)
C(23)-Re(2)-C(21)	91.0(4)
C(22)-Re(2)-C(21)	87.8(4)
C(23)-Re(2)-N(211)	97.0(4)
C(22)-Re(2)-N(211)	93.9(3)
C(21)-Re(2)-N(211)	171.8(3)
C(23)-Re(2)-N(221)	172.6(4)
C(22)-Re(2)-N(221)	95.5(4)

C(21)-Re(2)-N(221)	95.6(3)
N(211)-Re(2)-N(221)	76.3(2)
C(23)-Re(2)-N(22)	91.8(3)
C(22)-Re(2)-N(22)	176.7(3)
C(21)-Re(2)-N(22)	95.5(3)
N(211)-Re(2)-N(22)	82.8(2)
N(221)-Re(2)-N(22)	84.2(2)

Table A 10. Hydrogen bonds for complex **15Phe** [Å and °].

D-H...A	d(D-H)	d(H...A)	d(D...A)	<(DHA)
N(157)-H(157)...O(257)[1]	0.88	2.24	2.963(8)	139.7
N(257)-H(257)...O(157)	0.88	2.01	2.872(8)	164.6

Symmetry transformations used to generate equivalent atoms: [1] x,y,z+1

Table A 11. Crystal data and structure refinement for complex **15Gly.**

Identification code	**15Gly**
Empirical formula	$C_{26}H_{18}N_7O_6Re$
Formula weight	710.67
Temperature	100(2) K
Wavelength	0.71073 Å
Crystal system	Triclinic
Space group	$P\bar{1}$
Unit cell dimensions	a = 9.6772(2) Å
	b = 12.0421(3) Å
	c = 12.6759(3) Å
	α= 88.966(2)°
	β= 68.533(2)°
	γ = 68.542(2)°
Volume	1267.92(6) Å^3
Z	2
Density (calculated)	1.861 Mg/m^3
μ	4.849 mm^{-1}
Crystal size	0.45 x 0.32 x 0.12 mm^3
θ range for data collection	2.693 to 37.315°.
Index ranges	-16<=h<=16, -20<=k<=20, -21<=l<=21
Reflections collected	46810
Independent reflections	12721 [R(int) = 0.0320]
Completeness to θ = 36.500°	99.7 %
Absorption correction	Analytical
Max. and min. transmission	0.625 and 0.281
Refinement method	Full-matrix least-squares on F^2
Data / restraints / parameters	12721 / 0 / 362
Goodness-of-fit on F^2	1.065
Final R indices [$I > 2\sigma(I)$]	$R1$ = 0.0237, $wR2$ = 0.0543
R indices (all data)	$R1$ = 0.0262, $wR2$ = 0.0558
Largest diff. peak and hole	2.463 and -1.943 e.Å^{-3}

Table A 12. Selected bond lengths [Å] and angles [°] for complex **15Gly.**

Re(1)-C(2)	1.9206(17)
Re(1)-C(3)	1.9211(17)
Re(1)-C(1)	1.9230(19)
Re(1)-N(2)	2.1646(14)
Re(1)-N(11)	2.1720(14)
Re(1)-N(21)	2.1744(14)
C(2)-Re(1)-C(3)	89.41(7)
C(2)-Re(1)-C(1)	88.65(8)
C(3)-Re(1)-C(1)	86.50(8)
C(2)-Re(1)-N(2)	179.87(6)
C(3)-Re(1)-N(2)	90.54(6)
C(1)-Re(1)-N(2)	91.46(7)
C(2)-Re(1)-N(11)	95.32(6)
C(3)-Re(1)-N(11)	99.42(6)
C(1)-Re(1)-N(11)	172.87(7)
N(2)-Re(1)-N(11)	84.57(5)
C(2)-Re(1)-N(21)	96.96(6)
C(3)-Re(1)-N(21)	172.37(6)
C(1)-Re(1)-N(21)	97.80(7)
N(2)-Re(1)-N(21)	83.08(5)
N(11)-Re(1)-N(21)	75.88(5)

Table A 13. Crystal data and structure refinement for complex **19Phe.**

Identification code	**19Phe**
Empirical formula	$C_{27.50}H_{23}N_7O_{4.50}Re$
Formula weight	709.73
Temperature	100(2) K
Wavelength	0.71073 Å
Crystal system	Triclinic
Space group	$P\bar{1}$
Unit cell dimensions	a = 10.9419(5) Å
	b = 11.7035(5) Å
	c = 12.0764(5) Å
	α= 89.254(3)°
	β= 63.115(5)°
	γ = 73.746(4)°
Volume	1312.51(11) $Å^3$
Z	2
Density (calculated)	1.796 Mg/m^3
μ	4.680 mm^{-1}
Crystal size	0.575 x 0.181 x 0.097 mm^3
θ range for data collection	2.193 to 31.00°.
Index ranges	-15<=h<=15, -16<=k<=16, -17<=l<=17
Reflections collected	16059
Independent reflections	8374 [R(int) = 0.0275]
Completeness to θ = 31.00°	100.0 %
Absorption correction	Analytical
Max. and min. transmission	0.699 and 0.320
Refinement method	Full-matrix least-squares on F^2
Data / restraints / parameters	8374 / 1 / 384
Goodness-of-fit on F^2	1.028
Final R indices [I>2σ(I)]	R1 = 0.0263, wR2 = 0.0566
R indices (all data)	R1 = 0.0303, wR2 = 0.0585
Largest diff. peak and hole	1.439 and -0.627 e.$Å^{-3}$

Table A 14. Selected bond lengths [Å] and angles [°] for complex **19Phe.**

Re(1)-C(3)	1.917(3)
Re(1)-C(2)	1.918(3)
Re(1)-C(1)	1.931(3)
Re(1)-N(2)	2.164(2)
Re(1)-N(21)	2.171(2)
Re(1)-N(11)	2.175(2)
C(3)-Re(1)-C(2)	88.04(11)
C(3)-Re(1)-C(1)	88.88(11)
C(2)-Re(1)-C(1)	90.44(11)
C(3)-Re(1)-N(2)	92.09(9)
C(2)-Re(1)-N(2)	178.09(9)
C(1)-Re(1)-N(2)	91.47(9)
C(3)-Re(1)-N(21)	173.33(9)
C(2)-Re(1)-N(21)	93.98(9)
C(1)-Re(1)-N(21)	97.46(10)
N(2)-Re(1)-N(21)	85.69(8)
C(3)-Re(1)-N(11)	97.52(10)
C(2)-Re(1)-N(11)	95.49(9)
C(1)-Re(1)-N(11)	171.41(10)
N(2)-Re(1)-N(11)	82.61(8)
N(21)-Re(1)-N(11)	75.97(8)

Table A 15. Hydrogen bonds for complex **19Phe** [Å and °].

D-H...A	d(D-H)	d(H...A)	d(D...A)	<(DHA)
N(51)-H(51N)...N(4)[1]	0.881(18)	2.053(19)	2.923(3)	170(3)

Symmetry transformations used to generate equivalent atoms:

[1] 1-x,1-y,-z

A.3 Chapter 4

Table A 16. Crystal data and structure refinement for complex **23.**

Identification code	**23**
Empirical formula	$C_{23}H_{16}F_3N_4O_6ReS$
Formula weight	719.66
Temperature	100(2) K
Wavelength	1.54178 Å
Crystal system	Orthorhombic
Space group	*Pbca*
Unit cell dimensions	a = 18.8083(2) Å
	b = 12.79370(10) Å
	c = 19.9734(4) Å
Volume	4806.15(12) Å^3
Z	8
Density (calculated)	1.989 Mg/m^3
μ	11.362 mm^{-1}
Crystal size	0.48 x 0.03 x 0.015 mm^3
θ range for data collection	4.43 to 67.35°.
Index ranges	-22<=h<=22, -13<=k<=14, -23<=l<=23
Reflections collected	43235
Independent reflections	4285 [R(int) = 0.0581]
Completeness to θ = 67.35°	99.4 %
Absorption correction	Analytical
Max. and min. transmission	0.828 and 0.155
Refinement method	Full-matrix least-squares on F^2
Data / restraints / parameters	4285 / 0 / 406
Goodness-of-fit on F^2	1.145
Final R indices [I>2σI)]	R1 = 0.0261, wR2 = 0.0581
R indices (all data)	R1 = 0.0300, wR2 = 0.0597
Largest diff. peak and hole	0.997 and -0.871 e.Å^{-3}

Table A 17. Selected bond lengths [Å] and angles [°] for complex **23.**

Re(1)-C(301)	1.920(4)
Re(1)-C(201)	1.921(4)
Re(1)-C(101)	1.970(4)
Re(1)-C(2)	2.131(4)
Re(1)-N(21)	2.208(3)
Re(1)-N(31)	2.220(3)
C(301)-Re(1)-C(201)	88.83(15)
C(301)-Re(1)-C(101)	90.16(15)
C(201)-Re(1)-C(101)	89.55(15)
C(301)-Re(1)-C(2)	91.69(14)
C(201)-Re(1)-C(2)	97.38(15)
C(101)-Re(1)-C(2)	172.86(15)
C(301)-Re(1)-N(21)	95.42(14)
C(201)-Re(1)-N(21)	170.61(14)
C(101)-Re(1)-N(21)	98.79(13)
C(2)-Re(1)-N(21)	74.17(13)
C(301)-Re(1)-N(31)	178.81(14)
C(201)-Re(1)-N(31)	91.09(13)
C(101)-Re(1)-N(31)	91.03(13)
C(2)-Re(1)-N(31)	87.15(12)
N(21)-Re(1)-N(31)	84.48(12)

Table A 18. Crystal data and structure refinement for complex **24.**

Identification code	**24**
Empirical formula	$C_{25}H_{23}Cl_2F_6N_5O_3PRe$
Formula weight	843.55
Temperature	100(2) K
Wavelength	0.71073 Å
Crystal system	Triclinic
Space group	$P\bar{1}$
Unit cell dimensions	a = 10.6905(5) Å
	b = 11.4861(9) Å
	c = 13.9037(11) Å
	α= 110.318(7)°
	β= 101.341(5)°
	γ = 106.846(5)°
Volume	1445.84(17) Å^3
Z	2
Density (calculated)	1.938 Mg/m^3
μ	4.519 mm^{-1}
Crystal size	0.12 x 0.08 x 0.05 mm^3
θ range for data collection	2.94 to 31.00°.
Index ranges	-15<=h<=15, -16<=k<=16, -20<=l<=19
Reflections collected	27593
Independent reflections	9160 [R(int) = 0.0918]
Completeness to θ = 31.00°	99.1 %
Absorption correction	Analytical
Max. and min. transmission	0.859 and 0.745
Refinement method	Full-matrix least-squares on F^2
Data / restraints / parameters	9160 / 0 / 390
Goodness-of-fit on F^2	1.034
Final R indices [I>2σ(I)]	R1 = 0.0574, wR2 = 0.1235
R indices (all data)	R1 = 0.0689, wR2 = 0.1308
Largest diff. peak and hole	4.708 and -3.680 e.Å^{-3}

Table A 19. Bond lengths [Å] and angles [°] for complex **24.**

Re(1)-C(201)	1.927(6)
Re(1)-C(301)	1.928(6)
Re(1)-C(101)	1.950(6)
Re(1)-C(2)	2.137(6)
Re(1)-N(21)	2.200(5)
Re(1)-N(31)	2.209(4)
C(201)-Re(1)-C(301)	88.0(2)
C(201)-Re(1)-C(101)	88.3(2)
C(301)-Re(1)-C(101)	91.5(2)
C(201)-Re(1)-C(2)	102.0(2)
C(301)-Re(1)-C(2)	91.1(2)
C(101)-Re(1)-C(2)	169.5(2)
C(201)-Re(1)-N(21)	176.12(18)
C(301)-Re(1)-N(21)	93.9(2)
C(101)-Re(1)-N(21)	95.0(2)
C(2)-Re(1)-N(21)	74.62(19)
C(201)-Re(1)-N(31)	92.36(19)
C(301)-Re(1)-N(31)	176.2(2)
C(101)-Re(1)-N(31)	92.3(2)
C(2)-Re(1)-N(31)	85.12(18)
N(21)-Re(1)-N(31)	85.52(16)

Table A 20. Crystal data and structure refinement for complex **27.**

Identification code	**27**
Empirical formula	$C_{22}H_{18}F_6N_4O_3PRe$
Formula weight	717.57
Temperature	100(2) K
Wavelength	0.71073 Å
Crystal system	Monoclinic
Space group	*I* 2/*a*
Unit cell dimensions	*a* = 14.7806(2) Å
	b = 16.4531(2) Å
	c = 19.7556(3) Å
	β= 94.7550(10)°
Volume	4787.76(11) $Å^3$
Z	8
Density (calculated)	1.991 Mg/m^3
μ	5.223 mm^{-1}
Crystal size	0.42 x 0.30 x 0.085 mm^3
θ range for data collection	2.069 to 34.506°.
Index ranges	-22<=h<=22, -26<=k<=26, -31<=l<=31
Reflections collected	63285
Independent reflections	9797 [*R*(int) = 0.0347]
Completeness to θ = 33.00°	100.0 %
Absorption correction	Analytical
Max. and min. transmission	0.726 and 0.320
Refinement method	Full-matrix least-squares on F^2
Data / restraints / parameters	9797 / 0 / 336
Goodness-of-fit on F^2	1.056
Final *R* indices [$I>2\sigma(I)$]	*R*1 = 0.0263, *wR*2 = 0.0587
R indices (all data)	*R*1 = 0.0336, *wR*2 = 0.0618
Largest diff. peak and hole	1.653 and -0.558 $e.Å^{-3}$

Table A 21. Selected bond lengths [Å] and angles [°] for complex **27.**

Re(1)-C(3)	1.921(2)
Re(1)-C(1)	1.920(2)
Re(1)-C(2)	1.926(2)
Re(1)-N(11)	2.1763(19)
Re(1)-N(21)	2.1799(19)
Re(1)-N(51)	2.1996(19)
C(3)-Re(1)-C(1)	91.01(10)
C(3)-Re(1)-C(2)	90.14(9)
C(1)-Re(1)-C(2)	89.61(10)
C(3)-Re(1)-N(11)	97.42(9)
C(1)-Re(1)-N(11)	171.52(8)
C(2)-Re(1)-N(11)	91.23(9)
C(3)-Re(1)-N(21)	172.23(9)
C(1)-Re(1)-N(21)	95.47(8)
C(2)-Re(1)-N(21)	94.19(8)
N(11)-Re(1)-N(21)	76.06(7)
C(3)-Re(1)-N(51)	90.41(8)
C(1)-Re(1)-N(51)	93.79(8)
C(2)-Re(1)-N(51)	176.55(8)
N(11)-Re(1)-N(51)	85.32(7)
N(21)-Re(1)-N(51)	84.90(7)

Table A 22. Crystal data and structure refinement for complex **26.**

Identification code	**26**
Empirical formula	$C_{44}H_{31}F_6N_6O_{12.50}Re_2S_2$
Formula weight	1394.27
Temperature	100(2) K
Wavelength	0.71073 Å
Crystal system	trigonal
Space group	*R*-3
Unit cell dimensions	*a* = 32.6304(6) Å
	b = 32.6304(6) Å
	c = 12.8562(1) Å
	β= 94.7550(10)°
Volume	11854.62(18) Å^3
Z	9
Density (calculated)	1.758 g/cm^3
μ	4.754 mm^{-1}
Crystal size	0.36 × 0.22 × 0.21 mm^3
Reflections collected	131293
Independent reflections	13600 (R_{int} = 0.0274)
Refinement method	Full-matrix least-squares on F^2
Restraints / parameters	18 / 350
Goodness-of-fit on F^2	1.005
Final *R* indices [$I>2\sigma(I)$]	*R1* = 0.0215, *wR2* = 0.0590

Table A 23. Selected bond lengths and angles for complex **26.**

Re1—C102	1.9146 (17)
Re1—C103	1.9210 (15)
Re1—C101	1.9394 (16)
Re1—N21	2.1727 (12)
Re1—N11	2.1780 (13)
Re1—N1	2.2031 (13)
O101—C101	1.144 (2)
O102—C102	1.152 (2)
O103—C103	1.158 (2)
C102—Re1—C103	89.79 (7)
C102—Re1—C101	87.26 (7)
C103—Re1—C101	89.78 (7)
C102—Re1—N21	171.85 (7)
C103—Re1—N21	98.36 (6)
C101—Re1—N21	92.92 (6)
C102—Re1—N11	95.87 (7)
C103—Re1—N11	173.54 (7)
C101—Re1—N11	93.59 (6)
N21—Re1—N11	75.98 (5)
C102—Re1—N1	95.16 (7)
C103—Re1—N1	91.07 (6)
C101—Re1—N1	177.44 (6)
N21—Re1—N1	84.57 (5)
N11—Re1—N1	85.33 (5)

Table A 24. Hydrogen bonds for complex **26** [Å and °].

D—H···*A*	*D*—H	H···*A*	*D*···*A*	*D*—H···*A*
C2—H2···O2^{i}	0.95	2.43	3.253 (2)	145
C6—H6···O3^{ii}	0.95	2.41	3.275 (2)	151
C26—H26···O3^{ii}	0.95	2.56	3.147 (2)	120
C114—H11*H*···O102	0.98	2.41	3.33 (3)	156
C114—H11*J*···O101^{iii}	0.98	2.70	3.42 (2)	131

A.4 Chapter 5

Table A 25. Crystal data and structure refinement for complex **37Br**.

Identification code	**37Br**
Empirical formula	$C_{18}H_{13}BrN_3O_4Re$
Formula weight	601.42
Temperature	100(2) K
Wavelength	0.71073 Å
Crystal system	Monoclinic
Space group	$P2_1/n$
Unit cell dimensions	a = 11.5983(2) Å
	b = 8.8040(2) Å
	c = 17.5334(3) Å
	β= 97.770(2)°
Volume	1773.92(6) $Å^3$
Z	4
Density (calculated)	2.252 Mg/m^3
μ	9.133 mm^{-1}
Crystal size	0.367 x 0.335 x 0.208 mm^3
θ range for data collection	2.915 to 33.047°.
Index ranges	-17<=h<=17, -13<=k<=13, -26<=l<=23
Reflections collected	20788
Independent reflections	6368 [R(int) = 0.0292]
Completeness to θ = 31.00°	99.9 %
Absorption correction	Analytical
Max. and min. transmission	0.212 and 0.100
Refinement method	Full-matrix least-squares on F^2
Data / restraints / parameters	6368 / 0 / 245
Goodness-of-fit on F^2	1.062
Final R indices [I>2σ(I)]	$R1$ = 0.0241, $wR2$ = 0.0523
R indices (all data)	$R1$ = 0.0281, $wR2$ = 0.0538
Largest diff. peak and hole	1.585 and -1.777 e.$Å^{-3}$

Table A 26. Selected bond lengths [Å] and angles [°] for complex **37Br.**

Re(1)-C(101)	1.909(3)
Re(1)-C(103)	1.912(3)
Re(1)-C(102)	1.943(3)
Re(1)-C(2)	2.149(2)
Re(1)-N(21)	2.208(2)
Re(1)-Br(1)	2.6325(3)
C(101)-Re(1)-C(103)	88.67(11)
C(101)-Re(1)-C(102)	91.34(11)
C(103)-Re(1)-C(102)	89.26(11)
C(101)-Re(1)-C(2)	96.62(10)
C(103)-Re(1)-C(2)	100.37(10)
C(102)-Re(1)-C(2)	167.60(11)
C(101)-Re(1)-N(21)	93.17(10)
C(103)-Re(1)-N(21)	174.52(9)
C(102)-Re(1)-N(21)	95.85(10)
C(2)-Re(1)-N(21)	74.29(9)
C(101)-Re(1)-Br(1)	177.05(8)
C(103)-Re(1)-Br(1)	92.11(8)
C(102)-Re(1)-Br(1)	85.82(8)
C(2)-Re(1)-Br(1)	86.04(6)
N(21)-Re(1)-Br(1)	86.32(5)

Table A 27. Crystal data and structure refinement for complex **37Cl**

Identification code	**37Cl**
Empirical formula	$C_{18}H_{13}ClN_3O4Re$
Formula weight	556.96
Temperature	100(2) K
Wavelength	0.71073 Å
Crystal system	Monoclinic
Space group	$P2_1/n$
Unit cell dimensions	a = 11.4711(3) Å
	b = 8.7403(2) Å
	c = 17.4691(4) Å
	β= 96.938(3)°
Volume	1738.64(7) $Å^3$
Z	4
Density (calculated)	2.128 Mg/m^3
μ	7.174 mm^{-1}
Crystal size	0.591 x 0.322 x 0.148 mm^3
θ range for data collection	2.255 to 30.00°.
Index ranges	-15<=h<=16, -12<=k<=11, -24<=l<=24
Reflections collected	17324
Independent reflections	5075 [R(int) = 0.0296]
Completeness to θ = 30.00°	100.0 %
Absorption correction	Analytical
Max. and min. transmission	0.428 and 0.101
Refinement method	Full-matrix least-squares on F^2
Data / restraints / parameters	5075 / 0 / 245
Goodness-of-fit on F^2	1.045
Final R indices [I>2σ(I)]	R1 = 0.0227, wR2 = 0.0505
R indices (all data)	R1 = 0.0267, wR2 = 0.0522
Largest diff. peak and hole	2.064 and -1.114 e.$Å^{-3}$

Table A 28. Selected bond lengths [Å] and angles [°] for complex **37Cl.**

Re(1)-C(101)	1.913(3)
Re(1)-C(103)	1.920(3)
Re(1)-C(102)	1.940(3)
Re(1)-C(2)	2.157(3)
Re(1)-N(21)	2.210(2)
Re(1)-Cl(1)	2.5012(7)
C(101)-Re(1)-C(103)	88.90(12)
C(101)-Re(1)-C(102)	91.06(12)
C(103)-Re(1)-C(102)	89.18(11)
C(101)-Re(1)-C(2)	96.34(11)
C(103)-Re(1)-C(2)	100.47(11)
C(102)-Re(1)-C(2)	167.91(11)
C(101)-Re(1)-N(21)	92.55(10)
C(103)-Re(1)-N(21)	174.52(10)
C(102)-Re(1)-N(21)	96.07(10)
C(2)-Re(1)-N(21)	74.13(9)
C(101)-Re(1)-Cl(1)	177.19(8)
C(103)-Re(1)-Cl(1)	92.23(9)
C(102)-Re(1)-Cl(1)	86.39(8)
C(2)-Re(1)-Cl(1)	85.99(7)
N(21)-Re(1)-Cl(1)	86.56(6)

Table A 29. Crystal data and structure refinement for complex **38Br.**

Identification code	**38Br**
Empirical formula	$C_{22}H_{15}BrN_3O4Re$
Formula weight	651.48
Temperature	100(2) K
Wavelength	0.71073 Å
Crystal system	Triclinic
Space group	$P\bar{1}$
Unit cell dimensions	a = 7.3649(3) Å
	b = 7.9930(4) Å
	c = 18.0910(7) Å
	α= 83.816(4)°
	β= 82.945(3)°
	γ = 82.242(4)°
Volume	1042.73(8) $Å^3$
Z	2
Density (calculated)	2.075 Mg/m^3
μ	7.778 mm^{-1}
Crystal size	0.214 x 0.114 x 0.037 mm^3
θ range for data collection	2.808 to 30.0°.
Index ranges	-10<=h<=9, -11<=k<=11, -22<=l<=25
Reflections collected	12202
Independent reflections	6086 [R(int) = 0.0284]
Completeness to θ = 30.0°	99.9 %
Absorption correction	Analytical
Max. and min. transmission	0.762 and 0.397
Refinement method	Full-matrix least-squares on F^2
Data / restraints / parameters	6086 / 36 / 309
Goodness-of-fit on F^2	1.077
Final R indices [I>2σ(I)]	R1 = 0.0290, wR2 = 0.0636
R indices (all data)	R1 = 0.0329, wR2 = 0.0650
Largest diff. peak and hole	1.386 and -1.269 e.$Å^{-3}$

Table A 30. Selected bond lengths [Å] and angles [°] for complex **38Br.**

Re(1)-C(101)	1.865(6)
Re(1)-C(103)	1.905(4)
Re(1)-C(104)	1.902(9)
Re(1)-C(102)	1.964(4)
Re(1)-C(2)	2.111(3)
Re(1)-N(21)	2.270(3)
Re(1)-Br(1')	2.544(3)
Re(1)-Br(1)	2.5898(6)
C(101)-Re(1)-C(103)	90.3(2)
C(101)-Re(1)-C(102)	87.0(2)
C(103)-Re(1)-C(102)	85.27(14)
C(101)-Re(1)-C(2)	90.0(2)
C(103)-Re(1)-C(2)	97.19(14)
C(102)-Re(1)-C(2)	176.19(13)
C(101)-Re(1)-N(21)	93.7(2)
C(103)-Re(1)-N(21)	170.26(12)
C(102)-Re(1)-N(21)	103.80(12)
C(2)-Re(1)-N(21)	73.95(12)
C(104)-Re(1)-Br(1')	178.2(8)
C(101)-Re(1)-Br(1)	176.4(2)
C(103)-Re(1)-Br(1)	92.77(10)
C(102)-Re(1)-Br(1)	95.12(10)
C(2)-Re(1)-Br(1)	87.69(9)
N(21)-Re(1)-Br(1)	82.99(7)

Appendix B ^{1}H NMR Spectra Showing Full Range

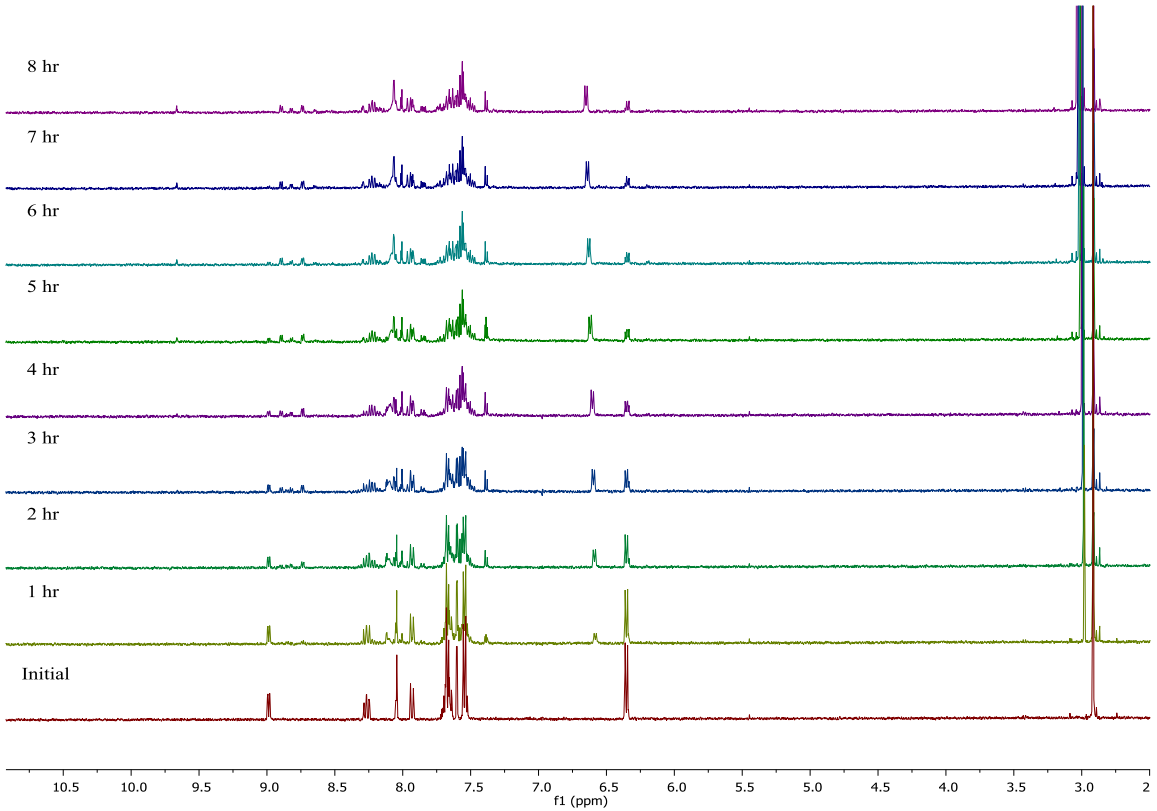

Figure A 1. ^{1}H NMR progression of the photolysis of [Re(**PyImPh**)$(CO)_3$(DMAP)]$^{+}$ in deuterated acetonitrile solution. The photolysis was performed by irradiating the sample at 365 nm (pen ray lamp) over a period of 8 hours.

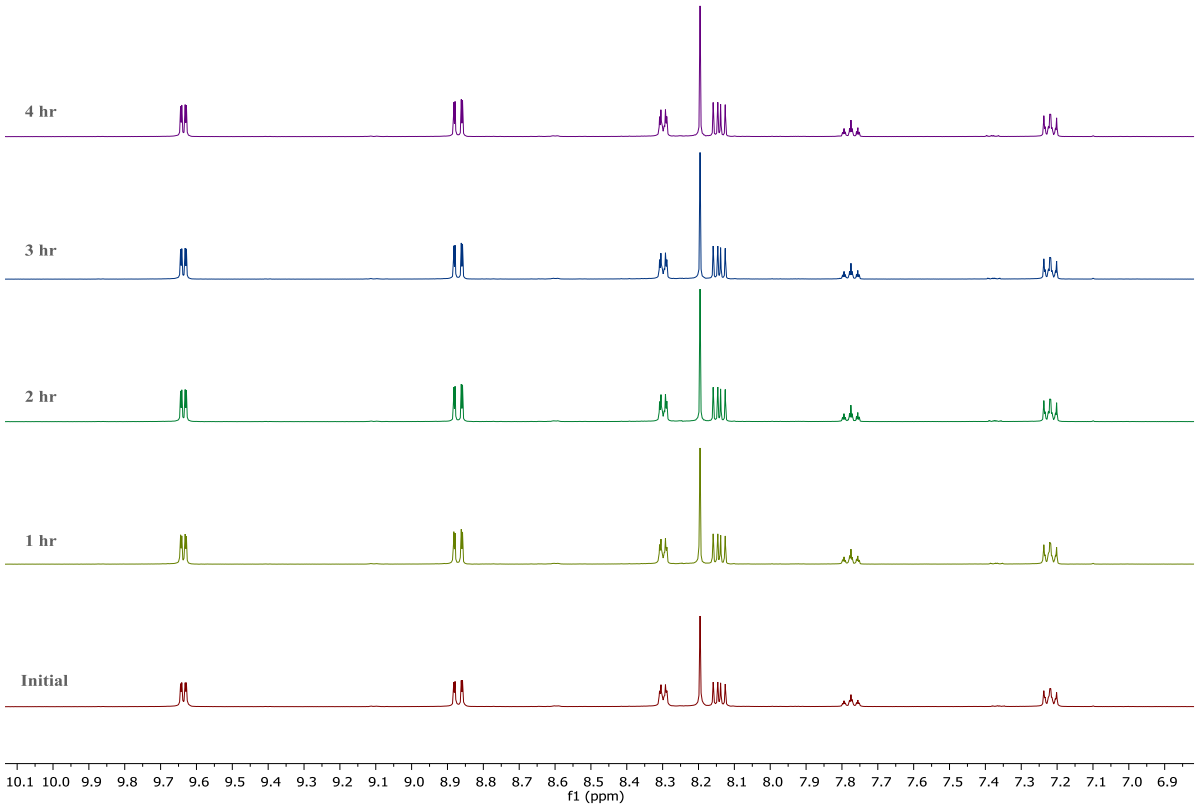

Figure A 2. ^{1}H NMR progression of the photolysis of [Re(**phen**)$(CO)_3$(Py)]$^{+}$ in deuterated acetonitrile solution. The photolysis was performed by irradiating the sample at λ_{ex} = 365 nm (pen ray lamp) over a period of 4 hours.

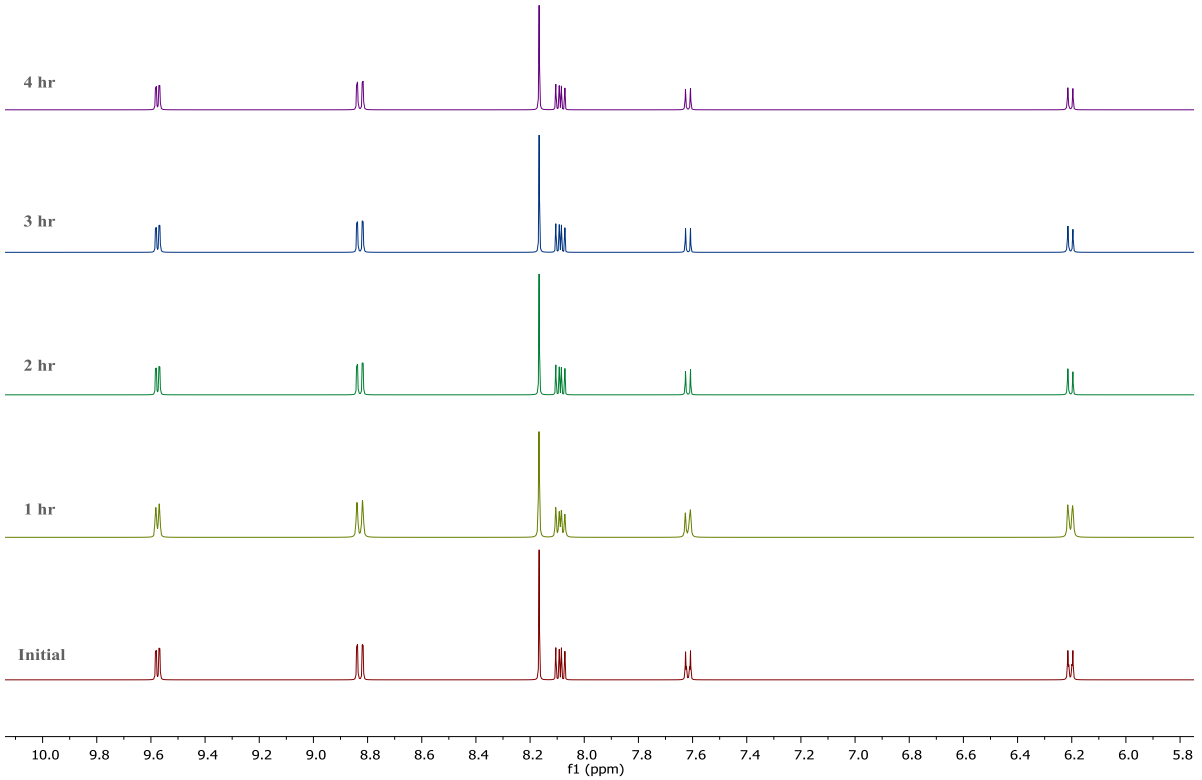

Figure A 3. ^{1}H NMR progression of the photolysis of [Re(**phen**)$(CO)_3$(DMAP)]$^{+}$ in deuterated acetonitrile solution. The photolysis was performed by irradiating the sample at 365 nm (pen ray lamp) over a period of 4 hours.

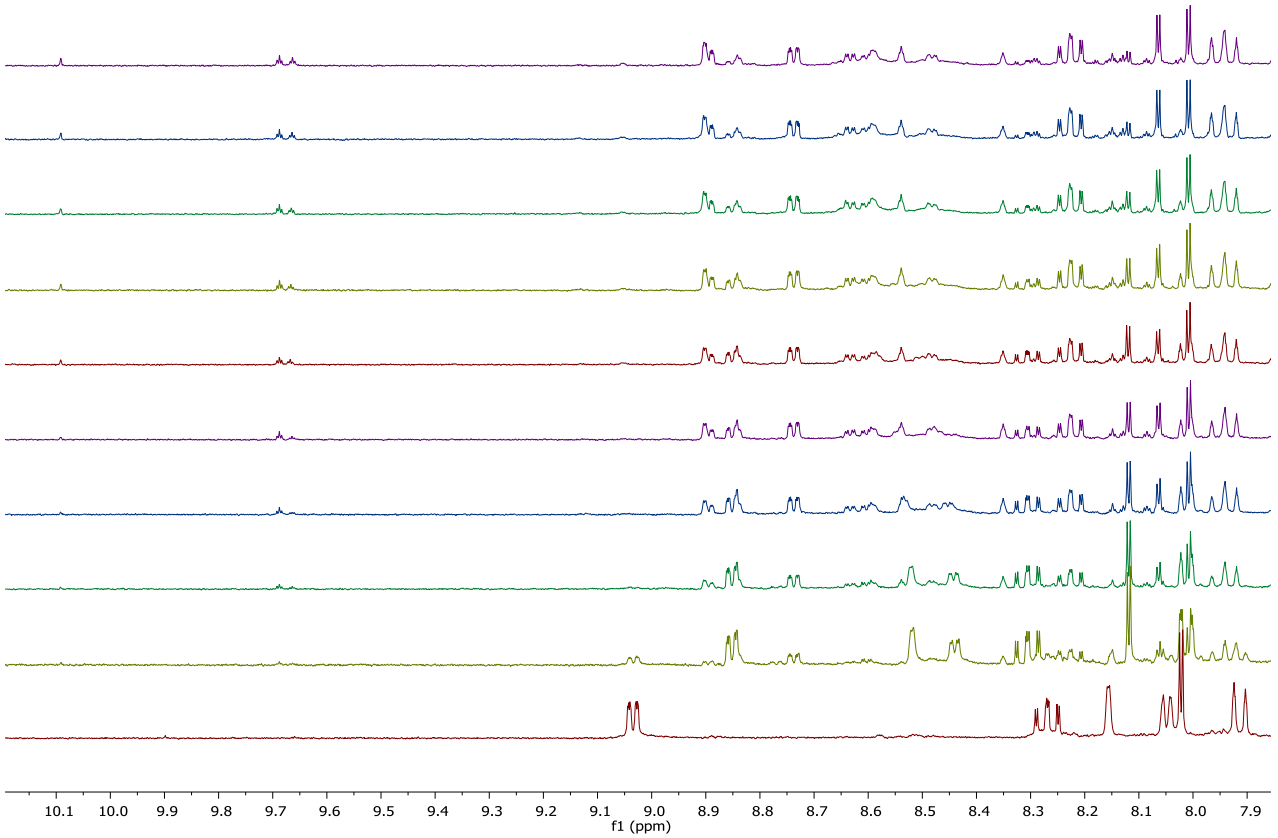

Figure A 4. ^{1}H NMR progression of the photolysis of [Re(**PyImPh**)$(CO)_3$(PyNHBu)]$^{+}$ in deuterated acetonitrile solution. The photolysis was performed by irradiating the sample at 365 nm (pen ray lamp) over a period of 8 hours.

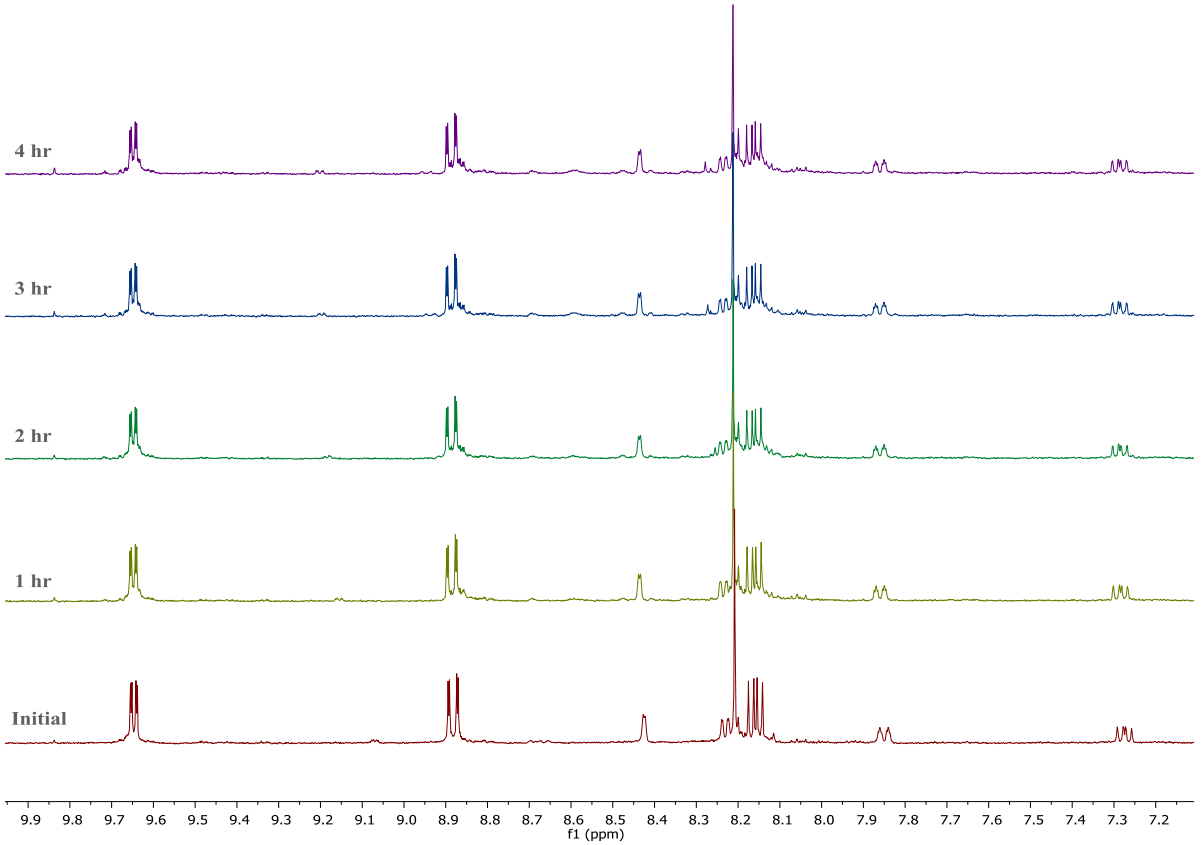

Figure A 5. ^{1}H NMR progression of the photolysis of [Re(**phen**)$(CO)_3$(PyNHBu)]$^{+}$ in deuterated acetonitrile solution. The photolysis was performed by irradiating the sample at 365 nm (pen ray lamp) over a period of 4 hours.

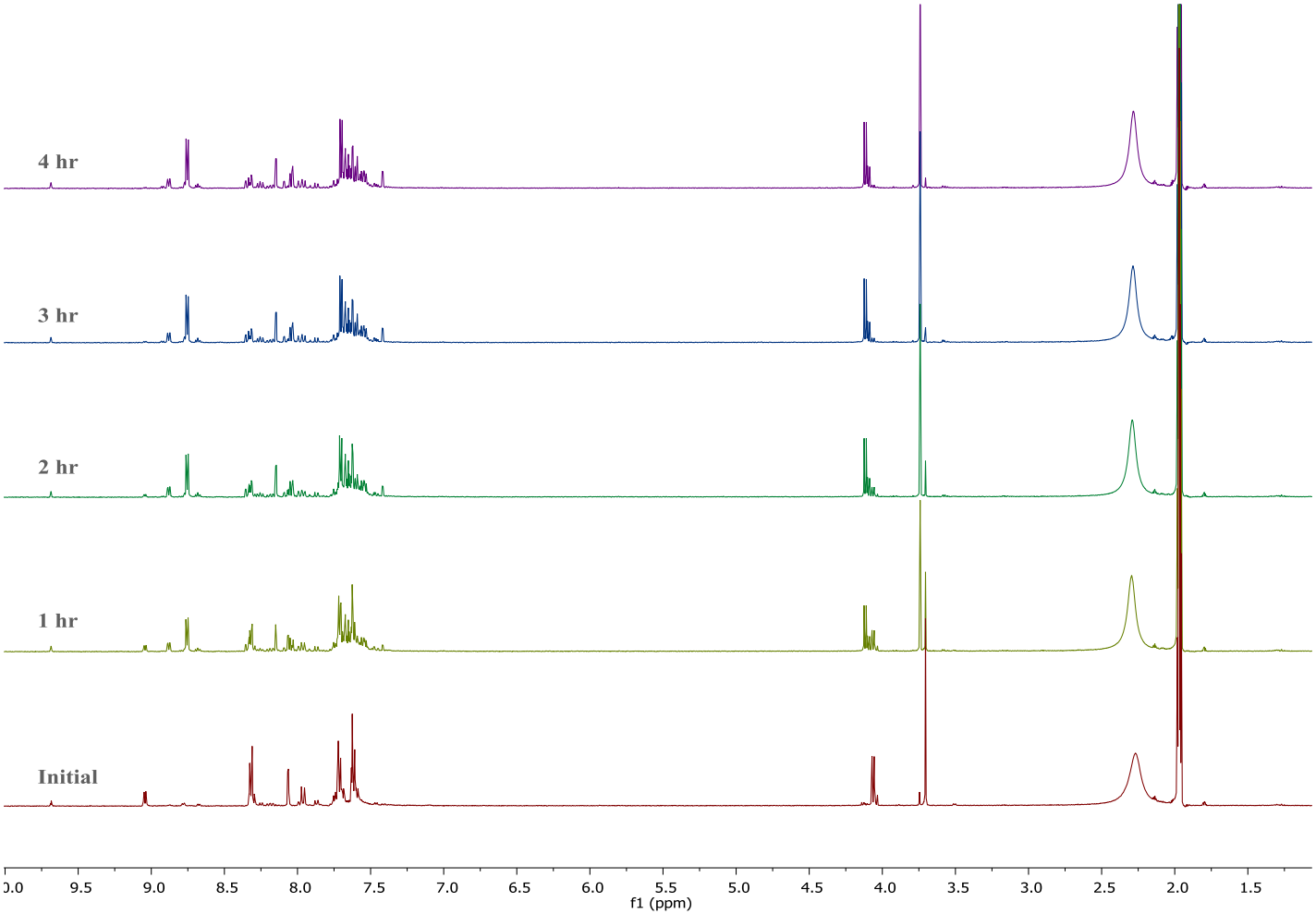

Figure A 6. 1H NMR progression of the photolysis of [Re(**PyImPh**)$(CO)_3$(Py**Gly**)]$^+$ in deuterated acetonitrile solution. The photolysis was performed by irradiating the sample at 365 nm (pen ray lamp) over a period of 4 hours.

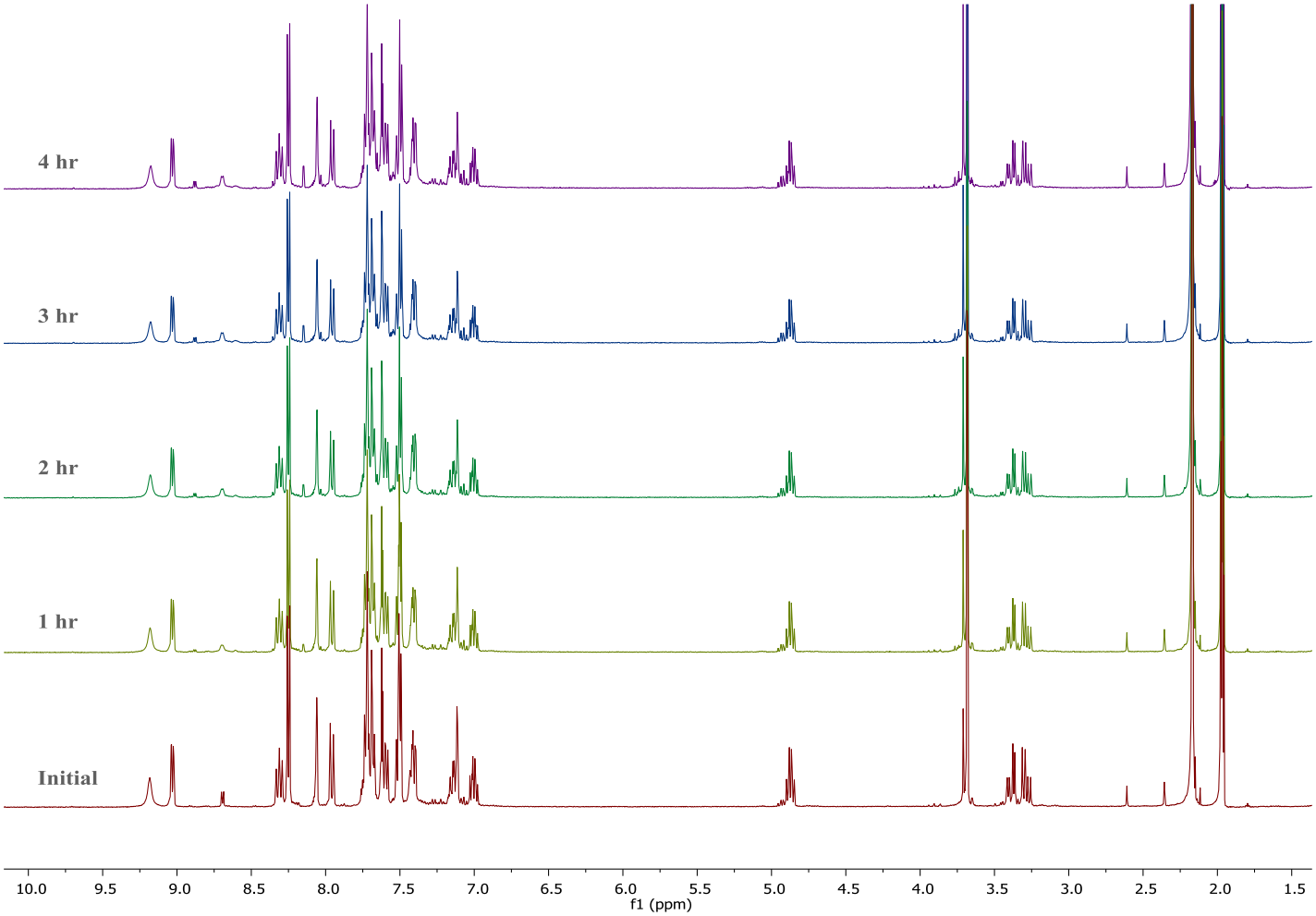

Figure A 7. ^{1}H NMR progression of the photolysis of [Re(**PyImPh**)$(CO)_3$(Py**Trp**)]$^{+}$ in deuterated acetonitrile solution. The photolysis was performed by irradiating the sample at 365 nm (pen ray lamp) over a period of 4 hours.

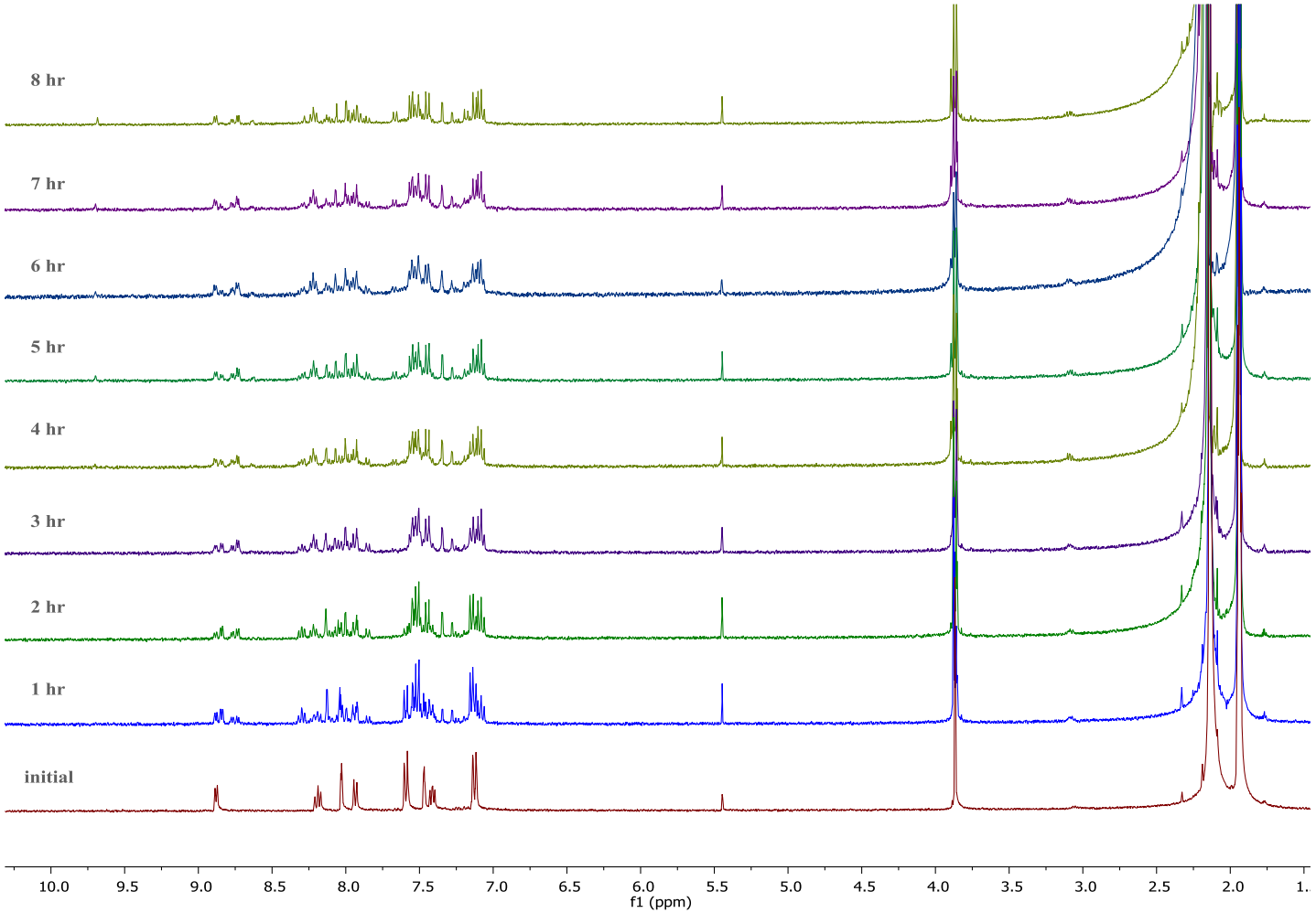

Figure A 8. ^{1}H NMR progression of the photolysis of [Re(**PyImPh**OMe)(CO)$_3$Br] in deuterated acetonitrile solution. The photolysis was performed by irradiating the sample at 365 nm (pen ray lamp) over a period of 8 hours.

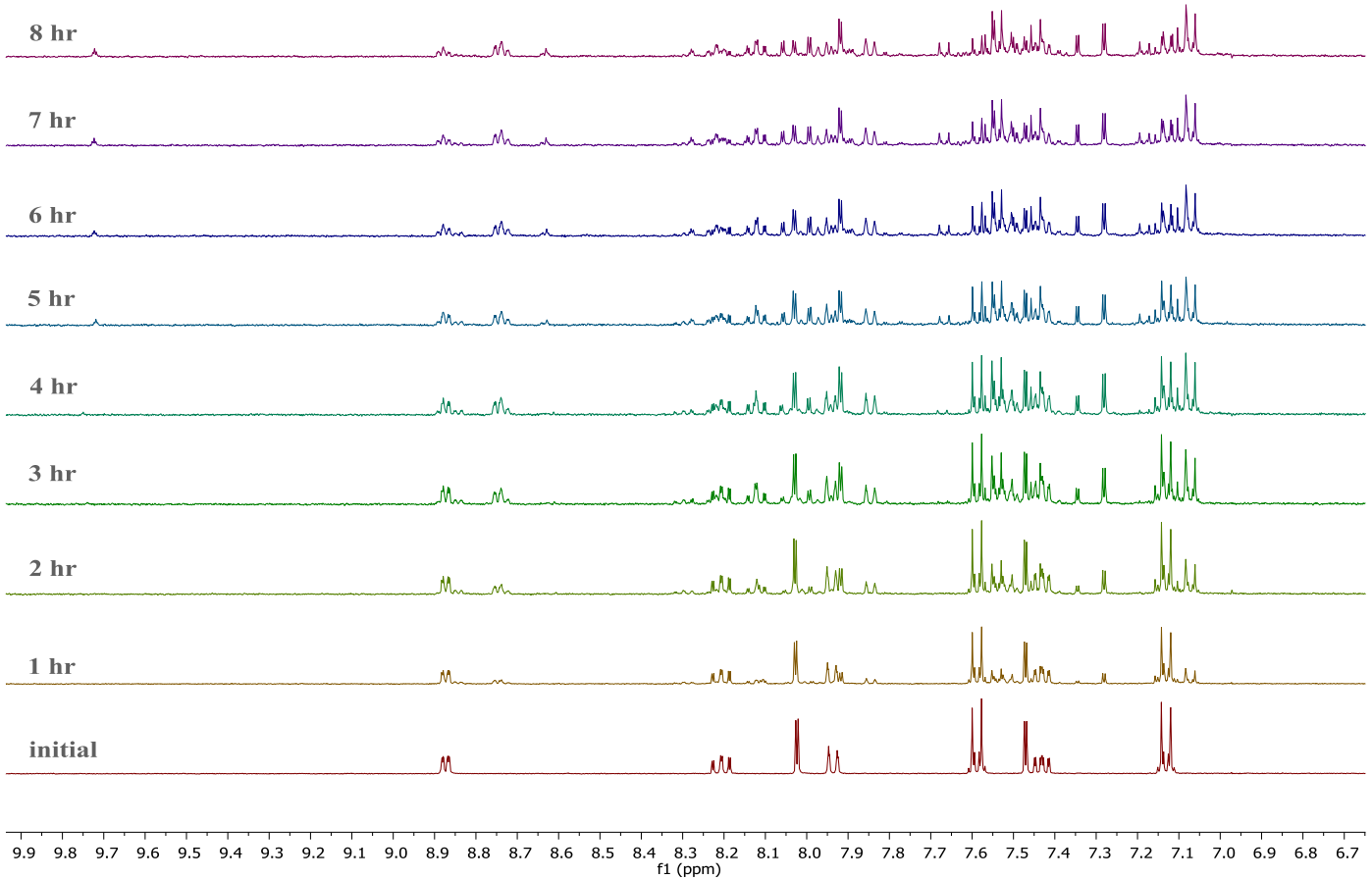

Figure A 9. ^{1}H NMR progression of the photolysis of [Re(**PyImPh**OMe)$(CO)_3$(Cl] in deuterated acetonitrile solution. The photolysis was performed by irradiating the sample at 365 nm (pen ray lamp) over a period of 8 hours.

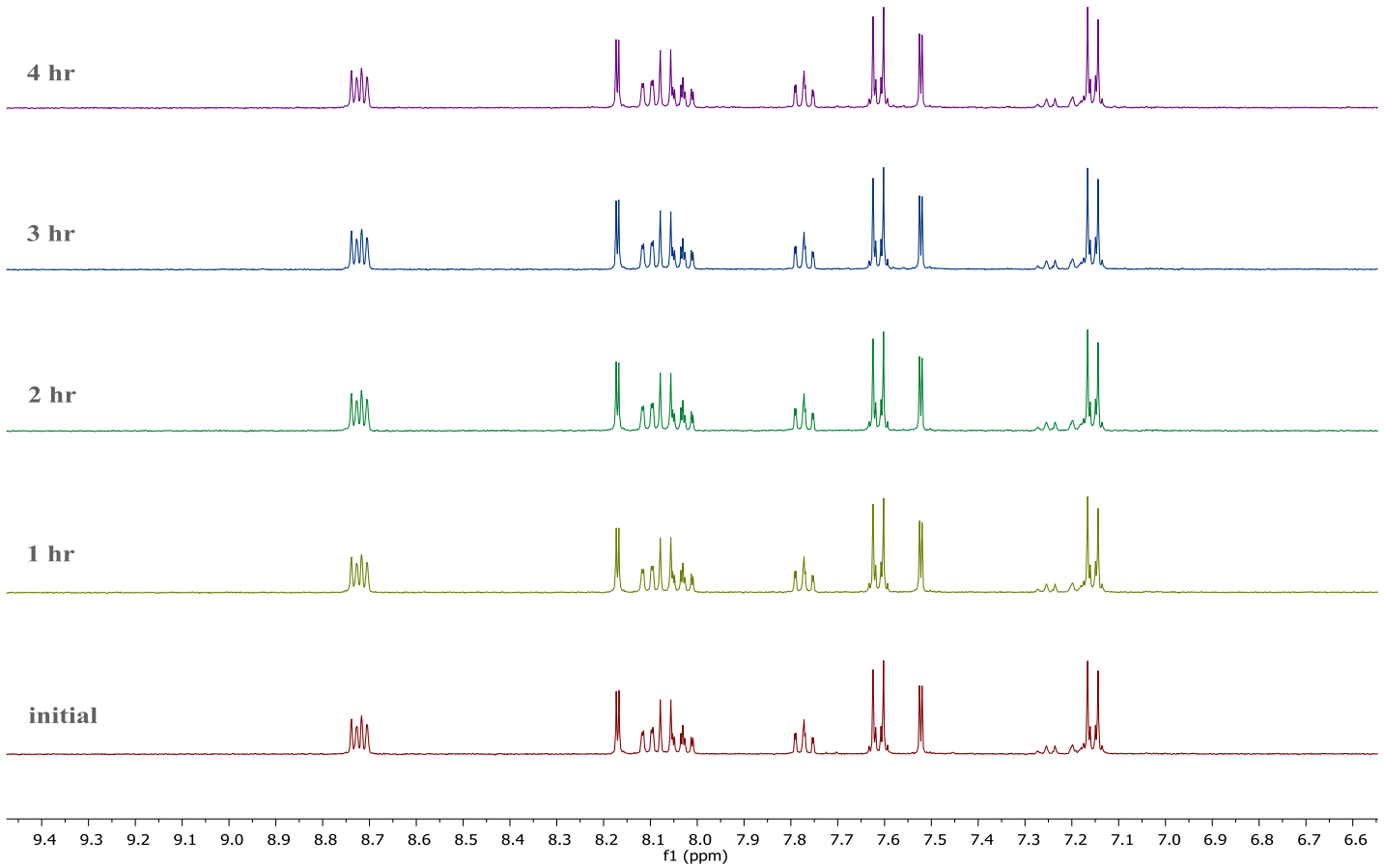

Figure A 10. ^{1}H NMR progression of the photolysis of [Re(**QuImPh**OMe)$(CO)_3$Br] in deuterated acetonitrile solution. The photolysis was performed by irradiating the sample at 365 nm (pen ray lamp) over a period of 4 hours.

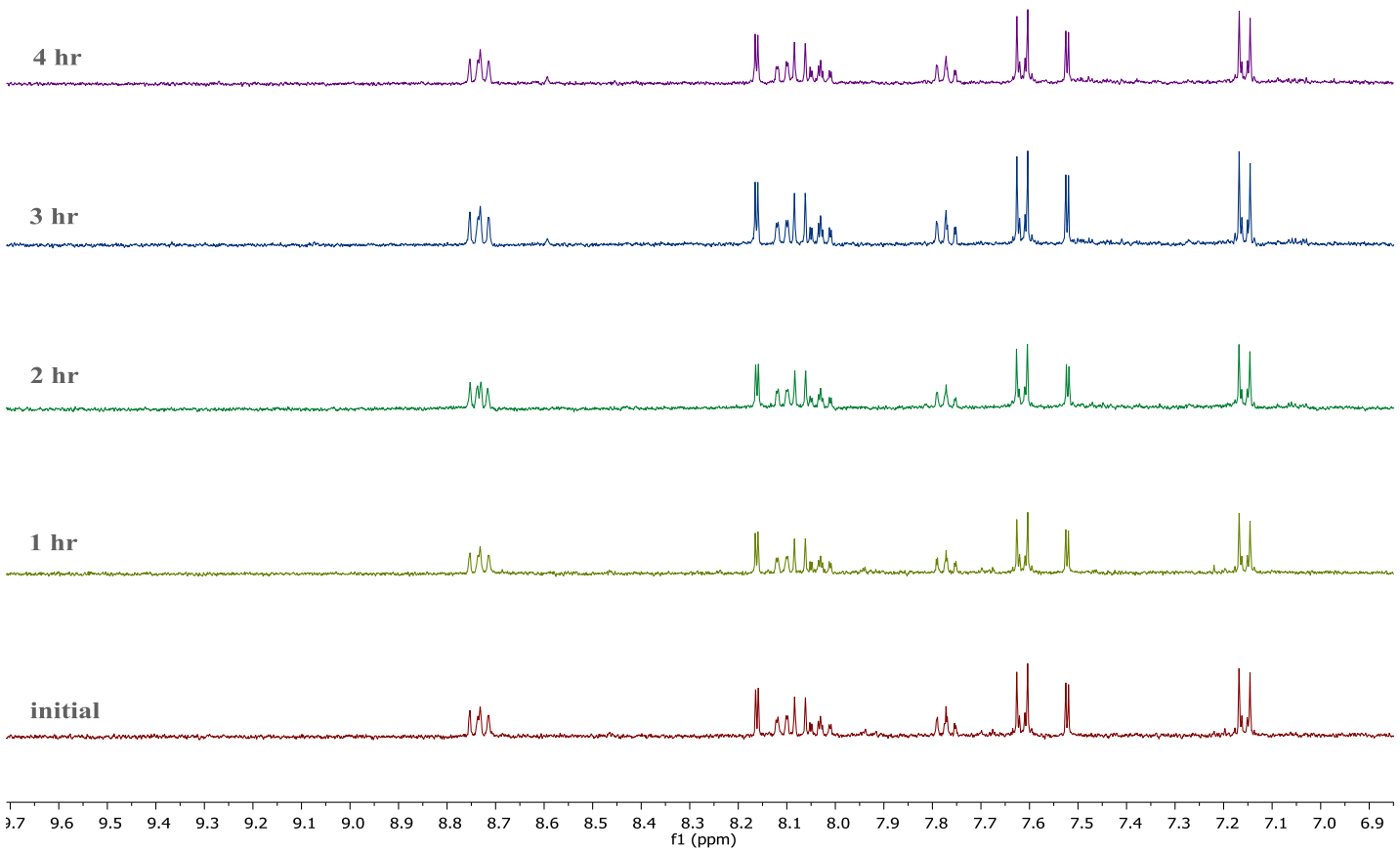

Figure A 11. ^{1}H NMR progression of the photolysis of [Re(**QuImPh**OMe)$(CO)_3$Cl] in deuterated acetonitrile solution. The photolysis was performed by irradiating the sample at 365 nm (pen ray lamp) over a period of 4 hours.

Appendix C Supplementary Images

C.1 Photolysis Using Polilamp

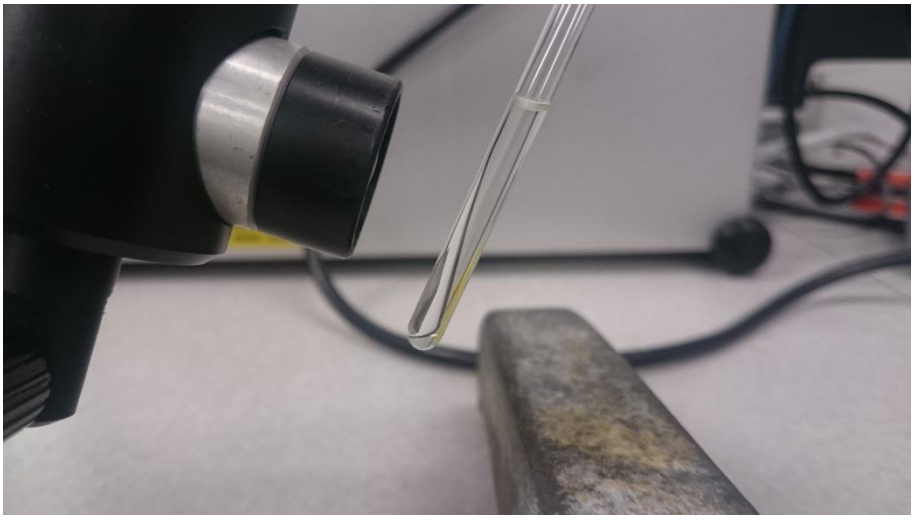

Figure A 12. NMR solution before photolysis.

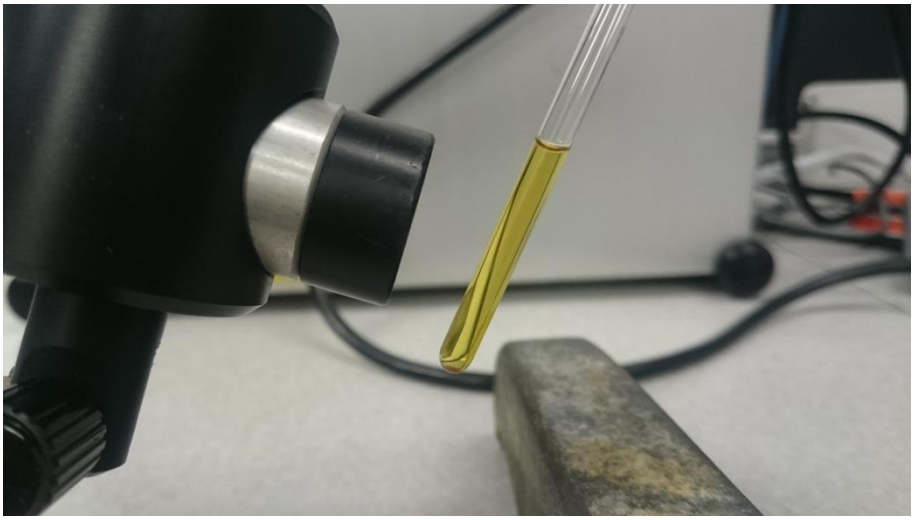

Figure A 13. NMR solution after photolysis.

Appendix D Flow Cytometry Gating at Varying Channels

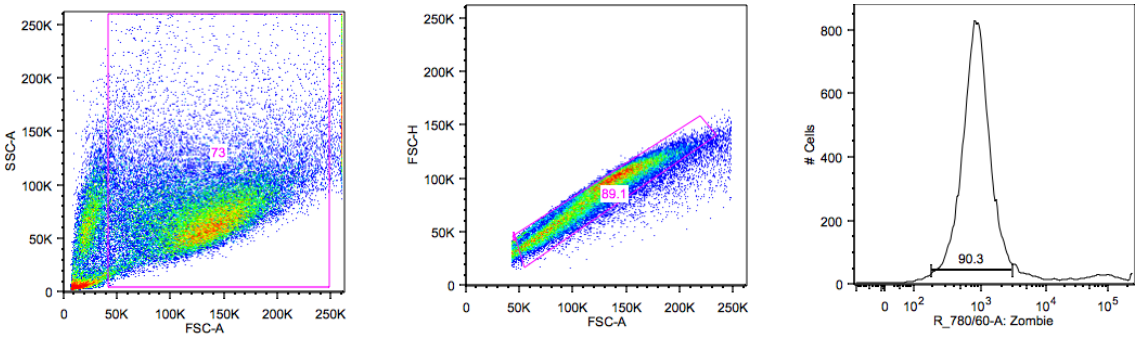

Figure A 14. Gating strategy – graph shown excluding debris, single cells and viable cells only, respectively.

D.1 [Re(**phen**)(CO)$_3$(**Tz**Ph4OH)]

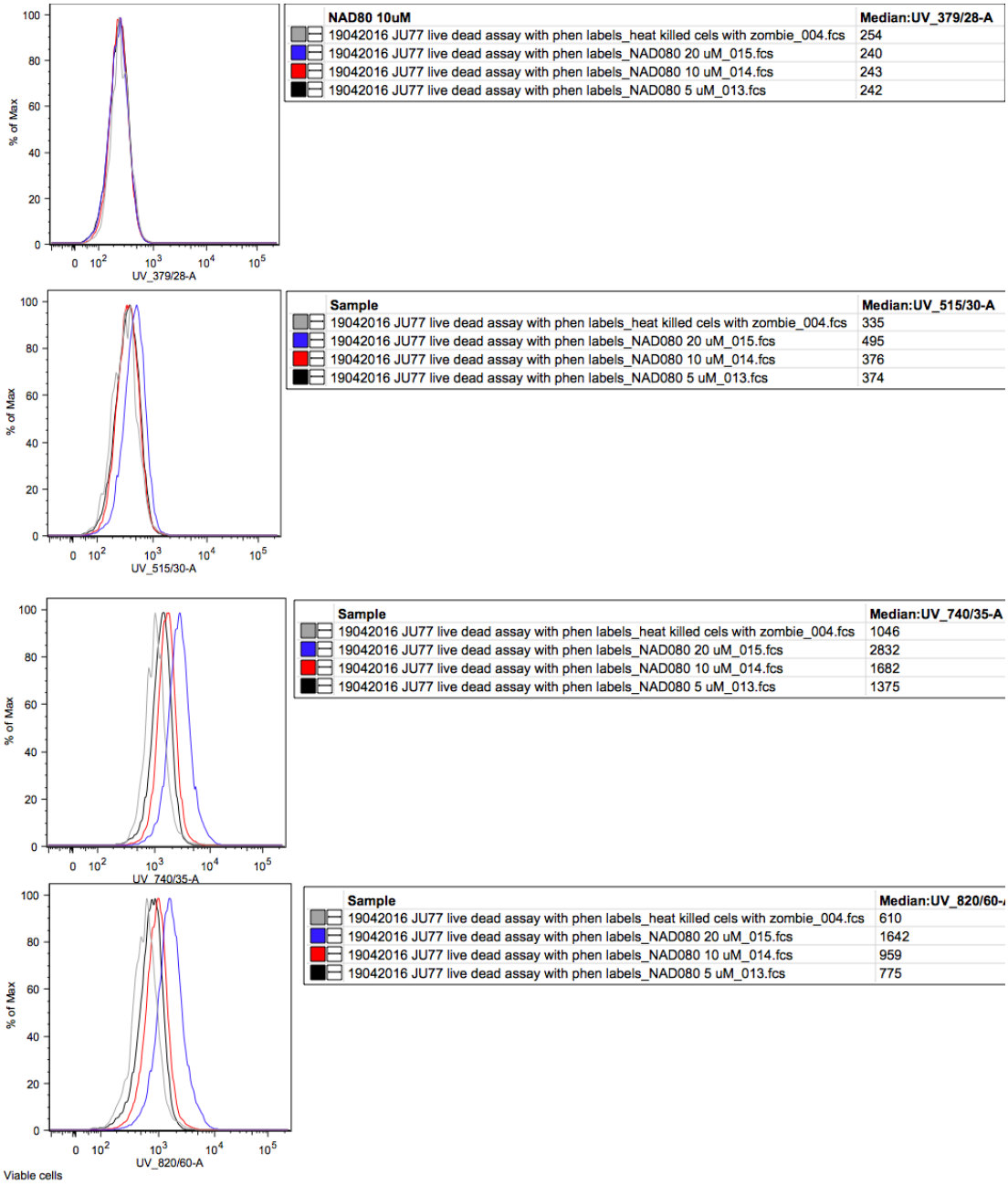

Figure A 15 Representative flow cytometry data of mean fluorescent intensities for complex **5** detected in the UV channel.

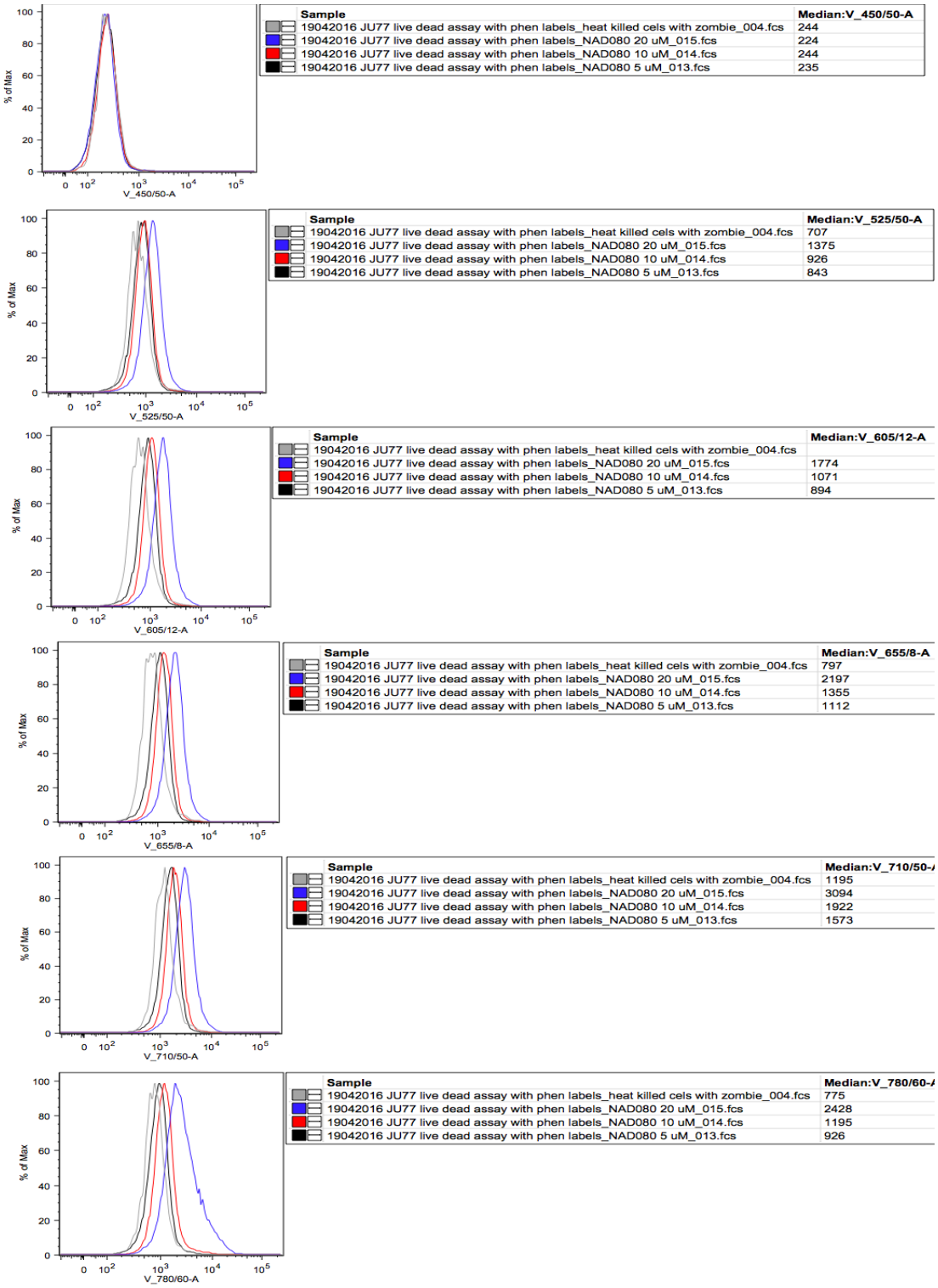

Figure A 16 Representative flow cytometry data of mean fluorescent intensities for complex **5** detected in the violet channel.

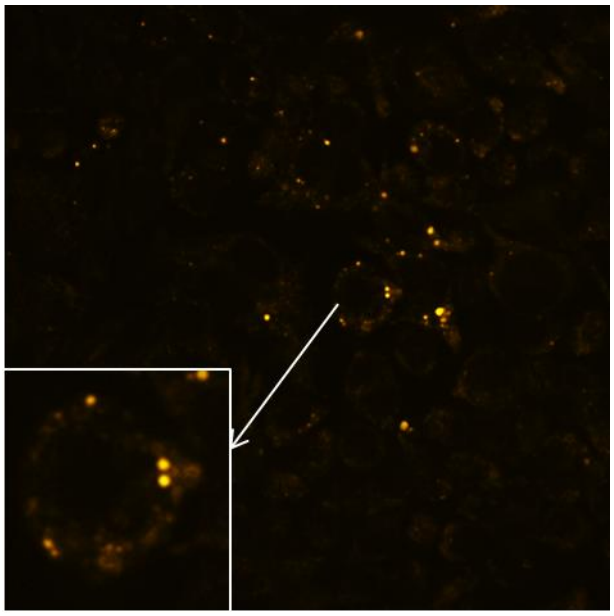

Figure A 17 Microscopy imaging of [Re(**phen**)$(CO)_3$(**Tz**Ph4OH)] in RAW264.7 cells at 10 μM concentration.

D.2 [Re(**phen**)(CO)$_3$(**Tz**Ph3OH)]

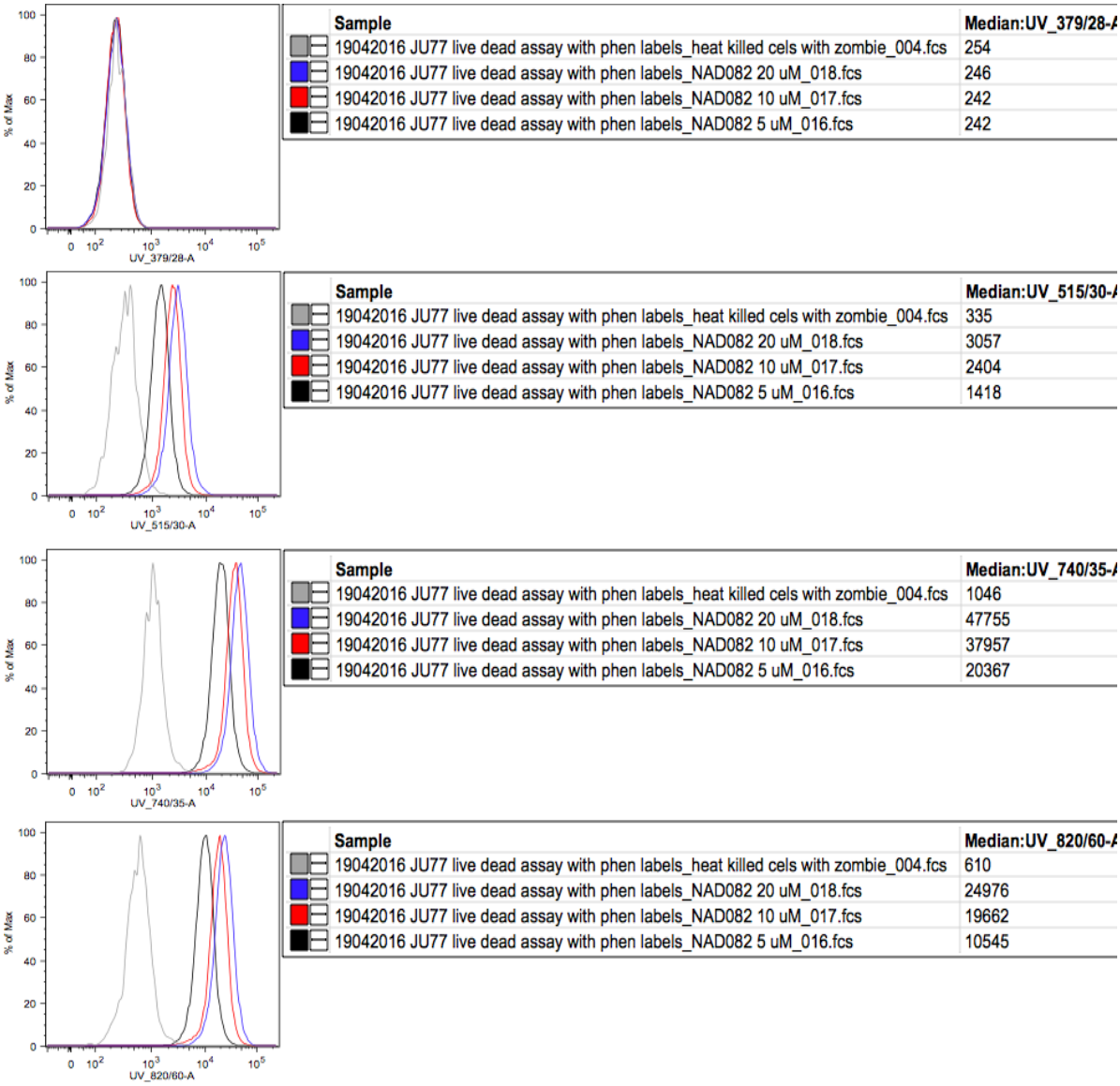

Figure A 18 Representative flow cytometry data of mean fluorescent intensities for complex **6** detected in the UV channel.

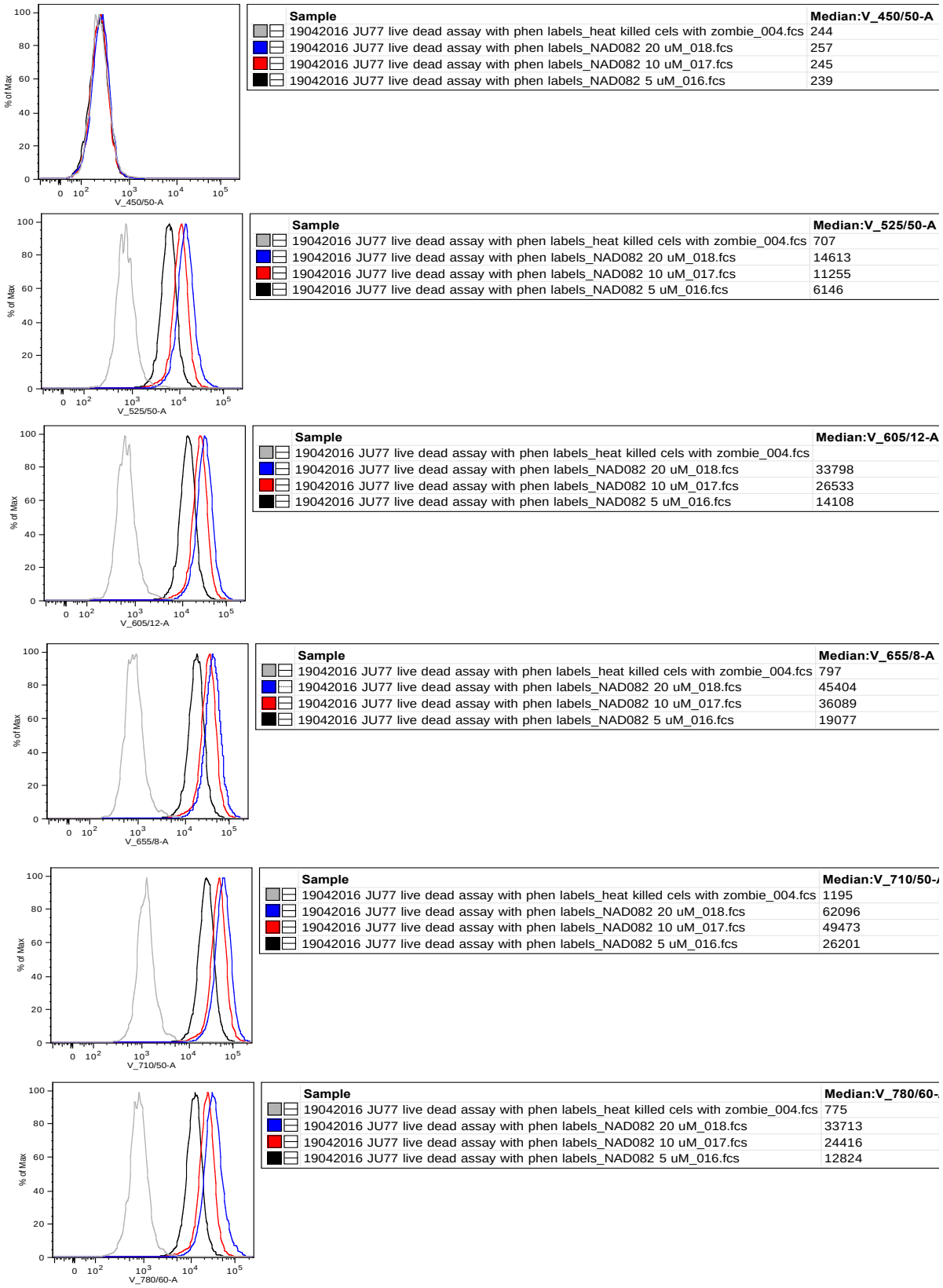

Figure A 19 Representative flow cytometry data of mean fluorescent intensities for complex **6** detected in the UV channel.

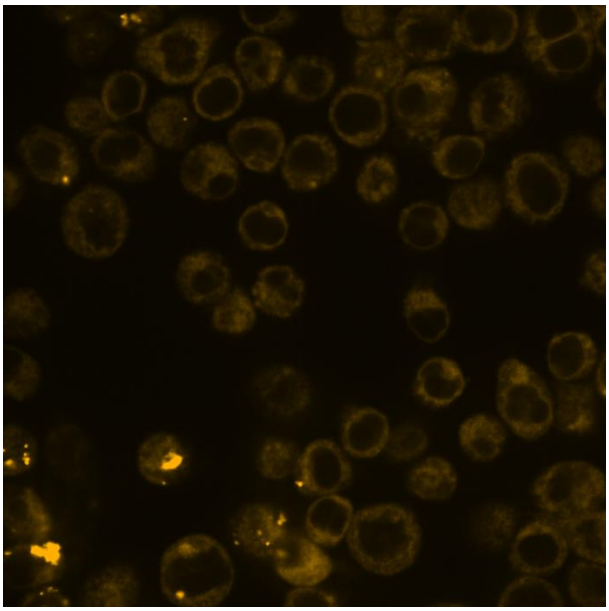

Figure A 20 Microscopy imaging of [Re(**phen**)$(CO)_3$(**Tz**Ph3OH)] in RAW264.7 cells at 10 µM.

D.3 [Re(**phen**)(CO)$_3$(**Tz**Ph4OMe)]

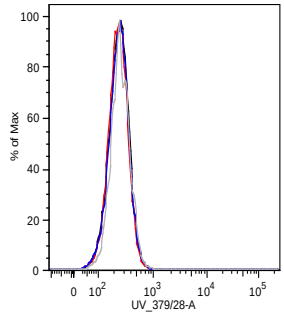

Sample	Median:UV_379/28-
19042016 JU77 live dead assay with phen labels_heat killed cels with zombie_004.fcs	254
19042016 JU77 live dead assay with phen labels_KU3520 uM_009.fcs	244
19042016 JU77 live dead assay with phen labels_KU35 10 uM_008.fcs	236
19042016 JU77 live dead assay with phen labels_KU35 5uM_007.fcs	243

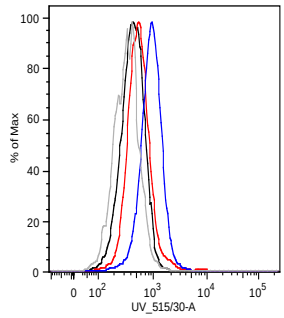

Sample	Median:UV_515/30-
19042016 JU77 live dead assay with phen labels_heat killed cels with zombie_004.fcs	335
19042016 JU77 live dead assay with phen labels_KU3520 uM_009.fcs	913
19042016 JU77 live dead assay with phen labels_KU35 10 uM_008.fcs	528
19042016 JU77 live dead assay with phen labels_KU35 5uM_007.fcs	425

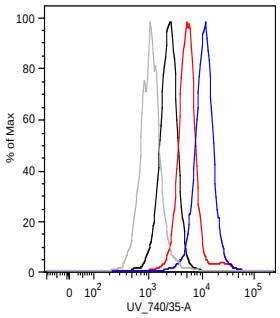

Sample	Median:UV_740/35-A
19042016 JU77 live dead assay with phen labels_heat killed cels with zombie_004.fcs	1046
19042016 JU77 live dead assay with phen labels_KU3520 uM_009.fcs	11284
19042016 JU77 live dead assay with phen labels_KU35 10 uM_008.fcs	5241
19042016 JU77 live dead assay with phen labels_KU35 5uM_007.fcs	2318

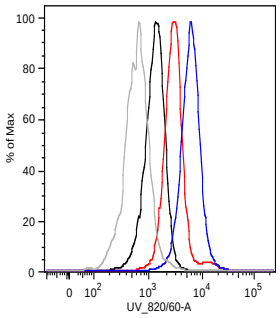

Sample	Median:UV_820/60-A
19042016 JU77 live dead assay with phen labels_heat killed cels with zombie_004.fcs	610
19042016 JU77 live dead assay with phen labels_KU3520 uM_009.fcs	6130
19042016 JU77 live dead assay with phen labels_KU35 10 uM_008.fcs	2874
19042016 JU77 live dead assay with phen labels_KU35 5uM_007.fcs	1298

Figure A 21 Representative flow cytometry data of mean fluorescent intensities for complex **7** detected in the violet channel.

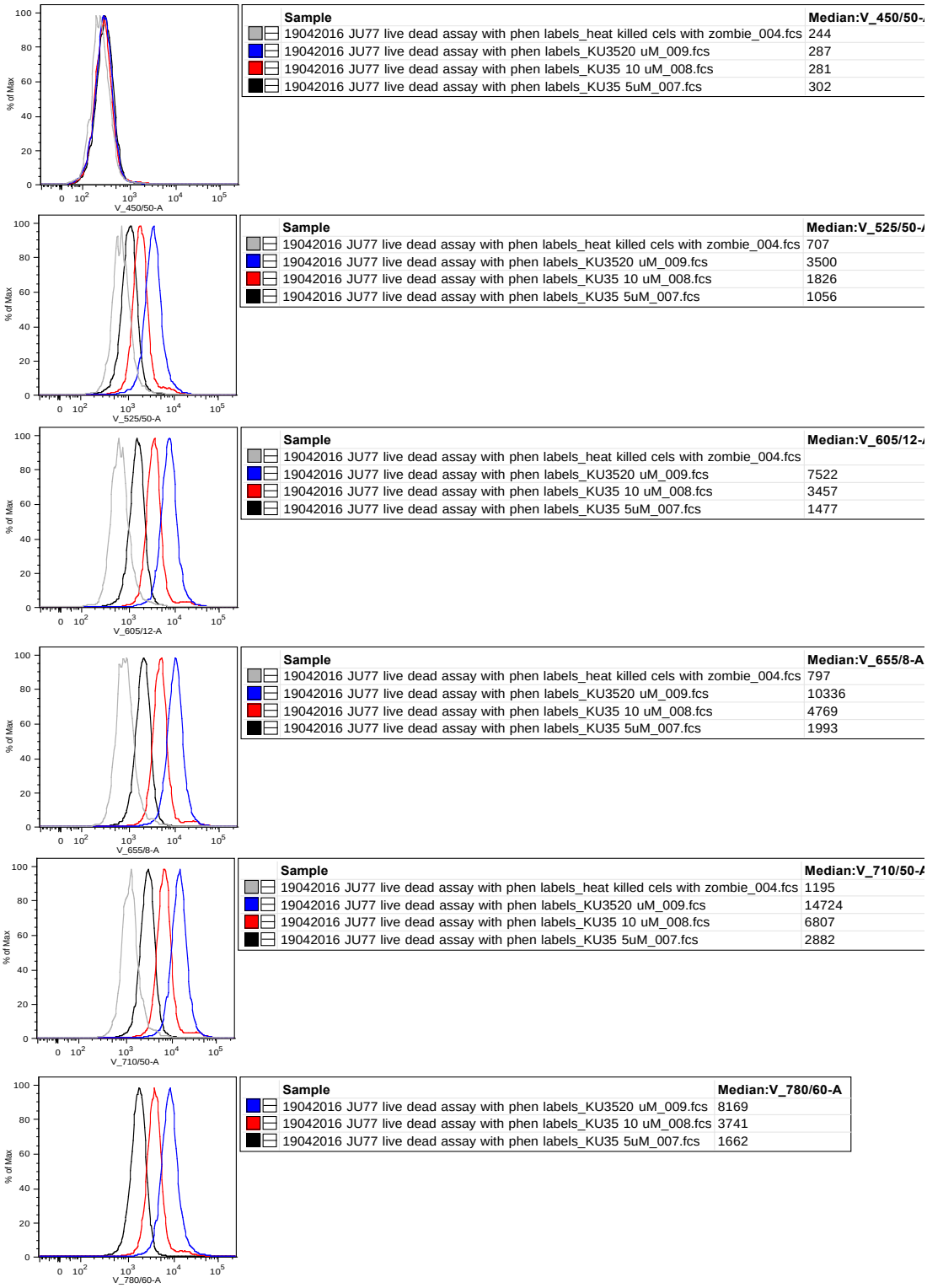

Sample	Median:V_450/50-A
19042016 JU77 live dead assay with phen labels_heat killed cels with zombie_004.fcs	244
19042016 JU77 live dead assay with phen labels_KU3520 uM_009.fcs	287
19042016 JU77 live dead assay with phen labels_KU35 10 uM_008.fcs	281
19042016 JU77 live dead assay with phen labels_KU35 5uM_007.fcs	302

Sample	Median:V_525/50-A
19042016 JU77 live dead assay with phen labels_heat killed cels with zombie_004.fcs	707
19042016 JU77 live dead assay with phen labels_KU3520 uM_009.fcs	3500
19042016 JU77 live dead assay with phen labels_KU35 10 uM_008.fcs	1826
19042016 JU77 live dead assay with phen labels_KU35 5uM_007.fcs	1056

Sample	Median:V_605/12-A
19042016 JU77 live dead assay with phen labels_heat killed cels with zombie_004.fcs	
19042016 JU77 live dead assay with phen labels_KU3520 uM_009.fcs	7522
19042016 JU77 live dead assay with phen labels_KU35 10 uM_008.fcs	3457
19042016 JU77 live dead assay with phen labels_KU35 5uM_007.fcs	1477

Sample	Median:V_655/8-A
19042016 JU77 live dead assay with phen labels_heat killed cels with zombie_004.fcs	797
19042016 JU77 live dead assay with phen labels_KU3520 uM_009.fcs	10336
19042016 JU77 live dead assay with phen labels_KU35 10 uM_008.fcs	4769
19042016 JU77 live dead assay with phen labels_KU35 5uM_007.fcs	1993

Sample	Median:V_710/50-A
19042016 JU77 live dead assay with phen labels_heat killed cels with zombie_004.fcs	1195
19042016 JU77 live dead assay with phen labels_KU3520 uM_009.fcs	14724
19042016 JU77 live dead assay with phen labels_KU35 10 uM_008.fcs	6807
19042016 JU77 live dead assay with phen labels_KU35 5uM_007.fcs	2882

Sample	Median:V_780/60-A
19042016 JU77 live dead assay with phen labels_KU3520 uM_009.fcs	8169
19042016 JU77 live dead assay with phen labels_KU35 10 uM_008.fcs	3741
19042016 JU77 live dead assay with phen labels_KU35 5uM_007.fcs	1662

Figure A 22 Representative flow cytometry data of mean fluorescent intensities for complex **7** detected in the violet channel.

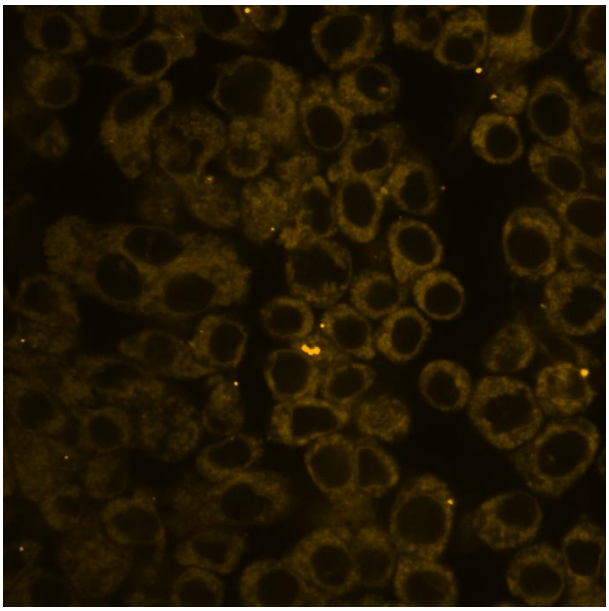

Figure A 23 Microscopy imaging of [Re(**phen**)$(CO)_3$(**Tz**Ph4OMe)] in RAW264.7 cells at 10 μM concentration.

D.4 [Re(**phen**)(CO)$_3$(**Tz**Ph3OMe)]

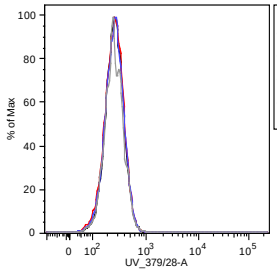

Zombie	Median:UV_379/28-
19042016 JU77 live dead assay with phen labels_heat killed cels with zombie_004.fcs	254
19042016 JU77 live dead assay with phen labels_KU38 20 uM_012.fcs	261
19042016 JU77 live dead assay with phen labels_KU38 10 uM_011.fcs	260
19042016 JU77 live dead assay with phen labels_KU38 5 uM_010.fcs	261

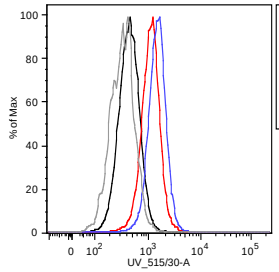

Sample	Median:UV_515/30-
19042016 JU77 live dead assay with phen labels_heat killed cels with zombie_004.fcs	335
19042016 JU77 live dead assay with phen labels_KU38 20 uM_012.fcs	1453
19042016 JU77 live dead assay with phen labels_KU38 10 uM_011.fcs	1089
19042016 JU77 live dead assay with phen labels_KU38 5 uM_010.fcs	434

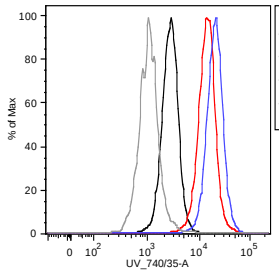

Sample	Median:UV_740/35-
19042016 JU77 live dead assay with phen labels_heat killed cels with zombie_004.fcs	1046
19042016 JU77 live dead assay with phen labels_KU38 20 uM_012.fcs	21311
19042016 JU77 live dead assay with phen labels_KU38 10 uM_011.fcs	14687
19042016 JU77 live dead assay with phen labels_KU38 5 uM_010.fcs	2723

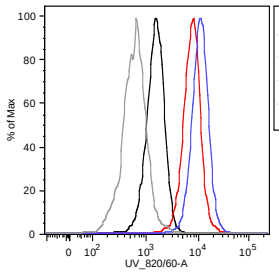

Sample	Median:UV_820/60-
19042016 JU77 live dead assay with phen labels_heat killed cels with zombie_004.fcs	610
19042016 JU77 live dead assay with phen labels_KU38 20 uM_012.fcs	11312
19042016 JU77 live dead assay with phen labels_KU38 10 uM_011.fcs	7790
19042016 JU77 live dead assay with phen labels_KU38 5 uM_010.fcs	1492

Figure A 24 Representative flow cytometry data of mean fluorescent intensities for complex **8** detected in the violet channel.

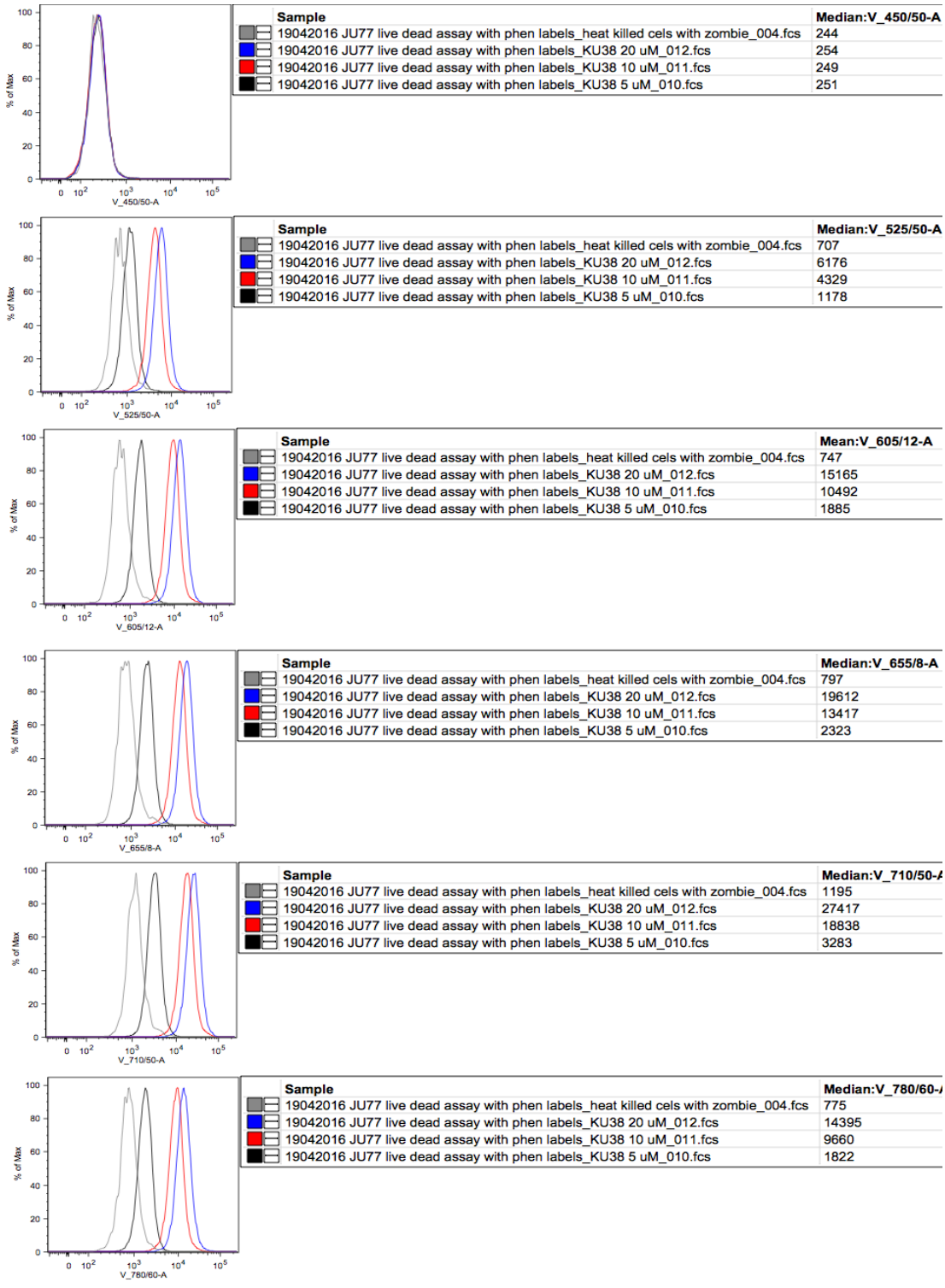

Figure A 25 Representative flow cytometry data of mean fluorescent intensities for complex **8** detected in the violet channel.

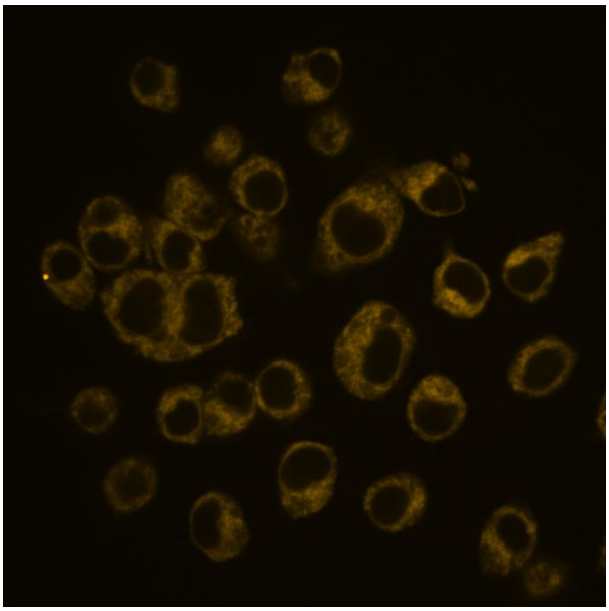

Figure A 26 Microscopy imaging of [Re(**phen**)$(CO)_3$(**Tz**Ph3OMe)] in RAW264.7 cells at 10 μM concentration.

D.5 [Re(**PyImPh**)$(CO)_3$(Py)]$^+$

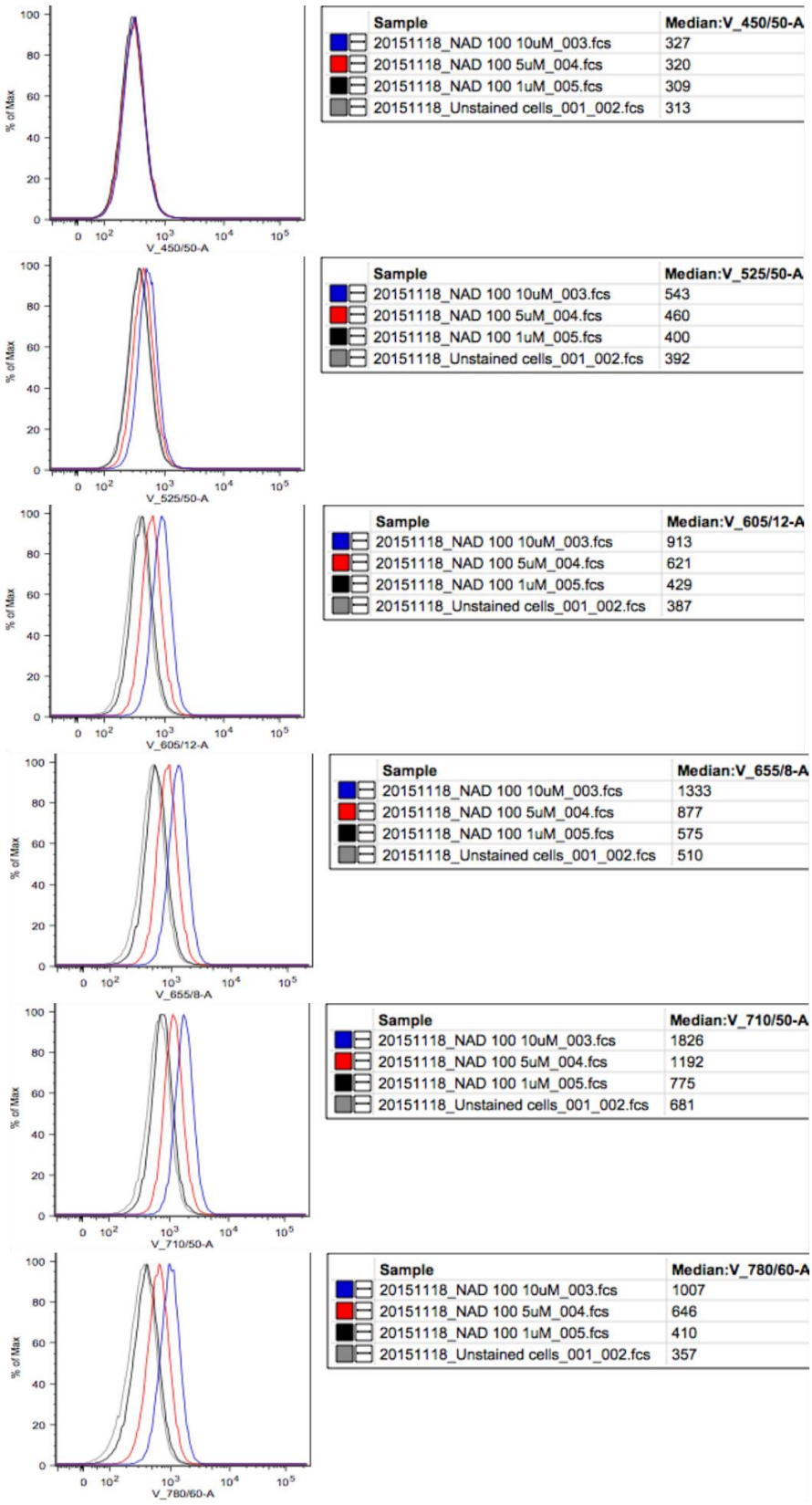

Figure A 27 Representative flow cytometry data of mean fluorescent intensities for complex **23** detected in the violet channel.

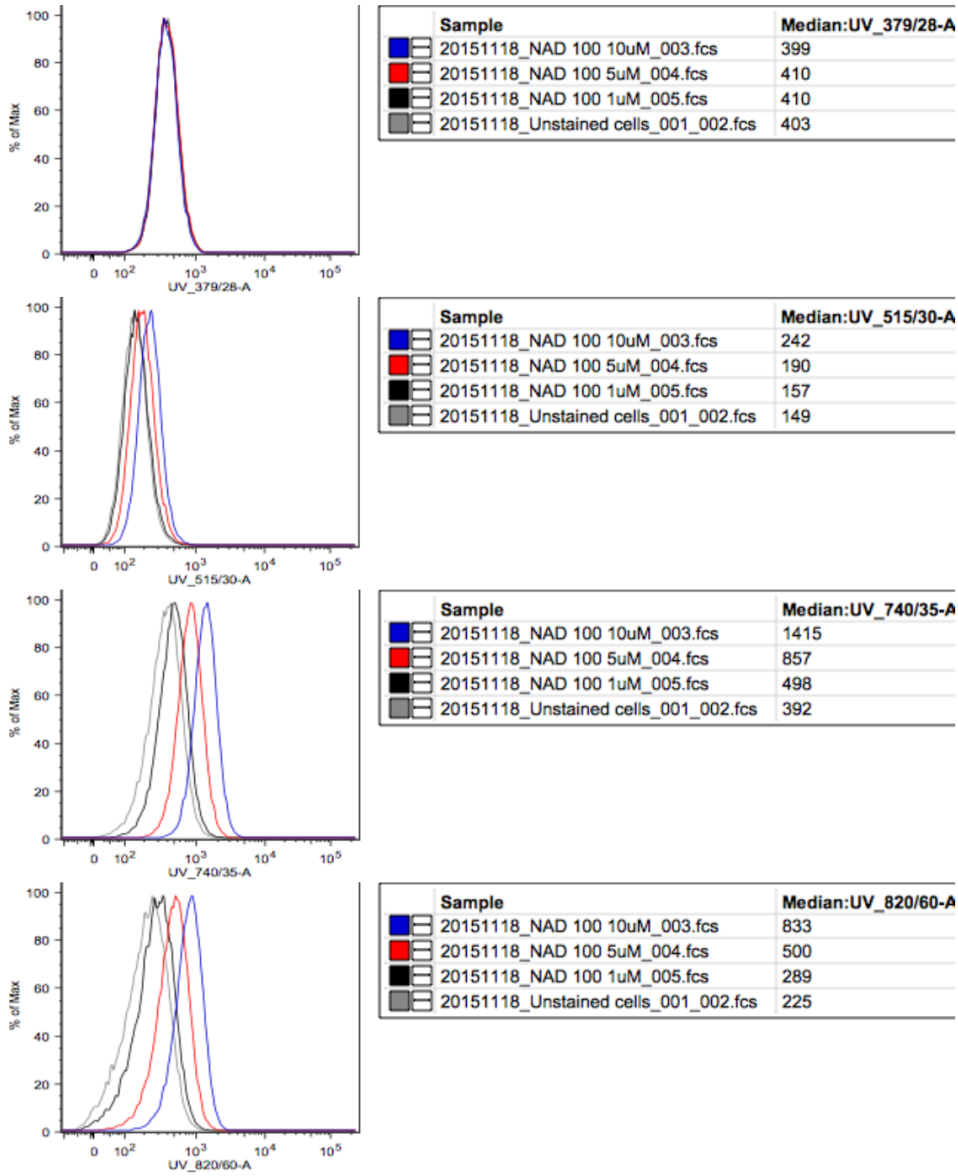

Figure A 28 Representative flow cytometry data of mean fluorescent intensities for complex **23** detected in the violet channel.

D.6 $[Re(\mathbf{PyImPh})(CO)_3(DMAP)]^+$

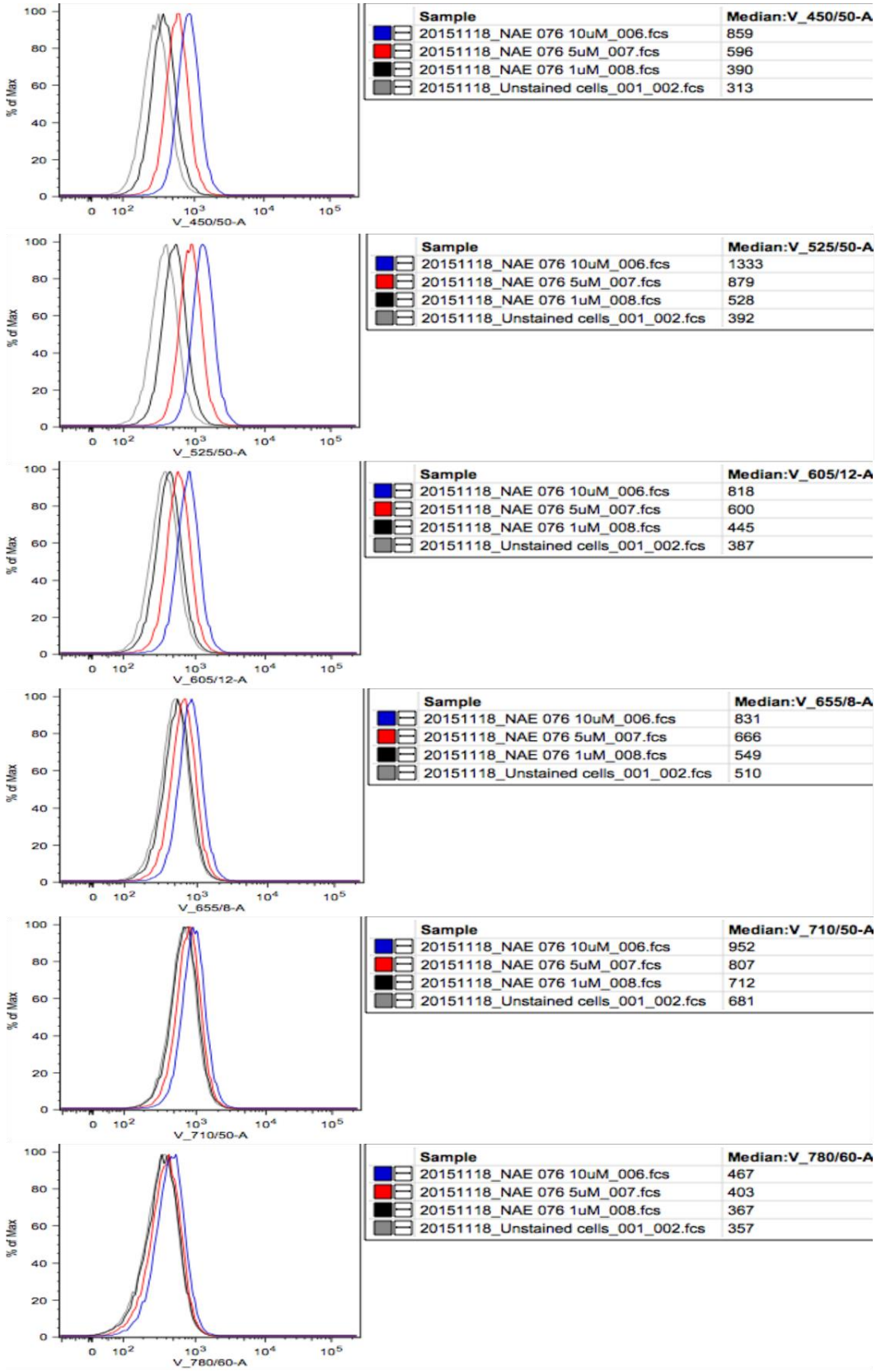

Figure A 29 Representative flow cytometry data of mean fluorescent intensities for complex **24** detected in the violet channel.

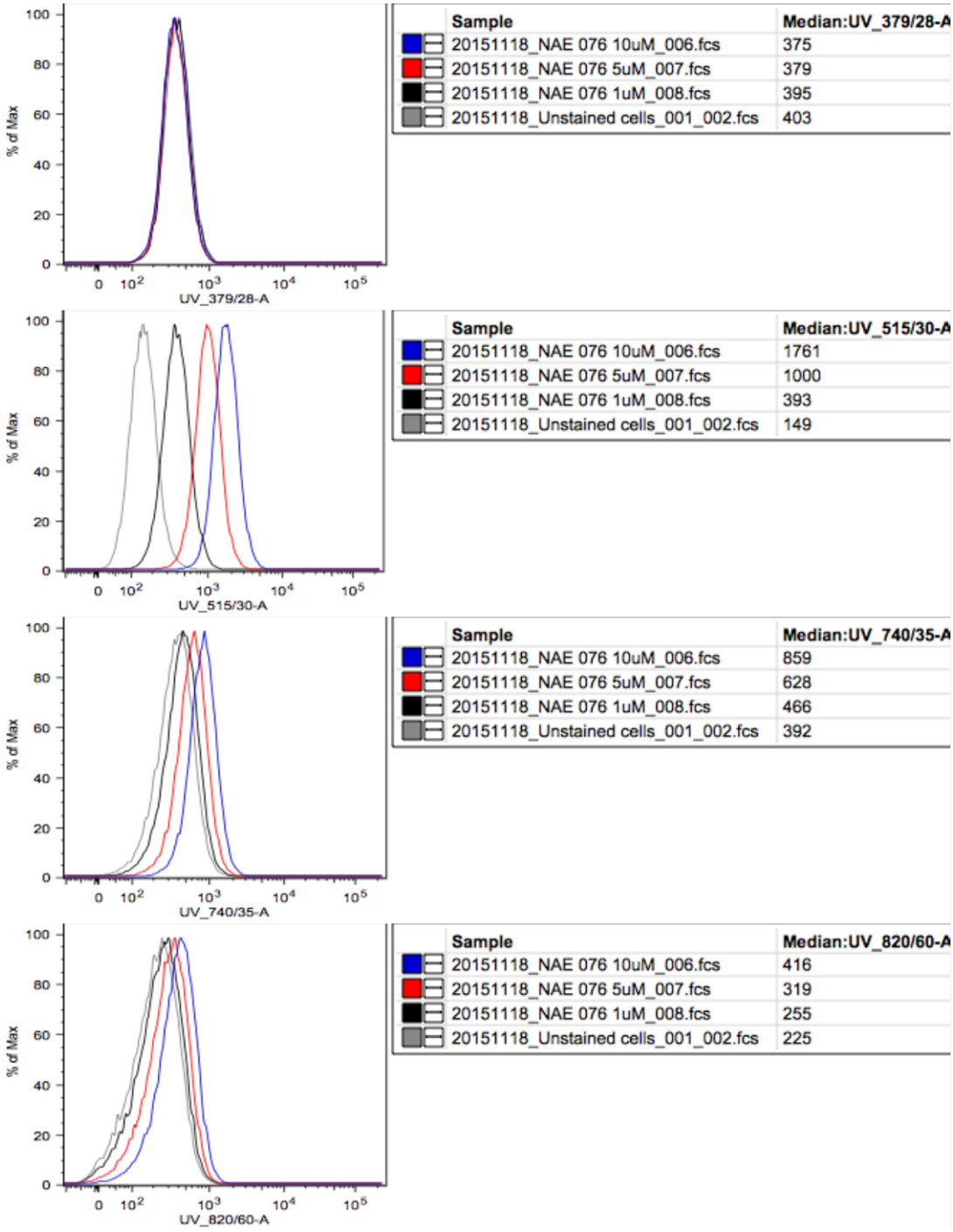

Figure A 30 Representative flow cytometry data of mean fluorescent intensities for complex **24** detected in the UV channel.

Appendix E Cytotoxicity Data

Table A 31. Cytotoxicity (live/dead) data for complexes **5-8** in JU77 cells.

	% cell death at concentration			
Complex	**Control**	**5 µM**	**10 µM**	**20 µM**
[Re(**phen**)$(CO)_3$(**Tz**Ph4OH)] (**5**)	6.00	9.70	12.30	13.80
[Re(**phen**)$(CO)_3$(**Tz**Ph3OH)] (**6**)	6.00	9.00	11.70	15.50
[Re(**phen**)$(CO)_3$(**Tz**Ph4OMe)] (**7**)	6.00	9.95	10.80	11.20
[Re(**phen**)$(CO)_3$(**Tz**Ph3OMe)] (**8**)	6.00	9.15	8.25	9.00

Table A 32. Cytotoxicity (live/dead) data for complexes **5-8** in RAW264.7 cells.

	% cell death at concentration			
Complex	**Control**	**5 µM**	**10 µM**	**20 µM**
[Re(**phen**)$(CO)_3$(**Tz**Ph4OH)] (**5**)	5.50	9.03	9.77	12.10
[Re(**phen**)$(CO)_3$(**Tz**Ph3OH)] (**6**)	5.50	9.24	10.25	13.40
[Re(**phen**)$(CO)_3$(**Tz**Ph4OMe)] (**7**)	5.50	11.94	11.98	13.86
[Re(**phen**)$(CO)_3$(**Tz**Ph3OMe)] (**8**)	5.50	11.83	12.70	14.40

Table A 33. Cytotoxicity (live/dead) data for complexes **23** and **24** in RAW264.7 cells.

	% cell death at concentration		
Complex	**5 µM**	**10 µM**	**20 µM**
23	5.40	5.70	5.20
24	7.50	7.30	33.00

Table A 34. Cytotoxicity (live/dead) data for complexes **23** and **24** in JU77 cells.

	% cell death at concentration		
Complex	**5 µM**	**10 µM**	**20 µM**
23	9.60	10.50	12.30
24	7.70	9.70	14.40